



**TECHNISCHE
UNIVERSITÄT
WIEN**

**VIENNA
UNIVERSITY OF
TECHNOLOGY**

DISSERTATION

DEMARCATING COAL FIRE RISK AREAS BASED ON SPECTRAL TEST SEQUENCES AND PARTIAL UNMIXING USING MULTI SENSOR REMOTE SENSING DATA

ausgeführt zum Zwecke der Erlangung des akademischen Grades eines
Doktors der Naturwissenschaften unter der Leitung von

Univ. Prof. Dipl. Ing. Dr. Wolfgang Wagner

Institut für Photogrammetrie und Fernerkundung

eingereicht an der Technischen Universität Wien
Fakultät für Technische Mathematik und Vermessung und Geoinformation

von

Claudia KÜNZER

0227503

Pasinger Str. 37, Planegg D-82152, Deutschland

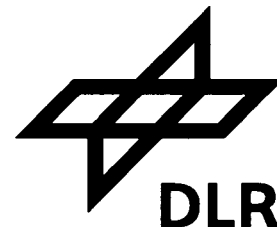
Wien, am 2005-01-03

A handwritten signature in black ink that reads 'Claudia Kunzer'. The signature is written in a cursive style with a large, stylized 'K'.

Coal Fire Research
Sino-German Research Initiative
German Remote Sensing Data Center (DFD)
German Aerospace Center (DLR)
Postfach 1116
D-82230 Wessling, Germany
http://www.coalfire.caf.dlr.de/intro_en.html



Claudia Künzer
German Remote Sensing Data Center (DFD)
German Aerospace Center (DLR)
Postfach 1116
D-82230 Wessling, Germany
Tel. +49 (0)8153-28-1338
email: claudia.kuenzer@dlr.de



Prof. Dr. Wolfgang Wagner
Vienna University of Technology
Institute of Photogrammetry and Remote Sensing
Gusshausstrasse 27-29/E122
A-1040 Vienna, Austria
Tel. +43 (0) 1-58801-12225
email: ww@ipf.tuwien.ac.at



Prof. Dr. Mathias Schardt
Graz University of Technology
Institute for Remote Sensing and Photogrammetry
Steyrergasse 30
A-8010 Graz, Austria
Tel. +43 (0) 316-873-6330
email: mathias.schardt@tugraz.at



Acknowledgements

This thesis was completed during my first three years working at the German Remote Sensing Data Center, DFD, of the German Aerospace Center, DLR in Oberpfaffenhofen, Germany. Many scientists, colleagues and friends have supported this work. Their encouragement, help and critical opinions have had a great influence on the outcome of this thesis. I am grateful to many people. The most important contributors I would like to thank here.

In the first place, I would like to thank Prof. Dr. Wolfgang Wagner (Vienna University of Technology, Institute of Photogrammetry and Remote Sensing, IPF), who was willing to supervise this thesis. I could always rely on him for support with the structure of this work, with technical details or general questions. As the former coordinator of the coal fire remote sensing project he always had a strong insight and interest in the project. I especially enjoyed the possibility to communicate very openly about all aspects of completing a PhD next to a full time job. His critical opinion, but at the same time very motivating impulses helped me to stay focused throughout the last two years.

I am grateful to my second supervisor Prof. Dr. Mathias Schardt (Graz University of Technology, Institute of Remote Sensing and Photogrammetry / Joanneum Research) for accepting the co-evaluation of this thesis. He contributed with many fruitful comments on topics of data preprocessing and signature analysis, as well as concerning the structure of this work.

My sincere thanks go to Dr. Stefan Voigt, (DLR-DFD), project coordinator of the geoscientific Sino-German coal fire project. He always shows interest in scientific topics and visions and he supported this work through constructive criticism and many discussions. I very much enjoy working within the dynamic and active environment of his team.

Dr. Harald Mehl, (DLR-DFD), head of the unit 'Environment and Geoinformation' at DFD and my former team-leader Dr. Günter Strunz, (DLR-DFD), both supported me in a quiet but consistent way. I enjoyed a very stable and friendly working atmosphere and always found an open door, when having organizational or thematic questions. Their guidance, constructive criticism and thoughts have always helped me a lot. Thank you.

I want to deeply thank my friend and former colleague Dr. Jianzhong Zhang, (Leica Beijing), for his help during the field campaigns in China, for long scientific and personal talks and last but not least for our close friendship, which developed during the three years of sharing an office. I am extremely thankful for having the chance, to experience the incredible variety of things, when looking at them from a completely different cultural perspective.

I am also grateful to Andreas Hirner and Anke Tetzlaff for their support and all the joint work during the last years working in the coal fire context at DFD.

Special thanks go to Prof. Dr. Patrick Hostert, (Humboldt University of Berlin), for answering numerous spectrometry related questions. He has been one of the persons during my former time at the University of Trier, who greatly increased my fascination for remote sensing related research. I am furthermore very thankful to Prof. Dr. Joachim Hill – supervisor of my diploma thesis – for making remote sensing lectures and seminars in Trier finest.

I am grateful to Prof. Dr. Stefan Dech (DFD / University of Würzburg), director of the German Remote Sensing Data Center, for caring about a friendly, motivated and dynamic atmosphere in his institute and within the different work units. He has always followed the Sino-German Coal Fire Research Initiative with great interest and enthusiasm.

In addition, I would like to express my sincere thanks to:

- ... Dr. Rolf Richter, (DLR-DFD), for his strong support with questions on radiative transfer, algorithm design or physics related topics. He always had at least five minutes, sometimes hours to spare and shared many helpful IDL routines.
- ... our colleagues Prof. Dr. Horst Rüter (HarbourDom), Dr. Fritz Bandelow, Dr. Hartwig Gielisch, (DMT), Prof. Dr. Christian Buhrow (TU-BAF), Prof. Uli Krause, Martin Schmidt (BAM) and Stefan Wessling (GGA) for the good cooperation, answers on geophysical questions and the willingness to close the gap between remote sensing, field geology and geophysics.
- ... Dr. Paul van Dijk, (ITC), for his help with geology related subjects and the sharing of his overall field experience during the fieldwork campaigns in 2002 and 2003.
- ... Christoph Hecker, (ITC), for his work contribution during the field campaign in 2003, interesting scientific discussions and the very good cooperation.
- ... my colleague Dr. Andreas Hirner, (DLR-DFD), for the good time during the 2004 field campaign and technical as well as moral support during the last half year.
- ... to the Chinese colleagues Yaorong Jia (Wuda mine), Yulin Sun (Wuda mine), Kong Bing (BRSC), Jing Li (BNU), Jiahong Li (NRSCC), Jianwei Ma (BRSC), Xianming Zhang (University of Delft, Netherlands), Yan Bo (BNU), Wang Xiaopeng (ARSC), and Zhang Songmei (NRSCC) for the good cooperation and the great support during the various field campaigns.
- ... Andreas Müller and Martin Habermeyer, (DLR-DFD), for lending the field spectrometer, providing the spectrometry laboratory and for answering many spectrometry related questions.
- ... Gao Yan, (former ITC master student) for her help with ground truth data collection during the field campaign in 2002.
- ... Dr. Anupma Prakash (University of Alaska, Fairbanks) for answering many questions related to coal fires from a distance and providing ground truth for the Jharia coal field.
- ... Martin Bachmann, (University of Würzburg), for his kind support with the preprocessing of laboratory and field spectra as well as for forwarding a lot of interesting scientific articles.
- ... Stefanie Holzwarth, (DLR-DFD), and Andrea Cihlar, (DLR), for the introduction to laboratory spectroscopy.
- ... Prof. Eckehart Jäger (University of Halle) for identifying the plant material from Inner Mongolia.
- ... my former interns Jens Wunderlich, David Mörth, Manuel Löhnertz, Lena Lieckfeld and Arne Bergau, who helped with the processing of data and literature collection.
- ... Dr. Jörn Hoffmann, Dr. Andreas Hirner, Dr. Stefan Voigt, Dr. Rolf Richter, Tanja Kraus, Dr. Gerd Rucker and Dr. Michael Schmidt for the proof reading of chapters.

Last but not least, very special thanks to my dear friends Torsten and Petra Riedlinger, Annette Wentzel, Stefan Schwarzer, Kerstin Kolodzie, Marcus Schneider, Lena Lieckfeld, Susanne Jansen, David Casey and Angela Porter, as well as my parents for all their general support, the necessary distraction from work and the great times outside DLR-DFD.

Abstract

Uncontrolled coal seam fires are a tremendous natural hazard and economic disaster occurring in over 15 coal producing countries worldwide. In China alone, coal fire related emissions of green house relevant gasses are equivalent to approximately 0.1 %-0.2 % of the annual human induced CO₂ input into the atmosphere. Toxic gasses released by the fires are a threat to human health. This is documented by increased lung cancer- and respiratory disease rates in the Chinese coal fires regions. Furthermore, subsurface coal fires, leading to volume loss underground, cause slow as well as sudden land surface movements and collapses. In addition, in the vicinity of coal fires vegetation degradation is commonplace.

China faces severe coal fire problems in over 50 coal fields located within China's coal belt, which stretches over 5000 km from East to West along the whole northern part of the country. The economic loss of coal due to burning coal seams in China is estimated to 20-30 Mio. tons per year. This is in the order of Germany's current annual production of hard coal. Since many of the coal mining regions affected by coal fires are sparsely populated remote areas, satellite remote sensing techniques are a cost efficient and powerful tool for local, regional and country-wide investigations.

This thesis presents a conceptual approach and two algorithms to automatically demarcate coal fire risk areas from Landsat-7 ETM+ and Aster remote sensing satellite data. The focus lies on multispectral data analyses to delineate areas, where coal fires are likely to occur. Such delineated regions can support the exclusion of false alarms from thermal anomaly detection. Furthermore, the demarcation of coal fire risk areas can highlight regions, which are in danger of coal fire ignition but do not show a thermal expression yet.

Based on field observations and mappings during three fieldwork campaigns in 2002, 2003 and 2004 it has been found that coal fire related thermal anomalies are always located adjacent to coal exposed to the surface. These surfaces can be outcropping coal seams, coal waste piles, coal storage piles or mining portals. Furthermore, coal fires lead to the degradation and decay of vegetation. Subsurface fires are not found underneath densely vegetated soil or bedrock. An additional phenomenon induced by very hot coal fires is the pyrometamorphosis of the surrounding bedrock. If the thermal intensity of a fire is high enough color and texture changes of the adjacent strata can occur. Depending on the spatial extent of this phenomenon it can be detected in remote sensing data.

Supported by the automated extraction of three surfaces classes- coal, dense vegetation and pyrometamorphic rock - two algorithms have been developed to automatically demarcate coal fire areas and future coal fire risk areas. The first is a knowledge-based spectral test sequence allowing for the mapping of the surfaces of interest. Coal surfaces are automatically extracted and the area in a certain radius is delineated, to yield possible coal fire risk areas. Within these regions densely vegetated areas are excluded. Furthermore, pixels of pyrometamorphic rock are highlighted. This algorithm runs fully automatic without any user interaction necessary.

The second approach relies on linear partial unmixing techniques. Coal surfaces, vegetated areas and pyrometamorphic regions are extracted based on a quantitative subpixel fraction estimation. An extensive spectral database including field and laboratory spectra of over 50 different surface samples collected during the field campaigns has been set up. This library provides the input reference spectra

for the partial unmixing analyses. Just like the knowledge-based test sequence, this method proves stable and solid enough for automation. Therefore, the two algorithms outperform standard surface extraction and classification approaches, where interactive input is always mandatory.

Surface extraction and coal fire area demarcation has been performed for a time series of eight ETM+ and two Aster scenes covering the main study areas in China. Furthermore, applicability has been tested on an ETM+ scene covering the area of Baotou, China, located outside the known study regions. In addition, transfer has been successfully tested on ETM+ scenes for the Jharia- and Rāy coal mining regions in India and the Leigh Creek coal mining area in Australia.

From the results of automated coal extraction an increase in mining activity in the order of 230 %-350 % could be obtained for the two main study areas in north central China during the past 15 years. Surface extraction accuracies were validated using an extensive set of over 50 ground truth polygons and seven mapped mixture grids. Accuracies ranged between 76 % and 100 % for all surfaces. Good surface extraction accuracies averaging 91 % have also been calculated for the transfer regions, where pyrometamorphic areas at a detectable scale did not exist.

Many new coal fire risk areas could be delineated next to the already well known coal fire areas located within the two Chinese study regions. They are presented in detailed maps at a spatial scale of 1:100,000. Within two of these risk areas formerly unknown coal fires could already be detected, when combining the automated coal fire area demarcation results and automated thermal anomaly detection as developed by ZHANG, J. 2004. These findings have been verified during two field campaigns in 2003 and 2004. This proves that formerly unknown coal fires can be extracted from remote sensing data exclusively.

The synergy effects of coal fire area demarcation and coal fire related thermal anomaly detection was furthermore assessed processing six scenes. The findings of the analyses reveal that coal fire area demarcation can clearly reduce false alarms resulting from automated thermal anomaly extraction. Many subtle thermal anomalies picked up from the thermal algorithm are related to industry, settlement, biomass fires, limestone processing and solar effects. If located outside the delineated risk areas they have a negligible probability to be coal fires. Thermal anomalies for all scenes processed could be reduced in number and overall area for 50 % on average for nighttime data and >80 % for daytime data. Thus, automated coal fire (risk) area demarcation is a powerful tool to focus thermal anomaly monitoring to the appropriate and relevant spots.

The results of this thesis prove the applicability of automated large scale coal fire area demarcation and can support the monitoring of coal fire areas and risk areas for the whole northern part of China.

Zusammenfassung

Unkontrollierte Kohleflözbrände sind eine Naturkatastrophe und ein wirtschaftliche Problem globalen Ausmaßes. Die Brände existieren weltweit in über 15 Kohle fördernden Ländern und führen nicht nur zur Vernichtung der wertvollen wirtschaftlichen Ressource, sondern auch zu treibhausrelevanten Emissionen. Es wird angenommen, dass Kohlebrandemissionen einem Equivalent von 0,1 % bis 0,2 % der jährlichen anthropogen verursachten CO₂ Emission entsprechen. Des Weiteren setzen sie toxische Gase frei, die sich schädlich auf die Gesundheit der Einwohner in den Kohlebrandregionen auswirken. Durch den Volumenschwund im Untergrund führen die Brände zudem zu langsamer Landabsenkung sowie Oberflächeneinbrüchen. Des Weiteren kommt es durch die aus Spalten emittierenden toxischen Gase zu Degradation und Absterben der Vegetation in der unmittelbaren Umgebung.

In China existieren Kohlebrände in über 50 Kohlefeldern, die sich über den nördlichen Kohleabbaugürtel erstrecken. Dieser Gürtel dehnt sich 5000 km von Osten nach Westen über den gesamten nördlichen Teil des Landes aus. Der wirtschaftliche Verlust durch Kohlebrände wird in China auf 20 bis 30 Mio. Tonnen pro Jahr beziffert. Dies entspricht in etwa der deutschen Jahresproduktion an Steinkohle. Viele der Kohleabbauregionen befinden sich in entlegenen, nur dünn besiedelten Gebieten. Daher stellt die Fernerkundung ein kostengünstiges und robustes Werkzeug dar, um die Brandregionen auf lokalem, regionalem und landesweitem Maßstab zu untersuchen.

Diese Arbeit stellt einen konzeptuellen Ansatz und zwei Algorithmen zur automatisierten Ausweisung von Kohlebrandgebieten und zukünftigen Risikogebieten basierend auf Landsat-7 ETM+ und Aster Satellitendaten vor. Der Fokus liegt hierbei auf der Analyse multispektraler Satellitendaten zur Abgrenzung von Gegenden, in denen Kohlebrände mit hoher Wahrscheinlichkeit auftreten. Solche ausgewiesenen Bereiche unterstützen die Differenzierung Kohlebrand-bedingter und anderer Thermalanomalien. Zugleich kann die Ausweisung von Kohlebrand-Risikogebieten die Überwachung von Regionen unterstützen, die ein hohes Gefährdungspotential für die Entstehung der Brände- aber noch keine thermalen Anomalien aufweisen.

Während drei Feldarbeitskampagnen in 2002, 2003 und 2004 konnte beobachtet werden, dass Thermalanomalien von oberflächennahen und unterirdischen Kohlebränden immer in der näheren Umgebung von Kohle an der Erdoberfläche auftreten. Dies können austreichende Kohleflöze, Kohleabraumhalden, Kohlelagerhalden oder Mineneingänge sein. Des Weiteren führen Kohlebrände zur Degradierung und dem Absterben von Vegetation in ihrer unmittelbaren Umgebung. Daher sind unterirdische Kohlebrände nicht unterhalb dicht mit Vegetation bedeckter Böden zu finden. Eine weitere Auswirkung der Brände ist die Entstehung pyrometamorphen Gesteines. Eine hohe thermale Intensität des Brandes vorausgesetzt, kommt es zu Farb- und Texturveränderungen des Umgebungsgesteines. Diese Auswirkungen können in Satellitendaten detektiert werden, wenn diese Gesteine in entsprechend großen Arealen an der Oberfläche exponiert sind.

Basierend auf diesen Beobachtungen wurden in dieser Arbeit zwei Algorithmen entwickelt, um die drei Oberflächentypen aus Fernerkundungsdaten zu extrahieren und Kohlebrandgebiete automatisiert auszuweisen. Bei dem ersten Algorithmus handelt es sich um eine wissensbasierte spektrale Testsequenz, die die automatisierte Extraktion von Kohle, dichter Vegetation und pyrometamorphem Gestein ermöglicht. Kohleflächen werden ausgewiesen und ein Bereich in einem bestimmten Radius wird abgegrenzt. Dieser Radius kann durch den Einfallswinkel der Schichten sowie eine

Tiefenbegrenzung von Kohlebränden definiert werden. Innerhalb des Radius' werden Gebiete dichter Vegetation eliminiert und pyrometamorphen Areale hervorgehoben.

Der zweite Ansatz basiert auf linear partieller Entmischung. Kohleflächen, Areale dichter Vegetation und pyrometamorphe Bereiche werden mit dieser quantitativen Methode bezüglich ihres prozentualen Sub-Pixel Anteiles extrahiert. Eine spektrale Datenbank, die aus Labor- und Feldmessungen von über 50 verschiedenen Proben erstellt wurde, dient als Referenzdatenbank für die Entmischung. Wie auch der wissensbasierte Ansatz ist diese Methode voll automatisierbar. Beide Algorithmen haben daher in Bezug auf eine großräumige Anwendung einen deutlichen Vorteil gegenüber gängigen überwachten Klassifikations- und Extraktionsmethoden, bei denen interaktive Schritte und ein deutlicher Einfluss des Bearbeiters unvermeidbar sind.

Oberflächenextraktion und die Ausweisung von Kohlebrandgebieten wurde für eine acht ETM+ Szenen umfassende Zeitreihe sowie zwei Aster Szenen für die beiden Untersuchungsgebiete in China vorgenommen. Zusätzlich wurden außerhalb der Untersuchungsgebiete Datensätze für die Gegend Baotou, in Nord-China sowie für die Jharia- und Rāy Kohleabbaugebiete in Indien und das Leigh Creek Kohleabbaugebiet in Australien analysiert, um den Transfer der Algorithmen zu demonstrieren. Basierend auf den Ergebnissen automatisierter Kohleextraktion kann ein deutlicher Anstieg der bergbaulichen Aktivitäten in den beiden chinesischen Untersuchungsgebieten innerhalb der letzten 15 Jahre aufgezeigt werden. Extraktionsgenauigkeiten wurden anhand umfangreicher Kartierungen von über 50 Arealen von Kohle-, Vegetation- und pyrometamorphen Gestein sowie dem Vergleich mit sieben kartierten Mischungs-Rastern berechnet. Die Produzenten Genauigkeiten liegen dabei in den Untersuchungsgebieten für alle Oberflächen zwischen 76 % und 100 %. In den drei Gebieten, in denen der Transfer der Algorithmen getestet wurde liegen sie im Mittel bei 91 %.

Neben den bekannten Kohlebrandbereichen in den beiden Untersuchungsgebieten konnten mehrere neue Kohlebrandgebiete und potentielle Risikogebiete ausgegliedert werden. Diese werden anhand detaillierter Karten vorgestellt. Innerhalb zwei dieser neu ausgewiesenen Kohlebrandgebiete konnten mehrere Thermalanomalien detektiert and bereits als vormals unbekannte Kohlebrände im Gelände verifiziert werden. Dadurch konnte gezeigt werden, dass mit Hilfe der automatisierten Ausweisung von Kohlebrandgebieten die Detektion unbekannter Kohlebrände in Fernerkundungsdaten möglich ist. Die Kombination der Ausweisung von Kohlebrandgebieten und Detektion von Thermalanomalien wurde anhand von sechs Szenen überprüft. Es konnte gezeigt werden, dass die Ausweisung von Brandgebieten die Zurückweisung fälschlich extrahierter Anomalien, die von Industrie, Siedlungen, Biomassebränden, Kalkbrennereien oder solaren Einflüssen resultieren, deutlich unterstützt. Sind Thermalanomalien außerhalb der ausgewiesenen Gebiete lokalisiert, handelt es sich mit hoher Wahrscheinlichkeit nicht um Kohlebrände. Thermalanomalien konnten hinsichtlich Anzahl und Gesamtgröße für alle prozessierten Szenen um über 50 % in Nachtszenen und über 80 % in Tagszenen reduziert werden.

Die Ergebnisse dieser Arbeit zeigen, dass eine großflächige automatisierte Ausweisung von Kohlebrandgebieten und Risikogebieten möglich ist. In Kombination mit der Auswertung thermaler Daten können somit rezente Kohlebrandbereiche und potentielle Risikogebiete gezielt mit Methoden der Fernerkundung überwacht werden.

摘要

煤火作为一种严重的自然灾害和经济灾害在世界上的15个产煤国都有发生。仅在中国，由煤火释放出的与温室效应有关的气体就占人类向大气释放二氧化碳总量的0.1%-0.2%。煤火释放的有毒气体威胁人类的健康，据记载，在中国煤火地区，肺癌和呼吸道疾病的比例正在升高。进一步地，地下煤火可产生地下空洞，从而引起或快或慢的地表运动和塌陷。同时，在煤火的周边地区，植被退化也经常发生。

中国正面对着50多个煤田火区的严重问题。这些火区位于中国的东西长5000公里，覆盖整个北方地区的产煤带。在中国，估计每年烧失煤炭2-3千万吨。这相当于德国当前煤年产量的三分之一。

由于受煤火影响的很多采矿区都位于人烟稀少，人迹罕至的地区，所以不论是对工区范围，区域范围，还是对国家范围的火区进行调查，遥感都可以作为一种经济且有效的工具。

本篇论文介绍了从Landsat-7 ETM+ 和 Aster 遥感数据上自动圈划煤火危险区的理论方法和两种算法。着重讨论通过多光谱数据分析技术来勾划煤火可能发生的区域。这些勾划出的可能发生煤火的区域可以用来支持排除从热异常探测中得到的噪音。

基于在2002，2003和2004年的三次野外观测和制图，我们发现与煤火有关的热异常总是发生在一种地表信息—煤体的周围。这些煤体包括煤层露头，煤矸石堆，煤堆，或矿井口。进一步地，煤火可引起植被的退化和坏死。在拥有茂密植被的土壤和基岩下，一般没有煤火。煤火产生的另一现象就是围岩的热变质。如果火的强度足够大，围岩的颜色和结构都会发生变化。这种现象是否能被遥感影像探测到则取决于它的空间分布范围。

基于对以下三种地表信息的提取—煤，茂密的植被和烧变岩—两种算法被开发出来用以自动勾划煤火区域和将来有可能发生煤火的区域。第一种算法是一个基于知识的光谱测试序列分析，它能对所需的地表信息进行制图。煤体被自动提取出来，同时与之有一定距离的区域也被勾划出来，以此来产生可能发生煤火的危险区。在这些区域中，拥有茂密植被的地区被排除在外。进一步地，拥有烧变岩的像元被强调。这一算法完全自动运行，没有任何的用户介入。

第二种方法基于线性亚像元分解技术。这是通过一种定量的亚像元比例估计方法，来提取煤体，植被区和烧变区。首先建立一个容量的光谱数据库，它包含50多种采自野外的不同的地表样品的野外和实验室的光谱数据。这一数据库为亚像元分解分析提供了输入参考光谱。同基于知识的光谱测试序列分析一样，这一方法结果稳定，足以自动实现。因此，这两种方法大大优于传统的地表信息提取方法和分类方法，因为在传统的分类方法中，人机交互式的输入是必不可少的。

首先，在中国的主要研究区内，地表信息提取和煤火区域勾划方法被应用到不同时相的八景ETM+和两景Aster影像上。接着，使用一景位于已知区外的，覆盖中国包头的ETM+，测试了方法的应用能力。最后，通过对覆盖印度Jharia及Ray煤矿和澳大利亚Leigh Creek煤矿的ETM+影像上的测试成功，证实了该方法的通用性。

从自动煤体提取的结果中可以看出，在中国北部的两个主要研究区，采矿活动的增长超过230%-350%。地表信息提取的精度是通过超过50个的地面验证多边形和7个混合栅格区域制

图来验证的。对所有地表信息类型来说，精度介于76 % and 100 %。在印度和澳大利亚的矿区，不存在能探测得到的烧变区，地表信息提取的精度据计算可好到平均为91 %。

在中国的两个研究区内，新提取出的很多煤火危险区都与已知的煤火区紧密相连。他们在详细的空间比例尺为1:100000的图件上有很好的呈现。在这些煤火危险区中，得知有两个含有未知煤火，这是通过叠加自动煤火区域圈划的结果和张建中于2004年开发的自动热异常探测的结果来实现的。这些新发现的煤火在两次野外验证中被证实。这说明只用遥感数据就可以探测未知煤火。

通过处理6景的影像，融合煤火区域的圈划结果和煤火热异常探测结果的效果得到了进一步的评价。结果显示，煤火区域圈划能有效地去除自动热异常提取中产生的噪音。从热算法中提取出的很多小的热异常是来自于工业，居民区，生物火源，石灰厂和太阳的影响。如果他们位于危险区外，他们是煤火的可能性就很小。所有景的热异常可以在数目上平均减少50 %-80 %。因此，自动的火区圈划对正确的煤火监测是一个有力的工具。

本论文的结果证明，遥感大面积的煤火区域圈划是可行的，同时他能支持对整个中国北方地区的火区及危险区的监测。

List of Contents

1. Introduction	1
1.1. Coal Fires.....	1
1.2. Remote Sensing of Coal Fires: Brief Status of Research.....	2
1.3. Research Objectives.....	5
1.4. Thesis Outline.....	7
2. The Study Areas: Wuda, Ruqigou / Gulaben and Environmental Coal Fire Impacts ..	9
2.1. Geographic Location.....	9
2.2. Geologic and Geomorphologic Characteristics	11
2.3. Climatic Characteristics	16
2.4. Hydrographic Characteristics.....	17
2.5. Soils and Natural Vegetation	17
2.6. Socio-economic Characteristics.....	19
2.7. Impact of Coal Mining and Coal Fires	21
3. Theoretical Background: Image Classification and Feature Extraction	24
3.1. Feature Space Manipulation Techniques.....	24
3.2. Unsupervised Classification Algorithms (UCA)	26
3.3. Supervised Classification Algorithms (SCA)	28
3.4. Contextual or Object Oriented Classification Approaches (OOC).....	30
3.5. Decision Tree Classifiers and Knowledge Based Methods (DTC).....	31
3.6. Artificial Neural Networks (ANN)	32
3.7. Binary Encoding (BE)	33
3.8. Spectral Mixture Analysis (SMA)	33
3.9. Spectral Angle Mapping (SAM).....	36
3.10. Spectral Feature Fitting (SFF)	37
3.11. Other Spectral Matching and Classification Techniques.....	38
3.12. Thermal Approaches for Geologic Mapping	39
3.13. Change Detection Studies.....	40
3.14. Assessing Classification and Surface Extraction Accuracy.....	40
4. Data Analyzed	42
4.1. Satellite Data.....	42
4.1.1. Landsat-7 ETM+ Data	42
4.1.2. Landsat-5 TM Data.....	44
4.1.3. Aster Data	44
4.1.4. Quickbird Data.....	45
4.1.5. ERS-2 SAR Data	45
4.2. Field- and Laboratory Spectral Measurements	46
4.2.1. Surface Spectra Measured During the Field Campaign.....	46
4.2.2. Laboratory Spectra Measured from Samples Collected During the Fieldwork.....	47
4.3. GIS Data	49
4.3.1. Available GIS Data.....	49

4.3.2. GPS Locations Measured During the Fieldwork in 2002 and 2003	49
4.3.3. Landcover Polygons Mapped During the 2002 and 2003 Fieldwork.....	49
4.3.4. Mixture Grids Mapped During the 2002- and 2003 Fieldwork.....	50
4.3.5. Coal Fires Mapped During the 2002- 2003 and 2004 Fieldwork.....	50
4.4. Maps and Descriptive Data	51
5. Data Preprocessing: Rectification, Calibration, Radiometry	52
5.1. Geometric Corrections.....	52
5.1.1. Principles of Geometric Distortions and Applied Correction Methods.....	52
5.1.2. Results and Validation.....	55
5.2. Radiometric Corrections for the Reflective Bands.....	56
5.2.1. Sensor Calibration	57
5.2.2. Atmospheric and Topographic Corrections.....	58
5.2.3. Results and Validation.....	62
5.3 Radiometric Correction of the Thermal Band	67
5.3.1. Principles and Methods Applied	67
5.3.2. Results and Validation.....	71
6. Conceptual Approach of Coal Fire Area Demarcation	73
6.1. Extraction of Coal Surfaces	73
6.2. Analysis of Vegetation Density.....	74
6.3. Pyrometamorphic Rocks	76
6.4. Automation of the Demarcation Scheme.....	77
7. Signature Analysis	81
7.1. Fundamentals of Spectral Surface Properties	81
7.2. Signature Analysis of Coal Based on Chemical and Physical Properties.....	82
7.3. Signature Analysis of Vegetation	86
7.4. Signature Analysis of Pyrometamorphic Rock.....	86
7.5. Signature Analysis and Spectral Properties of Other Surfaces.....	89
7.6. Separability of Surface Spectra and Temporal Spectral Variability.....	90
8. Knowledge Based Surface Extraction.....	100
8.1. Set Up of the Knowledge Based Test Sequence.....	100
8.1.1. Automated Extraction of Coal Surfaces	100
8.1.2. Automated Extraction of Densely Vegetated Areas.....	106
8.1.3. Automated Extraction of Pyrometamorphic Rock	108
8.1.4. Transfer of the test sequence to the Aster Sensor.....	111
8.2. Results of the Knowledge Based Test Sequence.....	112
8.2.1. Results for the Main Study Areas.....	112
8.2.1.1. Wuda	112
8.2.1.2. Ruqigou	117
8.2.2. Results for the Transfer Regions	122

8.2.2.1. Flinders Ranges, Leigh Creek, Australia.....	123
8.2.2.2. Jharia coal mining region, India	124
8.2.2.3. Baotou, China.....	126
8.3. Quantification and Error Analysis of the Test Sequence Results	127
8.3.1. Quantification and Error Analysis for the Main Study Areas.....	127
8.3.2. Quantification and Error Analyses of the Transfer Regions.....	132
8.4. Discussion.....	135
9. Quantitative Surface Extraction applying Partial Unmixing	138
9.1. Method.....	138
9.1.1. Concept and Mathematical Background.....	138
9.1.2. Design of Prototype Spectra and Spectral Interpolation.....	140
9.1.3. Analysis of Extreme Pixels.....	141
9.2. Results of the Partial Unmixing Analyses	143
9.2.1. Results for the Main Study Areas	143
9.2.1.1. Wuda.....	143
9.2.1.2. Ruqigou	148
9.2.2. Results for the Transfer Regions	152
9.2.2.1. Flinders Ranges, Leigh Creek, Australia.....	152
9.2.2.2. Jharia and Ray coal mining regions, India.....	153
9.2.2.3. Baotou, China.....	154
9.3. Quantification and Error Analysis of the Partial Unmixing Results.....	155
9.3.1. Quantification and Error Analysis of the Main Study Areas.....	155
9.3.2. Quantification and Error Analysis of the Transfer Regions	159
9.4. Discussion.....	160
10. Coal Fire (Risk) Area Demarcation and Synergy with the Thermal Algorithm.....	166
10.1. Demarcated Coal Fire Areas and Coal Fire Risk Areas.....	166
10.2. Synergy with the Thermal Algorithm.....	180
10.3. Discussion.....	187
11. Conclusions and Outlook.....	190
11.1. Conclusions	190
11.2 Outlook	196
12. References	198

List of Figures

- Figure 2-1:** Small area of pyrometamorphic rock
- Figure 2-2:** Sulfur minerals above a former coal fire
- Figure 2-3:** Thick Yellow River deposits – clay loam
- Figure 2-4:** Crusting of top soil on an alluvial fan
- Figure 2-5:** Shrubs on desert sand
- Figure 2-6:** Shrubs in a sparsely settled mining area
- Figure 2-7:** Coal processing factory
- Figure 2-8:** Coal processing factory
- Figure 2-9:** Calcite burning near a limestone mine
- Figure 2-10:** Clay mining
- Figure 2-11:** Coal mining in Ruqigou
- Figure 2-12:** Coal infrastructure in Wuda
- Figure 2-13:** Coal miner in Wuda
- Figure 2-14:** Housing of a coal miner in Wuda
- Figure 2-15:** Cracked surface due to coal fires
- Figure 2-16:** Coal fire in Wuda during daytime
- Figure 2-17:** Dead vegetation due to coal fires
- Figure 2-18:** Woman wearing a face mask against the gaseous emissions
- Figure 3-1:** Ideal (left) and realistic (right) distribution of four classes in a 2-D feature space. In most remote sensing data sets clusters of thematic classes overlap, complicating extraction
- Figure 3-2:** Classification tree with root node (R), internal nodes (Y/N) and terminal nodes (L)
- Figure 3-3:** Scheme of an Artificial Neural network (ANN) with input layers (I), processing nodes (P) and output layers (O),
- Figure 3-4:** Different types of mixed pixels, (FISHER 1997)
- Figure 3-5:** Principle of linear Spectral Mixture Analysis (SMA).
- Figure 3-6:** Principle of Spectral Angle Mapping (SAM). Material 1 and 2 can clearly be distinguished by the angle. In the 2-D feature space to the right, the two ellipsoids located on one vector (no angle difference) will be difficult to distinguish.
- Figure 4-1:** Location of the recording points for field spectral measurements and surface sample collection for later laboratory spectral measurements within the broader Wuda study area. Background: gray scale Landsat image (band 1) acquired during the same week as spectra- and surface sampling.
- Figure 4-2:** Concept of the mixing grids mapped during the fieldwork
- Figure 5-1:** Principle of terrain induced object displacement
- Figure 5-2:** Orthorectified panchromatic ETM+ band (left) next to ERS-2 amplitude image (right). Center location: 573529E, 4818025N, UTM, Z45N
- Figure 5-3:** Geometric accuracy compared with GPS ground truth before (a) and after (b) the orthorectification demonstrated on a subset of ETM+ scene 129/033; Center location: 650651E, 4377299N, UTM, Z48N.
- Figure 5-4:** Radiance components of the signal reaching the sensor (RICHTER 1998, modified)
- Figure 5-5:** Image input parameters in ATCOR-3 (image bands, DEM, aspect, slope, skyview and shadow file)

- Figure 5-6:** Regression analysis for 4 calibration targets inflight calibrating the scene 129/33 of 2000 here shown for bands 1-5.
- Figure 5-7:** Visual impression before (top row) and after (bottom row) the radiometric correction for a subset of the Landsat-7 ETM+ scene from India (a), Australia (b) and Baotou (c) used for later transfer purposes. Center locations: UTM, a: 385657E, 2624616N, Z45N, b: 256271E, 6655205S Z54S, c: 356912E, 4405175N, Z49N
- Figure 5-8:** Quality assessment of the radiometrically corrected scenes based on the recorded spectra
- Figure 5-9:** Landsat-7 ETM+ spectra of three different surfaces (Yellow River=dark turquoise, lake water=light turquoise, coal=black) before (left) and after (right) the atmospheric correction. Band number 6 on the x-axis is band 7 (MIR) of the Landsat ETM+ data.
- Figure 5-10:** Visual impression before (a) and after (b) the combined radiometric correction using ATCOR-3. Center location: 642959E, 4360922N, UTM, Z48N
- Figure 5-11:** Regression analysis of the cosine of the illumination angle versus scene reflectances before and after the topographic correction for eight pixels located on a sun-facing and sun opposing limestone ridge in the area around center location 661553E, 4360919N, UTM, Z48N
- Figure 5-12:** very hot temperatures shift the radiation maximum to the nIR resulting in bright pixel values not representing an optical phenomenon. Location: 639085E, 4374840N, UTM, Z48N
- Figure 5-13:** Subset of the thermal nighttime scene (ETM+) from 28.09.2002; DN's transferred to temperature in °C and atmospherically corrected, center location (right subset): 645646E, 4376164N, UTM, Z48N.
- Figure 5-14:** Subset of the thermal daytime scene from 12.02.2003; left: false color infrared image, right: DN's transferred to temperature in ° C. Light: high temperatures, dark: lower temperatures (atmospherically corrected with ATCOR-3), center location: 650695E, 4373295N, UTM, Z48N.
- Figure 6-1:** Concept of demarcating the area, in which coal fire related thermal anomalies with regard to the outcropping coal seam can be expected.
- Figure 6-2:** a, b: dead vegetation above coal fire # 8, Wuda syncline. c: heavy smoke, vegetation density 0%, d: slowly degrading vegetation along a new fire front.
- Figure 6-3:** Kriged vegetation density maps over the three coal fires #6, #8 and #12 as mapped in 2002 and the development of vegetation density above fire #8 between 2002 and 2003
- Figure 6-4:** Pyrometamorphic rocks exposed to the surface in Baijigou coal mining area. Photos: C. Kuenzer, September 2003, Location: 595837E, 4322295N
- Figure 6-5:** Unsupervised classification into 20 classes, the first ("darkest") class is colored in orange on superimposed on the grey scale classification result. Coal, shadow, deep water, water of the Yellow River and even dense agricultural vegetation are all assigned to one class. Center coordinate: 650705E, 4373287N
- Figure 7-1:** a: field spectra and +/- standard deviation (green and red) of pure coal (a) and of coal waste (b); c: 5 different coal laboratory spectra; d: 3 different coal waste laboratory spectra (highest spectrum mixed with coal waste dust); a'-d': continuum removed spectra of a,b,c and d.

- Figure 7-2:** a: field spectra of three main desert shrub types, pure; b: field spectra of the three desert shrubs with soil influence; c: three different sandstone samples of different locations measured in the spectral laboratory; (from highest to lowest: grey, yellow, light grey) and a dark red siltstone sample; d: four different desert sand samples of different locations measured in the spectral laboratory; a'-d': continuum removed spectra of a-d.
- Figure 7-3:** a: laboratory spectra of four different grey limestones; b: laboratory spectra of a light and a dark magmatic and metamorphic rock; c: laboratory spectra of four different yellowish to dark brown shale-sandstone mixes, the lowest is a shale with very high organic content; d: four laboratory spectra of four yellow to dark red pyrometamorphic rocks; a'-d': continuum removed spectra of a-d.
- Figure 7-4:** Radiometrically corrected Landsat-7 ETM+ spectra for different surfaces. 6=MIR, 7=TIR.
- Figure 7-5:** Spectral profiles over seven ETM+ bands for two spatial profiles: shadow (right, center location: 4321784N, 605360E), coal (left, center location: 4323488N, 595692E, UTM, Z 48N).
- Figure 7-6:** Spectral profiles over seven Landsat-7 ETM+ bands for two spatial profiles: shadow (left), coal (right), band 6 is the thermal TIR band and therefore is displayed behind channel 7, which represents the MIR.
- Figure 7-7:** Temporal spectral variability of three surfaces for eight time steps in Ruqigou mining area
- Figure 7-8:** Temporal spectral variability of four surfaces for eight time steps in Wuda area
- Figure 7-9:** Spatial spectral variability of 3 to 6 surfaces in the transfer regions Baotou in China, Jharia in India, and Leigh Creek coal mining area in Australia
- Figure 8-1:** Synthetic spectral mean channel over bands 1, 2, 3, 4, 5 and 7 (a); result after the first test: pixels, which passed the test are presented in white and include coal, shadow and very dark water pixels (b). Center coordinate: 650705E, 4373287N, UTM, Z48 N.
- Figure 8-2:** Spectral mean for bands 123457 and bands 123 for eight time steps for the Ruqigou area
- Figure 8-3:** Spectral mean for bands 123457 and bands 123 for eight time steps for the Wuda area
- Figure 8-4:** Visible band displayed in gray scale mode (a) and shadowed areas extracted by test 3 supported by available illumination data derived from a DEM. Here presented for the strongly shadowed area of Ruqigou. Center coordinate: 607794E, 4336506N, UTM, Z48N
- Figure 8-5:** Relationship between number of excluded shadow pixels and scene acquisition date; calculated for three scenes of the Ruqigou area for the months of August, October and December. As expected, the area eliminated by test 3 (pixels do not undergo further testing for "coal") increases with decreasing sun angles.
- Figure 8-6:** Pixels which passed tests 1, 2, 4 and 5 and were not excluded by test 3 (white) in the left image (a), result after the final relative temperature test 6 (b), Center coordinate: 650705E, 4373287N, UTM, Z48 N
- Figure 8-7:** SAVI image of Wuda area on 21.09.2002.
- Figure 8-8:** Spatial pattern of the average SAVI in buffer zones around the active coal fires #6, #7, #8 and #11 of Wuda syncline.
- Figure 8-9:** Result of the vegetation test for Wuda area, white: dense vegetation, black areas below the SAVI threshold. Center coordinate: 650705E, 4373287N, UTM, Z48 N

- Figure 8-10:** Coal mining area Ruqigou, Landsat image (a), Quickbird image (b). Center coordinate of both displayed subsets: 59443 E, 4322273 N, UTM Z48N, WGS84. Both images are displayed in real color combination: bands 1,2,3 = BGR. The pyrometamorphically changed rocks of reddish colour are clearly visible in the Quickbird image. Only a few pixel in the Landat image experience a strong enough spectral signal to be considered as a 30 × 30 m pixel representing pyrometamorph rock.
- Figure 8-11:** Workflow of the knowledge based test sequence (not every temporary output file is shown). After the SPM channels and the SAVI data is generated 16 equations and inequalities are tested for the automated extraction of coal, 2 equations are tested for the extraction of dense vegetation and 9 relationships need to be fulfilled for a pixel to be assigned to the class of pyrometamorphic rock.
- Figure 8-12:** Pixels automatically extracted as coal (white) for 8 time steps for the broader Wuda area (filtered).
- Figure 8-13:** Development of the number of coal pixels extracted from 1987 until 2003 for the Wuda area including all scenes processed (a), and excluding the winter scenes (b). The trend was calculated for the filtered results.
- Figure 8-14:** Difference between coal accumulation comparing September 2002 and February 2003. The summer/fall scenes acquired present a stable linear increase in coal surfaces over the past years The two winter scenes of December 2002 and February 2003 act as outliers. This can be explained with the heavy coal use during the winter month. It is obvious that coal storage and coal waste piles and the piles around the mine portals shrink in size during times when coal is increasingly used for heating and electricity production.
- Figure 8-15:** Pixels automatically extracted as coal for 8 time steps for the broader Wuda area (filtered). The color scheme represents how often a pixel was considered as a coal surface.
- Figure 8-16:** Pixels automatically extracted as coal (white) for 8 time steps for the Ruqigou area (filtered),
- Figure 8-17:** Development of the number of coal pixels extracted from 1987 until 2003 for the Ruqigou area including all scenes processed (a), excluding the winter scenes (b). The trend was calculated for the filtered results.
- Figure 8-18:** Pixels automatically extracted as coal for 8 time steps for the broader Ruqigou area (filtered). The color scheme represents, how often a pixel was considered as a coal surface. Center coordinate of main subset: 607794E, 4336506N, UTM, Z48N
- Figure 8-19:** Spectral mean for bands 123457 and bands 123 for the three transfer areas
- Figure 8-20:** Number of extracted coal pixels for the Leigh Creek area, Australia, the Baotou area in northern China and the Jahria coal mining region in India. An exceptional high amount of single scattered pixels is extracted in the scene from India. This scene has much larger coal occurrences than the regions of Baotou and Leigh Creek area, Australia.
- Figure 8-21:** Location of the transfer ETM+ scene from Australia
- Figure 8-22:** The Leigh Creek coal mining area (a), coal pixels extracted for the scene (b), this subset displays only 1/15th of the full scene. Center coordinate of subset: 6626009 S; 252463 E, UTM, Z54 S, WGS 84.
- Figure 8-23:** Location of the ETM+ transfer scene from India

- Figure 8-24:** Coal pixels extracted for the scene of India. The two subsets display only parts of the full scene. The upper two images (a, b) present the Jharia coal field. The lower two subsets (c, d) present a coal field approximately 100 km west of Jharia close to the small town of Rāy. Center coordinate of upper subset: 428060E, 2624047N, UTM, Z45 N, WGS 84. Center coordinate of lower subset: 307711 E, 2621553 N, UTM, Z45 N, WGS84.
- Figure 8-25:** Location of the ETM+ transfer scene from northern China
- Figure 8-26:** Original data (a) and coal pixels extracted for the scene of Baotou, northern China (b). The subset displays only part of the full scene. Center coordinate: 404361E, 4502452N, UTM, Z49 N, WGS 84.
- Figure 8-27:** Areal reduction with progression of the knowledge based coal extraction test sequence (a, b) and for the overall test sequence (c, d) for the broader Wuda and Ruqigou area. Exemplarily visualized for three time steps 2000, 2001 and 2002-09.
- Figure 8-28:** a: Extracted coal surfaces (white) and superimposed coal fire polygons. b: Extracted coal fire (risk) area (white) and mapped coal fire outlines for the year 2002-09 (red) for the broader area of Wuda. Center coordinate of the subset: 641952E, 4376514N, UTM, Z48N, WGS84. The Wuda coal fires are numbered from 1-17
- Figure 8-29:** a: Extracted coal surfaces (white) and superimposed coal fire polygons. b: Extracted coal fire (risk) area (white) and mapped coal fire outlines for the year 2002 (red) for the broader area of Ruqigou. Center coordinate of the subset: 595800E, 4325705 N, UTM, Z48N, WGS 84. The Gulaben coal fires are numbered from 21-25, the Ruqigou coal fires are numbered from 31-45. All together the mapped coal fire area (red polygons) covers 6,11 km².
- Figure 8-30:** Areal reduction with progression of the knowledge based coal extraction test sequence (a, b, c) and for the overall test sequence (d, e, f) for three transfer areas, Baotou in northern China, Leigh Creek in Australia and Jharia in India.
- Figure 9-1:** Results of partial unmixing to coal for the broader Wuda area, image from 1999. Bright pixel values indicate a high sub-pixel coal fraction, dark areas have lower sub-pixel fractions. Center coordinate: 650705E, 4373287N, UTM, Z48 N, 43km×36km
- Figure 9-2:** left: prototype spectrum of coal derived by creating a mean of all averaged input spectra measurements. The black spectra represent the mean spectra of 8 coal samples. Each was measured 20 times. Right: overall mean spectrum of coal interpolated to the SRF of Aster (blue), Landsat-5 TM (turquoise) and Landsat-7 ETM+ (violet); the resampled spectra are stacked with offset for better visualization.
- Figure 9-3:** Results of a PPI calculation (10k iterations) superimposed on band one (blue) of ETM+ 129/33 from 17.10.2000. Center co-ordinate of left subset: 650705E, 4373287N, UTM, Z48 N, 43km×36km
- Figure 9-4:** Partial unmixing results for the broader Wuda area for all 8 scenes. Light areas indicate a high spatial fraction of the input prototype spectrum (coal), while dark areas represent pixels with a smaller fraction of this surface. Mimicking surfaces include shaded areas and partially water. Center coordinate: 650705E, 4373287N, UTM, Z48 N, 43km×36km
- Figure 9-5:** Subpixel fraction of the input prototype surface (coal) plotted against the percentage of the scene area, which would remain, if the partial unmixing result is thresholded for the pixels containing equal or above the percentage subpixel fraction. All eight time steps were calculated and displayed.

- Figure 9-6:** Subpixel fraction of the input prototype surface (coal) plotted against the percentage of the scene area, which would remain, if the partial unmixing result is thresholded for the pixels containing equal or above the percentage subpixel fraction. Presented for Wuda, 20.09.1987 and 21.09.2002 (River not included).
- Figure 9-7:** Subpixel fraction of the input pattern surface (coal) plotted against the percentage of the scene area, which would remain, if the partial unmixing result is thresholded for the pixels containing equal or above the percentage subpixel fraction. Here only flat regions were included in the calculation to exclude shadow effects induced by differing sun angles, (a).(b) presents a zoom into (a) for better clarity.
- Figure 9-8:** Partial unmixing results for vegetation for the broader Wuda area for 1987-09 (a) and 2002-09 (b). Light areas indicate a high spatial fraction of the input prototype spectrum (pure Artemisia leaves), while dark areas represent pixels with a smaller fraction of vegetation. Center coordinate: 650705E, 4373287N, UTM, Z48 N, 43km×36km.
- Figure 9-9:** Linear spectral unmixing result for the broader Wuda area for 2002-09. The selected endmembers are coal (a), quartzite desert sand (b), arcotic sandstone (c) and Artemisia vegetation (d). Light areas indicate high subpixel fractions, while dark areas represent pixels with a smaller fraction of the endmember. Center coordinate: 640134E, 4377377N, UTM, Z48 N, 43km×36km
- Figure 9-10:** RMSE image (a) and color coded unmixing result (b). Here the endmember coal, vegetation and sandstone are displayed in red, green and blue. The RMSE image shows high errors for the vegetated areas. This goes in line with the confusion between desert sand and vegetation. Center coordinate: 640134E, 4377377N, UTM, Z48 N, 43km×36km
- Figure 9-11:** Partial unmixing results for the broader Ruqigou study area for all 8 scenes. Light areas indicate a high spatial fraction of the input prototype spectrum, while dark areas represent pixels with a smaller fraction. Mimicking surfaces include shaded areas. Center coordinate: 606211E, 4334381N, UTM, Z48N, 33km×28km
- Figure 9-12:** Subpixel fraction of the input pattern surface (coal) plotted against the percentage of the scene area, which would remain, if the partial unmixing result is thresholded for the pixels containing equal or above the percentage subpixel fraction. All eight time steps were calculated and displayed.
- Figure 9-13:** Subpixel fraction of the input pattern surface (coal) plotted against the percentage of the scene area, which would remain, if the partial unmixing result is thresholded for the pixels containing equal or above the percentage subpixel fraction. Presented for Ruqigou, 20.09.1987 and 21.09.2002.
- Figure 9-14:** Subpixel fraction result image for coal intersected with a 85% threshold, to retrieve pure coal surfaces; for the broader study area of Ruqigou, 1999 (a) and 2002-09 (b), Center coordinate: 606211E, 4334381N, UTM, Z48N, 33km×28km
- Figure 9-15:** Partial unmixing results for vegetation for the broader Ruqigou area for 1987-09 (a) and 2002-09 (b). Light areas indicate a high fraction (pure Artemisia leaves), while dark areas represent pixels with a smaller fraction of vegetation. Center coordinate: 610605E, 43327047N, UTM, Z48 N, 33km×28km.
- Figure 9-16:** Subpixel fraction image for pyrometamorphic rock (averaged prototype spectrum) for the broader Ruqigou area calculated for the scene from 2002-09. Center coordinate of a: 607794E, 4336506N, b and b': 595287E, 4325273N, UTM, Z48N, 33km×28km.

- Figure 9-17:** Fraction image of coal resulting from partial unmixing for the broader Leigh Creek area, Australia, (a) and fraction image of vegetation (b). Center coordinate: 6626009 S; 252463 E, UTM, Z54 S.
- Figure 9-18:** Thresholded 85% subpixel coal fraction image before (a) and after (b) the intersection with the temperature test (majority filtered). Center coordinate: 6626009 S; 252463 E, UTM, Z54 S, 60km×50km.
- Figure 9-19:** PMA result for the scene of India (only the Jharia area is presented). Original image (a), grey scale fraction image (b) and result after thresholding at the 85% fraction (majority filtered) (c). Center coordinate: 430324E; 2622931N, UTM, Z45N, 33km×25km
- Figure 9-20:** PMA result for the scene of India (only the Ray area is presented). Original image (a), grey scale fraction image (b) and result after thresholding at the 85% fraction (c). Center coordinate: 301422E; 2622092N, UTM, Z45N, 17km×13km.
- Figure 9-21:** PMA result for the scene of Baotou (only a subset is presented). Original image (a), grey scale fraction image (b) and result after thresholding at the 85% fraction (c). Also a post processing temperature test applied cannot improve the result presented in c. Center coordinate: 375443E; 4495960N, UTM, Z49N, 80km×60km.
- Figure 9-22:** Location of the seven mixture grids mapped during the field campaign in September 2002. Over 600 cells were mapped with regard to their percentage subcell fraction of the occurring surface components. The grids are superimposed on an ETM+ PMA result of 2002-09. Center coordinate of the presented subset 644123E, 4370610N, UTM, Z48N, 23km×10km
- Figure 9-23:** The three main grids mapped within Wuda syncline, Suhai Tu (left), Wuhushan (upper right) and Wuhushan south (lower right). The mapping result from the field in September 2002 (left side) as well as the PMA result for the partial unmixing to coal – also from a September 2002 scene - (right side) are shown. Orange boxes indicate areas, which were not mapped.
- Figure 9-24:** Thematic principle of class- or material membership infeasibility. Deviation from the prototype spectrum is given in noise δ units. The right part illustrates, where the desired pixels requested to be extracted are located. Pixels with a high PMA score and a low infeasibility (= high feasibility) are similar or tend to be close to the prototype input. DAMM, 2004, modified and extended.
- Figure 9-25:** Partial unmixing result post processed with infeasibility information. a: PMA result for Wuda from 2002-12, b: infeasibility calculation for the prototype spectrum of coal, c: 85% subpixel fraction thresholded image of the PMA score, d: intersected image of high PMA scores (>85 %) and low infeasibility scores (<10 %).
- Figure 9-26:** MNF transformed data. Color coded components 1-3 (a) and components 1-6 (b-g) demonstrating the increase in noise level from component 1 to 6.
- Figure 10-1:** Newly detected coalfires based on coal fire (risk) area demarcation and thermal anomaly detection in two parallel valleys 50 km southwest of Wuda. The coalfires were not known outside the local community beforehand. Extracted coal is displayed as a superimposed vector layer in light blue, thermal anomalies in yellow, demarcated coalfire (risk) areas in red, center coordinate: 611355E, 4342156N, UTM, Z48N.
- Figure 10-2:** Newly detected coalfires based on coal fire (risk) area demarcation and thermal anomaly detection 25 km southeast of Wuda. The coalfires were not known except to few local inhabitants. Extracted coal is displayed as a superimposed polygon vector

layer in light blue, thermal anomalies in yellow, the demarcated coalfire (risk) areas are superimposed in red. Center coordinate:669169E, 4365414N, UTM, Z48N

Figure 10-3: Newly detected coal fires based on coal fire (risk) area demarcation and thermal anomaly detection 25 km southeast of Wuda. Note the coal fire related smoke in figure 10-3 a and the improperly sealed former private mines in figure 10-3 b. The trench is excavated to prevent the spreading of the fire. Photos: a: C. KUENZER. b: J. ZHANG, June 2004

Figure 10-4: Thermal anomalies in numbers of pixels extracted (orange), anomalies rejected by the knowledge based coal fire area demarcation (dark grey) and anomalies rejected by PMA based coal fire area demarcation (light grey). Exemplarily presented for six satellite scenes. Displayed are a nighttime and daytime scene from 2002 of the two main study areas, a scene of these areas for 1987 and scenes for the three transfer areas in India, Baotou and Australia.

List of Tables

- Table 2-1:** Climate data for the main study areas
- Table 3-1:** Concept of an accuracy assessment error matrix
- Table 4-1:** Spectral and spatial properties of Landsat 7 ETM+ data versus Landsat 5 TM (in brackets)
- Table 4-2:** LS7 ETM+ scenes processed and analyzed in the framework of this thesis
- Table 4-3:** Spectral and spatial properties of ASTER data
- Table 4-4:** ASTER scenes processed and analyzed in the framework of the thesis
- Table 4-5:** Geologic surface samples measured in the spectral laboratory
- Table 5-1:** Elevation dependence of relief induced displacement (ETM+)
- Table 5-2:** Relief induced displacement in the main study areas relative to NN in Landsat-7 ETM+ data
- Table 5-3:** RMSE-results in orthorectification of Landsat-5 TM, Landsat-7 ETM+, Aster and Quickbird data
- Table 5-4:** MODTRAN 4 standard atmospheres applied
- Table 5-5:** Temperature of saturation in the low- and high gain bands of Landsat-7 ETM+
- Table 5-6:** Emissivity of different surfaces
- Table 5-7:** Thermal properties of geologic materials
- Table 7-1:** Physical and chemical properties of coals from the study areas
- Table 7-2 a:** Separabilities (D_E) for the most common surface classes in Wuda (no thermal band included)
- Table 7-2 b:** Separabilities (D_E) for the most common surface classes in Wuda (thermal band included)
- Table 7-3 a:** Separabilities (D_E) for the most common surface classes in Ruqigou (thermal band not included)
- Table 7-3 b:** Separabilities (D_E) for the most common surface classes in Ruqigou (thermal band included)
- Table 8-1:** Reduction of the full scene areas to coal fire risk areas based on the automated extraction of coal, a delineation based on this area and the exclusion of densely vegetated areas within this zone for the Wuda region
- Table 8-2:** Reduction of the full scene areas to coal fire risk areas based on the automated extraction of coal, a delineation based on this area and exclusion of densely vegetated areas within this zone for the Ruqigou region
- Table 8-3:** Reduction of the full scene areas to coal fire risk areas based on the automated extraction of coal, a delineation based on this area, exclusion of densely vegetated areas within this zone for the Leigh Creek region
- Table 8-4:** Reduction of the full scene areas to coal fire risk areas based on the automated extraction of coal, a delineation based on this area and exclusion of densely vegetated areas within this zone for the Jharia region
- Table 8-5:** Reduction of the full scene areas to coal fire risk areas based on the automated extraction of coal, a delineation around this area and exclusion of densely vegetated areas within this zone for the Baotou region
- Table 8-6:** Relevance of the single tests, filters and delineation for the areal reduction of the input data set for three exemplary time steps for the broader Wuda study area

- Table 8-7:** Relevance of the single tests, filters and buffers for the areal reduction of the input data set for three exemplary time steps for the broader Ruqigou study area
- Table 8-8:** Accuracy of the extracted coal (filtered) and dense vegetation pixels for Wuda
- Table 8-9:** Accuracy of the extracted coal (filtered), dense vegetation and burned rock pixels for Ruqigou
- Table 8-10:** Percentage of fire polygons mapped in the Wuda area during the field campaign in 2002 included in the delineated area from the 2002-09 scene for a 500m and a 1000 m buffer.
- Table 8-11:** Percentage of fire polygons mapped in the Ruqigou during the field campaign in 2002 included in the demarcated coal fire (risk) area from the September 2002 scene.
- Table 8-12:** Relevance of the single tests, filters and delineation for the areal reduction of the input data set for three exemplary time steps for the three transfer areas
- Table 8-13:** Relevance of the single tests, filters and delineation for the reduction of the input data. Averaged % reduction in comparison with the previous test sequence result calculated for all five areas
- Table 8-14:** Accuracy of the extracted coal (filtered) and dense vegetation pixels for Australia
- Table 8-15:** Accuracy of the extracted coal (filtered) and dense vegetation pixels for India
- Table 8-16:** Accuracy of the extracted coal (filtered) and dense vegetation pixels for Baotou
- Table 9-1:** Accuracy assessment for the 85 % thresholded coal fractions and 85 % thresholded vegetation fractions for the Wuda study area
- Table 9-2:** Accuracy assessment for the 85 % thresholded coal fractions and 85 % thresholded vegetation fractions for the Ruqigou study area
- Table 9-3:** Regression analyses between mapped subpixel fractions and the PMA result
- Table 9-4:** Accuracy of the extracted coal for Australia
- Table 9-5:** Accuracy of the extracted coal and dense vegetation pixels for India
- Table 9-6:** Accuracy of the extracted coal and dense vegetation pixels for Baotou
- Table 10-1:** Coal fire area demarcation supporting the exclusion of false alarms: knowledge based demarcation
- Table 10-2:** Coal fire area demarcation supporting the exclusion of false alarms: PMA based demarcation

List of Maps

- Map 1:** Location of the study areas Wuda and Ruqigou/Gulaben within China
- Map 2:** Geology of the main study areas Wuda and Ruqigou/Gulaben
- Map 3:** General characteristics and topography of the study areas Wuda and Ruqigou/Gulaben
- Map 4:** Demarcated Coal Fire Risk Areas and Thermal Anomalies for Wuda Syncline
- Map 5:** Demarcated Coal Fire Risk Areas and Thermal Anomalies for Southern Wuhai
- Map 6:** Demarcated Coal Fire Risk Areas and Thermal Anomalies Southeast of Wuhai
- Map 7:** Demarcated Coal Fire Risk Areas and Thermal Anomalies far Southeast of Wuda
- Map 8:** Demarcated Coal Fire Risk Areas and Thermal Anomalies East of Shizuishan City
- Map 9:** Demarcated Coal Fire Risk Areas and Thermal Anomalies East of the Newly Detected Coal Fires of 2004
- Map 10:** Demarcated Coal Fire Risk Areas and Thermal Anomalies for Ruqigou / Gulaben Mining Area
- Map 11:** Demarcated Coal Fire Risk Areas and Thermal Anomalies for the Valleys Hulusitai and Shitanjing
- Map 12:** Demarcated Coal Fire Risk Areas and Thermal Anomalies East of Shitanjing
- Map 13:** Demarcated Coal Fire Risk Areas and Thermal Anomalies for Leigh Creek Mining Area
- Map 14:** Demarcated Coal Fire Risk Areas and Thermal Anomalies for the City Area of Baotou
- Map 15:** Demarcated Coal Fire Risk Areas and Thermal Anomalies for the Jharia Mining Region
- Map 16:** Demarcated Coal Fire Risk Areas and Thermal Anomalies for the Rāy Mining Region

List of Symbols and Acronyms

$\tau_0(z)$:	Ground to sensor view angle transmittance with direct and diffuse components
$\beta(x,y)$:	Angle between the solar ray and the surface normal (illumination angle)
\approx :	Approximately
$^\circ$:	Degree
ϵ :	Emissivity
ϕ :	Orbit parameter of platform (gear)
σ :	Orbit parameter of platform (pitch)
κ :	Orbit parameter of platform (roll)
π :	Pi, = 3.14159265
\pm :	Plus-minus
ρ :	Reflectance
θ :	Sun zenith angle
\times :	Times (multiplication)
\neq :	Unequal
γ :	Viewing angle between point on earth's surface and sensor
λ :	Wavelength
Δ :	Difference
μm :	Micrometer
$\tau_s(z)$:	Sun to ground beam (direct) transmittance
ΔT :	Temperature difference between a diurnal solar cycle
ρ_{Terrain} :	Terrain reflected radiation obtained by weighting the reflected radiation in a 0.5 km surrounding of a pixel with the terrain view factor
τ_v :	ground-to-sensor transmittance
(x,y) :	Horizontal coordinates
ALI:	Advanced Land Imager
ANN:	Artificial Neural Network
Arc/Info:	GIS Software
ArcGIS:	GIS Software
ARSC:	Aerophotogrammetry & Remote Sensing Bureau of China
asl:	Above sea level
ASTM:	American Society of Testing and Materials
ATCOR:	Program for atmospheric and topographic correction
ATI:	Apparent thermal inertia
b:	Binary factor with b = 1 if a pixel receives a direct solar beam, otherwise b = 0
BE:	Binary Encoding
BNU:	Beijing Normal University
BRDF:	Bidirectional Reflectance Distribution Function
BRSC:	Bureau of Remote Sensing China
c:	Specific warmth
c:	Speed of light ($2.998 * 10^8$ m/s)
c_0 :	Calibration coefficient
c_1 :	Calibration coefficient
CAS:	Chinese Academy of Sciences
CCSM:	Cross Correlogram Spectral Matching

CH ₄ :	Methane
CO ₂ :	Carbon dioxide
cosθ _s :	Cosine of the sun zenith angle
Cpf:	Calibration parameter file
d:	Astronomical unit (earth to sun distance)
DCT:	Decision Tree Classifier
D _E :	Euclidean distance
DEM:	Digital Elevation Model
DFD:	Deutsche Fernerkundungsdatenzentrum
DLR:	German Aerospace Center
DN:	Digital Number
DN _{max} :	Maximum DN
DN _{min} :	Minimum DN
E:	East
E _{dif} :	Diffuse solar flux
E _{dir} :	Direct solar flux
E _g :	Global direct and diffuse flux on the ground
EM:	Endmember
EMR:	Electromagnetic Radiation
ENVI:	Environment for visualizing images, Image Processing Software
EO-1:	Earth Observing Mission 1
ERS-2:	European Radar Satellite 2
E _s :	Exatmospheric irradiance (TOA)
ETM+:	Enhanced Thematic Mapper of Landsat-7
F _{th} :	Thermal downwelling flux on the ground
GCP:	Ground Control Point
GIS:	Geographic Information System
h:	Height, terrain elevation
h:	Planck's constant ($6.63 \times 10^{-34} \text{ W*s}^2$)
HCMM:	Heat Capacity Mapping Mission
IDL:	Interactive Data Language
IFOV:	Instantaneous field of view
Imagine:	Image Processing Software
K:	Kelvin
k:	Bolzmann's constant ($1.3805 \times 10^{-23} \text{ W*S*K}^{-1}$)
k:	Thermal conductivity of an object.
km ² :	Square Kilometers
L:	Incoming radiance
L ₁ :	Reflected direct and diffuse radiation from the currently viewed pixel
L ₂ , L _p :	Path radiance
L ₃ :	Terrain reflected radiation from opposite hills
L ₄ :	Adjacency radiation
Landsat-7:	American earth observing satellite
Lat:	Latitude
L _{maxλ} :	Maximum radiance at wavelength λ
L _{minλ} :	Minimum radiance at wavelength λ
Lon:	Longitude

$L_p(z, \theta_v, \phi)$:	Path radiance depending on elevation and viewing geometry;
LS-7:	Landsat-7
L_{Sat} :	Radiance reaching the sensor
LST:	Land surface temperature
L_{Surf} :	Blackbody radiance at the ground surface ($W/m^2/\mu m/sr/\lambda$)
LTAP:	Long Term Acquisition Plan
m:	Meter
m^3 :	Cubic meter
MB:	Megabytes
MDC:	Minimum Distance Classification
MF:	Matched Filtering
Mio.:	Million
MIR:	Middle Infrared part of the EMR
MLC:	Maximum Likelihood Classification
MNF:	Minimum Noise Fraction Transformation
MODTRAN:	MODerate spectral resolution atmospheric TRANsmittance
Mtce:	Million tons of coal equivalent (refers to the intntl. standard of 29.3 GJ per ton of coal)
MTMF:	Mixture Tuned Matched Filtering
mW:	Milliwatts
N:	North
NDVI:	Normalized difference vegetation index
NIR:	Near Infrared part of the EMR
nm:	Nanometer
NN:	Neural Network
NO_x :	Nitrous Oxides
NRSCC:	National Remote sensing Center China
O_2 :	Oxygen
O_3 :	Ozone
OA:	Overall Accuracy
OOC:	Object Oriented Classification
p:	Density of a material
P:	Thermal inertia
PA:	Producers Accuracy
PAN:	Panchromatic
PCA:	Principal Component Analysis
PCS:	Principal Component Substitution
PGS:	Product Generation System
PMA:	Partial Mixture Analysis
PPC:	Parallelliped Classification
PPI:	Pixel Purity Index
q:	Weighing factor.
RMSE:	Root Mean Square Error
SAM:	Spectral Angle Mapping
SAR:	Synthetic Aperture Radar
SCA:	Supervized Classification Algorithms
SD:	Standard deviation
SFF:	Spetral Feature Fitting

SM:	Spectral Matching
SMA:	Spectral Mixture Analysis
SNR:	Signal to noise ration
SO ₂ :	Sulfur Dioxide
SPM:	Spectral Mean
sr:	Steradian
SRF:	Spectral Response Function
SSD:	Sum of Squared Distances
T:	Surface temperature
Tab.:	Table
tan:	Tangens
TCT:	Tasseled Cap Transformation
TIMS:	Thermal Infrared Multispectral Scanner
TM:	Thematic Mapper
TOA:	Top of the atmosphere
UA:	Users Accuracy
UCA:	Unsupervized Classification Algorithms
UTM:	Universal Transverse Mercator
VIS	Visible part of the EMR
$V_{\text{terrain}}(x,y)$:	Terrain view factor (0-1 range) calculated from the local slope or a horizon analysis (
W:	Watt
WGS84:	Spheroid Type
z:	Elevation information
Z:	Zone
Φ :	Slope of the upper hull curve

Any abbreviations missing in this list will be explained in text or can be found below the equations

1. Introduction

1.1. Coal Fires

Uncontrolled coal seam fires are an environmental and economic problem of international magnitude. They occur in many countries worldwide including China, India, Russia, the United States, Indonesia, Venezuela, Australia and South Africa, but also at a smaller scale for example in Germany, Romania or the Czech Republic (GLOVER 1998, PRAKASH & GUPTA 1998, PRAKASH et al. 1999, DENG et al. 2001, PENNIG 2002, BOEKEMEIER et al. 2002).

The term coal fire refers to a burning or smoldering coal seam, coal storage pile or coal waste pile. The adsorption of oxygen at the outer and inner surface of coal and resulting oxidation is an exothermic reaction. This leads to an increase in temperature within the coal accumulation. If the temperature exceeds approximately 80°C the coal can ignite and start to burn. This process, referred to as "spontaneous combustion", is the most common cause for coal fires of large extent. Spontaneous combustion processes can be accelerated through human impact. Mining operations expose formerly covered coal to oxidation processes and additionally lead to the accumulation of large coal waste and storage piles (CHAIKEN et al. 1980, KIM & CHAIKEN 1993, WALKER 1999, VAN GENDEREN & GUAN 1997). Coal fires can also be ignited by lightning, forest- or peat fires, mining accidents or careless human interaction (PAGE et al. 1997, RUECKER 2003, JIA 2002).

Depending on cause, location, age and burning intensity, coal fires can be classified into different types. Coal fires can be human induced, when coal seams in areas of mining activity start to smolder or burn due to anthropogenic causes. They can occur naturally, when the fire is a result of natural spontaneous combustion. Furthermore, underground and surface coal fires, cold and hot coal fires, paleo- and recent coal fires, as well as coal fires in coal-seams, coal waste- or coal storage piles can be differentiated (ZHANG, J., et al. 2004a). VAN GENDEREN & GUAN (1997) additionally classify shallow (0-10m), intermediate (10-30m) and deep fires (>30m), depending on their location underground. The oldest documented coal fire on a global scale, which has been burning for over 2,000 years, is located in New South Wales, Australia (ZHANG, J., et al. 2004a). Another case that has attracted strong public attention is the subsurface coal fire in Centralia in Pennsylvania, U.S., which started in 1962. Here, between 1980 and 1998 a whole city had to be evacuated and relocated. The slowly advancing coal fire underneath the city endangered houses and infrastructure. Even today the fire still leads to the collapse of formerly inhabited ground.

Coal fires in China are mentioned in historic documents as early as 1000 AC in the travel report of Li Dao Yuan, who explored Northwest China during the "Northern Song Dynasty" (960-1280 AC). Also the travel documents of Marco Polo (1254-1324 BC) mention the "burning mountains along the silk road" as well as paleo coal fires in Xinjiang, which are dated back to be of Pleistocene age (GIELISCH 2002, SCHNEIDER 1996). Today, China is the leading country concerning coal production, consumption and export, whereas Russia and the US rank first and second in terms of coal reserves on a global scale. Annual Chinese coal production averages above 1400 Mio. tons (WALKER, 1999). The energy supply for approximately 1.3 Billion Chinese people, of which over 25% live in cities, is mainly provided by coal. Oil accounts for only 20% of the total energy supply. Only two nuclear power plants exist and gas production is negligible. Next to coal, only hydroelectric power is of higher

relevance, showing increasing growth rates in Southwest China. Therefore, the country at present accounts for 28% of the world's coal use with projected requirements of 1632 Mio. tons coal equivalent in 2010 and faces the problem of numerous uncontrolled burning coal fires (DANIEL 1994, WALKER 1999, TODD & FENGJUN 1997).

Nowadays, the main coal fire areas stretch along the coal mining belt in China, which extends for 5000km from East to West along the North of the country. Here more than 50 coal fields affected by coal fires have been identified (VAN GENDEREN & GUAN. 1997). At present in China an estimated 20-30 Mio. tons of coal burn each year. This corresponds to the amount of Germany's annual hard coal production. Actually, the tenfold amount of the resource is lost, since coal adjacent to a coal fire becomes inaccessible. The economic loss of the valuable resource in China is estimated to sum up to total 4.2 Billion tons since 1960 (BETHGE, 1999). Thus, China faces the world's biggest problem of coal fires both in terms of the spatial area affected and the amount of coal lost each year.

Besides the economic loss, coal fires pose many environmental threats. The fires produce large amounts of greenhouse-relevant and partially toxic gasses including CO₂, CH₄, NO_x, N₂O, CO and SO₂. According to most recent estimations coal fires in China contribute about 0.1% to 0.2% of the annual human induced CO₂ emissions globally. They contribute 12% of all Chinese coal-based carbon emissions in the form of CO₂ (KUENZER et al. in review, WALKER 1999). In addition, coal fires lead to the degradation of their direct surrounding area through significant aerosol input to water sources and agricultural areas. Additionally, the toxic fumes released pose a threat to the health of the local inhabitants (SARAF et al. 1995, RATHORE & WRIGHT 1993, LIVINGOOD et al. 1999). Furthermore, land subsidence can occur due to the loss of volume underground, when a coal seam, supporting several layers of overlying strata, turns into ash. The resulting slow or very sudden subsidence can be a threat to infrastructure, local inhabitants and miners (CHEN 1997, GUAN 1989, RATHORE & WRIGHT 1993, ZHANG, X. 1998, WRIGHT & STOW 1999, PRAKASH et al. 2001). Each year, several thousand workers are killed in mining accidents, which are quite often also coal fire related (ZHANG et al. 2004a, BETHGE 1999, PENNIG 2002, BOEKEMEIER et al. 2002, JIA 2002).

These negative environmental impacts of coal fires explain the urgent need for methodologies to map, analyze and monitor the coal fire regions. Since many Chinese mining regions are located in remote areas, airborne or satellite remote sensing can play a key role for coal fire detection and monitoring. With respect to the large spatial extent of the Chinese coal mining belt and the number of existing coal fire areas, remote sensing is a powerful tool for the generation of land cover- and coal fire maps. Reflective and thermal indicators can be derived from satellite data to develop early warning- or risk assessment strategies and to implement priority schemes for future coal fire extinguishing activities.

1.2. Remote Sensing of Coal Fires: Brief Status of Research

Documented coal fire research based on remote sensing data started around 1963, when a company producing airborne thermal cameras, tested their equipment above burning coal waste piles in Scranton, Pennsylvania. The thermal imagery clearly showed the burning areas within the coal waste piles as light grey values (SLAVECKI 1964). Further aerial surveys with thermal cameras in the 1960s and 1970s were conducted by MOXHAM & GREENE (1967), GREENE et al. (1968), KNUTH et al. (1968), FISHER & KNUTH (1968), RABCHEVSKY (1972) and ELLYETT & FLEMING (1974). Their main research foci were investigations of coal fires in the U.S. at a very local scale (ZHANG, J., et al. 2004a).

These approaches were dominated by visual interpretation and the localization of the well-known fires within the imagery. Density slicing was used exclusively to extract the fires from the image data.

In the early 1980s coal fires were already studied in several countries. Still aerial remote sensing was the main tool applied. In 1983 multi-spectral scanner data and thermal infrared scanner data was used for the investigation of coal fires in the Chinese regions of Taiyuan Xishan in Shanxi province (GUAN 1984, LI 1985). Coal fire research based on aerial multispectral scanner data continued in India, where BHATTACHARYA et al. (1991, 1994), MUKHERJEE (1991) and PRAKASH (1995) investigated the Jharia coal field, generating coal fire maps derived from the aerial thermal data based on ground truth knowledge. Details on the capability of coal fire detection from airborne thermal scanner data are presented by ZHANG, X. et al. 2004.

The Jharia region was later studied based on satellite data by MANSOR et al. (1994), using thermal and mid-infrared NOAA-AVHRR and thermal Landsat-5 TM data. SARAF et al. (1995) as well as PRAKASH et al. (1997), PRAKASH & GUPTA (1998) and GUPTA & PRAKASH (1999) studied the coal fires in the Jharia coal field, using Landsat-5 TM thermal band data with 120m spatial resolution. Their studies focused on coal fire detection within the satellite data, supported by ground truth, as well as on depth estimation of subsurface coal fires. The spatial resolution of Landsat-5 TM was sufficient for the detection of surface fires but often proved too coarse to detect very deep or small coal fires (ZHANG, X. 1998). Even Landsat-5 TM nighttime data often was too coarse for the early detection of new coal fires (VAN GENDEREN & GUAN 1997). Furthermore, from 1997 on the thermal band of Landsat-5 was not longer operational.

Overall, studies applying Landsat-5 TM band 6 were mainly limited to the exact demarcation of hot and large surface coal fires and the rough localization of hot or large underground coal fires supported by field measurements. Research undertaken included the application of this satellite data to different locations, the evaluation of density slicing techniques for coal fire detection, and temperature retrieval in case of coal fires exceeding several pixels in size. Furthermore, time series analyses were pursued to describe the movement of the fires. First relief-based thermal calibration methods, differencing methods between thermal daytime and nighttime data and the combined interpretation of the two were employed. In addition, combining the information of Landsat band 6 with band 5 and 7 (1.55-1.75 μm and 2.08-2.35 μm) was tested. Based on the 'dual band method' developed by MATSON & DOZIER (1981), the size and temperature of very hot surface coal fires occupying sub-pixel portions could be calculated (ZHANG, X. 1998, ZHANG, X. et al. 1997, PRAKASH & GUPTA 1999). This approach has also been proposed for Aster data with 6 bands of 30m resolution in the SWIR and 5 bands of 90m resolution in the TIR (WANG, 2002). TETZLAFF (2004) discusses the detectability of coal fires with different sensors depending on the size and temperature of a fire. SPOT-XS data at 20m spatial resolution proved to be less useful for coal fire research. Due to the limited swath width of only 60 km and the lack of a thermal band the sensor never gained high relevance (VAN GENDEREN & GUAN 1997).

Generally, satellite data with a coarser spatial resolution than that of Landsat-TM was rarely used for coal fire research and did not yield promising results. Though MANSOR et al. (1994) could spot very hot surface coal fires in Jharia, ZHANG, X. (1998) showed that the spatial resolution of NOAA-AVHRR data (1km) in general is too low to detect underground coal fires in Northwest China. The same applies to unenhanced 1km resolution data from MODIS. In thermal pixels with a spatial

resolution of 1km the subsurface coal fire anomalies are usually not large- and not hot enough to have a measurable impact on the overall thermal signal of the pixel. However, HECKER (2003) could show that MODIS data with several thermal bands can support the extraction of thermal anomalies resulting from surface coal fires. Ratio images from MODIS nighttime data (band 20 versus band 32) were used to detect surface coal fires based on related thermal anomalies, even where the fires only covered a fraction of the pixel size. Nevertheless, in daytime ratio images these anomalies were masked by solar effects. Underground coal fires could not be detected.

Also sensors with an intermediate spatial resolution like the DLR sensor BIRD with 185m pixel size can only detect extremely hot surface coal fires in the mid infrared (3,4-4,2 μ m). However, surface coal fires, such as those found in the Jharia coal field in India, the site of over 70 major mine fires, (PRAKASH & GUPTA 1999, PRAKASH et al. 1997) or in the Ruqigou coal mining area of Ningxia Hui Autonomous Region, China, are not the standard case (GUPTA & PRAKASH 1998, ZHANG, J., et al. 2004a, VOIGT et al. 2004). Most coal fires are deeper subsurface fires. These underground fires pose a great challenge for detection and quantification by means of remote sensing. For these fires, leading to only subtle thermal surface anomalies, Landsat-7 ETM+ data with a spatial resolution of 60m in the thermal band is a promising data source for new developments in coal fire research as shown by ZHANG, J. (2004) and TETZLAFF (2004). For a very detailed overview on coal fire research before 2000 see ZHANG, J. et al. (2004a).

It can be concluded that the main foci in the field of remote sensing based coal fire research have been thermal investigations based on different airborne and spaceborne sensors. Different methods have been applied for the extraction of thermal anomalies. The detection capability of the thermal bands of NOAA-AVHRR, MODIS, BIRD, Landsat-5 TM, Landsat 7 ETM+ and Aster has been evaluated by many authors. The application of different techniques like density slicing (PRAKASH et al. 1997, ZHANG, X. 1998, ROSEMA et al 1999), automated statistical analysis (ZHANG, J. 2004), the dual band method (PRAKASH & GUPTA 1998, ZHANG, X. 1998) or multitemporal analysis (PRAKASH et al. 1999) has been pursued within recent years.

Coal fire research based on multispectral reflective remote sensing information has only been conducted in rare cases, focusing on local descriptions of coal fire area environments (VAN GENDEREN & GUAN 1997, PRAKASH & Gupta 1998, 1999, PRAKASH et al. 2001). Mostly, reflective parameters for coal fire detection were not considered to be as obvious and representative as thermal anomalies in satellite data with continuously improving spatial resolution in the thermal bands. Non-thermal data have only been used for the "synoptic overview" on the regional structure and tectonic setting of the study areas or the detection of burned rock related to paleo coal fires (VAN GENDEREN & GUAN 1997).

Starting in 2003 a Sino German Research Initiative has been addressing the problem of coal fires involving different research disciplines. Remote sensing, geology, geophysics, chemistry and mining technology contribute to investigations on coal fire area demarcation, thermal anomaly detection, fire quantification, 3D modeling, spontaneous combustion processes, fire dynamics and environmental impacts. This project on coal fires in China is funded by the German Ministry of Education and Science (BMBF) on the German side. The Ministry of Science and Technology (MOST) is responsible for funding on the Chinese side. The initiative is coordinated by the German Remote Sensing Data Center (DFD) of the German Aerospace Center (DLR). The research presented in this thesis was undertaken within the framework of this initiative and a foregoing remote sensing project.

The overall goal of the research initiative is to provide the scientific basis and techniques, which allow the efficient assessment, monitoring and development of extinction strategies for coal fires in China. Extinction strategies to reduce the Kyoto relevant emissions released through this environmental hazard shall be supported. The objectives of the remote sensing part of the project are to detect the coal fires from thermal Landsat-7 ETM+, BIRD and ASTER daytime and nighttime data operationally and to demarcate possible coal fire areas and future coal fires risk areas based on multispectral information. Furthermore, it is intended to analyze the landcover patterns in the coal fire areas.

Multitemporal land cover analysis can reveal where new mining areas develop and if uncontrolled private mining is spreading. This will help to understand the link between land cover changes, mining development and coal fires. It shall be observed if coal fires tend to grow or shrink, and how long extinguished fires will remain extinct. In combination with the research results of the other geoscientific disciplines the remote sensing results can support the overall understanding of coal fire related processes and the quantitative assessment of the problem. This can support the development of a comprehensive monitoring and extinguishing scheme.

Building on remote sensing based coal fire research completed before 2001, a major challenge in this recent project is the development of automated methods, which need to be applicable on a large spatial scale. To implement operational monitoring, techniques like knowledge based temperature thresholding, on screen digitization of features, manual land cover classifications or locally adapted image arithmetic are inefficient. Therefore – based on detailed regional studies –automated algorithms for coal fire detection and demarcation applicable over large geographic regions are being developed.

1.3. Research Objectives

This thesis aims at the automated demarcation of coal fire areas and coal fire risk areas. It focuses on multispectral data analyses to find spectral features or indicators, which can support the delineation of potential coal fire areas. At the same time coal fire area demarcation is developed to have a synergetic effect with the algorithm for thermal anomaly detection, implemented and presented by ZHANG, J. (2004).

Automated statistical analysis can reach good results extracting thermal anomalies resulting from coal fires from thermal nighttime data. This applies, although these anomalies usually show only a very subtle contrast towards the background pixels not influenced by coal fires (ZHANG, J. 2004). The majority of coal fires occur underground. In contrast to surface coal fires a lot of energy is absorbed by the overlaying bedrock. Therefore, subsurface fires do not produce very strong thermal signals. Anomalies are typically 3-10 °C warmer than the unaffected background. Thus, automated statistical analyses of thermal anomalies still leads to the extraction of anomalous pixels that are not related to coal fires, which cannot necessarily be distinguished from a coal fire anomaly. These are thermal anomalies caused by industry, settlement, biomass fires, limestone burning and uneven solar heating in both daytime and nighttime images (RATHORE & WRIGHT 1993, ZHANG, X. 1998, ZHANG, J. et al. 2004a). Especially the accurate automated extraction of coal fire related thermal anomalies from daytime data, which includes a strong solar component in the thermal band, remains challenging (DENG et al. 2001, ZHANG, X., 1998). Based on measurements, taken during the 2002 field campaign, ZHANG, J. (2004) could show that thermal anomalies – even in the close vicinity of very hot cracks – were masked by the effect of solar heating already one hour past sunrise.

This problem can usually be overcome with thermal nighttime data. Such data offers the advantage of a much lower solar influence within the thermal bands than found in daytime data. ROSEMA et al. (1999) could show that the difference between an east- and a west facing slope at 10:30 am can be over 12 K, while in nighttime data (22:30) the contrast is less than 2 K. However, nighttime satellite data is very expensive and difficult to acquire. It cannot be considered a standard product, which is accessible for large areas (DENG et al. 2001). Therefore, nighttime satellite datasets of Landsat or Aster cannot be employed for a large scale thermal monitoring nor can they alone be used as the base for coal fire detection. VAN GENDEREN & GUAN (1997) state that for operational routine coal fire detection the user will need to work predominantly with daytime data. This complicates the detection of coal fire related thermal anomalies. In the worst case, some fires will not even result in a thermal expression. New and deep fires are only detectable when heat is transferred through fractures or cracks, since it takes several years for exclusively conductive heat to manifest at the surface (ROSEMA et al. 1999, ZHANG, J. et al. 2004a). Even high temperature fires can exist closely beneath the ground surface and yet exhibit little or no surface expression. Research has found that even though 'hot spots' in large mine waste piles generally occur between 1.5 and 2.5 meters below the surface, thermal imaging equipment is often of limited benefit (WALKER 1999).

Furthermore, the absolute calibration of thermal daytime data to improve coal fire detection appears very challenging. To account for effects of uneven solar heating a very precise DEM is needed. To account for uneven heating due to differing surface inherent physical characteristics (albedo, density, conductivity etc.) detailed surface maps need to be provided. Furthermore, time integrated heating effects with respect to the overpass time of the satellite have to be taken into account (SABINS 1996, ZHANG, X., 1998.).

It becomes obvious that thermal anomaly detection as well as thermal calibration alone both face problems not easily overcome. Therefore, this work focuses on the demarcation of areas, where coal fires are likely to occur. It is assumed that information extracted from multispectral data will not only help to better understand landscape patterns and the temporal dynamics in the coal fire regions, but can furthermore support the analysis of thermal satellite imagery.

The following research questions will be addressed in this study:

1. How did coal mining activity in the study areas develop over the past 15 years and can changes of coal mining activity be qualitatively and quantitatively assessed from time series satellite data?
2. What influence do coal fires have on their surrounding environment and how can such influences be observed in reflective satellite data?
3. Which surfaces types or indicators can be extracted from satellite data, which support the demarcation of coal fire areas and probable coal fire risk areas?
4. Which approach proves most applicable to design a fully automated algorithm for the demarcation of coal fire areas based on multispectral remote sensing information?
5. Can such an automated algorithm be combined with existing thermal algorithms?
6. How will the combination of multispectral and thermal research influence the detection accuracy of coal fire related thermal anomalies?
7. What role does multispectral reflective information play for the demarcation of possible future coal fire risk areas?

1.4. Thesis Outline

Chapter 1 introduces the problem of coal fires on a global and China-wide scale. A short review on coal fire related remote sensing research undertaken since 1963 is presented. The current project framework as well as most recent challenges in coal fire research are introduced. This is followed by the definition of research objectives for this thesis. A short outline of this work is presented.

Chapter 2 gives an overview of the two main study areas in North-central China: Wuda and Ruqigou / Gulaben. The geographic location of these areas is specified and physical-geographic characteristics like geologic setting, geomorphologic appearance, climatic and hydrographic influences as well as dominating soil- and vegetation patterns are explained. Furthermore, the socio-geographic parameters are briefly introduced. The effects and hazards of coal fires dominating the local environmental situation are described.

Chapter 3 introduces the theoretical concepts as well as the status of research in the field of multispectral surface classification and spectral feature extraction. Here, the variety of mathematical statistical approaches for information extraction from satellite data is illustrated. This chapter forms the theoretical backbone for the two algorithms developed for coal fire area demarcation.

Chapter 4 presents the satellite-, field-, GIS- and map-data acquired for this research. The satellite data used is listed and the sensor characteristics of the different satellites are presented. In addition, the data collected and recorded during a one-month field campaign in the study areas in September 2002 and a three-week field campaign in September 2003 is presented. Available GIS data and maps are listed.

Chapter 5 deals with the spatial and spectral accuracy of the satellite data analyzed. The preprocessing of this data in a complete chain including orthorectification, sensor calibration and a combined atmospheric and topographic correction is explained. Results of surface reflectance retrieval over all wavelength are presented. The accuracy is assessed based on field and laboratory spectra of pseudo-invariant objects. Thermal data sets are corrected to land surface temperatures. Results of these analyses are presented and validated.

Chapter 6 presents the concept of coal fire area demarcation based on field observations and remote sensing analysis. This conceptual approach is the basis for the algorithms developed to delineate coal fire areas and risk areas.

In chapter 7 a detailed spectral signature analysis of the surfaces, which are considered to be of relevance for coal fire area demarcation as defined in chapter 6, is undertaken. This analysis explains the chemical, physical and spectral properties of the surfaces and materials of interest. The separability of these surfaces against each other, as well as against other spectral components present in the image data is discussed. The results and conclusions drawn from signature analysis form the basis for the algorithm design presented in chapter 8.

In chapter 8 the first algorithm for the automated demarcation of coal fire areas is presented. It is designed as a knowledge-based spectral test sequence. The chapter is subdivided into the methodological part, results, a validation and error estimation of these results, a spatial transfer to different regions and a discussion.

Chapter 9 presents a second – more quantitative – approach of automated surface extraction based on partial unmixing of image data. Partial unmixing bases on the fundamentals of linear spectral mixture analysis and supports the mapping of single surfaces within raster imagery. As in chapter 8, the methodological frame, results, validation and error estimation, a spatial transfer and a detailed discussion are presented.

In chapter 10 the two developed algorithms are applied to a large number of data sets. Results presented in chapter 8 and 9 are combined in the form of coal fire area maps and coal fire risk maps for several regions. Regions mapped include the two main study areas, their broader surroundings as well as the transfer areas. The transfer areas are located in north central China, India and Australia to demonstrate the spatial transfer of the algorithms employed. Furthermore, results of the combination of automated coal fire area demarcation and thermal anomaly detection as developed by ZHANG, J. (2004) are shown. The demarcation concept, the results of the developed algorithms and synergetic effects of multispectral and thermal analysis are discussed. Furthermore, the map products are evaluated concerning their practical value.

In chapter 11 a conclusion summarizes the most important results. An outlook on continuing coal fire research and questions to be addressed in the future is given.

2. The Study Areas: Wuda, Ruqigou / Gulaben and Environmental Coal Fire Impacts

2.1. Geographic Location

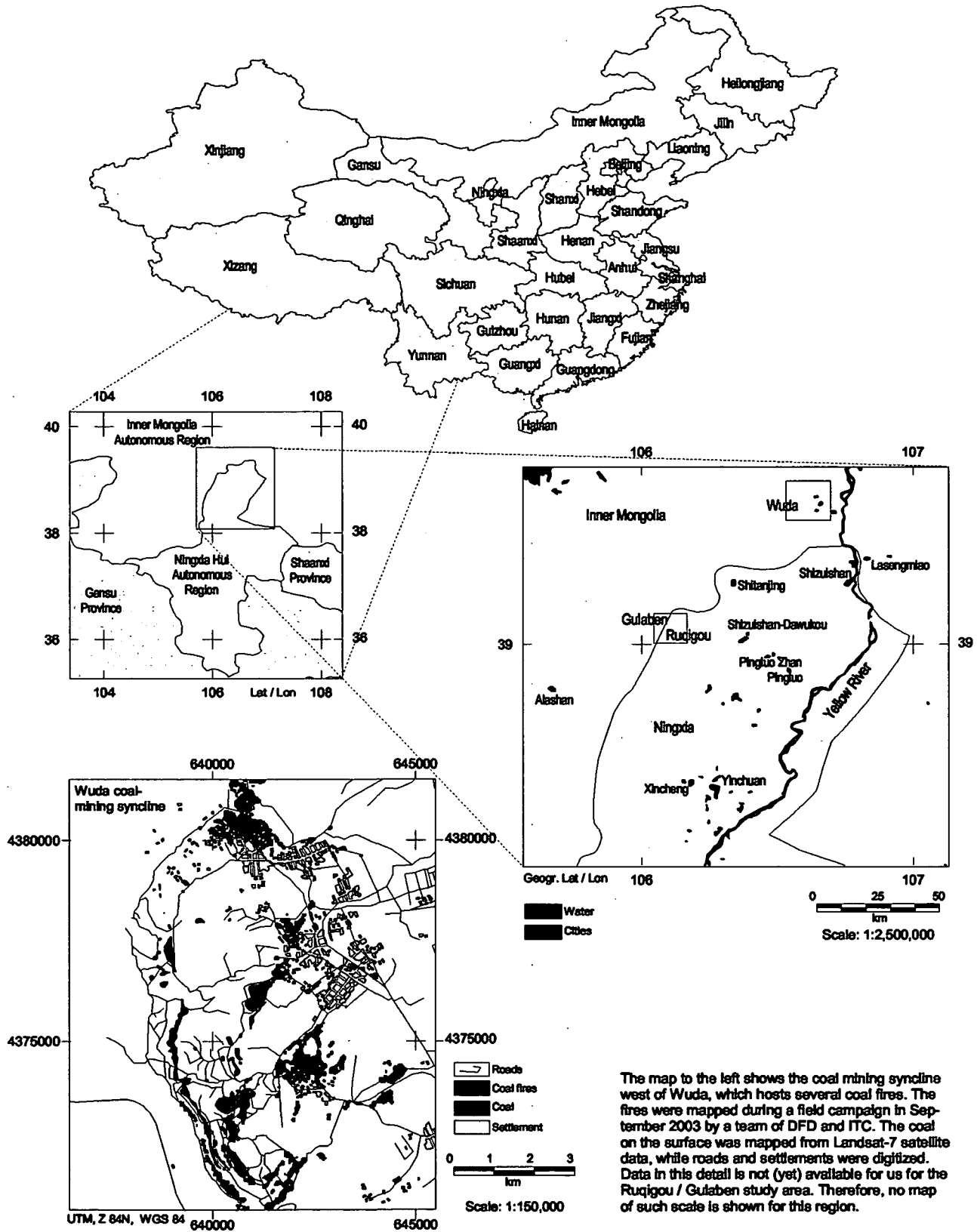
The field sites and mining areas of Wuda and Ruqigou / Gulaben are both located in North Central China. Although the surroundings of these two areas were investigated also, during the field campaigns a clear focus was research in these two mining areas. Accordingly, this chapter introduces the geophysical and socio-economical factors characterizing the two regions. It should be mentioned that during the field campaigns research was possible in Wuda region for 21 days in 2002 and 10 days in 2003 and 2004, while the Ruqigou area could only be studied in detail for three days in 2002 and 2003, respectively. Therefore, the Wuda region is the main area for general characterization, mapping, ground truthing and spectral as well as thermal measurements and receives a higher priority concerning data analysis within this thesis. In contrast to Ruqigou / Gulaben coal fires in the Wuda study area have not been internationally studied prior to the start of this project and information on the geographic characteristics were scarce. International publications were not available. Therefore, this chapter includes a novel synoptic overview of physical geographic characteristics of this region.

Wuda is located in Inner Mongolia Autonomous Region, which covers an area of 1,180,000 km² or about one-eighth of the country (PEOPLE'S REPUBLIC OF CHINA MINISTRY OF GEOLOGY AND MINERAL RESOURCES, 1991). The city borders the structural syncline hosting a large coal fire area investigated. It is located on the western side of the Yellow River, north of the Helan Shan mountain range, not far from the border to Ningxia Hui Autonomous Region. Ten kilometers west of Wuda the first dunes of the Badain Jaran desert can be found. The geographic location of Wuda city is approximately 39.51° North and 106.60° East (see map 1). The nearest bigger cities are Wuhai, located 20 km to the Northeast, Shizuishan-Dawukou, 75km southwest of Wuda and Yinchuan, the capital of Ningxia Hui Autonomous Region, which is located 150 km to the South. The broader study area of Wuda includes a region of approximately 1600 km², with Wuda at the center. Land elevations in this region vary from 1010 to 1980 meters above sea level.

The other study area, Ruqigou / Gulaben, is located in the northern part of the Helan Shan mountain range in Ningxia Hui Autonomous Region, which covers an area of 66,400 km² and therefore is 17 times smaller than Inner Mongolia Autonomous Region (PEOPLE'S REPUBLIC OF CHINA MINISTRY OF GEOLOGY AND MINERAL RESOURCES, 1990). The Helan Shan mountains strike from Southwest to Northeast for ca. 200 km along the northwestern border between Ningxia and Inner Mongolia. Their average height is 2000 meters; the highest peak, Helan Mountain, reaches 3557 meters. The mining area is located at approximately 39.07° North and 106.12° East, close to the border of Inner Mongolia Autonomous Region to the West (see map 1). The nearest larger cities are Shizuishan-Dawukou, 25 km east and Yinchuan, 70 km southeast of Ruqigou. Wuda is located 75km to the Northeast. The broader study area of Ruqigou includes the adjacent regions within a radius of 8 km around the city. This also includes the mining area of Gulaben – already located in Inner Mongolia – neighboring the Ruqigou syncline. Elevations in this region vary from 1400 to 2640 meters above sea level. Though coal mining- and coal fire areas in China are widespread, the areas of Wuda and Ruqigou offer the major advantage that different types of coal fires occur within a small region. Furthermore, different mining methods are applied, the areas were partially (Ruqigou) studied before (ROSEMA et al. 1999, PRAKASH et al. 1999, PRAKASH et al. 2001) and they offer sufficient accessibility.

Location of the Study Areas Wuda and Ruqigou / Gulaben in China

Orientation on a China-wide, provincial, regional and local scale



The map to the left shows the coal mining syncline west of Wuda, which hosts several coal fires. The fires were mapped during a field campaign in September 2003 by a team of DFD and ITC. The coal on the surface was mapped from Landsat-7 satellite data, while roads and settlements were digitized. Data in this detail is not (yet) available for us for the Ruqigou / Gulabien study area. Therefore, no map of such scale is shown for this region.

Layout and GIS: Claudia Künzer
 German Remote Sensing Data Center
 Environment and Geoinformation
 Germany



2.2. Geologic and Geomorphologic Characteristics

The geology of the broader area of northern Ningxia and south-central Inner Mongolia is rather complex, since the area is located within the transition zone between the different geotectonic units of eastern and western China. Detailed geologic descriptions can be found in PEOPLE'S REPUBLIC OF CHINA MINISTRY OF GEOLOGY AND MINERAL RESOURCES 1990 and PEOPLE'S REPUBLIC OF CHINA MINISTRY OF GEOLOGY AND MINERAL RESOURCES 1991, as well as ZHANG (1997), analyzing the area and its strata from oldest geologic times until today. This includes detailed discussions of processes of sedimentation, tectonics, erosion etc. of Archean-, Proterozoic-, Paleozoic- and the following younger units. Since the strata of interest in the Wuda study area are not older than Carboniferous next to some local deposits of Ordovician strata, older units will not be discussed. The same applies for Ruqigou, where the major area of interest consists of Triassic and younger strata, though Precambrian metamorphics do occur as well. Readers with deeper geologic interest are referred to the above sources. Map 2 gives an impression of the geology in the two study areas.

The north-south striking structural syncline located 5 km west of Wuda has a spatial extent of 35km² and holds a total reserve of 630 Mio. tons of coal. The coal layers originate from Upper Carboniferous and Lower Permian times (DAI et al. 2002). Mineable reserves are stated to be 27 Mio. tons with seam thickness varying between 1.5 and 12 meters. The coal layers are interbedded in different layers of coarse to fine-grained white to dark grey or yellowish sandstone and grayish-, brown- or green-yellowish shale with varying organic content also originating from the Carboniferous and Permian. Occurring formations are the Taiyuan-, Shanxi-, Xiashihezi- and Shangshihezi formation. The Taiyuan formation is the major coal bearing formation (DAI et al. 2002). The strata dip to the East with an average dip angle of 6 to 10°, but steeper dips occur as well. Quaternary alluvial layers of silt, shale and gravel unconformably cover small parts of the Permian and Carboniferous outcrops. Outside the syncline also Lower- and Middle Ordovician marine facies sediments including thick bedded dolomite and limestone occur. The Silurian and Devonian sequence is missing in the Helan Mountain area and its surroundings.

In the syncline area the coal layers have been mined under the authority of the "Wuda coal mine bureau" within the three coal mines of Wuhushan operating in the South, Huangbaici in the East and Suhai-Tu in the Northwest since 1958. In these three mines three different qualities of coal – fatcoal, cooking coal and steam coal – are being extracted from the 17 mineable of the overall 24 coal seams. The upper seven coal seams from Permian times, belonging to the Shanxi group, have an overall thickness of 88 meters and are characterized by a low sulfur and a high ash content. All lower seams from the Carboniferous belong to the Thairen group and have a high sulfur and low ash content. The heating value of the Wuda coal varies between 5000-7000 kcal/kg (JIA 2002, SUN 2003).

The broader Ruqigou / Gulaben study area is located in the Helan mountains – a significant boundary in the geographical zonation of China. They form the fold- and fault belt of the western rim of the transitional Ordos Basin, which has been affected by the Trans-Eurasian Tethys tectonism and the circum-Pacific tectonism including dual extensional and compressional shearing mechanisms (ROSEMA et al. 1999). The Helan Shan has undergone several phases of orogeny. In its present shape it was formed in a compressional regime between the Xiaosongshan thrust fault system in the Northwest and the Helanshan fault zone in the East during various tectonic phases of the Yanshan orogeny in the Jurassic. After erosion and basin formation during the late Jurassic a renewed uplift

began 25 Mio. years ago during the Himalayan period which is still continuing (ROSEMA et al. 1999). Today, in the North and West this mountain chain borders the desert with gentle hill slopes formed through broad alluvial fans. East of the mountains steep hill slopes form the transition to the large Yinchuan alluvial plain, which developed through the accumulation of deposits from the Yellow River.

The Ruqigou- and Gulaben coal fields belong to an asymmetrical Jurassic synclinal basin located at the western rim of the Paleo-Mesozoic sedimentary Ordos Basin. The Jurassic syncline stretches 14 km from Southwest to Northeast, 7 km from Southeast to Northwest and covers an area of approximately 80 km². The Gulaben area is located at the western rim of Ruqigou syncline at the transition to Houlugou anticline. Strata in the Ruqigou syncline show dip angles of 5-30° while 35- up to 75° are reached in Gulaben. The 10 main coal seams of the two regions were deposited under lacustrine-fluvial conditions during the Middle Jurassic and belong to the Yan'an formation. Due to the Yanshanian movement the covering layers were partially eroded and the coal seams are well exposed (ZHANG, X., 1997). Coal rank is high and ranges from low volatile bituminous coal to Anthracite with low ash and sulfur contents resulting in a very good export market. The Anthracite distribution corresponds spatially with an underlying magmatic intrusion into the Helan Shan complex during the early Yanshanian movement. It is assumed that this thermal intrusion supported the high-degree coalification (ZHANG, X., 1997). Ruqigou and Gulaben area together hold a proven geologic reserve of 1.04 Mio. tons with prospects ranging around 1 Billion tons. The coal is mined within three major mines: Ruqigou- and Baijigou underground mines and Dafeng open pit mine. The coal seams are interbedded in different layers of older Triassic (Yanchang formation) and younger Jurassic (Zhiluo formation) fine to coarse grained white to grey sandstones, purplish red mudstones, yellow-green siltstones and shales, occasional deposits of claystones and interbedded conglomerates. These strata were deposited during seven sedimentation cycles each of which represented a certain climate, ranging from dry to humid environments (CHEN 1997). Apart from this strata, some Quaternary alluvial deposits occur along the small seasonal rivers dissecting the syncline (ROSEMA et al. 1999).

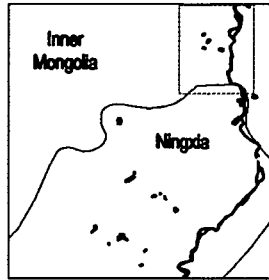
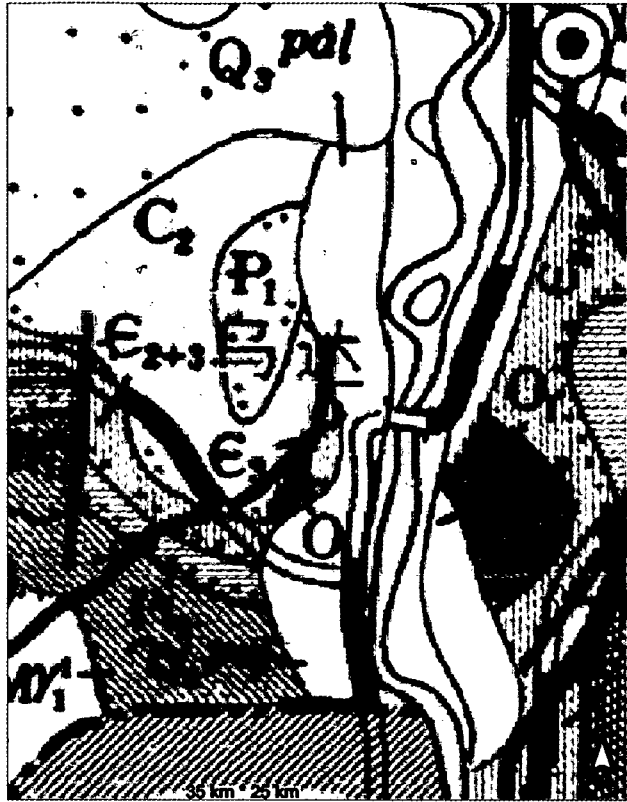
The tectonic system is characterized by several large and many small faults in the study area. These explain displacements and discontinuities in the Triassic and Jurassic strata. The most important one is the north-south running Westfoot fault west of the Helan Mountains, which has been active during all orogenic movements (Caledonian, Hercynian, Yanshanian and younger). Furthermore, the Eastfoot fault in the East of the orogenic complex demarcates the boundary between the mountains and the Yinchuan graben. The Xiaosongshan reverse fault in the Northwest of Ruqigou divides the Archean and Precambrian metamorphic sequences from the younger sedimentary cover. Additionally, the Zhenyiguan strike fault runs east-west through the northern part of the Helan Mountains (ZHANG, X. 1997).

A local geologic phenomenon resulting from coal fire induced metamorphism is the occurrence of pyrometamorphic rocks. These are rocks that have been baked or heated by coal fires, resulting in texture- and color changes due to oxidation and dehydration. Within the Wuda syncline they occur only locally in very small places (see figure 2-1), while in the Hongliang area within the Ruqigou basin they can be observed even at a larger spatial extent. Also newly formed fumarolic minerals such as salmiac, sulfur (see figure 2-1), gypsum and calcite indicate coal fire activity (LAPHAM et al. 1980, ZHANG, J. 1996, VAN GENDEREN & GUAN 1997, ZHANG, X. 1998, ZHANG, J. et al. 2004a).

Geology of the Study Areas Wuda and Ruqigou / Gulaben and Adjacent Regions

as presented by the People's Republic of China Ministry of Geology and Mineral Resources

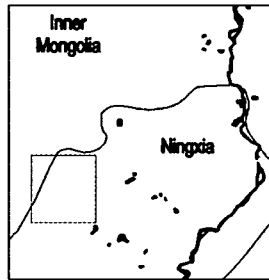
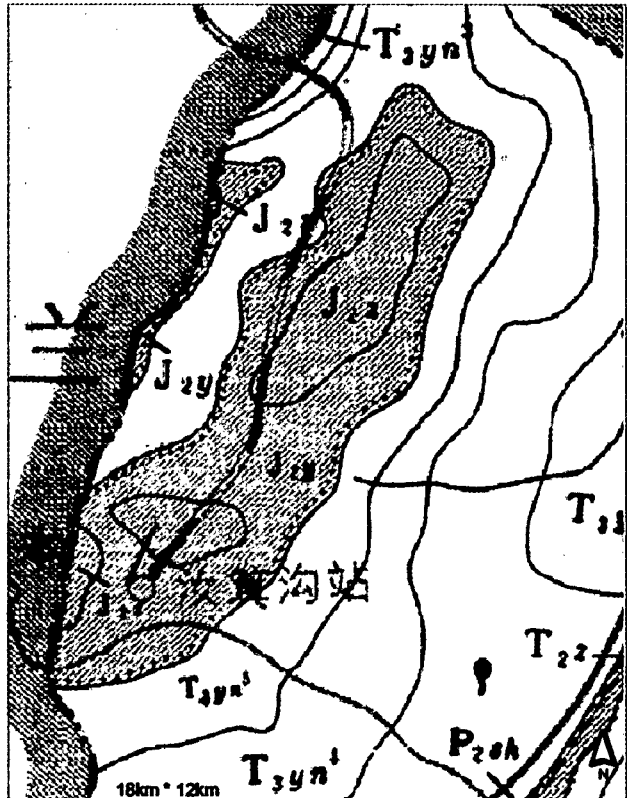
Wuda coal mining area and broader surrounding



Legend:

- Q4al: Undivided alluvial
- Q3pal: Undivided or combined: Malan loess, Pailouyingzi Fm., Talpingzhuang Fm., proluvial and alluvial
- P1: Combined including P1x and P1s Shanxi Fm., greyish yellow sandstone, shale with bauxite and coal beds
- C2: Undivided or combination of Aman Ul Fm. and Burnbat Fm.
- O1: Combined O1s, O1z, O1k: Shangmajigou Fm. carbonates w. shale, Liangjieshan Fm. dolomitic limestone and shale, Yeli Fm. dolomite w. shale
- E2+3: Combined, including E2m, E2x, E2z, E3g, E3c, E3f, limestone and dolomite dominated
- P2: Combined, including Wangquankou Group chert banded dolomite, siliceous limestone w. sandstone; Huangqikou Gr. low grade metaclastics
- Argn1: Clariishan Group lower part: migmatic sillimanite garnet, hypersthene garnet or cordierite garnet gneiss with granulite
- MY1: Migmatic granites
- Yellow River (Huang He)
- Province border of Ningxia and Inner Mongolia
- Fault zone

Ruqigou / Gulaben coal mining area and broader surrounding



Legend:

- J2z: Zhiluo Formation: conglomerate, feldspathic quartzose sandstone, shale, siltstone and coal seams
- J2y: Yan'an Formation: conglomerate, gravel-bearing sandstone, fine sandstone, siltstone, shale and coal seams
- T3yn5: Yanchang Formation: Fifth rock association: shale, quartzose sandstone and feldspathic quartzose sandstone
- T3yn4: Yanchang Formation: Fourth rock association: feldspathic quartzose sandstone, arkose, siltstone, mudstone
- T3yn3: Yanchang Formation: Third rock association: greywackeous arkose, siltstone, greyish black shale with locally thin bedded coal seams
- T3yn2: Yanchang Formation: Second rock association: greywackeous arkose, shale and sandstone
- T2z: Zhifang Formation: yellowish green, purplish red feldspathic quartzose sandstone, arkose, siltstone and mudstone
- P2sh: Shiqianfeng Formation: feldspathic quartzose sandstone, sandy shale, siltstone, mudstone and dacite liparite tuff
- Province border of Ningxia and Inner Mongolia
- Background of map
- Fault zone

Layout and GIS: Claudia Künzer
German Remote Sensing Data Center
Environment and Geoinformation
Germany

Data source: Geological Map of Nei Mongol Autonomous Region, the Peoples Republic of China, 1:1,500,000 and Geological Map of the Helan Mountains, 1:500,000

- Map 2 -





Figure 2-1: Small area of pyrometamorphic rock



Figure 2-2: Sulfur minerals above a former coal fire

Photos: C. Kuenzer, 09/2002, location: 638906E, 4377468N, UTM Z48N

Next to the sulfides and sulfates in rare occasions Selenium, oxides like Hematite, Arsenolite, Cassiterite, Downeyite and Halides like Mascagnite or Tschermigite can be found (LAPHAM et al. 1980).

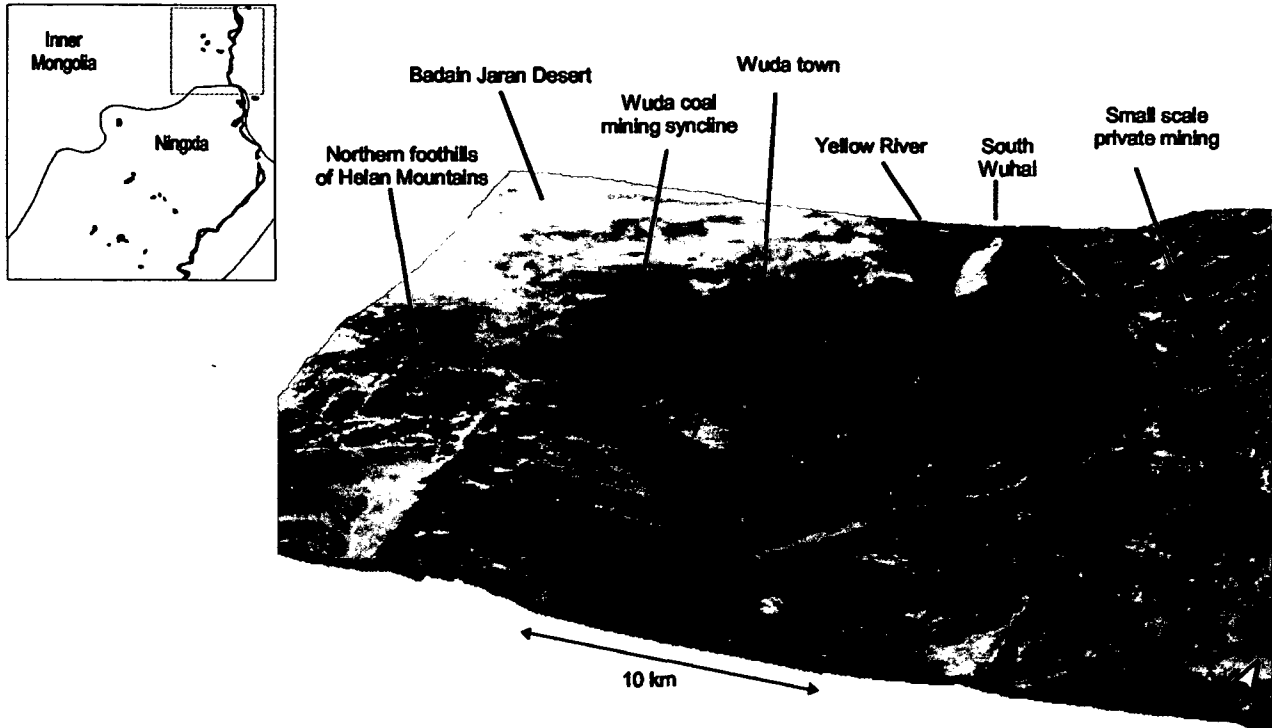
Geomorphologic features at this local scale are mainly dependent on the properties of the surface material. Apart from climate, this is the key parameter in the development of present-day morphology. Due to differential erosion hard rocks like sandstone outcrop in scarps, dip slope surfaces and plateaus, while soft bedrock like siltstone or shale with a lower resistance to weathering outcrop in gentle landforms (CHEN 1997). Four types of landforms occur in the Ruqigou study area: structural denudational landforms like dip slopes, face slopes and structural plateaus, denudational landforms that are near vertical scarps, denudational slopes, denudational valleys, asymmetric hills and foot slopes, alluvial landforms including flood plains, alluvial terraces and alluvial fans and anthropogenically induced landforms. This last type can be further classified into opencast coal mining areas with complete removal of overburden, opencast mining with partial removal of overburden, mine dump areas, underground coal mining areas, cut-slopes, artificial lakes, subsidence areas and residential areas (CHEN 1997).

The broader Wuda study area is characterized by less varying relief than the Ruqigou / Gulaben area, since the region is not located within the Helan Shan. The Wuda syncline itself has a slightly undulating terrain with gentle slopes. Elevations range from 1030 to 1350 meters. Opencast coal mining as in the Dafeng open pit mine of Ruqigou does not exist. Coal mining activities in general are of smaller scale. Therefore, resulting landscape changes due to mining are less accentuated. Furthermore, artificial lakes – such as those existing in the Ruqigou area – are also not present in the Wuda area. Land subsidence resulting from coal fires occurring due to the volume loss underground is widespread and shows as slow trough-like subsidence, sudden doline-like or large area subsidence. Furthermore, many small scale cracks and crack fields on the surface dissect the bedrock layers in both study areas (ZHANG, J. et al. 2004a, RATHORE & WRIGHT 1993, GANGOPADHYAY 2003).

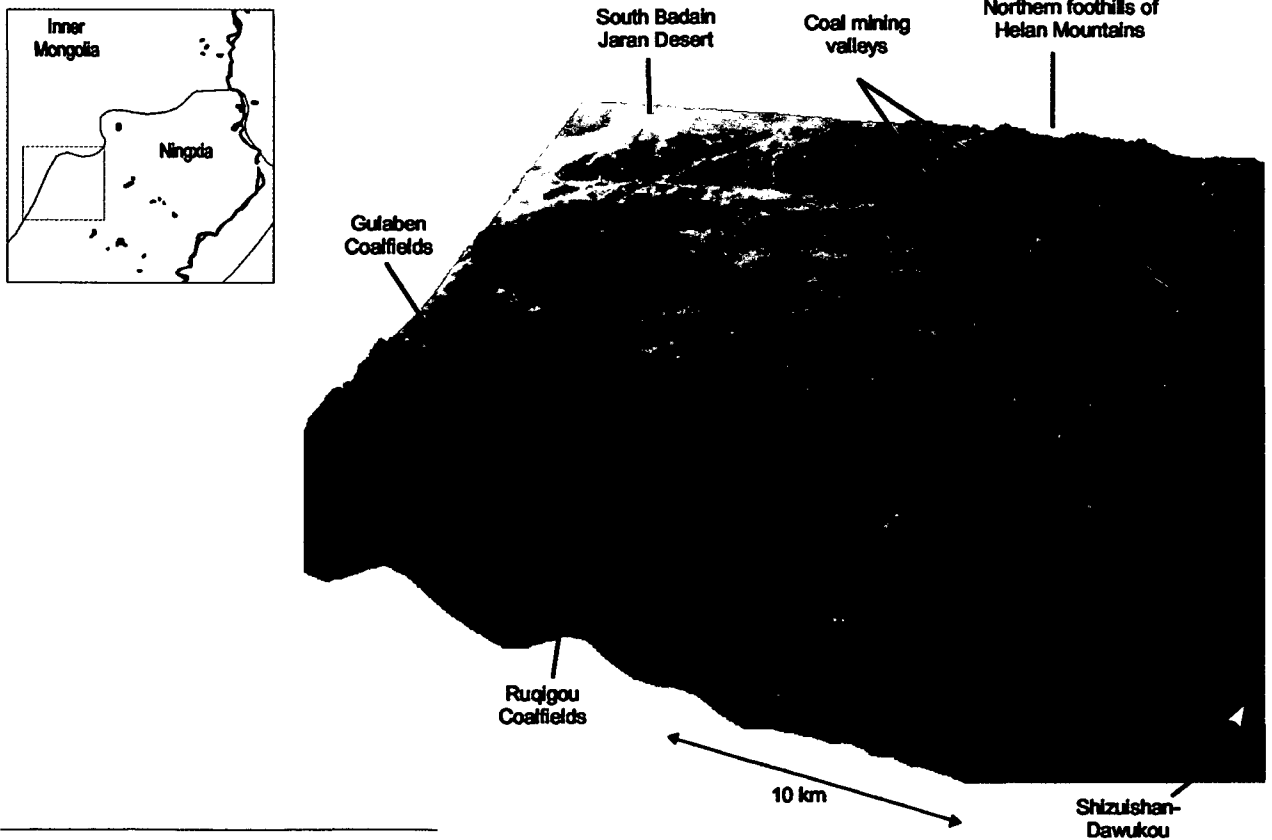
A general impression of the study areas topography is given with map 3 on the next page.

General Characteristics and Topography of the Study Areas Wuda and Ruqigou / Gulaben
as seen in Landsat-7 ETM+ data from September 2002 combined with a digital elevation model (DEM)

Wuda coal mining area and broader surrounding



Ruqigou / Gulaben coal mining area and broader surrounding



Layout and GIS: Claudia Künzer
German Remote Sensing Data Center
Environment and Geoinformation
Germany

Data source: Landsat-7 ETM+ scene of 21.08.2002, displayed: channels 7,5,3 as RGB draped over ERS derived digital elevation model (DEM), terrain elevation displayed with factor 4

- Map 3 -



2.3. Climatic Characteristics

The climate of Wuda, Ruqigou and the surrounding area can be characterized as a transitional climate between a B1sa climate and a CIIa climate, indicated by the climate classification of LAUER and FRANKENBERG (1986). The B1sa class represents a subtropic, strongly continental, semi arid climate, while CIIa indicates a middle latitude, strongly continental, fully arid climate. Diagnostic features for both are large daily and seasonal temperature amplitudes. Winters are cold and long, summers can be very hot, precipitation amounts are low and winds are strong.

The main climatic system influencing the study area is the East Asian Monsoon (XIE 2001). Unlike the Indian Monsoon, this monsoon outside the tropics at about 40° latitude does not necessarily bring large amounts of precipitation. In winter the polar front is pushed back far to the South. The weather in East Asia (China, Japan) at this time of the year is mainly influenced by the prevailing Westerlies and their traversing cyclones (lows). At the backside of frontal cyclones rapid intrusions of cool air from Inner Asia (near surface thermal Russian High) can occur, leading to near surface northerly to north westerly winds in Wuda, Ruqigou and adjacent regions. In early summer and summer the Inner Asian near surface thermal Low leads to a shift of the northeastern trade winds to southeastern winds on the continent. Due to their small vertical extent these southeastern trade winds can only transport small volumes of water. Precipitation in the study area is mainly autochthon resulting from the convergence of the Westerlies with the southeastern trade winds. Thus the cyclones are the main sources for precipitation. During the summer season southeasterly winds dominate the study area (WEISCHET 1988). Long term measurements at the climate station Yinchuan (1112m asl.) show an average annual temperature of 8.6°C, an average annual precipitation of 193 mm, an average absolute daily maximum of 39.3°C and an average absolute daily minimum of -30.6°C. In January the average daily temperature is -8.4°C, in July 17.7°C (URL 2-1). In Baotou (Inner Mongolia), 300 km northeast of Wuda average annual temperature is 6.4°C (RICHTER 1996). An average of 3,230 sunshine hours per year is recorded for Wuda. Climate data for Wuda, Ruqigou and Gulaben is presented in table 2-1 below.

Table 2-1: Climate data for the main study areas

	Wuda	Ruqigou	Gulaben
Precipitation	168 mm/a	238 mm/a	200 mm/a
Potential Evaporation	3,500 mm/a	2,720 mm/a	2500 mm/a
Temp. Min. / Max.	-26.7°C / 39.6°C	-31.0°C / 35.0°C	-45.0°C / 41.0°C

Source: HALIK et al. 2003, modified

In Wuda first nights with frost can be expected around the middle of September and in spring last frost nights occur around the end of April. In Ruqigou, the first and last frost days are shifted due to the location at higher elevation. At a broader scale, including the whole province of Ningxia and the south central part of Inner Mongolia, precipitation decreases from the South to the North. Therefore, precipitation in Wuda is substantially less than in Yinchuan. It averages 168 mm and is distributed to 7-20 days within the year (JIA 2003, SUN 2003). The annual precipitation curve for the broader study area shows single modal properties, with the highest rates occurring in July and August. Annual evaporation rates of well above 2500 mm lead to a water shortage in surface flows and underground (CHEN 1997, WU & ZHANG, 2003). For areas located alongside the Yellow River the influence of the

river can be seen in a slight weakening of daily as well as annual temperature amplitudes and the tendency for morning fog in adjacent regions. It should be noted that the presented average values underlie significant variations due to differing elevation zones, aspect and microclimatic phenomena (ROSEMA et al. 1999).

Concerning possible climatic trends analyses of meteorological data over the past half century indicate an increase in annual temperature and a decrease in annual precipitation for the broader study area. Increasing soil- and vegetation degradation, salinization and a decreasing number of small lakes and reed areas accompany these observations (WU et al. 2001, WU & ZHANG 2003). A phenomenon occurring on average at 75 days within the year are sandstorms, which lead to the intrusion of desert sand into agricultural areas and support the deflation of the top soil and coal dust (HALIK et al. 2003).

2.4. Hydrographic Characteristics

Due to the extremely small amount of precipitation, inland waters like lakes hardly exist (with some exceptions in the vicinity of Yinchuan) and most fluvial features in the region – like creeks, wadis, and small rivers – are seasonal. One exception and the most distinct hydrographic fluvial feature in the study area is the Yellow River, *Huang-He*, running from South to North through Ningxia Autonomous Region and into Inner Mongolia Autonomous Region. The river has not been channeled and the width of its bed shows annual changes. This results in extensive alluvial flood plains on both sides. The water of the Yellow river is extremely rich in sediment and has a light brown color. Although pollution levels are high the river is the most important water supply for agricultural irrigation. Over the course of the last 15 years the average water level of the river has declined due to the high water demand of the steadily growing mining communities (JIA 2003, SUN 2003, VERBURG et al. 1999). Two smaller rivers are the *Xi Ganqu* and the *Di'er Nongchang Qu* running parallel to the Yellow River along the foothills of the Helan Shan.

Further distinct hydrographic features close to Wuda are wadi beds with only seasonal water flow stretching from the foothills of the mountain chains East and West of the Yellow River towards their erosion base. The runoff from the mountains in the Wuda area is nearly 100% due to absence of soil and vegetation, accounting for large water volumes transported in the wadi beds in times of rainfall or snowmelt. In Ruqigou, three small braided rivers cross the basin, which have eroded deeply incised valleys. Their runoff is seasonal but can also reach high volumes during heavy rain events or snowmelt in the spring (ROSEMA et al. 1999). Ground water does not play an important role in the region since water for irrigation is pumped from the nearby rivers and, except for the Yellow River area, sufficient ground water horizons are usually out of reach. The groundwater quality in Wuda is not adequate for consumption due to its high mineral content. In Ruqigou and Gulaben the water supply is provided by water trucks.

2.5. Soils and Natural Vegetation

Bedrock materials for soil development in the region are sandstone, shale, limestone, desert sand, other aeolian deposits (loess) and river-terrace- or alluvial fan material with gravel and boulders. Due to the arid climate physical weathering outweighs chemical weathering and soil development progresses slowly. Therefore, large areas especially in the mountains and structural hill slopes have no soil cover but weathered bedrock, a cover of aeolian sand or coarse alluvial fan material. Soils

occur mainly on the irrigated river terraces of the Yellow River and on its actual floodplains as sandy, silty and loamy types. Clays are rare but can occur locally. Generally the soils of the region (except the ones influenced by rivers) belong to the class of grey to brown half-desert and desert soils including calcisols, gypsisols, leptosols, solonetz and solonchaks (DRIESSEN & DUDAL 1991). Within the US soil taxonomy they are classified as Inceptisols and Aridisols (BRADY & WEIL 1996).

Allocton alluvial loams sedimented by the Yellow River are the most fertile soils in the study area. Apart from these soils influenced by the river, soils developed from limestone dominated material are usually rich in clay minerals, bases and nutrients. They are therefore more fertile than soil developed from quartz dominated material with a more sour and less nutrient-rich character. The higher the amount of clay within a soil, the smaller the pores and the slower the infiltration of water. This leads to the genesis of small temporal wetlands after flooding along the Yellow River or after rain events in clay-rich plains. Water also plays a major role in the process of crusting. Some alluvial fans or even sand dune areas show a grayish crusting covering the top horizon or sand. This crusting contains fine silty material, coal dust and small organic particles of fluvial and aeolian origin baked together through the influence of intense precipitation and slow surface run off. Crusts reduce the soil's infiltration capacity, hamper the germination and development of vegetation and reduce the water retention capacity of the topsoil as well as aeration processes (VAN DER MEER & DE JONG 2001).



Figure 2-3: Thick Yellow River deposits – clay loam



Figure 2-4: Crusting of top soil on an alluvial fan

Photos: C. Kuenzer, 09/2002, location: 651654E, 4358416N, UTM Z48N

Vegetative cover in general is very sparse. Especially patches of trees are rare. The dominant tree species are Maple (*Acer campestre*, *Acer davidii*), Chinese Poplar (*Populus lasiocarpa*) and Chinese Ash (*Fraxinus chinensis*). Some wooded areas occur naturally, but often trees have been planted as barriers against wind and the aeolian intrusion of desert sand into agricultural fields or residential areas. The most common vegetation cover are dry desert shrubs with partially sclerophyllous leaves, which are dominated by *Tetanea mongolica*, *Reaumuria soongorica*, *Bassia dasyphylla* and species of *Artemisia* (JAEGER 2003). They occur in varying ground cover densities from zero to 80%. Annual drought-deciduous species show a high photosynthesizing capacity and water use efficiency during the short weeks when soil moisture is high and photosynthesis is possible.

Very rare in the close vicinity of Wuda, but more common further south, are belts of reed found at seasonal flooded flats close to the Yellow River. Sparsely distributed grasslands can be found in the Helan Shan mountains and on gentle hill slopes and alluvial fans (CHEN, 1997).

In most cases the areas covered with shrubs or grasslands are used to feed cattle, sheep and goats, which leads to strong grazing pressure. In several research projects it has been shown that more than 70% of the naturally vegetated surfaces in the study area are degraded and species structure and composition have been altered and simplified. Soil erosion is commonplace (JIA, 2001, XIE 2001).

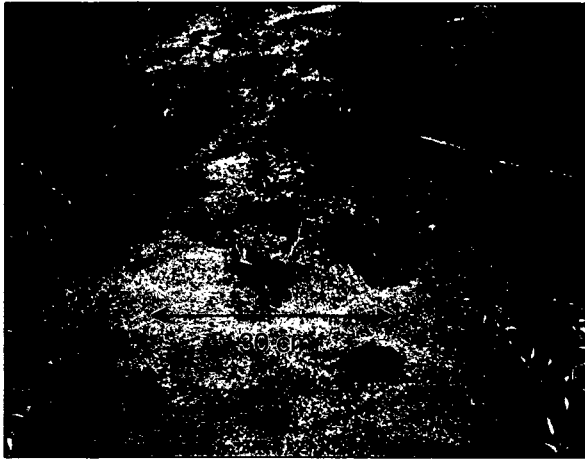


Figure 2-5: Shrubs on desert sand



Figure 2-6: Shrubs in a sparsely settled mining area

Photos: C. Kuenzer, 09/2002, locations: 646647E, 4368793N (2-5) and 641226E, 4371746E (2-6) UTM, Z48N

2.6. Socio-economic Characteristics

Ningxia Hui Autonomous Region has 5.3 Million inhabitants of Hui-, Han- or Manchu nationality. Many Chinese living in Ningxia are Muslims (URL 2-2). Inner Mongolia Autonomous Region has 22.3 Million inhabitants, who either belong to Han-, Hui-, Mongolian-, Daur-, Ewenki-, Oroqen- or Manchu ethnic groups. The broader study area around Ruqigou and Wuda has an estimated average population density of 25-50 inhabitants per km². The biggest cities are Shizuishan-Dawukou with 670,000 inhabitants, Wuda city with ca. 50,000 inhabitants and Wuhai city in the Northeast of Wuda with more than 100,000 inhabitants. The larger Wuhai district including the outskirts of the main cities has over 420,000 inhabitants. Ruqigou and Gulaben have approximately 40,000 and 3,000 inhabitants, respectively (HALIK et al. 2003). Houses are predominantly built of bricks or a mixture of loam and straw. Most of the households have electricity but running water is less common – many families have a weekly water supply in tanks. Street access is possible to most places, although some settlements can only be reached on dirt roads or wadis.

The predominant employment in the Wuda region and surroundings are coal mining and related activities. Coal mining takes place in state-run, locally-controlled and private mines. Coal mining related industry includes coal washing, coal cooking and coal power plants. Further industries in the area are limestone processing and related calcite and cement factories, dolomite processing, the exploration of phosphorus deposits, brick burning and loess mining. Also, gypsum production, clay mining, quartz mining, iron oxide processing and lead and zinc mining are found locally. A good network of roads and railways has been developed in the broader area, which enables the transportation of coal and other products to the neighboring provinces and bigger cities. However, especially the transport of coal and coal products by road produces a lot of fly-ash polluting the close vicinity of roads. Most of the secondary sector industries are emission intensive and cause heavy industrial smog, resulting in limited visibility and steadily increasing environmental pollution. In

addition to coal related industry and other industry the primary agricultural sector is another main source of income for the local inhabitants. Commercially grown food products include corn, wheat, sunflowers, rice, potatoes, soybeans, grapes, melons and vegetables. Many households also practice subsistence agriculture and cultivate small and highly fragmented patches of land. These activities are mainly restricted to the flood plains of the Yellow River, irrigated river terraces and other irrigated areas. Irrigation activities and cultivation of bare land have increased especially since the economic reform at the end of the 1980s with resulting land cover changes in the Yellow River Valley and plains (WU & ZHANG 2003). In Ruqigou and Gulaben agriculture is spatially very limited and in many areas hardly possible. The sparsely distributed grasslands in the Helan Shan and the shrub covered areas of alluvial fans are common grounds for grazing, facilitating livestock raising and wool production.



Figure 2-7: Coal processing factory

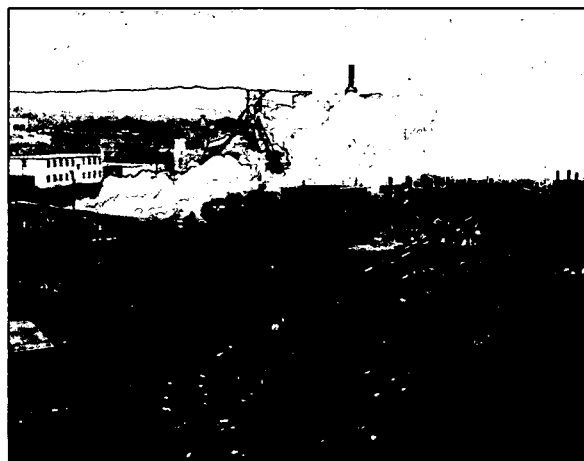


Figure 2-8: Coal processing factory



Figure 2-9: Calcite burning near a limestone mine

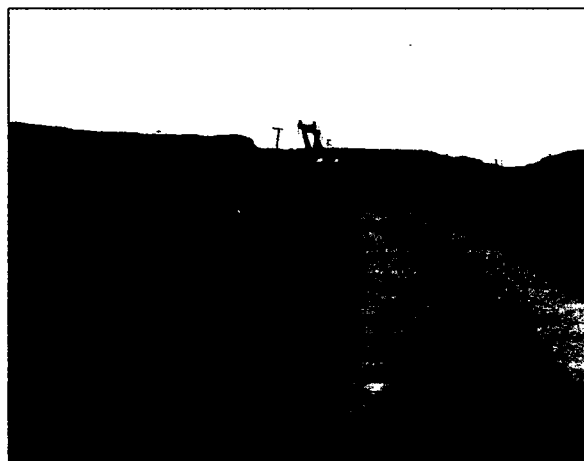


Figure 2-10: Clay mining

Photos: C. Kuenzer, 09/2002, locations: 673454E, 4360063N (2-7), 665130E, 4356929N (2-8), 663747E, 4361470N (2-9), 654976E, 4365744N (2-10), UTM, Z48N

Average wages range between 700 RMB per month (ca. 90 €) for a coal worker in a state run mine, who works an average of 10 hours a day, 400 RMB per month (ca. 50€) for a middle school teacher and less than 160 RMB (ca. 20€) per month for a small farmer (JIA, 2002). At the same time Chinese labor productivity is very low compared to other countries. The average coal output per employee is 163 t/y which is only 1/20th of that of a worker in e.g. South Africa (DANIEL 1994). Average life expectancy is 68.62 years and the illiteracy rate of 23.1% – of which 67.3% are women – is still quite high (URL 2-2).

2.7. Impact of Coal Mining and Coal Fires

Since commercial mining in the Wuda syncline started in 1958, 120 megatons have been mined by 2000. Mainly mechanized longwall methods are applied and the average mining depth of state run- or commercial mines is around 100m but can reach up to 200-300 m. The first coal fires in the area were discovered in 1961. The recent annual amount of coal being burned is estimated to be 200,000 tons. An acceleration of the process from year to year is observed. It is assumed that so far, over one Mio. tons of coal have been destroyed or became inaccessible due to coal fires. However, no attempt has been made to date to really quantify the total coal loss within the last 35 years. Knowledge about the influence of the numerous small profit mines is difficult to access. Today 8.8% of the three coal mining areas in the syncline are affected by coal fires and the coal fire area has an extent of 3.07 km² (JIA, 2002). Eight coal seams are burning: seams 1, 2, 4, 6, 7, 9, 10 and 12.

Small scale private mines with a low level of mechanization and poor safety standards pose the greatest threat concerning the development of new coal fires or the ventilation of existing fires. Private mining has been permitted since 1980 as long as mine shafts are not drilled deeper than 300 m from the mine entrance into the strata. However, many of the formerly over 100 small scale private mines scattered along the seam outcrops are now abandoned, after coal fires made mining too dangerous. Governmental laws led to the closure of many private mines. Since mine entries and ventilation systems were in most cases not properly sealed off, these abandoned private mines are still risk areas for spontaneous combustion of coal seams. The same is true for coal waste- and leftover coal storage piles. The coal in the Wuda area is particularly prone to this catalytic effect of self ignition.

The fires in Wuda are monitored by mine engineers and mine administrators and have been numbered to provide a common reference. In 2000, an assessment of the boundaries of the coal fires by satellite data, GPS-field measurements and geologic analysis was undertaken (JIA, 2002). Thermal measurements and borehole drillings supported these activities. The result is a map of Wuda syncline with 16 demarcated coal fire areas. Furthermore it was found that coal fires are burning not only close beneath the surface, but up to depths of 50-100 meters (JIA, 2002). Before 1989 most coal fires in Wuda were isolated and scattered in different locations. The isolated fires started to connect gradually between 1989 and 1995 (GANGOPADHYAY, 2003). The changes in coal fire dynamics observed between the field visits in 2002, 2003 and 2004 were dramatic. Fires 13-1 and 13-2 had merged, fire 6 and fire 8 had spread to the North and South and fire 3 had shifted southeast. A new very hot coal fire had developed between fires 6 and 8.

In Ruqigou and Gulaben governmental mining started in 1960. By this time many private small scale mines already existed. In the year 2000, 4 Mio. tons were mined in the three major mines of Ruqigou (Dafeng open pit mine, Ruqigou- and Baijigou underground mines) and 1 Mio. tons were produced in the 7 mines of the Gulaben area, belonging to the Inner Mongolia Taixi Anthracite Company, which exports 30% of the mined coal to the world market. About 55 private mines still exist next to these major mines. At present, the mines in the Ruqigou area are affected by at least 20 coal fires, most of which are currently under the process of extinction. In the Gulaben area, seven active fires are reported. All are related to former or present small scale commercial mining. In Gulaben alone the total coal fire area is estimated to 0.96 km². Here 10 Mio. tons of coal are affected and 500,000 tons of coal have already been lost. The total area affected by coal fires is assumed to cover more than 2.32. km² (Ruqigou / Gulaben).



Figure 2-11: Coal mining in Ruqigou



Figure 2-12: Coal infrastructure in Wuda



Figure 2-13: Coal miner in Wuda



Figure 2-14: Housing of a coal miner in Wuda

Photos: C. Kuenzer, 09/2002, locations: 598416E, 4327298N, (2-11), 639280E, 4373504N (2-12 to 2-14), UTM Z48N

Obvious indicators of underground coal fires in both study areas are abundant cracks in the surface as well as land subsidence due to the loss of volume underground (ZHANG, X., 1998, ZHANG, J., et al. 2004a). It has been found that joints in the geologic strata also play a leading role in subsidence occurrence and coal fire formation (CHEN 1997). In addition to rockfalls, landslides, cracks and large scale subsidence other environmental problems resulting from burning coal fires are manifold. Heavy smoke, rich of carbon-monoxide (CO), carbon-dioxide (CO₂), methane (CH₄), sulfur-dioxide (SO₂), nitrous oxides (NO_x) and other green-house relevant and toxic gases (e.g. H₂S, N₂O), emit from openings in the overlying strata. Chemical calculations indicate that burning of one ton of coal leads to an average emission of 1.17 tons of CO₂ and 0.17 tons of methane, with the latter having a 21-fold higher greenhouse potency than CO₂. The gases and the underground heat are responsible for the deterioration of vegetation directly above the coal fires. Additionally, coal ash and aerosols are also deflated to adjacent areas, where increasing air pollution can be noticed (HALIK et al. 2003).

A further environmental problem indirectly induced by coal fires is the steadily increasing water pollution. Since the self purifying capacity of a water body is (amongst others) depending on the water volume, the arid conditions and precipitation deficit raise the vulnerability of the area for water pollution through fluid mine waste, coal ash and toxic compounds (LAPHAM et al. 1980, RATHORE & WRIGHT 1993). Since the sparse water sources are used for irrigation, the pollutants easily reach the

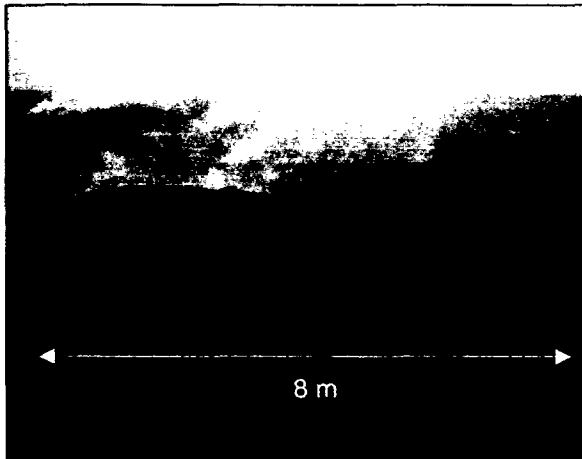


Figure 2-15: Cracked surface due to coal fires

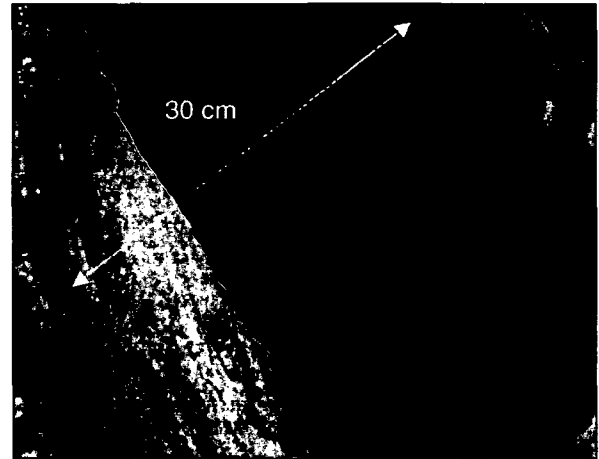


Figure 2-16: Coal fire in Wuda during daytime

Photos: C. Kuenzer, 09/2002, location: 639090E, 4374824N, UTM, Z48N

food chain. Compared to areas not affected by coal fires, elevated levels of copper (Cu), zinc (Zn), fluoride (F), lead (Pb) and cadmium (Cd) have been proven in common crops. Investigations of the health conditions of local inhabitants have furthermore shown a general decrease of immune system activity and an increased risk for respiratory tract illnesses, tuberculosis and lung cancer (CHEN 1997).

Though environmental impacts are obvious the main motivation for coal fire fighting in the study areas is an economic one. In all mining areas intensive fire fighting activities have been undertaken. In Ruqigou fire fighting already started in 1978. Due to the higher quality of coal in the Ruqigou-Gulaben area more governmental funding is provided for the development and application of extinguishing techniques than in Wuda and procedures in this region are more successful. Coal fires are fought by sealing off the fires, filling the cracks and openings, pouring water or colloidal mixtures into cracks or boreholes, covering fires with loess and excavating burning parts of the coal seam. All possible extinction methods either aim at the removal of the combustible, the lowering of the temperature, the cutting off of the oxygen supply or a combination of these. In Wuda over 10 Million Yuan (> 1.2 Million Euro) have been invested in coal fire fighting until 2003 (JIA, 2003). However, many fires are still burning, spreading and are not under control. Research has to be undertaken to improve the early detection and long term monitoring of coal fires.

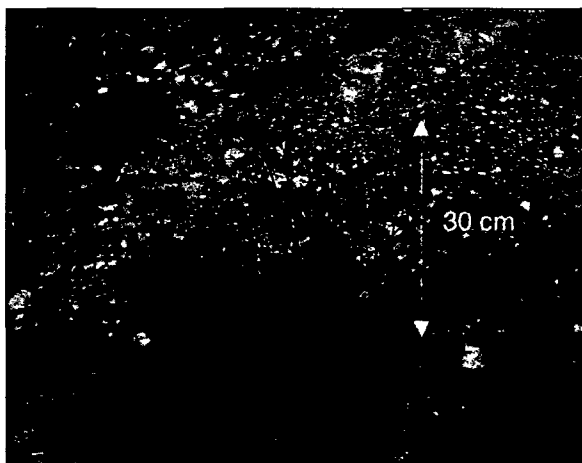


Figure 2-17: Dead vegetation due to coal fires



Figure 2-18: Woman wearing a face mask against the gaseous emissions, Photos: 2-17: C. Kuenzer, 09/2002, 2-18: S.Voigt, 08/2001

Photos: 2-17: C. Kuenzer, 09/2002, 2-18: S.Voigt, 08/2001

3. Theoretical Background: Image Classification and Feature Extraction

This chapter presents the theory and state of the art on image classification and feature extraction considering different approaches and techniques, combinations of the latter as well as case studies. This theoretic complex is the basis for the algorithm design for coal fire area demarcation.

Within the last decades several approaches and algorithms were developed to classify image data (FRIEDL & BRODLEY 1997, RICHARDS 1986, TSO & MATHER 2001, LILLESAND & KIEFER 1994). These methods base on the fundamentals of pattern recognition, where a pattern is defined as a vector of features describing an object. These features – in the case of image processing defining a pixel or a cluster of pixels – can be spectral reflectance, thermal emittance, radar backscatter, secondary derivatives like texture, spatial contextual information or physical values like elevation, slope or aspect. The final goal of the pattern recognition process is the establishment of a link between the patterns and class labels (TSO & MATHER 2001). The extensive number of approaches is roughly grouped into the main classes presented from chapters 3.2. to 3.12.. Generally speaking, spectral classifiers can be split into the two main categories of parametric and non-parametric classifiers. The first are defined by the assumption of an underlying probability distribution of the data, while the latter do not assume information about the probability distribution (CORTIJO & PEREZ DE LA BLANCA 1997, 1998, SCHOWENGERDT 1997). Furthermore, unsupervised and supervised classifiers, contextual and non-contextual methods can be distinguished (KRAUS 1990, KEUCHEL et al. 2003). Most important: it is impossible to say whether one classifier is better than another, since each classifiers performance depends on the data. Depending on their differentiation methodologies, some classifiers or extraction tools are preferred for multispectral data, while others are mainly used for hyperspectral data or work for both inputs. Some yield better results for global, others for local data sets; some require a trained image analysis expert or extensive ground knowledge, while others need no further input or expertise.

In the examples given, the field of radar data classification and feature extraction based on amplitude or coherence data and parameters like frequency is not treated. This would go beyond the scope of this work. Detailed studies in the field of radar based land cover type discrimination are presented by BLOM & DAILY (1982), DEROIN et al. (1998), BELCHANSKY & DOUGLAS (2000), BENEDIKTSSON & SVEINSSON (1997), HAAK (1984), HEIKKONEN et al. (1997), DOUSSET (1995), GAVEAU et al. (2003), HUBER (2001) and WAGNER et al. (2003), amongst others.

3.1. Feature Space Manipulation Techniques

A central problem for image classification and feature extraction results from the high data volume of multi-band satellite images or multitemporal time series (LUNETTA & ELVIDGE 1999, RICHARDS 1986). Hence, a common technique applied before pattern recognition is feature space manipulation to reduce the dimensionality of the often high-dimensional data cubes or to manipulate the data in a way that the maximum information content can be retrieved. TSO & MATHER (2001) give the example that in an 8 bit Landsat-7 ETM+ scene with 7 bands each pixel could theoretically occupy one of 7×10^{16} discrete locations in feature space. According to the Hughes phenomenon (HUGHES 1968) the effectiveness of a classifier will begin to decrease if a certain number of dimensions is exceeded. At

the same time it is known that e.g. the first three channels of Landsat TM or ETM+ data are highly correlated and often have correlation coefficients exceeding 0.9 (HILL 1993a). Feature space reductions and manipulations can therefore help to increase classification accuracy and enhance computing speed (LILLESAND & KIEFER 1994). Amongst many similar approaches the most common feature space manipulation techniques are Principal Component Analysis (PCA), the Minimum Noise Fraction transformation (MNF), Intensity-Hue-Saturation transformation (HIS), (TSO & MATHER 2001, RICHARDS 1986) and the Tasseled Cap Transformation (TCT). Since the last two are not of further relevance for this thesis it is referred to the literature, such as KAUTH & THOMAS (1976), LILLESAND & KIEFER (1994), RICHARDS, (1986), HILL (1993a), CRIST & CICONE (1984), DAVE (1981), SKAKUN (2003), KUENZER, (2001) and NETELER (1999).

The PCA is a variance analysis of a data set designed to remove the spectral redundancy amongst channels. Applying a PCA orthogonalizes the features within the n-dimensional feature space and orders the components according to their contribution to the overall variance of the data set. The first step in PCA is the calculation of the correlation matrix of the image bands followed by the extraction of eigenvalues and eigenvectors from that matrix and the final transformation of the feature space's former coordinate axis using these eigenvectors (RICHARDS 1986, TSO & MATHER 2001, NETELER 1999, BENEDIKTSSON & SVEINSSON 1997). Linear transformations in general are of the form:

$$DN' = W \cdot DN = \begin{bmatrix} W_{11} & \dots & W_{1K} \\ \dots & \dots & \dots \\ W_{K1} & \dots & W_{KK} \end{bmatrix} \begin{bmatrix} DN_1 \\ \dots \\ DN_K \end{bmatrix} \quad (3.1)$$

where W is the transformation matrix defining the weights for each of the spectral bands defining a coordinate rotation and scaling of the DN to DN' . PCA is of the form:

$$PC = W_{PC} \cdot DN \quad (3.2)$$

altering the covariance matrix of a data set C_{PC} according to:

$$C_{PC} = W_{PC} C W_{PC}^T \quad (3.3)$$

The detailed calculation of the PCs is presented in SCHOWENGERDT (1997) and RICHARDS (1986). Mathematically speaking, the PCA is a rotation of the original coordinate axes in the n-D feature space to then coincide with the principal axes of the data. The coefficients of the transformation are a function of the data spectral covariance matrix. Therefore, it is important to note that the PCA is data dependent. After applying a PCA, the first axis of the feature space points into the direction of the largest extent of the data cluster. The second axis points orthogonal to it into the direction of second largest variance and so forth. This indicates that with decreasing component number less of the variability within the data set is explained (LI & YEY 1998). The result of a PCA are PCA images with each band containing one component, being synthetic features, since the new axes resulting from the rotation are not pre-defined by the user. Due to the newly generated synthetic features, which are sometimes hard to interpret (LUNETTA & ELVIDGE 1999), preprocessing steps like an atmospheric or illumination correction are not necessarily mandatory (HILL 1993b).

The Minimum Noise Fraction transformation (MNF) – sometimes also referred to as Maximum Noise Fraction Transformation – produces components, which successively maximize the signal to noise ratio (TSO & MATHER 2001) requiring estimates of the variance-covariance matrices of signal and noise of an image, where the latter is often hard to obtain. The problem of PCA, where decreasing components do not necessarily lead to decreasing image quality, is overcome by sorting the transformed bands based on the SNR. The assumption for the estimation of noise is based on:

$$DN(x) = S(x) + N(x) \quad (3.4)$$

and the theory that variation of the Signal S between a pixel and its neighboring pixel is nearly 0, while noise N, varies and the difference between two neighboring pixels can be explained by varying noise; an assumption which is of course only true for very homogeneous surfaces and can also lead to problems if real structures within the image are explained as noise (SCHOWENGERDT 1997, UNDERWOOD et al. 2003).

The MNF transform (GREEN et al. 1988) is essentially a two cascaded Principal Components transformation, where the first transformation, based on an estimated noise covariance matrix, decorrelates and rescales the noise in the data. This results in transformed data, where the noise has unit variance and no band-to-band correlations. The second step applies a standard Principal Components transformation to the noise decorrelated data. For further spectral processing, the inherent dimensionality of the data can be determined by examining the final eigenvalues and the associated images. The data space therefore can be divided into two parts. One is associated with large eigenvalues and coherent eigenimages, while the second complementary part shows near-unity eigenvalues and noise-dominated images. By using only the coherent portions, the noise is separated from the data, thus improving spectral processing results (GREEN et al. 1998, RSI 2003).

3.2. Unsupervised Classification Algorithms (UCA)

Unsupervised classification approaches (UCA) aim to identify all spectral clusters without training data or ground truth of the area. To apply an unsupervised classification algorithm the user does not need a-priori knowledge of the image and in most cases only has to specify the initial number of clusters the algorithm shall generate. The most generally used method of unsupervised pattern recognition is the basic migrating means or ISODATA clustering algorithm. It accepts from the analyst the number of clusters to be located in the data. The algorithm then randomly locates artificial cluster centers within the multidimensional feature space, before assigning each pixel to the cluster with the closest arbitrary mean vector. To quantify spectral similarity, spectral distance measures like the Euclidean distance (D_E) are used, where the distance between two pixels x_1 and x_2 is calculated as:

$$D_E(x_1, x_2) = \|x_1 - x_2\| = \sqrt{(x_1 - x_2)^t (x_1 - x_2)} = \sqrt{\sum_{i=1}^n (x_{1i} - x_{2i})^2} \quad (3.5)$$

Here n represents the number of channels and t denotes the matrix transpose. Other than D_E many distance measures between two locations in feature space exist, such as the Mahalanobis distance, the Bhattacharyya distance, the Jeffries-Matusita distance or the divergence or angular distance. Definitions can be found in SCHOWENGERDT (1997).

Following the distance estimation, revised mean vectors for the single classes are computed in an iterative process until spatial change of the mean vector is below a certain significance threshold. A commonly used criteria for the quality of a clustering process is the sum of squared distances (SSD):

$$SSD = \sum_{C_i} \sum_{x \in C_i} (x - m_i)' (x - m_i) \quad (3.6)$$

where m_i is the center of the cluster and $x \in C_i$ is the assigned spectral vector.

Theoretically, the sum of the SSD would be 0 if only one spectral vector is assigned to each cluster. This would end the clustering process. Practically, iterative cluster analysis is ended through a defined convergence criterium: $SSD < SSD_{max}$. Then the analyst has to determine the land cover identity of each spectral class a posteriori (LILLESAND & KIEFER 1994, CIHLAR et al. 1998).

UCA can be important to observe the spectral characteristics of a data cluster before supervised approaches are applied. In recent years, emphasis has been put on the automatic determination of cluster numbers by the algorithm itself. The aim is to generate even more user independent methods, since it is assumed that with unsupervised methods the user has no a-priory knowledge of the area and therefore cannot necessarily define the cluster number, as it is often the case e.g. with numerous large scale and time series data sets (VIOVY 2000, CIHLAR et al. 1998). Therefore, UCA are a good substitute for the usually more accurate supervised methods, when aiming at a large scale applicability like global or continental land cover classifications using medium to low resolution satellite data like MODIS or AVHRR.

Furthermore, they can outperform supervised methods, when an evenly good or only slightly weaker classification result than with supervised methods can be achieved in a very fast time. This is especially the case, when aiming at the separation of classes with distinct spectral differences, as presented by THOMSON et al. (1998). They preferred unsupervised methods to classify coasts and river corridors where surface classes could be differentiated very well.

However, UCA have several limitations. Since the algorithms strive for an overall optimum spanning of the entire data set, UCA may miss specific detailed but relevant information. This will not occur in supervised approaches, where the analyst knows about the existence of such classes, however small they may be. (CIHLAR et al. 1998, SCHROEDER-BRZOSNIOWSKY, 2000).

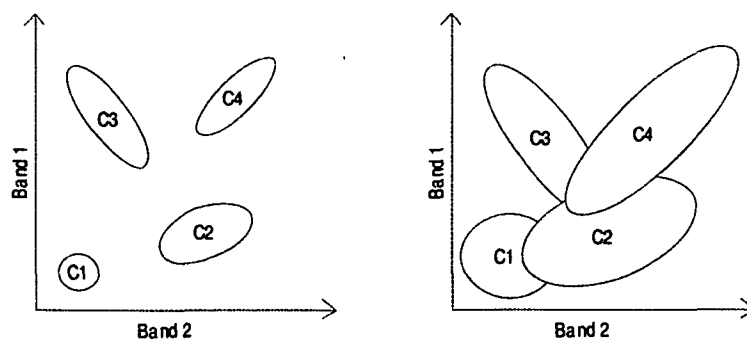


Figure 3-1: Ideal (left) and realistic (right) distribution of four classes in a 2-D feature space. In most remote sensing data sets clusters of thematic classes overlap, complicating extraction

A hybrid approach between the two was developed by CIHLAR et al. (1998) with their Classification by Progressive Generalization (CPG) algorithm. CPG is a combination of image enhancement, unsupervised classification and visual analysis including not only spectral but also spatial measures to overcome the disadvantages of UCA like cluster number definition or wrong weighting of clusters.

3.3. Supervised Classification Algorithms (SCA)

Supervised classification approaches (SCA) assume that the locations of some land cover classes / surface conditions are known accurately and the analyst therefore has a-priori knowledge of the area (CIHLAR et al. 1998).

One of the first supervised non-parametric methods developed was the minimum distance (MDC) approach. A minimum distance classifier uses the mean spectral value of classes defined through training data and computes the distance of an unknown pixel to the given class means. This distance between the pixel and the class centers is either measured as the Mahalanobis- or the Euclidean distance, with the first usually showing better classification results. The Euclidean distance, D_E is defined as shown in equation 3.5. The Mahalanobis distance, D_M , is given by:

$$D_M = (X_i - \mu_j)^t \times C_j^{-1} + (X_i - \mu_j) \quad (3.7)$$

where t denotes the matrix transposition and C_j^{-1} is the inverse of the variance-covariance matrix for cluster j . While D_M takes the shape of the frequency distribution for a given cluster within the feature space into account and therefore defines ellipsoidal clusters, D_E assumes equal variances and a correlation of 0 between the features resulting in circular clusters, sometimes leading to contrary assignments of a pixel with regard to cluster centers. In general, the pixel is assigned to the nearest class (TSO & MATHER 2001, KRAUS 1990). MDC was applied in the work of MALYUTO (2002) or CARR (1996) and others.

Contrary to the MDC method, the parallelepiped (PPC) supervised approach is always sensitive to variance considering the range of spectral values in each training class. The range can be defined as the highest and lowest digital number (DN) value in each spectral band creating a multidimensional box around the class signatures, the size of which depends on the class' inherent variance. PPC is quick and easy to implement. However, the classifier has difficulties when decision regions overlap as in the presence of covariance between two or more classes or if a pixel is not contained within the predefined parallelepipeds (TSO & MATHER 2001, LILLESAND & KIEFER 1994, KRAUS 1990).

The most frequently used maximum likelihood classifier (MLC) belongs to the class of parametric classifiers, assuming that the data is distributed according to a previously defined probability model. Parameters are defined by the training data. Each pixel $x_j \in R^d$ is classified independently by assigning it to the class $y_j \in \{\omega_1, \dots, \omega_m\}$, which has the highest a posteriori probability $P(y_j = \omega_k | x_j)$. The Bayes' rule is used to calculate these probabilities:

$$P(y_j = \omega_k | x_j) = (P(x_j | y_j = \omega_k) p(\omega_k)) / (\sum_i P(x_j | y_j = \omega_i) p(\omega_i)) \quad (3.8)$$

where $P(x_j | y_j = \omega_k)$ is the probability that x_j is observed for the given class ω_k whereas $p(\omega_k)$ denotes the a priori probability of the class ω_k , which is known approximately from ground checks. To

calculate $P(x_j | y_j = \omega_k)$ a multivariate Gaussian distribution with mean vector μ_k and covariance matrix Σ_k is assumed for each class ω_k :

$$P(x_j | y_j = \omega_k) \propto ((2\pi)^d |\Sigma_k|)^{-\frac{1}{2}} \cdot \exp\left(-\frac{1}{2} (x_j - \mu_k)^T \Sigma_k^{-1} (x_j - \mu_k)\right) \quad (3.9)$$

The resulting a posteriori probability (3.8) is maximized for a given data point x_j when it is assigned the label ω_{k^*} according to the classification rule:

$$k^* = \arg \max_{k=1, \dots, m} -\frac{1}{2} (x_j - \mu_k)^T \Sigma_k^{-1} (x_j - \mu_k) - \frac{1}{2} \ln(|\Sigma_k|) + \ln(p(\omega_k)) \quad (3.10)$$

This classification rule leads to quadratic decision boundaries between the single classes. The corresponding class-dependant parameters μ_k and Σ_k are estimated from the training data vectors x_i available for class k :

$$\mu_k = \frac{1}{n_k} \sum_{i=1}^{n_k} x_i \quad \text{and} \quad \Sigma_k = \frac{1}{n_k} \sum_{i=1}^{n_k} (x_i - \mu_k)(x_i - \mu_k)^T \quad (3.11)$$

Here n_k is the number of training samples for class k (KEUCHEL et al. 2003, SCHROEDER-BRZOSNIOWSKY, M., 2000, PAL et al. 2001). MLC therefore quantitatively evaluates both, the variance and the covariance of the individual classes when assigning an unknown pixel. A cluster of a defined class is described by its mean vector and its covariance matrix. Given these parameters the statistical probability of a pixel belonging to a particular predefined class can be computed. After evaluating the probability of membership for each of the predefined training classes the pixel is assigned to the class with the highest probability (RICHARDS 1986, YAN 2003). MLC yields the better results the farther the class means are separated from each other and the smaller the variance within the predefined classes (KRAUS, 1990). However, PATRONO (1996) states that it is often impossible to classify an entire image without segmenting or masking the original data.

The MLC approach has been applied on global (DEFRIES & TOWNSHEND 1994) and regional scales and has been modified by many authors (FRIEDL et al. 2002, KEUCHEL et al. 2003, STOLZ 1998, BARAL & GUPTA 1997). Furthermore, it has often been transformed from a so called hard classifier (0/1; either a pixel belongs to a class or not) to a semi-soft classifier, taking second and third pixel probabilities into account. Furthermore, neighborhood rules, exclusion rules or areal restriction have softened the MLC approach. Resolving the crispness of standard pixel based classifiers has been developed further e.g. with the supervised fuzzy maximum likelihood classifier proposed by WANG (1990). Here a pixel can be assigned to several classes as also presented in the study of STOLZ (1998). HUBERT-MOY et al. (2001) compared different parametric classification procedures and stress the variance of classification results and accuracies depending on the character of the study area. They state that each specific area needs an adapted classification strategy. However, overall MLC has often proven to obtain very good classifications results.

A disadvantage of MLC is the often overall “noisy” impression of output images. This can be improved through contextual methods or post-processing (WATSON & WILCOCK 2001). MLC and

other supervised approaches are furthermore limited when large areas are to be classified, which would require too much ground knowledge (cost of field data collection) (CIHLAR et al. 1998).

Though several large scale case studies prefer minimum distance, nonparametric supervised or unsupervised approaches, many research projects have clearly shown the general superiority of MLC if ground truth is available (SAN MIGUEL-AYANZ & BIGING 1997, STOLZ 1998). Comparisons of MLC with non-parametric supervised classifiers were presented by CORTIJO & PEREZ DE LA BLANCA (1997) and others. Differentiated routines like Support Vector Machine (SVM) approaches, which are supervised non-parametric algorithms have been developed only recently and are not yet applied routinely to remote sensing data (KEUCHEL et al. 2003).

3.4. Contextual or Object Oriented Classification Approaches (OOC)

While pixel based approaches only use the spectral information of the pixel, object oriented approaches (OOC) combine spectral and spatial information for classification. This is of advantage when objects with similar spectral information cannot be separated otherwise. Objects are generated by image segmentation, subdividing an image into separate regions based on measures like object statistics and -texture, object shape and topological object features. The concepts of segmentation based on "n-connectedness" and rule systems are presented in SCHOWENGERDT (1997). The segmentation process in the common OOC software *ecognition* allows segmentation based on primary features like gray tone and shape or – after an initial classification – a more advanced classification based segmentation. The multi-resolution segmentation is a bottom up region merging technique starting with one-pixel objects. The objects created on different scales can then be linked in a hierarchical object network defined by the user (BENZ et al. 2004).

Besides, OOC are soft classifiers, which take uncertainties in measurements, parameter variations, vague linguistic class descriptions and class mixtures into account. Soft classifiers base on fuzzy logic, which is a multi-value logic. It quantifies uncertain statements, where the boolean logic of "true" and "false" (or 1 and 0) is replaced by a continuous range $[0, \dots, 1]$ with 1 being "true", 0 being "false" and the values in between indicating a transition of the two. Therefore, fuzzy logic is able to approximate the real world in its complexity much better than boolean approaches. The fuzzy object feature classes are defined by membership functions (SCHOWENGERDT 1997, BENZ et al. 2004).

Overall, object oriented approaches are predominantly used for urban area classification or vegetation type and landscape-unit differentiation (ESCH 2003, BAUER & STEINOCHE 2001, KRESSLER et al. 2003, LOESCHENBRAND et al. 2003). They are generally preferred for the analysis and classification of high-spatial-resolution data like Ikonos-, Quickbird- or digital air photo data.

Some authors modified classic OOC approaches, combining them with common pixel based classifiers (KARTIKEYAN et al. 1998). KEUCHEL et al. (2003) demonstrated that the use of a contextual approach (Iterated Conditional Modes, ICM) in combination with an MLC could clearly smoothen classification results. Instead of hard classification fuzzy labelings can be used during the ICM approach handling mixed pixels more appropriately. STOLZ (1998) combined MLC and OOC using fuzzy logic theory for knowledge based classification of an agricultural area. SMITH & FULLER (2001) presented an improved method for operational land cover mapping using information on the separation landscape into land parcels to help classify the data on a per parcel basis in an object oriented approach.

Object oriented image analysis is still an extremely interactive process, since the user has to take many choices concerning cluster seeds, segmentation size, class definition etc. and over- or under-segmentation occurs easily. Furthermore, the interactive design of a class hierarchy is a tedious, time consuming process. The advantages and limitations of contextual or object oriented approaches are discussed in detail by HORNSTRA et al. (2000), ESCH (2003), MOELLER-JENSEN (1997), BENZ et al. (2004), and KARATHANASSI et al. (2000), and others.

3.5. Decision Tree Classifiers and Knowledge Based Methods (DTC)

A common and successful method to classify image data are non-parametric unsupervised decision tree classifier (DTC) approaches (CIHLAR et al. 1998). "A decision tree is defined as a classification procedure that recursively partitions a data set into smaller subdivisions on the basis of a set of tests defined at each branch or node in the tree. A tree is composed of a root node (formed from all of the data), a set of internal nodes (splits), and a set of terminal nodes (leaves)." (FRIEDL & BRODLEY 1996, p. 400). Classification of a pixel in this boolean scheme is performed following the path determined by the answers to the questions related to the nodes; from the root node until a leave node is reached (CORTIJO & PEREZ DE LA BLANCA, 1997).

HANSEN et al. (1996) underline the strengths of DTC approaches compared to standard MLC methods due to the possibilities of great flexibility in data analysis and interpretation by using the metrics, which are most useful for discriminating among cover types. HANSEN et al. (2000) used a DTC for a global land cover classification into 12 classes at 1km spatial resolution based on AVHRR data. As a first step the tree splits vegetated from non-vegetated areas in a hierarchical pattern splitting the resulting classes further until the final 11 different vegetation classes, and the class "bare ground" are distinguished. The rules at the tree intersections are purely quantitative, taking channel maxima and minima, NDVI derivates, channel means and amplitudes into account. BROWN DE COLSTOUN et al. (2003) employed a decision tree classifier to distinguish 11 classes in a forest dominated study area. WEN & TATEISHI (2001) produced a land cover classification for the whole of Asia using AVHRR data, taking land surface temperature (LST) derivates, NDVI derivates and elevation data into account. VOIGT (2000) developed a hierarchical threshold test sequence including three tests based on brightness temperature, one test based on the NDVI and two tests based on albedo to automatically differentiate the classes "cloud", "snow" and "no snow". The procedure is similar to a classification tree approach, though in the strict sense the definition of a tree is not fulfilled, since some leaves can be reached via more than one branch. However, the boundary between other knowledge based approaches and DTC is not sharp.

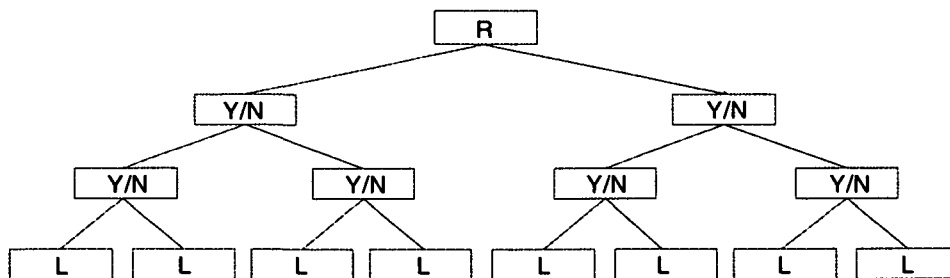


Figure 3-2: Classification tree with root node (R), internal nodes (Y/N) and terminal nodes (L)

FRIEDL & BRODLEY (1996) compared several types of DTC, including univariate, multivariate and hybrid trees, containing different classification algorithms within a single tree. They found that decision tree approaches – especially hybrid ones – generally outperform MLC approaches concerning classification accuracy. Later, MCIVER & FRIEDL (2002) incorporated ML based prior probabilities into decision tree classification to better differentiate natural versus agricultural vegetation classes.

Disadvantages of DTC include the fact that the development of a good tree is very time consuming and contains several iterations of training the tree, node-definition, adding or deleting of leaves, pruning of the tree etc. Furthermore, trees are sensitive to varying data quality and require detailed radiometric- and atmospheric correction (FRIEDL & BRODLEY 1996, BROWN DE COLSTOUN et al. 2003).

3.6. Artificial Neural Networks (ANN)

Many further methods for pattern recognition exist, among them neural networks (non parametric). A artificial neural network (ANN) consists of a series of layers (input layers, hidden processing layers, output layers) with a number of processing units or neurons linked to other neurons on subsequent layers. The input layers are an interface to the input data. The processing nodes contain summations and transformations and within the output nodes the output is calculated, as schematically shown in figure 3-3.

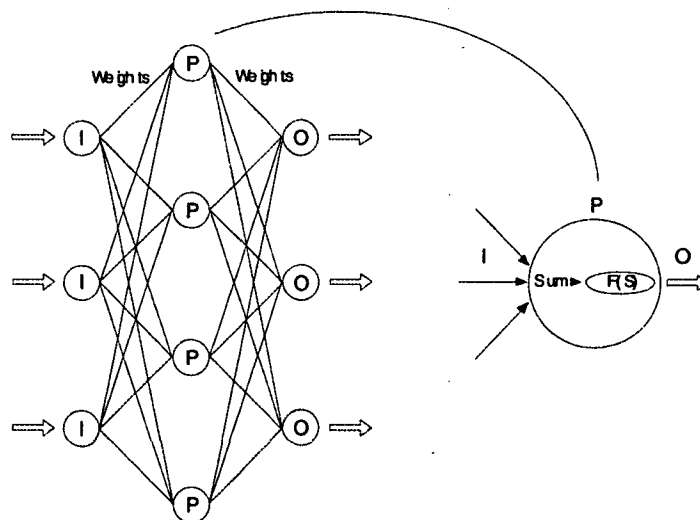


Figure 3-3: Scheme of an Artificial Neural network (ANN) with input layers (I), processing nodes (P) and output layers (O), (SCHOWENGERDT 1997), modified

The ANN's training stage is an iterative process converging to a stable solution by small incremental changes in system weights, which determine the decision boundaries (SCHOWENGERDT 1997). The ANN's learning strategy therefore specifies the initial set of weights and indicates how these weights and neuron values should be updated in order to improve performance. Mathematically speaking, most NN methods are based on the optimization (minimization) of a cost function. NN topologies can work in supervised or unsupervised modes. More details on the often highly complex NNs can be found in TSO & MATHER (2001), BENEDIKTSSON & SVEINSSON (1997) and KRAUS (1990). GOPAL et al. (1999) used a NN architecture named ARTMAP to classify 1° AVHRR data, which before had been

classified with an MLC approach by DEFRIES & TOWNSHEND (1994). They could improve classification accuracy when ARTMAP was trained with 80% of the input data. ABUELGASIM et al. (1996) employed an artificial neural network to identify five different land cover classes, while NIANG et al. (2003) used an automatic neural classification approach for ocean color mapping. YANG et al. (1998) employed NNs to classify different lithologies in Canada's Northwest Territories.

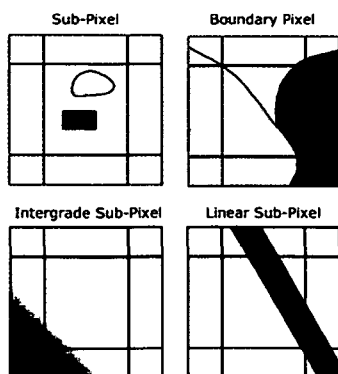
Nevertheless, in most cases the newer supervised neural network approaches have not gained much relevance, especially since their results rarely yield greatly increased classification accuracies compared with standard methods like MLC (NETELER 1999). FRIEDL & BRODLEY (1996) underline the drawback of neural networks, stating that they are time consuming, highly complex with regard to their algorithmic basis and therefore require substantial expertise and interaction or both.

3.7. Binary Encoding (BE)

Though the algorithms described above can be applied to hyperspectral data, they are more commonly used for multispectral input, while the following methods are mainly applied to the former. Though no algorithm has theoretical limitations in the number of bands processable, MLC (e.g.) will appear inefficient when applied to over 200 different bands.

Binary Encoding (BE) of the spectral dimension of a data set was an early approach to classify high spectral resolution data. The spectral radiances are coded based on a single DN threshold, which is specified. Values above the threshold are coded as one, while values located below the threshold are coded as zero. Therefore, a single bit in each channel can be used to code the spectrum (SCHOWENGERDT 1997). Discrimination can further be supported by encoding the derivative of the spectrum also to zero and one, depending if it is negative or positive. Modifications of BE can reach that the coded features are less sensitive to solar effects and atmosphere or BE results can be improved when using multiple thresholds (SCHOWENGERDT 1997). The BE coded spectra can be compared bit by bit using the "Hamming distance", which is "defined as the number of bits that are different in two binary numbers" (SCHOWENGERDT, 1997, p. 468). The drawback of binary encoding is – like for some other matching techniques – that it does not take the effect of compositional mixing into account (MARACCI, 1992). BE is presented in greater detail in MARACCI (1992). It was amongst others applied by KRUSE et al. (1990), mapping mineral composition of the Cuprite test site, Nevada.

3.8. Spectral Mixture Analysis (SMA)



Spectral Mixture Analysis (SMA) is based on the concept that spectral characteristics of a pixel are composed of a mixture of several spectral patterns resulting from different surface types in the pixel or simply an evenly mixed medium filling the pixel (e.g. water with sediment). Hence, spectral mixtures can be described with additive linear processes (SETTLE & DRAKE, 1993, MARACCI, 1992).

Figure 3-4: Different types of mixed pixels, (FISHER 1997)

Though the approach was already known in the 1970s it was not until the early 1990s that the method started to be applied on a broader basis by several authors. Especially with an increase of the integration of remote sensing data analysis results into models and the increasing need for quantitative data SMA is a promising approach.

In SMA pixels are transformed from the n -dimensional feature space to a mixing space, spanned up by endmembers, which are automatically defined (TOMPKINS et al. 1997) or derived / supplied by the user. Calculating the abundances (endmember fractions in a pixel) is possible with:

$$A \cdot X = R \quad \text{and} \quad X = A^{-1} \cdot R \quad (3.12)$$

where:

A: $m \times n$ -matrix of spectral endmembers (spectral library) in n spectral bands

X: vector of unknown abundances of the endmembers

R: measured reflection of the image pixel

So the unknown vector of abundances can be calculated by inverting the endmember-matrix, where the number of component spectra may not exceed the number of spectral bands.

In other terms, spectral mixtures can be derived based on an optimization of surface component percentages based on a residual error minimization of the input channels:

$$R_i = \sum_{j=1}^n f_j \times RE_{ij} + \varepsilon_i \quad \text{and} \quad \sum_{j=1}^n f_j = 1 \quad (3.13)$$

where:

R_i : spectral reflectance of a mixed spectrum in image band i

f_j : fraction of each endmember j calculated band by band

RE_{ij} : reflectance of the endmember spectrum j in band i

i : band number

j : each of the n image endmembers

f_j : residual error or the difference between the measured and the modeled DN in band i

ε_i : modeling error in band i

n : number of endmembers

The residual error ε_i of each of the image end-members is approximated by the measured and the modeled DN in band i . Minimizing ε_i in a least squares solution yields a unique solution to the unmixing equation. ε_i should – in an ideal case – be equal to the instrument noise, if only the endmembers of the selected model were present in the pixel. However, this case is very rare. Residuals ε_i over all spectral bands for a pixel can be averaged to receive the root mean square error (RMSE), which can be displayed as an image. It is calculated from the difference of the modeled (with SMA) and the measured (actual) pixel spectrum as:

$$RMS = \frac{1}{m} \sum_{k=1}^m \sqrt{\sum_{j=1}^n (R_{jk} - R'_{jk})^2 / n} \quad (3.14)$$

where:

m : number of pixels within the image

n : number of spectral bands

R_{jk} : modeled pixel spectrum
 R'_{jk} : real pixel spectrum

Furthermore, ε_i can also be calculated on a per channel basis to evaluate the quality of the model, with:

$$\varepsilon_i = R_i - \sum_{i=1}^n f_j \times RE_{ij} \quad (3.15)$$

(symbols and abbreviations as in 3.13.)

Since the sum of all spectral endmember reflection fractions including the RMSE needs to reach a sum of 1 (100%) as shown in equation 3.13. this approach is also referred to as “constrained” spectral unmixing. This additional condition of forcing the endmember fractions to sum up to unity (yielding an additional equation) allows the input of an additional endmember. In this constrained case the maximum number of endmembers is equal to the number of input bands plus one. In case the number of endmembers is lower than the number of bands, the linear equations are over-determined and can be solved applying a pseudo-inversion of the form:

$$X = (A^T A)^{-1} A^T R + E \quad (3.16.)$$

where X is the vector of unknown abundances of the endmembers, A is the $m \times n$ -matrix of spectral endmembers, R is the pixel reflectance and E the error term. A^T is the transposed matrix of A.

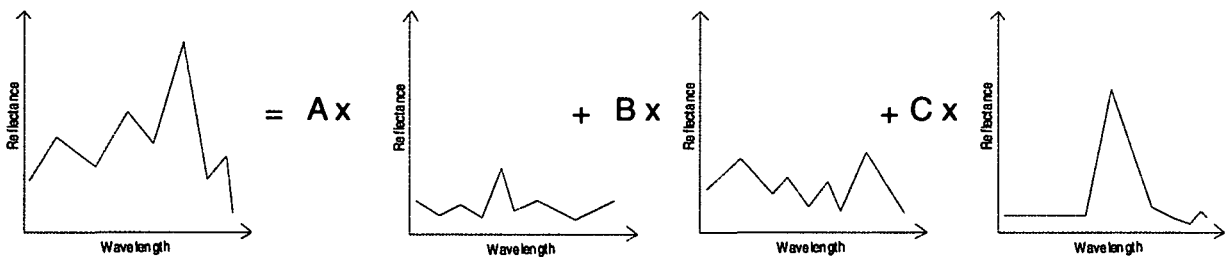


Figure 3-5: Principle of linear Spectral Mixture Analysis (SMA).

Advantages of SMA are the possibility to estimate surface fractions within a pixel in a standardized way. Furthermore, trends in fraction time series can be analyzed to perform change detection studies on a quantitative basis. HILL (1993b) states that spectral training is one of the major drawbacks to traditional parametric land cover mapping. Classification approaches and results are hardly reproducible. The classification process will furthermore be strongly biased by the analyst. It is therefore doubtful that mapping results can be compared objectively with reference maps from earlier dates. Here SMA can be a solution.

Furthermore, the axes defining the feature space do not have to be orthogonal like in PCA or TCT, but can be defined through the focus of the analyst, although with decreasing angle between the axes (increasing dimensions) redundancies grow. Problematic is that e.g. for Landsat data the number of extractable endmembers is reduced to three to four, due to the high correlation of the first bands

(RADELOFF et al. 1997, VAN DER MEER & DE JONG 2001, HILL 1998, MUECHER et al. 2000, GARCÍA-HARO et al. 1994).

Spectral unmixing approaches to assess human induced soil erosion or land degradation were amongst many others applied by HILL (1996b), KOCH (2000), HOSTERT (2001), and NETELER (1999). Studies in the field of vegetation discrimination were amongst others undertaken by COCHRANE & SOUZA (1998), FOODY & COX (1994), ROBERTS et al. (1998), BACHMANN (2002) and multi land cover mapping by DRAKE et al. (1999). ASNER & HEIDEBRACHT (2003) applied SMA to recent hyperspectral HYPERION satellite data while FARAND (1997) extracted endmembers from AVIRIS data to trace mine waste flows along a river streambed.

Standard SMA has been modified by many authors like VAN DER MEER (1999b), THESEIRA et al. (2002) and TOMPKINS et al. 1997. DRAKE et al. (1999) underline the problem of unmixing data that is nonlinearly mixed with a linear data model. Linear mixing assumes that each photon has only interacted with one material in the image. In reality – especially in highly vegetated areas – objects are not always opaque and significant amounts of transmission induce multiple scattering, resulting in nonlinear mixing (ROBERTS et al. 1993, BOREL & GERSTL 1994, RAY & MURRAY 1996). However, the vast amount of a-priory and additional data necessary for non-linear calculations make non-linear SMA rarely feasible (HOSTERT 2001).

In general, it needs to be remembered that all natural and most man made surfaces are mixed at some level of spatial resolution. Signature mixing therefore occurs at all scales and does not “disappear” as one increases the spatial resolution of the data set. However, since there is a “natural scale” to most surfaces depending on the research question, the decision to apply or not apply SMA can be met.

3.9. Spectral Angle Mapping (SAM)

A technique often used for the mapping of abundances is spectral angle mapping (SAM), which calculates the spectral similarity between a test reflectance spectrum and a reference reflectance spectrum, assuming that the data is correctly calibrated to apparent reflectance (VAN DER MEER & DE JONG 2001). The spectral similarity between the pixel, t , and the reference spectrum, r , is expressed in terms of the average angle, Θ , between the two spectra as calculated for each channel, i , as:

$$\Theta = \cos^{-1} \left(\frac{\vec{t} \cdot \vec{r}}{\|\vec{t}\| \|\vec{r}\|} \right) \quad (3.17)$$

which equals:

$$\Theta = \cos^{-1} \left(\frac{\sum_{i=1}^n t_i r_i}{\sqrt{\sum_{i=1}^n t_i^2 \sum_{i=1}^n r_i^2}} \right) \quad (3.18)$$

The spectra are seen as vectors in a multidimensional feature space. The dimensions are defined by the number of bands, n . The result of SAM is an image representing angular differences measured in radians ranging from 0 to $\pi/2$, which gives a qualitative estimate of the presence of absorption

features (VAN DER MEER & DE JONG 2001). The derived spectral angle maps therefore form a new data cube with the number of bands equal to the number of reference spectra in the mapping. The method is insensitive to illumination differences, since the SAM algorithm uses only the vector direction and not the vector length. Furthermore it is based on simple linear algebra, computationally easy and one can add and drop bands as desired. SAM is usually used as a first procedure to determine the mineralogy in high to hyperspectral resolution images of geologically interesting areas.

KRUSE et al. (2003) applied SAM to conduct mineral mapping investigations on AVIRIS and HYPERION data, VAN DER MEER et al. 1997 mapped ophiolite lithologies in Cyprus, and HORNSTRA et al. (2003) compare SMA to other classification methods from a conceptual point of view.

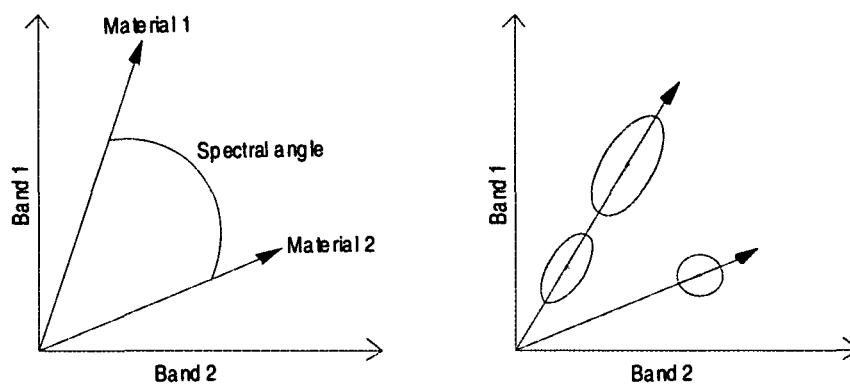


Figure 3-6: Principle of Spectral Angle Mapping (SAM). Material 1 and 2 can clearly be distinguished by the angle. In the 2-D feature space to the right, the two ellipsoids located on one vector (no angle difference) will be difficult to distinguish.

3.10. Spectral Feature Fitting (SFF)

Spectral feature fitting (CLARK & SWAYZE 1995) is a method matching pixel spectra to reference spectra based on their characteristic absorption features. The matching process is based on a least squares “best fit” approach. The better the fit, the smaller the sum of squared distances between the two spectra compared. The measure for this fit, the root mean square error (RMS), is used to create an RMS image, which indicates if pixels are more or less similar to the selected reference endmember (VAN DER MEER & DE JONG 2001, KOKALY et al. 2003).

CLARK & SWAYZE (1995) developed an algorithm named “Tetracorder” (formerly “Tricorder”) that uses a digital library of known materials and a fast, modified-least-squares method to determine, if a single spectral feature of a given material is present in an image. The algorithm can simultaneously map multiple materials using multiple spectral input features. It furthermore has the capability to analyze spectra step wise, using operator defined case sequences or gives the option of fit, band depth and continuum thresholding.

Preferably, continuum removed spectra are used and compared to known continuum reference spectra (CLARK et al. 1990). Absorption in a spectrum consists of the continuum and the individual features.

The absorption bands are characterized by parameters like wavelength position, depth, width, asymmetry, slope of the upper convex hull and area (URL 3-1). The continuum or background represents the overall albedo of the reflectance curve. This is removed to extract absorption features using the Hull technique, also referred to as continuum removal (VAN DER MEER & DE JONG 2001), normalizing the data. The hull consists of a series of line segments that connect various local reflectance maxima within the spectrum. Therefore, the upper convex hull is calculated as an enveloping curve on the pixel spectra having no absorption features. The hull difference is created by subtracting the hull from the spectrum and then adding 100% to the result (VAN DER MEER & DE JONG 2001, ZHANG, J., 1996). The continuum removed spectra can then be used for further characterization of absorption features (KOKALY et al. 2003, UNDERWOOD et al. 2002).

In general, absorption feature depth is proportional to the spectral abundance of the material in the pixel. In SFF several library spectra or other reference spectra are used for the calculation of fits and the spectrum with the best fit is chosen as the identified material. Identification of this spectrally dominant material does not imply though that other materials do not exist within the spectrum.

3.11. Other Spectral Matching and Classification Techniques

Spectral matching (SM) as applied by DE JONG (1994) works on a pixel by pixel basis based on the approach that a pixel spectrum of an image is matched with a reference spectrum for the entire- or parts of the spectral range respectively. The similarity index (SI) calculates the normalized Euclidean distance between two spectra in a user defined spectral window:

$$SI = \sqrt{\sum_{i=m}^n \frac{(W_i - R_i)^2}{(n - m + 1)}} \quad (3.19)$$

where W_i is the pixel spectrum, R_i is the reference spectrum and n and m are the band numbers of a user defined window. The lower the SI value, the better the match of the two spectra. Hence, a SI value of 0 indicates a perfect match. Prior to SI calculation the spectra should be corrected for their vertical offset.

DRAKE et al. (1999) found that spectral matching of pure library spectra to those in an image was an effective method to classify image data prior to SMA and to identify and locate endmembers for SMA, including the very purest pixels of each identified material (MARACCI 1992). VAN DER MEER (2000) introduced Cross Correlogram Spectral Matching (CCSM) to match known spectral signatures to unknown spectral signatures in order to determine the similarity of the two. His technique calculates cross correlograms between the two spectra, with

$$r_m = \frac{n \sum \lambda_r \lambda_i - \sum \lambda_r \sum \lambda_i}{\sqrt{[n \sum \lambda_r^2 - (\sum \lambda_r)^2][n \sum \lambda_i^2 - (\sum \lambda_i)^2]}} \quad (3.20)$$

where r_m is the cross correlation at matching position m , λ_i is the target spectrum, λ_r is the reference spectrum and n is the number of overlapping positions (= spectral bands). The reference spectrum is

shifted subsequently over m channels to shorter and longer wavelengths using the RMS, derived from the difference between the calculated CC and the ideal CC for the reference, as a measure for matching-success. As in any spectral matching procedure continuum removal is suggested prior to the operation. The advantages of CCSM are the insensitivity to gain factors, the fact that the CC is equally affected by random noise, the direct correlation of the correlation maximum with the relative position of absorption features and the option to compare target and reference statistically. A disadvantage is the fact that CCSM does not consider mixtures (VAN DER MEER 2000).

Further additional approaches are manifold, and it is often hard to determine, if an approach still belongs to the above defined methods or if it is modified strongly enough to be considered a stand-alone new method. Furthermore, many authors assign own names or abbreviations to their algorithms. ZHU & BLUMBERG (2002) and KEUCHEL et al. (2003) used support vector machine (SVM) algorithms based on statistical learning theory for accurate classification procedures of urban areas from Aster and TM data for general land cover classifications, respectively. PALACIOS-ORUETA et al. (1999) used a hierarchical foreground and background analysis to discriminate soil properties (organic matter and iron content) from two valleys in the Santa Monica Mountains, CA. RESMINI et al. (1997) employed a constrained energy minimization (CEM) algorithm on HYDICE data for mineral mapping at the Cuprite, Nevada, test site. To review all these less known hybrid approaches is not within the scope of this work. Review papers including most classification and feature extraction approaches are rare; however, good overviews can be found in TSO & MATHER (2001), RICHARDS (1986), SCHOWENGERDT 1997 and VAN DER MEER & DE JONG (2001) amongst others.

3.12. Thermal Approaches for Geologic Mapping

Geologic surfaces have been classified and mapped with all the methods presented and explained above. Examples for case studies are given in the respective subchapters. Still, there are some approaches specific to geologic mapping, which shall briefly be mentioned here also.

A common tool for data transformation of geologic data used prior to classification are PCA and IHS transforms. PCA is explained in 3.1, details on IHS transformation, rotating the Red-Green-Blue (RGB) color space to an Intensity-Hue-Saturation color (IHS) space are given by LILLESAND & KIEFER (1994). KENEA (1997) presents the often applied techniques of calculating a PCA or IHS transformation on geologic remote sensing data, decorrelation-stretching the transformed data and employing an inverse PCA or IHS transformation afterwards to spectrally improve the separability of geologic units and rocks with subtle mineralogical differences. Also CASACCHIA et al. (1999) applied these methods to differentiate rock units in Antarctica. Nevertheless, both methods result in changed pixel values and synthetic features. Hence, they are mainly applied for visual interpretation or classification procedures not relying on field spectra or radiometrically corrected input data as presented by MICKUS & JOHNSON (2001), who used Landsat-TM and SPOT data for the discrimination of sedimentary and volcanic units in Petrified Forest National Park, Arizona. They applied the transforms mentioned above and classified the data with an MLC approach as also done by KRISHNAMURTHY (1997).

Often times, different rocks do not have distinctly different spectral reflectance curves, since they might be of similar mineral content, grain size or water content. However, a common method for rock type discrimination is to incorporate a thermal band into the analysis. Different rock types may show a

different thermal behavior, due to different thermal inertias, which characterize the warming and cooling behavior of rocks. Therefore, an interesting approach to map different rock units is the classification of thermal image products generated by subtracting thermal nighttime data from thermal daytime data. KAHLE et al. (1976) e.g. mapped different geologic units based on airborne scanner derived diurnal temperature ranges (ΔT), which were studied as a function of albedo, slope, aspect and thermal inertia. Also ABRAMS et al. (1984) stress the fact that thermal radiance data can augment the surface reflectance data and provide additional information related to material composition. This applies especially, when coatings on exposed materials mask their true composition. They employed HCMM (Heat Capacity Mapping Mission) daytime and nighttime data to calculate thermal inertia images and generated image products consisting of thermal IR daytime-, thermal IR nighttime and VNIR daytime data, presenting a wide variety of rocks, which had similar colors or similar overall spectra in Landsat MSS data. They reached very detailed mapping results, but stated that the spatial resolution of HCMM (600 m at nadir) was a limiting factor. Also CRACKNELL & XUE (1996) discuss the possibilities to employ thermal information for geologic mapping. Thermal inertia images as well as the more easily derived apparent thermal inertia (ATI) images (SABINS 1996), ΔT images and emissivity images (HOOK et al. 1992) can be derived, if thermal daytime and nighttime data or data with different thermal bands exist.

3.13. Change Detection Studies

Independently of the classification or feature detection algorithm applied, typical applications for advanced studies are change detection analyses. An overview of the most commonly used change detection methods including image differencing, vegetative index differencing, selective PCA, direct multi-date unsupervised classification, post classification change differencing and combinations of the above is given by MAS (1999). Also in the range of spectral feature matching or SMA many differencing approaches, trend analysis studies of fraction images etc. are undertaken. The thematic foci of change detection studies are as manifold as the broad range of geoscientific research topics. YOUNG & WANG (2001) assessed the land cover changes of the whole of China using global Pathfinder AVHRR land cover data between 1982 and 1992 on the basis of NDVI time series. REES et al. (2003) mapped land cover changes in a reindeer herding area of the Russian Arctic to show the dynamics and temporal trends in phenology induced by grazing. PRAKASH & GUPTA (1998) investigated land cover changes in the Jharia coal mining area, India, and GREY et al. (2003) investigated urban area changes based on satellite radar interferometry. ANDRÉFOUET et al. (2001) analyzed the temporal development of coral reef environments, ABUELGASIM et al. (1999) employed fuzzy neural networks for the change detection of environmental damage after the first Gulf war and COLLINS et al. (1996) assessed changes in forest mortality. These are just a few examples representing the wide span of thematic applications with numerous published case studies in common remote sensing and geoscience journals.

3.14. Assessing Classification and Surface Extraction Accuracy

Classification and feature extraction is not complete without a quantitative error estimation called accuracy assessment. No classification or extraction of a certain surface will yield as good results as a ground mapping and a varying uncertainty of the classification results has to be expected for each classifier. Misclassifications mostly result from spectral ambiguities between classes, represented in feature space through overlapping pixel clusters, analyst-induced errors in training data selection or a

weak geometric co-registration of image data and ground truth data (STOLZ 1998). Classification accuracies are presented in so-called error matrices, which have the schematic form illustrated in table 3-1.

Quantitative measures for classification accuracy are the overall accuracy, the producer accuracy and the user accuracy. The overall accuracy is defined as the overall percentage of correctly classified pixels with respect to the combined set of training data. It is the least specific accuracy measure, since it does not yield information on the classification accuracy of the single classes. A class with a very high classification accuracy can “blur” the fact that e.g. the other remaining classes were classified with less accurate results. To account for this, many critical image analysts present their accuracy data including and excluding the class of “water” if water is present in the classification. Water – due to its good spectral separability and low class inherent variance – often yields class accuracies exceeding 95% and therefore improves the overall accuracy substantially.

Producer accuracy for a specific land cover class defines, how much of the training areas of this land cover class were classified correctly, and user accuracy is a measure defining the probability that a classification pixel, assigned to the specific land cover class, really represents that class. Therefore, producer and user accuracy can differ from each other, with the latter being the strictest and most objective measure for the definition of single class classification accuracy (CONGALTON & GREEN 1999).

Table 3-1: Concept of an accuracy assessment error matrix

		Reference Data				
		Class 1	Class 2	...	Class n	Row total
Classification Data	Class 1	a_{11}	a_{12}	...	a_{1n}	$\sum_{K=1}^N a_{1K}$
	Class 2	a_{21}	a_{22}	...	a_{2n}	$\sum_{K=1}^N a_{2K}$

	Class n	a_{n1}	a_{n2}	...	a_{nn}	$\sum_{K=1}^N a_{NK}$
Column total		$\sum_{K=1}^N a_{K1}$	$\sum_{K=1}^N a_{K2}$...	$\sum_{K=1}^N a_{KN}$	$N = \sum_{I,K=1}^N a_{iK}$

The overall accuracy can be calculated according to:

$$OA = \frac{\sum_{i=1}^k n_{ij}}{n} \quad (3.21)$$

the producers accuracy with:

$$PA = n_{jj} / n_{+j} \quad (3.22)$$

and the user’s accuracy with:

$$UA = n_{ij} / n_{i+} \quad (3.23)$$

with n_{i+} being the number of samples classified into category i in the remotely sensed classification and n_{+j} being the number of samples classified into category j in the reference data set and k representing the categories (CONGALTON & GREEN 1999, HUBERT-MOY et al. 2001). A good overview of accuracy measures and their appropriate use is also given by STEHMAN (1997).

4. Data Analyzed

Most of the data used for this thesis were collected for the data base in the framework of the BMBF project “Reception and project specific processing of remote sensing data for the support of current and future projects within the Sino-German environmental research co-operation”. Furthermore, a lot of data was acquired within the Sino-German coal fire research initiative “Innovative Technologies for the Exploration, Extinction and Monitoring of Coal Fires in North China”. A large number of Landsat-7 ETM+, Modis- and ERS-scenes was acquired during two DLR acquisition campaigns at a mobile ground station in Ulan Bator, Mongolia, in fall 2001 and spring 2002. Furthermore, data of the sensors Aster, ALI, Hyperion and Quickbird was available for the main study areas. However, the following subchapters will only present the data processed and analyzed within this thesis. Since this chapter only introduces the data, explanations on the geometric and radiometric quality and preprocessing of the data is presented in chapter 5.

4.1. Satellite Data

Landsat-7 ETM+ data is the main source of remote sensing information used in this thesis. Reasons for this are the broad spatial coverage of Landsat data, the sensors spatial resolution of up to 15 meters and its 7 spectral channels including a thermal band. Although bands are not overwhelming in number they are evenly distributed and well studied. The long term acquisition plan (LTAP) of the Landsat program predestines Landsat data for long term monitoring. The recording of land- and water surfaces started in 1972 with Landsat-1, therefore offering now 30 years of coverage (ARVIDSON et al. 2001, GOWARD et al. 2001, FLYNN et al. 2001). Furthermore, up to date thermal remote sensing research in the field of coal fire analyses focuses on the capabilities of Landsat-7 ETM+. This sensor promised new achievements compared to the ‘older generation’ of coal fire research undertaken with satellite data of lower spatial resolution. The utilization of ETM+ data for multispectral investigations pursued within this work will therefore grant the comparability and possible combination with ETM+ based approaches from thermal oriented research.

For small areas the analyses were also conducted for partially available Aster data. This sensor is of interest due to its 14 spectral bands. Furthermore Quickbird data was available for the two main study areas. ERS-2 SAR data was mainly used for rectification purposes based on amplitude and coherence data as well as for the derivation of terrain information. Although the easy data accessibility and the number of thermal channels of Modis might be interesting for coal fire research also, satellite data of this sensor was not used due to the low spatial resolution of the satellite (MASEK et al. 2001, Zhang, J. 2002).

4.1.1. Landsat-7 ETM+ Data

The spectral and spatial properties of Landsat-7 ETM+ are briefly presented in table 4-1. The satellite was launched into its near polar, sun synchronous orbit (inclination 98.2°) on April 15th of 1999. It has a repetition rate of 16 days and covers 90.6 % of the earth’s surface (ARVIDSON et al. 2001, GOWARD et al. 2001). Data is acquired in frames covering an area of approximately 183 km × 170 km at 10:00 a.m. local time. Frames acquired over the equator show a sidelap of adjacent swaths of 7.3 %, while at 80° latitude they overlap by 83.9 % (MASEK et al. 2001, USGS 1999). The LTAP grants the

4. Data Analyzed

option for short term special requests for science and government sponsored companies. Although mainly operating in the daytime mode, also nighttime data in the tIR band could be acquired within the project for thermal research. The nighttime frames are acquired at 10:00 p.m. local time. All channels show 8 bit data depth represented in a maximum of 256 digital numbers (DNs). Opposite to Landsat-5 TM, Landsat-7 ETM+ includes a panchromatic channel ranging from 0.52-0.9 μm with 15 m resolution and a thermal channel with 60 m resolution offering a high- and a low gain mode (FLYNN 2001). For more detailed information on the Landsat program and the satellite's characteristics see MIKA (2000) or URL 4-1. For Landsat data earlier than April 1999 the Landsat TM or MSS archives have to be consulted.

As shown in table 4-2 available scenes for this thesis covered regions of Ningxia and Inner Mongolia in China (for the main study areas also multitemporal coverage), as well as areas outside of China for later validation and the transfer of methods. These two scenes outside China cover the Jharia coal fields in Northeast India (PRAKASH et al. 1997) at approximately 23°42'N and 86°15'E and an area in South-central Australia at the foothills of the Flinders Range at approximately 30°18'S and 138°36'E. For all data the pre-requirement of nearly 0% cloud coverage was fulfilled.

Towards the end of this thesis it became clear that unexpected instabilities of the scan mirror of ETM+, which started to occur in May 2003, could not be fixed. Only a center stripe close the nadir line is unaffected. This challenge for the project and this work is discussed in chapter 10.

Table 4-1: Spectral and spatial properties of Landsat 7 ETM+ data versus Landsat 5 TM (in brackets)

Part of the electromagnetic spectrum	Band width / EMS-area [μm]	Spatial resolution	Depth [bit]
(1) visible (blue)	0.45 - 0.51, [0.45-0.52]	30 m, [30m]	8
(2) visible (green)	0.52 - 0.60, [0.52-0.60]	30 m, [30m]	8
(3) visible (red)	0.63 - 0.69, [0.63-0.69]	30 m, [30m]	8
(4) near Infrared (nIR)	0.75 - 0.90, [0.76-0.90]	30 m, [30m]	8
(5) middle Infrared (nIR 2)	1.55 - 1.75, [1.55-1.75]	30 m, [30m]	8
(6) thermal Infrared (tIR)	10.40 -12.50, [10.40-12.50]	60 m, [120m]	8
(7) middle Infrared (mIR)	2.09 - 2.35, [2.08-2.35]	30 m, [30m]	8
(8) panchromatic (PAN)	0.52 - 0.90, [none]	15 m, [none]	8

(Source: URL 4-2, SCHWARZ et al. 1999, MASEK et al. 2001)

Table 4-2: LS7 ETM+ scenes processed and analyzed in the framework of this thesis

Path/Row	Acquisition date	latitude [UL corner]	longitude [UL corner]	Sun elevation [dec. deg.]	Sun azimuth [dec. deg.]	day/night
129/033	12.08.1999	39.88 N	105.62 E	+ 58.59	+ 132.73	day
129/033	17.10.2000	39.88 N	105.55 E	+ 38.60	+ 155.63	day
129/033	04.10.2001	39.86 N	105.64 E	+ 42.96	+ 151.53	day
129/033	21.09.2002	39.87 N	105.58 E	+ 47.02	+ 147.12	day
129/033	10.12.2002	39.89 N	105.61 E	+ 31.63	+ 149.16	day
129/033	12.02.2003	39.88 N	105.62 E	+ 25.04	+ 158.22	day
129/033	03.05.2003	39.87 N	105.59 E	+ 30.52	+ 133.69	day
128/032	29.08.2002	41.28 N	107.45 E	+ 52.84	+ 139.80	day
098/081	15.11.2002	29.33 S	137.42 E	+ 59.53	+ 074.15	day
140/044	02.11.2001	24.05 N	087.81 E	+ 46.31	+ 147.98	day

It is obvious, that most scenes were acquired in fall, winter or spring. Due to the larger thermal contrast image data from these seasons is preferred to summer data with overall higher temperatures. Data acquired during the summer season should be avoided (ZHANG, X. 1998). Daytime data were used for automated coal fire area demarcation as well as for the investigation of parameters coinciding with thermal anomalies and coal fires respectively. Nighttime data were used for thermal anomaly extraction applying the algorithm of ZHANG, J. (2004) and combined analysis of the two approaches.

4.1.2. Landsat-5 TM Data

One Landsat-5 TM scene of path 129, row 33 covering the Wuda and the Ruqigou / Gulaben test sites, acquired on 20.09.1987 was available. The characteristics of Landsat-5 TM are shown in table 4-1. The major difference to ETM+ data is the weaker spatial resolution in the thermal band (120 m, no double gain setting) and the lack of a panchromatic channel (MASEK et al. 2001). Furthermore, TM data have a weaker SNR ratio and radiometric sensitivity. Also, Landsat-7 ETM+ concentrates a larger part of the image amplitude in the lower wavelength part of the spectrum associated with the actual image content, rather than shorter wavelengths associated with noise. Therefore, subtle land cover feature differences of darker objects (e.g. forest, water) might be less easy to resolve than in ETM+ data. The scene is the only fully cloud-free one available from the 1980s and offers the chance for long term change detection.

4.1.3. Aster Data

The spectral and spatial properties of the Aster sensor, installed on the satellite Terra and flying 30 min. behind Landsat-7, are briefly introduced in table 4-3. Since December 1999 Aster circles in a near polar, sun synchronous orbit, acquiring data since February 24, 2000, with a repetition rate of 16 days. Data is downlinked in frames covering an area of approximately 60 km × 60 km at 10:30 a.m. local time. Unlike Landsat-7, which acquires data constantly and therefore providing a near-worldwide coverage of frames (except the poles), ASTER only scans the earth's surface when specifically required by a customer. Thus it does not grant a sufficient areal coverage (EARTH REMOTE SENSING DATA ANALYSIS CENTER. 2000 & 2001, ABRAMS & HOOK 1995). Also nighttime data with five thermal bands, acquired at 10:30 p.m. local time, could be requested within the project. A major advantage of thermal nighttime data recorded by Landsat-7 or Aster is the effect that at 10 p.m. only few solar effects modify the thermal signal. Influences of uneven heating due to slope and aspect are minimized (PRAKASH et al. 1999. ZHANG, J., et al. 2003). However, the optimal time for thermal data acquisition would be around 5 a.m., when objects have the lowest temperature (ZHANG, X., 1998). For more detailed information on the Aster program and the sensors characteristics see URL 4-3.

Table 4-3: Spectral and spatial properties of ASTER data

Part of the electromagnetic spectrum	Band width / EMR-area [μm]	Spatial resolution	Depth [bit]
(1) VNIR	0.52 – 0.60	15 m	8
(2) VNIR	0.63 – 0.69	15 m	8
(3) VNIR nadir looking	0.76 – 0.86	15 m	8
(3) VNIR backward looking	0.76 – 0.86	15 m	8
(4) SWIR	1.6 – 1.7	15 m	8
(5) SWIR	2.145 – 2.185	30 m	8

4. Data Analyzed

Table 4-3 cont'd

Part of the electromagnetic spectrum	Band width / EMS-area [μm]	Spatial resolution	Depth [bit]
(6) SWIR	2.185 – 2.225	30 m	8
(7) SWIR	2.235 – 2.285	30 m	8
(8) SWIR	2.295 – 2.365	30 m	8
(9) SWIR	2.360 – 2.430	30 m	8
(11) TIR	8.125 - 8.475	90 m	12
(12) TIR	8.475 - 8.825	90 m	12
(13) TIR	8.925 - 9.275	90 m	12
(14) TIR	10.25 - 10.95	90 m	12
(15) TIR	10.95 - 11.65	90 m	12

(Source: URL 4-4)

Table 4-4: ASTER scenes processed and analyzed in the framework of the thesis

Path/Row	Acquisition date	Latitude (UL corner)	Longitude (UL corner)	Sun elevation [dec. deg.]	Sun azimuth [dec. deg.]	day/night
Ruqigou	08.09.2003	34.40	105.66	43.5	126.5	day
Wuda	24.09.2003	39.87	106.26	39.4	133.6	day

4.1.4. Quickbird Data

Quickbird is a high spatial resolution sensor, which was launched in October 2001. Quickbird circles in a 97.2° sun-synchronous near polar orbit at 450km altitude with an equatorial crossing time of 10:30 am. It acquires images in five bands, which are the panchromatic band, ranging from 0.45-0.9 μm , the blue band (0.45-0.52 μm), the green band (0.52-0.6 μm), the red band (0.63-0.67 μm) and the near Infrared (NIR) band, ranging from 0.76-0.9 μm . The nominal swath width at nadir is 16.5 km. The panchromatic channel has a spatial resolution of 0.6 meters per pixel, while the other multispectral bands have a resolution of 2.4 meters per pixel (URL 4-6). The data for the Wuda study area was acquired on October 5th 2003 and covers 64 km², while the data for the Ruqigou / Gulaben study area was acquired on September 22nd 2003 and covers an area of 81 km². For both acquisitions a nadir-mode was requested granting minimal viewing angles. Since the panchromatic and multispectral image channels fit well due to a parallax correction undertaken by the data provider they can easily be fused to integrate the high spatial information content of the 0.6 m panchromatic channel into the multispectral bands. A Quickbird standard product has a geometric accuracy in the desired map projection of +/- 14 meters RMSE. The geometric accuracy of the products is increased as presented in chapter 5. For further details on Quickbird see URL 4-6.

4.1.5. ERS-2 SAR Data

ERS-2 is an earth observing satellite, launched in 1995 and circling the earth at 800 km height in a polar orbit, thus covering 100% of the earth's surface. Instruments on board include an Active Microwave Instrument (AMI), a Radar Altimeter (RA), an Along Track Scanning Radiometer (ATSR) and a spectrometer, monitoring ozone, CFCs and trace gas levels (GOME) (BAMLER et al. 1996). The SAR data used in this thesis was recorded with the AMI. The instrument can record weather- and sun-independent, pulsing its microwave beam in an angle of 23° . Amplitude and coherence data as well as

digital elevation models (DEM), which were derived from SAR interferograms, were available for large areas of North-central and Northwest China. The data could be extracted from a database containing ERS-SAR data of the SAR-Topo team of DFD. ERS DEMs are characterized by a spatial resolution of 25 meters and a data depth of signed 16 bit, while amplitude and coherence data contain unsigned 8 bit information. The spatial accuracy of the DEM depends on many factors of which one is the local relief. It varies between 25-70 m in flat terrain and several hundred meters of up to a kilometer in strong relief (see also chapter 5.1). Further factors influencing the DEM accuracy are the option to calculate the digital elevation model from single pass interferometry data (Tandem data, which was only available in 1995/96), staples of data for one specific region and good baselines (URL 4-7). For the DEM generated for the Coal Fire Project Tandem data was not available and furthermore baselines and coverage were often not sufficient. Therefore a general overall quality assessment of the DEM, generated for an area of 780.000 km² focussing on the provinces of Ningxia and Xinjiang, cannot be pursued. The accuracy has to be assessed for individual use for specific areas. However, no reference for this DEM other than GLOBE with a much lower resolution or 1:100,000 topographic maps with only few elevation lines were available. The accuracy assessment had to be a qualitative one based on field observations and visual data comparison for the main study areas. SRTM products for central Asia were not available early enough to be incorporated in this work.

Other than the DEM, coherence data can be of interest for land surface characterization and classification, as shown amongst many others, by LE HÉGARAT-MASCALE et al. 2000, LIU et al. 2001 and WAGNER et al. 2003. However, the coherence data was not used within this study. The ERS datasets from which the coherence was derived, did not fit the Landsat data concerning data acquisition times.

4.2. Field- and Laboratory Spectral Measurements

4.2.1. Surface Spectra Measured During the Field Campaign

During the fieldwork conducted in Wuda in September 2002 spectra of the most important representative surfaces of the study area were sampled with a GER3700 single beam portable field spectrometer from the Geophysical and Environment Research Corporation (KUENZER et al. 2003). The instrument has a spectral range between 350-2500 nm, sampling with a 1.5 nm step in the range of 350-1050 nm, 6.2 nm in the range of 1050-1900 nm and 9.5 nm between 1900-2500nm. The spectral resolution in these three sampling intervals is 3nm, 11nm and 16nm respectively. The field of view is 3° under normal conditions. Although a fiber optic allows to furthermore use a FOV of 10°. Data depth is 16 bit in the range of 300-1050 nm and 15 bit in the range of 1050-2500 nm.

Spectra in the field were measured \pm 2 hours before/after noontime, when cloud coverage was less than 2/8th and weather conditions were sunny and clear. The recording process was kept as standardized as possible. A reference measurement with a Barium-Sulfate-panel (standard white, approximated 100% reflectance, Lambertian reflectance characteristics) was taken before each spectral measurement. Dividing the response of the target by the response of the reference yields the reflectivity of the target. A constant height of the spectrometer on a tripod granting the total fill of the FOV was calculated and kept stable during field measurements. Furthermore the geometry of reference and target was similar under all conditions (GER 1999, MILTON 1987, ROSEMA et al. 1999, MARACCI 1992).

Homogeneous large areas with an extent of several Landsat-7 pixels were chosen for the spectral measurements to grant the representativity of the spectra for a certain land surface class. For instance, desert sand was sampled in flat areas within large fields of sand dunes. When sampling vegetation spectra it was considered that staples of leaves (8 layers minimum) had to be recorded to receive highly saturated pure vegetation spectra and to exclude the signal of the underlying ground/soil (GUYOT 1990). Also mixtures of vegetation and soil were measured. For each set of recorded spectra additional information like GPS location, a digital photograph and a surface sample were collected.

Due to technical and logistic problems in China no spectra could be measured during the ETM+ daytime overflight on 21.09.2002 (clear sky, 0% clouds), but most spectra were collected five days before under the same illumination conditions and during the overpass time at around 10:00 a.m. local time. Hierarchical priorities were assigned to the surfaces selected for measuring to record most important spectra first. Within the four weeks of time during the field campaign in 2003 only few days were suitable for spectral measurements.

The focus of this thesis is to derive multispectral parameters for coal fire area demarcation. Since vegetation – based on field observations – is assumed to be one of the relevant parameters spectra of the dominant desert shrubs were recorded first. They could not be transported to Germany to be investigated under laboratory conditions (decay). Spectra of four different shrubs in a pure state as well as in mixtures with the underlying soil were collected. Furthermore, spectra of pure coal, coal dust, pure desert sand, crusted desert sand, pure solid sandstone of different colors, weathered sandstone, shale of different colors and limestones of different colors were acquired. Next to vegetation these were the main geologic constituents in the arid study area. The field spectra show no or a disturbed signal in the wavelengths, where the atmosphere is completely absorbing and therefore leading to a poor SNR ratio.

4.2.2. Laboratory Spectra Measured from Samples Collected During the Fieldwork

Due to time limits and weather conditions for some surface types no spectra could be recorded in the field. Therefore 28 kg of mainly rock- and soil samples were collected from the study areas and brought back to Germany. Here they were analyzed in the spectral laboratory of the hyperspectral working unit at DFD. Under laboratory conditions a 1000 Watt light source (Osram Halogen photo optic light source) illuminates the sample. The reflectance of the sampling surface is then measured with the GER3700 to retrieve the characteristic reflectance curve. As during the fieldwork, the reference is recorded before each measurement. In contrast to field-measurements, no atmospheric absorption and scattering processes influence the signal. Furthermore, laboratory measurements are highly standardized. The distance between the GER internal sensor and the surface was always approximately 40 cm in nadir position, the source of illumination was set up in 40 cm distance to the surface with an incidence angle of 30 °. Also the warm up time of 10 minutes for the spectrometer and the light source could be considered. Field- and laboratory measurements were undertaken as recommended by GER in the field- and laboratory handbook and represented a typical standard set up as e.g. used by HOSTERT 2001, BAUMGARDNER et al. 1985 or SCHLERF et al. 2003 and others.

4. Data Analyzed

Table 4-5: Geologic surface samples measured in the spectral laboratory

Coal	Sand	Sandstone	Shale	Limestone	Pyrometam.	Others
anthracite	pure desert	white	pure black	white	dark red	orange clay
cooking coal	pure wadi	light grey	pure brown	light grey	red	dark gneiss
coal dust	mix w. sst.	grey	mix w. sst.	dark grey	orange	granite
mine waste	mix w. lime	yellow	mix w. sand	yellowish	yellow	silt crusting
coal ash	mix w. shale	orange-red	mix w. soil	light brown	multicolor	wadi pebbles

Table 4-5 presents the samples recorded in the laboratory. The samples were not crushed to keep aggregates as found in the field. To account for different reflectance properties depending on viewing geometry each sample was measured 20 times from 4 directions (80 measurements) by horizontally rotating the sample for 90° respectively. A major advantage resulting from the climatic situation in the study areas was the fact that the surface samples were very dry when collected. No spectral variations between field and laboratory measurements depending on varying sample moisture occurred.

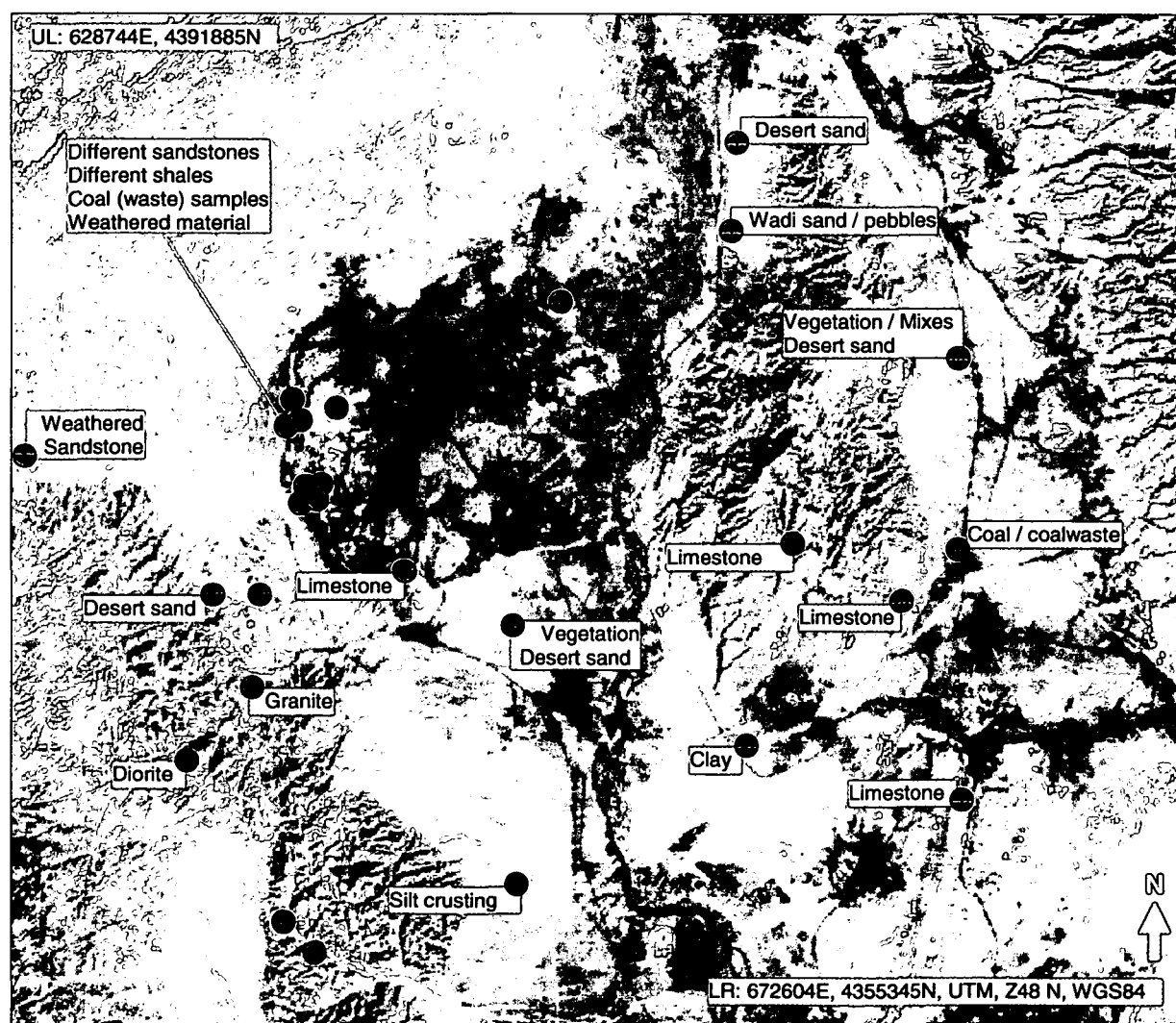


Figure 4-1: Location of the recording points for field spectral measurements and surface sample collection for later laboratory spectral measurements within the broader Wuda study area. Background: gray scale Landsat image (band 1) acquired during the same week as spectra- and surface sampling.

4.3. GIS Data

4.3.1. Available GIS Data

GIS data available for this research were very rare and had to be newly generated for most parts. Available data included data from the Digital Chart of the World (DCW) compiled by agencies that produce the Operational Navigation Charts (ONC) map series. The data is freely available via the Internet at a scale of 1:1,000,000. This database contains information on borders, major rivers, towns etc. and is only useful for a general overview of a region. It is too inaccurate to be used for scientific queries and was only useful for overview map generation (see e.g. map 1, chapter 2). To collect more digital information some data from 1:100,000 topographic maps was digitized for the broader study area including road and railway networks, settlements and mining related information.

4.3.2. GPS Locations Measured During the Fieldwork in 2002 and 2003

During the fieldwork campaign in 2002 the GIS database was extended by GPS (Garmin GPS 12). The complete road network of the broader study area was tracked by GPS and later converted into vector data sets readable in common GIS. Furthermore, distinct points like road intersections, railway bridges or edges of large buildings were measured and transferred to point-data sets to serve as ground control points. Also the locations of surface sampling points, spectral measurement points, digital photographs and coal fire related thermal anomalies were recorded. During all measurements the time was taken for sufficient averaging of the GPS measurement to receive estimated position errors (EPE) below 5 meters. However, it should be mentioned that according to users manuals and field guides a non-differential GPS can still yield displacements of up to 15 meters, even though the EPE display is indicating less. Nevertheless, GPS measurements in this project have the highest spatial accuracy compared with other reference data. During a second field campaign in 2003 high precision ground control points were recorded with three independent GPS and 5 minute position averaging times with a Garmin GPS12, a handheld GPS-GIS Compaq iPAQ computer (3950, GPS: EMTAC GPSJAQ D15A8) and a Garmin GPS 3 for the syncline areas in Wuda and Ruqigou / Gulaben. These data were used to rectify the high spatial resolution Quickbird data.

4.3.3. Landcover Polygons Mapped During the 2002 and 2003 Fieldwork

During the 2002 and 2003 fieldwork polygons of homogeneous landcover of 100 m × 100 m up to 1km×1km were mapped by GPS to act as ground truth for landcover classifications and their accuracy assessment within the framework of the project. Over 170 of such ground truth polygons were collected and transferred to vector-polygon data with descriptive attributes. Amongst these polygons are many, covering areas of coal outcrops or coal piles, which will be used as reference areas for the sensitivity analysis of the coal surface extraction algorithm. Also polygons of other land cover classes interesting for the approach to demarcate coal fire areas as outlined in the introduction are stored in this database.

4.3.4. Mixture Grids Mapped During the 2002- and 2003 Fieldwork

Seven detailed mixture grids of up to 500m×500m distributed within the Wuda mining area and broader surroundings were mapped. They act as ground truth for processes of unmixing activities within the project. Mapping took place during the fieldwork in 2002 and 2003. Therefore some grids are available in a “multitemporal” version. The grids have a cell size of 50 meters with each cell containing a percentage information of each individual surface, which is represented within the cell. This information was transferred in a multi-layer database with all the surface percentages adding up to 100 %. It was then included into a GIS to make the surface information available within its spatial context.

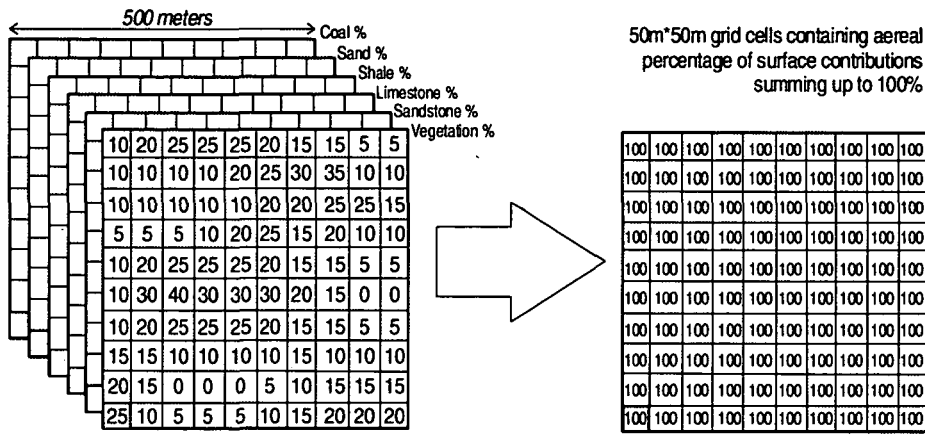


Figure 4-2: Concept of the mixing grids mapped during the fieldwork

4.3.5. Coal Fires Mapped During the 2002- 2003 and 2004 Fieldwork

During three field campaigns the coal fires in the Wuda and Ruqigou study area were mapped using GPS and thermal radiometers supported by handheld GPS-GIS units during the last campaign. The mapping of the year 2002 was undertaken by Zhang, J., Sun, Y. and Tetzlaff, A., the mapping in 2003 by Zhang, J., Tetzlaff, A., Kuenzer, C. and Hecker, C., the mapping in 2004 by Kuenzer, C., Hirner, A., Zhang, J and Y. Sun. While the Wuda coal fires were mapped for all these three years the coal fires of Ruqigou and Gulaben were only mapped in 2002, due to logistic and administrative reasons.

The mapping registered the locations of active cracks and subsidence holes exhaling hot gasses. Based on a large number of such thermal measurements as well as surface features like mining entrances, vegetation degradation, bedrock changes and subsidence phenomena the underground coal fire outlines were mapped the best way possible. However, the result of these mappings – polygon layers of subsurface coal fire outlines – can only approximate the size, extent and shape of the real coal fires. The mapping results are influenced by a lot of analyst interpretation. It was found that mapping results of 2003 and 2004 vary strongly from those in 2002, where the subsurface coal fire area has probably been mapped too large. The coal fire polygons are important to test, if the coal fire (risk) areas demarcated are precise enough to contain the actual known coal fires.

4.4. Maps and Descriptive Data

Topographic and thematic maps of China are difficult to obtain, especially when detailed scales are required. Expensive Russian military maps in the scale of 1:100,000 are available via the Internet. Two map sheets which only cover about 15% of one Landsat-7 satellite scene were ordered for both study areas. They could therefore not exclusively be used for geometric rectification procedures and were mainly used for an accuracy assessment of the orthorectification process within the distinct study areas. In addition they were used for vector extraction of infrastructure information. A list of further maps, which were of help for this thesis, is given below.

- Geologic Map of Ningxia 1:350,000⁺
- Tectonic Map of Ningxia 1:500,000⁺
- Geologic Map of Helan Mountains 1:500,000⁺
- Geologic Map of Inner Mongolia 1:1,500,000⁺
- Russian Military Map 1:100,000 “j48022” for Wuda[#]
- Russian Military Map 1:100,000 “j48033” for Ruqigou[#]
- Gulaben Topographic Map 1:50,000 *
- Gulaben Geological Structure Map 1:50,000 *
- Geologic and thematic map of Leigh Creek area, Australia, 1:250.000[#]

Items marked with * were only available as scanned versions on CD in Chinese coordinates not transferable to a known projection. Therefore they could only be used as ‘relative’ information and not support rectification or absolute object retrieval. Data marked with ⁺ was acquired in Beijing while data marked with [#] was ordered via the Internet.

Concerning descriptive data the scientific journal papers, book chapters and other publications mentioned in chapters 1.1. and 1.2. as well as the ones listed in the references at the end of this thesis have been accumulated. In addition some fieldwork reports and photographic material from past and current and project partners were available.

5. Data Preprocessing: Rectification, Calibration, Radiometry

Data preprocessing is of utmost importance when aiming at the retrieval of quantitative parameters from remote sensing data sets based on physical characteristics. Also for multitemporal or transferable studies a thorough preprocessing is the only option to guarantee the spatial and spectral comparability of data. SCHOTT (1997) from a conceptual point of view refers to an image processing chain approach based on spatial, radiometric and spectral preprocessing steps as links. Since each link in the chain is partially a result of previous links, the output product can only be as strong as the weakest link. Therefore putting emphasis on the quality of each link in the preprocessing chain can build the basis for a high quality output result.

5.1. Geometric Corrections

5.1.1. Principles of Geometric Distortions and Applied Correction Methods

The aim of each geometric correction procedure of satellite data is to rectify raster data in a way that all objects within the scene are located in their exact spatial topology towards each other within a projection system. Such a spatially exact topology between objects can be found in topographic maps, characterized by a parallel projection. Furthermore, the process of geometric correction can aim at the precise co-registration of satellite images towards each other. Coregistration is of high relevance for multitemporal studies (LUNETTA 1999, LILLESAND & KIEFER 1994, ROSEMA et al. 1999).

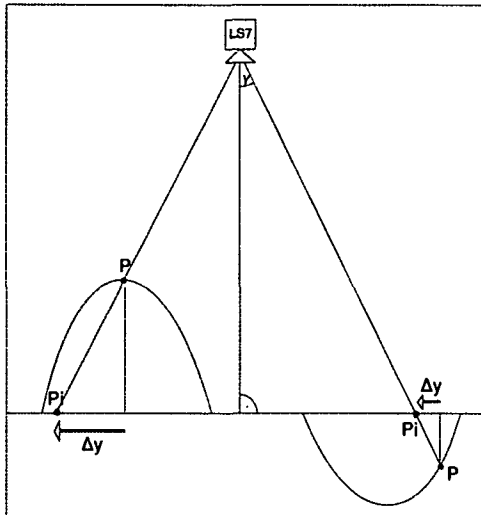
During the satellite's scanning process systematic and non-systematic shifts and displacements occur, which lead to a spatial displacement of objects within a scene. Systematic distortions result from many factors such as the earth's rotation during the scanning process, a shift in scan lines due to the forward movement of the satellite (scan time skew), a growing IFOV with increasing distance from the scene's nadir line (panoramic effect), instabilities in the satellite's scan rhythm as well as slightly different orientation of the instrument's detector axes (RICHARDS 1986, HOSTERT 2001, LÖFFLER 1994).

The systematic distortions of the Landsat-7 raw data (.fred-format or level 0R data) were resolved with the Product Generation System (PGS) of MacDonald Dettwiler (MDA). This system accounts for the systematic distortions as well as for basic radiometric calibration procedures based on regularly updated Landsat-7 calibration parameter files. A complete sensor calibration of the data is not included yet. For geometric registration the system uses altitude data contained in the Landsat-7 payload correction data files and the sensor's focal plane and detector alignment parameters from the .cpf-files. Systematically corrected Landsat-7 1G data have a spatial accuracy of approximately 50 meters in a scene with no significant relief (GOWARD et al. 2001). Details of these processor internal rectifications can be found in the MDA PGS handbook.

Non-systematic distortions result from instabilities of the satellite's orbit (κ , ϕ , σ , = roll, pitch and gear) and the terrain-induced object displacement orthogonal to the nadir line. These displacements need to be eliminated interactively in a parametric geocorrection approach reconstructing the image acquisition procedure. Therefore, sensor parameters, orbit description, local terrain elevation and projection parameters need to be known. This way a level 1T product can be generated leading to a more accurate result than non-parametric correction approaches (KRAUS 1990, LÖFFLER 1994).

Figure 5-1 demonstrates the principle of terrain-induced object displacement. The horizontal shift 'Δy' between the position P_i of an object in the image and the corresponding position P within an orthogonal projection can be calculated using equation 5.1:

$$\Delta y = h \times \tan \gamma \tag{5.1}$$



where h is defined by the terrain elevation of the object in P and γ is the viewing angle between the point on the earth's surface and the sensor. Terrain elevation h can either be derived from a topographic map or a DEM. The relief induced displacement increases with a growing positive or negative elevation difference from sea level as well as with growing distance of an object from the nadir-line of the satellite image (LÖFFLER 1994). Landsat-7 circles in a near polar orbit 705 km above the earth's surface (above nadir-line). At an average of 50 kilometers distance orthogonal to the nadir-line the distance to the satellite is about 706.77km (retrieved from $705^2+50^2=706.77^2$ and neglecting earth curvature).

Figure 5-1: Principle of terrain induced object displacement

The viewing angle of the satellite at this position can be derived from the modified Pythagorean relationships, where $\sin \gamma = 50/706.77$. Calculating the inverse sinus one retrieves a viewing angle of the sensor to a point at 50 kilometers distance from the nadir-line of 4.05°.

Applying formula 5.1 the terrain induced object displacement at several elevations as presented in table 5-1 can be calculated. Within the orthorectification process the shift of a pixel Δy can therefore be compensated.

Table 5-1: Elevation dependence of relief induced displacement (ETM+)

Elevation difference to sea level	Terrain induced displacement in 50 km distance orthogonal to the nadir line
0 - 500 m	0.00 m - 35.46 m
500 - 1000 m	35.46 m - 70.92 m
1000 - 2000 m	70.92 m - 141.84 m
2000 - 3000 m	141.84 m - 212.76 m
3000 - 4000 m	212.76 m - 283.68 m
4000 - 5000 m	283.68 m - 354.60 m

note that here the reference plane is always 0 meters (SL)

In the main scene (frame 129/33, LS-7) of the study areas Wuda is located in 38 km distance orthogonal to the nadir line while Ruqigou/Gulaben is located in 80 km distance from the nadir. The satellite scans the areas under an angle of 3.08° and 6.49° respectively. Expected displacements for these specific areas as well as for validation areas outside the study regions are shown in table 5-2.

Table 5-2: Relief induced displacement in the main study areas relative to NN in Landsat-7 ETM+ data

Coal Fire Area	Elevation Range [m]	Ø terrain amplitude	Distance to nadir of ETM+ scene	Relief induced displacement [m]	Number of pixels [15m]
China, Wuda	1010-1980	± 485 m	38 km	54.38–106.60 to SL max. 26.11 locally	3.6 – 7.0 1.6
China, Ruqigou	1400-2640	± 620 m	80 km	159.49 – 300.75 to SL max 70.63 locally	10.6 – 20.05 4.7
China, Baotou SE Australia India, Jharia	No orthorectification applied, terrain relatively flat to hilly				

A model approximating the Landsat-7 ETM+ orbit- and sensor parameters is included in the resampling algorithms of the geocorrection tools used, which also allows the spatial integration of a digital elevation model. It was routinely used for orthorectification of all scenes except the ones of the transfer areas. The amplitude, coherence and DEM tiles were extracted with the same spatial coverage as the equivalent Landsat-7 frame from the DEM database provided by the SAR-Topo team of DFD. The DEM tiles were resampled to 30 meters, to adapt to the size of most ETM+ channels. In small areas, which were not covered by the ERS-DEM, the data gaps were filled with small subsets from the GLOBE-DEM to grant a rough orthorectification even within these regions.

The link between the satellite scenes, the DEM and a reference with parallel projection was set through the careful selection of evenly distributed ground control points (GCPs) identifiable in the scenes as well as the reference. Since no maps, which covered the broader areas of interest sufficiently were available another geometric basis for GCP search had to be found. Therefore, the ERS SAR amplitude and coherence data proved to be suitable to look for distinct features existing in the SAR as well as the ETM+ data sets. Also GPS data (tracks along roads and distinct infrastructure intersections) measured during the field work could be used as a reference. For all daytime Landsat-7 scenes 20 GCPs evenly distributed within the images were chosen for geometric correction.

Using the coordinates of the GCPs defined in the satellite scene as well as in the reference, the transformation coefficients (where n is the number of coefficients) of the rectification using multiple regression can be calculated. The application of these coefficients to the GCPs of the distorted scene, allows the calculation of residual values in x - and y -direction. Resulting, one can calculate the 'Root Mean Square Error' (RMSE), which is a measure for the quality of a geometric correction:

$$RMSE = \sqrt{\frac{\sum(r(x)^2 + r(y)^2)}{n - p}} \quad (5.2)$$

The resampling technique used was the 'nearest neighbor' approach. It was preferred to the methods of bilinear interpolation or cubic convolution since it grants unchanged pixel values (RICHARDS 1986). In the worst case nearest neighbor resampling can lead to a shift of up to 0.5 pixels which can result in a 'blocky' structure in lineaments (KRAUS 1990, ROSEMA et al. 1999). However, for this work it is of utmost importance that pixel values stay unchanged. Figure 5-2 gives an example of an orthorectified Landsat-7 image next to the ERS-2 amplitude data.



Table 5-3 and figure 5-3 present the results of the orthorectification process for the different satellite scenes. To register the scenes of the main study areas towards each other and retrieve a time series of scenes comparable for change analysis, the frame 129/33 from 2001 was declared as the master-scene. It was corrected with the GPS data. Other data sets of the same- and neighboring frames were registered towards this master scene. All scenes were assigned to the UTM, Zone 48 N, coordinate system and the WGS84 datum. This is the common reference system in the project as well.

Figure 5-2: Orthorectified panchromatic ETM+ band (left) next to ERS-2 amplitude image (right). Center location: 573529E, 4818025N, UTM, Z48N

5.1.2. Results and Validation

Table 5-3 presents the results of the geo- and orthocorrection of satellite imagery of four different sensors. Due to the exact location of GCPs and including the DEM for orthorectification, RMS-errors indicating a shift of less than one pixel (subpixel accuracy) could be received for all scenes.

Table 5-3: RMSE-results in orthorectification of Landsat-5 TM, Landsat-7 ETM+, Aster and Quickbird data

Path/Row	Sensor	Date	Reference	RMSE x, (m)	RMSE y, (m)	RMSE tot.(m)
129/033	ETM+	12.08.99	2001 rectified	8.6177	9.1286	12.5537
129/033	ETM+	17.10.00	2001 rectified	5.6997	8.6340	10.3457
129/033	ETM+	04.10.01	GPS, ERS	8.9675	11.5214	14.5999
129/033	ETM+	21.09.02	2001 rectified	7.6434	7.1199	10.4458
129/033	ETM+	10.12.02	2001 rectified	10.6984	4.8891	11.7626
129/033	ETM+	12.02.03	2001 rectified	7.7086	7.8451	10.9986
129/033	ETM+	03.05.03	2001 rectified	6.3943	7.7073	10.0145
128/032	ETM+	28.09.02	no reference data and DEM available, data +/- 50m exact			
098/081	ETM+	15.11.02	no reference data and DEM available, data +/- 50m exact			
140/044	ETM+	02.11.01	no reference data and DEM available, data +/- 50m exact			
129/033	TM	20.09.87	2001 rectified	8.3564	8.9765	12.2640
Wuda	AST	24.09.03	2001 rectified	8.8802	7.5561	11.6599
Ruqigou	AST	08.09.03	2001 rectified	7.2751	6.7039	9.8929
Wuda	QB	05.10.03	GCPs field	2.2301	1.5610	2.7214
Ruqigou	QB	22.09.03	GCPs field	3.2333	5.3418	6.2441

To demonstrate the improvement of orthorectification versus a geometric correction without the integration of a DEM the residual errors of a rectification not including the DEM were plotted against elevation. A clear dependence on the terrain (elevation) could be noted in an R^2 exceeding 0.7. Including the DEM into the correction the relationship turned non significant, illustrated in an R^2 below 0.2 ($n=20$). Nevertheless, it should be mentioned that the quality of an orthorectification predominantly depends on the quality of the DEM included in the parametric approach. Strictly speaking, the RMSEs represent the accuracy close to the GCPs, but internal variation within the scene

can still occur (HOSTERT 2001). Also, the GPS data used as reference may already contain a spatial shift of up to 15 meters as mentioned in chapter 3. Therefore, the term ‘subpixel accuracy’ has to be used with care. Nevertheless, a visual control of the remaining shifts to assess the final spatial accuracy showed no preferred direction. With total RMSEs in the range of 7 to 18 meters for all ETM+ scenes, the quality of the individual geometric corrections can be considered good.

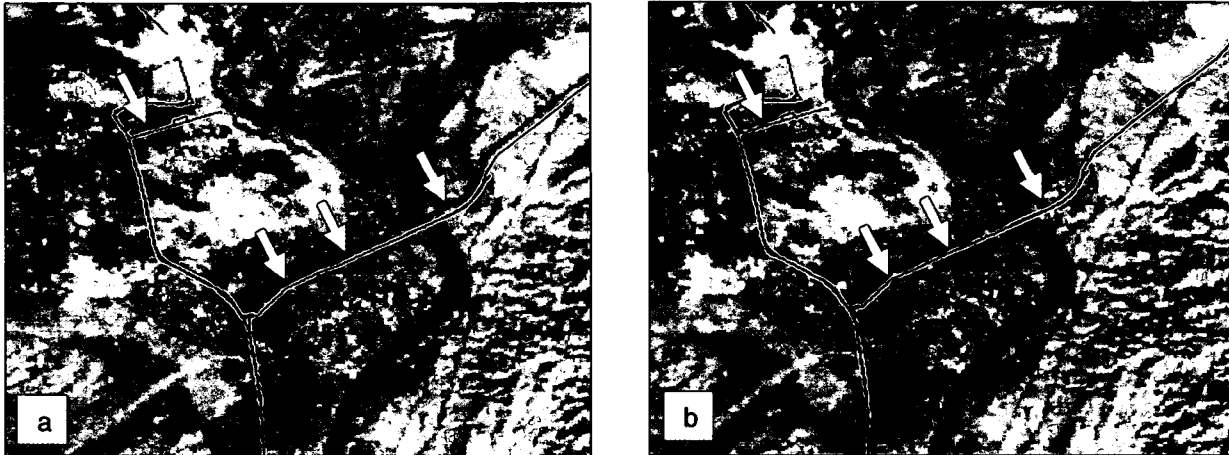


Figure 5-3: Geometric accuracy compared with GPS ground truth before (a) and after (b) the orthorectification demonstrated on a subset of ETM+ scene 129/033, Center location: 650651E, 4377299N, UTM, Z48N.

Since very detailed maps for the Wuda syncline are not available the Quickbird data was geometrically rectified on the basis of GPS based ground control points. These were collected on distinct points within the syncline during the satellite’s overpass time during the field campaigns in 2002 and 2003. Three different GPS of the same brand were used to map points, which were thought to be recognizable in the satellite images. Corners of house roofs, electric poles, water storage tanks, road intersections and similar features were located and mapped with GPS. Furthermore the height was estimated with an analogue altimeter (Thommen Classic 5000).

Drawings of the ground control points (GCPs) collected with GPS were generated and a small description as well as the x, y and z coordinates were noted, to relocate the GCPs within the high resolution satellite images. It turned out that only 70% of the collected ground control points in the field could be identified in the satellite data. This was especially true for the cemented foundations of electric poles. However, the other GCPs were distinct enough and the data could be rectified within the range of 2.5 meters.

An accurate orthorectification of imagery is also desirable for the following step in the processing chain – a combined atmospheric and topographic correction.

5.2. Radiometric Corrections for the Reflective Bands

Conditions for analysis of satellite data are best, when reflection changes detected by the sensor are caused by spectral characteristics of a surface exclusively. This is not the case though, since radiation reaching the sensor represents interactions of different factors. Illumination conditions caused by the sun-earth-sensor geometry or relief induced topographic illumination effects, aerosol and gas contents

and different reflectance patterns of different surfaces play an important role. Therefore, these factors have to be eliminated as far as possible in order to obtain calibrated images enabling the option to quantitatively compare different or multitemporal data sets. This can be achieved applying a combined atmospheric- and topographic illumination correction to the data (RICHTER 1998, RICHARDS 1986, SCHOTT 1997, SONG et al. 2001, HILL & MEHL 1995, KRAUS 1990, KRAUS 1989, HILL & MEHL 2003). Nevertheless, it should be mentioned that an atmospheric correction is not necessarily of importance when aiming at image classification of a single date image in flat terrain (SONG et al. 2001). However, in rugged terrain a topographic illumination correction is indispensable to improve classification results. When aiming at multitemporal or spatially comparable data sets, signature detection and comparison based on standard spectra or multitemporal unmixing, a thorough radiometric correction is a must. This applies especially with respect to classification-algorithms or change detection methods, which will be applied in one place and shall be transferred in other places and/or times, including a possible routine development (SONG et al. 2001, RICHTER 2003).

5.2.1. Sensor Calibration

The radiance L_{Sat} reaching the sensor passes the optics, a detector, electronics, undergoes analogue- to digital conversion and is finally quantified in a DN. A calibration function defines the transformation between the physical radiance quantity and the DN. Since sensor degradation effects are unavoidable over time, it is an important task to adjust the calibration coefficients of the linear calibration function. Each channel has its own coefficients and radiometric calibration function including the dynamic range of the specific channel:

$$L_{Sat} = L_{min\lambda} + ((L_{max\lambda} - L_{min\lambda}) / (DN_{max} - DN_{min})) \times DN \quad (5.3)$$

where $L_{min\lambda}$ and $L_{max\lambda}$ are the minimum- and maximum radiance and DN_{min} and DN_{max} are the minimum and maximum DN respectively. This can be expressed simplified as:

$$L_{Sat} = c_0 + c_1 \times DN \quad (5.4)$$

The calibration coefficients c_0 and c_1 are regularly updated based on onboard calibration methods and reflectance based vicarious calibration techniques (RICHTER 1998, THOME 2001). Onboard calibration for ETM+ includes an internal light source, a multifaceted optical device to direct solar radiation onto the focal plane and a full-aperture, full-optical-path solar diffuser (MARKHAM et al. 1996). However, onboard calibrators can not provide a calibration of higher accuracy than preflight laboratory calibrations, since the latter are used to calibrate the onboard devices. Therefore, (and due to the degradation problem of the optical elements and diffuser panel), vicarious calibrations based on ground measurements are regularly undertaken. Ideal test sites for this purpose have a high reflectance, high elevation (to minimize atmospheric influence), high spatial and spectral uniformity, minimal to no changes over the seasons, nearly Lambertian bidirectional reflectance distribution functions (isotropic reflectance) and good accessibility (THOME 2001). One of these ideal sites is the alkalic flat region White Sands Missile Range in New Mexico. Here, large amounts of ground based surface reflectance measurements (>15,000) at over 500 sampling points are used to calculate an average reflectance for the entire site. Measured reflectance and atmospherically corrected DNs of multitemporal scenes can then be compared. Landsat-7 – up to its failure in May 2003 – convinced with a great stability of all bands and only little degradation (THOME 2001, GOWARD et al. 2001).

5.2.2. Atmospheric and Topographic Corrections

Assuming a correct sensor calibration, the derivation of radiances from the DNs enables to derive the at satellite reflectance of a surface, ρ . The calculation uses incoming radiance and exatmospheric irradiance, also referred to as top of the atmosphere irradiance (TOA), E_s , which depends on the cosine of the sun zenith angle θ_s , and the earth-to-sun distance, d , in astronomical units:

$$\rho = (\pi \times L \times d^2) / (E_s \times \cos\theta_s) \quad (5.5)$$

However, only for a hypothetic case of a perfectly transmitting atmosphere equals ρ the reflectance of the object on the earth's surface. In reality the signal is modified by wavelength dependent atmospheric influences. These sometimes have such a strong impact that in the worst case the reflectance characteristics of a surface on the earth are totally masked. Although there is no agreement on which atmospheric radiative transfer code should be used to correct satellite data for atmospheric effects, there is the overall agreement that atmospheric correction is often a necessity for optical and thermal data. Most codes lead to results much alike (ATZBERGER 2002, HOLZER-POPP et al. 2002).

When electromagnetic radiation passes through the atmosphere it undergoes the processes of absorption and scattering (both add to extinction). Components of atmospheric extinction are gas absorption of mainly ozone, oxygen, water vapor and CO₂, Rayleigh scattering caused by gaseous air molecules with a radius of less than 10⁻⁴ μm , and Mie scattering caused by aerosol particles between 0.1 μm and 10 μm .

The resistance of the atmosphere to the transmission of electromagnetic radiation (EMR) – the optical thickness – is defined by the sum of the weakening influences of these three complexes (LÖFFLER 1994). Rayleigh scattering, showing a symmetrical phase function, is defined by $0,000873 \times \lambda^{-4,09}$, which is also referred to as the molecular optical thickness of a standard Rayleigh atmosphere. It imposes that scattering shows an inverse relationship with the wavelength. This means short wavelengths experience a stronger scattering than longer wavelengths.

Atmospheric correction therefore has to account for Rayleigh scattering, aerosol scattering and absorption and molecular absorption mainly caused by CO₂, O₂, O₃ and water vapor. The major atmospheric water vapour absorption bands are centered at approximately 0.94, 1.14, 1.38 and 1.88 μm , while CO₂ leads to absorption bands near 2.01 μm and 2.08 μm and O₂ at 0.76 μm . O₃, CO, N₂O and CH₄ produce noticeable features between 0.4 μm -2.5 μm . The Rayleigh contribution depends only on the pressure level and can easily be calculated analytically. The absorption effects caused by CO₂ and O₂ also depend on the pressure level, but they have a constant volume mixing ratio, so this influence can also be taken into account. Ozone and water vapor concentrations show large variations in space and time. Maps of O₃ or water vapor can be derived from meteorological satellite data. The remaining challenging task of atmospheric correction is the calculation of the spatially varying aerosol concentration (ATZBERGER 2002, ARANUVACHAPUN 1983, KRAUS 1989, RICHTER 2003).

As presented in figure 5-4, for a rugged terrain, the signal at the sensor consists of four components (L_1, L_2, L_3, L_4). These are the reflected direct and diffuse radiation from the currently viewed pixel, path radiance (depending on solar and viewing geometry), terrain reflected radiation from nearby hills and adjacency radiation caused by atmospheric scattering. L_4 therefore mainly depends on the

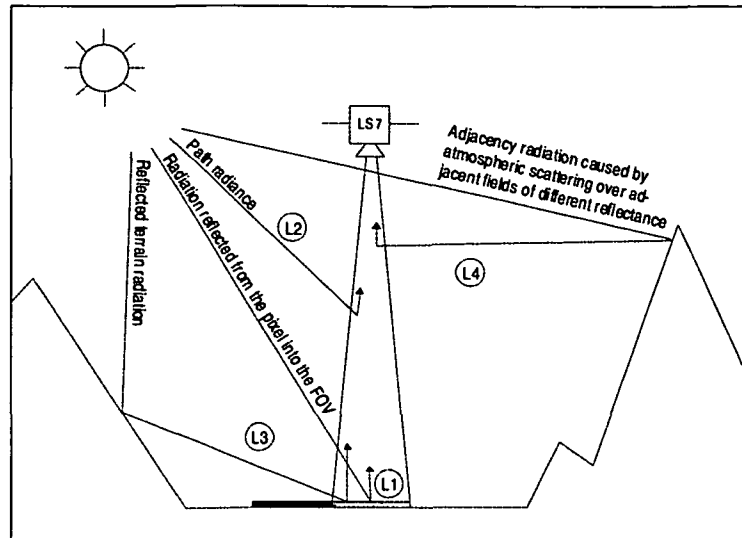


Figure 5-4: Radiance components of the signal reaching the sensor (RICHTER 1998, modified)

brightness difference between the pixel of interest and the surrounding neighborhood. Only L_1 contains the information of the actual surface properties, while L_2 , L_3 and L_4 have to be removed during the correction process.

Depending on slope and aspect a ground element (pixel) of a specific land cover class, which is exposed towards the sun, receives more energy than a pixel of the same land cover class exposed in opposite direction. Thus, the pixel exposed towards the sun will appear brighter. This effect increases the spectral variance within a single class, which can lead to misclassifications (TOKOLA et al. 2001, COLBY 1991, PROY et al. 1989). It has often been reported that this influence leads e.g. to the fact that deciduous forest areas on a sunny slope will be classified as meadow while, when located in shadowed areas, they will be classified as coniferous forest (HILL & MEHL 1995). Therefore these topographic effects should be considered within the radiometric correction process.

Many different radiative transfer codes for atmospheric correction exist; such as e.g. the 5S code (Simulation of the Satellite Signal in the Solar Spectrum) developed by TANRÉ et al. (1990) and further modified to the 6S code (Second Simulation ...) by VERMOTE et al. (1997), or codes developed by OUAIDRARI & VERMOTE (1999) and BERK & BERNSTEIN (1989). Atmospheric and topographic correction algorithms based on these radiative transfer codes were amongst others implemented by ARANUVACHAPUN (1983), HILL & STURM (1991), HILL & MEHL (2003), CHAVEZ (1996) and RICHTER (1998). CONGHE et al. (2001) stress that contrary to expectations, the more complicated algorithms do not necessarily lead to improved performance of surface classification and change detection results for imagery in flat terrain.

The Landsat-7 scenes used for this research were radiometrically corrected using the IDL code of the ATCOR 3 model developed by RICHTER (1998, 2003). This model takes the atmospheric and topographic effects as well as the optical mass into account. The optical mass is defined by the atmospheric column above a point on the earth's surface depending on its elevation.

The code calculates at-sensor radiances (L_{Sat}) for each pixel in each channel as the first step. Then, atmospheric transmittance, direct and diffuse solar flux and path radiance as needed for the atmospheric correction will be extracted from an atmospheric database compiled with MODTRAN-4

radiative transfer code (BERK & BERNSTEIN 1989). This database represents a wide range of atmospheric conditions based on manifold cross combinations of water vapor content (8 classes, 0.4-4.1 cm water vapor column), aerosol types (5 classes), ground elevations (6 classes, 0 km - 2.5 km), solar zenith angles (8 classes, 0°-70°) and visibility. It allows an approximated definition of atmospheric conditions for the satellite data without the need to recalculate the whole radiative transfer for each individual case (RICHTER 1998, 2003).

The properties of the selected standard aerosol type will be modified iteratively to match scene conditions based on the “dark dense vegetation / dark object approach” using dark pixels of known reflectance to derive the scene-specific optical depth. If several dark areas exist, a spatially varying map of the optical depth can be triangulated. In case no dark objects are available, a standard atmosphere with a user specified visibility can be used. For details on the dark object approach see KAUFMANN & SENDRA (1988) and SONG et al. (2001).

Since all scenes used for this research were completely haze- and cloud free an interactive masking of these areas was not necessary.

The four radiance components summing up to the radiation reaching the sensor (in $\text{mW cm}^{-2} \text{sr}^{-1} \mu\text{m}^{-1}$) have already been introduced in figure 5-4. Component L_1 is calculated as:

$$L_1 = \tau_v (\rho/\pi) (E_{\text{dir}} + E_{\text{dif}}) \quad (5.6)$$

where τ_v , ρ , E_{dir} , E_{dif} are ground-to-sensor transmittance, ground reflectance and direct and diffuse solar flux (RICHTER, 1998).

L_2 – path radiance (L_p) – is known from the radiative transfer code, while component L_3 is described by:

$$L_3 = \tau_v (\rho/\pi) \rho_{\text{TerraIn}} E_g \quad (5.7)$$

where E_g is the global direct and diffuse flux on the ground and ρ_{TerraIn} is an approximation of the terrain reflected radiation obtained by weighting the reflected radiation in a 0.5 km surrounding of a pixel with the terrain view factor V_{terraIn} . This factor is derived from $1 - V_{\text{sky}}$, with the latter representing the visible part of the sky hemisphere for a pixel (x,y) calculated from a DEM.

Neglecting the adjacency effect, L_4 , we receive:

$$L_{\text{Sat}} = c_0 + c_1 \text{DN} = L_1 + L_2 + L_3 \quad (5.8)$$

which can be transferred to:

$$\rho = \pi (d^2 L_{\text{Sat}} - L_p) / [\tau_v (E_{\text{dir}} + E_{\text{dif}} + \rho_{\text{TerraIn}} E_g)] \quad (5.9)$$

where d is the Earth-Sun distance in astronomical units. Equation 5.9 is extended to account for the directional dependence of the direct and diffuse solar radiation in a rugged terrain. The reflectance is then calculated iteratively starting with $\rho_{\text{terrain}}^{(0)} = 0.1$ and neglecting the adjacency effect:

$$\rho_i(x, y) = \frac{\pi \times \{d^2 [c_0 + c_1 \text{DN}(x, y)] - L_p(z, \theta_v, \phi)\}}{\tau_v(z, \theta_v) [b(x, y) E_s \tau_s(z) \cos \beta(x, y) + E_d^*(x, y, z) + E_g(z) \rho_{\text{terrain}}^{(i)} V_{\text{terrain}}(x, y)]} \quad (5.10)$$

representing the true reflectance ρ of each pixel in each band with:

x, y : horizontal coordinates corresponding to the georeferenced pixel positions;

z : containing the elevation information from the DEM;

DN: digital number;

$L_p(z, \theta_v, \phi)$: path radiance depending on elevation and viewing geometry;

$\tau_v(z)$: ground to sensor view angle transmittance with direct and diffuse components;

$\tau_s(z)$: sun to ground beam (direct) transmittance;

$\beta(x, y)$: angle between the solar ray and the surface normal (illumination angle);

b : binary factor with $b = 1$ if a pixel receives a direct solar beam, otherwise $b = 0$;

E_s : exatmospheric solar irradiance;

$E_d^*(x, y, z)$: diffuse solar flux;

$E_g(z)$: global flux (direct plus diffuse solar flux at a horizontal surface with elevation z);

$\rho_{\text{terrain}}^{(0)}$: initial value (constant for each band) of average terrain reflectance;

$\rho_{\text{terrain}}^{(i)}(x, y)$: locally varying average terrain reflectance, calculated iteratively ($i=1,2,3$) by low pass filtering the image with a box of $1\text{km} \times 1\text{km}$, i.e., twice the $R = 0.5\text{-km}$ range;

$V_{\text{terrain}}(x, y)$: terrain view factor (0-1 range) calculated from the local slope or a horizon analysis (RICHTER 1998).

Here, the reflectance ρ_i of a pixel is calculated iteratively based on the previously selected atmosphere (water vapour, aerosol type), the visibility map and the DEM. After three iterations the results indicate an asymptotic behavior not leading to distinct further improvements (RICHTER 1998).

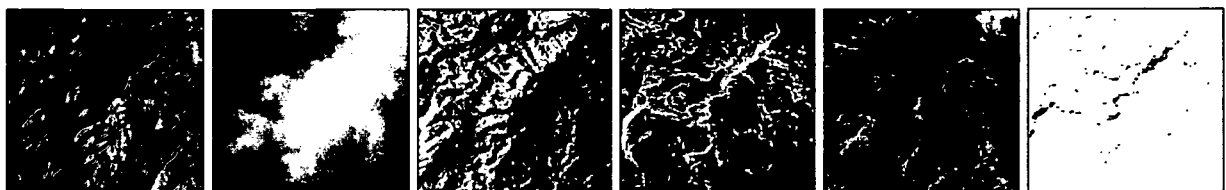


Figure 5-5: Image input parameters in ATCOR-3 (image bands, DEM, aspect, slope, skyview and shadow file)

The final reflectance ρ_f including the adjacency effect is calculated from the result of equation 5.10. and the local average reflectance in the $1\text{km} \times 1\text{km}$ neighborhood of a pixel:

$$\rho_r = \rho(x, y) + q[\rho(x, y) - \rho'(x, y)] \quad (5.11.)$$

where q is a weighing factor (stored in the database derived from MODTRAN-4 representing the ratio of diffuse to direct transmittance); which is extended further to include the range dependent exponential decrease of the adjacency effect (see RICHTER 1998 for further details).

5.2.3. Results and Validation

When correcting the multitemporal scenes of frame 129/33 from 1987, 1999, 2000, 2001, 2002 and 2003 it became obvious that the actual calibration files available for the specific time periods in ATCOR-3 did not yield good results in calibrating and correcting the data. Pixel values in the blue band dropped below zero pseudo-indicating either a strong sensor degradation or data inherent errors in the raw data. Furthermore, for many scenes even after the radiometric correction did image spectra not coincide with the spectra measured in the field and laboratory, which were used as reference for the radiometric correction quality assessment.

To account for this problem, a relative calibration procedure was performed. This procedure improves the spectral comparability of scenes after radiometric correction when dealing with time series of data. The calibration parameters of uncorrected scenes are calculated based on a corrected master scene (129/33 from 1999) using a linear regression. To compute the regression several surfaces, which do not spectrally change over time (bare sand, bare rock etc.) and which are often referred to as pseudo-invariant objects, will be spectrally compared. A regression for the different reflectance values in each band is derived. Four reference targets, which were pure desert sand, bare soil, pure Sandstone and mixed sand were chosen to apply this approach. The reference targets were located in homogeneous areas not influenced by mixed signatures or adjacency effects. The calibration coefficients were then calculated with a least squares fit approach applied to a linear regression equation (see figure 5-6). This process was repeated for all other scenes of this frame. The highly significant correlation derived from the linear regression proves the stability of the model and grants inter-scene as well as good spectra comparability.

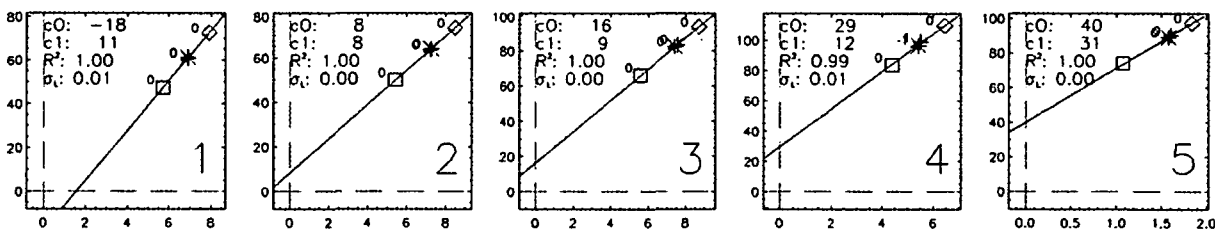


Figure 5-6: Regression analysis for 4 calibration targets inflight calibrating the scene 129/33 of 2000 here shown for bands 1-5. x-axis: reflectances in %/100, y-axis: reflectances in %. Four pseudo-invariant targets.

In some cases the generation of an own calibration file, which can be created based on the header file of the individual raw scene were sufficient to reach comparable signatures (e.g. for the two Aster scenes). Each header file contains the minimum and maximum radiance (L_{Sat}) recorded for each channel respectively. The coefficients c_0 and c_1 can be derived with:

$$c_0 = L_{min} / 10 \quad \text{and} \quad c_1 = ((L_{max} - L_{min}) / 254) \times 0.1 \quad (5.12.)$$

After the application of the individual parameter files the atmospherically corrected data of the time series fit very well. This could be proven comparing signatures of pseudo-invariant targets like pure sandstone, sand and light limestone over time. The atmospheres used for the correction of the different satellite scenes are presented in table 5-4.

*Table 5-4: MODTRAN 4 standard atmospheres applied. Scenes marked with a * were adjusted (calibration files, or relative calibration as presented on the last page)*

Path/Row	Sensor	Date	Solar azimuth	Solar zenith	MODTRAN atmosphere
129/033	ETM+	12.08.99	132.73	31.41	dry rural atmosphere
129/033	ETM+	17.10.00	155.63	51.39	dry rural atmosphere
129/033	ETM+	04.10.01	151.53	47.04	dry rural atmosphere
129/033	ETM+	21.09.02	147.12	42.97	dry rural atmosphere
129/033*	ETM+	10.12.02	149.16	58.36	dry rural atmosphere
129/033*	ETM+	12.02.03	158.22	64.95	dry rural atmosphere
129/933*	ETM+	03.05.03	133.69	30.52	dry rural atmosphere
128/032	ETM+	29.08.02	139.80	37.16	dry rural atmosphere
098/081	ETM+	15.11.02	74.15	30.46	fall desert atmosphere
140/044	ETM+	02.11.01	147.98	43.68	tropical rural atmosphere
129/033	TM	20.09.87	141.10	43.91	dry rural atmosphere
Wuda	AST	24.09.03	126.50	46.50	dry rural atmosphere
Ruqigou	AST	08.09.03	133.60	50.60	dry rural atmosphere
Wuda	QB	05.10.03	155.60	46.80	no atm. correction
Ruqigou	QB	22.09.03	152.70	41.70	no atm. correction

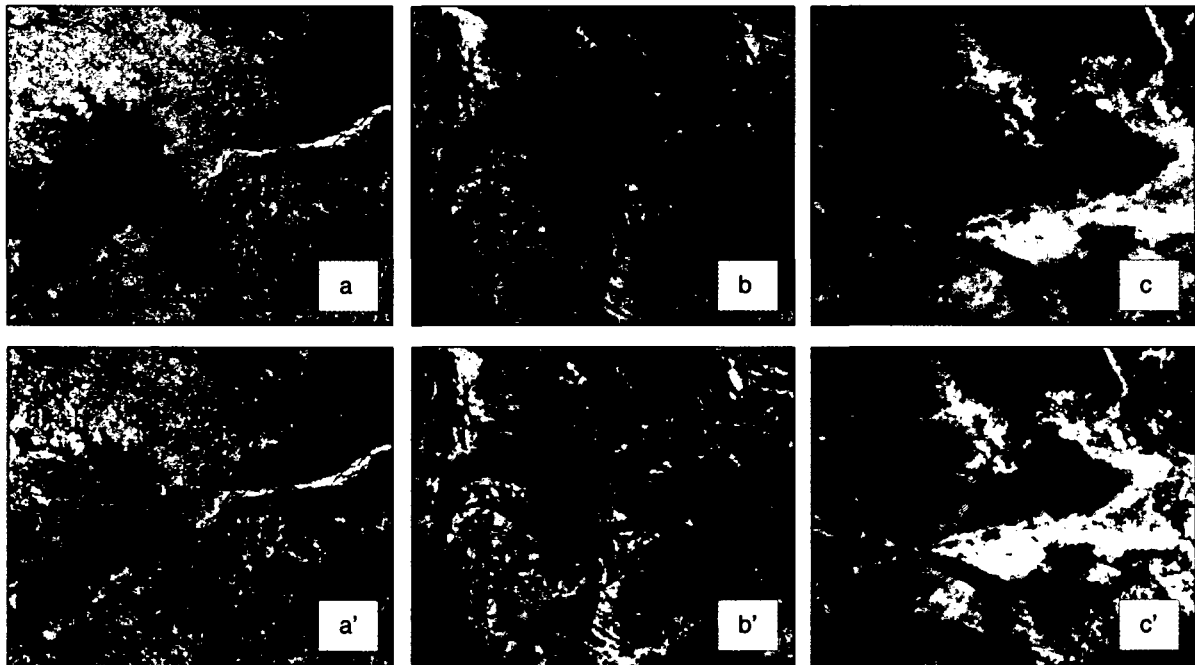


Figure 5-7: Visual impression before (top row) and after (bottom row) the radiometric correction for a subset of the Landsat-7 ETM+ scene from India (a), Australia (b) and Baotou (c) used for later transfer purposes. Center locations: UTM, a: 385657E, 2624616N, Z45N, b: 256271E, 6655205S Z54S, c: 356912E, 4405175N, Z49N

Figure 5-7 presents the result of atmospheric correction for the Landsat-7 transfer scenes. Due to the lack of a DEM and a relatively flat terrain ATCOR-2 was applied. It can clearly be seen that the amount of Rayleigh scattering still present in the top images has been reduced in the bottom row. The overall blur due to aerosol influence has decreased substantially.

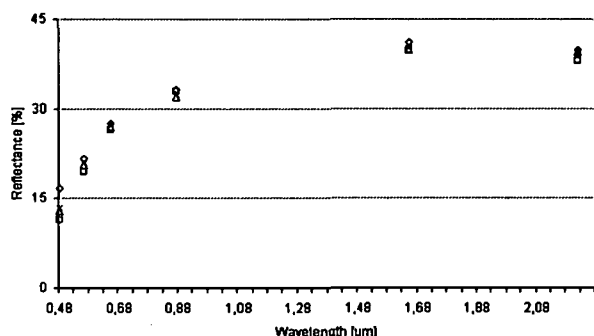


Figure 5-8- presents a comparison of a resampled desert sand reference spectrum measured in the spectral laboratory (\diamond) and three spectra collected in an atmospherically corrected image. The “ \times ” spectrum is from the same area as the sample (close to Wuda) and proves the high quality of the correction. The “ Δ ” and “ \square ” spectra are desert sand spectra from the scene of Baotou (128/032).

Figure 5-8: Quality assessment of the radiometrically corrected scenes based on the recorded spectra

Figure 5-9 presents two sets of spectral profiles of three different surfaces from the same scene in the coal mining areas before and after the correction. To compare DNs (before) with reflectances (afterwards) the DNs were transferred into reflectances at the top of the atmosphere (TOA-reflectance, ρ_{TOA}), also called ‘apparent reflectance’, defined by equation 5.5. TOA-spectra and surface spectra of the Yellow River (dark turquoise), water of a small lake (light turquoise), and coal (black) were compared. The overall impression of the ‘before’- and ‘after’ situation proves that the additive scattering part especially in the blue range of the spectrum could clearly be eliminated. Also the scattering in the NIR, which is visible in the spectrum of lake water before the correction, could be minimized. This was expected since clear water bodies reflect only visible EMR while the reflection in the NIR should be close to zero. Only turbid water bodies with large amounts of algae or sediment have a moderate surface reflectance of a few percent. High values of the Yellow River in the green, red and NIR are caused by high amounts of sediment and algae within the water. Especially the latter leads to the peak in the NIR.

Figure 5-10 presents two small subsets of frame 129/33 from 1999 before and after the combined atmospheric and topographic correction at the foothills of a metamorphic complex south of

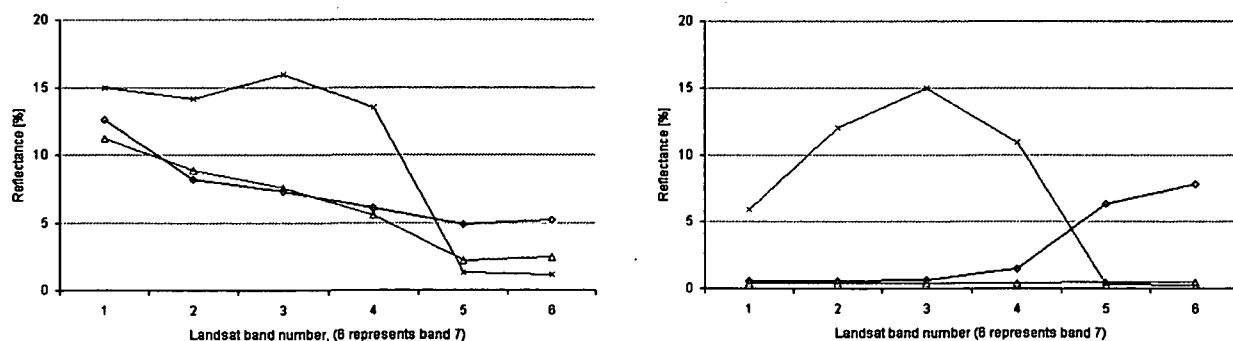


Figure 5-9: Landsat-7 ETM+ spectra of three different surfaces (Yellow River=dark turquoise, lake water=light turquoise, coal=black) before (left) and after (right) the atmospheric correction. Band number 6 on the x-axis is band 7 (MIR) of the Landsat ETM+ data.

Wuda grading into an alluvial fan in the East. The visual comparison illustrates that relief induced illumination effects could be reduced substantially through the combined radiometric correction of the data. Shadowed areas were clearly lightened up. Only after the topographic correction do similar objects have a similar spectral behavior. Nevertheless, not all areas can completely be equalized since some areas might be located within a core-shadow region where the signal does not receive any spectral signal of the surface. This is often the case in areas of extreme slopes or narrow and deeply incised valleys and canyons. Therefore no topographic correction can eliminate 100% of the relief induced radiometric effects present in the data.

The analysis of spectra before and after atmospheric- and topographic correction procedures (figure 5-9) as well as figures 5-7, 5-8 and 5-10 qualitatively support the success of the corrections. However, it should be mentioned that direct photometer measurements in the field during overflight times were not undertaken and a variable aerosol optical thickness over an area of nearly $180 \times 180 \text{ km}^2$ could not be assessed. Therefore, data other than spectral measurements to quantitatively assess the radiometric correction based on ground truth is not available and applicable.

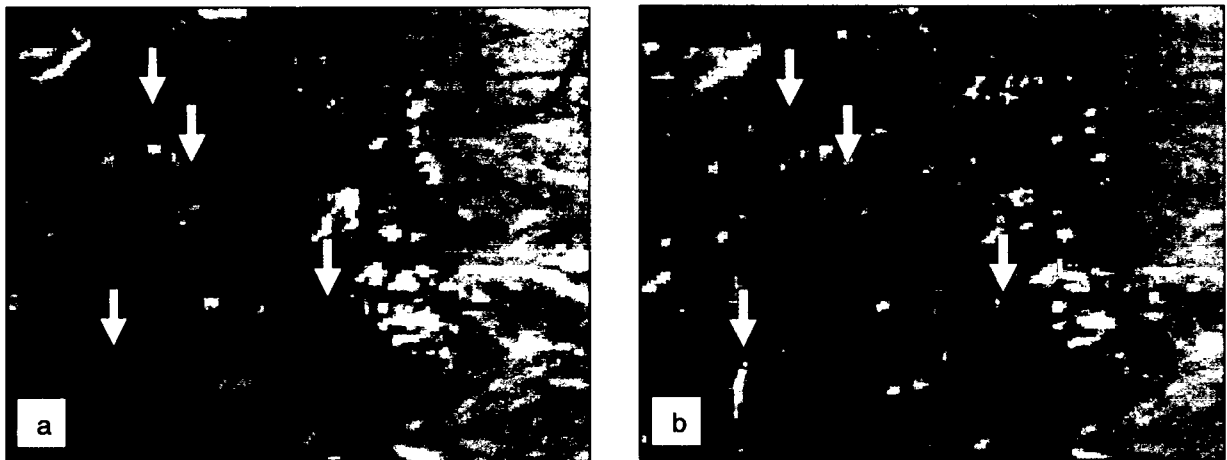


Figure 5-10: Visual impression before (a) and after (b) the combined radiometric correction using ATCOR-3. Center location: 642959E, 4360922N, UTM, Z48N

Nevertheless, an approximating quantitative validation for the reduction of topographic influences could be obtained on a statistical basis through a regression analysis of the relationship between the computed scene reflectances and the cosine of the illumination angle (HILL & MEHL 1995, RICHTER 1998). Before topographic correction, a significant correlation coefficient of $R^2 = 0.93$ is obtained, illustrating that small illumination angles cause high radiance values interpreted as high reflectance, while large illumination angles cause low radiance values interpreted as low reflectance. After the combined atmospheric and topographic correction the correlation coefficient is clearly reduced ($R^2=0.24$), indicating the successful removal of relief induced reflectance differences. This calculation is based on 8 pixels, where ground truth was available. The eight plots are all located on a small limestone ridge on the eastern side of the Yellow River. The surface consists of bare limestone covered with a sparse grass cover on the eastern and western slope. Two pixels are located in completely flat terrain near a road, while two are located on a steeper cliff – the others are located on the intermediate slope. For a larger area, where no ground truth is available though, the correlation coefficient is 0.73 before- and 0.28 after the combined correction. However, figure 5-10 demonstrates that some shadowed areas remain and that over-corrections occur as well.

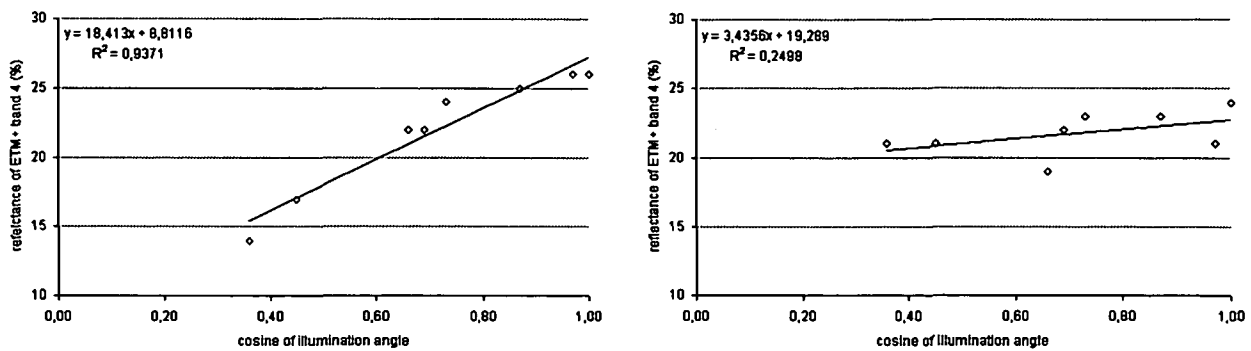


Figure 5-11: Regression analysis of the cosine of the illumination angle versus scene reflectances before and after the topographic correction for eight pixels located on a sun-facing and sun opposing limestone ridge in the area around center location 661553E, 4360919N, UTM, Z48N

Regarding inner class separability investigations (different vegetation types, differentiation of similar geologic units etc.) SCHARDT (1990) illustrated that a stratification of a study area based on topographic and illumination parameters is strongly supporting signature discrimination. He stratified his study area into classes of different elevation, slope, aspect and illumination and demonstrated the reflectance dependence of tree species signatures on these topographic / geometric parameters. Different tree types and age classes could then be differentiated taking this relief-dependent behavior into account. However, in this case the aim to extract certain surfaces does not require for as much precision as applied in the above investigation, but rather focuses on inter-class separability (vegetation from geology) than on inner-class separability (vegetation from vegetation). The accuracy of corrections reached in the presented preprocessing procedure is considered good and sufficient for further analysis.

Nevertheless, error sources in radiometric correction can still occur and should be mentioned. A critical point for atmospheric correction is the fact that surfaces – contrary to the default assumption in ATCOR3 – usually exhibit non-Lambertian reflectance characteristics as defined by their bidirectional reflectance distribution function (BRDF). If the BRDF of a surface is known, the reflected outgoing spatial radiance for a given – directionally varying – incoming radiance can be calculated (KRAUS 1989). RICHTER (1998) underlines that although accounting for the BRDF (which is optional in ATCOR3) can lead to improvements, difficulties may still remain. Although the isotropic- or Lambertian reflectance assumption is appropriate for sensors with a small scan angle ($< \pm 15^\circ$), the BRDF plays a role especially in mountainous terrain with large slopes and an extreme range of incidence angles influencing the resulting reflectance. Here, the Lambertian assumption may cause over-corrections of faintly illuminated areas, where local solar zenith angles, β , range from $60^\circ - 90^\circ$ (RICHTER 2003). However, in these regions the BRDF is no longer symmetrical and BRDFs recorded from flat areas cannot be applied.

SCHARDT (1990) underlines that BRDF effects are especially strong in vegetation types of different surface roughness depending on volume and leaf / stem geometry. However, these effects can not be accounted for in a large study area or in a transferable approach – otherwise ground truth and BRDF characteristics would have to be available for each scene. Also, most atmospheric / illumination correction codes cannot account for BRDF effects since land surface classes are rarely known a priori (HOSTERT 2001).

A further uncertainty is once again the quality of the DEM, which strongly influences the quality of the illumination correction. This refers back to the statement at the very beginning of chapter 5. For a detailed analysis of the influence of DEM inaccuracies on atmospheric correction see RICHTER (1998).

It becomes obvious that the derivation and correction of atmospheric and topographic influences based on a radiative transfer code and a radiometric correction algorithm is everything else but trivial and can only approximate conditions during the satellite's overpass. Nevertheless, it could be demonstrated above that for the data from varying times and locations used in this study, a combined radiometric correction leads to distinct improvements of the reflectance data of the scenes. However, manual adjustments to grant a quantitative comparability of time series of data was necessary.

5.3 Radiometric Correction of the Thermal Band

5.3.1. Principles and Methods Applied

The atmospheric correction of the thermal band 6 of ETM+ or thermal bands of other sensors is an integral part of the overall atmospheric correction. However, the radiometric calibration is demonstrated separately to account for differences in physical principles and correction procedures compared to the reflective bands.

All Landsat bands are acquired in either a low- or a high gain mode. Gain selection is defined in the gain strategy of the Long Term Acquisition Plan (LTAP), depending on acquisition time and the dominating surface types in a scene (percentages of land, desert, ice/snow, water, sea ice etc.). These are known a priori based on maps. Except for very specific requests the user has no influence on the gain setting in the reflective modes. Nevertheless, LS-7 band 6 will always be recorded and delivered in the low- and the high gain mode extending the dynamic range of the data.

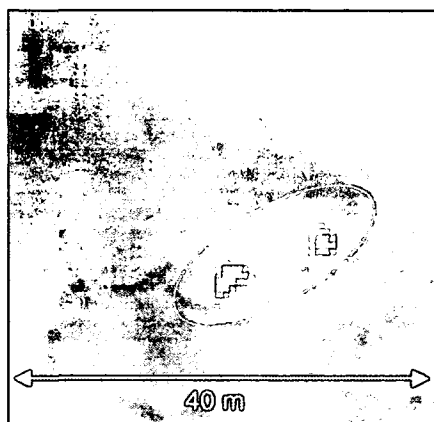
Still, detector saturation can occur if a surface has extremely high temperatures or a surface will thermally not be detected, if temperature decreases below a certain threshold. Table 5-5 lists the minimum and maximum temperatures in the low-gain and high-gain (in brackets) setting, indicating the lowest respectively highest pixel integrated temperature, which can be detected in a certain wavelength region. It should be noted that band 6 ranges from 10.4 μm to 12.5 μm only, to avoid effects of ozone adsorption. Its broad bandpass of 2 μm combined with only 60 m ground resolution enable a sufficient thermal energy yield.

Table 5-5: Temperature of saturation in the low- and high gain bands of Landsat-7 ETM+

channel	μm regions	Minimum temperature [$^{\circ}\text{C}$]	Maximum temperature [$^{\circ}\text{C}$]
1	0.45 - 0.51	1051 (1075)	1483 (1526)
2	0.52 - 0.60	900 (922)	1301 (1340)
3	0.63 - 0.69	755 (775)	1119 (1156)
4	0.75 - 0.90	595 (613)	926 (961)
5	1.55 - 1.75	206 (217)	417 (440)
6	10.40 - 12.50	-33 (-134)	51 (77)
7	2.09 - 2.35	92 (101)	258 (276)
8	0.52 - 0.90	702 (721)	1056 (1092)

(Source: Flynn et al. 2001, modified)

It can be seen that the mid Infrared band 5 can be used to detect thermal anomalies of very high temperatures leading to saturation in band 6 (ZHANG, X. 1998). Even the near Infrared channel 4 offers options for the detection of extremely high temperatures. It has not been used in coal fire research up to present, although successfully applied to lava-stream research, where higher temperatures are common (ROTHERY & FRANCIS 1990).



However, in the 60 cm resolution panchromatic Quickbird data this phenomenon can also be detected. Figure 5-12 to the left shows a small part of fire #8 in the Wuda syncline with a very hot crack observed during all three field campaigns. Here temperatures up to 800°C were measured. The brightness of the pixels in band 4 results from these very high temperatures and not from an reflective expression.

Figure 5-12: very hot temperatures shift the radiation maximum to the NIR resulting in bright pixel values not representing an optical phenomenon. Location: 639085E, 4374840N, UTM, Z48N

Though the low- and high-gain options offering a higher dynamic range are new compared to former Landsat-TM, the thermal bands of ETM+ are less suitable for high temperature studies. They saturate at 51° C and 77° C respectively, while TM band 6 saturated at around 90° C. It is also often stated that ETM+ still suffers from an antiquated 8bit dynamic range, limiting radiance steps to 256 instead of e.g. 4096 if a 12 bit system was used (FLYNN et al. 2001). Nevertheless, it is also important to underline that thermal contrasts in 8-14 μm data are much better than in 3-5 μm data (SABINS 1996). 8-14 μm data therefore have great advantages for terrain mapping.

In contrast to radiometric corrections of the reflective bands, for band 6 the physical principles of thermal absorption and -emission apply. Not the reflectance in percent has to be calculated, but the temperature of a surface in ° C or K. In the thermal spectral region (8-14μm) water vapor is the dominating disturbing parameter, while aerosol types play only a negligible role. These two mainly determine L_p and τ .

The radiance equation in the thermal spectral region can therefore be expressed as:

$$L_{Sat} = L_p + \tau_v \times \epsilon \times L_{Surf}(T) + \tau_v (1-\epsilon) \times F_{th}/\pi \quad (5.13)$$

with:

L_{Sat} : at-sensor radiance

L_p : thermal path radiance

τ_v : ground to sensor atmospheric transmittance

ϵ : surface emissivity

T: surface temperature

L_{Surf} : blackbody radiance at the ground surface

F_{th} : thermal downwelling flux on the ground

The second and the third term are the emitted surface radiance reaching the sensor and atmospheric radiance reflected at the surface and attenuated on the way to the sensor respectively. τ_v accounts for the influence of the constituents of the atmosphere. It is again a height dependent term derived from the MODTRAN database and the DEM. The emissivity is a surface inherent characteristic modifying the surface's thermal signal (RICHTER 2003, FLYNN et al. 2001, SCHMUGGE et al. 1991).

Planck's law (see equation 5.14) defines the radiation released by a black body. Very few terrestrial surfaces act as black bodies but rather as gray bodies, which re-emit only a percentage of the radiance incident on them. The emissivity term is defined by Kirchoff's law ($\epsilon_{(\lambda)} = 1 - R_{(\lambda)}$) where $R_{(\lambda)}$ is the spectral reflectance between 0 and 1. Emissivity varies depending on surface type and wavelength but is not temperature dependent (FLYNN et al. 2001). While materials with a high ϵ absorb large amounts of incidence energy and radiate large quantities of kinetic energy, materials with low ϵ absorb and radiate lower amounts of energy (SABINS 1996). Table 5-6 presents emissivities of common surfaces in the wavelength range of 8 to 14 μm .

Table 5-6: Emissivity of different surfaces

surface	Emissivity at 8-14 μm
Leaves	0.97
Sand	0.93
Asphalt	0.96
Water	0.99
Granite	0.82
Basalt	0.90
Ice	0.98
Wood	0.96

Source: KRAUS 1989

Correcting for emissivity effects can be done by classifying the optical channels of an image into different surface types and assigning an emissivity value to each land cover class. This approach is integrated in ATCOR-3, pre-classifying the image into three classes (water, vegetation, bare ground). Therefore, the emissivity problem is at least approximated. As soon as ϵ is known for a pixel the LST can be retrieved (SCHMUGGE et al. 1991, PRAKASH & GUPTA 1999, GANGOPADHYAY 2003).

RICHTER (2003) states that as a rule of thumb a 0.01 emissivity error leads to a temperature error of 0.5 K, while VIDAL (1991) assumes an error of 1 K. Therefore, a detailed emissivity correction would be recommended when aiming at the retrieval of very exact surface temperatures (BECKER 1987). Even if a-priori classification knowledge exists, this is difficult though, since the emissivity of a pixel depends on the composition of surfaces. In case of a mixed pixel mixed emissivities would have to be calculated. Approaches to derive the emissivity of surfaces were amongst others developed and applied by BECKER (1987), NERRY et al. (1990), HOOK et al. (1992) and KEALY & HOOK (1993). They mainly applied data other than Landsat – namely TIMS- or NOAA-AVHRR data in combination with extensive field measurements. CRACKNELL & XUE (1996) based their studies on Heat Capacity Mapping Mission (HCMM) data. Furthermore, soil moisture or general moisture of a surface play an important role. However, the correction performed with ATCOR for three broad classes is sufficient when aiming at the calibration of the thermal channel as an input into signature extraction algorithms. This applies also for the retrieval of thermal anomalies contrasting to the background and neglecting absolute temperature determination.

The relationship of the radiation emitted by a blackbody (L_{Surf}) at a given wavelength (λ) and kinetic temperature (T) can be derived from Planck's law:

$$L_{\text{Surf}(\lambda, T)} = (2hc^2 / \lambda^5) \times (e^{hc/\lambda kT} - 1)^{-1} \quad (5.14)$$

where L_{Surf} is the emitted radiation in $\text{W}/\text{m}^2/\mu\text{m}/\text{sr}$ at wavelength λ and temperature T in Kelvin, h is the Planck's constant ($6.63 \times 10^{-34} \text{ W} \times \text{s}^2$), c is the speed of light ($2.998 \times 10^8 \text{ m/s}$) and k is the Boltzmann's constant ($1.3805 \times 10^{-23} \text{ W} \times \text{S} \times \text{K}^{-1}$) (FLYNN et al. 2001, KRAUS 1989). Resulting, the higher the temperature of a surface, the more radiation it will emit at all wavelengths. To retrieve the brightness temperature of an object formula 5.14 can be rearranged to:

$$T_{(\lambda, k)} = (hc/\lambda k) \times (\ln((2hc^2)/\lambda^5 L_{\text{Surf}} + 1))^{-1} \quad (5.15)$$

Within ATCOR 3 surface temperature is retrieved on the basis of the visibility index (optical depth), water vapor, elevation and scan angle modified for the viewing geometry. While a slope and aspect correction is applied for the reflective bands, it is not performed in the thermal region. However, it would be reasonable to correct for the fact that – until a certain sensor overpass time – pixels are illuminated unevenly long and unevenly strong depending on their slope and aspect. In mountainous terrain uneven solar heating is the main source of confusion for coal fire induced thermal anomalies in daytime data (ZHANG, X. 1998, WARNER & CHEN 2001).

The calculation of this time integrated energy gain of surfaces is extremely complicated though. This results from the fact that different surfaces have different thermal behaviors (TIPLER 2000), amongst other physical parameters expressed by the thermal inertia. The thermal inertia, P ($\text{cal}/\text{cm}^2/\text{sec}^{-0.5}/^\circ\text{C}$), is defined as the resistance of a material against its heating for 1°C , depending on the specific warmth, c . This is the energy needed to rise the temperature of a material for 1°C (heat capacity C) per mass unit of the substance (m), the density of a material, p – the main determining factor – and the thermal conductivity, k , of an object.

$$P = \sqrt{c \times p \times k} \quad (5.16)$$

Variations of P result in changes of ΔT (KAHLE et al. 1976). ΔT is the difference between the maximum and minimum temperature occurring during a diurnal solar cycle. Low thermal inertias indicate low resistance to temperature changes resulting in a high ΔT . The opposite applies for surfaces with a high thermal inertia. With remote sensing, P can usually not be derived, since c , p and k can only be measured in the field. However, PRATT et al. (1977) as well as CRACKNELL & XUE (1996) introduce interesting approaches for the application of thermal inertia models – even to derive P from space.

Table 5-7: Thermal properties of geologic materials

Material	Thermal conductivity, K [cal/cm/sec/°C]	Thermal capacity, C [cal/g/°C]	Thermal inertia, P [cal/cm ² /sec ^{-0.5} /°C]
Clay soil, moist	0.0030	0.35	0.042
Sandstone	0.0120	0.19	0.074
Limestone	0.0048	0.17	0.045
Shale	0.0042	0.17	0.041
Sandy soil	0.0014	0.24	0.024

(Source: SABINS 1996)

Furthermore most surfaces within a 60×60 m thermal pixel are mixed surfaces and cannot be described or even approximated with one specific surface class. Additionally it is found that even the BRDF effect (which is actually a BEDF effect in the thermal wavelengths) is of relevance in the thermal region. The shape of the BRDF-curve (with respect to the viewing angle) is extremely dependent on the heterogeneity within a pixel. Due to all these complex facts so far no sufficient model for the topographic thermal correction of unbalanced energy gain and release exists. An approach for the optical wavelength region has been developed by SCHAAB (2000) modeling the incidence radiance on a pixel of a certain position (x,y,z) between sunrise and sunset or between two defined times during the day respectively (additive approach). Nevertheless, the model – aiming at the retrieval of the amount of light received by a plant (PAR) – is valid for radiation from the optical region only, assuming that light is reflected and not stored and later emitted like thermal radiation. ZHANG, X. (1998) employed a basic approach modeling solar heating based on a DEM, the azimuth and elevation angle of the sun and the overpass time of Landsat-TM. However, the model was only developed as a case study for a small area and is not available nor transferable for mass throughput. The same applies to neural network based calibration studies applied in the Kelazha coal fire area, Xinjiang, China by DENG et al. (2001).

5.3.2. Results and Validation

The accuracy of the temperatures retrieved after sensor calibration and atmospheric correction can be assessed based on ground truth temperatures measured during the overflight of the satellite during the field campaign in 2002. Figure 5-13 shows a subset of an atmospherically corrected Landsat-7 nighttime scene within the coal mining area of Wuda. The different colors illustrate different temperatures ranging from 1 to 29°C.

During the Landsat-7 nighttime overflight in 2002 the temperature of the Yellow River was measured as 14.2°C. During the daytime overflight in 2002 three geologic surfaces (coal, sandstone, desert sand) were investigated regarding their thermal behavior over a larger area. Derived and integrated at ground temperatures vary for less than 1.2° C indicating a good result of the thermal atmospheric correction.

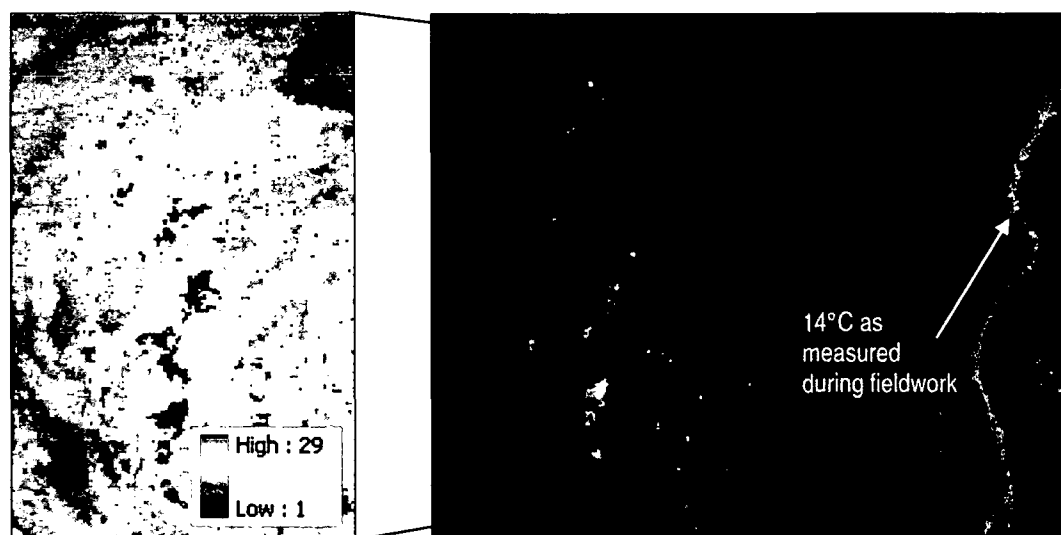


Figure 5-13: Subset of the thermal nighttime scene (ETM+) from 28.09.2002; DN's transferred to temperature in °C and atmospherically corrected, center location (right subset): 645646E, 4376164N, UTM, Z48N.

Additional temperature observations were not available, since temperatures – compared to spectral signatures change very quickly with time. Unfortunately, in 2003 during the overpass time of Landsat the sky was cloud covered. During the 2004 field campaign Landsat ETM+ was already suffering from the erroneous scan mirror effect.

The winter scene from 03.02.2003 presented in figure 5-14 is displayed as a false color composite image (left) and a temperature image (right). Temperatures range between -13°C (black) and 29°C (white). The Yellow River is frozen in most parts and temperatures range between -2°C to 1°C . Water temperature measurements from Wuhai in non frozen areas confirmed these temperature retrievals ($0-1^{\circ}\text{C}$). Coal surfaces ($15-22^{\circ}\text{C}$) and sun-exposed geologic surfaces are the warmest areas, while the deeply incised valleys on the eastern side of the Yellow River and the northwest exposed slopes in the northern Helan Mountains (-13 to 0°C) are the coldest regions. When radiometrically correcting winter scenes it has to be taken into account that negative temperature values may occur and therefore the data has to be handled as “signed” 8 bit instead of “unsigned” 8 bit data.

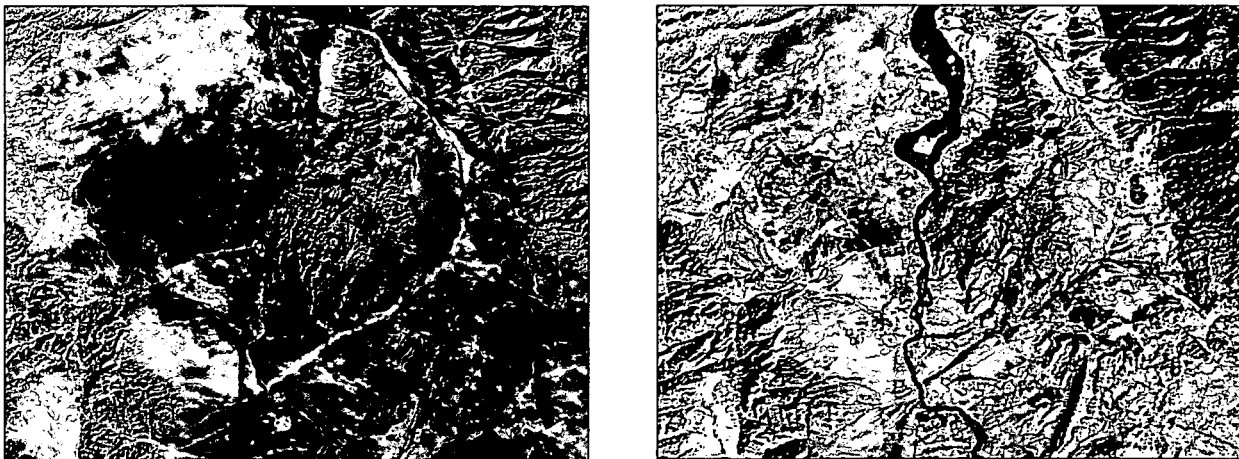


Figure 5-14: Subset of the thermal daytime scene from 12.02.2003; left: false color infrared image, right: DN's transferred to temperature in $^{\circ}\text{C}$. Light: high temperatures, dark: lower temperatures (atmospherically corrected with ATCOR-3), center location: 650695E, 4373295N, UTM, Z48N.

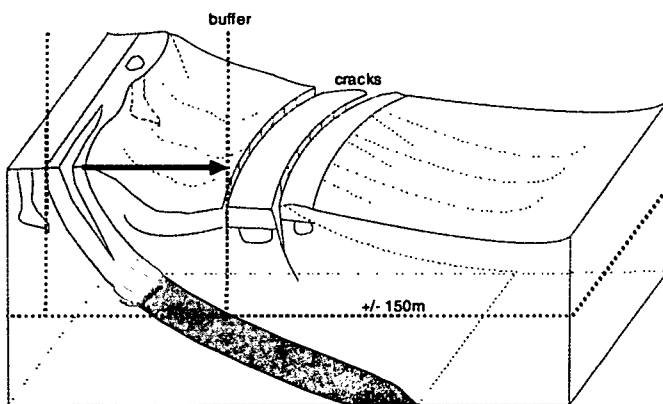
6. Conceptual Approach of Coal Fire Area Demarcation

The following chapter presents the conceptual approach developed on how to demarcate currently active and future coal fire risk areas. The conceptual approach of coal fire area demarcation is based on observations made during the field campaigns in 2002 and 2003.

Coal fire occurrence is not related to certain elevation zones or aspect and slope regimes – information, which could be derived from a DEM. Coal fires are also not related to certain geologic land cover types, since the coal seams can be interbedded in strongly differing bedrock layers of very different spectral behavior. Coal fires can occur in densely settled as well as uninhabited and remote areas. They are also not restricted to a certain climate. The roughest demarcation base for coal fires in China is a vector data set representing coal bearing regions along the borders of former sedimentary basins. These are areas, where coalification occurred. However, coal fires can still occur outside this limited area in case of coal waste pile fires or coal storage pile fires.

6.1. Extraction of Coal Surfaces

At risk for coal fires are abandoned and active mines, coal seams, coal waste piles, coal storage piles, coal washery discard and coal with overlaying material like shale or mudstone, which provides extensive fuel resources and speeds up the self heating. Coal fires can therefore only occur in the vicinity of outcropping coal seams, coal waste- or coal storage piles and related coal accumulations (PRAKASH et al. 2001, KUENZER et al.2004a). Thus, the detection of the signature “coal” and knowledge of the distribution of coal is crucial for monitoring purposes in the region and the demarcation of possible coal fire- and coal fire risk areas.



Even though coal fires occur underground and the surface thermal anomalies may not be located directly related to a coal Surface (e.g. a sandstone layer, which is overlaying a burning coal seam) coal fires are restricted to a certain depth. In general, coal fires in China occur no deeper than ± 150 m underground. Deeper coal fires would not be sufficiently supplied with oxygen (JIA 2002, SUN 2003).

Figure 6-1: Concept of demarcating the area, in which coal fire related thermal anomalies with regard to the outcropping coal seam can be expected.

Provided, that the dip angle of a coal seam is known, a zone around the detected coal surface can be delineated, demarcating the area, where coal fires can occur. The farthest horizontal distance of a possible underground coal fire (or thermal anomaly) relative to the location, where the corresponding coal seam crops out at the surface can therefore be calculated with:

$$Dp_{\max [m]} = Bf_{[m]} \times \tan \gamma_{da} \quad (6.1.)$$

where Dp_{max} is the maximal coal fire depth in meters (constant), B_f is the delineation radius in meters and γ_{da} is the dip angle of the seam. The tangent of a 3° dip angle is 0.05, that of 30° 0.57 and that of 45° is 1. This would lead to a delineation radius of 2862 meters, 259 meters and 150 meters respectively. Since dip angles shallower than 3° are extremely rare a buffer of 3.0 km will be broad enough to demarcate all areas, where underground coal fires can possibly occur and lead to thermal surface expressions.

If a coal seam is dipping with e.g. 30° westwards into the ground a coal fire related thermal anomaly on the surface should only occur directly above or west of the outcropping coal seam. Therefore, the delineation buffer around a detected coal seam should only extend in the direction of dip. However, two circumstances are hampering this approach. Firstly, a remote sensing image only shows the coal on the surface. Even if a perfectly linear coal seam is cropping out no information of the strike direction and dip angle can be retrieved. Many coal surfaces are furthermore not outcropping seams but anthropogenic moved material in the vicinity of the seams. Vector data sets containing strike and dip angle do not even exist for the Wuda or Ruqigou area, nor for the rest of China. Secondly, coal fire related thermal anomalies can also occur with no coal present below the thermal anomaly. PRAKASH et al. (1999) and ZHANG, J. (2004) demonstrated, that the thermal pattern in thermal remote sensing data acquired over coal fire areas actually is the pattern of cracks. The strongly heated exhaust gasses travel through cracks and vents in the bedrock and can also exhaust in opposite dip direction.

For a transferable large scale approach it is necessary to develop a method to detect coal surfaces in satellite imagery automatically, without manual surface classification procedures like training sample selection being needed.

6.2. Analysis of Vegetation Density

Furthermore, during the field campaigns in 2002, 2003 and 2004 it could be observed, that underground coal fires do have an influence on the vegetation occurring on the surface above the fires. Elevated temperatures and especially the highly toxic fumes resulting from the coal fires and exhaling through fractures and cracks lead to the deterioration of plants.

To quantify these observations vegetation density was mapped in the field in 2002 and 2003 above three coal fires (#6, #8, #12) and their unaffected surroundings within the Wuda syncline. This mapping was part of the mixture grid mapping presented in chapter 4. The assessment of vegetation density was undertaken in three grids located above the fires with 50 meter cells extending for several hundreds of meters in North-South- and East-West direction, respectively. Furthermore, four grids outside the coal fire areas were mapped. For each grid cell the vegetation density was estimated by three persons individually, quantifying the percentage of each 50 meter raster cell covered with vegetation. The three different estimates did not vary substantially. If estimates differed for more than 5 % an average was taken as the vegetation density percentage for the specific grid cell. Furthermore 5 randomly located 200 m line intersects were mapped in each of the three grids (15 intersects) and vegetation density was estimated in $10\text{ m} \times 10\text{ m}$ subplots to compare them to the broader raster estimations. In addition, the vegetation density grid estimates of late September 2003 were compared to the vegetation density pattern observable in the early October 2003 high resolution Quickbird data (60 cm panchromatic channel), where each single shrub can be identified. This data showed a good visual coincidence with field measurements. However, it is known, that estimations – be it from high

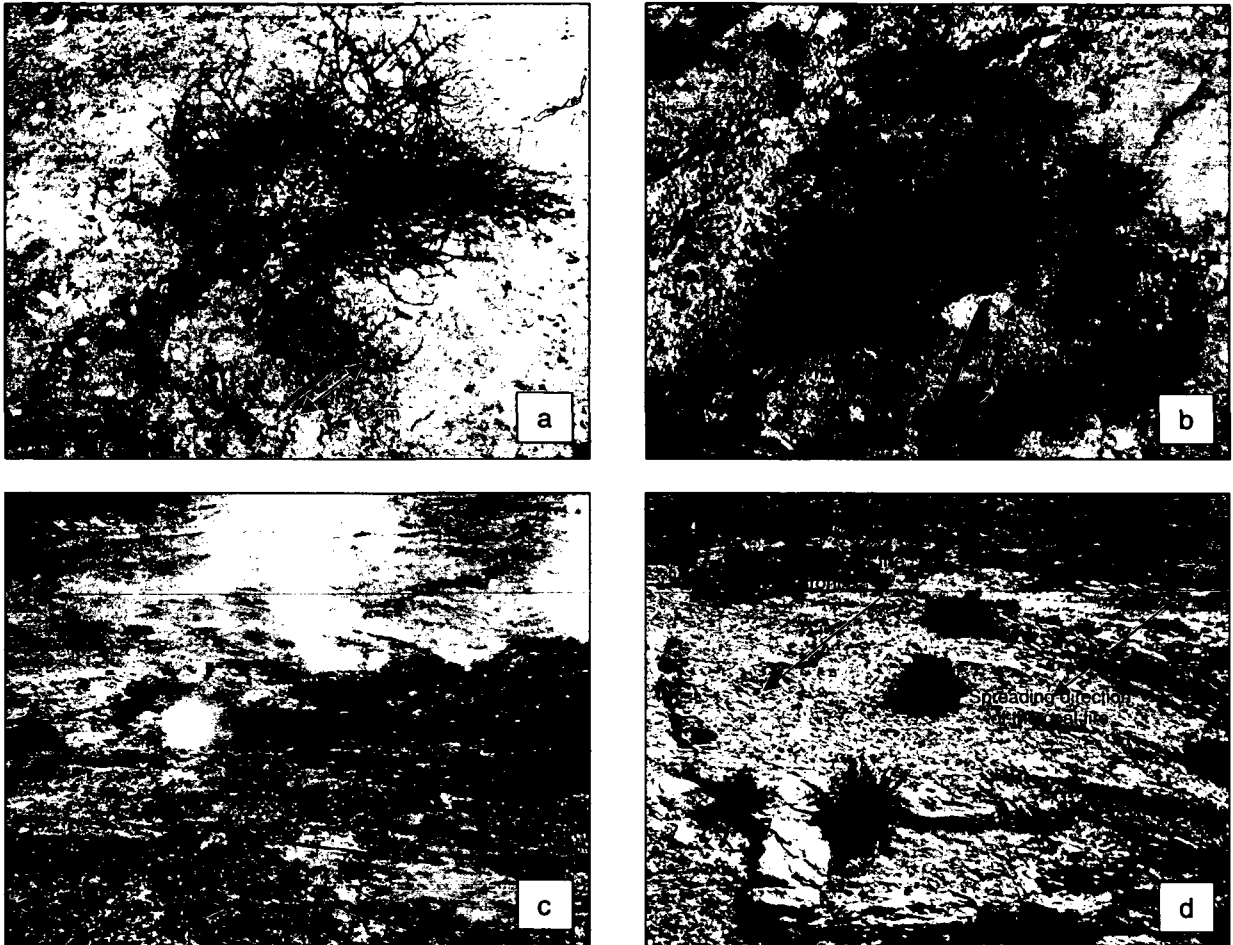


Figure 6-2, a-d: a, b: dead vegetation above coal fire # 8, Wuda syncline. c: heavy smoke, vegetation density 0%, d: slowly degrading vegetation along a new fire front. Photos: C. Kuenzer, 09/2003

spatial resolution remote sensing data or from field mappings – will always contain analyst influence and may to some degree contain estimation error (SMITH et al. 1990).

For reasons of better visualization of natural phenomena, which are more suitably represented in a continuous map with “floating” boundaries than in a strict raster, the estimated vegetation density values were assigned to the center of the raster cells and an ordinary kriging interpolation was applied. Thus, kriged vegetation density maps were generated for the three fire areas and their surrounding as presented in figure 6-3. The locations of thermally anomalous areas within the test grids mapped were located by GPS and are superimposed on the maps. They represent deep cracks or vents, which show temperatures strongly differing from the background and exhalating toxic fumes.

Since it was announced by the fire fighting team and mining engineers in Wuda in September 2003, that fire # 8 had extended to the North between September 2002 and September 2003, the vegetation grid above fire # 8 was remapped in September 2003. Already during the mapping process it could be visually observed, that the area with dead and degraded vegetation had also extended to the North. No active fire zone of all 16 fires in the Wuda coal mining syncline showed any substantial vegetation density on the bedrock surface of the underground fires. The absence of vegetation is of course not an indicator for a coal fire. Low vegetation densities occur as well in settled areas, on bare bedrock or in deserts. However, dense vegetation will not be found above active coal fires.

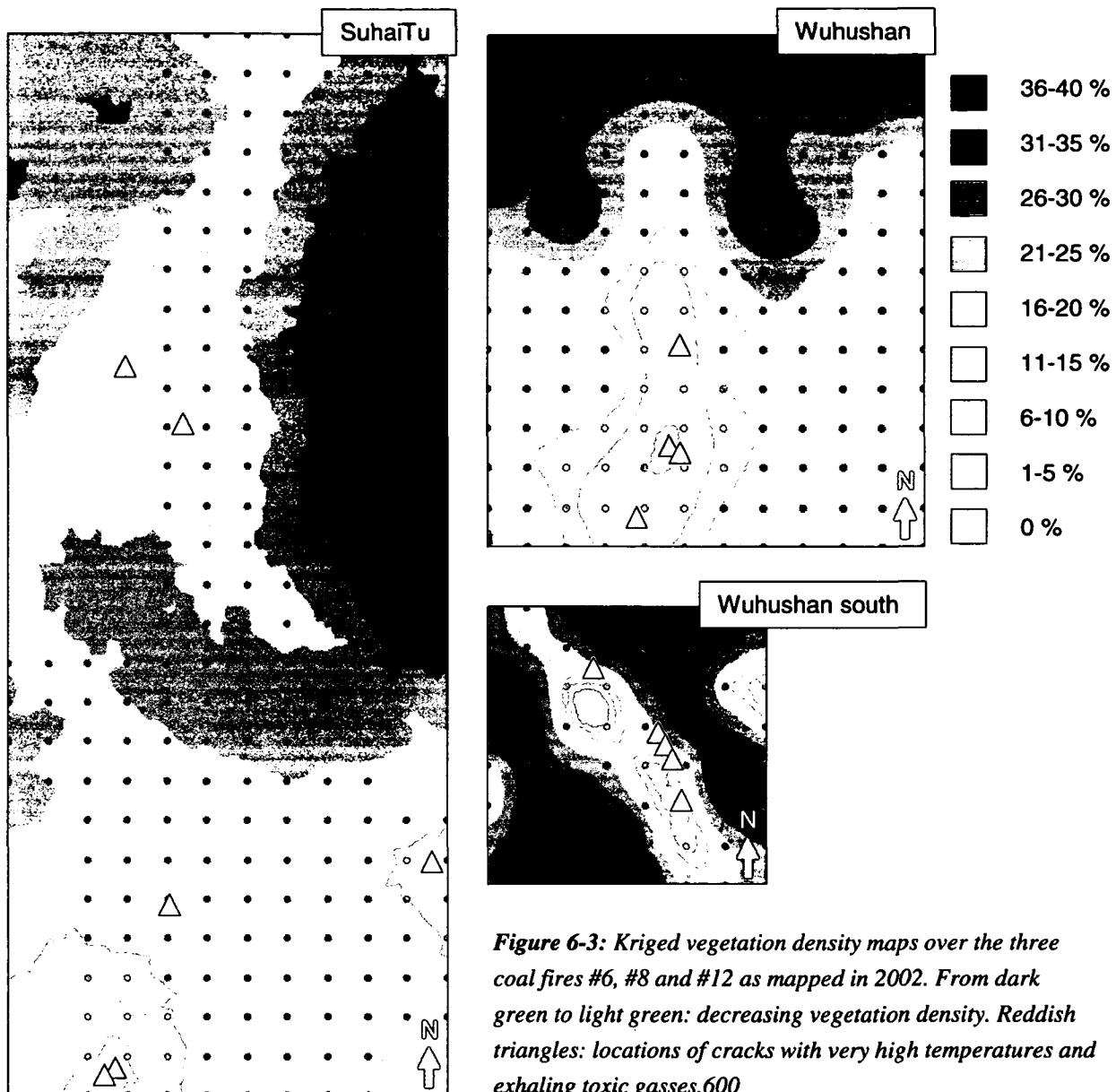


Figure 6-3: Kriged vegetation density maps over the three coal fires #6, #8 and #12 as mapped in 2002. From dark green to light green: decreasing vegetation density. Reddish triangles: locations of cracks with very high temperatures and exhaling toxic gasses.600

6.3. Pyrometamorphic Rocks

As presented in chapter 2 coal fires lead to the generation of fumarolic minerals and pyrometamorphic rocks. Fumarolic minerals are newly generated minerals through coal fire influence. Minerals from the original bedrock layers are dissociated by the heat and transfer along the cracks to the surface, where they re-crystallize around the crack. Compared to burned rocks fumarolic minerals occur in such small spatial expressions that they can not be detected in remote sensing data.

Pyrometamorphic rocks are rocks metamorphosed at different stages through the heat of the nearby coal fire. In literature these rocks are classified into three categories. Firstly baked rocks are described, which have been heated to a relatively low temperature of 300-800°C and which still keep their original texture but show changes in color due to dehydration and oxidation. Secondly, porcelanite-like rocks exist, which have been heated between 600-1400° C and therefore have hardened. They show a ceramic texture and color has been changed greatly. Thirdly, molten rocks are generated when

the coal fire adjacent bedrock is heated to 1500-2000° C. Molten rocks commonly occur very close to the burning centre of the coal seam. The granulated minerals in the rocks melt and form a lava-like black rock (ZHANG, J. 1996). Pyrometamorphic rocks found in the field are mainly of red or yellowish color and can visually clearly be distinguished from non affected samples.

Large areas of burned rock in the Ruqigou / Gulaben area are clearly visible in multispectral Quickbird data, acquired on September 22nd 2003. These surfaces clearly depict the present- or former occurrence of coal fires. It needs to be stated though that burned rock can be decades old and the coal fire may not burning anymore. However, a remote sensing based detection of burned rock from Landsat or Aster data can support differentiation within the delineated coal fire risk areas. ROSEMA et al. (1999) investigated possible methods to find the most suitable satellite bands for classification of rock into burnt and non-burned species using band ratioing and supervised and unsupervised classification. They question the large scale detectability in 30 m Landsat-TM data, since the features dividing burned and non-burned rock are not deterministic. A large overlap exists, when plotting spectra of burned and non burned rock at low spectral resolution against each other. Furthermore, the stratigraphy in the Ruqigou area investigated consists of banded shale and sandstone layers with a thickness of only a few meters, hampering the detection of burned rock in a 30 m pixel. The area of burned rock might only cover a subpixel fraction. Nevertheless, it shall be investigated, if burned rocks can be extracted from strictly calibrated data with the help of extensive ground truth and representative field- and laboratory spectra.

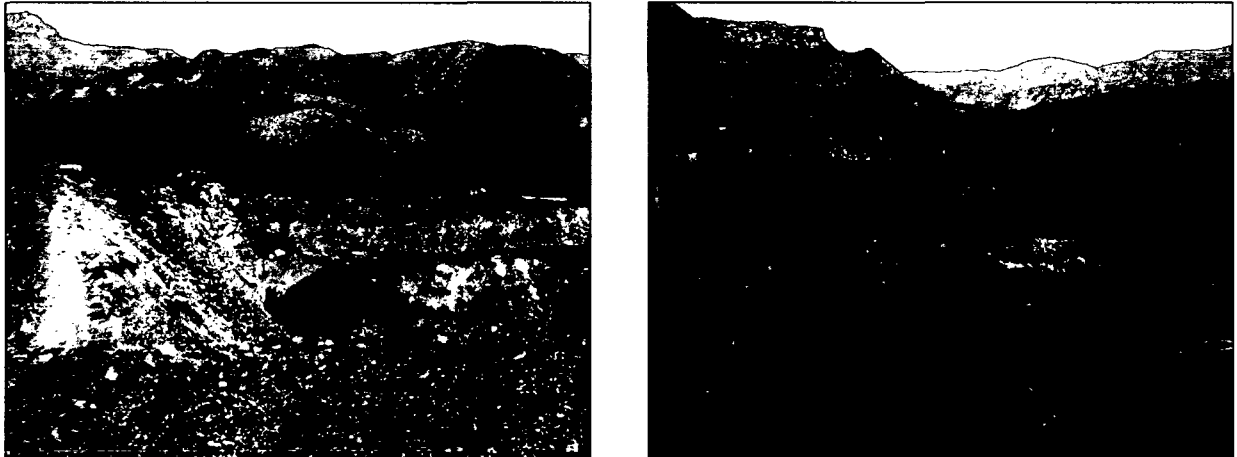


Figure 6-4: Pyrometamorphic rocks exposed to the surface in Baijigou coal mining area. Photos: C. Kuenzer, September 2003, Location: 595837E, 4322295N

6.4. Automation of the Demarcation Scheme

In brief, coal fire area demarcation can be pursued with the following steps. Firstly, coal has to be automatically extracted from remote sensing satellite data. Secondly, an area around the extracted coal surfaces is delineated automatically based on a certain radius. The radius is defined by the average dip angle of the coal seams in the area or a large enough general distance is chosen. Thirdly, within the demarcated area, where coal fire related thermal anomalies are likely to occur, densely vegetated areas can be excluded. This includes the exclusion of forests, dense agricultural areas or natural vegetation, which would not exist, if a coal fire was burning underneath. Therefore, areas of dense vegetation

have to be extracted automatically from remote sensing data. In a fourth step, pyrometamorphic rock should be detected in the multispectral data. Areas of pyrometamorphic rock occurrence give an indication that a coal fire is existing or has been burning in former times. The regions can be highlighted within the demarcated coal fire (risk) areas.

CIHLAR et al. (1998) state, that visual image interpretation and classification to date is still the most successful classification methodology, since the human eye and brain efficiently incorporate color, shape, texture, pattern, shadows, height and other information simultaneously, even if the full spectral feature space cannot be recognized. Manual supervised classifications benefit from this fact through a lot of manual fine tuning processes, which are applied to the data.

However, the goal of this study is to provide an algorithm for coal fire area demarcation, which is applicable on a large spatial scale, can be applied to multi-sensor remote sensing data and minimizes analyst interaction. Coal surfaces, areas with high vegetation density as well as pixels containing pyrometamorphic rock need to be extracted from remote sensing data without analyst interaction. Therefore, from the classification and feature extraction methods presented in chapter 3 a combination of existing approaches needs to be selected, which can meet this demand.

Great advantages of automated data processing and analyses include the following aspects:

- Standardized production and products
- Objectiveness of results
- Mass throughput, large areas processable
- Operational data interpretation
- Increased complexity of products (the time savings due to automation gives room for further research in other fields)
- Low cost of production

For the two approaches presented in this thesis, it was decided not to change the dimensionality of the multispectral data space. All possible input channels for feature extraction except the – if present – panchromatic channels as in ETM+ or Aster imagery were kept. In case of Landat-7 these are 7 bands (1, 2, 3, 4, 5, 7, 6), where the latter is the thermal channel, additionally useful for surface discrimination. Feature space reduction produces synthetic DN's, which can only with difficulty be related to their actual surface features as in the case of PCA or MNF. Since one approach aimed at is to use the field and laboratory spectra of coal, vegetation and burned rock for a spectral comparison, synthetic features would not be helpful. Therefore, the approaches of PCA or MNF rotations were excluded from possible transformation options for the automated mapping of surfaces. Although in many cases the redundancies in multispectral data of the visible channels are a disturbing factor and two of the three visible bands are often deleted, these three to four channels are of higher relevance here due to the exceptional albedo of coal in this EM range. Here the reflectance values for blue, green and red are expected to be nearly identical. Furthermore these channels are of relevance for the exclusion of shadowed areas.

The input data into the two algorithms developed is therefore a geometrically, radiometrically as well as atmospherically corrected reflectance image. An antecedent orthorectification is preferred for an optimum radiometric result in areas with strong relief. A high-quality illumination correction as

presented in chapter 5 can only be applied if the spatial match between the satellite image and a DEM is guaranteed.

A challenge in the extraction of the surface class “coal” is the fact that this surface usually occupies only an extremely small fraction of the image and its multidimensional feature space. The same applies for signatures of pyrometamorphic rock, which is expected to occur only in a few pixels spanning far less than 0.00001% of the scene. An unsupervised approach could therefore not be chosen. Since UCA strive for an overall optimum spanning of the entire data set specific details that are relevant, are missed out easily. This has already been discussed in detail in chapter 3. Furthermore,



UCA would classify the image into several classes without the ability to specify the classes “coal”, “vegetation” or “burned rock” without user interaction. Unsupervised classes are also too inaccurate due to the random location of cluster centers within the initial cluster generation. In pre-studies UCA were applied to classify the image data resulting in classification accuracies well below 40% with coal, shadow and water classes often being mixed and confused. This is shown in figure 6-5. An unsupervised approach is therefore not employed for the feature extraction aimed at here.

Figure 6-5: Unsupervised classification into 20 classes, the first (“darkest”) class is colored in orange on superimposed on the grey scale classification result. Coal, shadow, deep water, water of the Yellow River and even dense agricultural vegetation are all assigned to one class. Center coordinate: 650705E, 4373287N

Standard supervised approaches all need the input of training data, which is often not available or – if ground truth exists - has to be generated in a tedious, time-consuming, interactive process. Therefore, also common supervised classification like training based maximum likelihood algorithms do not fulfill the requirements for an automated algorithm. Very detailed supervised classifications of Wuda and Ruqigou were performed in a change detection study of Wuda and Ruqigou between the time span of 1987 until 2002. The maximum likelihood based classification was accompanied by additional decision rules derived from a DEM and a priory knowledge. 15 classes were extracted in the Ruqigou subset, while 25 classes could be differentiated for the Wuda area. Overall classification accuracies for the 2002 scenes exceeded 85% in both cases. Details on this supervised change detection study can be found in KUENZER et al. 2004a and KUENZER et al. 2004b.

Object oriented analysis is still a highly interactive procedure with many decisions to be taken. This makes results hardly reproducible. Furthermore, for most areas, where the algorithm shall be applied, no knowledge base exists or can be generated. To generate a complex system of fuzzy knowledge based classification a large amount of additional information is necessary. For the surfaces and regions investigated here class membership functions are hard to obtain. The surface “coal” is only weakly

defined through parameters other than the spectral signal. From the field campaigns it is known that coal can occur in the neighborhood to every pixel (all geologic surfaces, settlement, all vegetation types, on the banks of rivers or lakes, etc.) and is – due to its natural occurrence in outcropping coal seams – also not limited to certain elevation or slope and aspect regimes. Furthermore the texture of coal surfaces – the class inherent variance of reflectances – is not unique. Coal can be mixed with other surfaces, may contain impurities, is accumulated in different layering densities and covers areas of different size.

Neural Network classifiers are due to their “black-box” character resulting from the processes within the internal neurone layers often hard to understand. Repetitive- or learning processes of the network are often highly complex. The drawbacks of ANNs are presented in chapter 3. Furthermore, no experiences with ANNs were made before; therefore the technique of neural network programming was not considered any further.

Linear spectral unmixing to a set of endmembers also hampers automatic surface extraction for datasets covering several different regions. The algorithm aimed at here shall focus on the extraction of the surface coal, dense vegetation and burned rock independent of other surface components. Especially pyrometamorphic rock is not assumed to be a typical endmember. A spectral unmixing approach would require the availability of typical endmember spectra for larger areas of China including Ruqigou / Gulaben, the transfer test site in Baotou and the transfer regions in India and Australia. Especially the spatial transferability of the algorithm would not be guaranteed using SMA, since for each scene a spectral mixture model would have to be defined. The assumption that a large part of the spectral variance within a scene can be computed with only a few mixtures is – in many cases – not appropriate (HOSTERT 2001).

Spectral feature fitting (SFF) and binary encoding are techniques only applicable to hyperspectral data. Such data is not used within the course of this thesis. Therefore these approaches are not given further consideration. However, to apply automated surface extraction to hyperspectral images, SFF is an approach, which allows for automation and could be integrated in an automated algorithm.

The above mentioned approaches such as UCA, SCA, OOC, or ANN, can produce highly accurate classification results when interactive data handling is not a limitation. However, for a fast, automated and not too complex algorithm, which shall firstly fulfill the goal to define coal fire risk areas, secondly the needs of the project (mass data throughput and transferability) and thirdly grant the compatibility with the thermal algorithm developed by ZHANG, J. (2004), these methods seem not sufficient.

In pre-studies and tests with numerous scenes two approaches were developed, which differ clearly in their theoretic background to extract a spectral signature. Therefore the two approaches will be presented in the separate chapters 8 and 9. Beforehand a detailed signature analysis of the surfaces existing in the areas (in short) and the surfaces of interest (in detail) is given in chapter 7.

7. Signature Analysis

In this chapter the general chemical and physical influences on surface reflectance spectra are briefly introduced (7.1.) before the spectra of coal (7.2.), vegetation (7.3.), pyrometamorphic rocks (7.4.) and the other surfaces (7.5.) sampled in the study areas and measured under field and laboratory conditions are analyzed. Here, the focus lies on the spectral difference of the surfaces of interest as defined in chapter 6. Finally, the temporal and spatial variability of spectral signatures as occurring in the numerous Landsat scenes investigated is presented in 7.6.

7.1. Fundamentals of Spectral Surface Properties

When photons are incident on a surface they interact with the electrons of the material. The absorption of a photon of a specific energy may cause the transition of an electron to a higher state resulting in absorption features within the reflectance spectra. The absorption of electromagnetic waves by an object depends on the frequency of the waves and the energy level of the object (HUNT et al. 1971).

Absorption features can be produced by electronic and vibrational processes. Electron transition can occur as molecular orbital transitions, charge transfers, crystal field absorptions, color centers and conduction bands while vibrational transitions occur as fundamental bands, overtones and combination tones, effects of phase changes and isotope effects (GAFFEY et al. 1993). Electron transitions produce bands, which are very broad and occur mostly in the UV and the VIS but rarely in the IR. Between 1.3 μm and 2.5 μm vibrational transitions play the major role in the interaction of EMR with the object. For the surface classes in the study areas (rocks, soil, vegetation) the absorption features of the spectra are mainly characterized by vibrational processes, which are overtone combinations of water molecules (H_2O), hydroxyl ions (OH^-), carbonate ions (CO_3^{2-}) and iron oxides (Fe_2O_3) producing relatively sharp features (HUNT & SALISBURY 1970, HUNT & SALISBURY 1971, HUNT et al. 1971). Within the range of the used satellite sensors and the GER the reflectance of water is very low. Wet samples therefore have a lower reflectance than dry samples. This was also demonstrated by ZHANG, J. (1996) comparing spectra of similar rocks of differing water contents. Very characteristic water related bands occur near 1.4 μm and 1.9 μm . An indication for a hydroxyl band is given, if a band near 1.4 μm but none at 1.9 μm exists. Also sulfuric minerals can produce bands at 1.4 μm and 1.9 μm respectively due to OH^- and H_2O vibrations. The OH^- ion furthermore produces bands at 0.95 μm , 1.4 μm - 1.5 μm and 2.2 μm - 2.3 μm , with the second occurring if the hydroxyl ion is attached to Aluminum (Al-OH), while the latter indicates a combination with Manganese (Mg-OH). The frequent occurrence at 1.4 μm results from OH^- being present in many materials as well as due to the OH^- stretching mode whenever water is present in a molecule. Influences of ferric components are given at 0.6 μm - 0.7 μm and 1.8 μm (ferric ion), 0.8-0.9 μm and 1.0-1.1 μm (trivalent ferrous), while carbonate related CO_3 combinations and overtones occur at 1.85 μm - 1.87 μm , 1.97-2.0 μm , 2.12 μm - 2.16 μm , 2.30 μm - 2.35 μm and 2.50 μm - 2.55 μm .

The original chemical composition of a sample is often altered by the degree of weathering, which is a complex process. Spectral changes depend on the influence of hydrolysis and oxidation or reduction within the sample. Depending on the bedrock type weathering can increase or decrease the overall reflectance over all wavelengths. Furthermore, the reflectance curves also depend on the grain size of the sample (surface roughness, BRDF), time, slope and azimuth (light-source – sensor - object

geometry, normalized by illumination correction). For laboratory spectral measurements these influences were eliminated as far as possible (see chapter 4). However, in satellite data they influence the reflectance spectrum of a pixel. A detailed review of the processes relevant in reflectance spectroscopy is given in HUNT et al (1971), HUNT & SALISBURY (1970) and HUNT & SALISBURY (1971) and VAN DER MEER & DE JONG (2001), with the first three being classics in that field.

A common technique for the analysis and differentiation of spectra is the investigation of continuum removed spectra as explained in chapter 3.10. The continuum removed spectra can be used for the characterization of absorption features with regard to their wavelength position, depth, width, asymmetry, slope of the upper convex hull and area. The position of the absorption band, λ , is the minimum reflectance value over the entire wavelength range of the absorption feature. The depth, D , of an absorption feature is the reflectance value at the absorption feature's shoulders minus the reflectance value at the absorption band minimum. The width, W , symmetry, S , and slope of the upper hull, Φ , are defined by

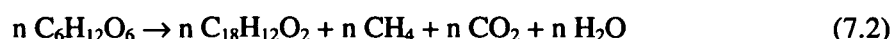
$$W = A_{\text{all}} / 2 D, \quad S = 2 (A_{\text{left}} / A_{\text{all}}) - 1, \quad \Phi = \tan^{-1} (R_e - R_s) / (\lambda_e - \lambda_s) \quad (7.1)$$

where A_{all} is the integral left and right of the absorption band minimum ($A_{\text{left}} + A_{\text{right}}$), which form the total area under the convex hull. The symmetry, S , ranges from -1 to 1 with an S of 0 indicating a completely symmetric absorption feature. To calculate the slope of the upper hull, Φ , a ratio of R_s and R_e (the reflectance) and λ_s and λ_e , which are the wavelength at the starting and the ending point of the absorption feature is calculated. Resulting from waveform characterization five images (position, depth, width, symmetry and slope of the upper hull) can be generated supporting the similarity analysis between a reference spectrum (e.g. laboratory spectrum) and the pixel spectra of images (VAN DER MEER & DE JONG 2001, MARACCI 1992, URL 3-1). However, for Landsat- and Aster data studied here absorption features are not accentuated enough to compare these images. This technique is of course of great benefit when coal fire area demarcation based on automated surface detection would be transferred to hyperspectral data.

7.2. Signature Analysis of Coal Based on Chemical and Physical Properties

Coal is defined as a type of bedrock developed from organic matter, where the carbon content exceeds 50% weight wise or 70% volume wise. The organic compounds of coal are called macerals. These are microscopic pieces, which can be classified depending on their form, morphology, reflectance- and fluorescence behavior into Vitrinites, Liptinites and Inertinites with their specific subgroups. Since different plant species and mixtures of plant compounds (leaves, stems, roots etc.) lead to the genesis of different maceral compositions with knowledge about these one can differentiate different types of coal. Next to macerals coal also contains variable amounts of water, different gasses and minerals, like clay-minerals, sulphur-minerals, carbonates, phosphates, sulfates, silicates, iron disulphides and salts (YANG 1995). Coal can furthermore be classified into different ranks depending on the strength of metamorphosis and - depending on the coal's purity and homogeneity - into different grades. The genesis of coal occurs in several steps. Alive or deteriorating plant material, which is cut off from O_2 , is decomposed by anaerobic bacteria. This process leads to a relative accumulation of carbon since other components are being split up and recycled. The process of anaerobic rotting leads to a change of soil-color towards darker blackish tones. In moors a similar process proceed under water; the

relative enrichment of carbon leads to the darkening of the moor and the steady growth of its layers. If the moor is furthermore covered and experiences strong pressure from above, temperatures rise. This leads to an acceleration of the coalification process (LENZ & WIEDERSICH 1993). The following chemical equation describes this process:



Simplified, cellulose is broken down to coal, methane, carbon-dioxide and water. The strength of coalification determines the rank of the coal ranging from anthracite (highest) via average mineral coal to brown coal (lowest). 24% of all coal stems from Carbonic times, 17% from Permian times, 4% from Jurassic times and some smaller percentages from Cretaceous and Triassic times. Therefore, coal varies in age between 345 and 65 Mio. years. The majority of mineral coals is around 280 Mi. years old. In Tertiary times 54% of the overall world's coal was accumulated as brown coal (lignite) indicating an age of 65 Mio. years and younger (LENZ & WIEDERSICH 1993, SCHRÖTER et al. 1992).

Physical and chemical coal properties like rank, density, moisture content and many others are major influencing factors for the process of spontaneous combustion, leading to coal fires worldwide. Laboratory tests for example have indicated that Lignites have self heating temperatures (SHTs) of 35-36°C, medium- to low volatile bituminous coal between 110-135°C and anthracite above 140°C (SMITH & LAZZARA, 1987). The self heating risk therefore decreases with increasing coal rank (BANERJEE, 1985). Next to physical coal properties also the geological setting of the coal seams, the dip angle of the coal seam, the neighborhood to other seams, the amount of overburden, the speed of coal mining, air pressure gradients, aeration, moisture content and oxygen supply as well as tectonic movements play a major role (YANG 1995). Due to all these interfering factors, the prediction of self heating and spontaneous combustion in coal mining areas is very complex and sometimes not even possible. In the field it could be observed that slack, coal waste and coal dust are the most likely materials for spontaneous combustion especially when exposed to sun and sufficient aeration. Very dense coal is not so likely to catch fire (ROSEMA et al. 1999). Detailed discussions on the proneness of different coal types for self heating or spontaneous combustion can be found amongst others in BANERJEE (1982, 1985), BANERJEE et al. (1972), COWARD (1957), BYLO (1960), MUENZER (1975) and PENG (1983).

Coal from the Wuda coal field is mainly used as cooking coal. Most seams within the syncline are dominated by Vitrinite macerals, contain a high amount of clay minerals, show a high sulphur content stemming from former sea water sulfates and low Liptinite contents (DAI et al. 2002). The energy-content also referred to as heating value of Wuda coal varies between 5000 and 7000 kcal/kg (where 1kcal/kg equals 4,1868 KJ/kg). This defines the energy amount released when burning the coal in an adiabatic calorimeter. This heating value characterizes a "flame"-or "gas-flame" coal, which – with regard to the standardized ASTM-ranking – indicates a "high volatile bituminous coal" (BANDELOW, 2003). The density of coal for the Ruqigou area varies between 950 and 1550 kg /m³. In this area Vitrinites and Inertinites dominate the macerals. Liptinites were not found (ROSEMA et al. 1999). Coal in Ruqigou and Gulaben is high rank anthracite coal, which shows an extremely small probability for spontaneous combustion. The heating value of Ruqigou / Gulaben coal varies between ca. 6950 and 8050 kcal/kg. Detailed studies on the physical and chemical properties of Ruqigou / Gulaben coal can be found in ROSEMA et al. (1999) and were undertaken just recently by the German „Bundesanstalt fuer Materialforschung“ (BAM), Berlin. Their analysis results are presented in table 7-2.

Table 7-1: Physical and chemical properties of coals from the study areas

Chemical and Physical Properties	Wuda	Ruqigou	Gulaben
C in %	53.818 ± 1.810	74.972 ± 4.586	85.720 ± 2.414
H in %	3.611 ± 0.088	2.904 ± 0.045	3.242 ± 0.042
N in %	0.897 ± 0.054	0.653 ± 0.033	0.683 ± 0.052
Water content in % of mass	1.57 ± 0.015	2.62 ± 0.11	0.97 ± 0.02
Ash content in % of mass	38.56	13.73	6.19
Calorific value in kJ/kg	21063	29226	33661
Density in kg/m ³	1551	1563	1486

Source: data provided by M. Schmidt of BAM, 02/2004

Figure 7-1 on the next page shows typical coal spectra measured in field as well as in the laboratory and their continuum removed equivalents. Common for all coal samples is a very low reflectance in the VIS and NIR region of the EMS. This results from an overall low albedo since most coal absorbs the different wavelengths in even quantities. The strong absorption of coal (and hydrocarbons) in the VIS and NIR occurs due to electronic transitions in molecular orbitals. Mature organic compounds with a high carbon content demonstrate conjugate structures and conjugate ring structures. Electron transitions in these systems occur at lower energies, shifting the maximum of absorption into the NIR and VIS. Furthermore, C-C charge transfer can occur in molecules and band gap transitions also play a major role. These band gap transitions occur especially in high grade coals with numerous conjugated double bonds. Here the electrons in the bonding orbitals are so mobile that they behave like free electrons in semi-conductors (GAFFEY et al. 1993. Furthermore, all spectra are relatively featureless, especially, when compared with other surface spectra.

Differences in the slope between VIS and NIR as well as the general reflectance level result from different carbon contents, particle sizes and impurities. Overall, reflectance decreases with increasing carbon content and the depth of water related features decreases as well. This can be noted in figure 7-1 c, which shows 5 different coal samples. While the top spectrum represents a lower quality coal from the Wuda coal field the spectrum with the lowest overall reflectance is a high rank anthracite coal from Gulaben of extremely high carbon content (see table 7-1). The slight features at 1.4 μm and 1.9 μm of the laboratory spectra presented in figure 7-1 c and -d result from a vibrational H₂O and OH overtones and sulfuric components present within the samples. Features around 1.5 μm and 1.8 μm result from sulphate in the samples.

In figure 7-1 d coal waste laboratory spectra of different origin are presented. While reflectance spectra with the highest overall reflectance presents coal waste mixed with shale impurities and ash from the Wuda coal field the lowest reflectance spectra presents a coal waste sample from an anthracite mine in Ruqigou (see table 7-1). A further influence important for coal spectra is particle size. In strong absorbing materials the depth of penetration is small and the regular part of reflection causes reflectivity to decrease with decreasing particle size. Coal of the same origin and chemical constitution may therefore differ in the overall reflectance level. This can explain the difference of the lowest and the middle spectrum in figure 7-1 d, where the middle spectrum was also collected in Ruqigou, but consists of a medium grounded coal powder.

7. Signature Analysis

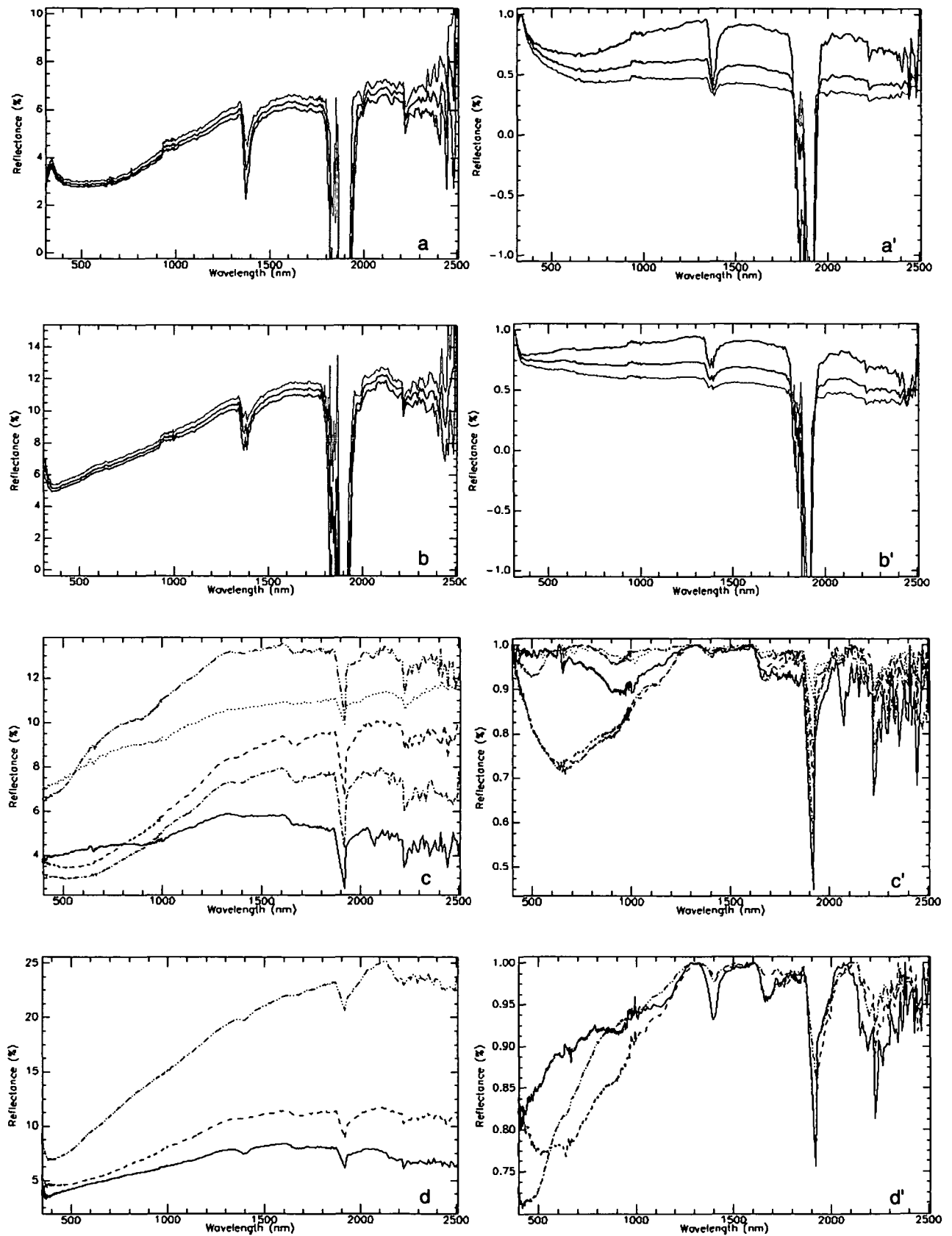


Figure 7-1 a-d: a: field spectra and +/- standard deviation (green and red) of pure coal (a) and of coal waste (b); c: 5 different coal laboratory spectra; d: 3 different coal waste laboratory spectra (highest spectrum mixed with coal waste dust); a'-d': continuum removed spectra of a,b,c and d.

7.3. Signature Analysis of Vegetation

Since coal is the major surface of interest in this study the signature analysis of vegetation, burned rock and the other surfaces is presented shorter and focuses on the separability with coal spectra. Most surfaces related to the occurrence of coal are spectrally clearly distinguishable from the reflectance pattern of coal itself. Due to the geologic time scale, coal occurrences are mainly associated with Permian, Carboniferous or Jurassic bedrocks, mainly sandstones, shale and limestones, recently deflated desert sands and weathered mixtures of the above. Vegetation, water and anthropogenic surfaces may occur as well.

Figure 7-2 depicts the spectra of three typical desert shrubs occurring in the two coal mining areas. Characteristic features here are the – compared to coal – varying reflectance in the VIS, a slight peak in the green band, the high reflectance in the NIR and a steady decline in the MIR range. While in the blue and red range leaf pigments absorb most of the EMR for charge transfer processes in chlorophyll, green light is - relatively seen - reflected more strongly. Overall, reflection is weak in the VIS (0.4 μm - 0.7 μm) and very high in the NIR (0.7 μm - 1.3 μm). Here the refractive index discontinuity between air and the leaf cells leads to the strong reflectance. Reflection decreases again past 1.3 μm with local maxima around 1.6 μm - 1.7 μm and 2.2 μm , where mainly the water content of the plant influences the degree of absorption (SCHARDT 1990). The absorption features at 0.66 μm - 0.68 μm result from chlorophyll-a and -b and carotinoids, while atmospheric- and plant water results in features at 1.4 μm -1.45 μm and plant- and atmospheric water is responsible for the feature at 1.9 μm . Cellulose (mesophyll) is usually responsible for features at 1.22 μm , 1.48 μm , 1.93 μm , 2.28 μm , 2.34 μm and 2.48 μm of which the second and third can be noted, while the others are hardly differentiable from noise in the MIR. Lignin results in features at 1.45 μm , 1.93 μm , 2.05 μm - 2.14 μm , 2.27 μm , 2.33 μm , 2.38 μm and 2.5 μm . The latter are located within the more noisy MIR range. The most common leaf protein usually results in features at 1.5 μm , 1.68 μm , 1.74 μm , 1.94 μm , 2.05 μm , 2.17 μm , 2.29 μm and 2.47 μm , of which only the last four can be guessed, while dry plant materials lead to diagnostic ligno-cellulose absorption features at 2.1 μm and 2.3 μm . Overall, the field spectra past 2.0 μm are too noisy to allow for hard statements. Variability of the three spectra results from differences in chlorophyll content, mesophyll structure and water content. However, like for all surfaces, reflection differences are not only a result of different chemical constituents but may also occur due to morphological differences of leaf surfaces (surface roughness) and leaf geometry. Spectra of vegetation mixed with their underlying bedrock or soil material are presented in figure 7-2 b. The higher reflectance in the VIS of the underlying material becomes apparent and the peak in the green disappears. The reflectance in the NIR is reduced and the 1.4 μm absorption band is slightly less accentuated due to a lower overall water content. The MIR reflectance is increased due to an increasing soil influence.

7.4. Signature Analysis of Pyrometamorphic Rock

The spectra of pyrometamorphic rock are presented in figure 7-3 d. When a rock is heated by a coal fire it undergoes dehydration and oxidation. Dehydration of free water occurs between 45°C and 200°C, for bound water above 100°C and for constitutional water between 500-700°C. With increased heating (>500°C) organic compounds turn to gas. Ferrous compounds like iron-sulphide oxidize to Fe_2O_3 . For pyrometamorphic rocks exposed to higher temperatures overall spectral reflectance decreases with increasing temperature exposure.

7. Signature Analysis

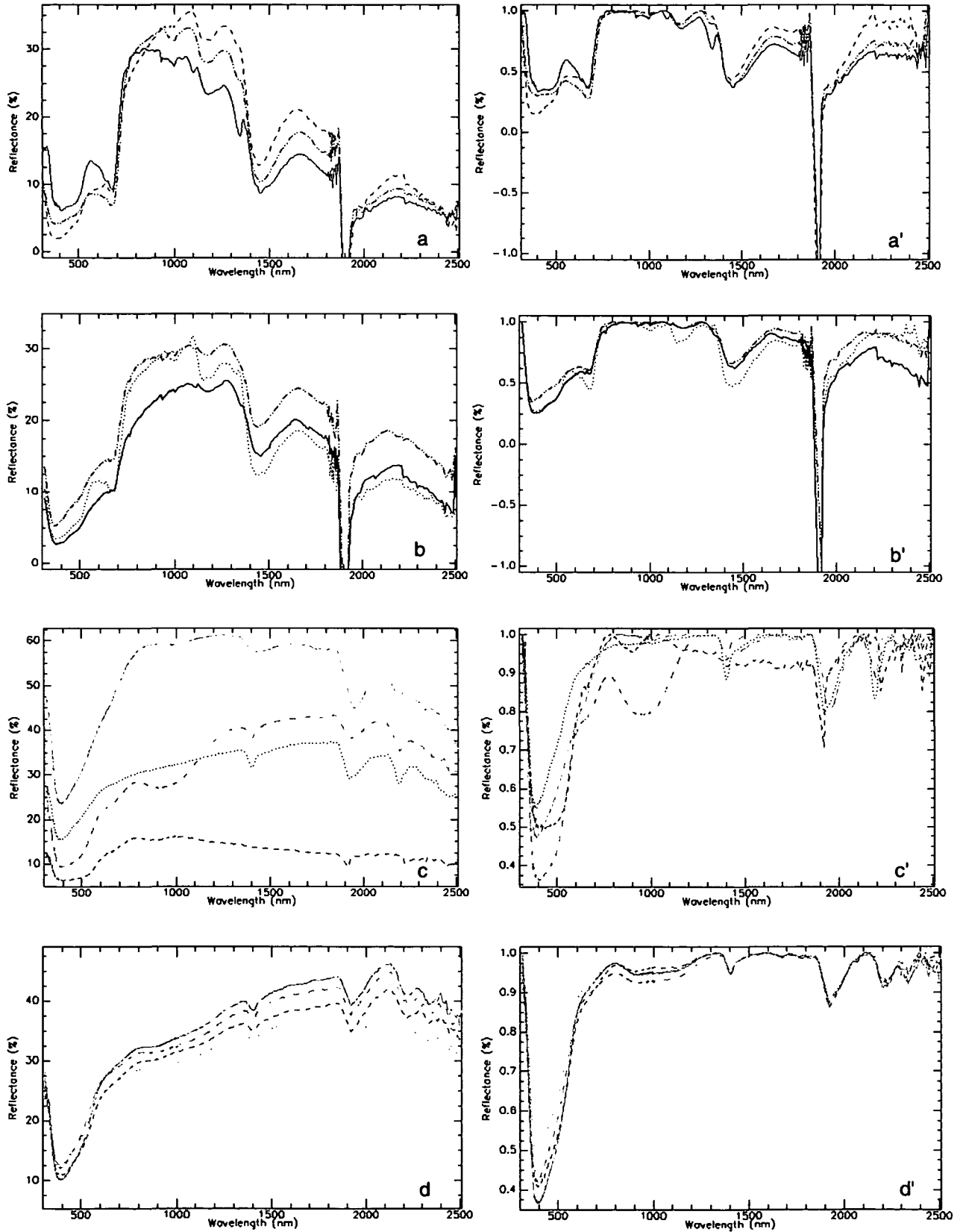


Figure 7-2 a-d: a: field spectra of three main desert shrub types, pure; b: field spectra of the three desert shrubs with soil influence; c: three different sandstone samples of different locations measured in the spectral laboratory; (from highest to lowest: grey, yellow, light grey) and a dark red siltstone sample; d: four different desert sand samples of different locations measured in the spectral laboratory; a'-d': continuum removed spectra of a-d.

7. Signature Analysis

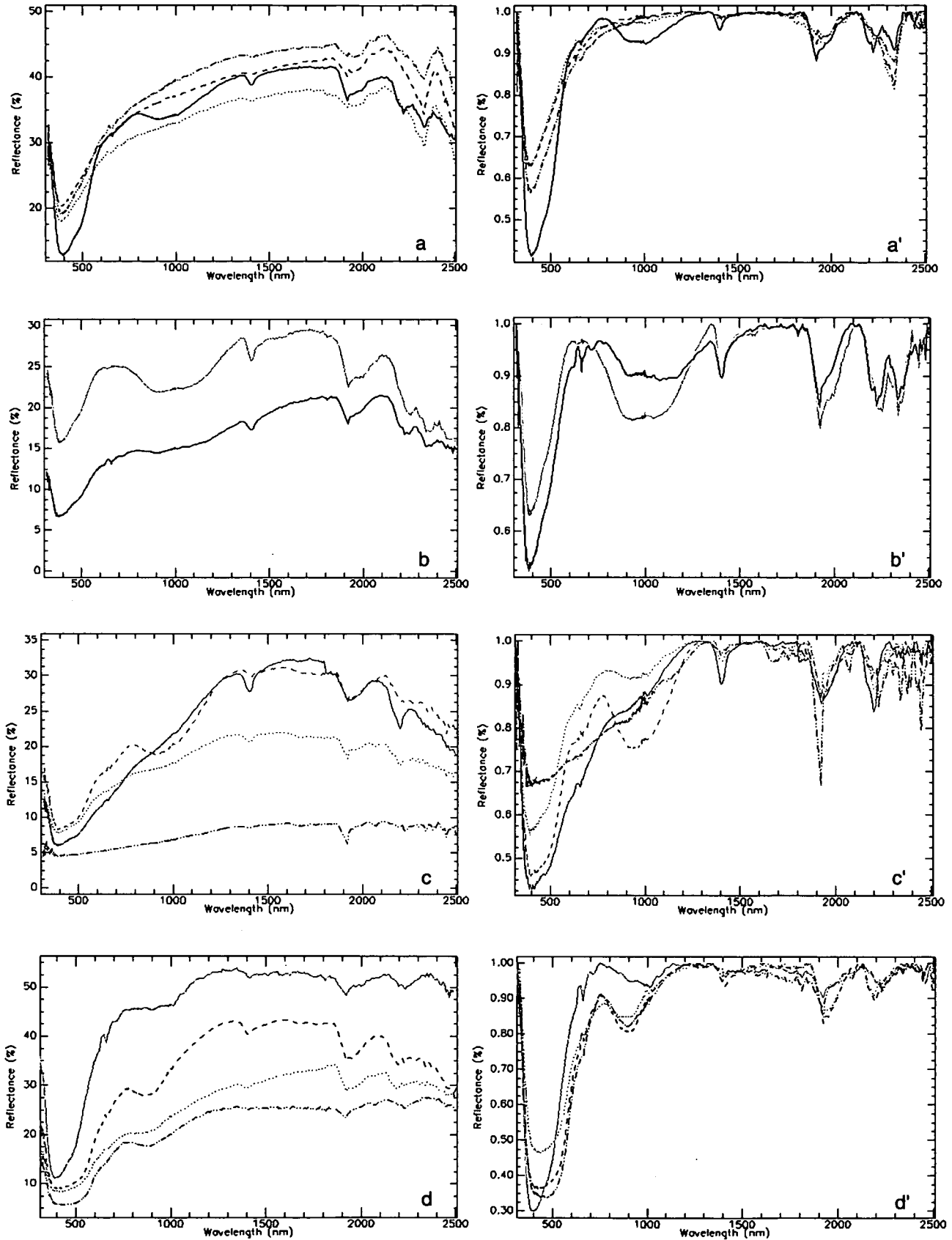


Figure 7-3 a-d: a: laboratory spectra of four different grey limestones; b: laboratory spectra of a light and a dark magmatic and metamorphic rock; c: laboratory spectra of four different yellowish to dark brown shale-sandstone mixes, the lowest is a shale with very high organic content; d: four laboratory spectra of four yellow to dark red pyrometamorphic rocks; a'-d': continuum removed spectra of a-d.

The final stage of a pyrometamorphic rock is a molten rock in which all minerals are remolten and solidified, including a high content of magnetic minerals. The stronger the pyrometamorphosis, the weaker accentuated are the H₂O and OH related bands at 1.4 μm and 1.9 μm (ZHANG, J. 1996). The four rock samples show an overall reflectance exceeding 15 % for all samples. The sample of yellow-orange burned rock shows a very high overall reflectance, ferrous features around 0.9 μm resulting from Goethite and Hematite and H₂O influence of water within the probes at 1.4 μm and 1.9 μm . From the rock's inner structure one can conclude that before pyrometamorphosis the sample was a clay bearing siltstone. The 1.4 μm band decreases in depth with decreasing overall spectral reflectance as does the 1.9 μm feature in the three red pyrometamorphic rocks. It is assumed that the dark red sample with the lowest reflectance underwent the strongest pyrometamorphosis, since it shows the least absorption features and the lowest overall reflectance. Hematite dominates this sample's absorption behavior around 0.9 μm . While the yellow-orange sample was collected at a relatively new active underground coal fire in Ruqigou, the red samples were collected at an old very large fire already surrounded by inactive parts and cooled pyrometamorphic rock.

7.5. Signature Analysis and Spectral Properties of Other Surfaces

The spectral properties of sandstone (figure 7-3c) differ clearly from the spectral characteristics of coal. All four laboratory samples exhibit a very high overall reflectance and display strong absorption bands at 1.4 μm and 1.9 μm resulting from liquid water in microscopic fluid inclusions in the samples. The "dent" in the yellow sandstone spectrum at around 0.8 μm - 0.9 μm results from ferrous oxides (Goethite) present in the sample, while the grey sandstone gives a slight indication for a carbonatic influence between 2.3 μm and 2.4 μm . Features at 2.2 μm indicate the influence of clay minerals involving Al-OH vibrations.

Figure 7-3 c also demonstrates the effect, that rock surfaces of lower surface roughness show overall lower reflectances over all wavelengths than very smooth surfaces. Though the grey and light grey sandstone samples do not differ substantially in color, the grey sample consists of much smaller grains and has a smoother surface. It also contains glimmer and feldspar particles. This phenomenon was demonstrated by ZHANG, J. (1996), who compared spectra of polished and original surfaces of the same bedrock. Differences result from the phenomenon that the number of photons scattered out of a sample is reduced when surface roughness increases (HUNT et al. 1971). The light grey sandstone sample exhibits no iron related absorption features. The red siltstone sample has a very different spectral behavior. It was collected 50 km east of Ruqigou, where wine red sandstone and siltstone bands of steep dipping angle exist. A slight ferric (Hematite) influence occurs around 0.9 μm . Compared to the sandstone the overall reflectance is much lower. Except for the light grey sample all samples indicate this ferric influence noticeable around 0.9 μm . For sandstones the spectral expression of the degree of weathering is not as accentuated as for shale or mudstones. Weathering usually lowers the overall reflectance slightly, while absorption features remain similar.

Desert sand (figure 7-2d) has very high overall reflectances between 1.0 μm and 2.5 μm due to the high quartzite content. Influences of crystal water and OH vibrational modes at 1.4 and 1.9 μm . Features past 2.2 μm may results from noise but could also indicate impurities induced through Al-OH vibrations from clay mineral influences. Spectra do not vary substantially even though the samples were collected at four different locations.

The limestone spectra presented in figure 7-3 a show an O₂ band near 0.67 μm. One sample shows ferrous influences (Siderite) between 0.85 and 1.1 μm (black solid line), while all samples indicate H₂O and OH vibrational modes at 1.4 and 1.9 μm and the typical carbonate bands between 2.2 μm and 2.4 μm. The iron bearing sample furthermore contains very small Bitumen minerals. While features at 2.31 μm indicate dolomitic dominance, features at 2.34 indicate calcitic influences (LONGHI et al. 2001). The overall reflectance is much higher than that of coal and confusion is unlikely. The same applies for vegetation.

Spectra of magmatic and metamorphic rocks (figure 7-3b) are characterized by strong ferric influences (chlorite) between 0.85 μm - and 1.1 μm, which occur as a broad “dent” before an increase around 1.35 μm. H₂O and OH induced absorption bands at 1.4 μm and 1.9 μm and an overall higher average reflectance than that of coal occur. Compared to sandstone or limestone a distinct spectral transition between the VIS, NIR and MIR induced by a strong ferric influence characterize these samples. The lower spectrum represents a gneiss, which could have been a granodiorite, while the overall lighter sample is a strongly weathered granite with high quartz and chlorite content. Past 2.2 μm Al-OH and Fe-OH vibrational modes occur. The finest grained light sample shows an overall higher reflectance and stronger accentuated features.

The four spectra of shale-sandstone mixes and pure shale in figure 7-3 c display very distinct features. The spectrum with the lowest overall reflectance (black, dash-dots) is nearly identical to a coal spectrum. While the features before 0.4 μm result from noise of the GER the features at 1.4 and 1.9 μm indicate fluid water inclusions, OH vibrational modes and sulphuric components in the samples. The feature between 0.6 μm and 0.7 μm, visible in the solid brown- and the dashed brown shale-sandstone mix spectra, may result from an influence of Goethit. The strong feature in all except the lowest spectrum at 1.35 μm may result from Kaolinit. Ferrous oxides yield a band at 2.1 μm for the lower two samples and an Illit influence can be guessed past 2.2 μm, while the strong band at 2.2 μm is induced by OH (LONGHI et al. 2001).

7.6. Separability of Surface Spectra and Temporal Spectral Variability

Resulting from signature analysis of the field and laboratory samples, spectra, which are harder to differentiate from coal, are dark shale with high organic contents as presented in figure 7-3c. These surfaces show similar spectral properties to those of coal in the VIS as well as the NIR and MIR wavelength range. The boundary between coal and shale with high organic content is spectrally and mineralogically not sharp. Therefore, it is possible, that these shales will be extracted as coal and vice versa. However, this type of shale was not found in larger surface outcrops. It usually occurs in slim bands associated with a coal seam. With a high organic content shale also has the potential to ignite spontaneously. The same spectral confusion could occur with very dark completely molten pyrometamorphic rock. However, such rock could not be found in relevant quantities in the study area.

In the satellite imagery (image spectra) additional surfaces exist, which will be hard to differentiate from the surface coal. Firstly, surfaces which are covered by thick coal dust will be extracted as coal, since spectral information does not enable to differentiate thematic classes. Coal, which will be denoted can be coal seams, coal waste piles, coal storage piles, mine works and areas, where a surface is covered and therefore masked by thick coal dust. Except for the last phenomenon – often found along roads leading to mines – all other areas may experience coal fires.

Secondly, difficulties may also arise from water bodies, which are rare in the study areas but occur in the chosen transfer areas (India, Australia). It can be seen in figure 7-4 that water bodies with a lack of sediment and suspended material show very low reflectances in the VIS as well as the NIR and MIR. Thirdly, the same applies for strongly shadowed areas of deeply incised valleys and shadowed mountain ridges, where even illumination correction could not resolve the spectral signal to a clear surface spectrum. Such shadowed areas show little reflection in the VIS, NIR and MIR as demonstrated in figure 7-4. Other surfaces like limestone, sandstone or desert sand (all dashed) should not play a major role in class confusion with coal surfaces and vegetation.

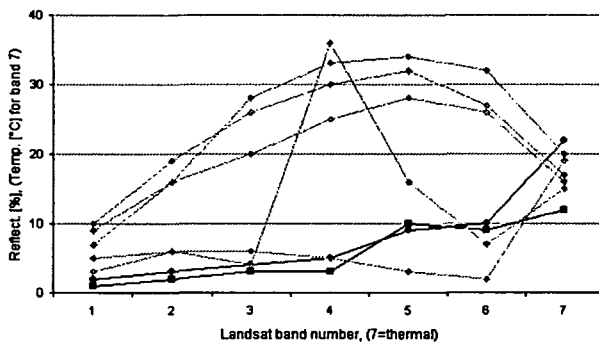


Figure 7-4: Radiometrically corrected Landsat-7 ETM+ spectra for different surfaces. 6=MIR, 7=TIR. The image spectra of coal (black diamonds) and shadow (black squares) run nearly parallel and can only be differentiated by temperature differences. Water (grey diamonds) shows a similar spectral behavior in the first four bands but differs in the far NIR and MIR. The separability of coal, vegetation, or geologic surfaces, like sandstone, limestone and desert sand (upper three signatures) is high.

The separabilities of the main surface classes can also be quantitatively analyzed calculating the Euclidean distance (D_E) as specified in chapter 3, equation 3.5. The following tables (7-2, a & b) show these separabilities as calculated for the main 15 spectral classes occurring in the Wuda region for Landsat-7 ETM+ data. In the first case only channels 1, 2, 3, 4, 5 and 7 are included, while in the second separability calculation the thermal band is included also. To calculate D_{ES} identical regions of interest were generated for each land cover class. They are based on existing ground truth and spectra within the area were averaged. Class distances for these mean vectors were calculated for the 6-band- and the 7-band image respectively. The size of the regions of interest (exceeding 20 pixels each) granted a representative number of pure image-derived surface spectra to be incorporated for each class' calculation. These 20 or more pixels were located within ground truth polygons mapped during the 2002 field campaign. Therefore, the distance measure was calculated based on the scene of September 2002. Compared to D_E the Mahalanobis distance would also take class variance into account, while the D_E only refers to the center vector of the class. Except for the "water" and the "calcite" class Mahalanobis distances were similar to the Euclidean distance presented in tables 7-2.

Within the two tables orange cells mark Euclidean distances lower than 15, while green cells indicate Euclidean distances above 50. In table 7-2 a the thermal band is not included in the calculations, while table 7-3 b shows the separabilities calculated from all Landsat-7 input channels. Blue fields indicate D_E 's which were below 15 and increased with the thermal channel included, while light blue fields indicate, where D_E 's ranged between 15 and 50 and increased as well. What is illustrated in figure 7-4 can also be quantitatively seen in table 7-2. Lake water, shadowed regions and coal related material are most likely to be confused with coal. Classes, which can be differentiated easily, are sandstone, desert sand and calcite. Especially the latter surface, which only occurs in one place within the broader Wuda region shows great D_{ES} compared to all other classes. All three problematic classes (lake water, shadow and coal related material) can be differentiated more easily when the thermal band is included into the analysis. Especially shadow can be separated based on the temperature difference to coal.

7. Signature Analysis

Note, that in 7-2a the dimension is reflectance [%] while in 7-2b another unit [°C] is included. This results in the fact that the inter class separabilities can not be compared unit wise but only relative, which is sufficient for the proof aimed at here. Depending on surface temperatures, cases may occur, where coal, water and shadow can not be separated in untransformed data. This can occur if they have a very similar temperature and spectral signature at the same time. Nevertheless, comparing table 7-2a and 7-2b it is illustrated that for most classes the incorporation of the thermal band improves the inter class separability. Hence, the thermal band will be included into the approaches for automated surface extraction.

Table 7-2 a: Separabilities (D_E) for the most common surface classes in Wuda (no thermal band included)

	Coal	Veg., dense	Veg., med	Veg., sparse	Water, river	Water, lake	Limestone	Sandstone	Metamorphic	Shadow	Desert sand	Calcite	Settlement	Weathered	Coal related
Coal		27	22	36	23	11	40	52	29	11	56	82	20	40	15
Veg., dense			15	28	28	26	34	43	24	34	47	72	22	32	20
Veg., med				16	28	22	22	34	12	33	37	66	9	21	9
Veg., sparse					39	34	7	19	9	47	20	53	16	6	21
Water, river						15	42	50	31	27	57	74	26	41	24
Water, lake							37	48	25	18	53	75	18	37	15
Limestone								13	13	52	16	47	20	2	25
Sandstone									24	63	12	35	32	14	37
Metamorphic										40	28	56	9	12	13
Shadow											67	93	31	51	27
Desert sand												42	36	16	40
Calcite													64	48	68
Settlement														20	5
Weathered															25

Table 7-2 b: Separabilities (D_E) for the most common surface classes in Wuda (thermal band included)

	Coal	Veg., dense	Veg., med	Veg., sparse	Water, river	Water, lake	Limestone	Sandstone	Metamorphic	Shadow	Desert sand	Calcite	Settlement	Weathered mix	Coal related
Coal		29	23	36	25	12	41	52	29	17	56	82	21	40	19
Veg., dense			15	29	28	26	34	44	25	34	48	72	22	33	23
Veg., med				17	29	22	23	34	12	33	37	66	9	22	12
Veg., sparse					40	34	7	19	10	49	21	53	16	6	21
Water, river						16	43	51	32	28	58	74	27	42	27
Water, lake							37	48	25	20	53	75	19	37	17
Limestone								13	13	53	16	47	20	2	26
Sandstone									24	64	12	35	32	14	37
Metamorphic										41	29	56	9	12	14
Shadow											68	93	33	52	31
Desert sand												42	36	16	41
Calcite													64	48	69
Settlement														20	8
Weathered mix															25

Only in Ruqigou does burned rock occur in large enough quantities to occur in the satellite image. However, after visual analysis and compared with ground truth it is assumed that even in the most recent Landsat image from May 2003 not more than 10 pixels in a 6- to 7-D feature space of more than 50 Million pixels are spectrally mainly influenced by pyrometamorphic rock. However, D_{ES} of

7. Signature Analysis

pyrometamorphic pixels to coal, slightly vegetated surfaces, agriculturally used surfaces, water, weathered bedrock mix, sandstone and shade were calculated as presented in table 7-3. The same color scheme as for table 7-2 a and b applies.

Table 7-3 a: Separabilities (D_E) for the most common surface classes in Ruqigou (thermal band not included)

	Pyro. rock	Coal	Veg. sparse	Agricultural	Water (lake)	Weathered mix	Sandstone	Shadow
Pyro. rock		52	9	42	55	14	11	54
Coal			51	24	8	41	56	3
Veg. sparse				38	54	14	12	53
Agricultural					28	34	46	25
Water (lake)						43	58	9
Weathered mix							15	43
Sandstone								58

As for the separabilities calculated for the region of Wuda, the D_E of coal, water and shadow are very small. Confusion is expected from pyrometamorphic rock with sparsely vegetated areas, weathered surfaces and sandstone. Good separabilities have sandstone against water, coal or shadow and pyrometamorphic rock against coal and water.

Table 7-3 b: Separabilities (D_E) for the most common surface classes in Ruqigou (thermal band included)

	Pyro. rock	Coal	Veg. sparse	Agricultural	Water (lake)	Weathered mix	Sandstone	Shadow
Pyro. rock		55		46	59		11	58
Coal			51	25	8	41	56	
Veg. sparse				38	54	14	12	53
Agricultural					28	35	47	25
Water (lake)						43	58	
Weathered mix							15	45
Sandstone								59

When the thermal band is included the degree of differentiation for coal, shadow and water from each other increases slightly. Furthermore, the separability of pyrometamorphic material from sparsely vegetated areas and weathered mix increases. The same applies for agricultural areas, weathered- and sandstone surfaces.

The weak separability of pyrometamorphic rock from sparse vegetation or weathered- and sandstone surfaces presented in table 7-3 a can be explained through the fact that the spectral signal – especially when the pyrometamorphic rock is “young” or did not experience extreme temperatures – does not differ very significantly from the original rock spectrum. This could also be observed in figure 7-3. Pyrometamorphic rocks in the first stage react with a slight reflectance increase in the NIR, which is why slightly vegetated areas lead to confusion. Pyrometamorphic rocks of the third stage were not found in larger quantities and could not be detected in the image – if they would exist in larger areas to influence a 30×30 m pixel signature, confusion with coal or dark shale would be likely.

The extreme low separability of coal and shadow (table 7-3 a) improves when the TIR information is included. Euclidean distances of coal and water stay the same. This is due to the fact that water and coal in the image chosen for separability analysis show similar temperatures. Therefore, the additional thermal information can not raise differentiability here. The spectral distance between pyrometamorphic rock and sparse vegetation as well as weathered surfaces increases slightly due to an overall higher temperature of burned rock surfaces compared to vegetated surfaces. Good separation is expected from pyrometamorph material with coal, water, shadow and densely vegetated areas in agricultural regions. This will support coal fire area demarcation in that respect that coal signatures, vegetation signatures and pyrometamorph signatures will not interfere with each other.

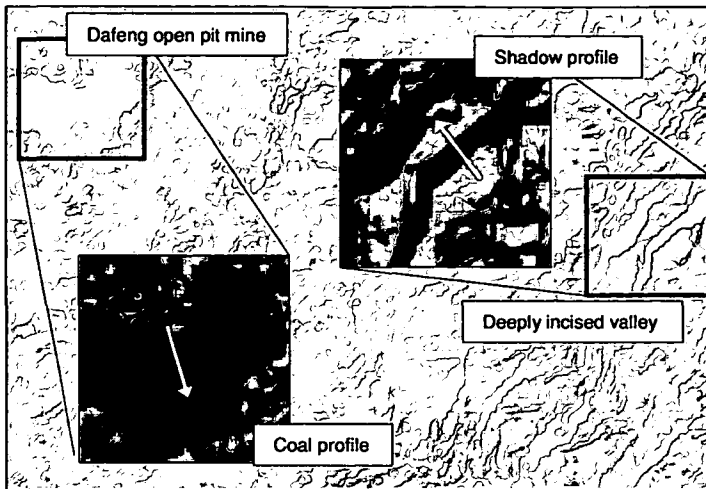


Figure 7-5 shows part of the Ruqigou coal mining area. The right subset displays a deeply incised valley south-east of the Ruqigou syncline. The right subset shows the Dafeng open pit coal mine northeast of Ruqigou.

Figure 7-5: Spectral profiles over seven ETM+ bands for two spatial profiles: shadow (right, center location: 4321784N, 605360E), coal (left, center location: 4323488N, 595692E, UTM, Z 48N).

Both spatial profiles cover an extent of 600 meters. Along this profile line spectra of each pixel in all wavelengths were plotted, which is illustrated in figure 7-6 on the next page. The left profile runs from a very slightly vegetated sandstone surface in the Southeast over the dark ca. 300 meter wide valley and covers part of a vegetated sandstone surface on the northern side of the valley. The right profile covering the Dafeng coal mine starts in a vegetated waste pile area of former covering bedrocks and gravel, proceeds from North to South over the whole extend of the open coal pit and ends on a slightly vegetated bedrock waste pile in the South.

Figure 7-6 illustrates the typical spectral behavior of the individual spatial profiles. For the valley profile the following observations can be made. The spectral signals (left column in figure 7-6) of the slightly vegetated sandstone surface in the South spectrally “behaves” like a mixture of a pure bedrock spectrum with a slight vegetation influence as seen in LS-7 band 4. Here the reflectance in the NIR reaches nearly 34 %. However, the sandstone influence is the dominant spectral influence within the pixels, which is clearly seen in the VIS profile. Here an increase in reflectance from blue to green and red is observed. No distinct peak in the green occurs. Furthermore, overall VIS reflectances are very high. On the northern side of the valley the vegetation influence is stronger. Here the NIR reflectances are higher. The valley itself shows no reflectance in the VIS and a neglectable reflectance in the NIR. It is a fully shadowed region, which – even with the support of illumination correction – could not be spectrally resolved to a surface signal. The slight reflectance in the MIR is almost negligible.

Nevertheless, it is of importance that the valley has a thermal emission (see ETM+ band 6), which reaches the sensor unhindered by the shading- and scattering processes occurring in the optical range. The temperature of the shaded valley, ranging between 7°C – 30°C, is clearly lower than the surrounding sandstone temperature, which ranges around 35°C-40°C. The “inner” part of the valley, which shows no spectral signal in the VIS (within the dashed orange margins in figure 7-6) ranges between 7°C-15°C, while the “valley margin” ranges between 10°C-30°C. This is an important observation. Based on tables 7-2 and 7-3 it is assumed, that the thermal band will increase the separability of coal and shadow. However, shadow has to be differentiated into the “inner shadow” or shadow region and the “shadow margin”. These shadow margin areas run parallel to the valley edge and have a great potential for the confusion with coal. Their VIS-, NIR- and MIR expression mimics the one of coal. Temperatures reach values only slightly below coal temperatures (see right column in figure 7-6). In cases, where these shadow margin areas show temperatures which overlap with coal temperature standard deviation a spectra-based separation in non transformed data will not be possible.

7. Signature Analysis

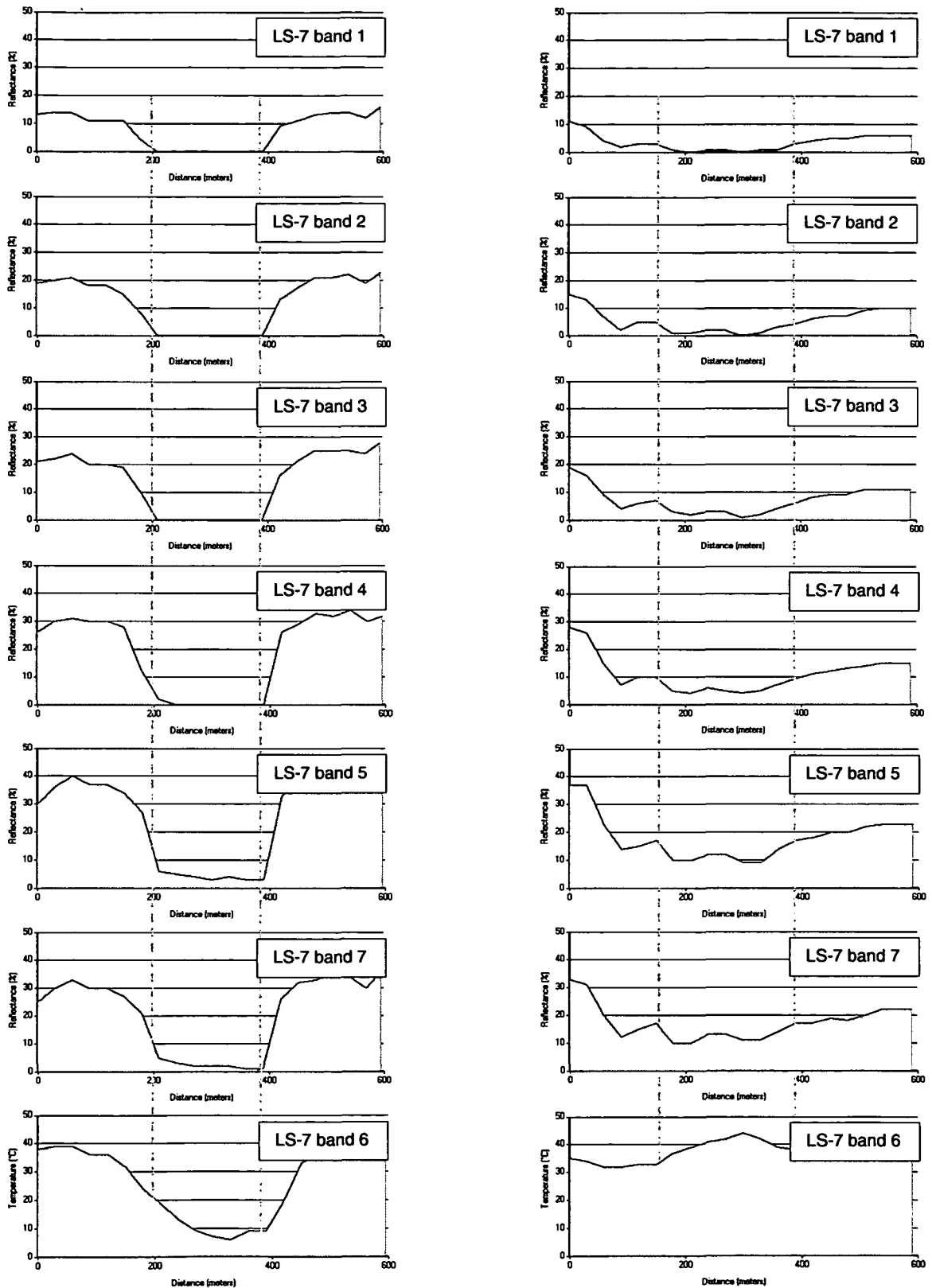


Figure 7-6: Spectral profiles over seven Landsat-7 ETM+ bands for two spatial profiles: shadow (left), coal (right), band 6 is the thermal TIR band and therefore is displayed behind channel 7, which represents the MIR.

7. Signature Analysis

The right column of figure 7-6 shows the spectral behavior of the surfaces covered by the profile, over all bands. While the reflectance of the Dafeng coal in the VIS and NIR is very low, reflectance values increase in the far NIR and MIR averaging slightly over 10%. Opposite to the shadowed area, where temperature decreases, a clear temperature increase against the surrounding areas of former cover bedrock waste piles can be noted.

Figure 7-7 and 7-8 illustrate the temporal spectral variability of the surfaces coal, shadow and shadow margin for Ruqigou and Wuda, for all the scenes processed and analyzed. For Wuda, the Yellow River is included as a reference for a surface with a low daily and medium yearly temperature amplitude. The thermal band is displayed as band 7, since this spectral region represents the longest wavelengths.

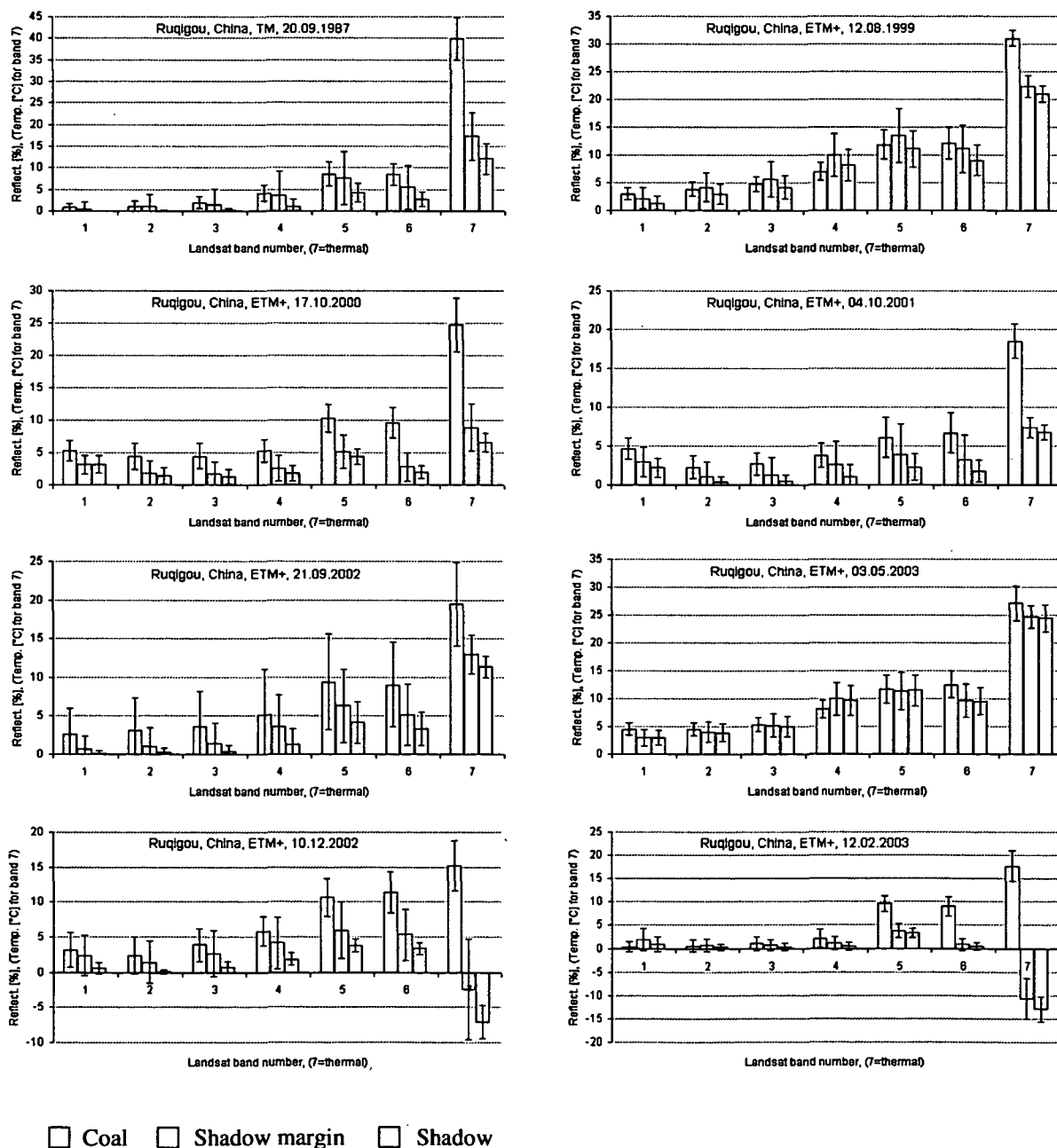


Figure 7-7: Temporal spectral variability of three surfaces for eight time steps in Ruqigou mining area

7. Signature Analysis

From each scene for the three and four surface classes respectively, signature clusters were collected, exceeding 20 pixels to grant representativity. For shadow and shadow margin these signature clusters were distributed evenly over the image. They could be defined based on analyst knowledge with the support of an illumination file. This file was created with the DEM and the appropriate sun angle depending on the date of the scene. Water from the Yellow River could be identified in the time series from 1987 until today without necessary ground truth polygons. The definition of clear coal signature clusters was supported by ground mappings of 2002 and 2003 for the datasets of September, December, February and May and by old mining information available from the Wuda mines and from former projects (ROSEMA et al. 1999). The mean of the signature clusters as well as the standard deviation of the surface class was calculated for each ETM+ band as shown in the diagrams.

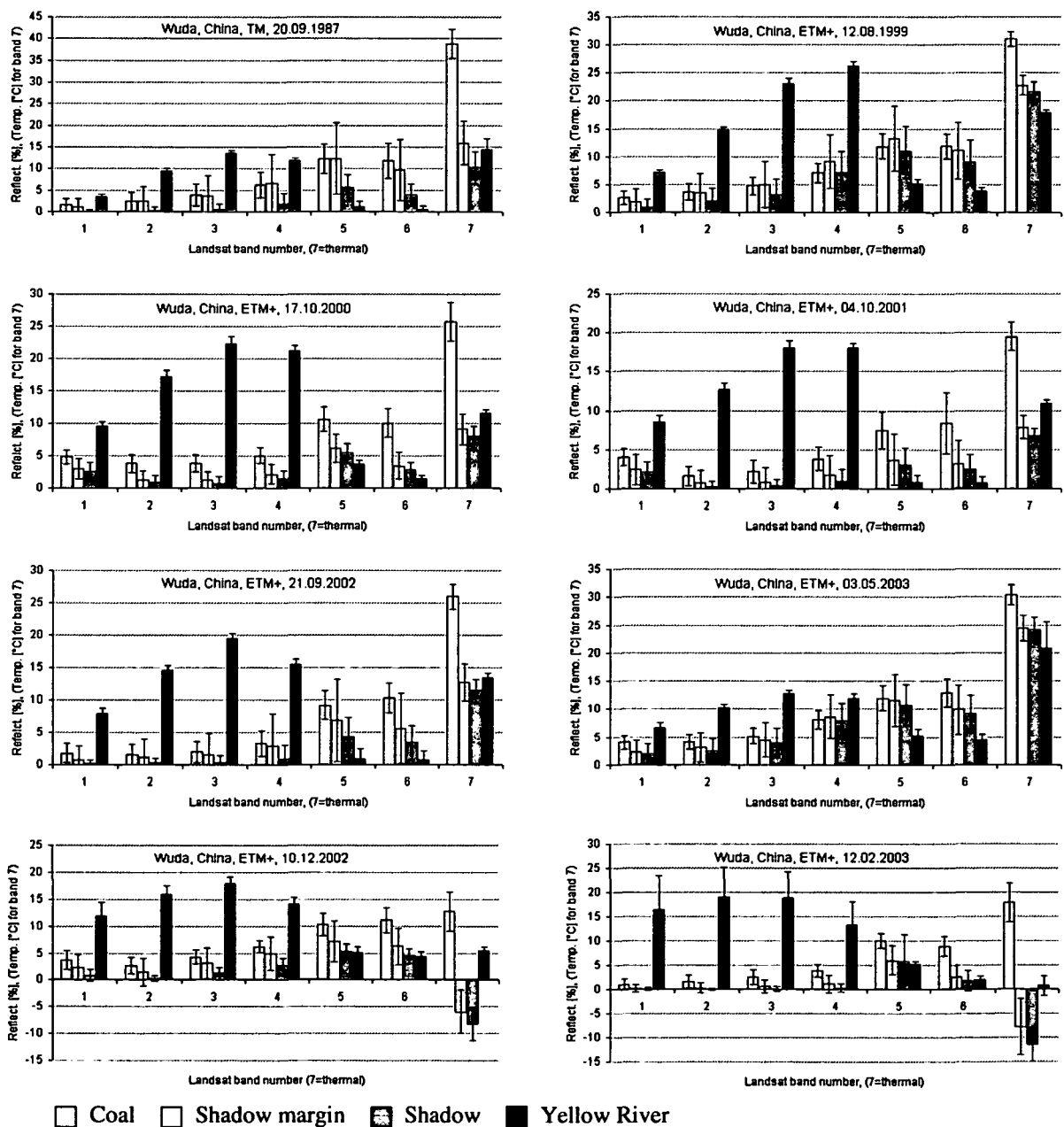


Figure 7-8: Temporal spectral variability of four surfaces for eight time steps in Wuda area

Figure 7-7 displays the averaged mean spectra of the three surfaces of interest including the surface specific error bars (+/- one standard deviation) for Ruqigou. The following statements are made:

1. Over all wavelengths and during all times do reflectance and emittance spectra of shadow margin exceed the mean values of shadow in the VIS, the MIR and the TIR.
2. Spectra of coal in band 1, 2 and 3 have in all but the 1987 scene a slightly higher reflectance than shadow margin and shadow. They are never zero.
3. Coal reflectances (taking standard deviations into account) do not exceed 8% reflectance for bands 1, 2 and 3 – except for the scene from 09/2002
4. Coal reflectances (taking standard deviations into account) do not exceed 10% reflectance for band 4 – except for the scene from 09/2002
5. In all images but the 1999 scene do coal surfaces reflect more radiation in band 5 and 6 (actually official Landsat-7 ETM+ band 7) than shadow and shadow margin.
6. For all scenes and during all times do mean coal signatures show over 7% reflectance in bands 5 and 6. When the standard error is taken into consideration, all coal surfaces exceed 5% reflectance – except in the scene from 09/2002
7. Coal surfaces show the highest temperatures in all scenes and at any time. Negative temperatures do not occur. Mean temperatures exceed 15 degrees in all scenes.
8. Shaded surfaces in winter have negative temperatures at 10:30 satellite overpass time. Shade margins exhibit mean negative temperatures, but a much higher temperature variance.
9. The positive and negative standard deviation for coal and shadow margin in the thermal band overlap in two (09/2002, 05/2003) out of eight scenes.
10. The positive and negative standard deviation for coal and shadow in the thermal band overlap in one (05/2003) out of eight scenes.
11. The spectral variance within all bands for the scene of September 2002 is extraordinarily high for all surfaces. This scene has outlier characteristics.

Figure 7-8 displays the averaged mean spectra of the four surfaces of interest including the specific error bars (+/- one standard deviation) for Wuda. Interpretation allows the following statements:

1. Statements 1, 2, 3, 6 and 8 for the scenes of Ruqigou fully apply for the scenes of Wuda.
2. Statement 4 for the scenes of Ruqigou fully applies for all scenes of Wuda, where spectral reflectances of coal never exceeds 10% in band 4.
3. Statement 5 for Ruqigou applies for the Wuda region as well, except when the standard deviation is taken into consideration. Under these circumstances coal surfaces do not reflect more EMR in band 5 and 6 than shadow and shadow margin for the scenes from 1987, 1999 and 09/2002.
4. Concerning statement 9 for Ruqigou it needs to be noted that in Wuda the positive and negative standard deviation for coal and shadow margin in the thermal band overlap in no scene.
5. Unlike for the region of Ruqigou there seems to be no outlier in the scenes of Wuda. This is expected, since radiometric calibration and correction could be undertaken with higher accuracy. More spectral ground samplings were available for Wuda. Furthermore, the terrain in Wuda is less challenging for scene radiometric normalization.

7. Signature Analysis

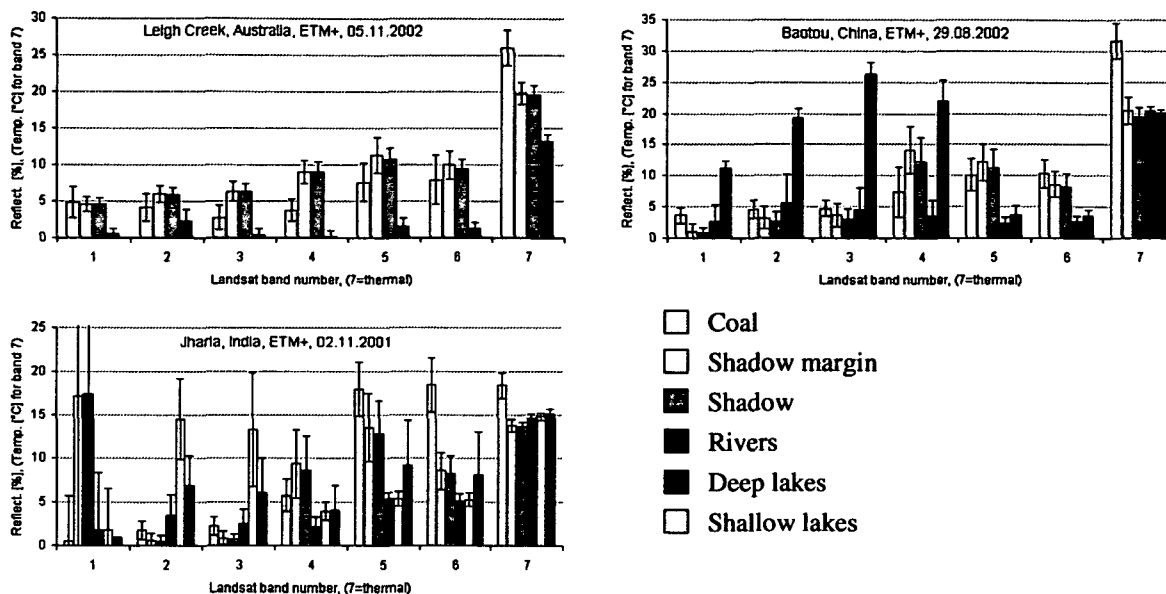


Figure 7-9: Spatial spectral variability of 3 to 6 surfaces in the transfer regions Baotou in China, Jharia in India, and Leigh Creek coal mining area in Australia

- The Yellow River exhibits reflectances in band 1, 2, 3 and 4, which always exceed reflectance values of coal, shadow and shadow margin. In band 5 and 6 the Yellow River exhibits lower reflectances than coal, shadow and shadow margin for all 8 time steps.
- Temperatures of the Yellow River are in all scenes close to those of shadow and shadow margin. This does not apply for the winter scenes, where temperatures of the river are higher. One exception is the scene from February 2003, where the Yellow River is frozen and negative temperatures occur. The frozen surface also explains the extremely high variability of the reflectance in the VIS and NIR (bands 1-4) in this scene.
- Except for the phenomenon mentioned under statement 7, spectra of the Yellow River present very low standard deviations of reflectances in all bands.

Figure 7-9 displays the averaged mean spectra of up to six surfaces of interest including the specific error bars (+/- one standard deviation) for the Leigh Creek in Australia, the Baotou area in China and the Jharia area in India. The following statements can be made:

- Statements 1, 2, 3, 4, 6, 7, 9, 10, 12 and 13 concluded for the 8 time steps of Ruqigou fully apply for the three scenes of the transfer areas, which were acquired over regions far away from the study areas. No exceptions occur.
- Statement 6 and 8 made for Wuda also apply for the scene of Baotou, which includes the northern part of the Yellow River.
- Statement 2 concluded from the Ruqigou region and applicable for the Wuda region does not apply in the transfer areas. The reflectance of coal in bands 1, 2 and 3 is only in the scene of Baotou higher than the reflectances for shadow and shadow margin. For the scenes of India and Australia coal exhibits lower spectral values in these three bands.

The insights and understandings gained from the signature analysis will support the automated surface extraction as presented in the following two chapters 8 and 9.

8. Knowledge Based Surface Extraction

8.1. Set Up of the Knowledge Based Test Sequence

Based on the analysis results of the multitemporal and multispatial signature analysis presented in chapter 7 a sequential knowledge based approach for the extraction of coal, vegetation and burned rock has been developed. The test sequence developed here bases on the principles of knowledge based classification or decision tree classification as presented in chapter 3.5. In this subchapter (3.5.) examples for other decision trees or test sequences in literature are given. The sequence designed here incorporates information on the spectral signature over all bands, single band thresholds, synthetic bands, information from the digital elevation model and land surface temperature (LST) information. Threshold conditions defining yes-no nodes were defined supported by the signature analysis in such way as to yield the best results for each scene without adapting thresholds specifically. Therefore, many empirical tests were performed on over numerous Landsat and Aster data sets. The knowledge based sequence can therefore run on multilayer Landsat-5 TM, Landsat-7 ETM+ and Aster data including all channels except the panchromatic band. This band was excluded due to its large file size (equivalent to 4 multispectral bands) and the “smearing” of wavelength information due to the large bandwidth. The test sequences act as filters defining boundary conditions to determine, if a pixel will be counted to the class “coal” or “no coal”, “dense vegetation” or “no dense vegetation”, “pyrometamorphic rock” or “no pyrometamorphic rock”. Though none of the threshold tests alone is sufficient to clearly demarcate the specified areas the combination of the criteria gives good results for the automated extraction. In the following, the designed test sequences for the three surface classes are presented.

8.1.1. Automated Extraction of Coal Surfaces

Test 1: Synthetic spectral mean test SMP_{123457}

From all input bands except the thermal channel a synthetic band is calculated, containing the spectral mean (SPM) of each pixel over all bands. This mean channel gives an indication of the albedo of a surface over the whole covered wavelength region. Surface classes like coal, water or shadow have low spectral mean values due to their overall low reflectance in the VIS, NIR and MIR.

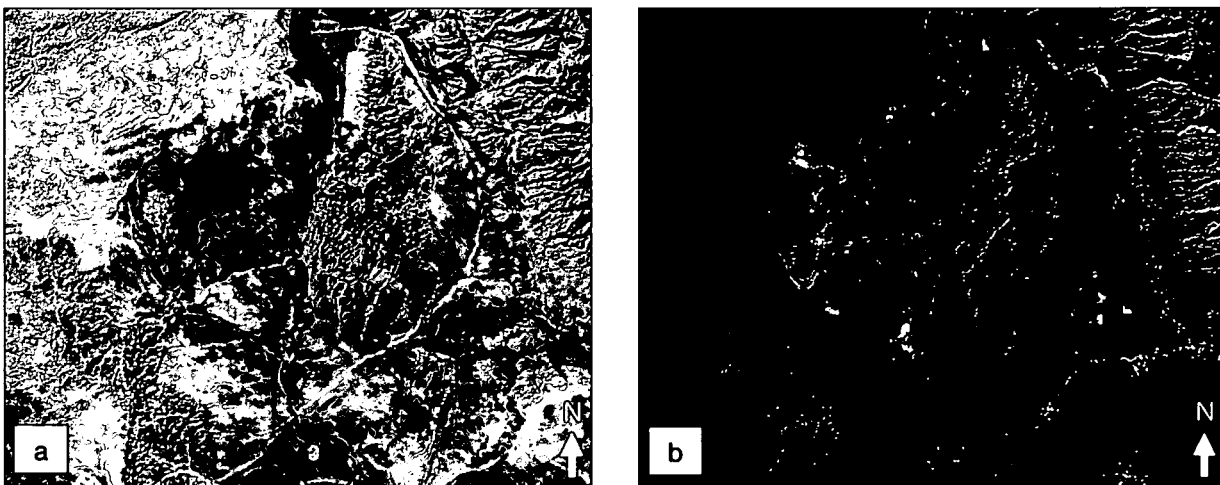


Figure 8-1 a-b: Synthetic spectral mean channel over bands 1, 2, 3, 4, 5 and 7 (a); result after the first test: pixels, which passed the test are presented in white and include coal, shadow and very dark water pixels (b). Center coordinate: 650705E, 4373287N, UTM, Z48 N.

In the strict sense of course shadow will yield now spectral signal. However, the principle of shadow and shadow margin has already been introduced in chapter 7 and is of importance for the separation of surface classes. This concept is also presented in the spectral mean figures 8-2 and 8-3.

$$\rho [\%] \text{SPM}_{123457} \geq 1 \text{ and } \rho [\%] \text{SPM}_{123457} \leq 10 \quad (8.1)$$

For the synthetic mean channel of bands 1, 2, 3, 4, 5 and 7 a lower threshold was defined at an average reflectance of 1 % and an upper threshold was defined at 10 % reflectance as demonstrated by equation (relation) 8.1.

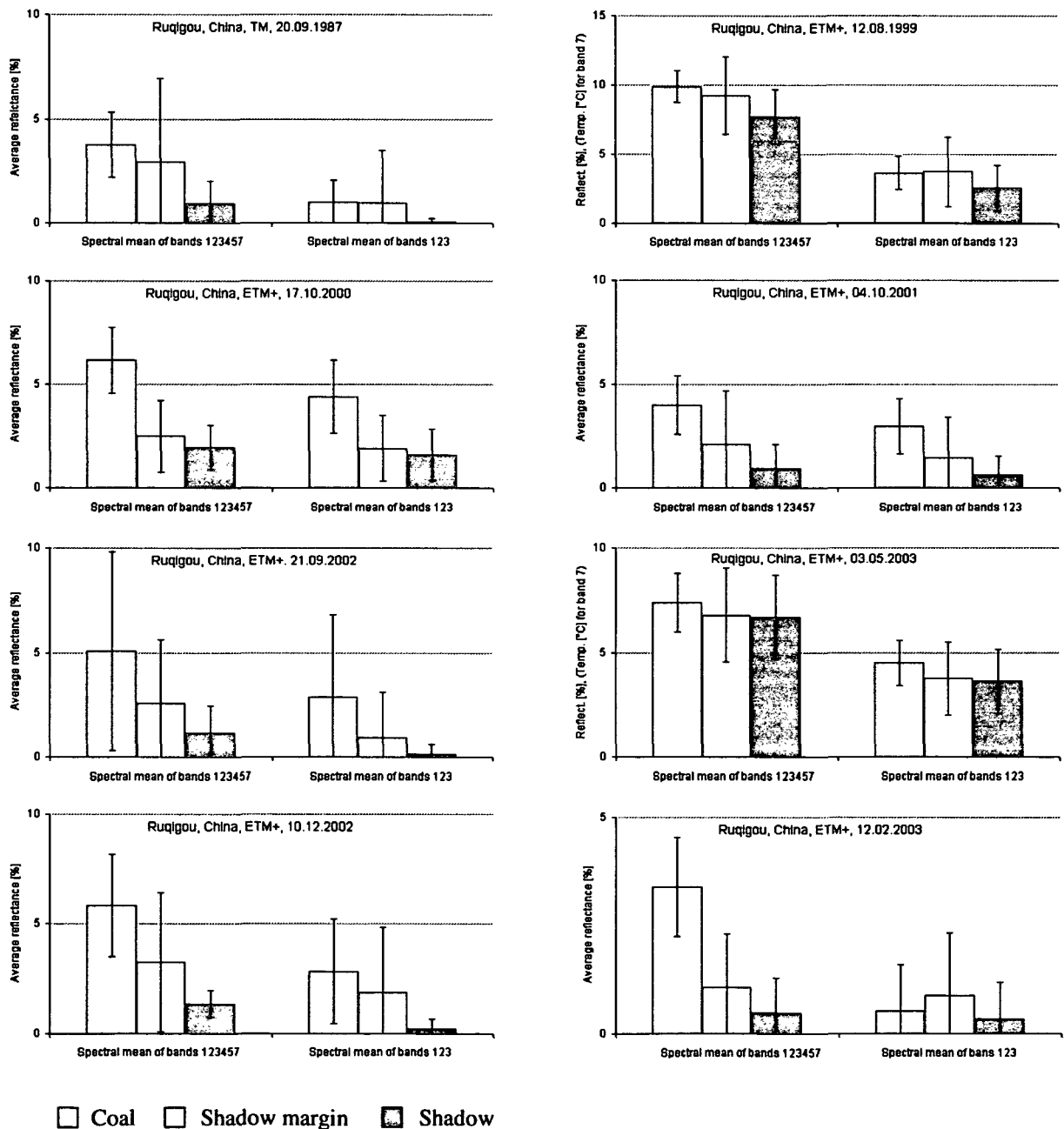


Figure 8-2: Spectral mean for bands 123457 and bands 123 for eight time steps for the Ruqigou area. Presented are the surface types coal, shadow margin and shadow.

As it could already be noted in the signature analysis diagrams representing signature mean and variance in chapter 7 the effect of radiometric differences becomes also apparent in figure 8-2. If all scenes would have a perfectly adjusted radiometry variation in SPM mean and variance should not occur or should only occur within a very slim range. However, it can be noted that even after a very thorough preprocessing radiometric inter scene variations still remain. They may result from changes in the material, different illumination conditions and different atmospheric conditions as well as sensor instabilities. Much time was spent for the calibration of the time series and it is assumed that the time series correction results can hardly be improved. This shows the limits of quantitative remote sensing, where even ground reflectances or land surface temperatures always underly a certain error range.

Test 2: Synthetic spectral mean test SPM_{123}

Additionally, a SPM was calculated over the visible bands 1, 2 and 3. For the synthetic mean channel of bands 1, 2, and 3 a lower threshold was defined at an average reflectance of 1 % and an upper threshold was defined at 7 % reflectance.

$$\rho [\%] SPM_{123} \geq 1 \text{ and } \rho [\%] SPM_{123} \leq 7 \tag{8.2}$$

These first two thresholds help to demarcate coal surfaces from other geologic surfaces. Shadow, shadow margin, deep water and some outlier pixels like e.g. very few pixels of the Yellow River can not be excluded or separated yet.

The thresholds were defined based on the analyses of the spectral mean characteristics of coal, shadow and shadow margin as presented in figure 8-2 for Ruqigou and figure 8-3 for Wuda. For Ruqigou the SPM_{123457} ranges between 3 % and 8 % not taking the standard deviation (SD) into account. Including the SD it ranges between 2 % and 9 %, including the outlier scene of 09/2002 between 1 and 10 %. For the spectral mean of coal for bands 1, 2 and 3 reflectance varies between 1% and 5%, including the SD and the outlier scene between 0% and 7%. The lower margin is not defined at 0% due to test 3. For Wuda the SPM_{123457} ranges between 4% and 8% not taking the SD into account. Including the SD it ranges between 3 % and 9 %. For the spectral mean of coal for bands 1, 2 and 3 reflectance varies between 2 % and 4 %; including the SD between 0% and 5%. Pixels of the Yellow River usually do not interfere with the thresholds defined – however, in figure 3-8 it can be seen that for the scene of 1987 the river reaches a very low SPM_{123457} . It lies within the error range of coal.

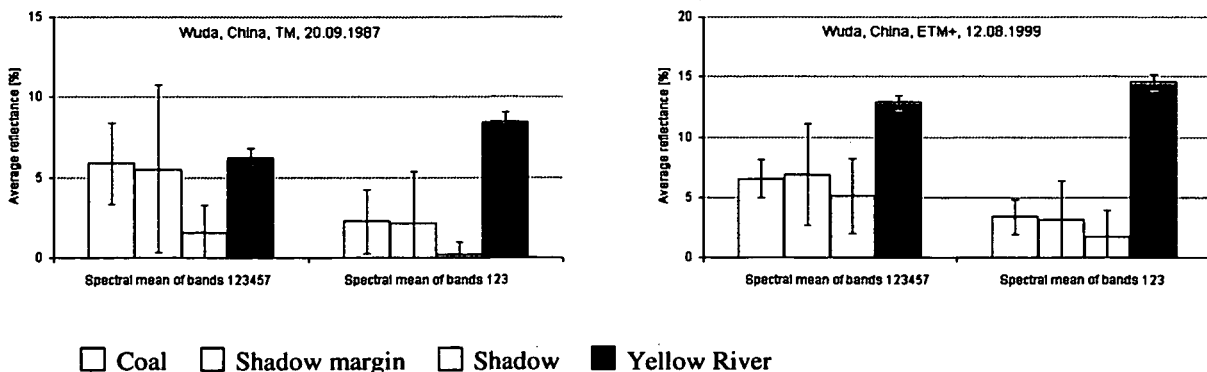


Figure 8-3: Spectral mean for bands 123457 and bands 123 for eight time steps for the Wuda area

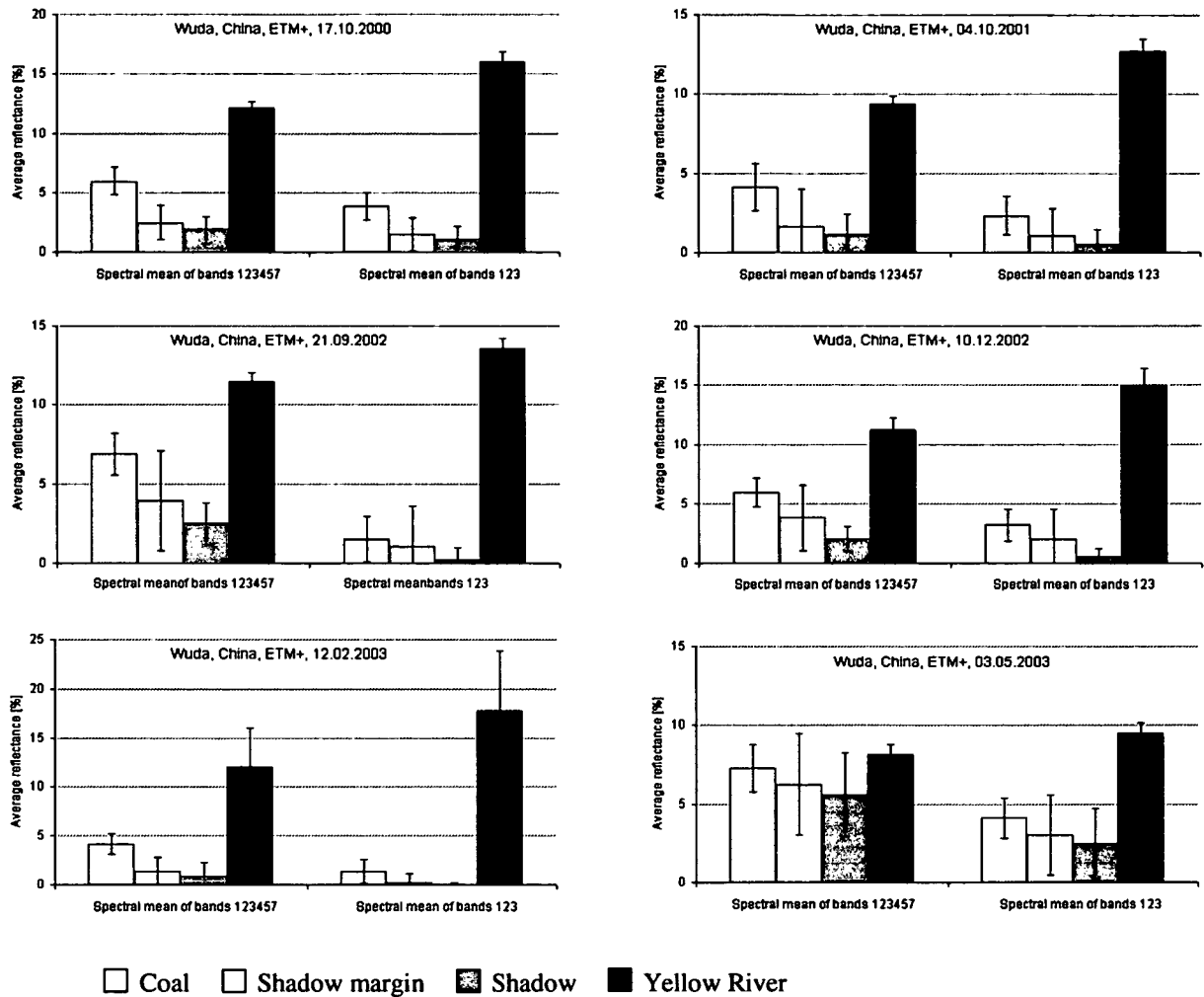


Figure 8-3 cont'd: Spectral mean for bands 123457 and bands 123 for eight time steps for the Wuda area

Test 3: Shadowed area tests

As discussed in chapter 7, conflict situations may occur, where it will be difficult to separate coal from deep clear water or shadow in radiometrically corrected but non transformed images. This is also obvious in figure 8.1., where some shadowed areas were extracted east of the Yellow River, in the central limestone complex and to a slight extend in the southwestern metamorphic complex. These pixels also passed the two spectral mean tests. They can be further reduced with the following tests:

$$\text{Shadow file from ATCOR} = 0 \quad (8.3.)$$

$$\rho [\%] \text{ SPM}_{123457} = 0 \quad (8.4.)$$

$$\rho [\%] \text{ SPM}_{123} = 0 \quad (8.5.)$$

$$\rho [\%] \text{ band 1} = 0 \quad (8.6.)$$

$$\rho [\%] \text{ band 2} = 0 \quad (8.7.)$$

$$\rho [\%] \text{ band 3} = 0 \quad (8.8.)$$

The first test includes the shadow-file, which is created during illumination correction in ATCOR (see chapter 5). This test is similar to the retrieval and exclusion of shadowed areas out of a DEM-derived illumination file directly. This calculation does not have to be repeated, since this file already exists.

Fully shadowed regions (shadow file = 0) are defined as areas, where the pixel consists purely of shade and the geometry between the pixel (relief), sun and satellite does not allow for a return signal in these wavelengths. In contrast, other shadowed pixels may only contain part of a shadow (e.g. shadow margin) and therefore allow for a weakened spectral signal. Such shadowed areas, which are not excluded in the shadow file can fulfill all or some of the equations 8.4 to 8.8. They can therefore be excluded and will not be interpreted as coal surfaces. Only pixels not fulfilling any of the equations will continue in the test sequence.

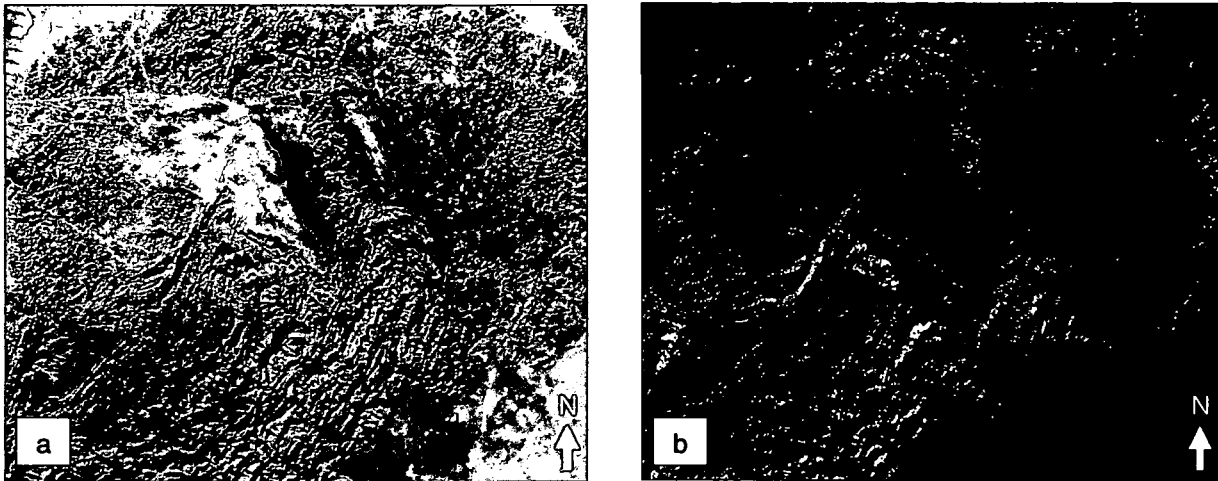


Figure 8-4 a-b: Visible band displayed in gray scale mode (a) and shadowed areas extracted by test 3 supported by available illumination data derived from a DEM. Here presented for the strongly shadowed area of Ruqigou. Center coordinate: 607794E, 4336506N, UTM, Z48N

Figure 8-5 on the next page demonstrates the relationship between the extent of the shadowed area excluded with the tests presented above in relation to the acquisition date of the satellite scene. It can be noted that the scene acquired in summer (high sun elevation angle) yields a smaller proportion of shadowed areas than the scene from fall. The fall scene again yields a smaller proportion of shadowed areas than the scene acquired at very low sun angles in winter.

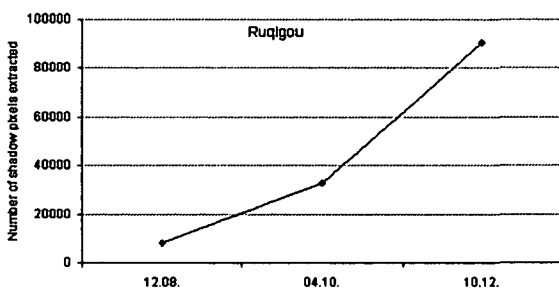


Figure 8-5: Relationship between number of excluded shadow pixels and scene acquisition date; calculated for three scenes of the Ruqigou area for the months of August, October and December. As expected, the area eliminated by test 3 (pixels do not undergo further testing for “coal”) increases with decreasing sun angles.

Test 4: NIR test

This test excludes pixels, which’ reflectance is too high in the NIR band 4 to belong to the class coal. Pixels, which pass this test continue in the testing sequence, pixels, which do not pass the test are excluded for further analysis. See chapter 7 for signature analysis of band 4.

$$\rho [\%] \text{ band 4} \leq 10$$

(8.9.)

Test 5: Test for water surface exclusion

This test supports the exclusion of water surfaces, which might still be left within the remaining pixels, which passed tests 1 and 2 and 4 and were not excluded by test 3. Water surfaces often have low overall albedo and therefore may pass test 1 and 2. Their differentiation criterion to coal is that they usually exhibit lower reflectances in band 5 and band 6. Here, the spectrum of water has decreasing reflectances from blue to the MIR. (The Yellow River is a special case due to its high sediment and algae content and is usually already excluded by test 2 and 4).

$$\rho [\%] \text{ band } 5 \geq 5 \quad (8.10.)$$

$$\rho [\%] \text{ band } 6 \geq 5 \quad (8.11.)$$

$$\rho [\%] \text{ bands } 4, 5, 7 > 0 \quad (8.12)$$

Pixels, which do pass this test continue in the test sequence, pixels which do not fulfill the criteria of inequalities 8.10. and 8.11. are assumed to be water surfaces. If inequality 8.12. is fulfilled these are either shadow surfaces (which were already excluded by test 3, equation 8.4), or water surfaces of extremely low reflectance. See chapter 7 for signature analysis in the above mentioned bands.

Test 6: Temperature test

As mentioned in chapter 7 the inclusion of the thermal band can improve the separability of classes. The thermal band (calibrated and radiometrically corrected to LST as presented in chapter 5) is included in the threshold sequence to exclude all pixels, which passed test 1 and test 2, did not pass test 3 and passed tests 4 and 5, but which have temperatures not suitable for coal surfaces.

Problematic about this test is that the temperature behavior of a surface changes over the year. Daily and annual amplitudes of a surface are not only a function of the surface's thermal inertia but also of longitude and latitude, elevation, microclimatic location and strongly depend on the seasons climate, shading, wind, snow cover etc. It is not possible to define a fixed absolute temperature threshold applicable for several regions and multi date imagery. Even though for each scene an adjusted temperature threshold can be defined, which yields – judged on the basis of visual validation – an optimal coal extraction for each scene, such individual thresholds are not applicable for a transferable

algorithm. Therefore – next to an absolute threshold fitting all scenes – a relative temperature test was defined. This relative approach is transferable from scene to scene. It might not yield as exact results as an absolute threshold but allows for multi scene processing.

$$\rho [^{\circ}\text{C}] \text{ band } 6 \geq 16 \quad (8.13.)$$

$$\rho [^{\circ}\text{C}] > \text{Global mean band } 6 [^{\circ}\text{C}] \quad (8.14.)$$

Here ρ is emission of thermal radiation, which may not be confused with emissivity. With condition 8.14. it is tested, if the pixel under investigation has a temperature exceeding the global mean of the thermal band. This is based on the finding that shaded pixels (cooler) are located left of the global mean of band 6, whereas coal pixels are located right (warmer) of the global temperature mean. See chapter 7 for temperature behavior of the surfaces for the individual scenes.

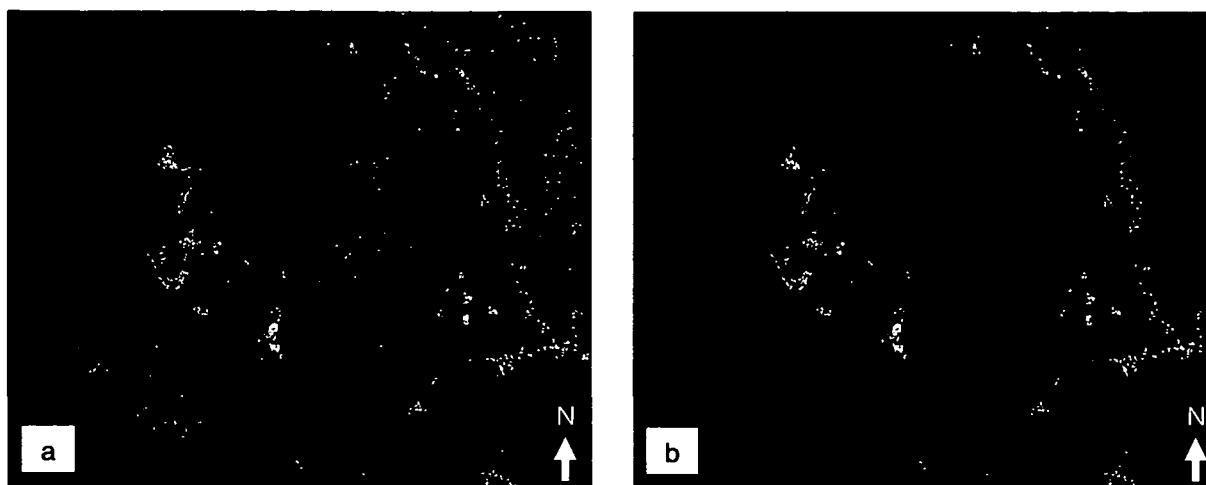


Figure 8-6 a-b: Pixels which passed tests 1, 2, 4 and 5 and were not excluded by test 3 (white) in the left image (a), result after the final relative temperature test 6 (b), Center coordinate: 650705E, 4373287N, UTM, Z48 N

Pixels, which pass test 1, 2, 4, 5 and 6 and which do not pass test 3 are defined as coal pixels. This final result of the knowledge based coal extraction developed undergoes a majority filtering with a 3×3 matrix. This statistical filter excludes single scattered pixels, which are likely to be false alarms. Though these are small in number they would lead to the definition of larger coal fire risk areas when a single pixel is surrounded with a delineation zone. Following this filter application, a delineation area with 500 meter radius is calculated around the areas designated as coal.

8.1.2. Automated Extraction of Densely Vegetated Areas

It is impossible to map vegetation density in such a disturbed and undulating terrain over a larger area without the help of color air photographs and highly interactive interpretation- and analyzing techniques. Therefore, the question arose, how the observation in the field (zero or only dead and degraded vegetation above active coal fires) could be incorporated into the coal fire area demarcation scheme without the need for ground vegetation mapping and additional data. Therefore, a vegetation index – a commonly used measure for vegetation density and vigor – (CRIPPEN, 1990) is derived from the preprocessed satellite data. The use of spectral indices is straightforward and computationally easy. Nevertheless, the drawbacks are that their performance for senescent vegetation is not satisfactory and that the impact of the soil background on spectral indices is often significant. In case of the most commonly used Normalized Differential Vegetation Index (NDVI), 20% of the variation can be explained by soil color background (VAN DER MEER & DE JONG 2001, KUEMMERLE 2003). Therefore many studies focused on SMA to map vegetation quantitatively. However, within this knowledge based test sequence it is not the goal to map vegetation on a quantitative basis, but to roughly differentiate low, medium and high vegetation density in the satellite data. The NDVI is defined as :

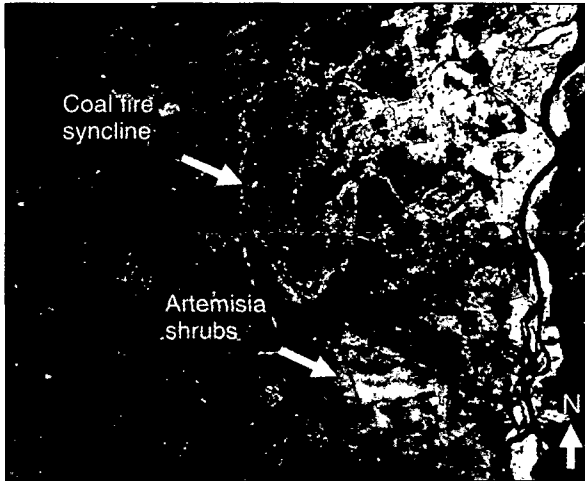
$$\text{NDVI} = (\rho_{\text{NIR}} - \rho_{\text{Red}}) / (\rho_{\text{NIR}} + \rho_{\text{Red}}) \quad (8.15)$$

where ρ_{NIR} is the reflectance in the NIR and ρ_{Red} is the reflectance in the red channel; in the case of Landsat-7 $\text{NDVI} = (\text{band 4} - \text{band 3}) / (\text{band 4} + \text{band 3})$. The NDVI is extensively used to monitor vegetation on country-wide, continental or global scales. However, it is a less reliable indicator of vegetation biomass if the ground cover is low, as it is the case in arid and semi-arid regions

(SCHOWENGERDT 1997, CRIPPEN 1990). Here, the Soil Adjusted Vegetation Index (SAVI) is more efficient in estimating vegetation density:

$$SAVI = (\rho_{NIR} - \rho_{Red}) / (\rho_{NIR} + \rho_{Red} + L) (1 + L) \quad (8.16)$$

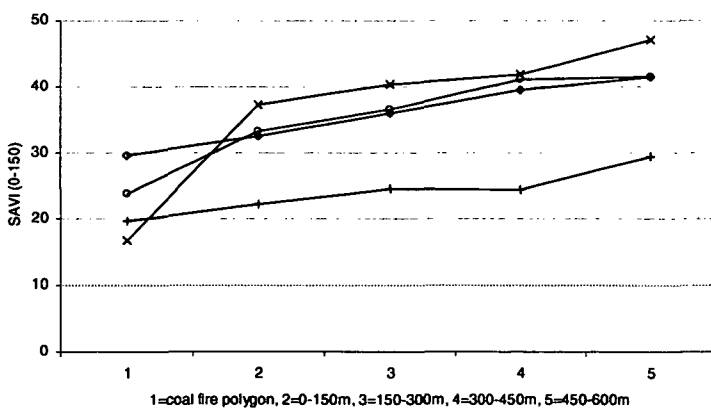
where L is a constant between zero and one, which is empirically determined to minimize the sensitivity of the vegetation index to soil background reflectance variation. When L is zero, the SAVI equals the NDVI. For intermediate vegetation cover the SAVI ranges around 0.5. This value proved



useful based on the results of other projects in similar areas and was applied here also. Due to the mainly arid study areas as well as semi-arid transfer areas (two out of three), the SAVI was preferred to the NDVI and was used for further analysis. In figure 8-7 the relationship between vegetation density and the SAVI distribution becomes apparent. Lowest SAVI values can be found in the area covered by the Yellow River. Very high SAVI values occur within the agricultural areas alongside the river. The lighter part in the central South is an alluvial fan densely covered with *Artemisia* shrubs.

Figure 8-7: SAVI image of Wuda area on 21.09.2002.

To quantitatively prove the relationship between coal fire existence and very low vegetation density in these areas the following calculations were undertaken. The SAVI image was scaled from originally -1.5 to 1.5 (float) to 0-150. To analyze the behavior of the SAVI in relation to the 16 coal fires located within the Wuda syncline statistical parameters were investigated with respect to the coal fire areas mapped in 2002 and 2003. Therefore an algorithm was developed, which calculates the minimum,



maximum and mean of the SAVI data within the 16 coal fire polygons. Following, these statistic parameters of SAVI were calculated separately within the fire zone and four buffer zones of equal size in increasing distance to the mapped coal fire polygon. Resulting, a regional increase of the SAVI with growing distance from the coal fire polygon could be detected as presented in figure 8-8.

Figure 8-8: Spatial pattern of the average SAVI in buffer zones around the active coal fires #6, #7, #8 and #11 of Wuda syncline.

There is no positive relationship stating that a low NDVI or SAVI gives any distinct indication on the occurrence of a coal fire area. Regions of extremely little to no vegetation cover also exist e.g. in settled areas, along infrastructure and industry or in non vegetated parts of the desert. However, above active coal fires no dense vegetation will exist. The goal of vegetation extraction within the knowledge based test sequence must therefore be to automatically extract areas of high vegetation density. These can be excluded as a currently active coal fire area.

Test 1: Test for densely vegetated areas

To extract areas, which are agriculturally used as well as areas, which are covered by a higher density of semiarid shrub coverage, the following two inequalities prove to be a transferable and reliable combination. The thresholds were found via empirical tests with all scenes.

$$SAVI_{xy} > 0.4 \tag{8.17}$$

$$SPM_{123457} > 10 \tag{8.18}$$



Figure 8-9: Result of the vegetation test for Wuda area, white: dense vegetation, black areas below the SAVI threshold. Center coordinate: 650705E, 4373287N, UTM, Z48 N

The first condition yields all pixels, whose SAVI is higher than 0.4. The threshold could not be set in a relative way (e.g. > Global Mean) because the SAVI is a data independent index. In a scene, where land cover classes are evenly distributed (from bare ground to densely vegetated areas all surface cover types available) the SAVI usually ranges between -1.5 and 1.5, with the mean ranging around 0. In subsets created with no vegetation present (pure desert sand) the SAVI ranges between -0.2 and 0.2. In subsets created containing agricultural fields exclusively the SAVI ranges between 0.5 and 1.2. Based on numerous empirical studies it was therefore concluded to set the threshold at +0.4. Pixels passing this test will be excluded from delineated risk areas.

8.1.3. Automated Extraction of Pyrometamorphic Rock

The extraction of burned rock from satellite data can only be applied for the region of Ruqigou. The largest area of pyrometamorphic rock observed in the field in the Wuda region was not of sufficient size to fill the spectral signal of a Landsat pixel. For the Ruqigou area the situation is comparable but not as unfavorable. Here, mapped ground truth of sufficient size for the years 2002 (from mapped polygons) and the year 2003 (from mapped polygons and Quickbird data) exist and approximately 4-5 Landsat pixels in the Ruqigou coal fire area can be visually observed in the data. These might be sufficiently influenced by the spectral signal of pyrometamorphic rock. However, the algorithm will have to search for 4-5 pixels within several million pixels. The burned rock detection is only applied

for the Ruqigou scenes of September 2002 and May 2003, since for the other dates no ground truth is available. The visual retrieval from older date satellite data is not possible for such a complex surface.

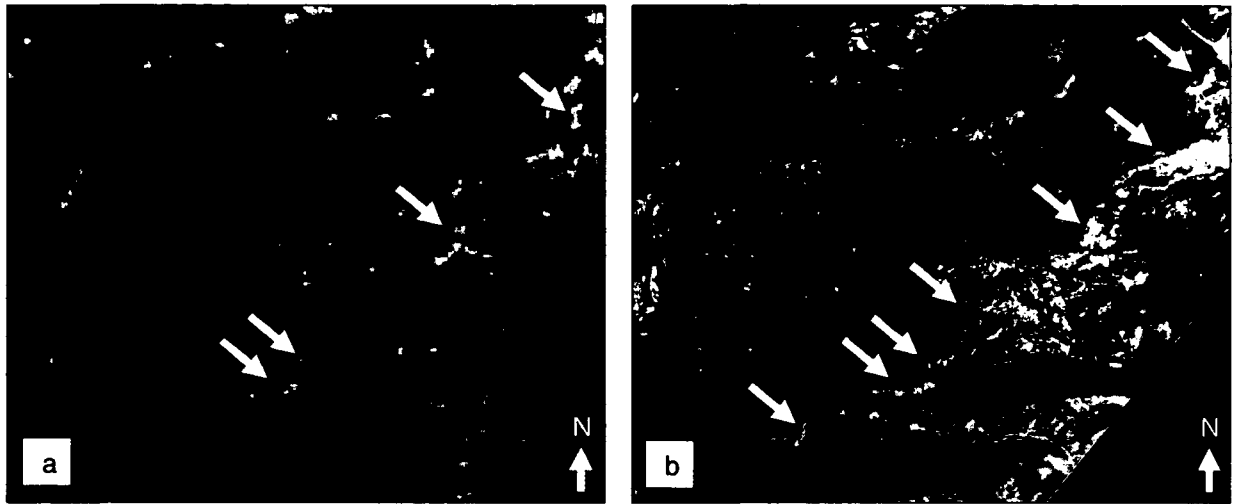


Figure 8-10: Coal mining area Ruqigou, Landsat image (a), Quickbird image (b). Center coordinate of both displayed subsets: 59443 E, 4322273 N, UTM Z48N, WGS84. Both images are displayed in real color combination: bands 1,2,3 = BGR. The pyrometamorphically changed rocks of reddish color are clearly visible in the Quickbird image. Only a few pixel in the Landsat image experience a strong enough spectral signal to be considered as a 30×30 m pixel representing pyrometamorph rock.

Test 1: Test for spectral characteristics of burned rock

This test is purely based on the spectral observations of the 4 pixels (figure 8-10a), which coincide with the locations of pyrometamorphic rock mapped during the field campaigns. The test analyses all spectral channels including the SPM bands as well as the thermal band for the fulfillment of the following relations:

$$\rho [\%] \text{ band 1} > 10 < 20 \quad (8.19.)$$

$$\rho [\%] \text{ band 2} > 15 < 25 \quad (8.20.)$$

$$\rho [\%] \text{ bands 3} \geq 25 \leq 33 \quad (8.21.)$$

$$\rho [\%] \text{ band 4} \geq 25 \leq 38 \quad (8.22.)$$

$$\rho [\%] \text{ band 5} > 35 \leq 50 \quad (8.23.)$$

$$\rho [\%] \text{ bands 7} > 35 \leq 50 \quad (8.24.)$$

$$\rho [\%] \text{ band } 6_{\text{thm}} \geq 20 \leq 25 \quad (8.25.)$$

$$\rho [\%] \text{ SPM}_{123457} > 25 \leq 35 \quad (8.26.)$$

$$\rho [\%] \text{ SPM}_{123} \geq 20 \leq 25 \quad (8.27.)$$

Test 2: Test for the size of clusters extracted in test 1

Signature analysis and empirical tests with the two scenes of Ruqigou revealed that the spectral behavior of the pyrometamorphic rock pixels visually identified are very similar to those of pure desert sand, not covered by vegetation. This is the case due to the age of pyrometamorphic rocks exposed in Ruqigou. Pyrometamorphic rocks of the final stage with a very low featureless spectrum are not abundant in the region (yet). The pyrometamorphic rocks present are characterized by a very

high overall reflectance, little absorption features and can easily be mimicked by a pure desert sand pixel not influenced by vegetation. Therefore the extraction results based on test 1 yield large desert sand regions also. The following assumption can help to further decrease the area extracted: pyrometamorphic rocks will not be found in clusters exceeding 5 Landsat pixels.

$$\text{Area Cluster}_{xy} \leq 5 \text{ pixels} = 4500 \text{ m}^2 \quad (8.28)$$

For no area in the world do coal fire related publications report of pyrometamorphic areas of larger extent. Even the very well known large occurrences in the Kelazha area in northwestern China (Xinjiang Autonomous Region, 50 km southwest of Xinjiang's capitol Urumqi) which were studied based on airborne data by ZHANG, J. (1996) do not cover an area larger than 4500 m². Therefore, a clustering followed by a "sieving" procedure supports the elimination of some of the surfaces, which were wrongly extracted. The pixels which passed pyrometamorphic test 1 are clustered based on an eight pixel neighborhood. Clusters which exceed the size of 5 pixels will not pass the second test and are not considered to be pyrometamorphic pixels.

Figure 8-11 demonstrates the single steps and calculations of the algorithm. A ETM+ or Aster stack of surface reflectance data undergoes the testing for the three surfaces of interest as described above.

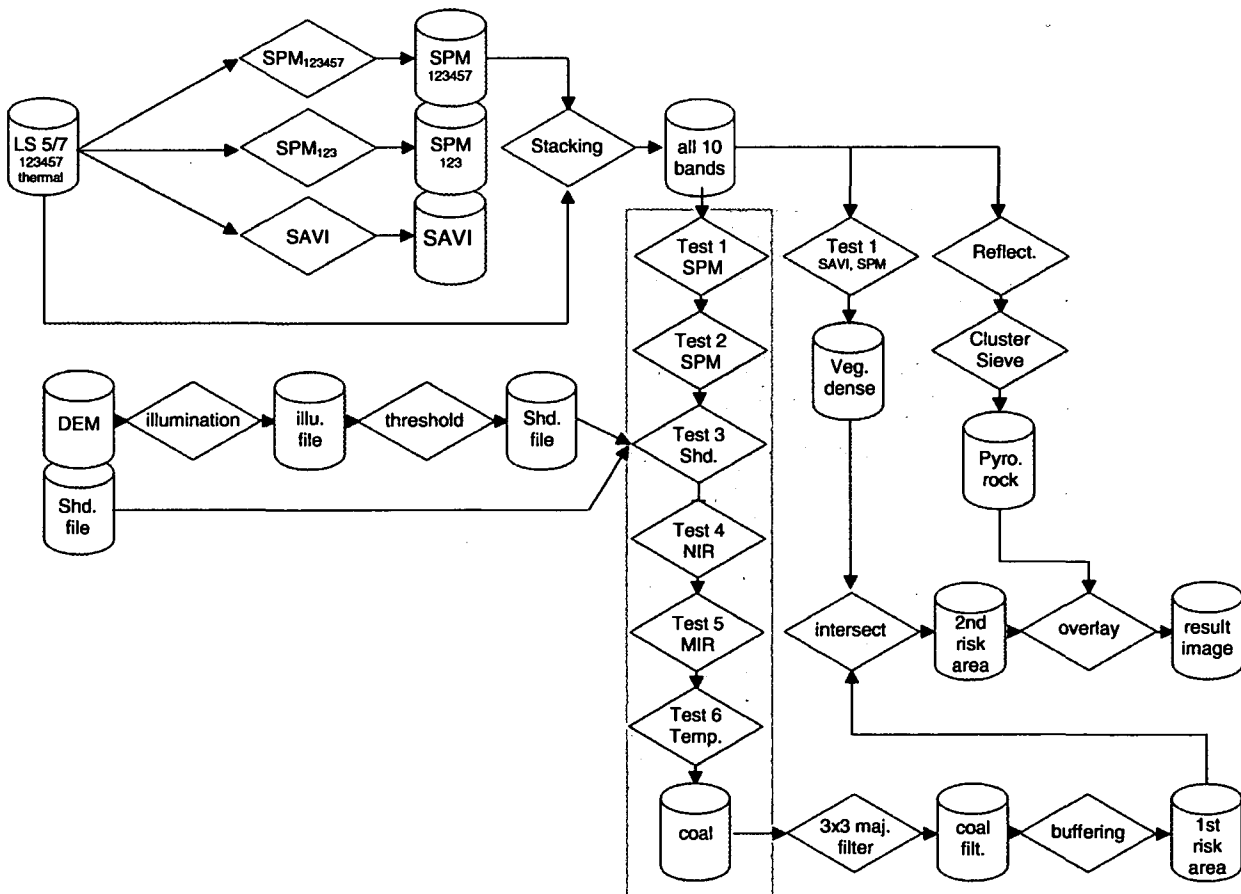


Figure 8-11: Summarized workflow of the knowledge based test sequence (not every temporary output file is shown). After the SPM channels and the SAVI data is generated 16 equations and inequalities are tested for the automated extraction of coal, 2 equations are tested for the extraction of dense vegetation and 9 relationships need to be fulfilled for a pixel to be assigned to the class of pyrometamorphic rock.

8.1.4. Transfer of the test sequence to the Aster Sensor

The above test sequence presented the boundary conditions and thresholds for the automatic extraction from Landsat TM-5 and ETM+ data. The following tests present the same approach for Aster data. Since Aster has more multispectral and thermal bands than Landsat and center wavelengths and bandwidths do not exactly overlap, the sequence had to be adjusted to this sensor. The fundamentals and assumptions for the applied filters are the same. Thus, only the equations and inequalities for the single tests are presented.

Test 1: Synthetic spectral mean test $SMP_{12345789}$

$$\rho [\%] SPM_{12345789} \geq 1 \text{ and } \rho [\%] SPM_{12345789} \leq 11 \quad (8.30)$$

Test 2: Synthetic spectral mean test SMP_{12}

$$\rho [\%] SPM_{12} \geq 1 \text{ and } \rho [\%] SPM_{12} \leq 7 \quad (8.31)$$

Test 3: Shadowed area tests

$$\text{Shadow file from ATCOR} = 0 \quad (8.32.)$$

$$\rho [\%] SPM_{123457} = 0 \quad (8.33.)$$

$$\rho [\%] SPM_{123} = 0 \quad (8.34.)$$

$$\rho [\%] \text{ band 1} = 0 \quad (8.35.)$$

$$\rho [\%] \text{ band 2} = 0 \quad (8.36.)$$

$$\rho [\%] \text{ band 3} = 0 \quad (8.37.)$$

Test 4: NIR test

$$\rho [\%] \text{ band 4} \leq 8 \quad (8.38.)$$

Test 5: Exclusion of water surfaces

$$\rho [\%] \text{ band 5} \geq 7 \quad (8.39.)$$

$$\rho [\%] \text{ band 6} \geq 5 \quad (8.40.)$$

$$\rho [\%] \text{ bands 3, 4, 5, 6, 7, 8, 8} > 0 \quad (8.41)$$

Test 6: Temperature test

$$\rho [^{\circ}\text{C}] \text{ band 6} \geq 16 \quad (8.42.)$$

$$\rho [^{\circ}\text{C}] > \text{Global mean band 6 } [^{\circ}\text{C}] \quad (8.43.)$$

Test 1: Test for densely vegetated areas

$$SAVI_{xy} > 0.4 \quad (8.44.)$$

$$SPM_{123457} > 10 \quad (8.45.)$$

Test 1: Test for spectral characteristics of burned rock

$$\rho [\%] \text{ band 1} > 15 < 25 \quad (8.46.)$$

$$\rho [\%] \text{ band 2} > 18 < 30 \quad (8.47.)$$

$$\rho [\%] \text{ bands 3} \geq 20 \leq 35 \quad (8.48.)$$

$$\rho [\%] \text{ band 4} \geq 22 \leq 35 \quad (8.49.)$$

$$\rho [\%] \text{ band 5} > 19 \leq 30 \quad (8.50.)$$

$$\rho [\%] \text{ band 6} > 17 \leq 30 \quad (8.51.)$$

ρ [%]bands 7 > 20 ≤ 30	(8.52.)
ρ [%]bands 8 > 20 ≤ 35	(8.53.)
ρ [%]bands 9 > 20 ≤ 30	(8.54.)
ρ [%] band 13 _{thm} ≥ 20 ≤ 30	(8.55.)
ρ [%] SPM ₁₂₃₄₅₇₈₉ > 20 ≤ 32	(8.56.)
ρ [%] SPM ₁₂ ≥ 16 ≤ 28	(8.57.)

Test 2: Test for the size of clusters extracted in test 1

$$\text{Area Cluster}_{xy} \leq 5 \text{ pixels} = 4500\text{m}^2 \quad (8.55.)$$

8.2. Results of the Knowledge Based Test Sequence**8.2.1. Results for the Main Study Areas****8.2.1.1. Wuda**

For the Wuda area eight time steps were processed as presented in figure 8-12. Most prominent areas of coal occurrence are the well known syncline in the central West, the north-south stretching band of mainly wild and private mining in the East and industry related accumulations in the southern center, the northern center and the Southeast. The pixels extracted as coal include hardly any shadow pixels. Only very few are recognizable in the winter scene of December 2002 acquired during a very low sun angle. Pixels of the Yellow River or a small lake existing on the western side of the Yellow River, northeast of the syncline were not extracted. Furthermore, already visually a clear increase from 1987 to 1999 and from 1999 to September 2002 can be noted. The temporal development was quantitatively analyzed and is presented in figure 8-13. Extraction accuracies in comparison with ground truth will be presented in chapter 8.3., where a quantification of the results and error analysis are included.

First visual comparisons of the original imagery and the extracted pixels support the observation that the algorithm tends to slightly underestimate the area covered by coal. This is a logical consequence of the algorithm design, which is based on thresholds mainly derived from class inherent standard deviations for a certain spectral band. For each surface class pixels exist, which have a spectral reflectance in one or the other band not located within the margins of the SD. However, thresholds had to be set to keep inter class confusions as low as possible and to minimize the extraction of false alarms. Therefore, it was expected that the coal area is more likely to be under- than overestimated. Another limitation for the definition of the test sequence was the need for a large spatially and time independent applicability. Each natural phenomenon or process has its defined measurement scale. Hence, it is clear that an algorithm aimed at the applicability in China and Australia, in spring and in summer, in strongly alpine as well as flat terrain will have a higher tolerance level concerning extraction accuracy when focusing on single pixels. It can be concluded that only very pure coal pixels are extracted by the knowledge based test sequence. Mixed pixels in the surrounding of a mine, which are heavily influenced by coal dust are not extracted if they are not located within the SD margins. This explains why industrial accumulations with clear boundaries are – visually interpreted – extracted with a higher accuracy than some pixels along the border of wild coal waste piles with fluent transitions to the surrounding bedrock or material. Figure 5-12 on the next page visualizes all extraction results for the Wuda area. The central coordinate of the presented subset is 650705E, 4373287N, UTM, Z48 N. An industrial storage pile south of Wuda is highlighted.

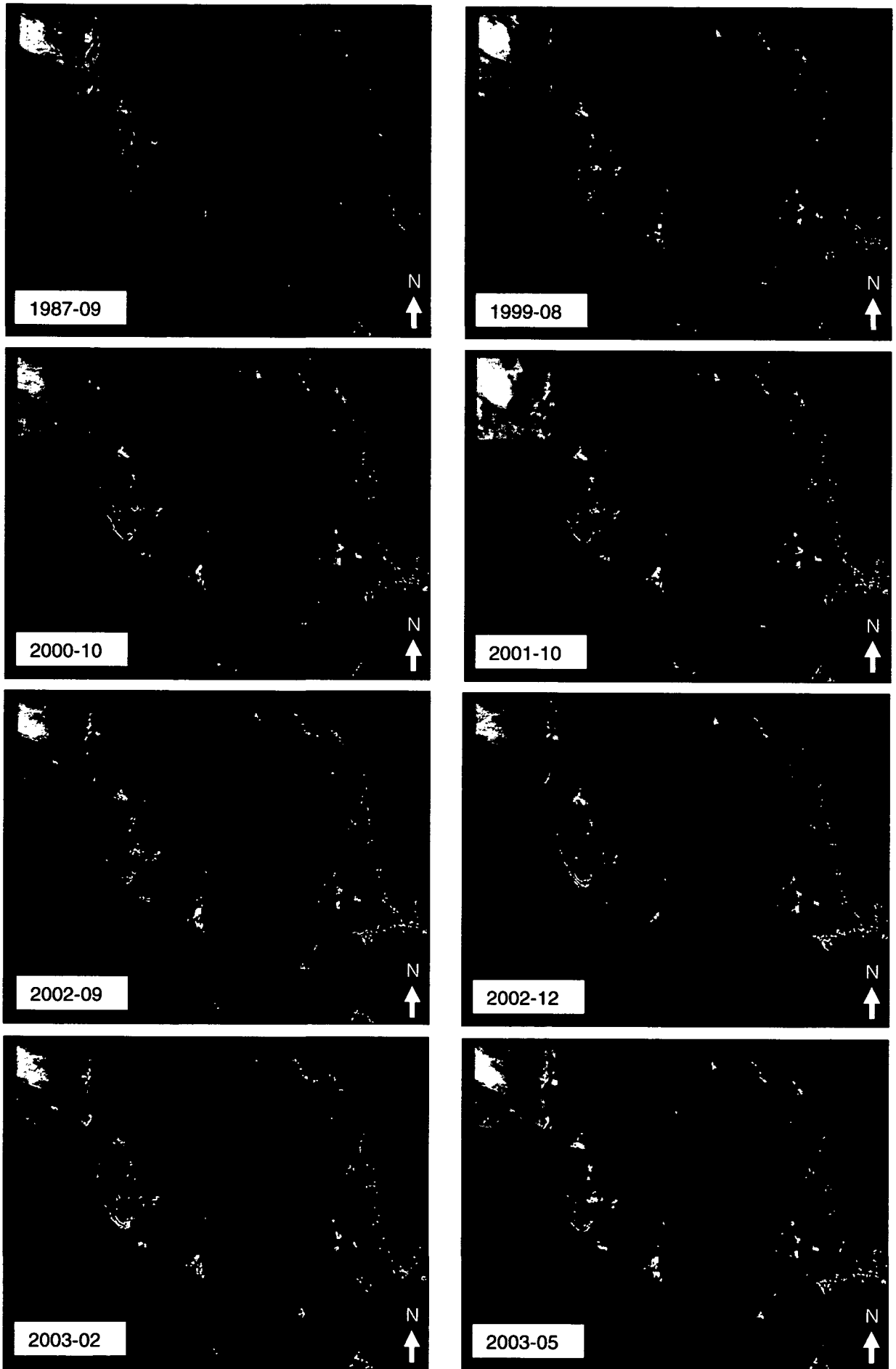


Figure 8-12: Pixels automatically extracted as coal (white) for 8 time steps for the broader Wuda area (filtered).

Figure 8-13 presents the number of coal pixels extracted with the knowledge based algorithm. Light grey columns represent unfiltered results, whereas dark columns represent the final majority filtered result. With the winter scenes included in the time series the trend of the time series is described by the equation presented in figure 8-13 (left). The strength of the relationship between an increase of coal surfaces over time is described by an R^2 of 0.84 (stability index r is 0.91). The level of significance, α , is with 0.1% very high. When winter scenes are excluded the trend of the time series is described by the equation presented in figure 8-13 (right). The strength of the relationship between an increasing area covered by coal detectable in the Wuda area with progressing time is represented with an R^2 of 0.94 (stability index r is 0.96). The level of significance, α , is 0.1%. Both significance levels were retrieved calculating the critical value, t , from equation 8-29 (where n is the number of samples) and following comparison with the critical values of the Student t-distribution for differing significance levels and degrees of freedom (BAHRENBERG et al. 1990). The gap of lacking data between 1987 and 1999 was considered in the calculation. Also the fact that for the years 1999, 2000 and 2001 only one scene exists, whereas 2002 and 2003 are represented by 2 scenes was taken into account.

$$t = \frac{r\sqrt{n-2}}{\sqrt{1-R^2}} > t_{n-2, \alpha/2} \quad (8.29)$$

A reason why the winter scenes can be optionally excluded for the investigation of the development of coal areas in Wuda over time is the fact that coal is heavily used in winter. Therefore storage piles decrease in area, as demonstrated in figure 8-14. This aggravates the quantitative comparison of the coal extraction results of winter scenes relative to the other scenes, which were acquired during times when coal is less heavily used.

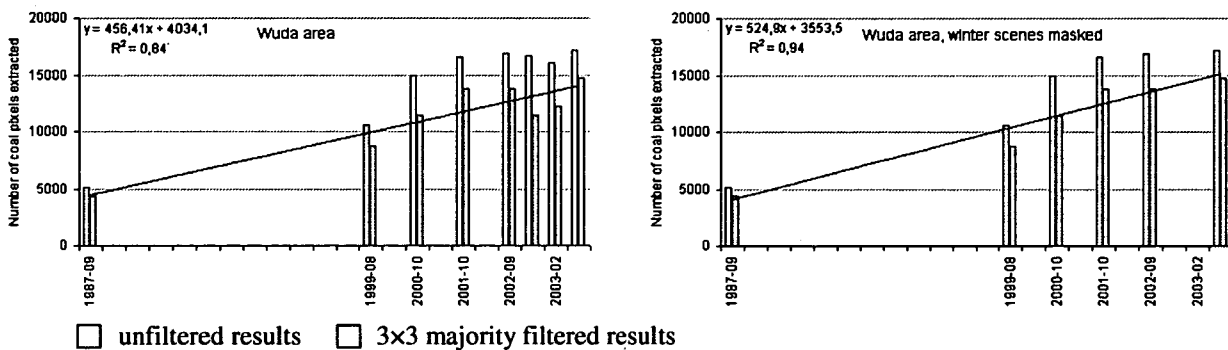


Figure 8-13: Development of the number of coal pixels extracted from 1987 until 2003 for the Wuda area including all scenes processed (a), and excluding the winter scenes (b). The trend was calculated for the filtered results.

Opposite to Ruqigou, radiometrically and concerning thresholds the winter scenes did not cause problems for coal extraction. The scenes were neither snow covered, nor are coal areas in Wuda located within deeply incised valleys supporting the masking of coal by shadow at low sun angle acquisition dates. The reflectance and temperature patterns for the scene from February 2003 have acceptable conditions for coal extraction. In the Wuda part of scene 129/33 from 12.02.2003 the Yellow River is nearly completely frozen. Temperatures of the frozen river range between -1 and 1°C. The thawed southern part ranges around 4°C. Coal surfaces range on average between 16 and 22°C,

and coal fire related pixels reach 25 to 36°C. The average background temperature (histogram mean) is 13.4 °C. Shadowed areas range between 0 and -11°C depending on location and elevation. The deeply incised valleys east of the Yellow River are on average cooler (-8 to -11°C) than the shadowed areas of the central limestone complex closer to the river or the northern foothill areas of the Helan Shan. Since coal is not located in shadowed areas, a spectral- and a temperature threshold are sufficient to differentiate coal from shadow and extract the coal surfaces with high accuracy.

It is not within the scope of this work to discuss every individual scene. A good impression on the spectral reflectance and temperature patterns of each scene is given with the figures representing the results of the signature analyses (chapter 7).

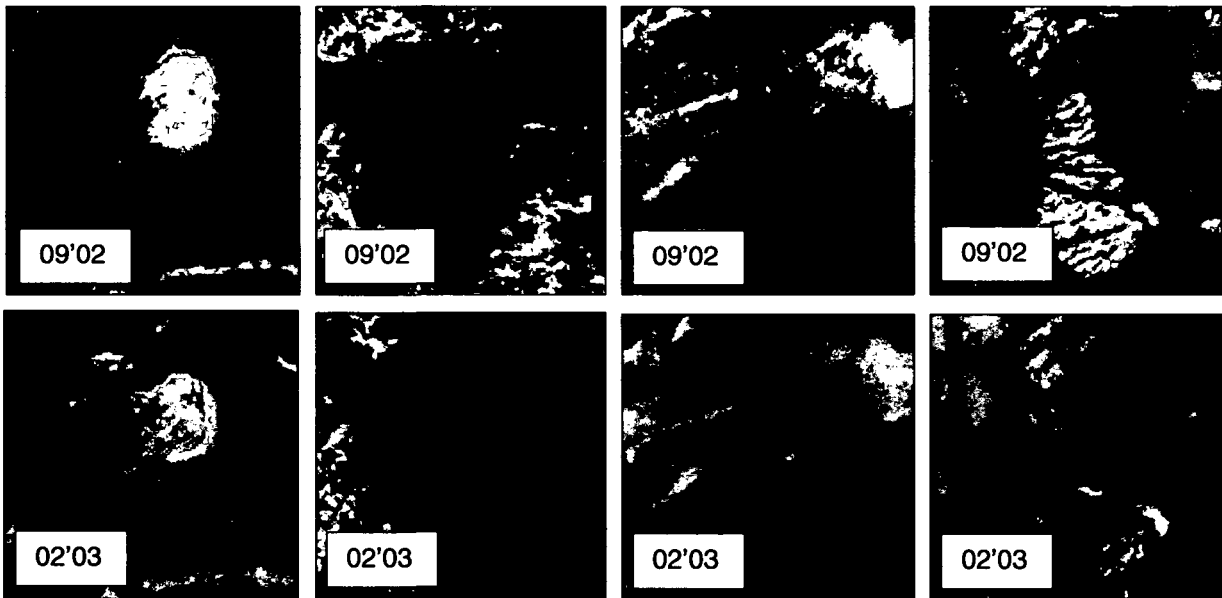


Figure 8-14: Difference between coal accumulation comparing September 2002 and February 2003. The summer/fall scenes acquired present a stable linear increase in coal surfaces over the past years. The two winter scenes of December 2002 and February 2003 act as outliers. This can be explained with the heavy coal use during the winter month. It is obvious that coal storage and coal waste piles and the piles around the mine portals shrink in size during times when coal is increasingly used for heating and electricity production.

The extraction of dense vegetation based on the SAVI image threshold tests yielded eight binary images as presented in figure 8-9. Unless for the surface of coal it is impossible to use this extracted data for a time series comparison since the scenes are not all from the same months. Furthermore, the time series is too incomplete to draw hard conclusions on vegetation trends (like degradation, desertification or the like). Coal exposure is mainly related to human activity and the time scale to monitor changes lies in the range of months to years. Vegetation distribution is dependent on the macro climate, the specific micro climate of a location, the present weather situation, human impacts, grazing impacts etc. and the time scale to monitor changes is in the order of years to decades. Especially in desert environments a few days of rain can lead to a rapid “awakening” and growth of desert shrubs hampering temporal comparison. Even comparing scenes of the same month will not allow the derivation of trends unless the time series consists of sufficient samples (at least 10 scenes of the same month) (HOSTERT 2001). However, the topic of degradation is of high relevance especially for the broader surrounding of the study area of Wuda and will be tackled in the future of the project when further Landsat archive scenes are available.

Table 8-1 presents, how many coal pixels (filtered) were extracted for each time step and how many pixels are included in the delineated area. In addition it is presented how many pixels within this area can be subtracted again, due to high vegetation density. Final remaining pixels indicate probable coal fire- or coal fire risk areas. Furthermore the areal percentage of this risk area in relation to the overall scene size is calculated. Tests for the extraction of burned rock were not undertaken in the Wuda study area, since these surfaces do not exist with sufficient spatial extent. The delineation radius for all areas was set to 500 m. This represents an average dip angle of approximately 15°. In Wuda and Ruqigou most seams dip with a steeper angle. Hence, a smaller buffer would be needed. However, the delineation radius was purposely selected larger to account for lower dip angles and to account for the fact that exact information on dip angles for the transfer regions is not available.

Table 8-1 indicates that for all eight time steps the original area of the input data (1605 km²) is reduced to less than 13 %, which can be considered as a coal fire risk area. Coal extraction yields remaining regions, which – for all time steps – remain below 0.82% of the original input data size. The coal covered area as well as the buffer region is increasing over time. Though the number of coal pixels extracted in the two winter scenes is lower than of the preceding and following years, the buffer area for these two scenes is very large. This results from the fact that for the winter scenes more single scattered (shadow related or outlier) pixels were extracted. These are not eliminated by the majority filter and with a 500 m buffer generation lead to a disproportionally larger delineated area.

Dense vegetation exclusion within the buffer zone minimizes this region for 1.8 % on average. The final remaining area – for no scene larger than 12.71 % of the original input data extent – can now be used to investigate thermal anomaly occurrence concerning their plausibility to be coal fire related anomalies. Complete coal fire risk maps will be presented in chapter 10.

Table 8-1: Reduction of the full scene areas to coal fire risk areas based on the automated extraction of coal, a delineation based on this area and the exclusion of densely vegetated areas within this zone for the Wuda region

Date	Overall pixels	Extracted coal pixels, [km ²]	Buffer region pixels, [km ²]	Veg. exclusion, pixels [km ²]	Area [km ²] remaining	% of scene
1987-09	1783397	4409 (03.96)	123362 (111.02)	1970 (1.77)	109.25	6.80
1999-08	1783397	8776 (07.89)	169210 (152.28)	2557 (2.30)	149.98	9.34
2000-10	1783397	11464 (10.31)	203208 (182,88)	643 (0.57)	182.31	11.35
2001-10	1783397	13764 (12.38)	209463 (188.51)	2410 (2.16)	186.35	11.61
2002-09	1783397	13784 (12.40)	207871 (187.08)	6932 (6.23)	180.85	11.26
2002-12	1783397	11496 (10.34)	227150 (204.43)	342 (0.30)	204.13	12.71
2003-02	1783397	12210 (10.98)	199412 (179.47)	129 (0.11)	179.36	11.17
2003-05	1783397	14790 (13.31)	202824 (182.54)	1182 (1.06)	181.41	11.30

Figure 8-15 on the next page presents an image calculated for the Wuda area indicating, how often for the eight time steps processed a pixel was counted as a coal surface. The black area indicates regions, where coal was never detected. The colored regions present areas, where coal was detected between one and eight times. It can be noted in the two zooms that the central areas of coal waste and coal storage piles are stable over time and appear as coal surfaces in all images. The coal storage pile of Wuda's biggest coal processing plant in the North of the image experiences an increase of the area covered by coal reminding of concentric circles. The steady growth of this pile is hereby demonstrated.

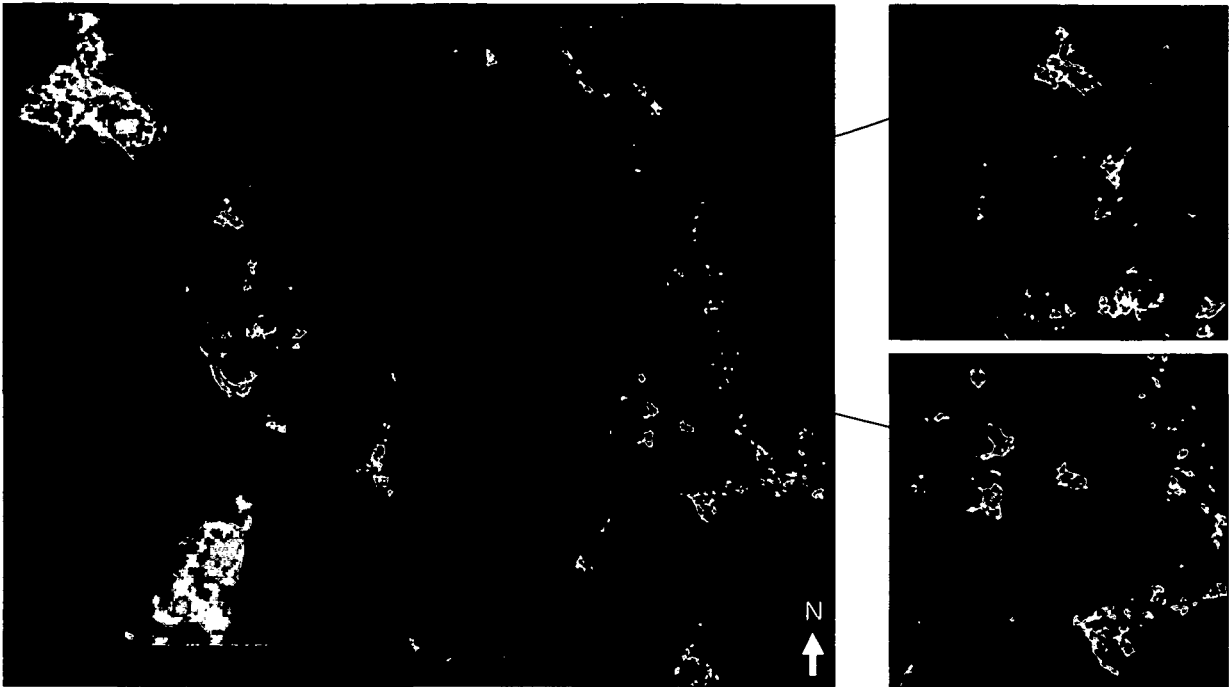
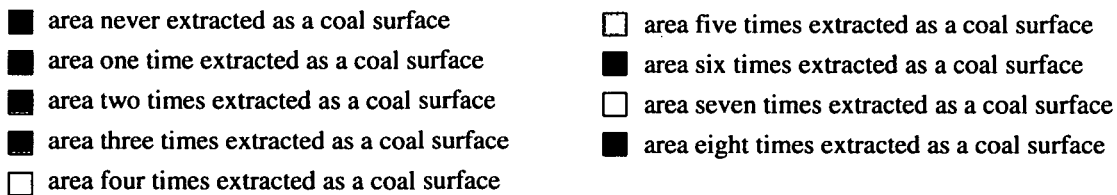
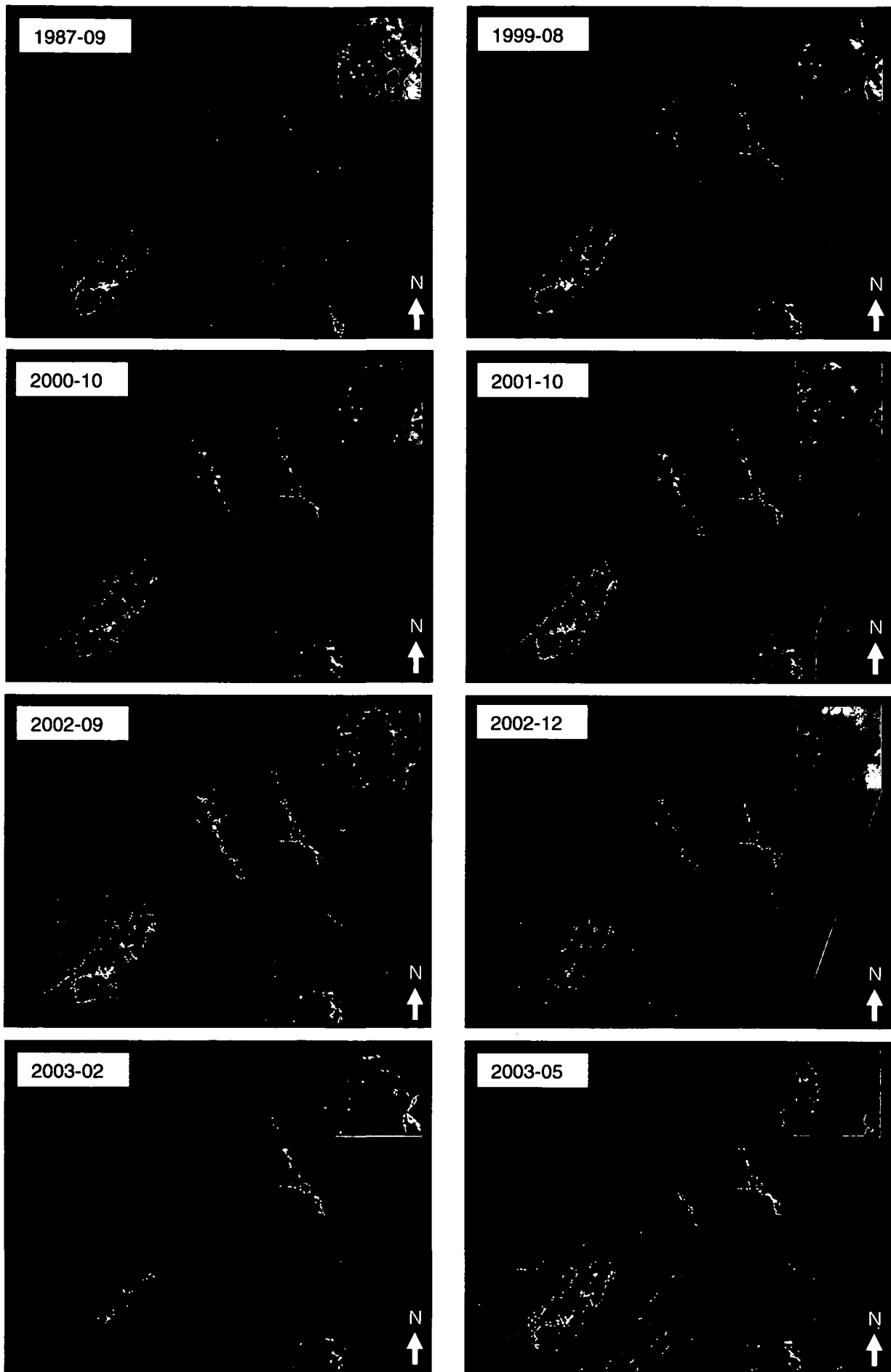


Figure 8-15: Pixels automatically extracted as coal for 8 time steps for the broader Wuda area (filtered). The color scheme represents how often a pixel was considered as a coal surface.



8.2.1.2. Ruqigou

For Ruqigou coal extraction results are presented in figure 8-16. The central coordinate of the presented subset is 667794 E, 4336506 N, UTM, Z48N, WGS84. Except for the two winter scenes – based on a first visual impression – results look very good. This applies although the alpine terrain is highly complex. The challenge to extract a surface only occurring at very limited quantities and the proneness of coal spectra to be easily mimicked by shadow is overcome. Especially for the scenes of 1999, 2000 and 2001 hardly any shadow pixels were extracted and a clear increase in the coal covered area can be noted. Also a large increase from 1987 to 1999 is recognizable. The two parallel running northeast to southwest stretching valleys of Hulusitai and Shitanjing were not yet developed in 1987. Furthermore, the northeastern part of the Ruqigou syncline has been developed strongly over time. Coal accumulations in the very Southeast of the displayed area are coal storage piles closely located to settled areas. Visual comparisons of the extracted area with the small Landsat image presented look very good. Only for the scene from December 2002, where a thin snow layer covers the coal piles, no pixels were extracted. Compared to 1999, 2000 and 2001 in 1987 and 2002 some random shadow pixels are extracted, which will influence risk area definition. The winter scenes of 2002 and 2003 do not fit the visual trend of an overall increase of coal accumulations on the surface. The reason for this is explained in the following paragraphs.



118 *Figure 8-16: Pixels automatically extracted as coal (white) for 8 time steps for the Ruqigou area (filtered),*

Figure 8-16 presents the coal pixels extracted with the knowledge based algorithm. Again, light columns represent unfiltered results. These are meaningless, due to a high number of single scattered pixels extracted along shadow margin areas. Dark columns represent the final majority filtered result. With the winter scenes included in the time series, the trend for the development of coal surfaces over time is described by the equation presented in figure 8-16 (left). The strength of the relationship between the spatial development of coal surfaces and progressing time is represented by an R^2 of less than 0.15 (stability index, r , is 0.38). This is by no means significant (significance level, α , is $>10\%$). When winter scenes are excluded the trend of increasing coal surfaces detectable in the Ruqigou area with progressing time is described by the equation in figure 8-16 (right). The strength of the trend is represented by an R^2 of 0.72 (stability index, r , is 0.85). This result is of high significance, represented by a level of significance, α , slightly above 1%. The gap of lacking data between 1987 and 1999 was considered in the calculation, as well as the fact that for the years 1999, 2000 and 2001 only one scene exists, whereas 2002 and 2003 are represented by 2 scenes.

Ruqigou winter scenes – contrary to Wuda – definitely had to be excluded for a realistic approximation of the development of coal areas over time. This was not so much due to the – not necessarily considerable – fact that coal is heavily used in winter and therefore piles decrease in size. The scene of February 2003 is to approximately 40% snow covered. This hinders the quantitative comparison of the coal extraction result relative to the other scenes. The scene from December 2002 is also not representative. Due to the low sun angle shaded areas are very large. Even illumination correction could not “light up” most of the shaded valleys. In this scene the “worst case scenario” occurs, where a lot of coal surfaces are located in fully shadowed regions. Therefore, coal extraction of sufficient comparability to the other scenes is not possible. This finding however was expected and it is assumed that no knowledgeable image analyst would order low sun angle winter data (also including a high chance of snow cover) for land cover studies, which are seasonally independent.

The phenomenon of decreasing coal pile sizes in winter as observed for the Wuda area could visually not be detected for the Ruqigou area. Several reasons can explain this observation. Compared to Wuda, which is surrounded by urban sprawl and which can be considered a larger agglomeration, Ruqigou is a mountain village with much less inhabitants. The coal demand for households and heating will therefore be considerably smaller. Furthermore, Ruqigou coal is mainly mined for national and international export. Mining is much more industrialized and private wild mining like in Wuda east of the Yellow River – undergoing strong fluctuations – is not as apparent.

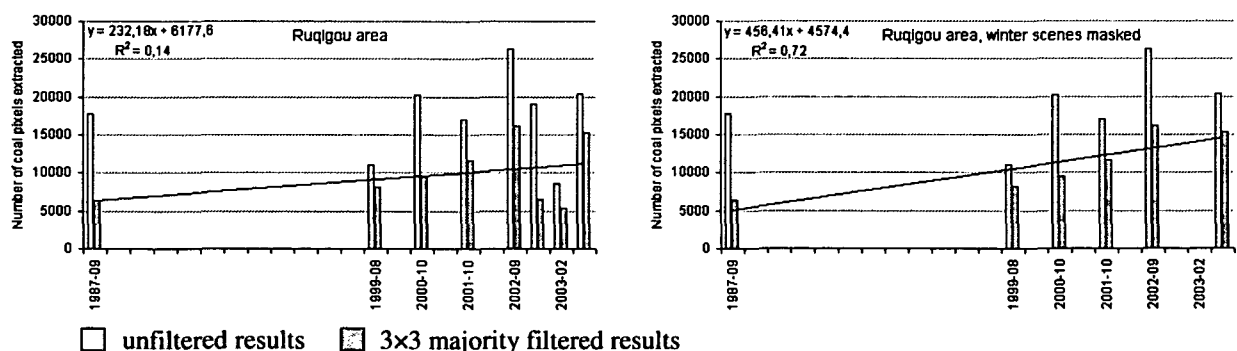


Figure 8-17: Development of the number of coal pixels extracted from 1987 until 2003 for the Ruqigou area including all scenes processed (a), excluding the winter scenes (b). The trend was calculated for the filtered results.

Based on first visual comparisons in Ruqigou the coal covered area is not underestimated, but extracted with high accuracy. This is the result of a compromise, which had to be undertaken concerning the transferability of the algorithm. The filtering of the output result for the Wuda area leads to a decrease in extracted surfaces. In Wuda shadowed regions are less accentuated than in Ruqigou and deeply incised valleys leading to bigger shadowed areas are large in size and spatially limited (mainly east of the river). From visual analysis it could be concluded that for the Wuda region the unfiltered results actually were closer to the real outline of coal surfaces than the filtered results.

However, in Ruqigou unfiltered results were not acceptable due to a lot of small shadow margin clusters extracted all over the Helan Shan mountain range. Therefore, the compromise was taken to decide for very good results in Ruqigou and still good results in Wuda and take the slight underestimation in the Wuda region into account. In addition the phenomenon of mixed pixels is less accentuated in Ruqigou. Here the terrain limits the spatial extent of coal accumulations.

Table 8-2 indicates that for all eight time steps the original area of the input data (1852 km²) is reduced to an area of less than 18 % of the input data. This remaining area can be considered as a coal fire (risk) area. For all scenes an average of 12.2 % remains. Coal extraction alone yields an area, which – for all time steps – remains below 0.78 % of the original input data size. Unless for Wuda, the larger delineated region is not consistently increasing over time, even when winter scenes are not included. In the alpine terrain of Ruqigou the size of the delineation radius largely depends on the quality of the output result of test 3 from the coal extraction test sequence (removal of shadow). In case the reflectance or temperature behavior of shadow and shadow margin are unfavorable, a lot of scattered pixels will be extracted. If not excluded by the majority filter, these pixels will lead to a disproportionally larger overall delineation area. The delineation zone development in Ruqigou over time therefore does not allow for any statement on the spatial development of coal fire risk areas.

Dense vegetation exclusion within the delineated zone reduces the demarcated coal fire risk area of Ruqigou for 7.82 km² on average. The final remaining area is for no scene larger than 17.98 % of the original data input. This demarcated area can now be investigated for thermal anomalies detected by the algorithm developed by ZHANG, J. (2004).

For the Ruqigou scene of September 2002 4441 pixels of pyrometamorph rock were extracted (3.9 km²). When this result is intersected with the delineation area – (since it is assumed that pyrometamorphic rock does not occur outside the delineation zone) – 181 pixels (= 0.16 km²) remain. Since only 4 of these 181 pixels can be validated and for many pixels no ground truth in the form of mapped polygons or high resolution data is available, this number can not be interpreted. It is assumed though that this result still contains some desert sand pixels, which occurred in small enough clusters to pass the pyrometamorphic rock test 2 and which are located within the margin of the demarcated risk area.

For the Ruqigou area in May 2003 all in all 8341 pixels indicating pyrometamorphic rock were extracted. When this result is intersected with the delineated area 706 pixels (= 0.63 km²) remain. This result is expected to be highly exceeding the realistic dimensions, since an increase in the exposure of pyrometamorphic rocks for about 0.5 km² within only half a year is considered very high.

Detailed coal fire risk maps will be presented in chapter 10.

8. Knowledge Based Surface Extraction

Table 8-2: Reduction of the full scene areas to coal fire risk areas based on the automated extraction of coal, a delineation based on this area and exclusion of densely vegetated areas within this zone for the Ruqigou region

Date	Overall pixels	Extracted coal pixels, [km ²]	Delineated region pixels, [km ²]	Veg. exclusion, pixels [km ²]	Area [km ²] remaining	% of scene
1987-09	2058820	6438 (5.79)	318681 (286.81)	14150 (12.73)	274.08	14.79
1999-08	2058820	8093 (7.28)	160863 (144.77)	8022 (7.21)	137.56	7.42
2000-10	2058820	9515 (8.56)	259066 (233.15)	3156 (2.84)	230.31	12.42
2001-10	2058820	11662 (10.49)	196747 (177.07)	5769 (5.19)	171.88	9.27
2002-09	2058820	16205 (14.58)	326470 (293.82)	18017 (16.21)	277.61	14.98
2002-12	2058820	6527 (5.87)	371670 (334.50)	1426 (1.28)	333.22	17.98
2003-02	2058820	5459 (4.91)	116001 (104.40)	247 (0.22)	104.18	5.62
2003-05	2058820	15241 (13.71)	330037 (297.03)	18763 (16.88)	280.15	15.11

The algorithm was also applied to the whole ETM+ scene 129/33 from September 2002, which is the most recent scene available for the area. The scene from May 2003 is unfortunately cloud covered for the region south of the study areas. The September scene covers an area of 52439.65 km². 43.49 km² could be extracted as coal, the delineated area includes 890 km² before- and 827 km² after vegetation exclusion. The remaining area is equal to 1.5 % of the input data set.

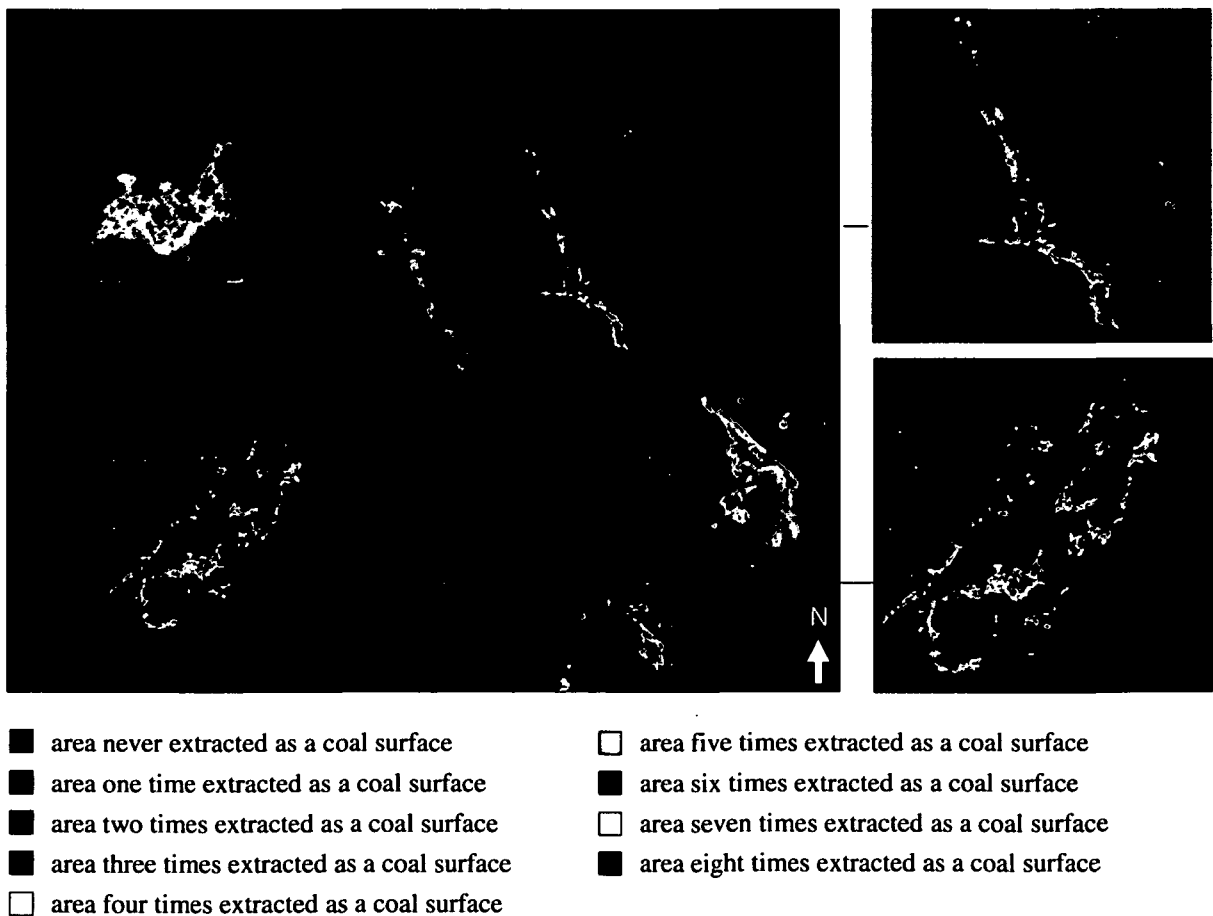


Figure 8-18: Pixels automatically extracted as coal for 8 time steps for the broader Ruqigou area (filtered). The color scheme represents, how often a pixel was considered as a coal surface. Center coordinate of main subset: 607794E, 4336506N, UTM, Z48N

8.2.2. Results for the Transfer Regions

To demonstrate the large scale transferability of the developed knowledge based sequence the algorithm was applied to three totally different locations outside the study areas. These are represented by Landsat-7 ETM+ scene 140 / 044 located in India as listed in chapter 4 and a scene (098 / 081) from the southern hemisphere in Australia. For both areas – the Jharia mining region (western India) and the Flinders Mountains (southeast Australia) all channels were available and the data was preprocessed as presented in chapter 5. Furthermore, a scene outside the common test areas in China was processed. It covers the northernmost part of the Yellow River, including the city of Baotou in Inner Mongolia (scene 128 / 032).

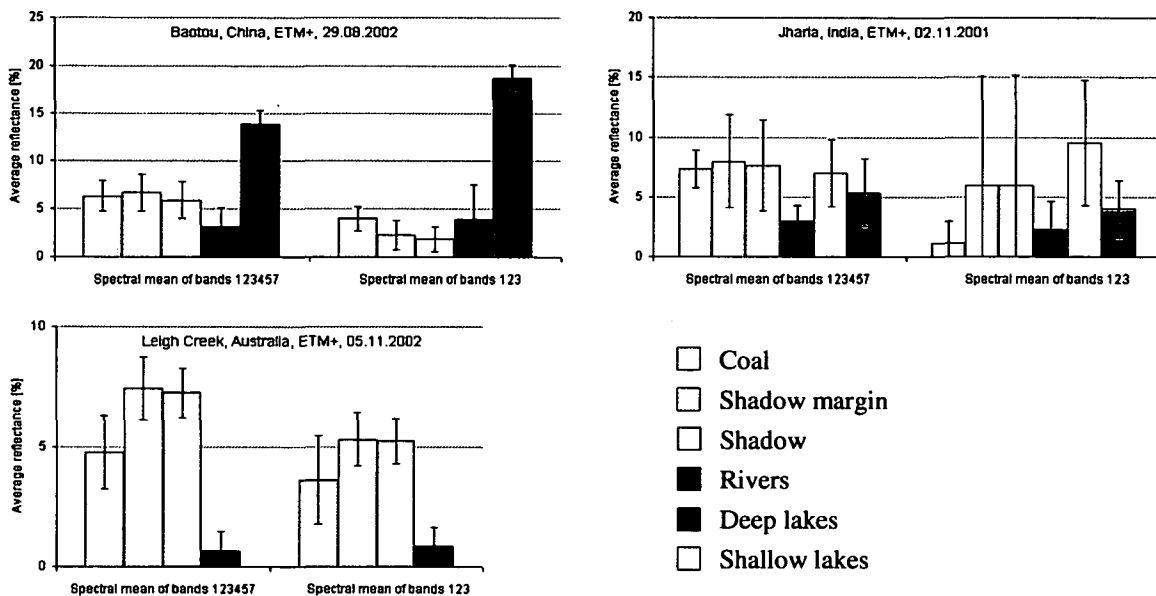


Figure 8-19: Spectral mean for bands 123457 and bands 123 for the three transfer areas

As presented in figure 8-11 synthetic spectral mean bands were also calculated for the transfer areas. The mean and SD of SMP_{123457} and SPM_{123} are presented in figure 8-19. The same threshold filters were applied as for the ETM+ scenes of Wuda and Ruqigou.

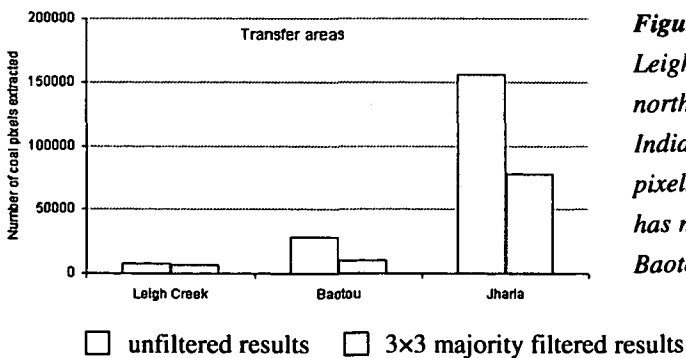


Figure 8-20: Number of extracted coal pixels for the Leigh Creek area, Australia, the Baotou area in northern China and the Jharia coal mining region in India. An exceptional high amount of single scattered pixels is extracted in the scene from India. This scene has much larger coal occurrences than the regions of Baotou and Leigh Creek area, Australia.

8.2.2.1. Flinders Ranges, Leigh Creek, Australia

The Flinders Ranges in Australia are about 400 km long and belong to the few elevated land masses of the continent. Due to the semi-arid to arid environment they are only sparsely covered with vegetation.



They offer a good insight in their geologic structure, when observed from satellite. The coal mining area present in the Landsat-7 scene is the Leigh Creek open pit coal mine, which is located at the southwestern foothills of the Flinders Range. Here, Triassic coal was discovered in 1888 and coal mining started in 1943. Leigh Creek is South Australia's only coal mine and supplies coal to the power station at Port Augusta. Here it is used as fuel to produce 40% of Adelaide's electricity. Currently 2.7 Mt/year of coal are won by open-cut methods (URL 8-1).

Figure 8-21: Location of the transfer ETM+ scene from Australia

For the scene from Australia the visual impression of coal extraction looks very good. 6786 pixels were extracted as coal from the large ETM+ subset processed containing over 3.7 Mio. Pixels. The extraction result therefore contains less than 1.46 % of all pixels within the scene. The clear deep (dark) water reservoirs south of Leigh Creek coal mining area (highlighted in white framed boxes, figure 8-22 left) were not extracted. Dense vegetation in this scene only exists in very low covering densities. An exception are the vicinities of riverbeds dissecting the image as well as the shores of two artificial lakes. The inclusion of the thresholded SAVI result could decrease the coal fire risk area from 50.05 to 49.91 km² (see table 8-3).

Pyrometamorphic rock could not be detected in the area. Though no detailed information on this subject was available, it is assumed that this type of rock does not exist. No larger long burning coal fires are reported for the Leigh Creek coal field. Furthermore the coal is mined with open pit mining and the ventilation – cooling the exothermal reaction of carbon and oxygen – is considered good. The coal is furthermore mined with heavily industrialized methods and under frequent supervision. If a coal fire would occur at all it is assumed to be extinguished fast. Therefore, no favorable environment for the genesis of pyrometamorphic rock exists. A coal fire area risk map is presented in chapter 10.

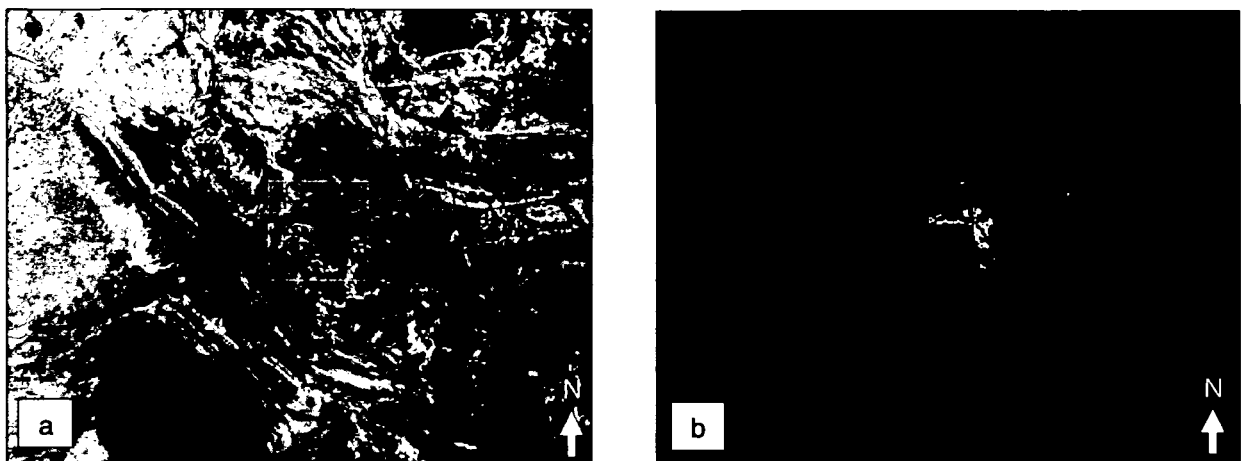


Figure 8-22: The Leigh Creek coal mining area (a), coal pixels extracted for the scene (b), this subset displays only 1/15th of the full scene. Center coordinate of subset: 6626009 S; 252463 E, UTM, Z54 S, WGS 84.

Table 8-3: Reduction of the full scene areas to coal fire risk areas based on the automated extraction of coal, a delineation based on this area, exclusion of densely vegetated areas within this zone for the Leigh Creek region

Date	Overall pixels	Extracted coal pixels, [km ²]	Deli. region pixels, [km ²]	Veg. exclusion, pixels [km ²]	Area [km ²] remaining	% of scene
2002-11	3788996	6786 (6.10)	55621(50.05)	164 (0.14)	49.91	1.46

8.2.2.2. Jharia coal mining region, India

The Jharia area in India has an extremely high industrial density. It hosts a well known coal field, formerly researched intensively in the context of coal fires by BHATTACHARYA & REDDY (1994), SARAF et al. (1995) and PRAKASH & GUPTA (1998, 1999). Jharia is the largest coal field in India located about 250 km northwest of Calcutta and 1150 km southeast of Dehli. To the South the coal fields are bordered by the Damodar River. More than 90 surface- and subsurface coal fires were reported in this region. Located 100 km southwest of Jharia the Rāy coal field can be found. The environment has a very high average vegetation density. Tropical monsoon forest still exists in close vicinity of the coal fields. Monthly average temperatures exceed 18°C.

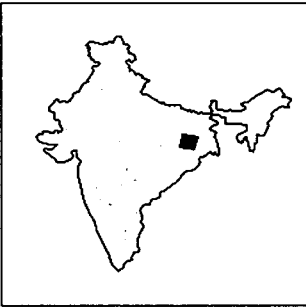


Figure 8-23: Location of the ETM+ transfer scene from India

As illustrated in table 8-4 77665 coal pixels were extracted from the scene available for India. This compares to an area of 0.13 % of the whole scene. Already after visual investigation it could be noted that coal extraction for India worked not as well as for the Chinese areas or the Australian transfer region. The problem is not so much that the existing coal areas were not demarcated properly by the algorithm. Other areas not representing coal were extracted also. These are for the most parts water bodies like rivers and lakes as it can already be seen in figure 8-24 (upper right). From chapter 7 as well as figure 8-19 it was already clear that in this tropical environment coal and the surfaces similar to coal have a different spectral pattern. For all surfaces and in all wavelengths bands as well as the SPM channel did the surfaces coal, river water, deep lake water and shallow lake water have very high SDs, complicating differentiation. This results in many scattered “coal” pixels, which are actually false alarms and lead to an inappropriate increase of the delineated area.

Dense vegetation is abundant in the region. Areas, which can be excluded from the demarcated zone are therefore very large. Vegetation exclusion reduces the delineated zone from 3178 to 778 km². The remaining area considered as a coal fire risk area contains only 1.48 % of the whole scene input into the knowledge based test sequence.

Pyrometamorphic rock does exist in very small quantities in the Jharia area. The outcrops are not large enough though, to be picked up in a 30 × 30 m pixel (personal communication with A. PRAKASH, July 2004).

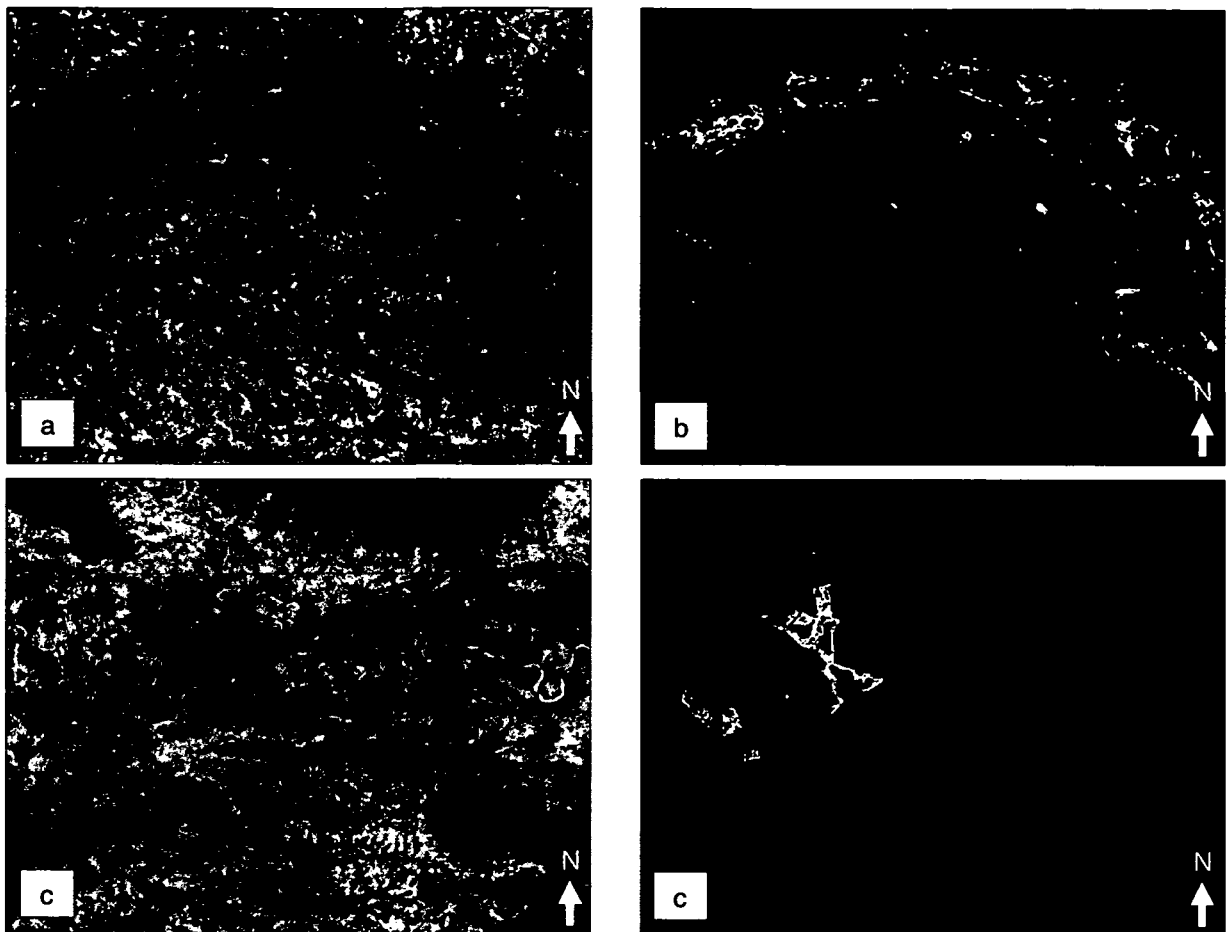


Figure 8-24: Coal pixels extracted for the scene of India. The two subsets display only parts of the full scene. The upper two images (a, b) present the Jharia coal field. The lower two subsets (c, d) present a coal field approximately 100 km west of Jharia close to the small town of Rāy. Center coordinate of upper subset: 428060E, 2624047N, UTM, Z45 N, WGS 84. Center coordinate of lower subset: 307711 E, 2621553 N, UTM, Z45 N, WGS84.

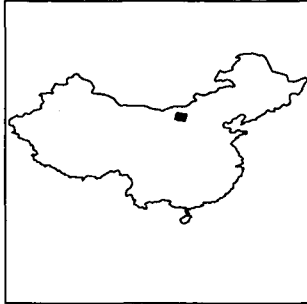
Table 8-4: Reduction of the full scene areas to coal fire risk areas based on the automated extraction of coal, a delineation based on this area and exclusion of densely vegetated areas within this zone for the Jharia region

Date	Overall pixels	Extracted coal pixels, [km ²]	Buffer region pixels, [km ²]	Veg. exclusion, pixels [km ²]	Area [km ²] remaining	% of scene
2001-11	58440921	77665 (69.89)	3532214 (3178.9)	2667462 (2400.7)	864752 (778.27)	1.48

It can be noted that the delineated region for the broader Jharia area is very large, which results from the erroneously extracted areas. Every little lake or surface, which was extracted as coal, is delineated with a 500 m radius delineation. At the same time, dense vegetation exclusion reduces this delineated area substantially. It plays a much larger role concerning the final remaining coal fire (risk) area than for the study areas. Even though next to the extraction of real coal a lot of other surfaces were extracted, the final area sums up to less than 1.48% of the spatial extent of the original data input. The surface extraction accuracies are presented in subchapter 8.3.. The transferability of the algorithm for such a different environment as for tropical India is discussed in subchapter 8.4..

8.2.2.3. Baotou, China

Baotou in Inner Mongolia, China, is located approximately 320 km northeast of Wuda. The city has approximately 1.8 Mio inhabitants, located 15 km north of the Yellow River's northernmost outreach.



Further east the river turns South to flow towards the northeast Chinese lowland. North of Baotou the Yin Shan mountain range rises. However, the broader Baotou area and the area to the South is flat. The climate is a semi-arid to arid half desert climate comparable to Wuda and surrounding. Fertile flood plains along the Yellow River are used for irrigated agriculture. Coal mined in the Baotou area is used for iron and steel processing based on iron ore, which is mined in Baiyunebo, about 150 km north of Baotou.

Figure 8-25: Location of the ETM+ transfer scene from northern China

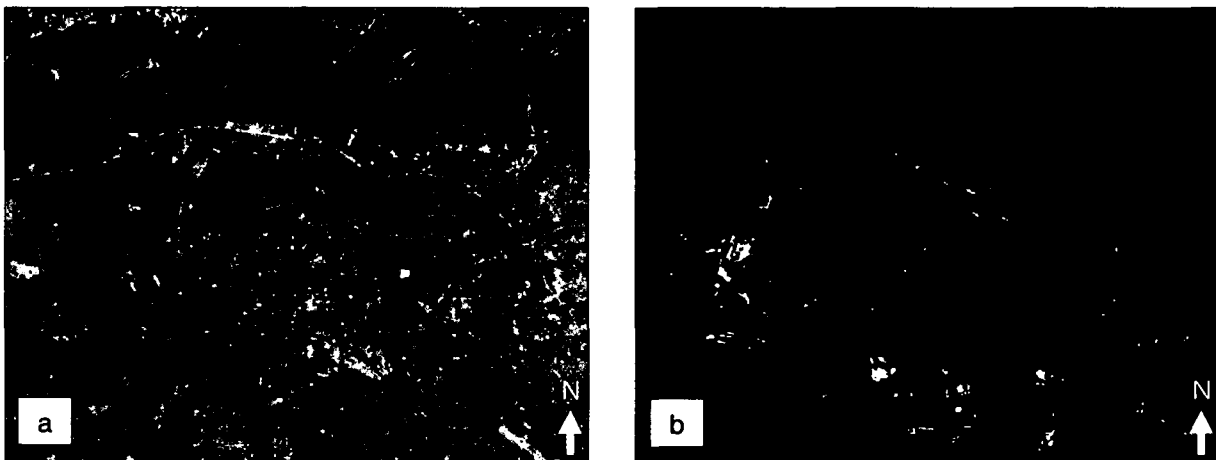


Figure 8-26: Original data (a) and coal pixels extracted for the scene of Baotou, northern China (b). The subset displays only part of the full scene. Center coordinate: 404361E, 4502452N, UTM, Z49 N, WGS 84.

Few coal pixels were extracted from the scene of Baotou. Confusion with water did not occur, only a few shadow margin areas were extracted as coal also. A DEM or shadow file did not exist for the area. Therefore the shadow removal was not 100 %. However, visual interpretation indicates that all coal areas were extracted with high accuracy. Table 8-5 presents the detailed numbers for the full scene. Extracted coal pixels make less than 0.016 % of the full feature space, the delineated area covers 0.9 % of the whole scene before- and 0.59 % after dense vegetation exclusion. Finally, less than 0.59 % of the scene remain as a coal fire risk area. The algorithm could not detect pyrometamorphic rock in the area. It is not known that pyrometamorphic rock exists. A detailed coal fire risk map for the scene of Baotou is presented in chapter 10.

Table 8-5: Reduction of the full scene areas to coal fire risk areas based on the automated extraction of coal, a delineation around this area and exclusion of densely vegetated areas within this zone for the Baotou region

Date	Overall pixels	Extracted coal pixels, [km ²]	Buffer region pixels, [km ²]	Veg. exclusion, pixels [km ²]	Area [km ²] remaining	% of scene
2002-08	61731741	10388 (9.34)	557669 (501.90)	189140 (170.22)	368529 (331.67)	0.59

8.3. Quantification and Error Analysis of the Test Sequence Results

8.3.1. Quantification and Error Analysis for the Main Study Areas

Figure 8-27 a to d illustrate the performance of the algorithm for coal extraction for three time steps for the Ruqigou and the Wuda area. The pixel numbers refer to the pixels remaining after test 1 until after test 6 and after the filtering of the result. The starting point (number of pixels of the original input data set) is not included in figure 8-27 a and b for better visualization. See figure 8-27 c to d for the performance of the full coal fire risk area demarcation scheme. The quantitative extraction results enable the investigation of the influence and importance of the different tests (filters) for spatial reduction.

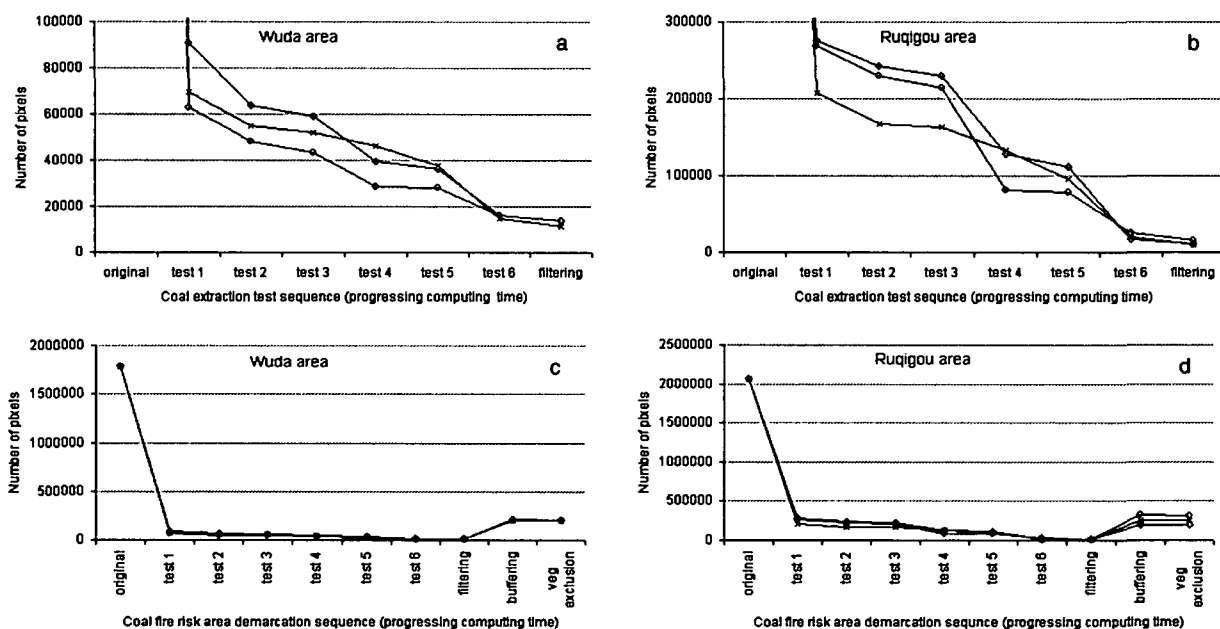


Figure 8-27: Areal reduction with progression of the knowledge based coal extraction test sequence (a, b) and for the overall test sequence (c, d) for the broader Wuda and Ruqigou area. Exemplarily visualized for three time steps 2000, 2001 and 2002-09.

In tables 8-6 and 8-7 the impacts of the different tests are presented on a quantitative basis via the number of pixels, which are left after each test. Furthermore, the percentage of the area excluded by each test compared to the result of the antecedent test is calculated. In both tables the last column represents the mean of this percentage over the three time steps investigated. As presented in table 8-6 for the Wuda study area test 1 already reduces the data for further testing to an average of 4.17% of the input data set size. As stated in subchapter 8.2. this test already enables the exclusion of all surfaces but coal, shadow, shadow margin and water. Therefore it has a significant influence. Tests 2, 3, 4 and 5 reduce the area of their previous test result between 18- and 25 % respectively. Test 6 leads to a clear reduction of the result of test 5 for about 52 %. Therefore, the SPM test 1 as well as the relative temperature test 6 can be considered two very stable and important tests for coal extraction in Wuda. The situation for Ruqigou is similar. An areal reduction of over 87 % after test 1, a more or less equal influence of test 2, 3 and 5 reducing the area for further 5- to 15 % and an areal reduction by test 4, reduces the spatial outcome of test 3 for even 42 %. As for Wuda, test 6 yields a very dominant

areal reduction exceeding 75% of the test 5 result. The majority filtering procedure after test 6 furthermore filters about 18% of the pixels for the Wuda area and eliminates over 40% of the pixels for the Ruqigou area. The reason for a stronger effect of the final filter in the Ruqigou region can be explained with the alpine terrain, including a larger spatial coverage with shadow- and shadow margin regions. More single scattered pixels remain after the six coal extraction tests. For both areas delineating an area around the extracted coal surfaces defines an area for further investigation. The resulting spatial increase is for Ruqigou larger than for Wuda. More single clusters are distributed in Ruqigou. Vegetation exclusion in the two semiarid to arid regions diminishes the final risk area for only 2-3%.

Table 8-6: Relevance of the single tests, filters and delineation for the areal reduction of the input data set for three exemplary time steps for the broader Wuda study area

	2000-10 Pixels	% of previous	2001-10 Pixels	% of previous	2002-09 Pixels	% of previous	Mean % previous
Original size	1783397		1783397		1783397		
After test 1	69320	3.89	90929	5.10	62737	3.52	4.17
After test 2	54812	79.07	63930	70.31	48161	76.77	75.38
After test 3	51679	94.28	59035	92.34	43433	90.18	92.27
After test 4	46113	89.23	39457	66.84	28769	66.24	74.10
After test 5	37554	81.44	36165	91.66	28228	98.12	90.41
After test 6	14962	39.84	16008	44.26	16318	57.81	47.30
After filtering	11464	76.62	13764	85.98	13784	84.47	82.36
After delineation	203208	1772.58	209463	1521.82	207871	1508.06	1600.82
After veg. exclusion	202565	99.68	207053	98.85	200939	96.67	98.40

Table 8-7: Relevance of the single tests, filters and buffers for the areal reduction of the input data set for three exemplary time steps for the broader Ruqigou study area

	2000-10 Pixels	% of previous	2001-10 Pixels	% of previous	2002-09 Pixels	% of previous	Mean % previous
Original size	2058820		2058820		2058820		
After test 1	207788	10.09	275779	13.40	268383	13.04	12.17
After test 2	167788	80.75	242706	88.01	230047	85.72	84.82
After test 3	163088	97.20	230709	95.06	214740	93.35	95.20
After test 4	132894	81.49	128726	55.80	80882	37.67	58.32
After test 5	95797	72.09	111833	86.88	78232	96.72	85.23
After test 6	20245	21.13	16794	15.02	25565	32.68	22.94
After filtering	9515	47.00	11662	69.44	16205	63.39	59.94
After delineation	259066	2722.71	196747	1687.08	326470	2014.63	2141.47
After veg. exclusion	255850	98.76	190978	97.07	308453	94.48	96.77

Tables 8-8 and 8-9 present the accuracy assessment for the extraction of coal and dense vegetation based on the equations presented in the theory of accuracy assessment illustrated in chapter 3. Tables 8-10 and 8-11 illustrate the accuracy of the demarcated coal fire risk area on the basis of the coal fire field mappings from the year 2002 for Wuda and for Ruqigou.

As seen in table 8-8 for the extraction results from 1987 and 1999 no ground truth is available. For 2000 a small map subset including the industrial coal storage piles within the mine was available. For 2002 and 2003 map data as well as ground truth mappings and for the latter high resolution Quickbird data was used.

Table 8-8: Accuracy of the extracted coal (filtered) and dense vegetation pixels for Wuda

Date	Prod. accuracy, coal	Prod. accuracy, dense vegetation
1987-09	not available	not available
1999-08	not available	not available
2000-10	93.21% (Wuda mine)	not available
2001-10	not available	not available
2002-09	92.10% (mapping)	95.04% (mapping)
2002-12	90.34% (mapping)	not available, winter
2003-02	92.79% (mapping)	not available, winter
2003-05	93.89% (Quickbird & mapping)	96.32% (Quickbird & mapping)

The mixture grids presented in chapter 4, which were mapped during the field work in 2002 could be used here for validation of the coal extracted for the scene of Wuda from September 2002. Within the three grids 15 50m cells were mapped exceeding 90% coal influence and can be regarded as pure coal. All but four of these cells are located within coal surfaces extracted for the scene from September.

In Ruqigou (table 8-9) for 1987 no ground truth was available. For 1999 digital data from a former Sino-Dutch project could be used for the producer accuracy calculation. For the year 2000 Ikonos data provided by ARSC (Aerophotogrammetry and Remote Sensing China, Xi' An) was available. For 2002 and 2003 field mappings and for the later year high resolution Quickbird data was available. Pyrometamorphic rock was mapped in the field in 2002 as well as on the basis of the Quickbird data from 2003 and was only extracted for these two years. It needs to be pointed out that no user's accuracy could be calculated. The producer's accuracy for the extraction of burned rock is 100% for 2002 and 2003 and 93.64% for 2000. Although this indicates that the area mapped in the field is extracted as a pyrometamorphic area by the algorithm, the probability that a pixel, extracted as pyrometamorphic rock really belongs to this class probably very low.

Table 8-9: Accuracy of the extracted coal (filtered), dense vegetation and burned rock pixels for Ruqigou

Date	Prod. accuracy, coal	Prod. accuracy, dense veg.	Prod. accuracy, pyro. rock
1987-09	not available	not available	not available
1999-08	95.98% (ITC project data)	not available	not available
2000-10	94.11% (Ikonos)	Not available	not available
2001-10	not available	not available	not available
2002-09	95.65% (mapping)	94.45% (mapping)	100% (mapping)
2002-12	94.24% (mapping)	not available, winter	not available
2003-02	93.45% (mapping)	not available, winter	not available
2003-05	95.96% (QB & mapping)	93.62% (QB & mapping)	100% (mapping)

Table 8-10 and figure 8-28 present how much of the coal fire polygons mapped for Wuda in 2000 is located within the automatically demarcated coal fire areas. Both field mappings were intersected with the risk areas derived from the 2002-09 data set. The same is presented in table 8-11 and figure 8-29.

Table 8-10: Percentage of fire polygons mapped in the Wuda area during the field campaign in 2002 included in the delineated area from the 2002-09 scene for a 500m and a 1000 m buffer.

Fire #	Demarcation 2002 (500 m)	Demarcation 2002 (1000m)
Fire # 1	99.87	99.87
Fire # 2	0.00	97.01
Fire # 3	12.92	71.04
Fire # 4	100.00	100.00
Fire # 5	0.00	96.61
Fire # 6	92.14	99.60
Fire # 7	44.50	99.60
Fire # 8	89.20	99.08
Fire # 9	100.00	100.00
Fire # 10	77.60	98.73
Fire # 11	97.89	99.29
Fire # 12	99.36	99.35
Fire # 13	100.00	100.00
Fire # 14	100.00	100.00
Fire # 15	0.00	100.00
Fire # 16	100.00	100.00
Fire # 17	0.00	60.02

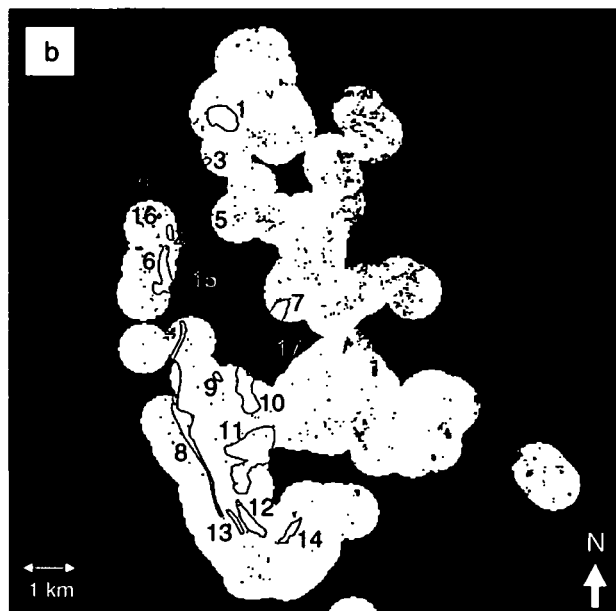
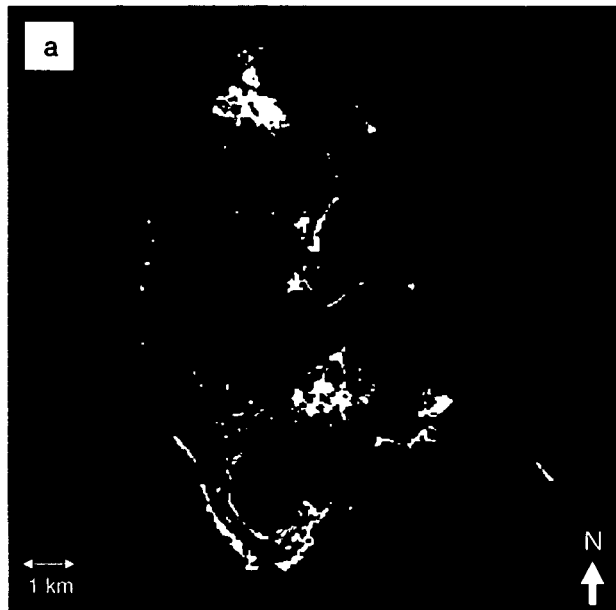


Figure 8-28: a: Extracted coal surfaces (white) and superimposed coal fire polygons. b: Extracted coal fire (risk) area (white) and mapped coal fire outlines for the year 2002-09 (red) for the broader area of Wuda. Center coordinate of the subset: 641952E, 4376514N, UTM, Z48N, WGS84. The Wuda coal fires are numbered from 1-17

It can clearly be seen that a delineation radius of 500 m around coal surfaces for the Wuda area is too small to cover all mapped coal fire polygons. Fires #2, #3, #5, #15 and #17 are not included in the coal fire risk area. Even though these fires are relatively “cold” and have negligible surface expressions, all underground coal fires should be included in the demarcated area. Applying a 1 km demarcation radius clearly improves the coverage of coal fires. Except for fire #3 and fire #17 all fires are covered sufficiently between 96.61% and 100%. Values slightly below 100% occur due to vegetation extraction and subtraction.

The weaker results from the 500 m delineation result from two causes. Firstly, coal fire polygons in the field do not really represent the underground situation. It is known that the fires were mapped rather too big than too small. Furthermore, it has already been mentioned that the coal extraction for Wuda (after filtering) tends to underestimate the coal covered surfaces. For Ruqigou the coal extraction result has slightly higher accuracies. Here a 500 m radius for the delineation of a risk area covers all coal fires sufficiently.

Table 8-11: Percentage of fire polygons mapped in the Ruqigou during the field campaign in 2002 included in the demarcated coal fire (risk) area from the September 2002 scene.

Fire #	Demarcation 2002 (500 m)
Fire # 21	96.90 %
Fire # 22	94.78 %
Fire # 23	91.66 %
Fire # 24	99.98 %
Fire # 25	90.52 %
Fire # 31	98.36 %
Fire # 22	100 %
Fire # 33	98.68 %
Fire # 34	97.18 %
Fire # 35	95.55 %
Fire # 36	96.07 %
Fire # 37	99.56 %
Fire # 38	99.40 %
Fire # 39	100 %
Fire # 40	98.05 %
Fire # 41	97.29 %
Fire # 42	100.00 %
Fire # 43	99.62 %
Fire # 44	99.18 %
Fire # 45	91.88 %

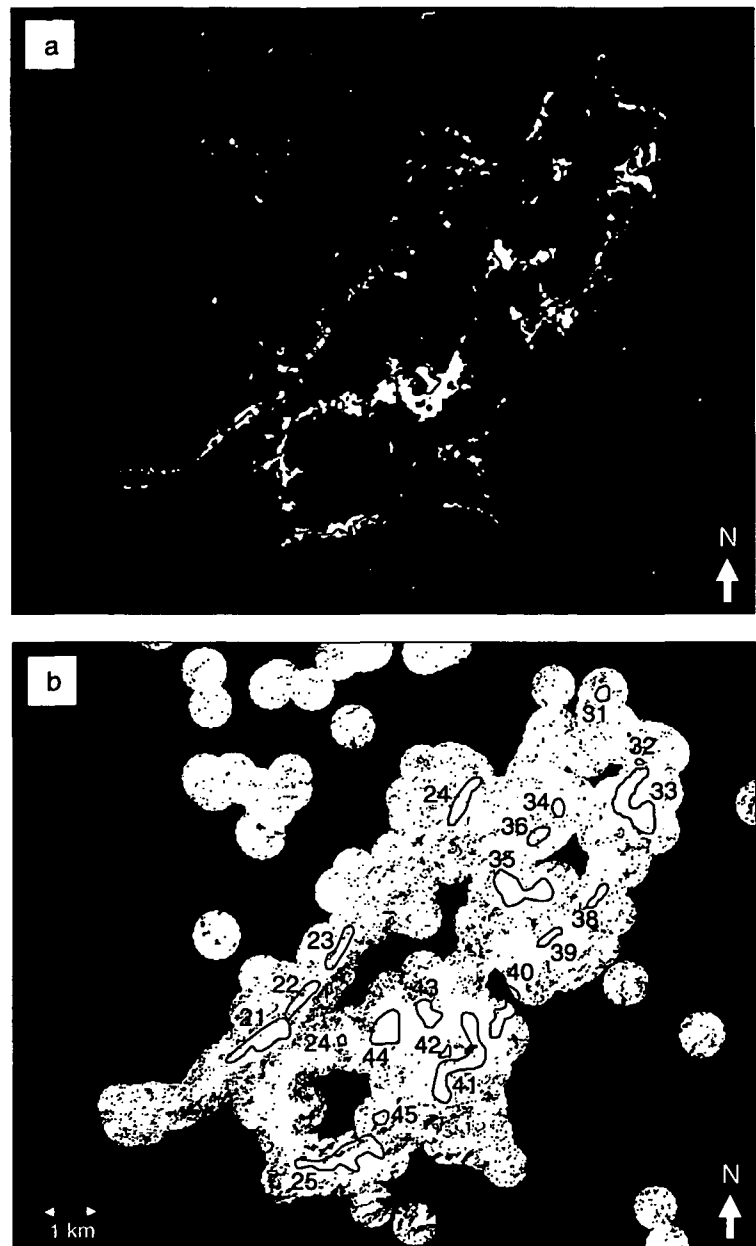


Figure 8-29: a: Extracted coal surfaces (white) and superimposed coal fire polygons. b: Extracted coal fire (risk) area (white) and mapped coal fire outlines for the year 2002 (red) for the broader area of Ruqigou. Center coordinate of the subset: 595800E, 4325705 N, UTM, Z48N, WGS 84. The Gulaben coal fires are numbered from 21-25, the Ruqigou coal fires are numbered from 31-45. All together the mapped coal fire area (red polygons) covers 6,11 km².

It is important to rather overestimate the delineation radius to grant the coverage of all possible coal fire risk areas than to choose the radius too small. An exclusion of thermal anomalies extracted with the thermal algorithm of ZHANG, J. (2004), which might actually be coal fire related thermal anomalies has to be avoided. This phenomenon is also addressed when combining the results of automated coal fire area demarcation with thermal analysis.

8.3.2. Quantification and Error Analyses of the Transfer Regions

Table 8-12 and figure 8-30 present the test sequence performance for Baotou, Australia and India. For Baotou tests 1 and 6 have a high impact as well as test 4 and 5, which filter for the spectral properties of coal in the NIR and exclude large areas covered by lakes or the Yellow River. Test 3 can exclude about 30% of the remaining pixels left after test 2, even though no DEM is available. These are shadowed pixels located within the mountain range stretching from West to East north of Baotou. Also vegetation exclusion plays a major role in the reduction of the delineated coal fire risk area. It averages 30%. For Australia the SPM and the temperature filter work very good for areal reduction. The same applies for test 4, which can exclude nearly 70% of the resulting pixels from test 3. Test 3 itself has nearly no impact, which was expected, since there are hardly any shadowed areas in the scene. For the scene in India the average percentage exclusion varies from the overall pattern recognizable for the scenes from the (semi-) arid regions. While the first test leads to a large reduction and the second is of similar influence as for the other scenes, test 3 can largely reduce the result of test 2. Here, all shadowed areas and a lot of very dark water surfaces, which may have 0% reflectance in one of the channels are reduced. Furthermore, some topographic (shadow) influences can be excluded.

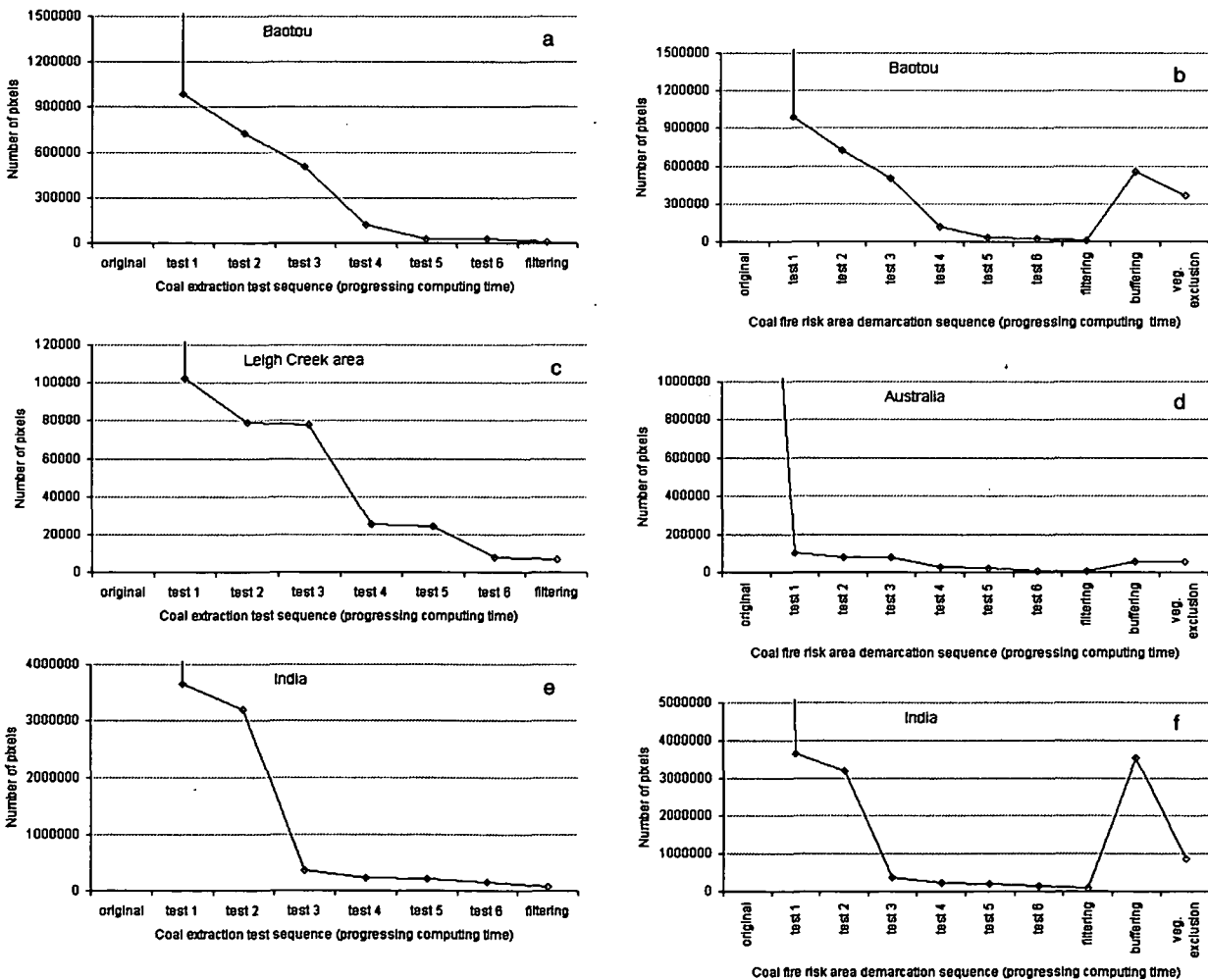


Figure 8-30: Areal reduction with progression of the knowledge based coal extraction test sequence (a, b, c) and for the overall test sequence (d, e, f) for three transfer areas, Baotou in northern China, Leigh Creek in Australia and Jharia in India.

8. Knowledge Based Surface Extraction

Test 6 only yields a reduction of 24% of the test 5 result. Temperatures of water, shadow and coal are within the upper range of the thermal histogram. The temperature based differentiation of the three in this tropical environment works not as well. Shadow and some water surfaces, which have identical temperatures to coal cannot be differentiated.

Very obvious is the strong areal reduction of the demarcated probable coal fire risk area based on the exclusion of dense vegetation. In the tropical environment densely vegetated areas or agricultural land reach close to the coal mining areas and basically the whole scene is strongly covered with vegetation.

Table 8-12: Relevance of the single tests, filters and delineation for the areal reduction of the input data set for three exemplary time steps for the three transfer areas

	Australia Pixels	% of previous	Baotou Pixels	% of previous	India Pixels	% of previous
Original size	3788996		61731741		58440921	
After test 1	102501	2.71	991319	1.61	3652999	6.25
After test 2	78803	76.88	722701	72.90	3197152	87.52
After test 3	78193	99.23	504798	69.85	369950	11.57
After test 4	25425	32.52	123039	24.37	224567	60.70
After test 5	24735	97.29	31456	25.57	206789	92.08
After test 6	7840	31.70	28616	90.97	155820	75.35
After filtering	6786	86.56	10388	36.30	77665	49.84
After delineation	55621	819.64	557669	5368.40	3532214	4548.01
After veg. exclusion	55457	99.71	368529	66.08	864752	24.48

Table 8-13 presents the overall mean of the single test results calculated from the average means of Wuda and Ruqigou as well as the mean of Baotou, Australia and India. Test 2, 3 and 5 demonstrate an equal influence around 20-25 % areal reduction compared to the antecedent test result, while test 4 and test 6 lead to a clear reduction around 50%. The final majority filter excludes 37 % of the leftover pixels. Delineation with a 500 m radius increases the remaining area for nearly the 50-fold. Following vegetation exclusion does not play an as important role, as presented in this table. The strong decrease of nearly 28% results from the influence of the overproportional influence of the scene from India.

Table 8-13: Relevance of the single tests, filters and delineation for the reduction of the input data. Averaged % reduction in comparison with the previous test sequence result calculated for all five areas

Sequential step	Mean % of previous for all input data sets
After test 1	5.38
After test 2	79.50
After test 3	73.62
After test 4	50.00
After test 5	78.11
After test 6	53.65
After filtering	63.00
After delineation	2895.67
After veg. exclusion	77.09

Tables 8-14 to 8-16 show the producer accuracy for the surfaces extracted in the transfer regions. Unlike for Wuda or Ruqigou ground truth had to be collected from publicly available data of former projects, the internet and data received via personal contacts. Quantitative statements on mapping methods or geometric precision of this ground truth data can not be made.

Table 8-14: Accuracy of the extracted coal (filtered) and dense vegetation pixels for Australia

Date	Prod. accuracy, coal	Prod. accuracy, dense vegetation
15.11.2002	98.03% (geol. & geomorph map)	not available

For the scene in Australia 98% of the area of the 4 polygons representing coal surfaces, which were available from the geologic and geomorphologic maps, were filled with coal pixels extracted. This is a very good result. Coal in Leigh Creek area is clearly distinguishable from the surrounding bedrock and due to the arid climate and industrialized mining methods land surface class borders are very distinct. However, it has to be mentioned that ground truth polygons for other land cover classes did not exist and no user accuracy could be calculated. The probability of a pixel extracted to be coal can therefore only be assessed on a visual basis. Since – next to the coal mining region – hardly any (except very few shade) pixels were extracted, the user's accuracy must also be very good. Vegetation extraction did not play a major role in the further areal decrease of the coal fire (risk) area region.

Table 8-15: Accuracy of the extracted coal (filtered) and dense vegetation pixels for India

Date	Prod. accuracy, coal	Prod. accuracy, dense vegetation
02.11.2001	87.51%	99%

For the scene from India 5 polygons derived from former maps and classifications processed for the Jharia area were available for coal and for agriculturally used fields respectively. The producer accuracy of coal is with 87% good. However, the extraction result is weaker than for the other scenes. Two possible reasons can explain this phenomenon. Firstly, for Australia real maps with ground truth were available. Even though the scene from Australia was not orthorectified, the location of geologic / geomorphologic units could easily be transferred to the satellite data, granting that no shift between ground truth and satellite data exists. Secondly, in India only projected ground truth polygons were available and the geometry had to be trusted. A slight mismatch between the polygons and the satellite data therefore might be possible. Furthermore, in India coal has a less distinct signal. The SD in the individual wavelength regions is very high and borders between pure coal and the surrounding areas are fluent.

Just as for Australia no producer accuracy could be calculated. However, opposite to Australia it is assumed that the user accuracy is much lower. A lot of pixels, which do not represent coal surfaces were extracted by the algorithm. These are mainly small clear lakes with a high water temperature and mixed pixels containing coal dust or similar material.

Table 8-16: Accuracy of the extracted coal (filtered) and dense vegetation pixels for Baotou

Date	Prod. accuracy, coal	Prod. accuracy, dense vegetation
29.08.2002	92.22%	96.64%

For the Baotou area the extraction accuracy for coal is 92%. A producer accuracy of 96% for the dense vegetation extraction based on SAVI thresholding analysis is reached. This is considered a very good result. Ground truthing was possible based on personal information. Users accuracy could not be assessed. However, only few shadow pixels were extracted as coal in the mountain range north of Baotou. Since no DEM for the area was available, an illumination correction could not be performed and a shadow file did not exist. If a DEM would exist the users accuracy – only assessable on a visual basis – would increase.

8.4. Discussion

Disadvantages of a knowledge based approach are the necessity of a very detailed empirical study of the spectral and thermal behavior of the surfaces of interest. These analyses are scientifically interesting and definitely help to understand the physical processes involved, as well as to point out the geophysical parameters of biggest impact. However, the thresholds defined will to some degree always be influenced by the decision of the analyst. This applies even if their span for specific classes is based on statistical parameters like mean and standard deviation in certain wavelength regions.

Furthermore, knowledge based approaches, as developed here, only allow the hard classification of pixels. Either the pixel is assigned to a class or not. A fuzzy classification is not implemented. This again leads to the discussion introduced in chapter 3, where object oriented fuzzy approaches are presented in 3.4 and the nature of materials occurring as mixtures is presented in 3.8. The knowledge based test sequence applied does not allow for the description of the sub-pixel constituents or the fraction proportions of the mixture. Time series of data – when fed into a knowledge based test sequence – have to be preprocessed extremely accurately to grant inter date comparability of one and the same spatial subset. This task can be very challenging – especially if spectrometer measurements of pseudo-invariant objects like deep clear water surfaces, bare bedrock or stable artificial surfaces like concrete or asphalt etc. are not present within a scene (HOSTERT 2001).

Clear advantages of the knowledge based method are the high extraction accuracy, which can be reached compared with ground truth data as presented in 8.3. as well as the adaptation of the method to local or regional surface characteristics. Compared to standard MLC classifications tested the knowledge based approach delivers results of higher accuracy. This observation is only based on one maximum likelihood classification result available for the area though. Nevertheless, the knowledge based sequence avoids error sources occurring in supervised maximum likelihood approaches where already the improper selection of a training area may have a negative impact on a result. The differentiation in only two classes (coal, no coal or similar) furthermore avoids confusion with a larger number of other classes. Once thresholds are defined decision trees or test sequences are easy to implement in common programming languages (e.g. IDL) based on queries, intersections and masking. Computing time is even for 10 band datasets (see figure 8-11) of over 50 Mio. pixels very fast. Furthermore, the output results are easy to interpret, since no gray scale outputs exist. Binary images are generated, either indicating areas which passed or did not pass a certain test within the test sequence.

In addition, the implementation of a knowledge based approach is very valuable for projects, where a certain area will be monitored over the course of many years. Once the thresholds are known and prove to be stable the algorithm can be applied to the scenes on a yearly basis. A certain surface can be

extracted without any further modifications necessary. The advantage is then that the results are reproducible by every image analyst starting the sequence. Provided that the thresholds are not modified, results will always be stable. They are also comparable on a temporal scale as presented in chapter 8.2., since all surfaces extracted in different years were extracted with exactly the same thresholds. Therefore, pixels of similar spectral and thermal behavior are extracted and compared. Further advantages of test sequence approaches are a very fast computing time, a realization option in most image processing environments and the easily apprehendable algorithm background.

Concerning the set up of the test sequence many alternative scenarios for the design could be thought of. For the cases presented here, slightly better results could be reached, when individual thresholds for each scene were tested. However, it was tried to develop a scheme applicable for a larger area and over several time steps. Therefore, the relevance of very good individual scene extraction accuracy was given a lower priority than the goal, to retrieve good results for a larger group of data sets. This is a common trade off between interactive very precise analysis and mass data throughput.

Coal extraction results and coal fire area demarcation for the scenes of Wuda and Ruqigou is for all scenes very good – except for the two winter scenes in Ruqigou. It is a clear consequence and unavoidable that snow cover will disturb the comparison of time series data. The weak extraction results in the Ruqigou winter scene in relation to the other scenes is not a weakness of the algorithm itself. This is indicated by good extraction accuracies, since the ground truth polygons mapped happened to be in areas not snow covered. Also the scene of September 2002 yielded good results, though this scene was considered to be an outlier after signature analysis. It is assumed that the high SDs of the surfaces for this scene resulted from improper selection of pure areas for signature analysis. Therefore, the elevated SDs were only seemingly elevated and did not influence the extraction result in a negative way. Since the result for the September 2002 scene was very good, signature analysis for this scene was not repeated. The fact that coal extraction accuracies for Ruqigou (except the mentioned winter scenes) are slightly higher than for Wuda results from the slight underestimation of coal for the Wuda region. Extraction accuracies for Wuda range between 90.34% and 96.32% and for Ruqigou producer's accuracies range between 93.45% and 95.98%. This result of coal extraction is considered very good.

Coal extraction accuracies for the transfer regions are also very good. The same applies for the SAVI thresholded areas of dense vegetation mapped in densely vegetated areas. One exception is the coal extraction for the Indian transfer region, which “only” reaches 87% (this can actually still be considered a good result). This stems from two influences. Firstly, the geometry of the coal polygons used for ground truthing available was not created by the author and a sufficient registration between the polygons and the satellite data had to be trusted. Furthermore, the coal surfaces in India have a much higher SD than the coal surfaces in the semiarid regions. Here, exposed coal experiences the influence of a humid subtropical atmosphere, monsoonal rains and resulting extensive chemical weathering and vegetation growth. The consequences of this phenomenon can be noted in figure 8-25, where coal surfaces occur substantially lighter in color than for the other regions. Boundaries to surrounding rock, soil and vegetation appear smeared and fuzzy. It was tried to adapt the algorithm to yield better results for India (different processing scenarios with adaptations of the temperature test and tests regarding the reflectance behavior of coal) without lowering extraction results for the semi-arid to arid regions. This could not be achieved.

Additionally the vegetation exclusion approach applied for this densely vegetated region diminishes almost the whole delineated area created after coal extraction. For tropical or densely vegetated environments vegetation exclusion is of higher relevance, than for sparsely vegetated arid and semi-arid regions. Though no field work in the study area was undertaken personally, communications with A. PRAKASH (2004-08) revealed that the coalfield is primarily covered and surrounded by shrubby vegetation. Most of the few trees in the Jharia coalfield are not natural forests but are replanted by the mining authorities. Thus it is very unlikely to find subsurface coal fires under dense vegetation in this area.

The areas from the ETM+ scenes of Australia and Baotou are – like the main study areas - set in a semiarid to arid environment. Therefore, geologic surfaces can be identified very clearly. Physical weathering outweighs chemical weathering and the morphosis of surfaces due to the influence of water (weathering, plant growth, moss, coatings etc.) is less accentuated than in India. Thus, the spectral properties of coal in Australia and Baotou are better comparable to the ones investigated in the main study areas.

The good temporal and spatial transferability of the algorithm could be proven on a number of scenes. Not only did the test sequence yield good results for very different seasons and years within the study areas. The extraction for three regions not related to the study areas yielded good results as well. This applied even though the three transfer scenes were radiometrically not adjusted to the study area data sets. The transfer to regions outside of China and in different climatic regimes gives reason to the assumption that the test sequence will be able to extract coal and coal fire risk areas for large regions.

Concerning coal fire area demarcation and support of the thermal algorithm the knowledge based algorithm can clearly reduce the area, which has to be taken into account when investigating thermal anomalies. For the broader Wuda region, the area to be investigated could be reduced to an average of down to 10.6 % of the input data size over all eight time steps. For Ruqigou an areal reduction down to 12.1 % on average over all eight time steps could be achieved. Including the full Landsat scene 129 / 33 only 1.5 % of the scene is remaining as a probable coal fire risk area.

In the transfer regions, for the broader area of Leigh Creek the remaining coal fire risk area sums to 1.4% of the original data input. For the Indian- and the Baotou region 1.48 % and 0.59 % of the original input data size remain respectively.

Hence, the developed knowledge based test sequence for coal fire area demarcation can minimize the area for thermal investigation substantially and eliminate all false alarm thermal anomalies located outside the demarcated coal fire (risk) areas.

Furthermore, the test sequence was transferred to run on Aster satellite data as well. Only few tests had to be slightly modified to automatically extract the three surfaces of interest (see 8.1.4.). Two Aster scenes presented in chapter 4 were processed and the test sequence was applied to both scenes. Although Aster has more spectral bands than ETM+ it could not be found that the sensor has advantages for the extraction of coal or dense vegetation. Extraction accuracies varied between 91.59% and 93.21% and 93.01% to 96.88% for both classes respectively. However, pyrometamorphic rocks could be extracted with 100% producers accuracy (as for ETM+) but less additional pixels resulted from the test sequence. The users accuracy is thus higher than for ETM+ data.

9. Quantitative Surface Extraction applying Partial Unmixing

9.1. Method

9.1.1. Concept and Mathematical Background

To implement an algorithm realizing feature extraction in a non-knowledge based approach a second method to automatically derive coal-, vegetation- and pyrometamorph surfaces from image data is applied. This approach employs the spectra collected during the field campaigns and from laboratory measurements. It is based on the fundamentals of Spectral Mixture Analysis (SMA) presented in chapter 3.8. Unmixing applications and neighboring applications offer the great advantage of quantitatively mapping a material within a pixel. They account for the fact that most materials in the real world are mixed and that only few regions exist, where 100% spectrally pure pixels can be found.

The method applied here is a so called partial unmixing approach (partial mixture analysis, PMA), since the unmixing equation will only be solved partially. This is an especially useful approach when the research focus is not to solve a complex mixture model but to assess, if a target signature is present in a scene or how much of the target material is present in a pixel. Therefore, the scene can be described by the target endmember and a composite endmember of all other scene materials. This basically reduces the problem to a two component mixing algorithm (BOARDMAN et al. 1993, KRUSE et al. 2000). Unlike in SMA only the abundances of one known endmember against an unknown background are calculated. This is based on the principle that the signal of the desired spectrum (being available as a library spectrum) is maximized, while the variance of the background image spectra is suppressed. This technique known from radio signal processing is also referred to as matched filtering.

Several methods exist to enhance a requested target signature against a suppressed background or to estimate the fractional contribution of a given pixel to the reflectance spectrum of this pixel. Correlation analysis can be employed to enhance a requested target signature. Furthermore, DRAKE et al. (1999) employ a distance function, which subtracts the to 1 normalized sum of the distances of the endmember signal from the pixel signal over all bands. Also orthogonal subspace projection or constrained energy minimization have been applied for this purpose.

In a geometric sense partial unmixing finds a projection of the n-dimensional spectral space which stretches the full range of the requested target spectrum but hides the variability of the background. Since the spectra, which span the background, are unknown in most cases, the algorithm uses statistical methods to derive the composite background spectrum from the image data itself. Thus for

$$A \cdot X = R \quad \text{and} \quad X = A^{-1} \cdot R \quad (9.1)$$

Known from chapter 3, where:

A: $m \times n$ -matrix of spectral endmembers (spectral library) in n spectral bands

X: vector of unknown abundances of the endmembers

R: measured reflection of the image pixel

$m \times n$ -matrix A is composed of the requested material spectrum (coal) and the background spectrum of the image.

The algorithm compares the prototype spectra supplied for the matrix calculations with the unknown pixel spectrum and maximizes the desired material within the unknown spectrum. The result of partial unmixing applying a single prototype spectrum is a gray scale image representing the relative degree of match of the image spectrum to the reference spectrum, where 1.0 is a perfect match (=100%). Linear mixing required the fraction images thus can also be regarded as images, representing the contribution of the input material to the overall spectral signal of the pixel in percent.

Figure 9-1 shows the result of partial unmixing to the supplied material (represented by a given pattern spectrum) coal. Very bright areas indicate high matches, while dark pixels contain hardly any or no coal. Every pixel above a certain threshold can now be defined as a pure coal pixel, which is used as a kernel for areal delineation. It can be seen that all areas within the subset for the broader Wuda area, which contain coal are represented by very bright DN's. Areas like the desert in the Northwest or the northern foot hills of the Helan Shan, where no coal occurs, are represented by very dark pixel values. However, also some areas with intermediate grey level pixel values indicate the contribution of coal to the pixel signal, even though no coal is present in this area. This phenomenon occurs due to the maximization of the desired surface spectrum within the unknown pixel spectrum leading to an overestimation of the target surface within all pixels. This phenomenon and methods to account for this overestimation are discussed in 9.3.. Furthermore, next to coal surfaces also shadowed regions show high fraction values, though no coal is present within the pixels. This spectral mimicking of shadow and coal in non-transformed data can only be solved by a masking of shadowed areas, applied to the partial unmixing result.

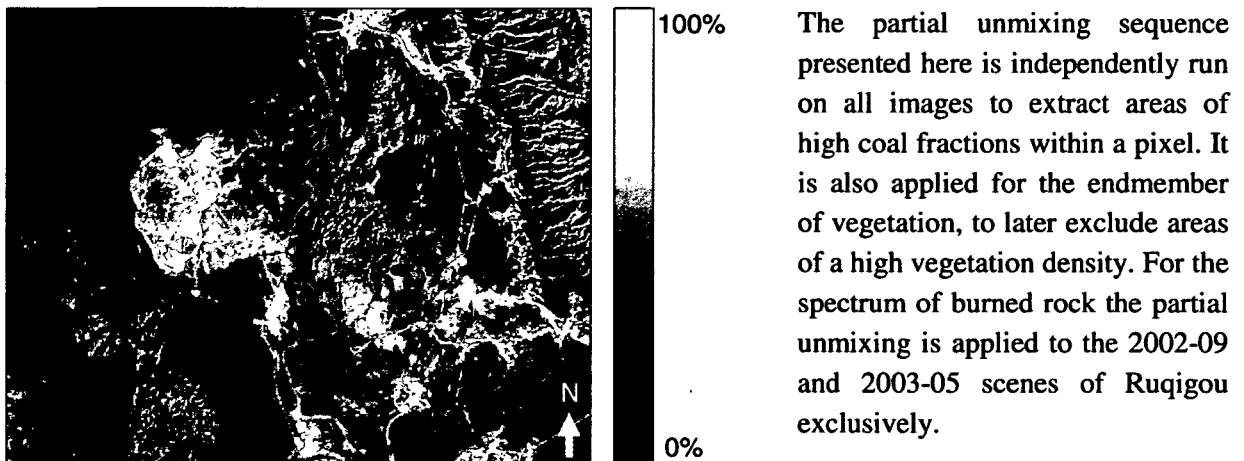


Figure 9-1: Results of partial unmixing to coal for the broader Wuda area, image from 1999. Bright pixel values indicate a high sub-pixel coal fraction, dark areas have lower sub-pixel fractions. Center coordinate: 650705E, 4373287N, UTM, Z48 N, 43km×36km

PMA is often applied to MNF transformed and inverted data. MNF transformation has been introduced in chapter 3.1. MNF transformation not only orders the data according to the noise content of the transformed components, but also allows for the better differentiation of classes. As for PCA, MNF leads to a better representation of the data space. For the Landsat scenes presented here, MNF transformed images allow for a better differentiation of e.g. coal and shadow. The problem is that a PMA analysis on MNF transformed data has to be performed with MNF transformed spectra also. The transformation parameters applied to the individual scene have to be applied to the spectra to grant the comparability of synthetic pixel spectra with the defined reference spectra. This means that an

individual set of MNF transformed prototype spectra would have to be generated for each individual scene. Original input prototype spectra could not be transferred from scene to scene as it is the case for non-transformed data. This clearly limits the suitability of MNF transformed data for automation.

9.1.2. Design of Prototype Spectra and Spectral Interpolation

A representative spectral library, generated from the field- and the laboratory spectra presented in chapter 4 was generated as an input library for the partial unmixing process. So called “prototype spectra” were artificially generated (see figure 9-2). They are representative for coal, vegetation and burned rock. Therefore, all mean coal-, vegetation- and pyrometamorph spectra of the different samples were used to calculate an overall mean. These spectra were visually compared to typical image spectra of homogeneous regions in the input data sets. The plausibility of these spectra was furthermore quantitatively tested based on SAM analysis presented in 3.9 and 9.1.3..

The prototype spectra were interpolated to the bandwidths of Landsat-5 TM, Landsat-7 ETM+, and Aster. Depending on the input image type the equivalent spectra are used for partial unmixing. Advantage of this interpolation is an improvement of the signal to noise ratio due to the averaging of the higher resolution spectrum to broader bandwidths. Spectral simulation is possible, when the source sensor has a spatial and spectral resolution finer than the target simulated sensor (as applicable in the case of the GER). Simulation of a spectrum includes estimating the Gaussian spectral response function (SRF) of each channel using the band center and width (full-width-half-maximum, FWHM) with:

$$R_i(\lambda) = \frac{1}{\sigma\sqrt{2\pi}} e^{-0.5(\lambda-\mu)^2/\sigma^2} \quad (9.2)$$

where μ is the band center, σ is the standard deviation (equivalent to the FWHM) of the channel and λ is the wavelength relative to μ and $R_i(\lambda)$ the spectral response. The integral over the SRF is 1.

The channels of the higher resolution imaging spectrometer GER, which are within the wavelength range of the selected ETM+ or Aster channels are integrated by dividing them into the derived SRF. It is assumed that the initial SRF of the input data channels are a single bright source (continuous input spectrum) using:

$$\rho_{res}(\lambda_i) = \frac{\int_{\lambda_1}^{\lambda_2} \rho(\lambda) R_i(\lambda) d\lambda}{\int_{\lambda_1}^{\lambda_2} R_i(\lambda) d\lambda} \quad (9.3)$$

where $\rho_{res}(\lambda_i)$ is the resampled spectrum using the continuous spectrum $\rho(\lambda)$ and the SRF $R_i(\lambda)$ (VAN DER MEER & DE JONG 2001). The convolution is achieved integrating between the lower (λ_1) and upper (λ_2) wavelength limit of the designated image channel. Since the spectral resolution of the image data to be simulated is lower than that of the image data, band matching has to be applied. Here the bands, which position in terms of wavelength of the band center is closest to the channel to be simulated, are used for the simulation (VAN DER MEER & DE JONG 2001, ABRAMS & HOOK, 1995). Opposite to the coal spectrum, for the vegetation spectrum it was not of utmost importance to be of high representativity for a certain type of plant or plant architecture. The goal of vegetation extraction

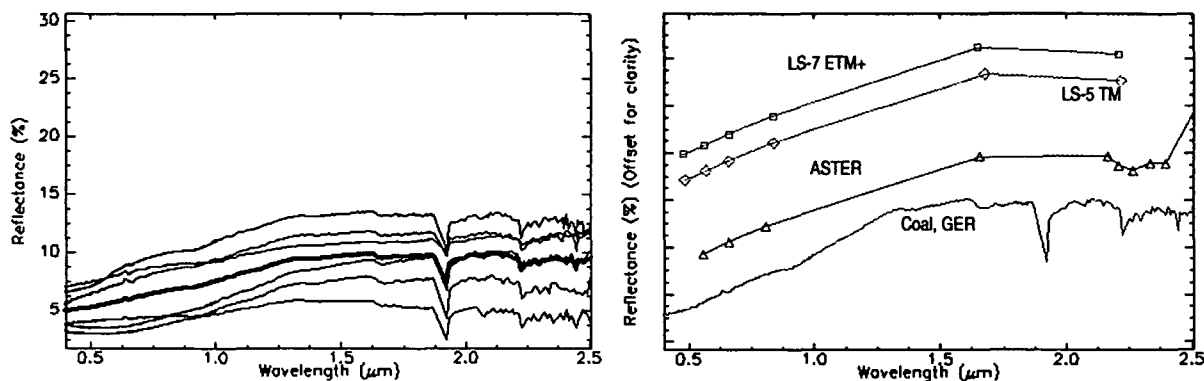


Figure 9-2: left: prototype spectrum of coal derived by creating a mean of all averaged input spectra measurements. The black spectra represent the mean spectra of 8 coal samples. Each was measured 20 times. Right: overall mean spectrum of coal interpolated to the SRF of Aster (blue), Landsat-5 TM (turquoise) and Landsat-7 ETM+ (violet); the resampled spectra are stacked with offset for better visualization.

is simply to exclude areas of high vegetation density and the vegetation spectrum shall support the detection of highly vegetated areas (dense agricultural areas or areas of very dense desert vegetation). Therefore, it is assumed that a pure spectrum of the desert shrub *Artemisia* (exclusively leaves, 8 layers, no soil reflection) will also support the extraction of all other vegetation types. Already KEMPER (2003) states that most land cover studies have to consider the spectral reflectance of vegetation, even if this is not the focus of the study, since vegetation is omnipresent on the land surface. A rough prototype spectrum is sufficient for the approach pursued here. Even though the overall reflectance level of vegetation may vary the shape of reflectance curves for green leaves is similar for most species.

The spectra of pyrometamorphic rocks vary strongly as presented in the signature analysis chapter 7. Therefore, next to an overall mean prototype spectra the average sample spectra of the different types of pyrometamorphic rock were also available as an input to the partial unmixing.

9.1.3. Analysis of Extreme Pixels

In this subchapter an endmember modeling is presented, supporting the selection of the endmember “coal” not only as an input to partial unmixing, but also as a candidate for a high quality spectral mixture model. Two major types of endmembers (EM) exist. Firstly, EM can be “derived” EM, extracted from the images itself (the purest pixels). This has the advantage that all EMs reflect under similar atmospheric conditions. However, such EM are hardly transferable. Secondly, “known” EM stem from spectral libraries or own ground- and laboratory spectral measurements. EM fed into SMA need to fulfill the conditions of physical and statistical purity. This is only given for materials, which characterize the limiting vectors of feature space and ideally explain all other spectral signatures enclosed by such a polyhedron (HOSTERT 2001). The objective pre-selection of EM into a mixing model – afterwards controlled by the analyst – is an approach, which tries to minimize possible errors during the set up of the model. Also for partial unmixing it is of advantage when materials or surfaces requested to extract are located at extreme positions in the n-D feature space. Even if the actual EM requested and available as a spectrum (reference EM) is already known, it can be tested, if the material (e.g. coal) belongs to a cluster in an extreme position defining one axis of the thematic mixture space.

The data was therefore analyzed for the best spectral EM inherent in the image data. Therefore, principal component analysis (BATESON & CURTISS 1996), neural networks (GARCÍA-HARO et al. 1999) or the pixel purity index (PPI) are often used methods (KRUSE et al. 2000, HOSTERT 2001). The PPI is a means of finding the most spectrally pure or extreme pixels in multi- or hyperspectral imagery and can be applied on original calibrated data or on MNF transformed data. It is computed by repeatedly projecting n-dimensional scatter plots (the data cluster) onto a random unit vector. The extreme pixels of each projection are recorded and the total number of times each pixel is marked as extreme is noted. After a larger number of iterations (commonly several thousands) a PPI image is created. In this image the DN of each pixel corresponds to the number of times the pixel was recorded as extreme (VAN DER MEER 1999a, KRUSE et al. 2000). Figure 9-3 shows the result of a PPI calculation for the scene 129/33 from 17.10.2000 performed with 10,000 iterations. This grants a high representativity of the extracted pixels.

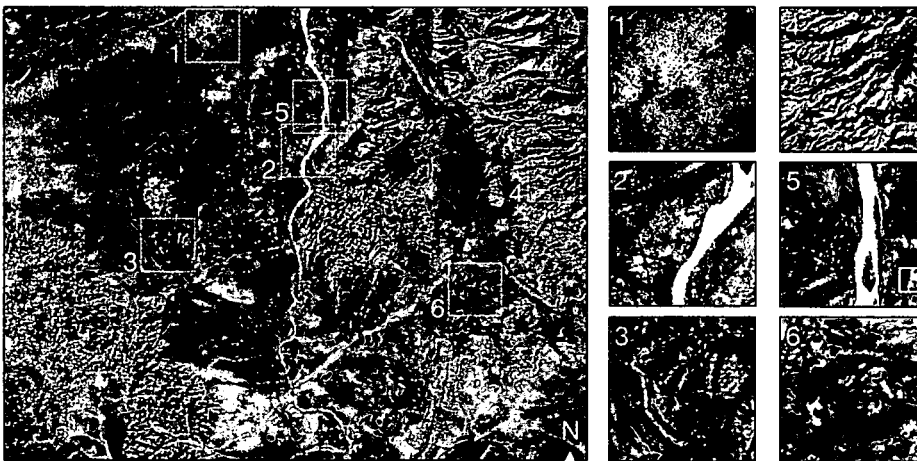


Figure 9-3: Results of a PPI calculation (10k iterations) superimposed on band one (blue) of ETM+ 129/33 from 17.10.2000. Center coordinate of left subset: 650705E, 4373287N, UTM, Z48 N, 43km×36km

According to this result (purest pixels) the ideal endmembers for a complete unmixing would be pure coal, pure uncovered desert sand, dense agricultural vegetation, Yellow River water and shadow. The PPI also leads to the extraction of EMs, which are spectrally extreme, but are not relevant for the composition of the scene or the phenomena under investigation. One example is the storage pile of the calcite factories east of the Yellow River (white box in subset 5) – a very bright and extreme surface, which only occurs close to very few factories. These surfaces would not be included in a mixture model. Furthermore, the water of the Yellow River is not assumed to really be an extreme EM, since it consists of a mixture of several pure components (water, sediment, algae etc.). The results of PPI therefore need to be interpreted by an analyst applying n-D visualization (HOSTERT 2001). However, here the PPI was calculated to compare image derived pure spectra with the input reference spectra (coal and vegetation) for partial unmixing. The similarity of image spectra resulting from PPI analysis and reference spectra of the same locations was calculated via a spectral angle mapping approach as presented in chapter 3.9. Interpolated laboratory spectra of coal and desert sand yielded spectral angles close to zero when compared with the pixel spectra of the marked extreme pixels. Resampled field vegetation spectra differed slightly stronger, when compared with dense agricultural vegetation pixels. This can be neglected in the present case. Also for Ruqigou a 10,000 iteration PPI image was calculated, indicating the surfaces coal / shadow, dense vegetation, calcite piles resulting from limestone burning (not really an EM), some water covered irrigated surfaces and alluvial fans, which show a crusting, as EMs.

9.2. Results of the Partial Unmixing Analyses

9.2.1. Results for the Main Study Areas

9.2.1.1. Wuda

Figure 9-4 shows the partial unmixing results for the broader Wuda area for all 8 Landsat scenes. The extraction results for 1987 and 2003 vary in that respect that here the Yellow River also yields very high fraction percentages. Next to coal, in all scenes shadowed areas are also extracted with very high percentages. With partial unmixing alone, applied to untransformed data, it is impossible to separate these two. Here a post-processing (e.g. test 6 of the knowledge based test sequence for coal extraction) or a masking of shaded terrain can help to exclude these areas.

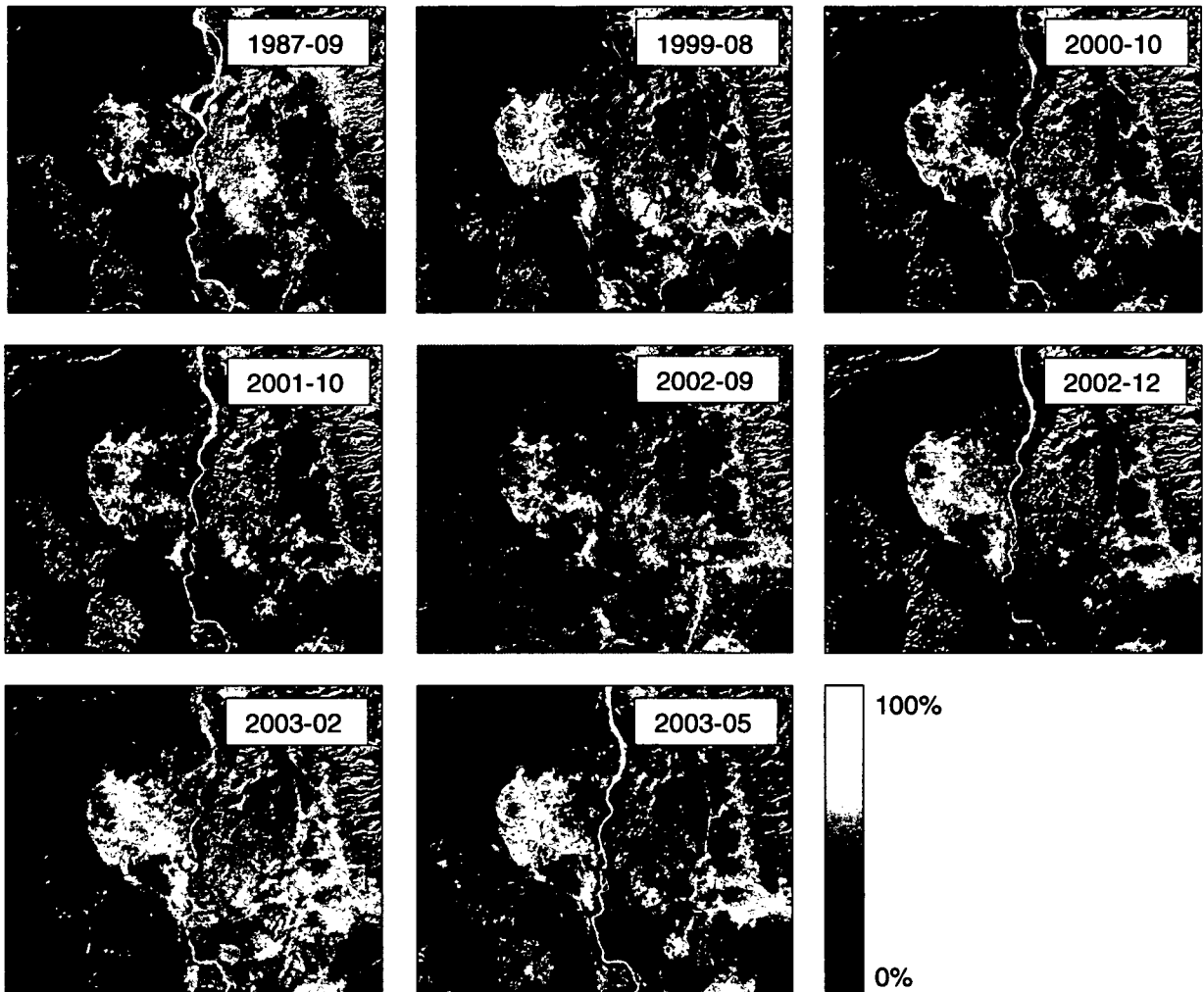


Figure 9-4: Partial unmixing results for the broader Wuda area for all 8 scenes. Light areas indicate a high spatial fraction of the input prototype spectrum (coal), while dark areas represent pixels with a smaller fraction of this surface. Mimicking surfaces include shaded areas and partially water. Center coordinate: 650705E, 4373287N, UTM, Z48 N, 43km×36km

It furthermore strikes that the light area does not necessarily increase steadily over time, as coal does for the broader Wuda study area. This results from the high amount of shadow mapped also as well as from differences in scene calibration. Even though the scenes were synchronized as exact as possible, variations still occur. This has been presented in chapter 7. Unmixing approaches are much more sensitive to such variations than the knowledge based test sequences. The latter operates with broader threshold ranges than a spectral matching approach and includes arithmetic functions, inequalities and a combination of rules for the extraction.

For all scenes processed a cut off percentage of 85% yields best results in defining areas considered as pure coal. This threshold was found based on numerous empirical tests. When thresholding the images at an 85% subpixel fraction, not only coal is extracted but also shadow and water. Even after thresholding, scenes of different acquisition dates can hardly be compared. Figure 9-6 illustrates this inter scene variability as well as sun angle induced variations in shadow sizes. The diagram presents the percentage of the scene area, which would be considered as coal, if the image was thresholded at a certain threshold. E.g. if the partial unmixing result of December 2002 is thresholded at the 90% fraction (where all pixels including more than 90% of the fraction “coal” would be considered) these pixels would add up to 5.79 % of the scene area.

If only the surface coal would influence this area, it would be expected that the curves of the different years increase in their offset. Furthermore, with progressing time the area extracted at a certain fraction threshold should increase over time. Due to the above mentioned reasons this is not the case. Especially when investigating the winter scenes the shadow effect is obvious. Although the two winter scenes both have a lower overall area covered with coal compared to summer or fall scenes (see chapter 8), the two should have similar areas covered by coal. The knowledge based test sequence even indicated a slight increase from December to February. As visible in figure 9-5 the scene of February 2003 (pink) yields – especially within the lower fraction thresholds – lower results, than the scene from December. This phenomenon occurs due to larger shadowed areas in December.

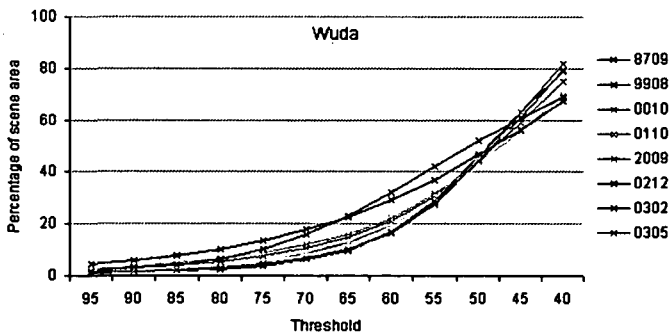


Figure 9-5: Subpixel fraction of the input prototype surface (coal) plotted against the percentage of the scene area, which would remain, if the partial unmixing result is thresholded for the pixels containing equal or above the percentage subpixel fraction. All eight time steps were calculated and displayed.

However, if the development between two scenes, acquired under completely similar illumination conditions is compared, the phenomenon of increasing coal surfaces over time can be demonstrated. Figure 9-6 presents the area in percent of the scene if the scene is thresholded at varying fraction thresholds for the scene from 20.09.1987 and 21.09.2002. If all pixels exceeding a partial unmixing result of 85 % fraction of the input surface (coal) were thresholded, the “coal” covered area in the broader Wuda study area would occupy 1.76 % of the scene in 1987 and 4.58 % in 2002. This indicates an increase for 260 % from 1987 to 2002. This result coincides well with the result from the knowledge based test sequence, where from September 1987 to September 2002 an areal increase for about 300% is calculated (compare table 8-1, chapter 8).

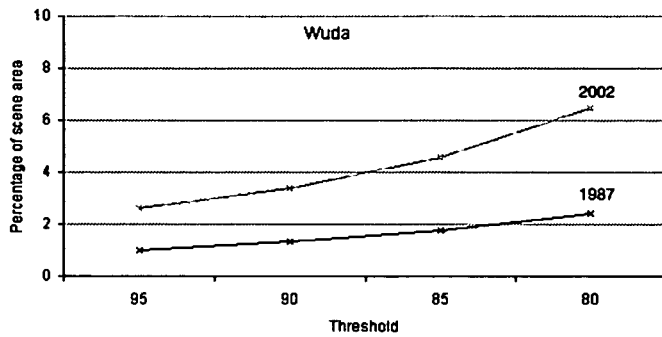


Figure 9-6: Subpixel fraction of the input prototype surface (coal) plotted against the percentage of the scene area, which would remain, if the partial unmixing result is thresholded for the pixels containing equal or above the percentage subpixel fraction. Presented for Wuda, 20.09.1987 and 21.09.2002 (River not included).

Absolute numbers can not be compared, since it has already been stated that the knowledge based test sequence tends to underestimate the coal area in Wuda. With the partial unmixing approach coal is overestimated, due to the phenomenon of “false positives”, explained in 9.3. Exclusion of shadowed areas from the thresholded images is possible with a post filtering based on the rules developed for the knowledge based test sequence. Already the application of the temperature test included in the coal extraction sequence yields good results. Additional majority filtering can furthermore smoothen the result, before a radius for the demarcation of coal fire risk areas is defined.

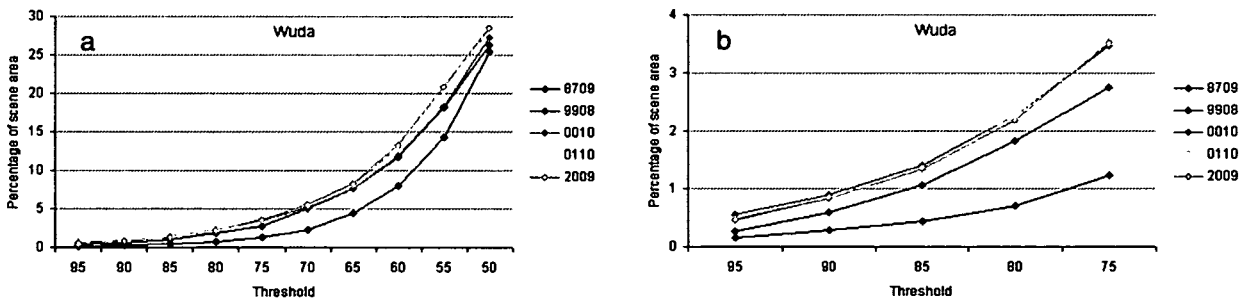


Figure 9-7: Subpixel fraction of the input pattern surface (coal) plotted against the percentage of the scene area, which would remain, if the partial unmixing result is thresholded for the pixels containing equal or above the percentage subpixel fraction. Here only flat regions were included in the calculation to exclude shadow effects induced by differing sun angles, (a).(b) presents a zoom into (a) for better clarity.

For figure 9-7 all shadowed areas in the Wuda study area were excluded based on an interactive masking of these areas. A clear increase from 1987 to 1999 can be noted. From 1999 to the following years the coal area increases further. This supports the results presented in chapter 8. However, no clear trend can be formulated for the years 2000 to 2002. The scene of 2003 even had to be excluded from the calculation, since PMA thresholding lead – next to coal – to the extraction of major parts of the Yellow River (see figure 9-4), thus tampering the time series.

Figure 9-8- shows the results of the vegetation fraction computation for the broader area of Wuda for the years 1987-09 and 2002-09. The densely vegetated agricultural areas along the Yellow River show very bright values, indicating a high subpixel vegetation fraction. In the southeastern quarter of the image some bright patches can be noted, which are smaller agricultural plantations adjacent to small villages and industrial areas. Low subpixel vegetation density occurs in the Badain Jaran desert in the northwestern quarter of the image. Coal surfaces also show a low vegetation density. In the remaining

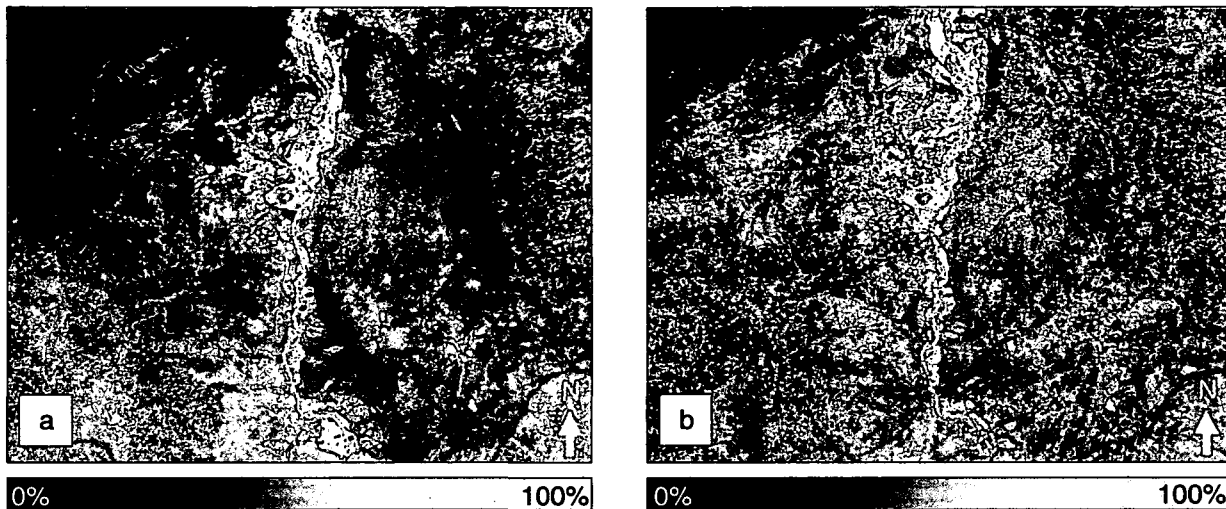


Figure 9-8: Partial unmixing results for vegetation for the broader Wuda area for 1987-09 (a) and 2002-09 (b). Light areas indicate a high spatial fraction of the input prototype spectrum (pure *Artemisia* leaves), while dark areas represent pixels with a smaller fraction of vegetation. Center coordinate: 650705E, 4373287N, UTM, Z48 N, 43km×36km.

area vegetation cover varies depending on geologic substrate, water accessibility, slope and aspect. Just like for SAVI results presented in chapter 8, the PMA result of subpixel vegetation fraction estimation can be thresholded to exclude densely vegetated areas from probable coal fire (risk) areas, which are delineated through coal extraction and delineation.

The thresholding and intersection method is simple and has already been presented in chapter 8. Therefore intermediate results are not shown here. Detailed maps with demarcated coal fire areas are presented in chapter 10. The extraction of pyrometamorphic rock was not pursued for the Wuda area.

The quality assessment of the partial unmixing result can not only be assessed based on ground truth and mapped mixture grids. Also the result of a linear spectral unmixing can be used, to indirectly validate the partial unmixing result for a certain surface. Therefore, next to the partial unmixing, a linear mixing model was set up for the broader Wuda study area. SMA has been applied employing the four selected endmembers coal, pure desert sand, sandstone (arcotic) and vegetation. Linear spectral unmixing results are presented in figure 9-9. Fraction images coincide very well with the ground knowledge available for the area. Figure 9-9a (coal) clearly presents the coal covered areas within the syncline as well as coal covered roads and coal storage- and waste piles as brightest pixels. In figure 9-9b (pure desert sand) the pixels in the area of the Badain Jaran desert in the Northwest are extracted with very high subpixel fractions. Only the lakes located within the desert appear as dark spots. It is unclear why pure desert sand is partly confused with vegetation. In figure 9-9c (sandstone) the sandstone plateau within the Wuda syncline is clearly extracted. Furthermore sandstone ridges in the southwestern corner (northern foot hills of the Helan Shan) can clearly be noted. As for coal, the visual impression of extraction accuracy for this surface is very convincing. Figure 9-9 d shows the fraction image for vegetation. Agricultural fields west of the mining town Wuda are represented by very bright values. Overall, the linear unmixing result is very satisfying. Its use for quantification and error assessment will be presented in subchapter 9.3..

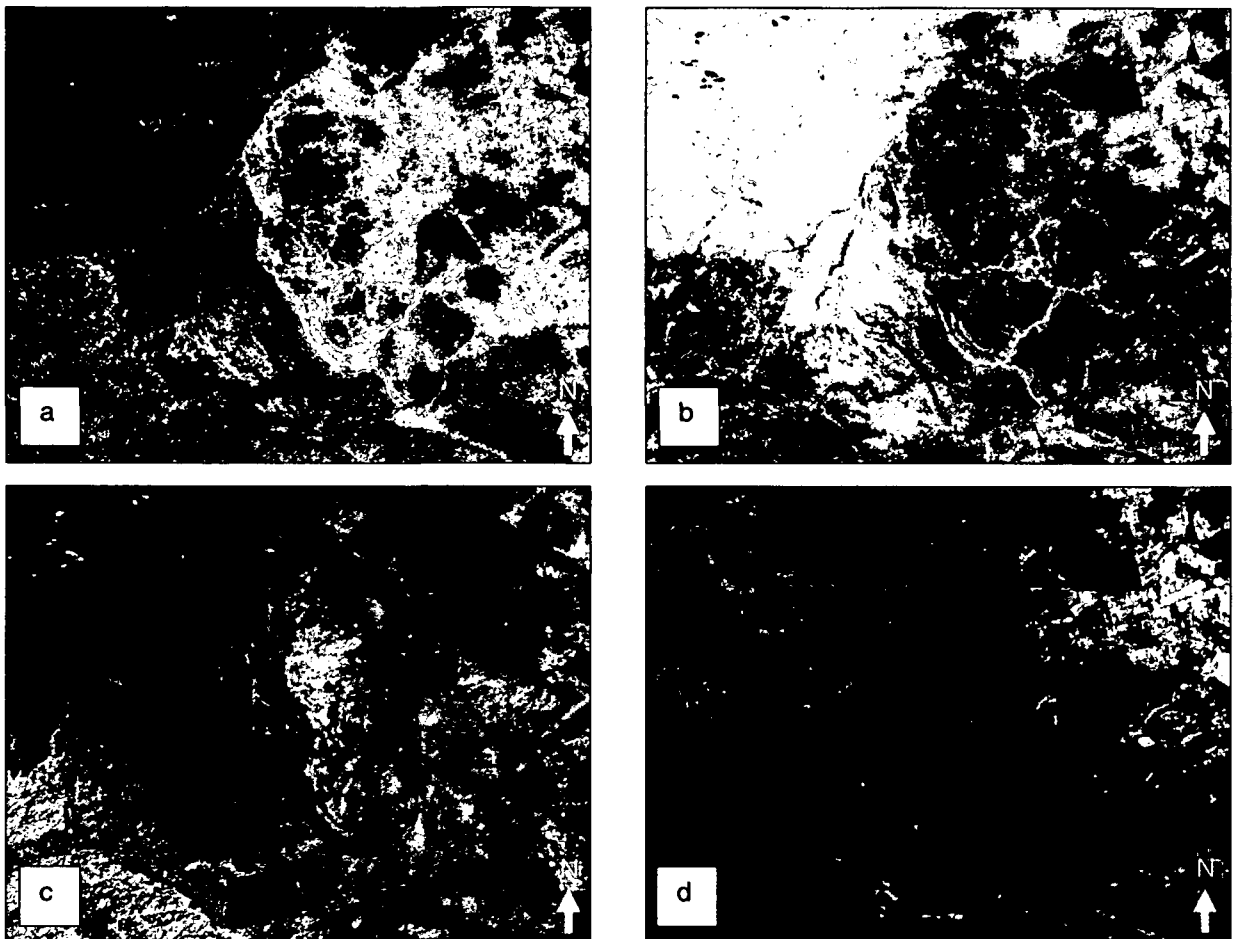


Figure 9-9: Linear spectral unmixing result for the broader Wuda area for 2002-09. The selected endmembers are coal (a), quartzite desert sand (b), arcotic sandstone (c) and Artemisia vegetation (d). Light areas indicate high subpixel fractions, while dark areas represent pixels with a smaller fraction of the endmember. Center coordinate: 640134E, 4377377N, UTM, Z48 N, 43km×36km

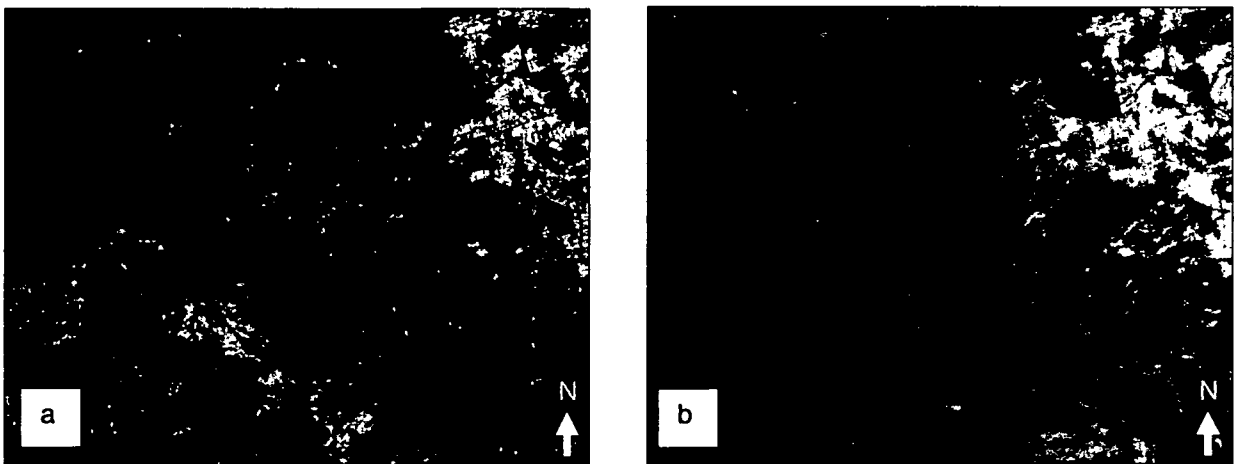


Figure 9-10: RMSE image (a) and color coded unmixing result (b). Here the endmember coal, vegetation and sandstone are displayed in red, green and blue. The RMSE image shows high errors for the vegetated areas. This goes in line with the confusion between desert sand and vegetation. Center coordinate: 640134E, 4377377N, UTM, Z48 N, 43km×36km

9.2.1.2. Ruqigou

Figure 9-11 presents the partial unmixing results for the broader Ruqigou area for all 8 ETM+ scenes. In all scenes the Ruqigou / Gulaben coalfields as well as the coal mining valleys of Hulusitai and Shitanjing in the Northeast were extracted. However, especially the winter scenes (2002-12 and 2003-02) yield visually insufficient results, since large shadowed areas were extracted. Visually good results were retrieved for the scenes of 1999, 2002-09 and 2003-05, where relief influence is minimized.

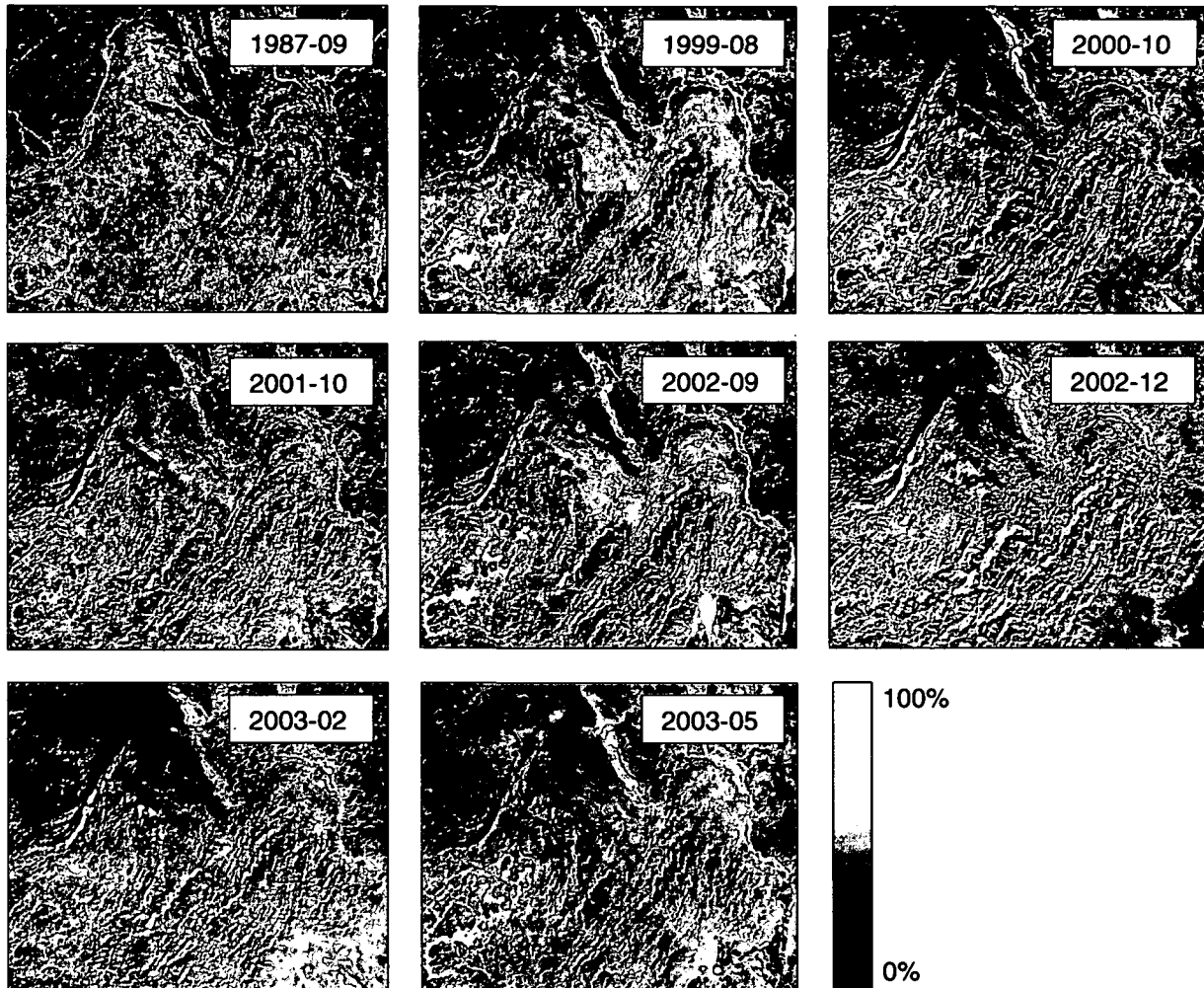


Figure 9-11: Partial unmixing results for the broader Ruqigou study area for all 8 scenes. Light areas indicate a high spatial fraction of the input prototype spectrum, while dark areas represent pixels with a smaller fractions. Mimicking surfaces include shaded areas. Center coordinate: 606211E, 4334381N, UTM, Z48N, 33km×28km

Figure 9-12 illustrates the inter scene variability as well as sun angle induced variations in shadow sizes. Again, multitemporal inter scene comparability for the evaluation of temporal trends is not given. However, if the development of two scenes acquired under similar illumination conditions is compared the increase of coal surfaces in the broader Ruqigou area becomes apparent.

It has to be remembered that the Ruqigou area is located in extremely difficult terrain. Elevation in the region processed varies between 950 and 2650m. Valleys are deeply incised. This compares to SMA applied in the central Alps. Such terrain limits analyses accuracies for most applications.

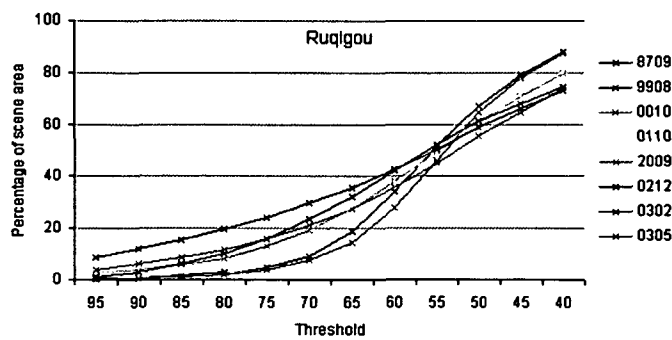


Figure 9-12: Subpixel fraction of the input pattern surface (coal) plotted against the percentage of the scene area, which would remain, if the partial unmixing result is thresholded for the pixels containing equal or above the percentage subpixel fraction. All eight time steps were calculated and displayed.

With the 85 % threshold in 1987 1.35 % of the input area was extracted as coal. In 2002 the 85 % thresholded already covers 5.54 % percent of the input scene. This indicates an increase for nearly 400 %, which is more than indicated by the knowledge based extraction. Here an increase of 250 % is calculated (compare table 8-2, chapter 8).

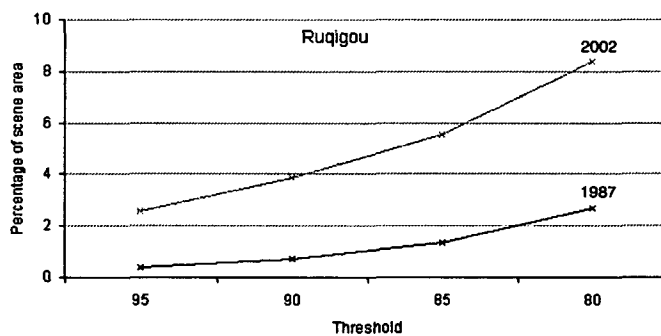


Figure 9-13: Subpixel fraction of the input pattern surface (coal) plotted against the percentage of the scene area, which would remain, if the partial unmixing result is thresholded for the pixels containing equal or above the percentage subpixel fraction. Presented for Ruqigou, 20.09.1987 and 21.09.2002.

It is important to note the fact that for Ruqigou a slightly smaller area was processed than with the knowledge based algorithm. This is a consequence of scene boarder effects, not influencing the test sequence, but influencing the partial unmixing. Therefore, the results can only be compared on a relative basis. The subset input into partial unmixing for the Ruqigou area has a higher areal coverage of coal mining areas and therefore coal extraction results are relatively seen higher and the increase appears stronger. However, both results are considered to lie in an adequate range to indicate the timely expansion, ranging between 250% and less than 400% for the Ruqigou area.

An advantage of the Ruqigou / Gulaben area is that no larger water surfaces (except a very small pond in the far Southeast) exist. Therefore, PMA for coal will only extract coal and shadow surfaces, with the latter varying depending on sun angle. However, quantitative statements resulting from partial unmixing approaches and similar approaches still need to be handled with care. This is discussed in detail in chapter 9.4.

Interactive shadowed area masking as presented in figure 9-7 for the Wuda study area was not performed for Ruqigou, since the terrain is too complex. However, it is obvious that without the influence of water, shadow and shadow margin the multitemporal comparison of extracted coal surfaces will show an overall increase over time.

Figure 9-14 presents the PMA coal fraction result of the Ruqigou area from 1999 thresholded with an 85 % threshold (a), and 2002-09 (b) to extract coal surfaces exclusively. The tresholded images were

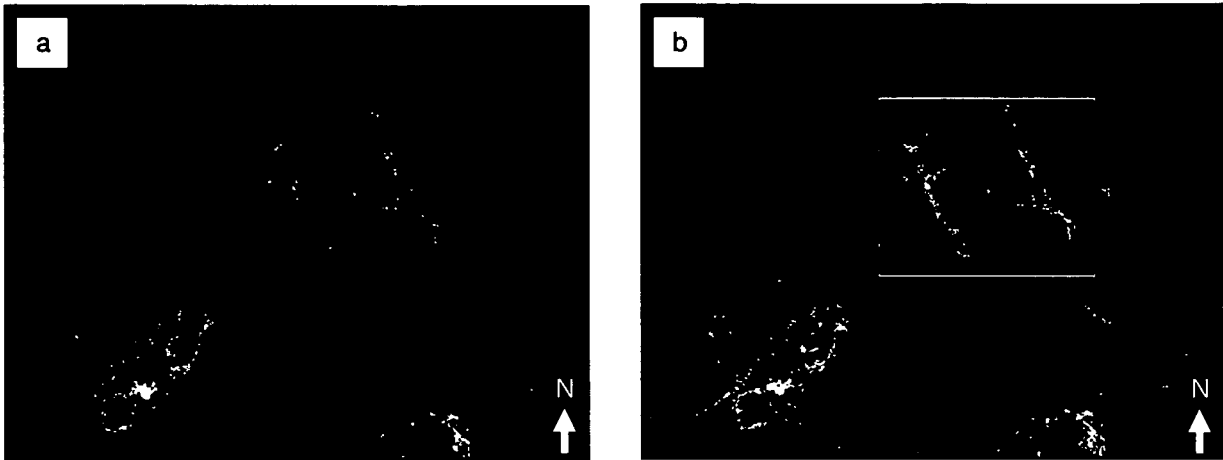


Figure 9-14: Subpixel fraction result image for coal intersected with a 85% threshold, to retrieve pure coal surfaces; for the broader study area of Ruqigou, 1999 (a) and 2002-09 (b), Center coordinate: 606211E, 4334381N, UTM, Z48N, 33km×28km

furthermore majority filtered. The expansion of mining operations in the valleys of Hulusitai and Shitanjing (white box in b) can be noted clearly.

Figure 9-15 presents the result of PMA estimation for the vegetation fraction for the broader Ruqigou area for the scenes of 1987-09 (a) and 2002-09 (b). Densely vegetated areas in the southeastern quarter of the subset can be observed. Further densely vegetated patches can be found in the small oasis in the northwestern quarter at the northern border of the subset. Also southwest of Ruqigou some denser mountainous vegetation can be found. Coal surfaces are represented with very low values. In the other regions vegetation density varies depending on geologic substrate and terrain. Thresholding, intersections, delineation and coal fire risk area reduction, which can be achieved by dense vegetation exclusion, are presented in chapter 10.

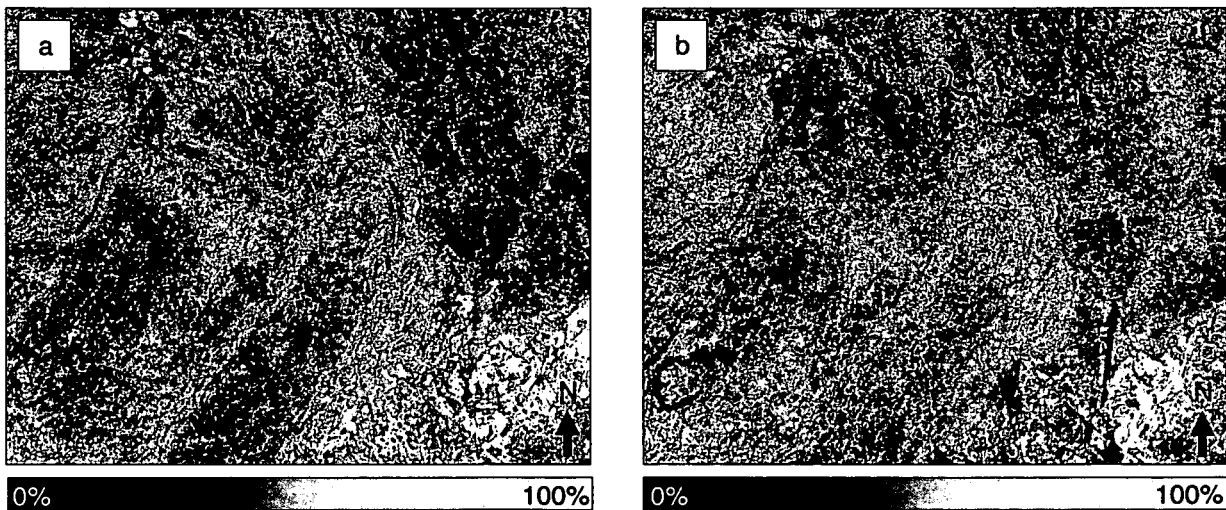


Figure 9-15: Partial unmixing results for vegetation for the broader Ruqigou area for 1987-09 (a) and 2002-09 (b). Light areas indicate a high fraction (pure Artemisia leaves), while dark areas represent pixels with a smaller fraction of vegetation. Center coordinate: 610605E, 43327047N, UTM, Z48 N, 33km×28km.

To extract pyrometamorphic rock, PMA was applied for the scenes of Ruqigou from September 2003 and May 2003. The result shows lighter areas in the mining area of Ruqigou, but also large areas covered with pure desert sand were extracted. This problem was already addressed in chapter 8. The overall PM result appears very blurred. Most pixels – except strongly vegetated areas in the Southeast and an area covered by a thin cloud – show the contribution of the input signal to at least some extent.

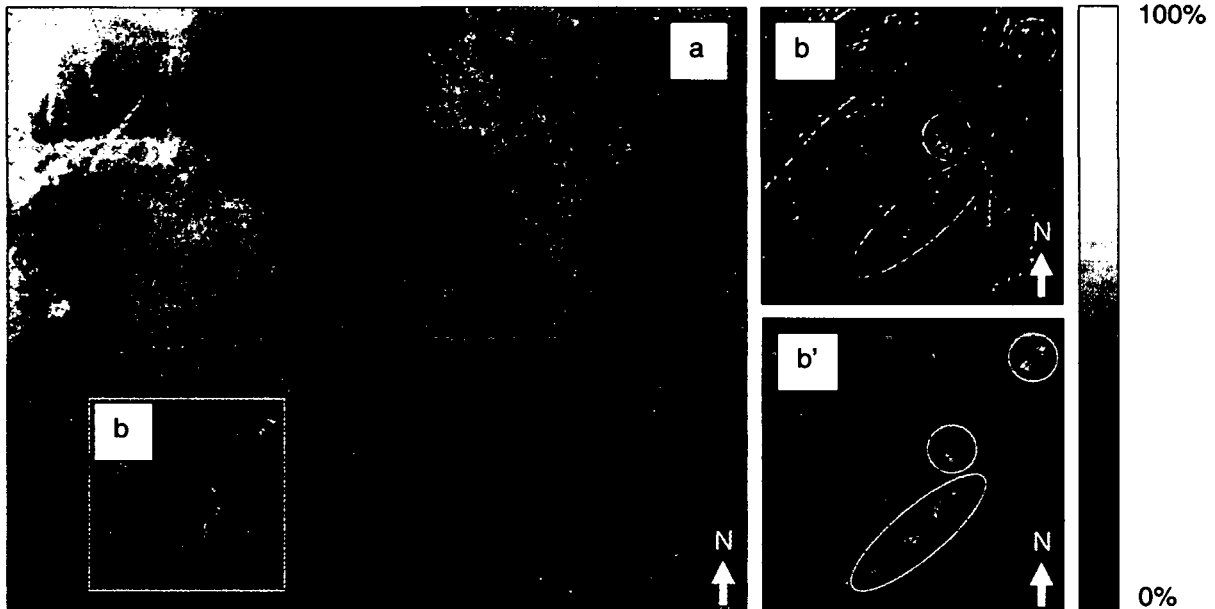


Figure 9-16: Subpixel fraction image for pyrometamorphic rock (averaged prototype spectrum) for the broader Ruqigou area calculated for the scene from 2002-09. Center coordinate of a: 607794E, 4336506N, b and b': 595287E, 4325273N, UTM, Z48N, 33km×28km.

Though the pyrometamorphic areas within the structural syncline were extracted with clearly higher fractions, the result cannot be used for the automated mapping of pyrometamorphic rock, unless some post filters are applied. Visual comparison of thresholded fractions (>70%) and the original data demonstrated that the pyrometamorphic regions reached PMA scores exceeding the threshold (indicating a very good producer accuracy). However, too many pixels with surfaces unaffected by pyrometamorphosis show similar high scores. PMA was also calculated for the single pyrometamorphic spectra instead of the averaged prototype spectra to account for the high variability of these rocks (and spectra). Visual comparisons yielded no improvement to the PMA result retrieved with the averaged prototype spectrum. One reason for this weaker extraction is the fact that pyrometamorphic pixels are not considered extreme pixels. However, the general extraction of the desired pixels was successful and pyrometamorphic regions can be extracted from the multispectral ETM+ data in a knowledge base test sequence,- as well as a PMA approach. Only for an automated mapping approach not influenced by analyst interpretation do pyrometamorphic pixels not give sufficient indication for distinct spectral recognition.

Linear unmixing with a multi EM model was not performed for the Ruqigou area. Only limited ground knowledge of this area exists and it is not sure, which endmembers (next to coal and vegetation) would yield an unmixing result of high accuracy.

9.2.2. Results for the Transfer Regions

9.2.2.1. Flinders Ranges, Leigh Creek, Australia

Figure 9-17 a represents the PMA result for the coal prototype spectrum for the Leigh Creek area, Australia. Next to coal, some deep lakes, shaded areas and also some geologic surfaces are represented by high subpixel fractions. The visual impression for the Leigh Creek area shows a good result of the fraction image thresholding at 85% subpixel coal fraction. Next to the coal mining area, which is clearly distinguishable, three deep dark artificial lakes south of the mining area as well as some shadowed areas were extracted. These can not be removed through the application of a majority filter. However, the postprocessing – intersecting the 85% thresholded coal subpixel fraction result with the temperature test of the knowledge based test sequence – can fully remove these areas. As outlined by figure 9-16 b dense vegetation for the Leigh Creek region only occurs along seasonal river beds and small creeks as well as along the shores of the reservoirs. In the remaining area vegetation density is clearly correlated with geology, where some strata shows a higher vegetation density than other surfaces. A coal fire (risk) area map is presented in chapter 10.

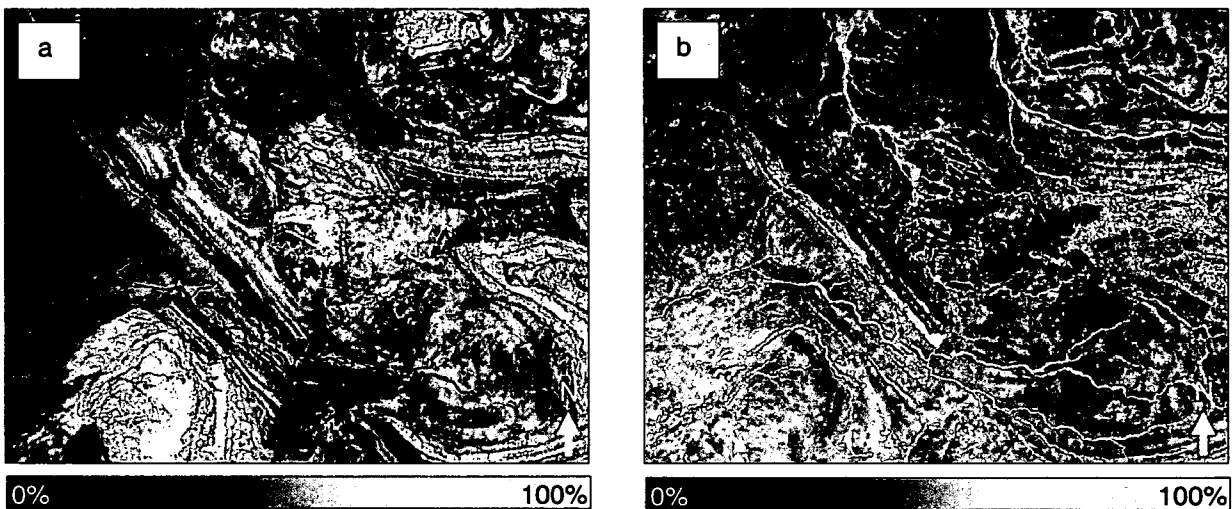


Figure 9-17: Fraction image of coal resulting from partial unmixing for the broader Leigh Creek area, Australia, (a) and fraction image of vegetation (b). Center coordinate: 6626009 S; 252463 E, UTM, Z54 S.

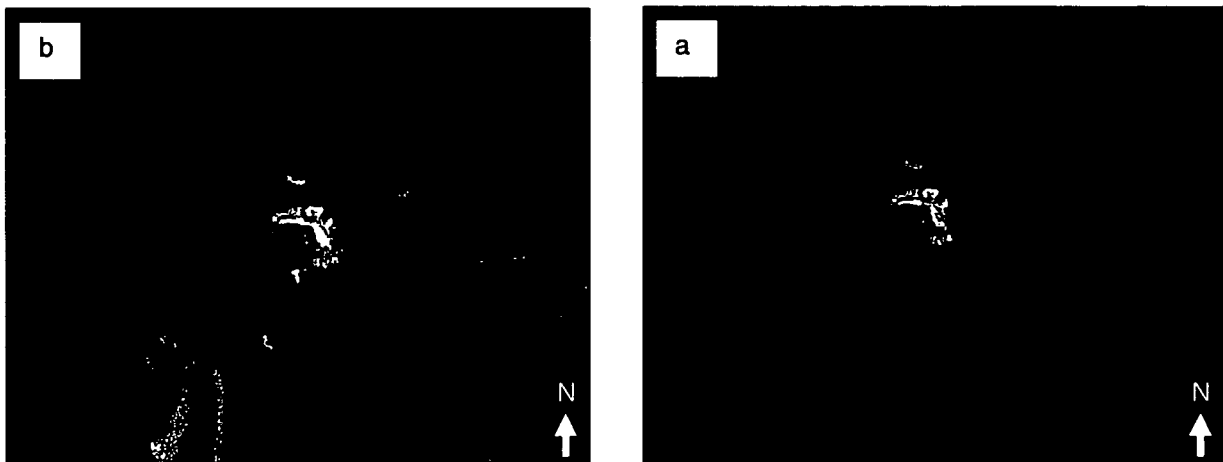


Figure 9-18: Thresholded 85% subpixel coal fraction image before (a) and after (b) the intersection with the temperature test (majority filtered). Center coordinate: 6626009 S; 252463 E, UTM, Z54 S, 60kmx50km.

9.2.2.2. Jharia and Ray coal mining regions, India

The PMA result for the scene of India looks very good. It can be noted that the coal surfaces clearly visible within the multispectral image are distinctly extracted in the PMA result. The result of PMA thresholding at the 85% fraction yields the image shown in figure 9-19 c. However, it also can be noted in figure 9-19 b that not only coal surfaces, but also their affected surrounding (mixtures with coal dust etc.) are extracted as very bright subpixel fractions. Pure coal surfaces are therefore slightly overestimated. The same applies for the coal field close to the town Ray presented in Figure 9-20 a, b and c.

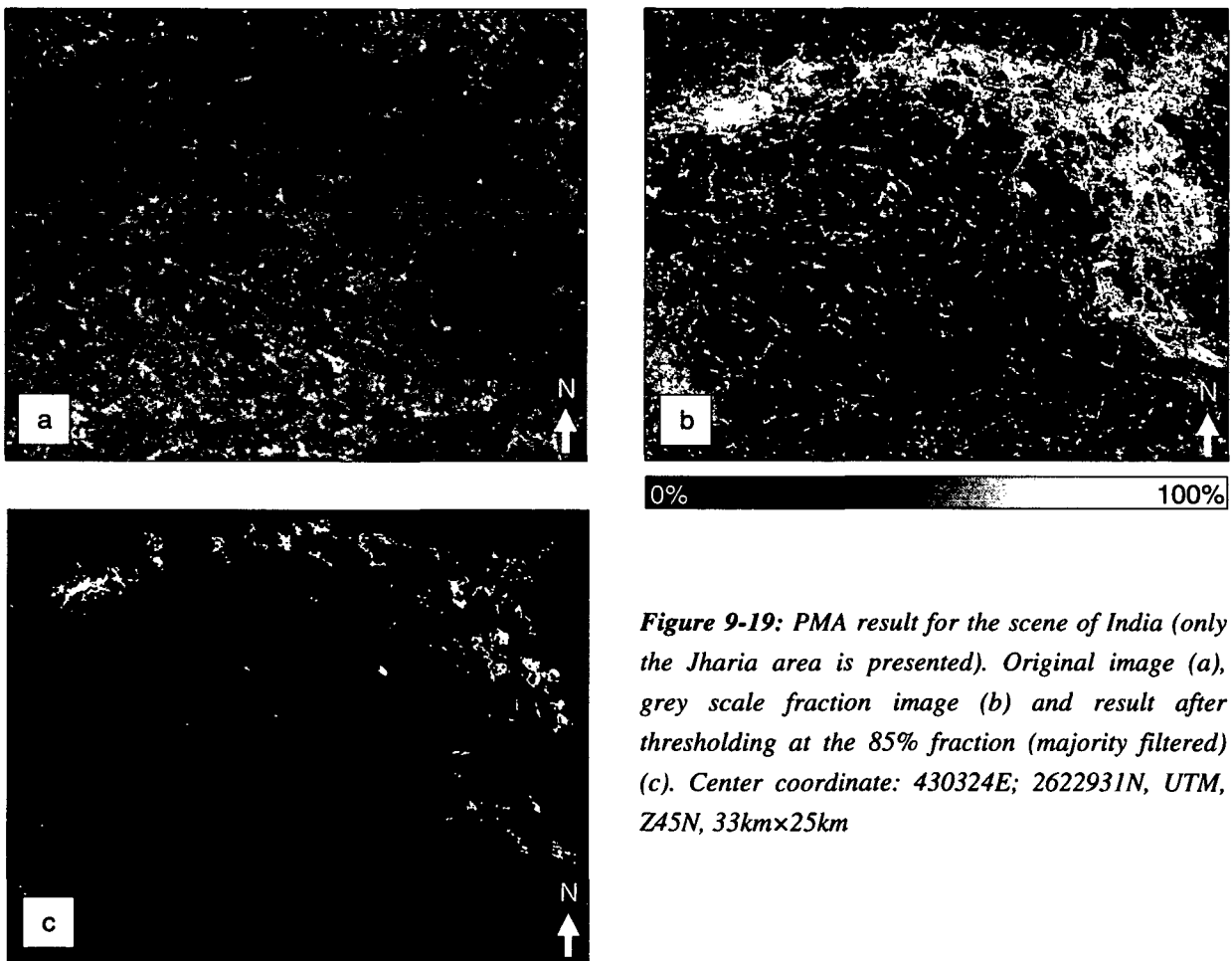


Figure 9-19: PMA result for the scene of India (only the Jharia area is presented). Original image (a), grey scale fraction image (b) and result after thresholding at the 85% fraction (majority filtered) (c). Center coordinate: 430324E; 2622931N, UTM, Z45N, 33km×25km

Results will be quantified in the next chapter. It is well known that the Jharia coal fields are affected by several coal fires. For the coal mining region close to the town Ray no information on coal fire occurrence could be found in international references. Also PRAKASH (2004, personal communication), who is very familiar with the Jharia area could not give detailed information on the Ray area 100 km west of Jharia. However, the coal outcrops in this region are very distinct and are the second largest in the ETM+ scene acquired for India. Therefore, for this area coal fire demarcation and coal fire risk maps will also be generated. Figure 9-20 presents the partial unmixing result to the prototype spectrum for this area.

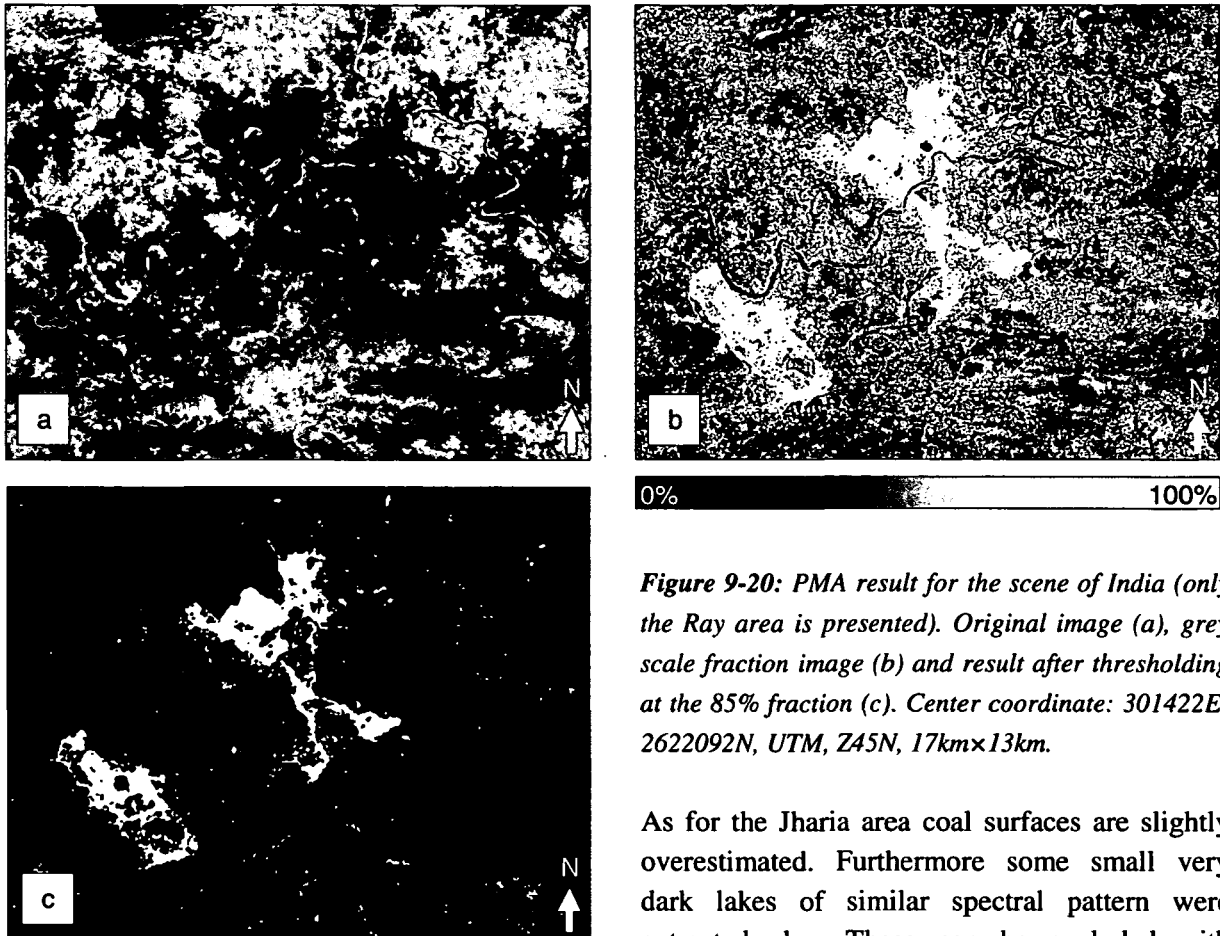


Figure 9-20: PMA result for the scene of India (only the Ray area is presented). Original image (a), grey scale fraction image (b) and result after thresholding at the 85% fraction (c). Center coordinate: 301422E; 2622092N, UTM, Z45N, 17km×13km.

As for the Jharia area coal surfaces are slightly overestimated. Furthermore some small very dark lakes of similar spectral pattern were extracted also. These can be excluded with temperature based post processing as

implemented in the knowledge based spectral test sequence presented. PMA vegetation extraction posed not problem for the scene of India. Most of the scene is extracted with high subpixel fraction values. Only riverbeds, lakes, coal accumulations, settlements and bare fields indicate low subpixel fractions for the vegetation endmember. Based on automated coal extraction, a delineation of this area with a 500 m delineation radius and the exclusion of densely vegetated areas, probable coal fire areas were demarcated for the whole ETM+ scene of northeastern India. Demarcated coal fire areas and thermal anomalies retrieved from the application of the thermal algorithm developed by ZHANG, J. (2004) are presented in chapter 10.

9.2.2.3. Baotou, China

Partial unmixing results for the Baotou area are presented in figure 9-22. All coal covered areas are represented by very bright pixels, indicating high coal fractions. However, many pixels were extracted with high subpixel prototype fractions, although no coal is present within these pixels. Even after a thresholding at 85 % subpixel fraction a large percentage of pixels erroneously extracted as coal remains. The whole scene of Baotou covers over 60 Mio. Pixels. 1.4 Mio pixels remain after a 85% fraction thresholding. Next to coal especially the settled areas were recognized. Confusion between coal and dark asphalt occurs. Though these two surfaces show slightly differing spectral profiles, the maximization of the requested signal leads to the extraction of similar surfaces also. This problem will be addressed in more detail in the discussion (chapter 9.4.).

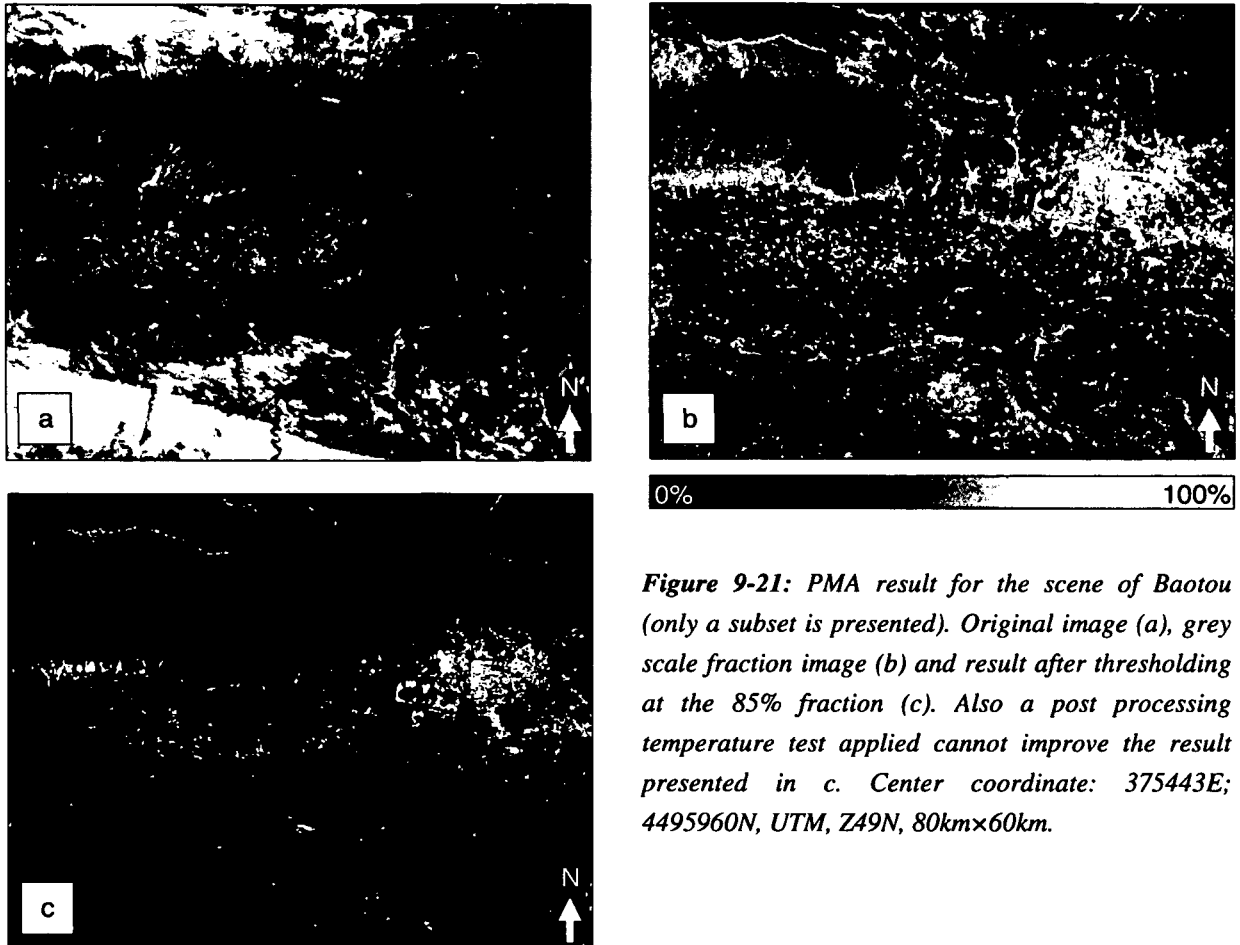


Figure 9-21: PMA result for the scene of Baotou (only a subset is presented). Original image (a), grey scale fraction image (b) and result after thresholding at the 85% fraction (c). Also a post processing temperature test applied cannot improve the result presented in c. Center coordinate: 375443E; 4495960N, UTM, Z49N, 80km×60km.

Majority filtering can slightly improve the result presented in 9-21 c. However, the PMA result for Baotou will lead to the derivation of too large coal fire risk areas. Here the result of coal fire area demarcation based on a spectral test sequence outperforms PMA analysis. A comparison of accuracy, feasibility and demarcation results for both algorithms applied will be presented in chapter 10.

9.3. Quantification and Error Analysis of the Partial Unmixing Results

9.3.1. Quantification and Error Analysis of the Main Study Areas

Here only the producers accuracies for the two main study areas over all time steps for the individual surfaces are shown. This is to avoid redundancy with chapter 8. For information on the sources of ground data refer to chapter 8.

Table 9-1: Accuracy assessment for the 85 % thresholded coal fractions and 85 % thresholded vegetation fractions for the Wuda study area

Date	Prod. accuracy, coal	Prod. accuracy, dense vegetation
1987-09	not available	not available
1999-08	not available	not available
2000-10	87.91 % (Wuda mine)	not available
2001-10	not available	not available
2002-09	89.65 % (mapping)	91.03 % (mapping)
2002-12	54.02 % (mapping)	not available, winter

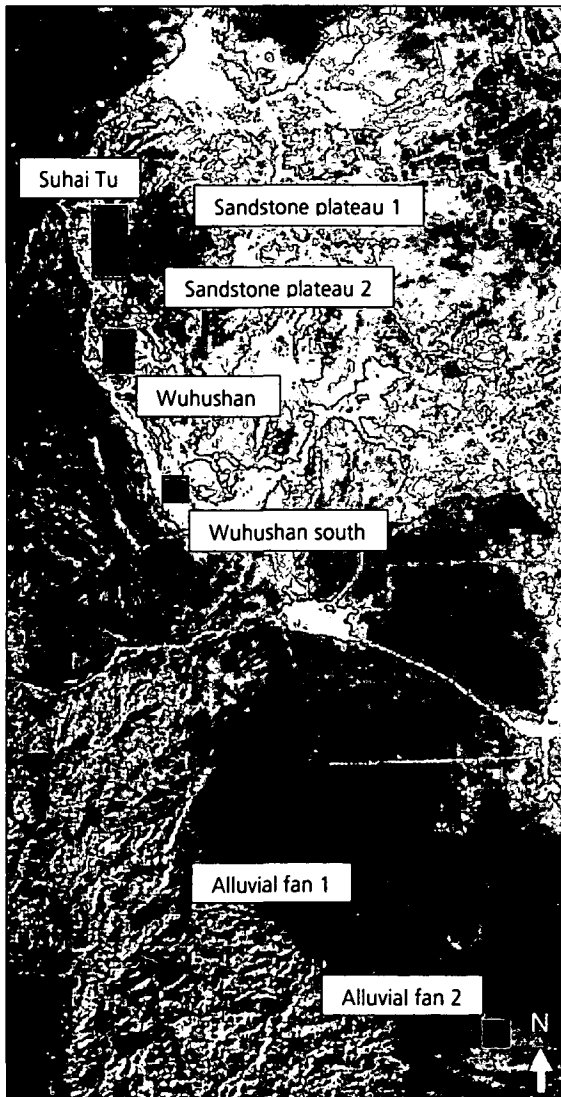
9. Quantitative Surface Extraction applying Partial Unmixing

Table 9-1 cont'd

Date	Prod. accuracy, coal	Prod. accuracy, dense vegetation
2003-02	61.72 % (mapping)	not available, winter
2003-05	76.47 % (Quickbird & mapping)	88.31 % (Quickbird & mapping)

Table 9-2: Accuracy assessment for the 85 % thresholded coal fractions and 85 % thresholded vegetation fractions for the Ruqigou study area

Date	Prod. accuracy, coal	Prod. accuracy, dense veg.	Prod. accuracy, pyro. rock
1987-09	not available	not available	not available
1999-08	89.45 % (ITC project data)	not available	not available
2000-10	89.98 % (Ikonos)	not available	not available
2001-10	not available	not available	not available
2002-09	91.42 % (mapping)	86.22 % (mapping)	100.00 % (mapping)
2002-12	32.81 % (mapping)	not available, winter	not available
2003-02	29.11 % (mapping)	not available, winter	not available
2003-05	77.87 % (QB & mapping)	83.59 % (QB & mapping)	97.13 % (mapping)



Extraction accuracies accuracies for coal in Wuda range between 54.02 % and 89.65 %. Excluding the winter scenes 76.47 % to 89.65 % are reached. Similar good results for dense vegetation between 88.31 % and 91.03 % indicate the good suitability of PMA for the mapping of a single surface of interest. The same applies for the Ruqigou area, where producers accuracies for coal range between 77.87 % and 91.42 % not taking winter scenes into account. Dense vegetation was mapped with 83.59 % to 86.22 % producer accuracy. The extremely good accuracy for the extraction of pyrometamorphic rock mimics the fact that next to the ground truth areas also many other regions yielded very high subpixel scores.

Figure 9-22: Location of the seven mixture grids mapped during the field campaign in September 2002. Over 600 cells were mapped with regard to their percentage subcell fraction of the occurring surface components. The grids are superimposed on an ETM+PMA result of 2002-09. Center coordinate of the presented subset 644123E, 4370610N, UTM, Z48N, 23km×10km

As shortly introduced in chapter 4, seven mixture grids were mapped during the 2002 field campaign. These grids can be used to assess the PMA result on a very detailed basis. The location of the seven grids is shown in figure 9-22. The grids Suhai Tu, Wuhushan and Wuhushan south are located above active coal fires and their surrounding (fires #6, #8 and # 13 respectively). While – next to other surface types – coal and vegetation do occur in some of the cells of these three grids, the two grids on the sandstone plateau as well as the two grids mapped on the alluvial fan do not contain coal.

However, the PMA result for coal indicates a coal fraction in all of the cells of the “Sandstone plateau 1” grid. The fraction values for the 15 grid cells range between 21 % and 45 % coal fraction (n=15). The average coal fraction value for the whole grid is 28 %. For the grid “Sandstone plateau 2” fraction values for coal – though no coal is present – range between 24% and 41%. The average is 29 % (n=23). The two grids on the alluvial fan do not contain coal either. However, the average for “Alluvial fan 1” ranging between 26 % and 37 % is 31 % (n=11). For the large grid “Alluvial fan 2” (n=185) PMA coal fraction values range between 29 % and 45 % with an average of 36 %.

This phenomenon of fraction overestimation due to the maximization of the prototype spectrum is typical for partial unmixing approaches. Therefore fraction estimates – especially in the lower fraction range – have to be interpreted with care. Figure 9-23 presents the mapping results for the subpixel coal occurrence (as mapped in the field) next to the result of PMA. Orange boxes within the PMA results mark regions, which were not mapped. Here dangerous terrain limited the mapping.

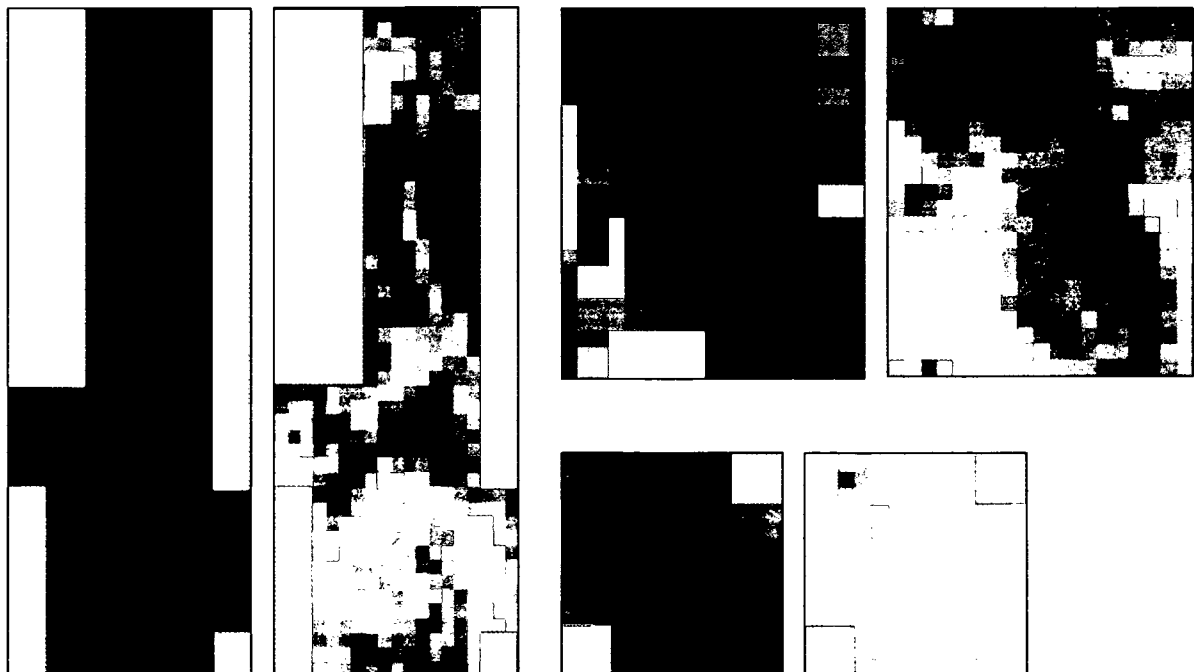


Figure 9-23: The three main grids mapped within Wuda syncline, Suhai Tu (left), Wuhushan (upper right) and Wuhushan south (lower right). The mapping result from the field in September 2002 (left side) as well as the PMA result for the partial unmixing to coal – also from a September 2002 scene - (right side) are shown. Orange boxes indicate areas, which were not mapped.

For these grids regression analyses were undertaken to investigate the relationship between the subpixel field mapping and the partial unmixing result. Correlation coefficients for the seven mapped grids for analyses between mapped coal and the PMA coal fraction as well as between vegetation and the PMA vegetation fraction are presented in table 9-3. They are not considered of satisfying significance and indicate insufficient explanation. Also cross correlation analysis shifting the grids against each other as well as cross validation excluding certain values or value ranges did not lead to an improvement of these coefficients. Even though this validation is unpleasant it was decided to present it here. Most unmixing or partial unmixing analysis only validate results based on thresholding the fraction images above a certain percentage and comparing the retrieved areas with ground truth polygons. This validation method has also been applied to the PMA results as presented before. Results were very good. The application of mapped mixture grids acquired during field campaigns is only presented in rare cases.

KUEMMERLE (2003) plotted the results of a field mappings of woody vegetation components and herbaceous vegetation components against unmixing results of these fractions and yielded R²s of 0.71 and 0.54 respectively. This result was achieved even though the ETM+ data set used was acquired two years after the field mapping. In his case only eleven pixels could be compared with ground truth. He found that SMA leads to an overestimation of the vegetation component when ground covering densities are low. This coincides with an overestimation of vegetation for about 20% in the two grids mapped (Sandstone plateau 1 and Sandstone plateau 2) where no vegetation was present. Furthermore it is likely that PMA (due to the maximization approach) overestimates a surface of low overall contribution much more, than SMA.

Table 9-3: Regression analyses between mapped subpixel fractions and the PMA result

	R ² for coal mapping versus coal fraction images	R ² for vegetation mapping versus fraction images
Suhai Tu	0.35	0.46
Wuhushan	0.18	0.23
Wuhushan South	0.21	0.31
Sandstone plateau 1	no coal existing, offset of 28 %	no vegetation exists, offset of 20 %
Sandstone plateau 2	no coal existing, offset of 29 %	no vegetation exists, offset of 22 %
Alluvial fan 1	no coal existing, offset of 31 %	0.42
Alluvial fan 2	no coal existing, offset of 36 %	0.51

Reasons for the weak results between modelling and field data can be the co-registration of the data. However, shifts for the datasets were in the subpixel range and it was tried to compensate any unknown effect with cross correlation. This did not improve the results. Therefore, the main problem is assumed to be the mapping method of the mixture grids in the field. A human analyst has a clearly different view onto a certain grid cell within the field than a nadir looking sensor system. While the sensor has an near orthometric view, the analyst's fraction estimation will always be biased by a limited field of view. It is likely that the vegetation fraction is overestimated, while soil fractions are underestimated (KUEMMERLE 2003). Surfaces with high contrasts to their surrounding might be mapped with a larger spatial subpixel proportion than is actually covered. In addition, for the surface "coal" mimicking effects with shadow lead to a phenomenon, which also needs to be mentioned. A

pixel can contain terrain induced shadow (e.g. shade from a mountain) and so called micro-shadow. These are shadow components included in a totally flat pixel, which are induced by vegetation or surface roughness. This component will always mimic a slight portion of “coal” to be available in each pixel. However, regarding the overall patterns in figure 9-23 presenting mapping and PMA results for the three largest grids the approximate distribution of areas of higher coal occurrence can be noted. Though this statement is based on visual analysis exclusively, it is suggested that the overall patterns can be recognized in the field mapping results as well as in PMA results.

Comparisons of the PMA result of from 2002-09 (ETM+) with the SMA coal fraction image of the same scene yielded an R^2 of 0.46, which is of some significance considering that over 1 Mio pixels (n) are plotted against each other. However, when only the 85% thresholded fraction score of both images are compared an overlap area of 73% indicates a good accordance of both results. The SMA result thresholded at 85% tends to slightly underestimate coal surfaces.

9.3.2. Quantification and Error Analysis of the Transfer Regions

To not create redundancy with chapter 8, here only the producer accuracies for the three transfer scenes and the individual surfaces are shown. For information on the sources of ground data as well as information on the transfer areas refer to chapter 8. The accuracy refers to subpixel fractions exceeding 85% for coal, which – based on visual analysis – was considered to be pure coal. Vegetation is thresholded at the 65 % fraction. User accuracies could not be calculated since no ground truth for the numerous other land cover surfaces did exist.

Table 9-4: Accuracy of the extracted coal for Australia

Date	Prod. accuracy, coal	Prod. accuracy, dense vegetation
15.11.2002	92.23 %	not available

Table 9-5: Accuracy of the extracted coal and dense vegetation pixels for India

Date	Prod. accuracy, coal	Prod. accuracy, dense vegetation
02.11.2001	86.87 %	89.03 %

Table 9-6: Accuracy of the extracted coal and dense vegetation pixels for Baotou

Date	Prod. accuracy, coal	Prod. accuracy, dense vegetation
29.08.2002	91.55 %	67.33 %

The results for the Leigh Creek area in Australia, where – according to ground truth – 92.23 % of the coal covered surfaces could be extracted is very good. Even though user’s accuracies can not be calculated, very few pixels outside the coal field were additionally extracted as coal. These can be eliminated based on post processing. The user’s accuracy is assumed to be high. The results for India are also sufficient. A producer accuracy of 86.87 % for coal and 89.03 % for dense vegetation clearly indicates that PMA analysis employing a prototype spectrum is successful. Results are slightly weaker

than for the other two transfer areas. The completely different environment in a tropical climate zone and very high standard deviations of most surfaces can be responsible for this observation.

PMA for the scene of Baotou yields good extraction accuracies for coal and dense vegetation. However, as presented in figure 9-21 a lot of additional pixels were extracted with high subpixel fraction percentages, indicating a low user's accuracy.

9.4. Discussion

General advantages of the partial unmixing approach compared to other methods are manifold. Most classification techniques like UCA, SCA, OOC; ANN, visual interactive delineation of classes and also the knowledge based system presented in chapter 8 can only provide a qualitative measure of class membership. A pixel either belongs to a class or not – the conclusion drawn is a hard statement, which often only approximates real ground conditions.

In general, the quantitative sub-pixel information derived from a spectral unmixing or partial unmixing approach is considered of much higher value – especially since the sub-pixel scale allows for fuzzy class transitions and contributes to the fact that most real materials occur in dimensions smaller than the pixel size (KUEMMERLE 2003, TOMPKINS et al. 1997). The partial unmixing approach presented here can contribute to the facts that land cover does not fit in square raster grid cells and that pixels are usually not homogeneous, no matter how small they are. The algorithm does not pretend the pixel to be a geographical object (FISHER 1997). Furthermore, fraction images ranging between 0-100% contribution of a material are easier to interpret than DN's (ADAMS et al. 1995). However, since the PMA results are thresholded for coal fire area demarcation, the advantage of subpixel fraction percentages is not necessarily of advantage for coal fire area demarcation. Nevertheless, the fraction images generated in the process of risk area demarcation can be used for time series analysis with respect to increasing pollution with coal dust and associated materials.

General disadvantages of partial unmixing are the extraction of false positives or the tendency of overestimating a materials abundance within a pixel. If all scene materials are accurately known, a complete SMA approach will yield better results than partial unmixing (KRUSE et al. 2000). However, it is often not reasonable that all endmembers are exactly known and this concept hinders the spatial transferability of the SMA approach – especially when aiming at the extraction of a certain surface. This is the reason that no full SMA approach was implemented for coal fire area delineation, which needs to be applicable not only for the well known study regions.

The slight disadvantage of PMA of maximizing the spectral response, which may lead to the definition of “false positives”, can be overcome applying a so called “infeasibility calculation”. This calculation reduces the number of false positives found in partial unmixing results. Infeasibility images are in noise sigma units indicating the feasibility of the partial unmixing result. Pixels of high infeasibility are likely to be partially unmixed false positives, while correctly mapped pixels show a low infeasibility value and a PMA score above the background distribution around zero. 2-D scatter plotting of the partial unmixing result against the infeasibility image can be used to identify pixels with low infeasibilities and high matching scores (KRUSE et al. 2000).

Although, infeasibility image calculation is included in the common software package ENVI, the calculation of infeasibility images is not published and available. According to RSI the algorithm implemented is under closure, since it was developed for US defense related purposes (RSI, personal communication, 04-2004). Although output results look good and can improve extraction accuracy substantially, the algorithm was only applied for tests with the data. It can not be included in

the surface extraction scheme, since the mathematical background is not fully clear. Discussions and contacts with several experts of hyperspectral image analysis (SETTLE, HOSTERT, VAN DER MEER, personal communication 04/05-2004) indicated that the infeasibility calculation – though commonly applied and published – is hardly understood to its full extent. Emails to the programmer of the infeasibility measure (BOARDMAN) remained unanswered.

Figures 9-24 and 9-25 demonstrate the thematic principle of infeasibility calculation and show the result of a partial unmixing additionally intersected with the result of infeasibility calculation. It has to be noted that infeasibility calculation is performed on MNF transformed data.

For the combined approach the background statistics are used just as in PMA to define the variability of the unknown natural dominant endmembers. The known signature of the requested material is used for the definition of one corner of the mixing simplex. This fixed point has a well known noise distribution. The background covariance, equivalent to the eigenvectors and eigenvalues (see MNF in chapter 3) define the shape, size and orientation of the spectral scatter (KRUSE et al. 2000).

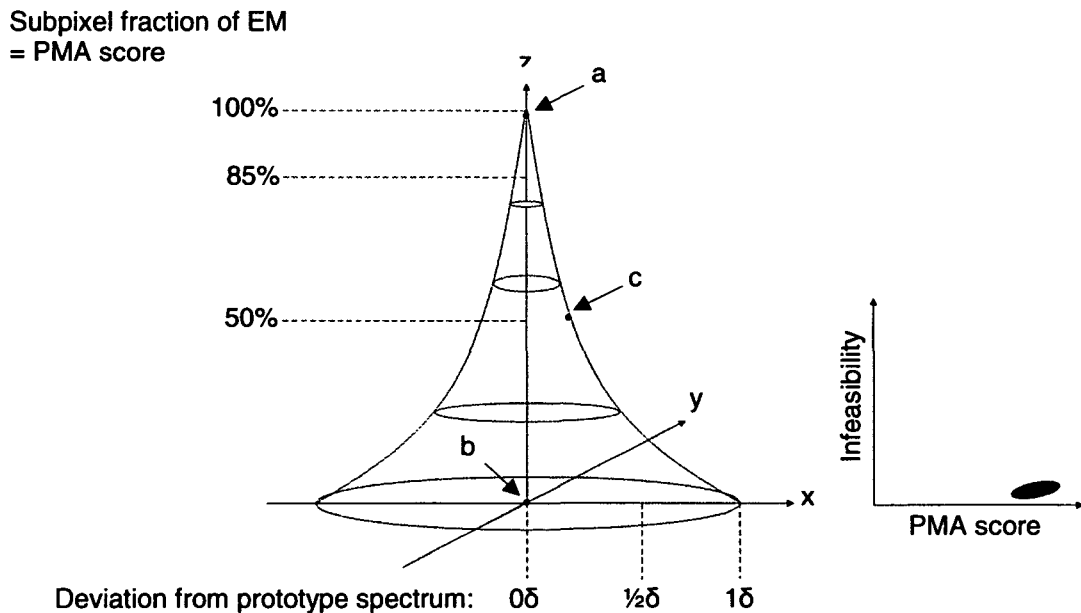


Figure 9-24: Thematic principle of class- or material membership infeasibility. Deviation from the prototype spectrum is given in noise δ units. The right part illustrates, where the desired pixels requested to be extracted are located. Pixels with a high PMA score and a low infeasibility (= high feasibility) are similar or tend to be close to the prototype input. DAMM, 2004, modified and extended.

Simplified, the basic assumption is that after PMA each pixel consists of a spectral mixture of the demanded EM (e.g. coal) and a background spectrum summing to 100 %. If the EM is approximated to 100 % the pixel is a pure pixel. If the PMA score is 0 % the pixel can be each arbitrary pixel within

the background. Through MNF transformation all background pixels are arranged around a point with uniform Gaussian variance. The prototype spectrum is an extreme pixel in feature space. The resulting feature space is approximately cone shaped. The extreme pixel is located at the peak of the cone and the cone-basis represents the distribution of background pixels defined through a radius, which is equal to the variance δ of the background distribution. The center point of the cone basis equals a background spectrum with 0 % fraction of the endmember (DAMM 2004, KRUSE et al. 2000). In figure 9-24 the x- and y axis span the background covariance of the feature space, while the z axis defines the percentage of the PMA score, which defines the subpixel fraction of the EM. Pixel "a" located in the synthetic space is equal to the requested endmember and matches the prototype spectrum to 100 %, while pixel "c" does not belong to the EM, shows a 50 % PMA score and $\frac{1}{4} \delta$ deviation from the prototype spectrum. Pixel "b" represents the prototype with a 0 % fraction but 0 δ deviation (DAMM 2004).

A combined PMA and infeasibility calculation was computed for MNF transformed data for a "difficult" scene of the Wuda study area. PMA calculations of the scene of 2002-12 acquired during lowest sun angles yielded – next to coal – large shadowed areas as well as parts of the Yellow River as high PMA scores. These phenomena could be eliminated with a post processing applying a relative temperature test. However, it should be evaluated, how the PMA result can be improved if a combined PMA and infeasibility calculation is applied. Figure 9-25 a shows the result of PMA for this scene,

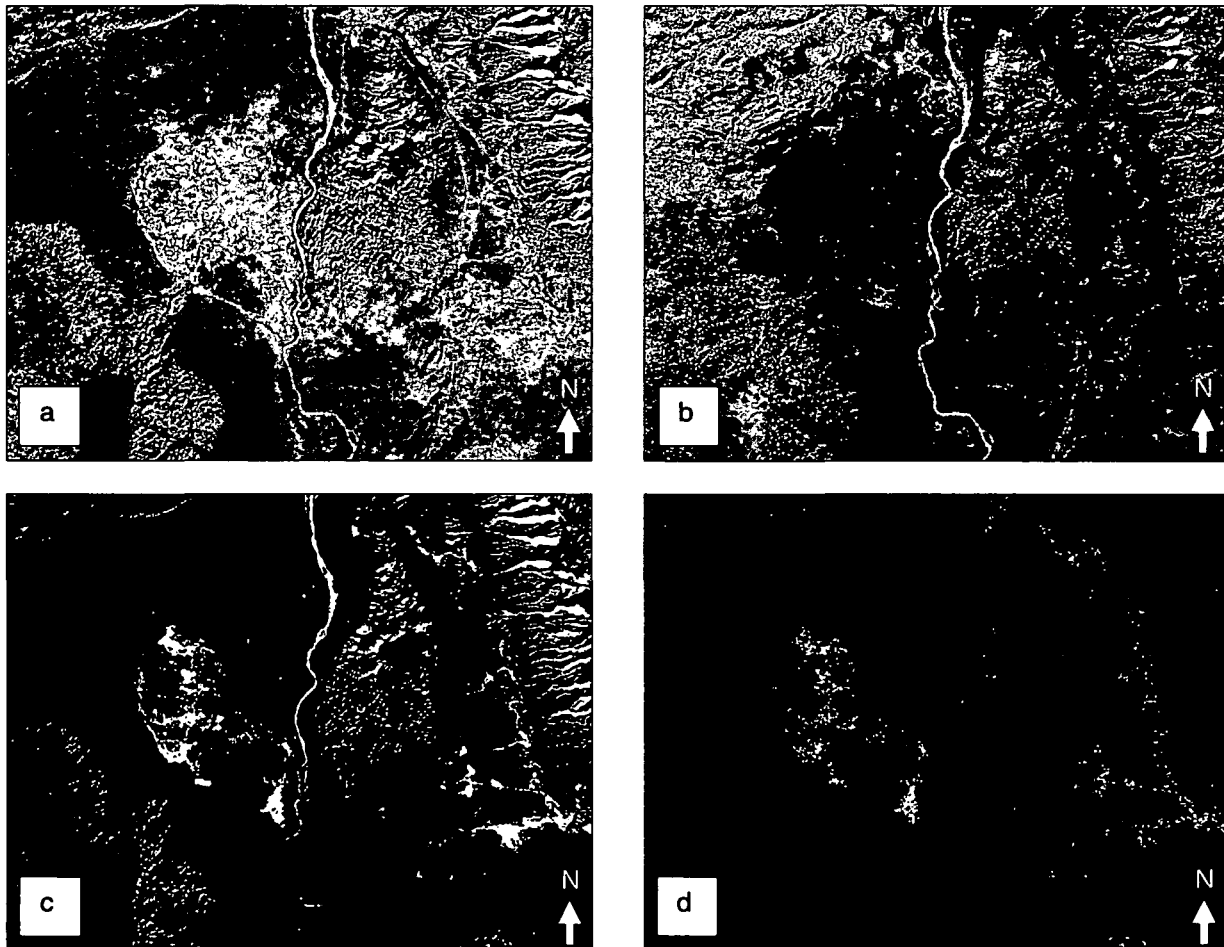


Figure 9-25: Partial unmixing result post processed with infeasibility information. a: PMA result for Wuda from 2002-12, b: infeasibility calculation for the prototype spectrum of coal, c: 85% subpixel fraction thresholded image of the PMA score, d: intersected image of high PMA scores (>85 %) and low infeasibility scores (<10 %).

while figure 9-25 b shows the infeasibility image for the PMA result. Dark values (low infeasibilities = high feasibilities) represent pixels with a high likelihood that a high PMA score represents the prototype spectrum. Lighter areas are unlikely to represent this spectrum. Visually, it can already be noted that some very bright areas in the PMA image (Yellow River, shadowed valleys in the center and East) show only high infeasibility scores. With an intersection of these results the requested surfaces (coal) can be extracted with higher accuracy. Figure 9-25 c illustrates the PMA score intersected at an 85% subpixel fraction threshold. Some areas not representing coal are still included (which are usually eliminated with a knowledge based post processing). However, if the two images (a and b) are intersected and only pixels are extracted, which show an PMA result exceeding 85 % and an infeasibility score below 10 % only the surfaces presented in figure 9-25 d remain. Though some coal surfaces are lost also, the result is very appealing. The shadowed areas in the East could be separated from coal, since these two are better distinguishable in synthetic MNF transformed data.

It is hoped that the mathematic basis for the calculation of infeasibility images will be accessible in the future. Not only for coal fire area demarcation but in the general context of PMA routines would this measure strongly support spectra based surface extraction.

Apart from false positives, misclassifications in partial unmixing can occur when endmembers are mimicked by other spectra. ADAMS et al. (1995) report about soils, which are mimicking dry grasses not resolvable in TM data. This mimicking phenomenon also occurs for coal and shadow in non-transformed images. However, a temperature based post processing enabled to eliminate the shadow regions and therefore only "lose" coal surfaces, which are located directly in the shade.

An additional fact, which influences the partial unmixing results and would also influence SMA results is that small amounts of a strongly absorbing species dispersed in a weakly absorbing medium will have a disproportionably strong effect on the spectrum of the mixture (GAFFEY et al. 1993). This applies for the material coal. This strongly absorbing material will in all subpixel approaches be slightly overestimated. However, this problem does not have a strong influence due to the threshold defined at 85% abundance. The validity of the assumption that spectral mixtures in a pixel are linear has already been discussed in chapter 3.8. Of course most processes in the real world are hardly ever linear and can only be approximated by linear or other defined mathematical (e.g. logarithmic, n-order polynomial etc.) assumptions. Also spectral mixtures in a pixel may better be approximated by non-linear processes. This makes the unmixing process very complex and would not allow for transferability. Non linear mixing is usually employed, when BRDF measurements are available, a small test site is investigated, or the distribution of several materials existing within a pixel is stable over a larger area. Non-linear unmixing is by many authors considered an approach not realistically applicable for larger areas, for transferable algorithms or for application-oriented remote sensing projects. Furthermore, the cost benefit effect of increased processing and programming against the gain of subpixel unmixing accuracy is by many authors considered too weak, to account for non-linear EMR-surface interactions (see chapter 3.8.).

With regard to the explicit results achieved here, it has to be questioned if the quantitative comparison of subpixel fraction results and the thresholding of images to derive scene proportions on a multitemporal basis, is appropriate. Though the Landsat time series was radiometrically processed and adjusted with great care and spectra of pseudo-invariant objects were measured and available for a

relative calibration, the scenes still showed non-linear shifts within the different spectral bands. This could already be noticed in the results of signature analysis in chapter 7.

In chapter 5 it was already demonstrated that even though radiometric correction was considered good, illumination correction can not account for all shadowed areas. The quality of illumination correction is not only dependent on the correction code applied, but also on the quality of the DEM, coregistration of scenes and other factors. Therefore, in satellite data of strongly alpine terrain shaded areas will always remain. Especially for such strongly alpine terrain like the Ruqigou / Gulaben area (>2500 m) the partial unmixing approach for a surface (coal) mimicking shadow cannot reach equal results as in flat terrain. Though producer's accuracies for Wuda and Ruqigou do not differ substantially, it is assumed that users accuracies for Wuda are much higher. Even though the combination of partial unmixing and a temperature based post processing leads to sufficient results, the knowledge based approach seems to be the more applicable and robust method, also yielding results of higher accuracy. PMA implies a quantitative accuracy and stability of output (though subpixel fraction composition is only computed in mixing space), which – in difficult terrain – has to be questioned.

In medium complex terrain as for the Wuda study area or the Leigh Creek transfer region, the PMA approach yields very good results. Time series analysis can be presented without doubts. Especially when neglecting the steeply incised valley region east of the Yellow River (which actually can already be considered as alpine terrain again) the extraction of coal and also investigations of vegetation density is well in accordance with ground truth polygons. The weaker results of the comparison of modeling results and mapped mixture grids have already been explained. It is assumed that especially the interactive mapping based on subpixel fraction estimation introduces a strong error, which later hampers quantitative comparison even though patterns look similar.

The results of PMA for the extraction of pyrometamorphically altered rock are not convincing in that respect that too many false pixels were extracted also. This is supported through the fact that pyrometamorph pixels (the ca. 5 100% ones, which exist) are not considered extreme pixels by a PPI calculation and similarities to other materials (in this case desert sand) are likely. Although – as for the knowledge based test sequence presented in chapter 8 – the PMA pyrometamorphic fraction result shows very high fractions in the appropriate areas, such high fractions can also be found elsewhere. However – opposite to several studies – as presented in figure 9-14, pyrometamorphic areas can be extracted from multispectral remote sensing data. This could be achieved with the knowledge based as well as with the PMA approach. They are both fully appropriate, if a known area is investigated within a highly interactive analysis. Nevertheless, for the automated extraction of pyrometamorphic rock from multispectral remote sensing data, partial unmixing is not considered a good choice.

Applying the prototype spectrum of coal to three regions in far distance of the well known study sites and particularly on other continents and still retrieving extraction accuracies for coal and vegetation of 86.87 %-91.55 % and 67.33 % and 89.03 % respectively allows for the following conclusions. As long as scenes are thoroughly radiometrically preprocessed to at ground reflectance and LST prototype spectra build from a large number of standardized and averaged measurements a spectral library set up in one region is – special surfaces requested – transferable to another region. A great advantage for this study was that coal does not vary as strongly in its spectral behavior as do e.g. different plant species. The coalification process is mostly similar all over the world and hard coal spectra – when

resampled to ETM+ resolution – do not vary substantially unless heavily altered by weathering or burning.

For the vegetation fraction no distinct unmixing to a certain plant species was required but only areas of dense vegetation cover had to be extracted. A prototype spectrum showing typical vegetation features like the low reflectance in the VIS with a peak in band 2 the strong increase from red to NIR and the decrease from band 4 to 5 was sufficient to retrieve most densely vegetated pixels.

Single scene PMA could have been slightly improved using MNF transformed data and spectra. Figure 9-26 presents an MNF color composite of MNF component 1-3 for the Wuda area as well as all 6 MNF components to demonstrate the increasing noise level. Although a noise reduction in 6-band ETM+ data is not of utmost importance MNF also leads to a better representation of feature space. This partially simplifies the separation of certain surface classes.

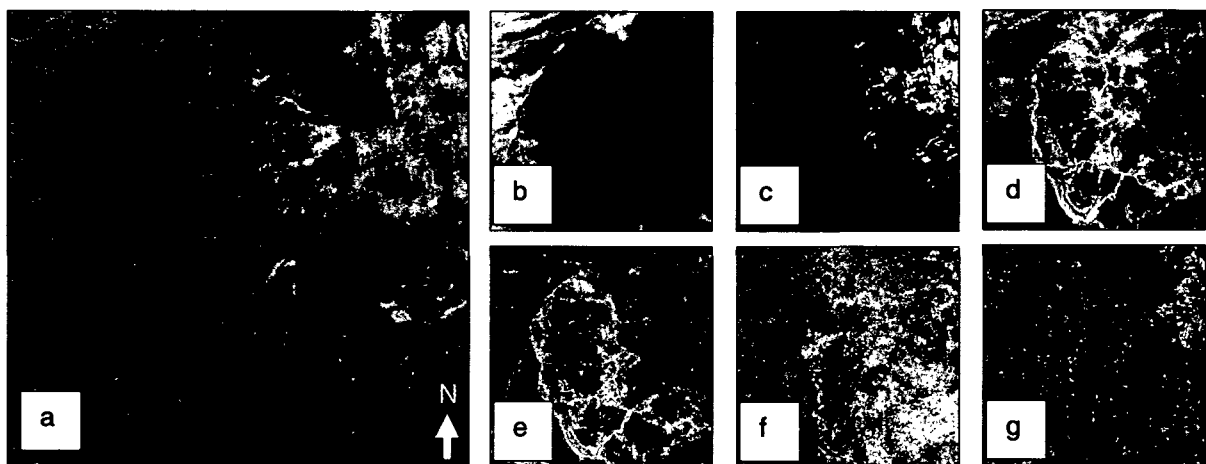


Figure 9-26: MNF transformed data. Color coded components 1-3 (a) and components 1-6 (b-g) demonstrating the increase in noise level from component 1 to 6.

Since MNF transformed PMA requires the application of MNF transformed spectral libraries for each image, the MNF transformation and inversion prior to PMA was not considered an option for a fully automatic extraction chain. However, for individual scene processing the differentiation of the two classes shadow and coal works better on MNF transformed data. When interactive processing is not a limitation it is therefore recommended, to MNF transform the data, extract and MNF transformed image endmember from a location of known ground purity and to apply PMA afterwards.

Compared to maximum likelihood approaches performed earlier in the project (KUENZER 2004b) the knowledge based as well as the PMA approach – once implemented – yielded faster results of equal or even better accuracy. In chapter 10 the comparison of the two presented approaches for automated surface extraction is addressed.

10. Coal Fire (Risk) Area Demarcation and Synergy with the Thermal Algorithm

10.1. Demarcated Coal Fire Areas and Coal Fire Risk Areas

The following 13 maps present the demarcated coal fire areas and coal fire risk areas retrieved from automated coal fire area demarcation. The maps show recent and probable future coal fire areas, which should stay under a regular investigation for:

1. Wuda coal mining syncline area, 2002 (map 4)
2. Region northeast of Wuda east of Yellow River, 2002, northern part (map 5)
3. Region east of Wuda east of Yellow River, 2002, middle part (map 6)
4. Region southeast of Wuda east of Yellow River, 2002, southern part (map 7)
5. Future coal fire risk area around Wuda, I, 2002 (map 8)
6. Future coal fire risk area around Wuda, II, 2002 (map 9)

7. Ruqigou / Gulaben coal mining area 2002 (map 10)
8. Coal mining valleys of Hulusitai and Shitanjing, 2002 (map 11)
9. Future risk areas around Ruqigou / Gulaben, 2002 (map 12)

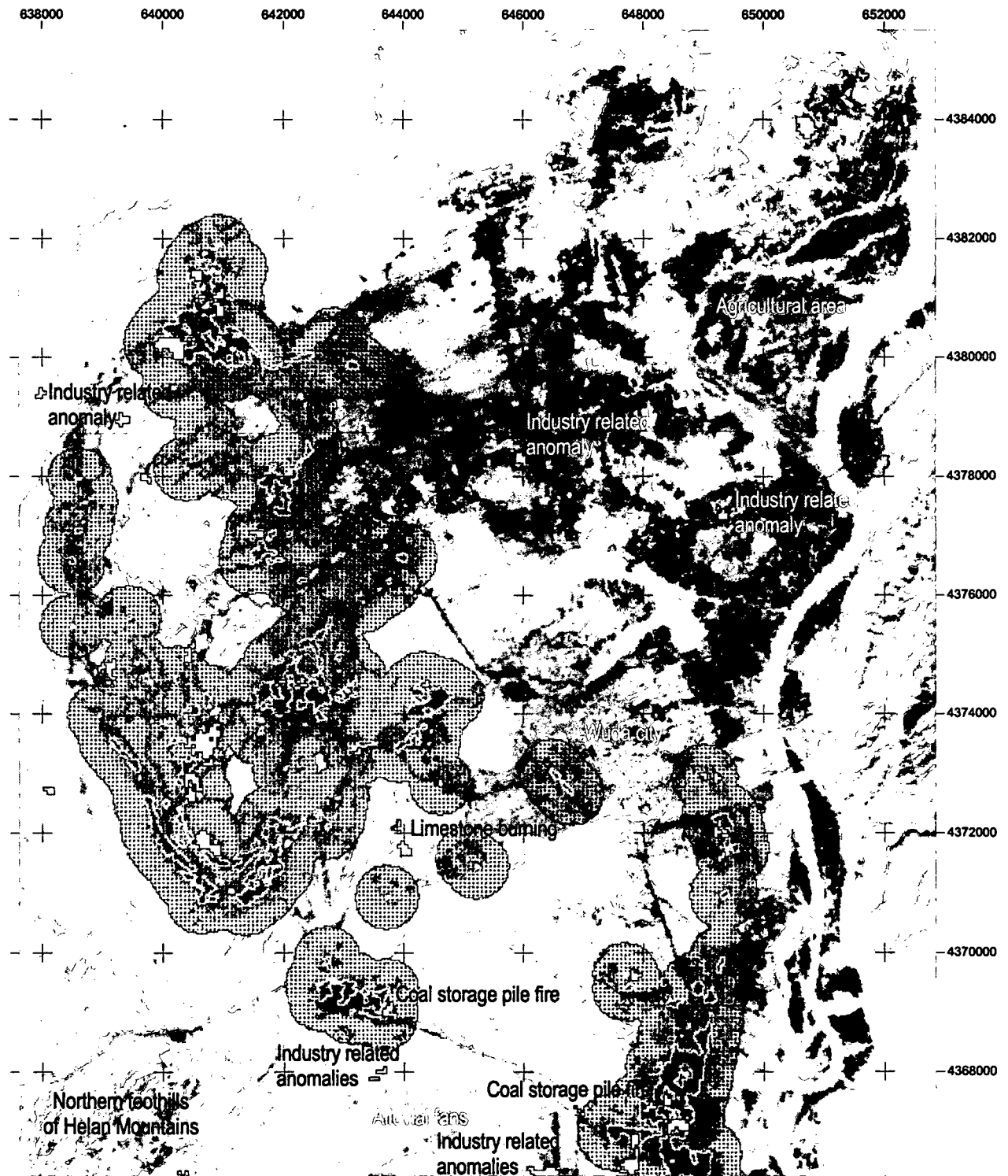
10. Leigh Creek area, southeast Australia (map 13)
11. Baotou region, north central China (map 14)
12. Jharia area, northeastern India (map 15)
13. Rāy area, 100 km southwest of Jharia, northeastern India (map 16)

The maps contain information on the setting of the region (based on the satellite data available), automatically extracted coal surfaces, automatically demarcated coal fire risk areas and automatically extracted pixels of pyrometamorphic rock. Furthermore, thermal anomalies detected by the thermal algorithm are superimposed on the maps. Thermal anomalies are differentiated for anomalies located within the demarcated coal fire area and anomalies outside these areas. All maps are presented in the UTM coordinate system. The maps designed for the Chinese regions will be supplied to the project partners and the local authorities in the provinces of Ningxia and Inner Mongolia.

In subchapter 10.2. the synergy of automated coal fire area- and coal fire risk area demarcation and thermal anomaly extraction as developed by ZHANG, J. (2004) is presented. Aspects of coal fire area demarcation, not yet mentioned within the methodic discussion in chapters 8.4. and 9.3. are discussed.

Demarcated Coal Fire Risk Areas and Thermal Anomalies for Wuda Syncline

- derived from Landsat ETM+ daytime data of 21.09.2002 and ETM+ nighttime data of 28.09.2002 -



- Thermal anomalies within demarcated coal fire risk area
- Thermal anomalies outside demarcated coal fire risk area
- Automatically demarcated coal fire risk area
- Automatically extracted coal surfaces

The map presents the region west of the coal mining town Wuda. The "ear-shaped" structural syncline, where coal is mined, is located in the center. Within this syncline 17 coal fires are known. The yellow thermal anomalies in this area result from these coal fires. However, many thermal anomalies extracted from the thermal nighttime data are not coal fire related. This is indicated in the map. Coal and coal fire risk areas were demarcated with the knowledge-based algorithm. The combination of the two methods (risk area demarcation and anomaly detection) allows for a differentiated analysis.

Layout and GIS: Claudia Künzer
 German Remote Sensing Data Center
 Environment and Geoinformation
 Germany

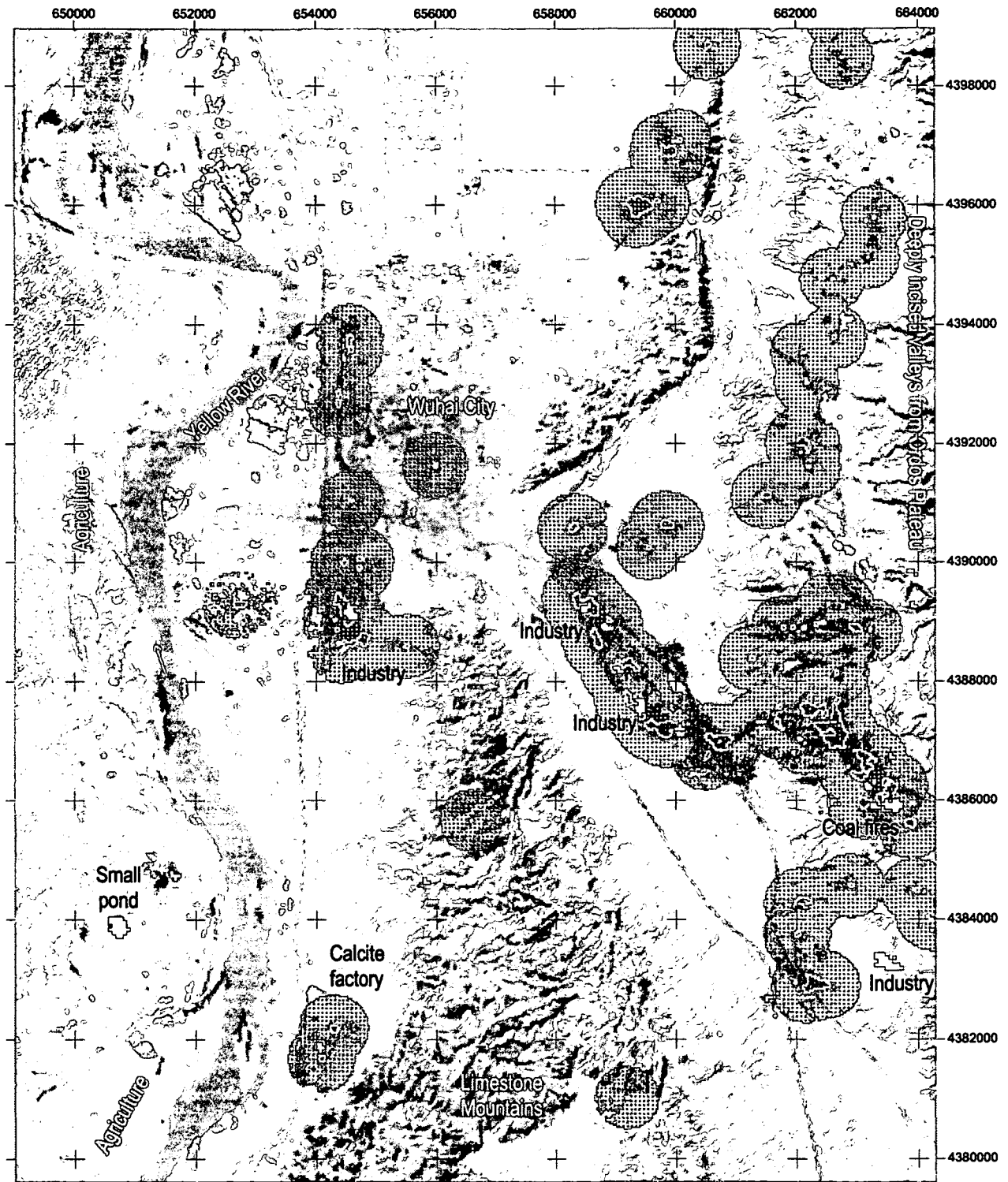
Scale 1: 100,000

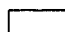
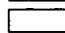


0 1 2 3 4
 km
 Projection: UTM, Zone 48 N, Datum: WGS 84



Demarcated Coal Fire Risk Areas and Thermal Anomalies for Southern Wuhai

- derived from Landsat ETM+ daytime data of 21.09.2002 and ETM+ nighttime data of 28.09.2002 -

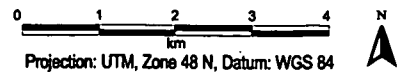


-  Thermal anomalies within demarcated coal fire risk area
-  Thermal anomalies outside demarcated coal fire risk area
-  Automatically demarcated coal fire risk area
-  Automatically extracted coal surfaces

The map presents the region south of the bigger city of Wuhai. This city is located 20 km northeast of Wuda. The north-south striking valley east of the Yellow River and east of the larger limestone complex hosts several coal industries but also many wild private mines. These are at risk for coal fire ignition. Most anomalies on this map are industry related. However, the area has to stay under close observation for spontaneous combustion - especially the northeastern corner of the map.

Layout and GIS: Claudia Künzer
 German Remote Sensing Data Center
 Environment and GeoInformation
 Germany

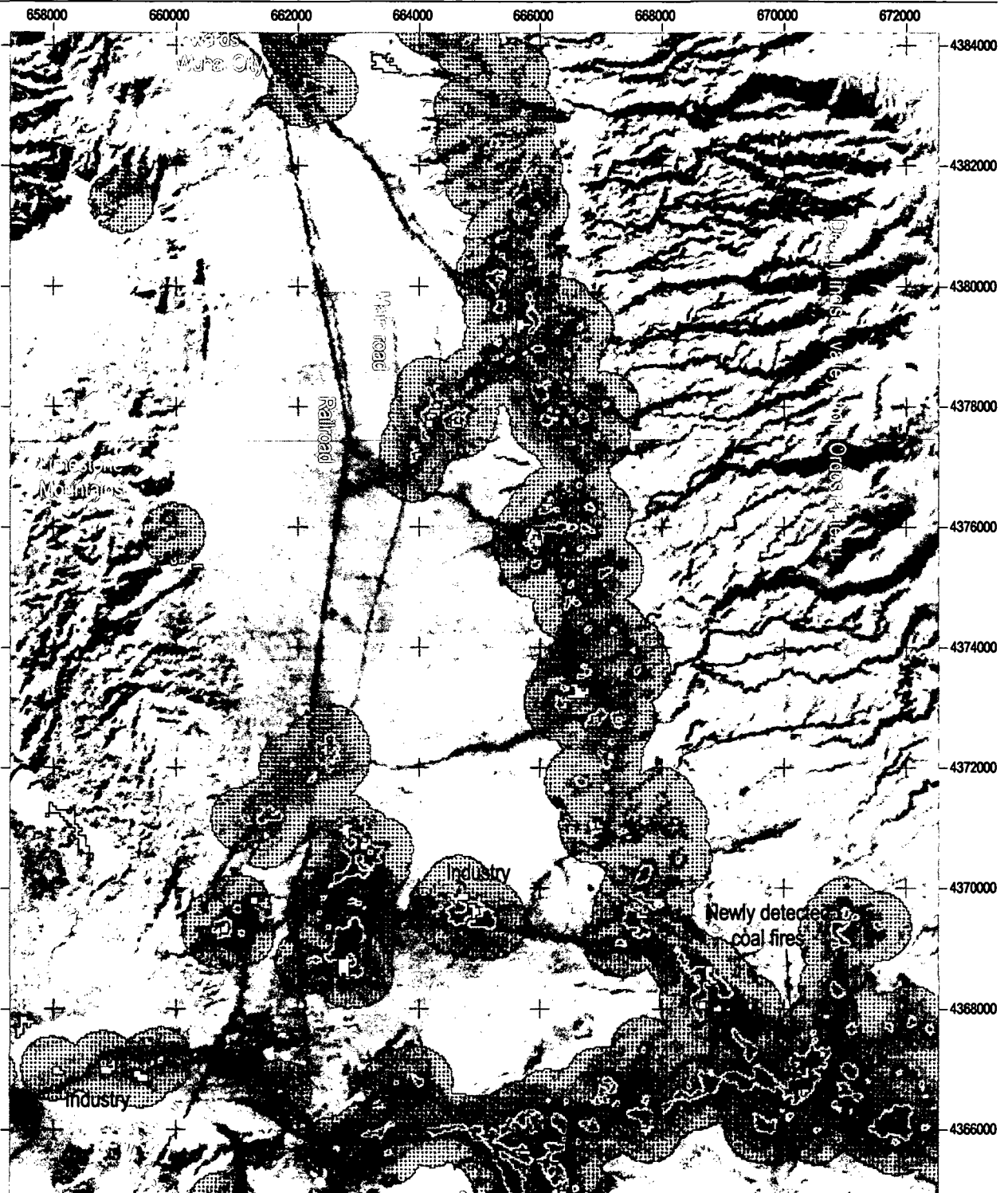
Scale 1: 100,000

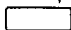
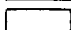

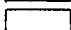


Projection: UTM, Zone 48 N, Datum: WGS 84

Demarcated Coal Fire Risak Areas and Thermal Anomalies Southeast of Wuhai

- derived from Landsat ETM+ daytime data of 21.09.2002 and ETM+ nighttime data of 28.09.2002 -



-  Thermal anomalies within demarcated coal fire risk area
-  Thermal anomalies outside demarcated coal fire risk area
-  Automatically demarcated coal fire risk area
-  Automatically extracted coal surfaces

The map presents the north-south stretching valley east of Wuda and east of the Yellow River. The river is located west of the limestone complex. Several coal seams dip to the East towards the Ordos Plateau. Here, a lot of wild and small scale mines exist. New coal fires resulting from unproperly sealed mines have already been detected in the south-eastern corner of the map. The coal accumulations and thermal anomalies close to the road are related to industry. Especially the northern and central areas in the map need to be observed closely in the future.

Layout and GIS: Claudia Künzer
 German Remote Sensing Data Center
 Environment and Geoinformation
 Germany

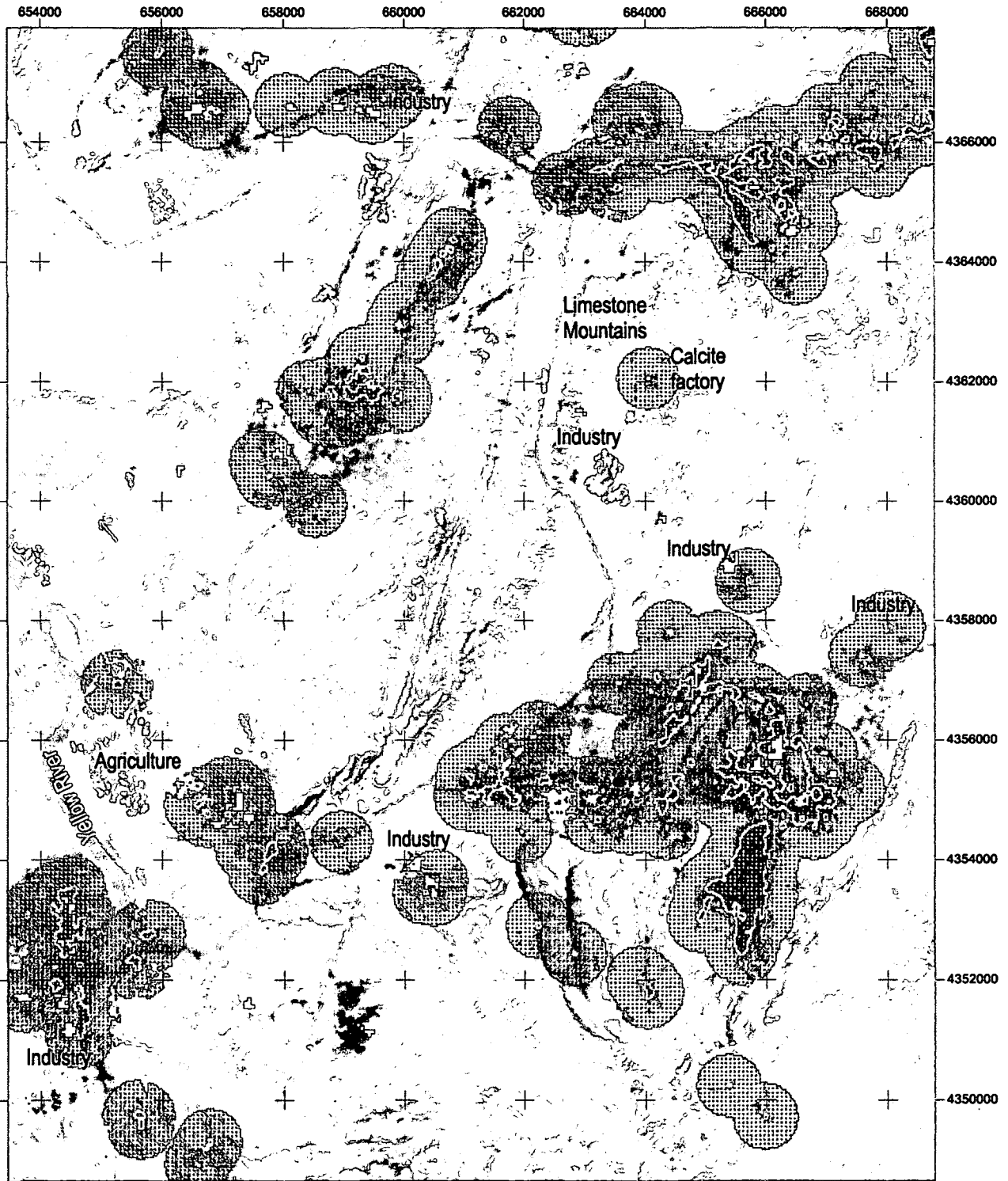
Scale 1: 100,000

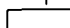
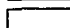


0 1 2 3 4
 km
 Projection: UTM, Zone 48 N, Datum: WGS 84



Demarcated Coal Fire Risk Areas and Thermal Anomalies far Southeast of Wuda

- derived from Landsat ETM+ daytime data of 21.09.2002 and ETM+ nighttime data of 28.09.2002 -



-  Thermal anomalies within demarcated coal fire risk area
-  Thermal anomalies outside demarcated coal fire risk area
-  Automatically demarcated coal fire risk area
-  Automatically extracted coal surfaces

All extracted coal surfaces are industry related accumulations in the form of coal waste and coal storage piles. The only exception are the coal surfaces in the far northeastern corner of the map. Thus, anomalies in this map all result from industrial activities or burning coal storage and waste piles. The region presented is located approximately 25 km southeast of Wuda. Factories and processing plants are rapidly increasing in this area. Coal cooking, washing and iron processing can be found.

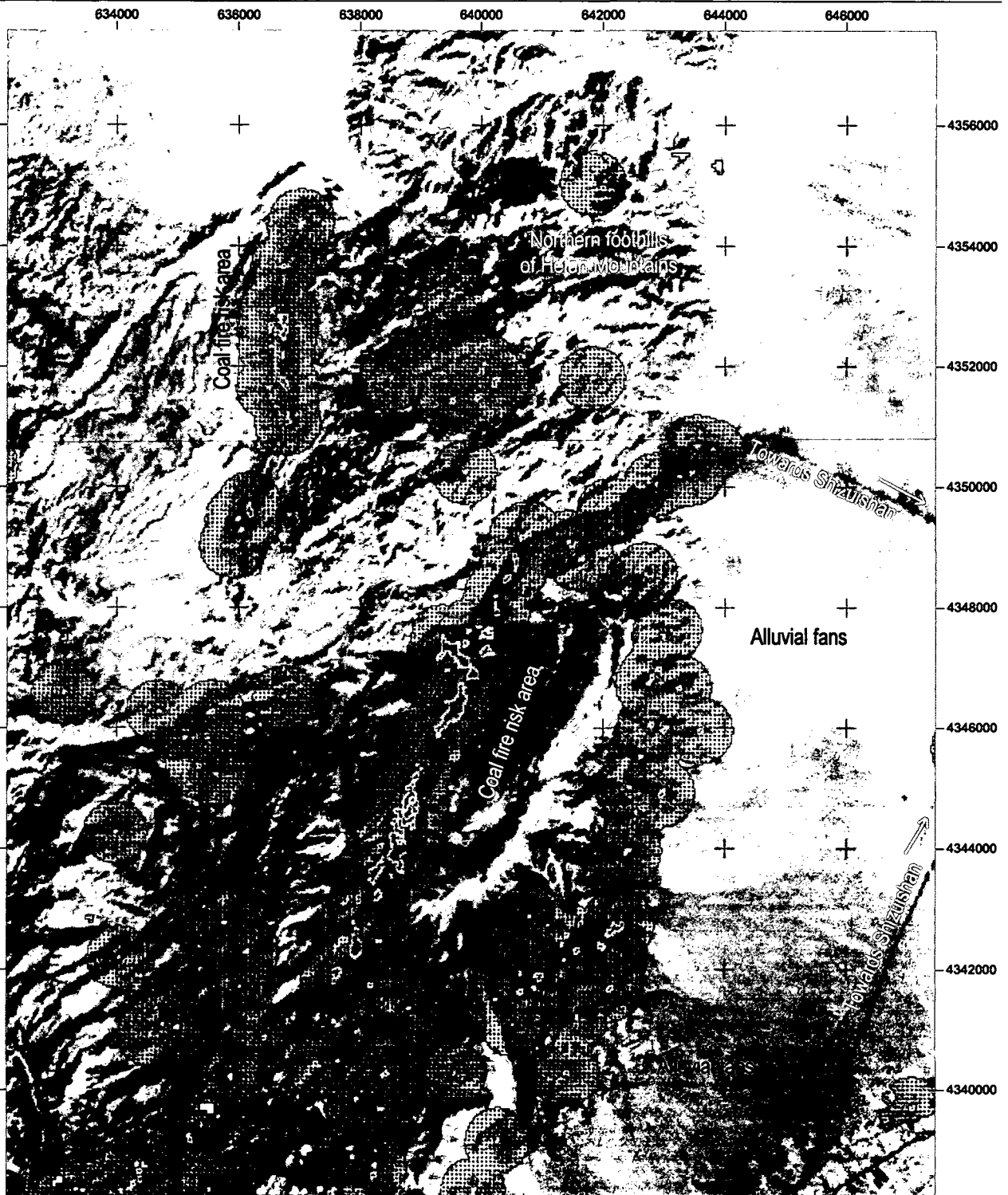
Layout and GIS: Claudia Künzer
 German Remote Sensing Data Center
 Environment and Geoinformation
 Germany


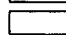

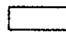
Scale 1: 100,000



Demarcated Coal Fire Risk Areas and Thermal Anomalies East of Shizuishan City

- derived from Landsat ETM+ daytime data of 21.09.2002 and ETM+ nighttime data of 28.09.2002 -



-  Thermal anomalies within demarcated coal fire risk area
-  Thermal anomalies outside demarcated coal fire risk area
-  Automatically demarcated coal fire risk area
-  Automatically extracted coal surfaces

This map presents a larger coal fire risk area approximately 30 km southwest of Wuda and 12 km east of Shizuishan City. Largest coal accumulations can be found in two valleys stretching from North to South. No thermal anomalies were extracted from the nighttime thermal data. However, these areas need to stay under close observation. It is very likely that coal fires will ignite in the valleys.

Layout and GIS: Claudia Künzler
 German Remote Sensing Data Center
 Environment and Geoinformation
 Germany

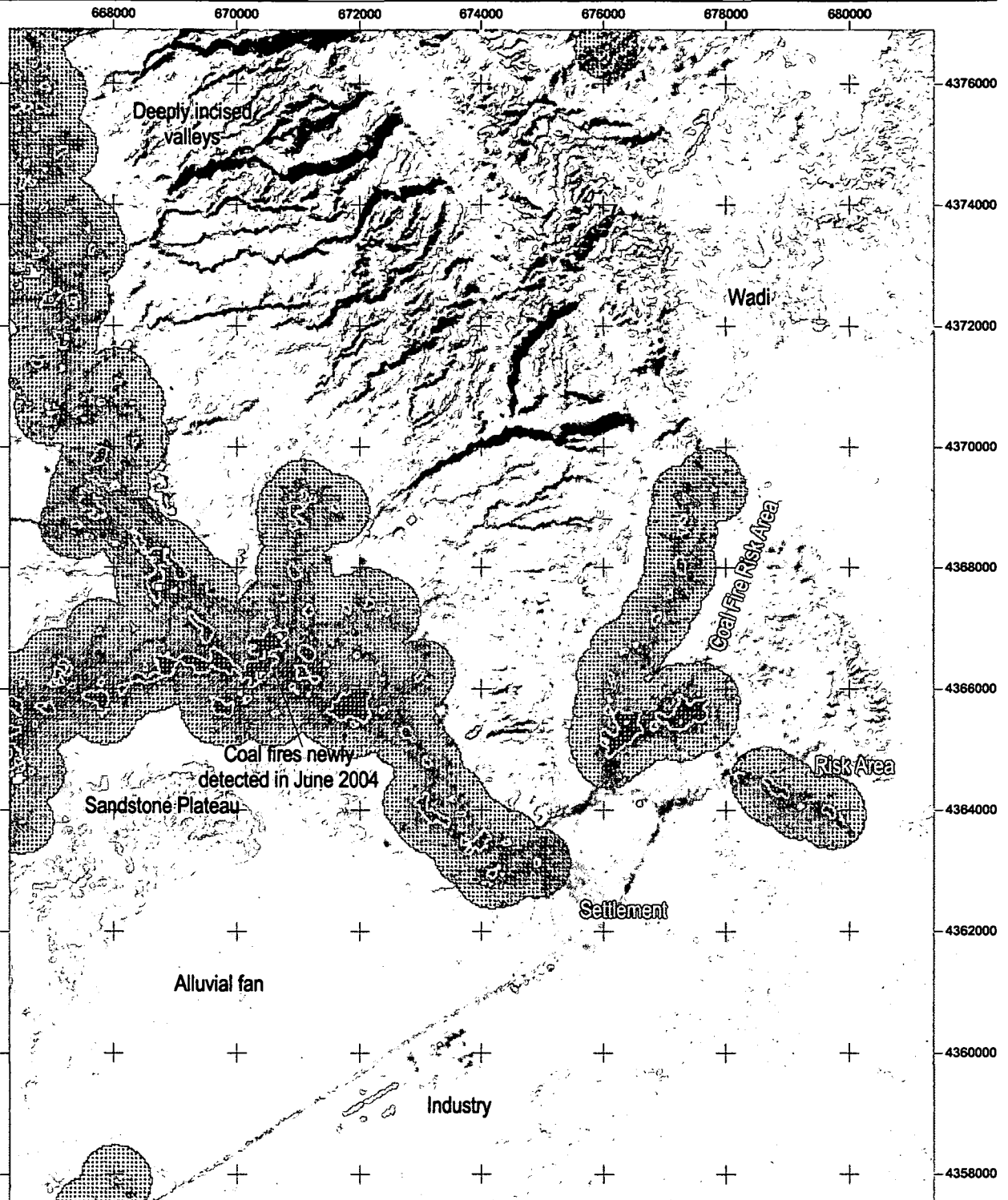
Scale 1: 100,000

0 1 2 3 4
 km
 Projection: UTM, Zone 48 N, Datum: WGS 84



Demarcated Coal Fire Risk Areas and Thermal Anomalies East of the Newly Detected Coal Fires of 2004

- derived from Landsat ETM+ daytime data of 21.09.2002 and ETM+ nighttime data of 28.09.2002 -

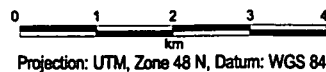


- Thermal anomalies within demarcated coal fire risk area
- Thermal anomalies outside demarcated coal fire risk area
- Automatically demarcated coal fire risk area
- Automatically extracted coal surfaces

Map 9 presents a coal fire risk area, which is located east of the coal fires, which were newly detected in June 2004. The risk area hosts several wild coal mines and is easily accessible by road. The danger of coal fire ignition is rated high. Just as the whole valley east of the Yellow River this area has to be monitored on a regular basis. Furthermore, just south of the newly detected fires some coal accumulations related to mines were extracted. These are also considered of risk for spontaneous combustion.

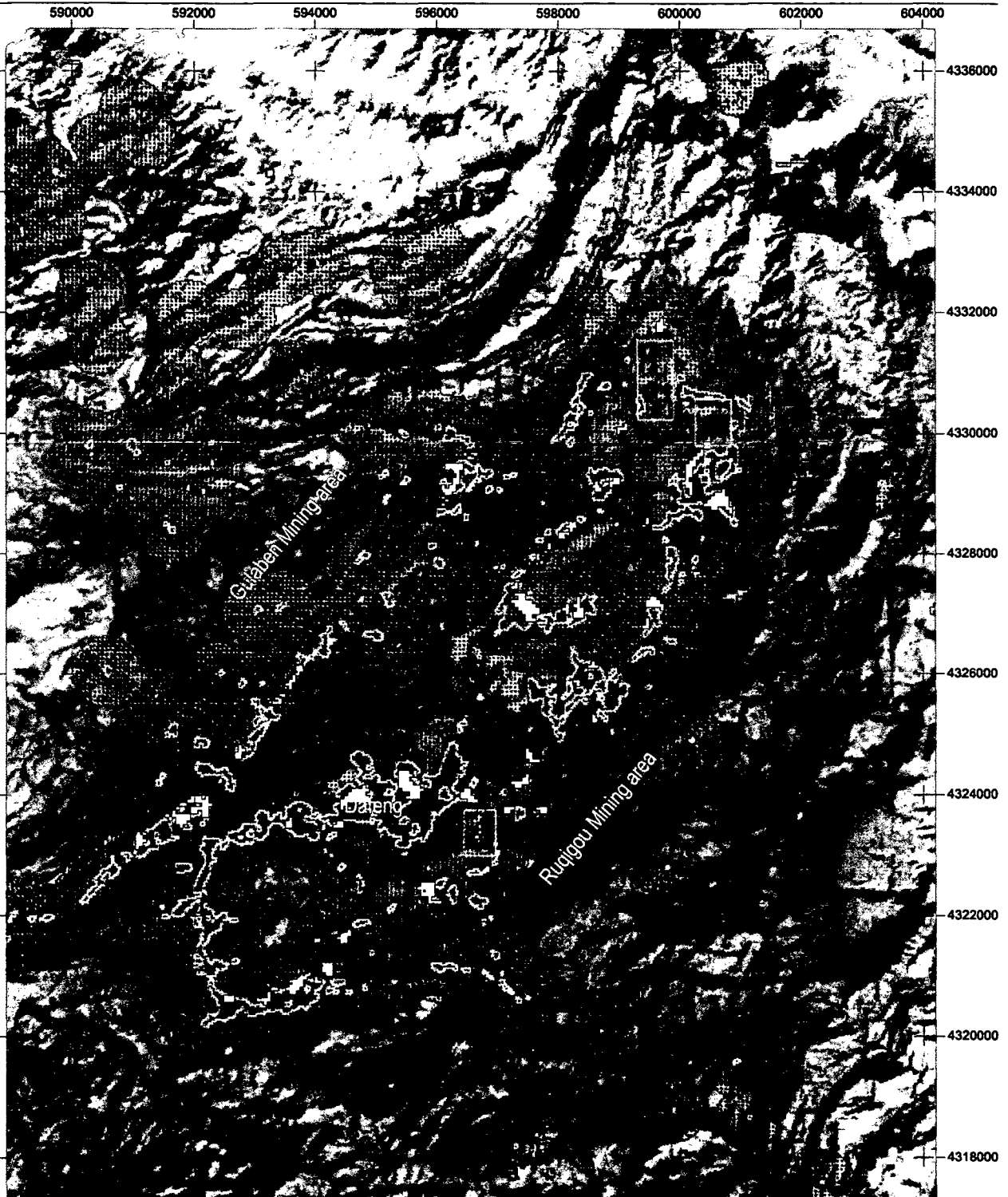
Layout and GIS: Claudia Künzer
 German Remote Sensing Data Center
 Environment and Geoinformation
 Germany

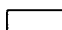
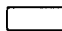
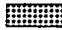
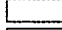

Scale 1: 100,000



Demarcated Coal Fire Risk Areas and Thermal Anomalies for Ruqigou / Gulaben Mining Area

- derived from Landsat ETM+ daytime data of 21.09.2002 and ETM+ nighttime data of 28.09.2002 -



-  Thermal anomalies within demarcated coal fire risk area
-  Thermal anomalies outside demarcated coal fire risk area
-  Automatically demarcated coal fire risk area
-  Automatically extracted coal surfaces
-  Pyrometamorphic rock

The map presents the Ruqigou / Gulaben coal mining region. Elevations in this area exceed 2000 m. All of the yellow thermal anomalies are either coal fire or industry related. Satellite pixels dominated by the spectral signature of pyrometamorphic rock were extracted and are shown in pink. Areas of their occurrence are highlighted by pink boxes. Most of the coal fires in the Ruqigou / Gulaben area are currently under extinction. Remote sensing is a good tool to observe if extinguished fires will stay extinct.

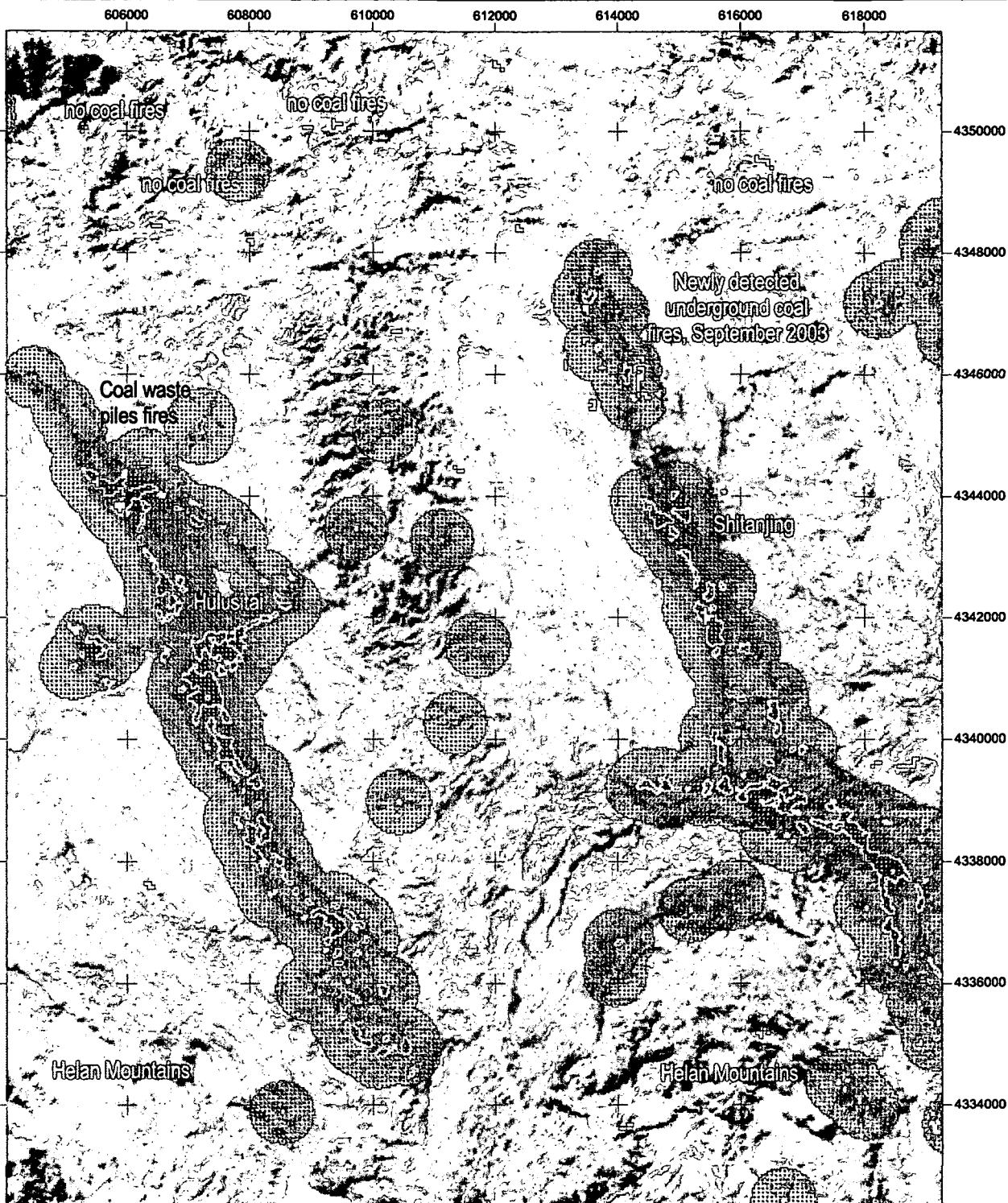
Layout and GIS: Claudia Künzer
 German Remote Sensing Data Center
 Environment and Geoinformation
 Germany

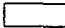



Scale 1: 100,000



Demarcated Coal Fire Risk Areas and Thermal Anomalies for the Valleys of Hulusitai and Shitanjing

- derived from Landsat ETM+ daytime data of 21.09.2002 and ETM+ nighttime data of 28.09.2002 -



-  Thermal anomalies within demarcated coal fire risk area
-  Thermal anomalies outside demarcated coal fire risk area
-  Automatically demarcated coal fire risk area
-  Automatically extracted coal surfaces

Map 11 presents the coal fire (risk) areas of the two valleys of Hulusitai and Shitanjing. In September 2003 an unknown underground coal fire and coal waste pile fires could be observed. These fires were unknown to the Wuda mining authorities located only 50 km northeast of the valleys. In both valleys coal mining once was a prospering industry. Today many mines are abandoned and were only improperly sealed. Some villages, where mine workers lived are abandoned ghost towns.

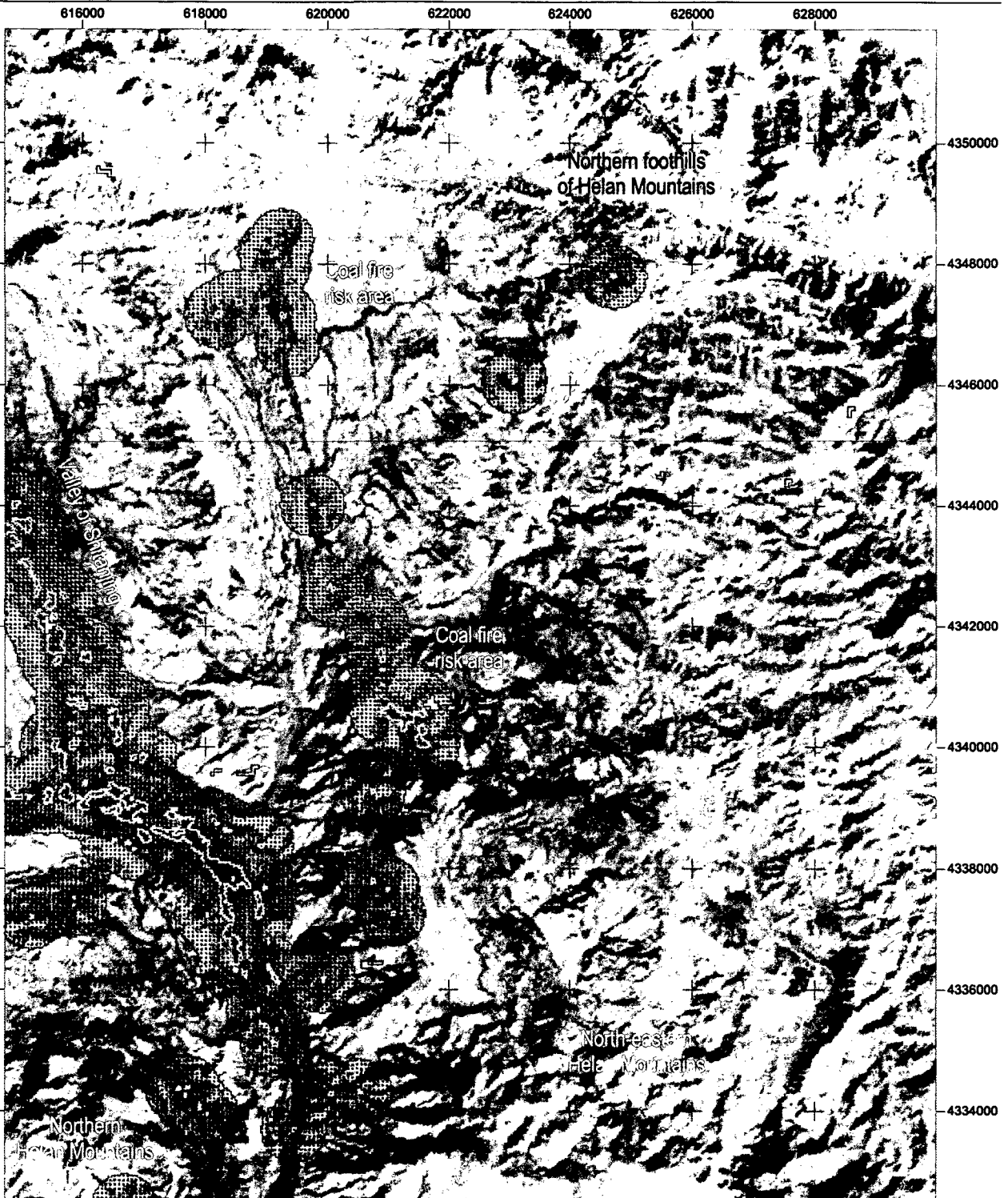
Layout and GIS: Claudia Künzer
 German Remote Sensing Data Center
 Environment and GeoInformation
 Germany

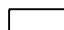
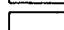

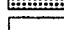
Scale 1: 100,000



Demarcated Coal Fire Risk Areas and Thermal Anomalies East of Shitanjing

- derived from Landsat ETM+ daytime data of 21.09.2002 and ETM+ nighttime data of 28.09.2002 -



-  Thermal anomalies within demarcated coal fire risk area
-  Thermal anomalies outside demarcated coal fire risk area
-  Automatically demarcated coal fire risk area
-  Automatically extracted coal surfaces

Map12 presents an area at risk of coal fires east of the valley of Shitanjing. This region has not been investigated yet. Several small coal accumulations were extracted in this area. Numerous small scale mine entries can be observed in the satellite data. The two thermal anomalies already existing could not be verified yet. However, the area needs close observation and should be monitored in the future.

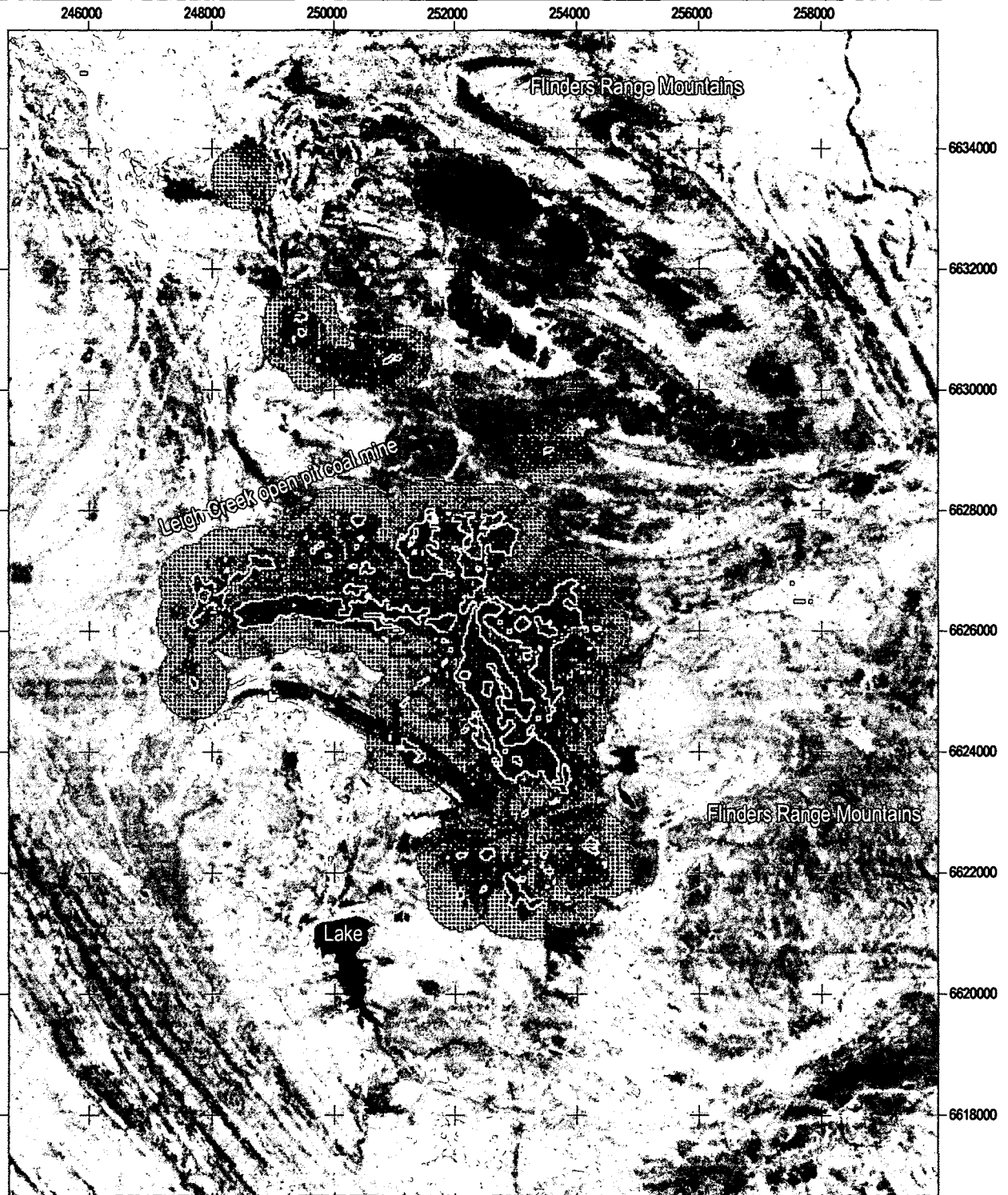
Layout and GIS: Claudia Künzer
 German Remote Sensing Data Center
 Environment and Geoinformation
 Germany

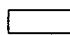
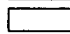

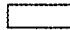
Scale 1: 100,000



Demarcated Coal Fire Risk Areas and Thermal Anomalies for Leigh Creek Mining Area

- derived from Landsat ETM+ daytime data of 15.11.2002 -

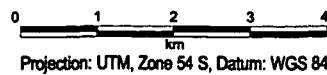


-  Thermal anomalies within demarcated coal fire risk area
-  Thermal anomalies outside demarcated coal fire risk area
-  Automatically demarcated coal fire risk area
-  Automatically extracted coal surfaces

Map 13 presents a coal fire risk area map for Leigh Creek mining region in south-western Australia. East of the mining area the Flinders ranges rise. Coal was extracted very precisely. Only 3 small shadowed areas were extracted also. It is not known if coal fires exist in this mining region. Thermal anomalies can therefore not be specified. They can also result from pure albedo influences.

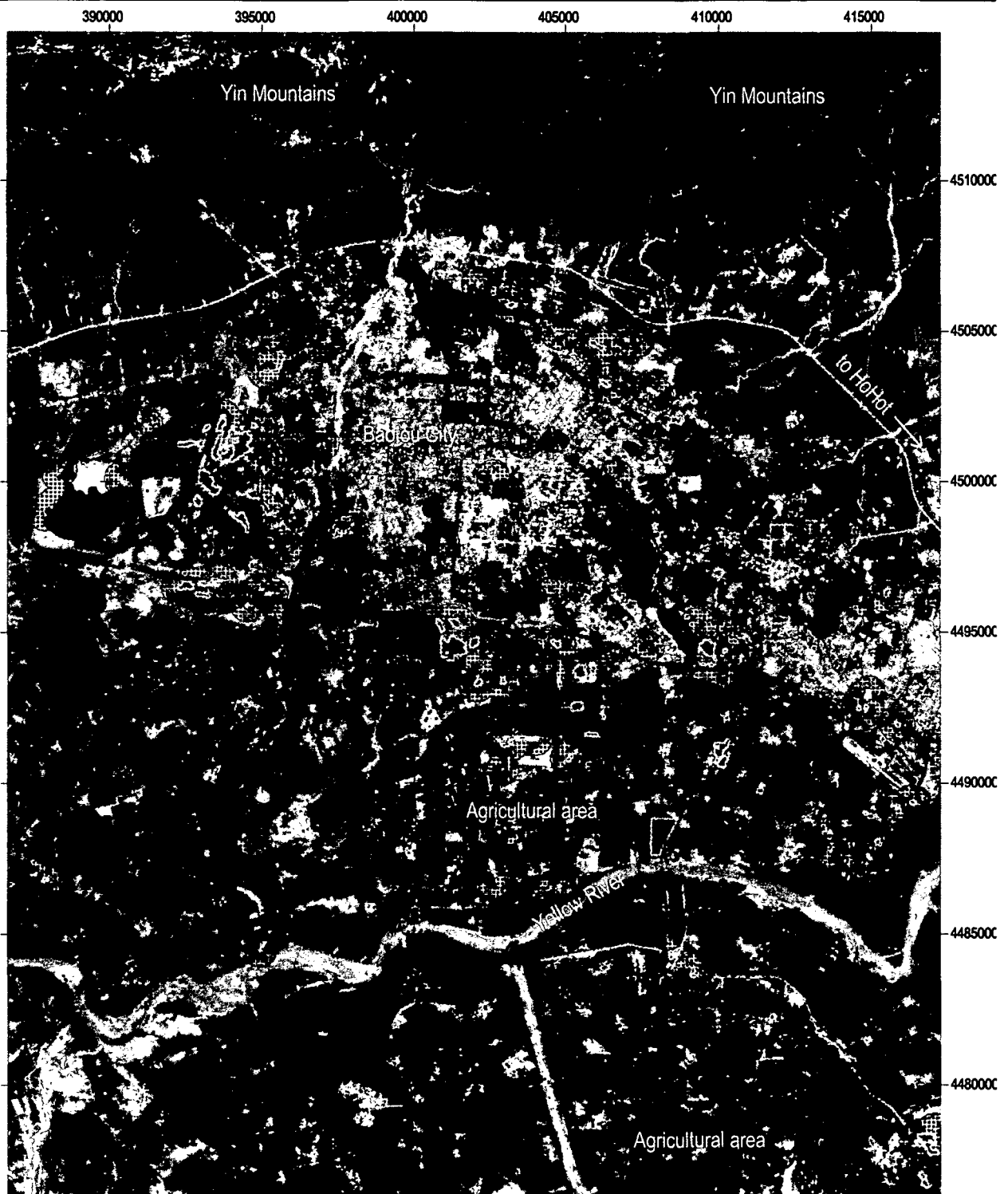
Layout and GIS: Claudia Künzer
 German Remote Sensing Data Center
 Environment and Geoinformation
 Germany

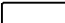
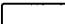

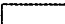
Scale 1: 100,000



Demarcated Coal Fire Risk Areas and Thermal Anomalies for the City Area of Baotou

- derived from Landsat ETM+ daytime data of 29.08.2002 -



-  Thermal anomalies within demarcated coal fire risk area
-  Thermal anomalies outside demarcated coal fire risk area
-  Automatically demarcated coal fire risk area
-  Automatically extracted coal surfaces

This map is the only one in scale 1:200,000 to provide a better overview of the region. The city of Baotou is located in the center. It lies appr. 15 km north of the Yellow River. Many coal accumulations were extracted within the city limits and along infrastructure. The thermal anomalies within demarcated coal fire risk areas are not necessarily coal waste or storage pile fires. Thermal anomalies were extracted from daytime data and may also stem from pure albedo effects.

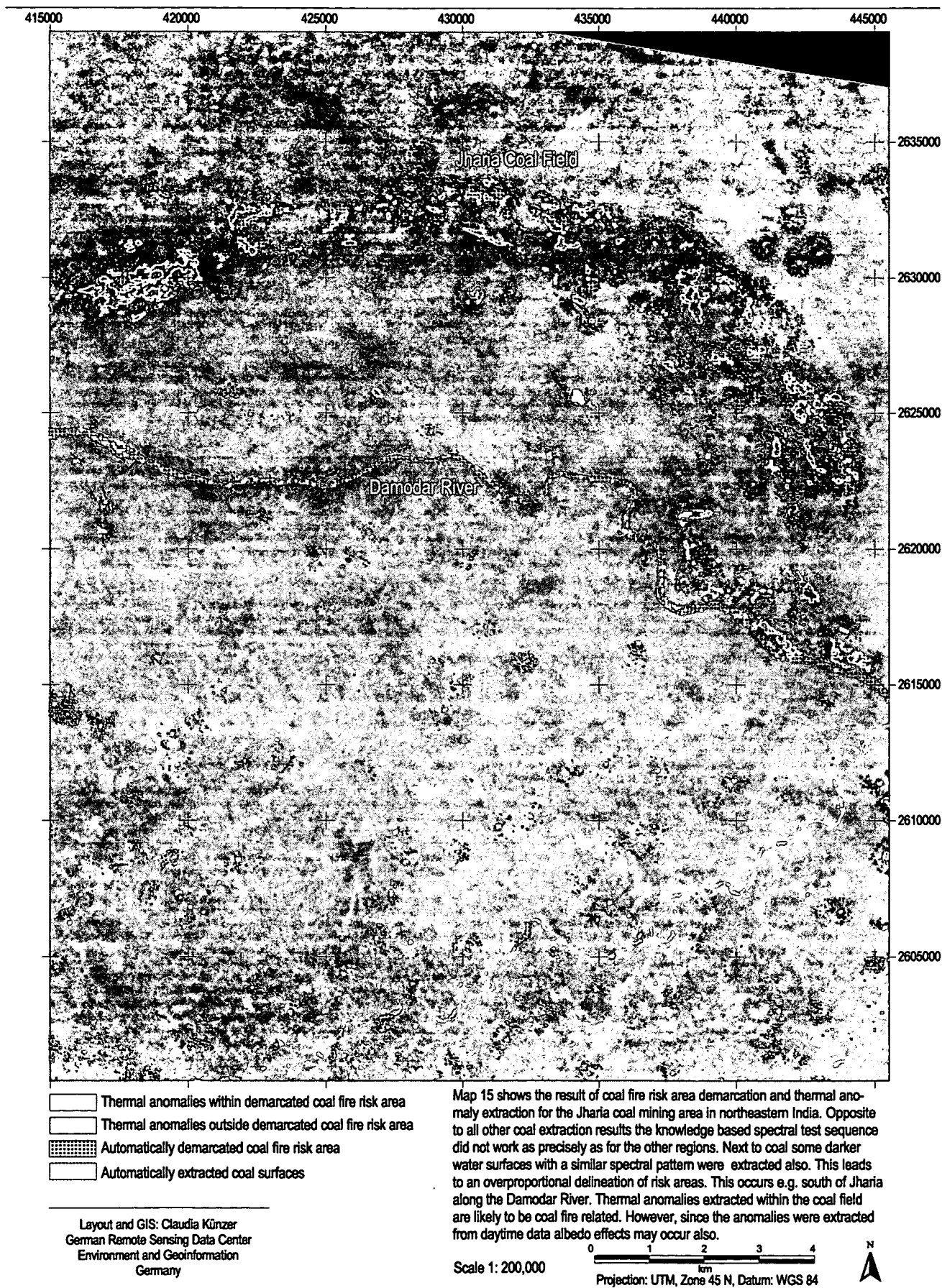
Layout and GIS: Claudia Künzer
 German Remote Sensing Data Center
 Environment and Geoinformation
 Germany

Scale 1: 200,000



Demarcated Coal Fire Risk Areas and Thermal Anomalies for the Jharia Coal Mining Area, India

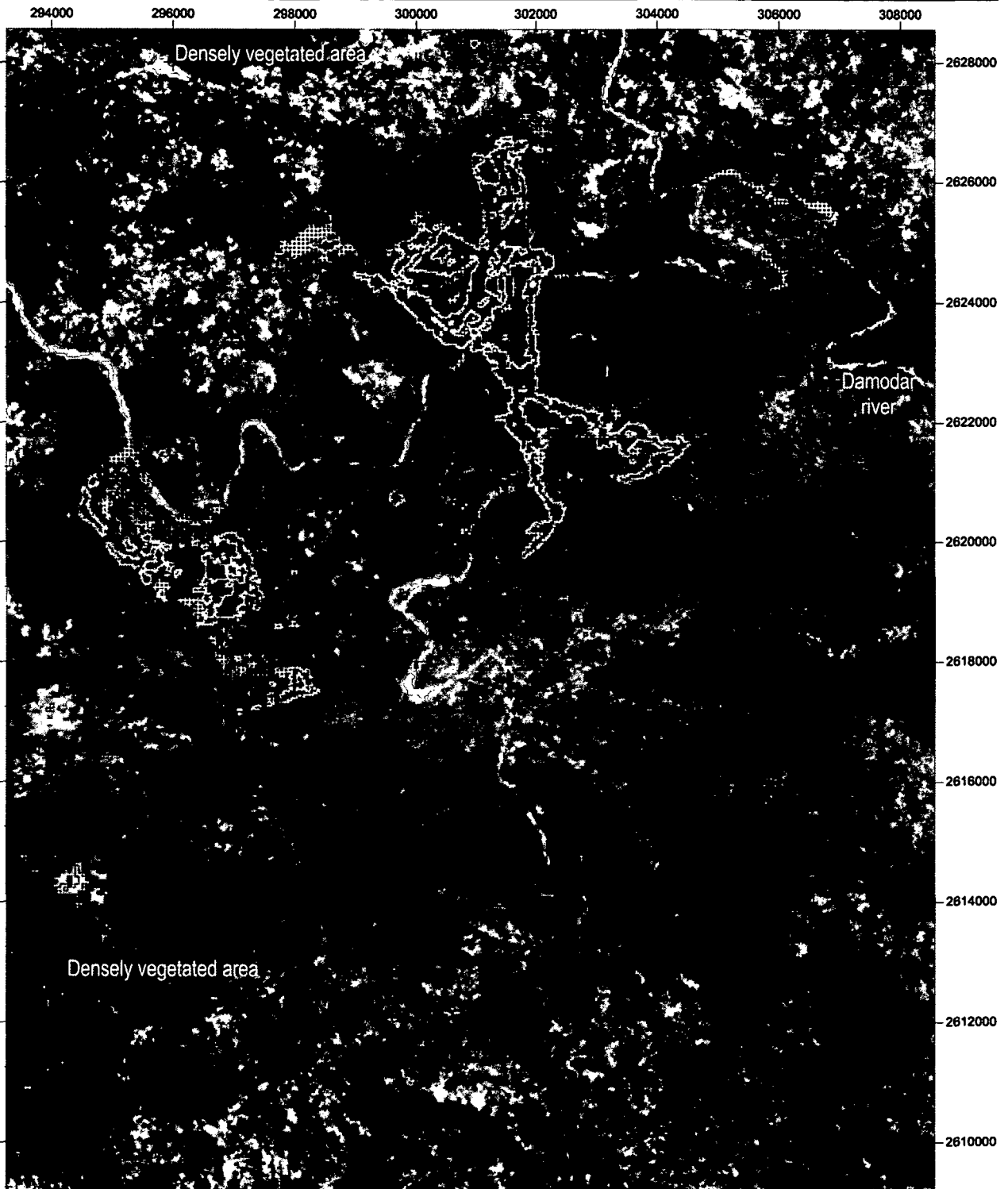
- derived from Landsat ETM+ daytime data of 02.11.2001 -

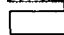
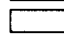

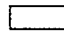


Landsat-7 ETM+ daytime data of 02.11.2001 used for coal extraction and coal fire risk area demarcation. The same data set was used for thermal anomaly extraction.

Demarcated Coal Fire Risk Areas and Thermal Anomalies for the Ray Area, India

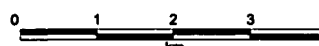

- derived from Landsat ETM+ daytime data of 02.11.2001 -



-  Thermal anomalies within demarcated coal fire risk area
-  Thermal anomalies outside demarcated coal fire risk area
-  Automatically demarcated coal fire risk area
-  Automatically extracted coal surfaces

Map 16 presents a probable coal mining area in northeastern India close to the town of Ray. This area lies in approximately 100 km distance west of the well-known Jharia coal field. It is not known if coal fires exist in this region. Thermal anomalies may also result from albedo effects. In this map the further spatial decrease of the demarcated coal fire risk area based on the exclusion of dense vegetation becomes very apparent. It is unclear what causes the large thermal anomalous cluster in the South of the map.

Layout and GIS: Claudia Künzer
 German Remote Sensing Data Center
 Environment and Geoinformation
 Germany

Scale 1: 100,000

 Projection: UTM, Zone 45 N, Datum: WGS 84


10.2. Synergy with the Thermal Algorithm

The success of the combination of the multispectral feature extraction algorithms for coal fire area demarcation presented here with the thermal anomaly extraction algorithm developed by ZHANG, J. (2004) could be proven, when 6 new coal fires could be detected from remote sensing data exclusively in 2003. They were validated in the field in September 2003. Furthermore, a second formerly unknown and new coal fire, which was only suspected based on the information extracted from remote sensing data exclusively (3 thermal anomalies located within delineated risk area) could be verified in the region east of Wuda and east of the Yellow River during the field campaign in June 2004.

The algorithm for automated thermal anomaly extraction from the thermal bands uses raw satellite data (DN values) as input for sub-image statistical analysis. Within a moving window of varying size the histogram for these subsets of the scene are investigated concerning the occurrence of thermal anomalous pixels. Image histogram statistics of coal fires were studied in very detail from different known coal fire areas. The average statistical "behavior" of coal fires within thermal images was determined. Specific features within the subset histograms (first turning point after the main maximum) could be defined as thresholds allowing the separation of thermally anomalous pixels from background pixels.

Due to the concept of a moving window, each pixel within the scene is sampled several times. Depending on how often a pixel is regarded as thermally anomalous, it is declared as a thermal anomaly. The advantage of this approach is that contrary to an overall threshold definition regional thermal anomalies will be extracted. The thermal anomalous pixels are then clustered based on an 8-neighbourhood. These thermal anomalous clusters are numbered and statistically investigated for their minimum-, maximum- and mean DN, their standard deviations and their spatial coverage. For example, coal fire areas do not exceed a certain size. If the algorithm picks out a thermally anomalous cluster of several square kilometers it is probably a sun illuminated slope. Warm water surfaces can be excluded based on the cluster's temperature variance. While water surfaces show a very low temperature variance, coal fire clusters are characterized by high variances.

This way, the final output image only contains thermal anomalies of small size, having a reasonable chance of being coal fires. Nevertheless, automated statistical analysis of thermal anomalies also leads to the extraction of anomalous pixels not related to coal fires. These cannot necessarily be distinguished from a coal fire anomaly. Such anomalies are smaller sun illuminated surfaces, which pass the areal threshold mentioned above, solar illumination effects of small extent even occurring in night time data, thermal anomalies resulting from the heating of houses, industry, the burning of agricultural fields or garbage, limestone burning or even forest or grassland fires. The demarcated coal fire (risk) areas can serve as a spatial limitation to exclude many of these thermal anomalies not stemming from coal fire influence.

The combination of the information automatically extracted from multispectral as well as thermal data can support the demarcation of areas with a high potential for coal fire occurrence. Within a subset of Landsat-7 ETM+ scene path 129, row 33 of 21.09.2002 several areas for coal fire occurrence were extracted with the multispectral approach. The northernmost area close to the city of Wuda hosts several coal fires already well known. The same applies for the westernmost area Ruqigou / Gulaben.

Both areas are well studied and also contain several well known coal fires. Areas never investigated so far are the north south striking coal outcrops east of the Yellow River and the coal outcrops in the two valleys of Hulusitai and Shitanjing. These valleys run parallel to each other from Northwest to Southeast, approximately 50km southwest of Wuda. The demarcated coal fire risk areas contain several thermal anomalies. Such areas, where some thermal anomalies were located within the automatically extracted coal fire (risk) areas, were checked during the recent field campaigns in 2003 and 2004.

On September 13th 2003 a field trip was organized to the very remote area shown in figure 10-1. The coal fire fighting team of Wuda, joining on the survey, did not know about the area visited beforehand, nor did they have any information on possible coal fires in that region. Once arrived in the area, which is very sparsely settled and only accessible via dirt roads, information from the local inhabitants revealed that the region once was a prospering coal mining area. However, production has decreased drastically due to financial problems. With the help of GPS, the thermal anomalies, extracted from the satellite data were located within an area of very rugged terrain of former coal waste piles, abandoned mines and heavily disturbed coal outcrops. Five of the thermal anomalies proved to be coal fires in an actual coal seam, while the other anomalies resulted from fires in a coal waste pile. Therefore, all six anomalies could be verified as coal fire anomalies. In this coal fire area, the fire temperatures ranged from 170 to 340 °C.

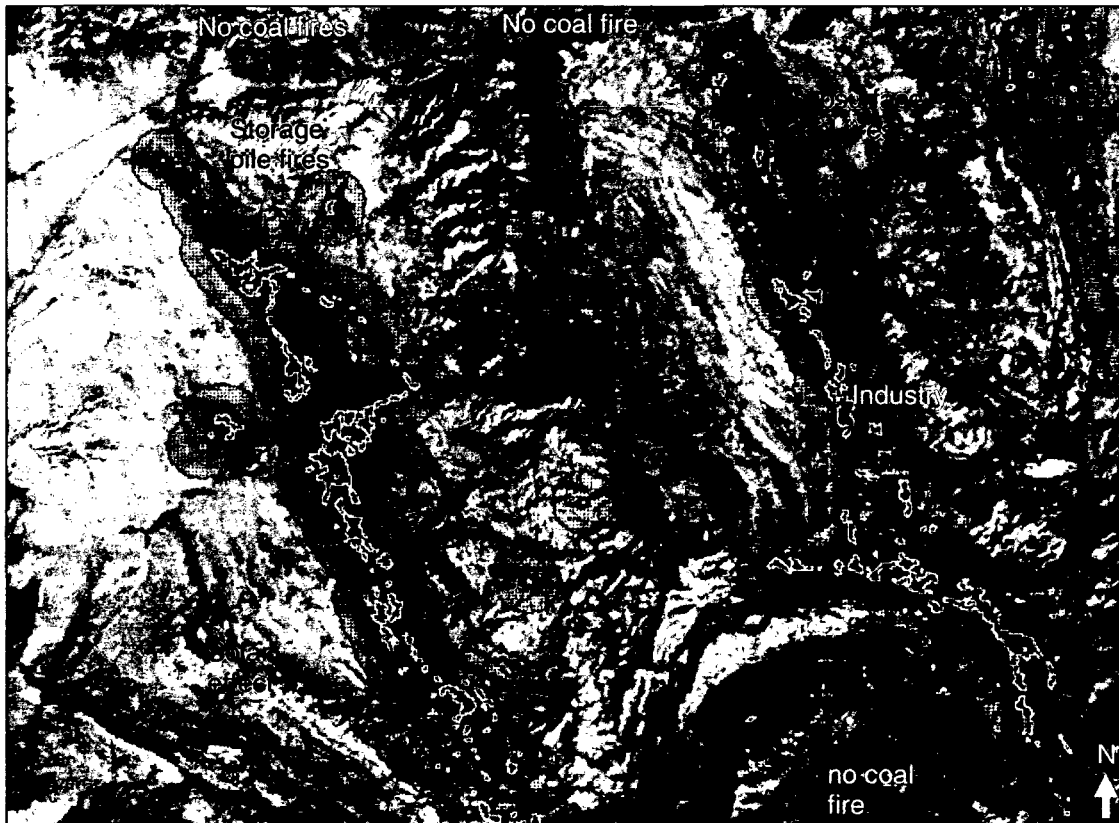


Figure 10-1: Newly detected coal fires based on coal fire (risk) area demarcation and thermal anomaly detection in two parallel valleys 50 km southwest of Wuda. The coal fires were not known outside the local community beforehand. Extracted coal is displayed as a superimposed vector layer in light blue, thermal anomalies in yellow (located within the demarcated area), and green (located outside the demarcated area), demarcated coal fire (risk) areas in red, center coordinate: 611355E, 4342156N, UTM, Z48N.

On June 18th 2004 a field trip was undertaken to the eastern side of the Yellow River, approximately 25 km southeast of Wuda. Based on remote sensing data analysis exclusively, also this area showed indication to host at least one coal fire. The thermal anomalies extracted and located within the demarcated coal fire areas proved to be an underground coal seam fire the direct local inhabitants new about. However, it was unknown to the authorities of Wuda and Wuhai city (SUN, Y. 2004). According to a local worker the fire had developed in wild private coal mines, which were abandoned and improperly sealed. Though the local people tried to seal these mines with sand and loess just recently, it is difficult to control the fire, which now has been burning for 2 years and is spreading rapidly.

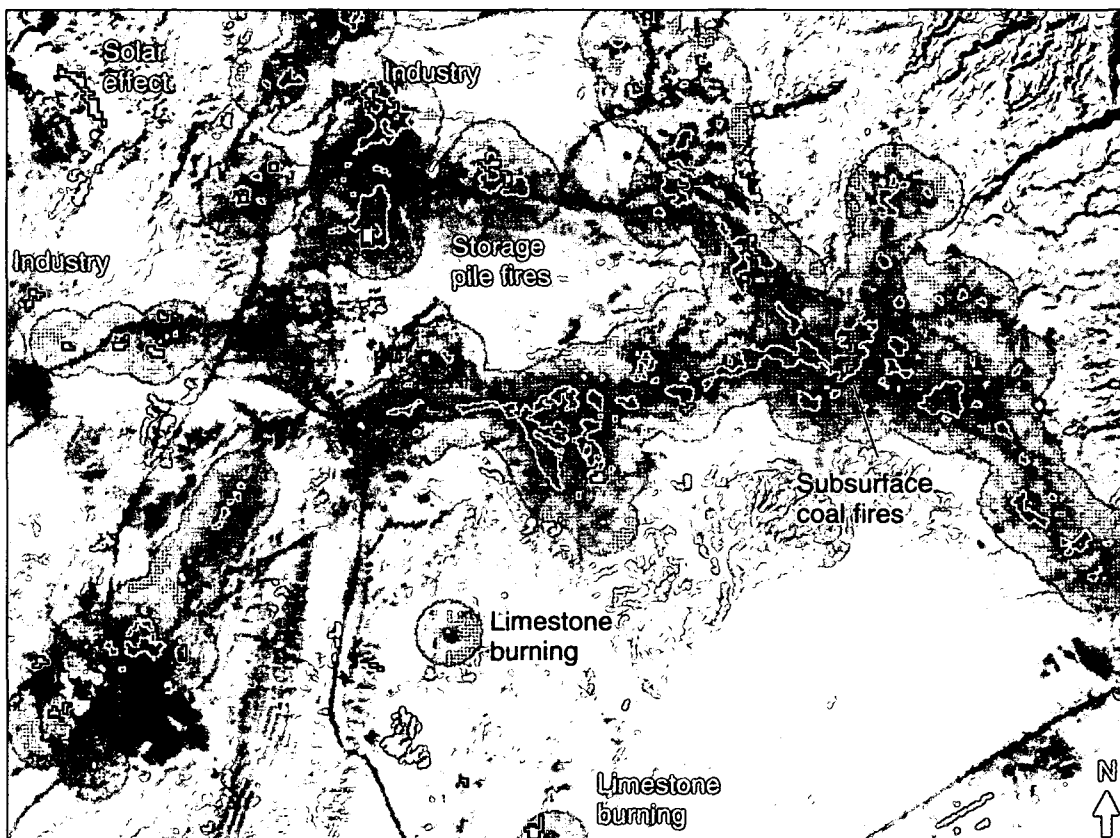


Figure 10-2: Newly detected coal fires based on coal fire (risk) area demarcation and thermal anomaly detection 25 km southeast of Wuda. The coal fires were not known except to few local inhabitants. Extracted coal is displayed as a superimposed polygon vector layer in light blue, thermal anomalies in yellow (inside the demarcated area) and green (outside the demarcated area), the demarcated coal fire (risk) areas are superimposed in red. Center coordinate: 669169E, 4365414N, UTM, Z48N

In the area presented above active mining is still ongoing. Coal fire fighting is undertaken, trying to separate the burning part of the coal seam from the unaffected part through a trench. However, to date the fire is not under control and spreads along dip and strike direction. According to Sun, Y. (2004) without the remote sensing analysis the coal fire would have remained unknown to anyone but the local workers. In the context of coal fire extinguishing actions planned for the broader Wuda area in the following year, this area can at least be included into extinguishing strategies. Figures 10-3 a and b illustrate the situation in this area. The eastern side of the Yellow River east of Wuda is considered as an area very prone to coal fires. It is expected that more coal fires will spread within the wild mining operations in the future.

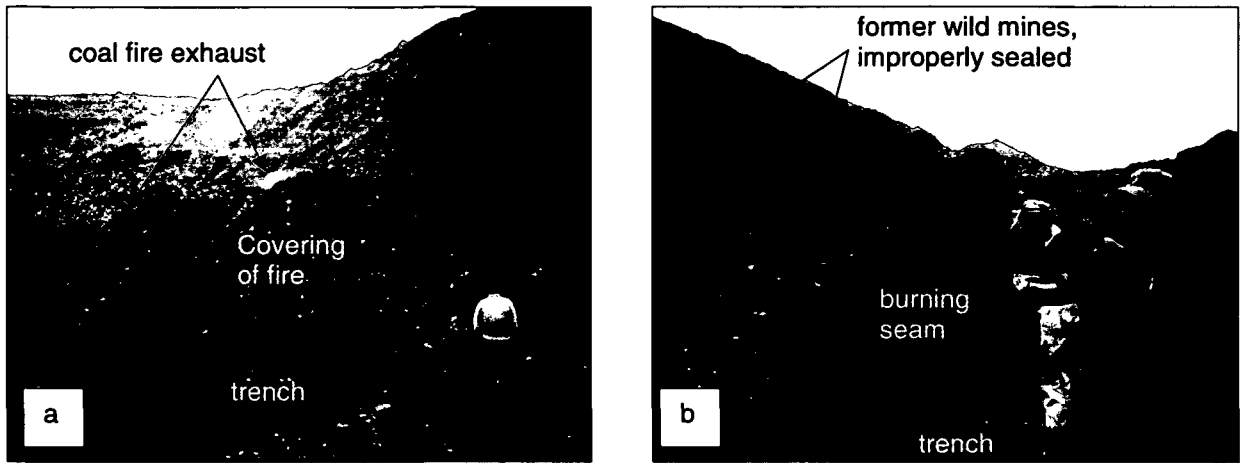


Figure 10-3 a,b: Newly detected coal fires based on coal fire (risk) area demarcation and thermal anomaly detection 25 km southeast of Wuda. Note the coal fire related smoke in figure 10-3 a and the improperly sealed former private mines in figure 10-3 b. The trench is excavated to prevent the spreading of the fire. Photos: a: C. KUENZER. b: J. ZHANG, June 2004

To quantify the synergetic effects of the thermal anomaly detection algorithm and the coal fire (risk) area demarcation algorithm, it is investigated, how many false alarm anomalies can be rejected through coal fire (risk) area demarcation.

Table 10-1: Coal fire area demarcation supporting the exclusion of false alarms: knowledge based demarcation

	Anomalies in # pixels extracted by thermal algorithm	Anomalies in # pixels rejected by coal fire risk area algorithm	Anomalous area before coal fire area demarcation [km ²]	Anomalous area after coal fire area demarcation [km ²]
226 / 211 ETM+ night 28.09.2002	451	243 (500m) 211 (1000m)	14.49	6.77 (500m) 7.54 (1000m)
129 / 033 ETM+ day 21.09.2002	10,911	9449 (500m) 8884 (1000m)	61.46	10.77 (500m) 13.22 (1000m)
129 / 033 ETM+ day 20.09.1987	9,817	9,078 (500m) 8593 (1000m)	100.41	8.48 (500m) 11.22 (1000m)
140 / 044 ETM+ day 02.11.2001	6,067	4533 (500m)	42.84	14.92 (500m)
128 / 032 ETM+ day 21.08.2002	15,653	15036 (500m)	83.90	3.90 (500m)
098 / 081 ETM+ day 15.11.2002	1334	1300 (500 m)	7.25	0.14 (500 m)

Table 10-1 and table 10-2 demonstrate how many pixels were extracted as thermally anomalous from ETM+ nighttime and daytime data, how many of these thermally anomalous pixels were located outside the demarcated coal fire (risk) areas and how large the overall coal fire risk area is with regard to the size of the full original scene. While table 10-1 focuses on the improvement of thermal outputs applying the knowledge based spectral test sequence for coal fire area demarcation, table 10-2 presents the results achieved with PMA analyses and demarcation.

The thermal algorithm was applied on the nighttime scene of September 28th 2002. 451 thermal anomalies were extracted for this scene and the overall thermal anomalous area covers 14.49 km². Applying the knowledge based coal fire demarcation algorithm presented in this thesis (chapter 8), with a 500 m delineation radius 243 of the 451 thermal anomalous clusters are rejected as probable coal fire anomalies, while 208 clusters remain. With a delineation radius of 1000m 211 anomalies are rejected. The spatial coverage of remaining coal fire related anomalies is 6.77 km² and 7.56 km² respectively. The number and area of thermal anomalies regarded as probable coal fire related anomalies by the algorithm of ZHANG (2004) can be reduced for about 50 % by the knowledge based coal fire area demarcation algorithm.

In the daytime scene covering Wuda and Ruqigou (129/033 from 21.09.2002) 10911 anomalies were extracted by the thermal algorithm. Coal fire risk area demarcation with a delineation radius of 500m rejects 9449 of these anomalies. With a 1000m radius 8884 anomalies are rejected. The area considered as coal fire related anomalies can therefore be reduced from 61.46km² to 10.77km² (500m) and 13.22 (1000m) respectively. Between 87% and 81% (500m, 1000m) of the anomalies can be rejected. The thermal anomalous area is reduced for 83%.

From the daytime scene 129/33 covering Wuda and Ruqigou acquired on 20.09.1987 a total of 9817 thermal anomalies was detected. 9078 of these anomalies can be rejected when coal fire area demarcation is performed with a 500 m delineation radius. 8593 anomalies are considered false alarms if a 1000 m radius is applied. The thermal anomalous area can be reduced from over 100 km² to 8.48 km² and 11.22 km² respectively. Thus over 90 % of the thermal anomalies do not need to be observed with regard to coal fire analyses.

From the daytime scene from India 6067 thermally anomalous clusters were extracted applying the thermal algorithm. 4433 anomalies are rejected by the coal fire area demarcation algorithm. The thermally anomalous area is reduced from 42.84 km² to 14.92 km². This equals a reduction in anomalies for 70 % and a reduction of the thermal anomalous area for 65 %.

In the daytime scene of Baotou 15653 thermal anomalies were extracted as probable coal fire anomalies. The overall thermal anomalous area the algorithm considers as coal fire anomalies is 83.9 km². 15036 of the 15653 anomalies are rejected by coal fire area demarcation. The thermally anomalous area is reduced from 83.90km² to 3.09km².

For the scene from Australia thermal anomalies 1334 were extracted fo which 1300 were rejected. The thermal anomalous area within the demarcated coal fire risk area zone cover 0.14km².

Table 10-2: Coal fire area demarcation supporting the exclusion of false alarms: PMA based demarcation

	Anomalies in # pixels extracted by thermal algorithm	Anomalies in # pixels rejected by coal fire risk area algorithm	Anomalous area before coal fire area demarcation [km ²]	Anomalous area after coal fire area demarcation [km ²]
226 / 211 ETM+ night 28.09.2002	451	254 (500 m) 225 (1000 m)	14.49	7.09 (500m) 8.28 (1000m)
129 / 033 ETM+ day 21.09.2002	10,911	9888 (500 m) 9569 (1000 m)	61.46	8.61 (500 m) 10.09 (1000 m)
129 / 033 ETM+ day 20.09.1987	9,817	9353 (500 m) 9034 (1000 m)	100.41	7.50 (500 m) 9.29 (1000 m)
140 / 044 ETM+ day 02.11.2001	6,067	4834 (500 m)	42.84	7.12 (500 m)
128 / 032 ETM+ day 21.08.2002	15,653	8380 (500 m)	83.90	42.80 (500 m)
098 / 081 ETM+ day 15.11.2002	1334	1296 (500m)	7.25	0.16 (500m)

Applying the PMA based coal fire demarcation algorithm presented in this thesis (chapter 9), 254 (500 m) and 225 (1000 m) of the 451 thermal anomalous clusters from the 129/33 nighttime scene are rejected as probable coal fire anomalies. The spatial coverage of coal fire related anomalies is reduced from 14.49 km² to 7.09 km² and 8.28 km² respectively. As for the knowledge based algorithm, this reduces the number of anomalies and their spatial extent for about 50%.

For the daytime scene covering Wuda and Ruqigou (129/033 from 21.09.2002) with PMA based demarcation a reduction of anomalies exceeding 80% is achieved. This coincides well with the results from knowledge based coal fire area demarcation.

In the daytime scene covering Wuda and Ruqigou (129/033) on 20.09.1987 overall 9817 anomalous clusters are extracted. They can be reduced for over 90 % applying coal fire area demarcation. The thermally anomalous area to investigate decreases from over 100 km² to 7.5 km² and 9.29 km² respectively – depending on the delineation radius.

For the scene from India 4838 of the 6067 anomalies can be rejected as coal fire related thermal anomalies. The thermally anomalous area to be investigated is covers 7.12 km². A reduction for over 80% could thus be achieved.

For the scene from Baotou with a 500 m delineation radius 8380 of the 15653 extracted thermal anomalies from daytimes data can be rejected with PMA based coal fire area demarcation. The

thermally anomalous area to be investigated is thus reduced from 83.90 km² to 42.80 km². This equals an reduction of approximately 50%. This reduction is lower compared to other daytime data sets, where a reduction of 90% can be achieved. It can be explained with the fact that for the scene of Baotou next to coal some other surfaces – like dark asphalt – were extracted also. The delineation zone is very large. Thus, only a smaller percentage of the thermal anomalies is rejected.

For the scene covering the Leigh Creek coal mining area in Australia 1334 themal anomalous clusters were extracted from the daytime thermal band. Over 90% of these anomalies can be rejected and the remaining thermal anomalous area covers only 0.16 km² compared to 7.25 km² before demarcation.

Figure 10-4 demonstrated the rejection of thermal anomalies with the knowledge based approach and the PMA approach. Except for the scene from Baotou the PMA based approach leads to the rejection of equal (nighttime scene and scene of Australia) or more pixels, than the knowledge based approach. The delineated area resulting from the PMA based approach is thus on average slightly smaller than the demarcated coal fire (risk) areas defined with the knowledge based test sequence. However – except for the scene of Baotou – both methods yield results much alike demonstrating the comparability of output results.

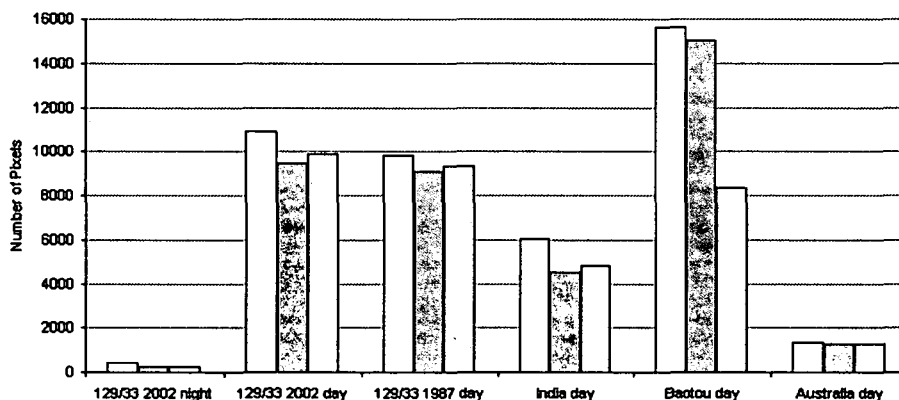


Figure 10-4 : Thermal anomalies in numbers of pixels extracted (orange), anomalies rejected by the knowledge based coal fire area demarcation (dark grey) and anomalies rejected by PMA based coal fire area demarcation (light grey). Exemplarily presented for six satellite scenes. Displayed are a nighttime and daytime scene from 2002 of the two main study areas, a scene of these areas for 1987 and scenes for the three transfer areas in India, Baotou and Australia.

In nighttime data the thermal algorithm extracts a substantially lower number of thermal anomalies than in daytime data. The nighttime and daytime scene of 2002 were acquired with only one week time difference. Effects of uneven solar heating due to aspect and slope and especially uneven heating of surfaces due to their albedo and emissivity lead to the extraction of many false alarms.

The false alarm reduction capability presented in table 10-1 and 10-2 and figure 10-4 as well as the discovery of formerly unknown coal fires from remote sensing data exclusively shows the powerful capabilities of the combined approach of coal fire area demarcation and thermal anomaly detection. This encourages the goal, aimed at within the project, to set up a detection- and monitoring system for coal fires in larger areas of northern China. Furthermore, automated coal fire area demarcation shows a great potential to highlight possible coal fire risk areas, not yet showing a thermal expression.

10.3. Discussion

The demarcated coal fire (risk) areas presented in maps 4 to 16 serve several purposes. They help the local people and mining authorities to get a regional overview over existing and probable coal fire risk areas within their municipalities. A ground survey check of present coal fire areas demarcated and presented in the maps on a regular timely basis can support the early detection of new fires in the adjacency of the existing ones. Furthermore the dynamics of the fires can be observed with the thermal algorithm. The algorithms can not help to monitor very small spatial changes of coal fires, but the extinction of a fire or the rapid growth of a fire can be detected.

Furthermore, the multispectral approach to demarcate coal fire risk areas allows the definition of regions potentially prone to coal fires. These regions should not only be visited during regular field checks, but should also get a high priority for satellite monitoring as e.g. by the satellite Aster. This sensor combines the advantages of several multispectral and thermal bands. For a focused monitoring this sensor is a good replacement for Landsat-7, now that sensor instabilities lead to a failure of ETM+ in late May 2003.

Map 4 presents automatically extracted coal surfaces, demarcated coal fire risk areas thermal anomalies for the region of Wuda syncline. The coal fire related thermal anomalies are all located within the demarcated risk area. Additionally, thermal anomalies resulting from industry were extracted also. Most thermal anomalies extracted from nighttime data are closely related to coal surfaces. Next to coal seam fires, coal waste pile and coal storage pile fires are commonplace in the area.

Map 5 presents the same features for the area south of Wuhai. Here thermal anomalies – also extracted from thermal nighttime data – occur close to coal accumulations, which are mainly industry related. However, there are some private wild mines directly east of the city of Wuhai, where no thermal anomalies are present yet. However, this area including the typical tiny round coal accumulations indicating private mining entrances is probably very prone to coal fire genesis. Also the valley extending south of Wuhai east of the central limestone mountains host many small scale mines and is prone to coal fire genesis.

Map 6 depicts the main part of this valley. Industry related coal waste and storage piles, small scale mines and wild coal digging is commonplace. In the very southern corner of the map a subsurface coal fire could be verified in June 2004. The area marked on the map as “newly detected coal fires” is the same shown in the photographs of figure 10-3.

In map 7 all larger coal accumulations, which are related to coal processing industry in the far Southeast of Wuda, were extracted. Demarcated coal fire risk areas around these industrial accumulations (especially in the South of the map) are actually not necessary. This demonstrated that a spectra based algorithm cannot distinguish thematic classes. Coal – occurring as coal seams, coal waste piles, coal storage piles, thick coal dust – can not be differentiated further.

Map 8 presents a coal fire risk area east of Shizuishan City, which is supposed to be at high risk for coal fire ignition. Coal is mined in two valleys stretching North-South in the northern foothills of the Helan Shan. Thermal anomalies do not show up yet. However, the area should be observed closely.

The same applies for the coal fire risk areas directly south and east of the fires, which were newly detected in June 2004. These areas are presented in map 9. Driving time from Wuda to this area is about 2 hours. A regular field check could help to detect coal fires early after ignition. This would guarantee a fast and easy extinction of the fires, once they flare up.

Map 10 presents the Ruqigou / Gulaben study area. Coal was extracted with high accuracy. The demarcated coal fire risk area coincides well with the actual occurrence of coal fires in this region. Over 20 coal fires induce thermal anomalies in nighttime data. Most of the anomalies in the map are coal fire related. Only very few are false alarms of unclear cause.

Maps 11 and 12 depict coal fire risk areas in the valleys of Hulusitai and Shitanjing, north of Ruqigou. These valleys are located in approximately 50 km distance to Wuda in the North. Both valley once had prospering coal mining communities. However, reserves have been exhausted several years ago and many mining operations were only improperly sealed. Unknown coal fires could be detected and verified in September 2003. The valley east of Shitanjing has not been visited so far. Nevertheless, this valley, showing a lot of small round coal accumulations (wild mines), is prone to coal fire ignition.

The further maps present the automatically extracted coal surfaces and demarcated coal fire risk areas for the transfer regions. In these regions the thermal anomalies cannot be assigned to certain causes, since field checks were not possible. In the city area of Baotou several coal industries exist. Furthermore coal storage pile fires occur. However, it is not known, where exactly they are located. For the Leigh Creek mining area in Australia it is not known if coal fires do exist. The thermal anomalies for the Jharia coal field are likely to be coal fire related. However, no updated information on the coal fire locations is currently available. The same applies for the coal field of Ray.

Comparing the knowledge based and the PMA approach for coal fire area demarcation the first proves to be more robust and easier to implement in common programming languages. It is therefore already used for mass data throughput within the project. However, the PMA based approach is a good tool if detailed knowledge trees do not yet exist and a certain surface type covering a high subpixel fraction shall be extracted fast and without much analyst interaction. As demonstrated in figure 10-4 both methods yield similar results for coal fire area demarcation. The extraction accuracy of the knowledge based approach is slightly higher but does not imply a general overall advantage

To improve coal fire risk maps and coal fire risk area demarcation many parameters could additionally be included. The implementation of further exclusion parameters and indicators, leading to a higher differentiation within the demarcated coal fire areas was not in the scope of this work. However, possible improvements include the following options:

- 1) Industry and settlement produce thermal anomalies resulting from fires, waste burning, and industrial thermal emission amongst others. Since a lot of industry in the study areas is coal related it may occur that a thermal anomaly occurs next to a coal surface (e.g. a coal stock pile), which actually belongs to a coal burning plant. The thermal anomaly therefore does not necessarily have to be a coal storage pile fire, but can result from a very near close by chimney. It is very hard to automatically extract settlement and industry from multispectral remote sensing imagery. This general challenge is complicated through the fact that settlements in the study areas are often built from materials, which are hardly distinguishable from natural surface materials. Main houses are build of loam and straw or

bricks. Roofs are flat and usually covered with weathered material, coal dust or pebbles. This does not apply for industrial complexes, but these also do not have clear characteristic spectral features. Industrial complexes could most likely be extracted taking image texture and context as well as lineament analysis into account. However, the exclusion of settled areas and industry within the demarcated coal fire (risk) areas could support the exclusion of some false alarms, which might be located within the risk areas.

2) In addition – as presented in chapter 2 – limestone mining and burning is a commonly undertaken activity within the area. Thermal anomalies, which occur close to very distinct and visibly bright surfaces of processed limestone (calcite) are not very likely to be coal fires. The calcite or dolomite signatures could be excluded from the data set in an approach similar to knowledge based or partial unmixing coal extraction.

3) Coal fires often lead to cracks and slow as well as sudden land subsidence within their surrounding. The specification of subsidence areas within the demarcated risk areas based on differential SAR interferometry is to date still very difficult (HOFFMANN et al. 2003). However, the indication on subsidence could increase the coal fire existence probability within these areas.

4) Further parameters of interest are the closeness of the demarcated areas to settlement, their accessibility via infrastructure and the infrastructure density within the risk areas. This would pay toll to the fact that coal fires are not only started due to fully natural spontaneous combustion in an untouched environment. Most coal fires' ignition is related to human interaction. A short distance to settlements and a high infrastructure density in the vicinity as well as within the demarcated risk areas could raise the potential risk within the designated areas. Also the structural and economical development of a region plays an important role. Proper mining techniques and industrialized methods hamper coal fire ignition, while practices like wild private mining with inappropriate ventilation, low security standards and insufficient sealing support spontaneous combustion processes.

5) Provided that a digital global data set of sufficient accuracy of all coal basins would be available, coal fire risk areas could be limited to these regions. This way only the risk area demarcation for coal waste and coal storage piles further away from their mining origin would be hampered. For China such a dataset at the scale of 1:500,000 was available from USGS. Even though this dataset is not considered fully complete, for the scenes of China processed no demarcated coal fire risk area extends into a region, which is not designated as a coal bearing area. For India and Australia such information was not available for this thesis.

6) As mentioned in chapter 7 different coal types show a differing proneness to spontaneous combustion. While the highly compacted high ranking anthracite coals of Ruqigou / Gulaben are actually not so prone to spontaneous combustion, the low quality coals of Wuda with high sulfur contents and a lower density ignite easier. A differentiation of different coal types within demarcated coal fire areas could therefore support the differentiation within the demarcated risk areas concerning coal fire ignition probability.

7) Also climatic parameters like sunshine hours, average temperatures, aridity, precipitation etc. may influence the proneness of an exposed coal seam, coal waste- or coal storage pile for spontaneous combustion. These factors could be included through rasters allowing the factorial weighting of areas.

11. Conclusions and Outlook

In this thesis a conceptual approach for the automated demarcation of coal fire risk areas has been designed. Based in this concept, two algorithms have been developed to automatically retrieve coal fire risk areas from multi sensor remote sensing data.

These algorithms are based on detailed field observations, the results of extensive signature analyses in satellite imagery and analyses of spectral measurements recorded on surface samples from the study areas. A knowledge-based spectral test sequence and a partial unmixing approach are employed to demarcate coal fire risk areas. The delineation approach is embedded in an integral coal fire area demarcation-, detection- and quantification scheme developed within the project. The algorithms presented have been demonstrated to be robust tools for coal fire area demarcation. They work automatically and enable to screen unknown areas for the probability of coal fire occurrence. Furthermore, they have been applied successfully to images acquired by different sensors and to coal mining regions on other continents. The delineation of coal fire risk areas based on the automated extraction of coal and analysis of vegetation density is cheaper and faster than tedious interactive mapping and standard classification approaches. This is of great advantage in countries, where detailed and updated land cover maps do not exist. Combined with approaches for coal fire related thermal anomaly detection the multispectral demarcation approach now enables the operational detection and monitoring of coal fire areas and coal fire risk areas in large regions, such as northern China.

11.1. Conclusions

With respect to the questions raised on page 6 in chapter one the following conclusions can be drawn:

1. Both study areas – Wuda and Ruqigou/Gulaben – have undergone a substantial increase in mining activity between 1987 and 2003. This is indirectly observed in the rapid expansion of coal covered surfaces in both areas. From 1987 to 2003 coal covered surface areas increased by over 100 % in both regions. The coal covered area in Wuda currently ranges at 3.7 times the area covered in 1987. In Ruqigou the area covered increased by a factor of 2.7. This finding is based on the application of a knowledge-based spectral test sequence applying identical thresholds for surface extraction to eight available ETM+ scenes. This result agrees with investigations on the development of coal covered areas using linear partial unmixing. Results of the automated mapping were evaluated based on an extensive set of over 50 coal ground truth polygons and seven mixture grids mapped in the field. Extraction accuracies for the surface coal in the study areas range from 77.87 % and 95.98 % for both approaches. The linear trends of increasing coal covered surfaces is statistically stable for both study area time series investigated.

While a quantitative estimate of the coal covered area increase has been obtained, the absolute coal covered area in 1987 and 2003 can only be estimated within a larger error range. The requirements for the algorithm – to be applicable for different times and in several regions – limits the individual extraction accuracy. It has been demonstrated for the Wuda region that knowledge-based coal extraction results tend to slightly underestimate the area of coal covered surfaces. This slight

underestimation is observed for all time steps. In Ruqigou the coal covered area could be estimated with slightly higher accuracies. Here, the total coal covered area within the broader study area sum to 13.7 km² in 2003.

Coal mining activities in Ruqigou have expanded within the main mining area. The open pit mine of Dafeng has grown over time, as have the coal fields of Gulaben and north of Baijigou. Furthermore, mining activities in the two valleys of Hulusitai and Shitanjing have strongly increased since 1987. A spread of small scale private mines cannot be detected visually in Ruqigou / Gulaben. For this region it is observed that coal mining is expanding within the industrially mined areas.

In the broader Wuda study area an increase in coal surfaces is not only noted in the area of the three major mines, but also outside the Wuda mining syncline. A rapid spread of small scale unlicensed private mines can be observed east of the Yellow River. Here, the foot-slopes along a former river valley are dotted with small mine openings and coal waste and storage piles. Many of these did not exist in 1987. Furthermore, industrial coal processing has spread dramatically in the broader Wuda surrounding. This can be seen in the increase of coal storage piles located near roads and settlements farther away from the actual mining operations. A temporal investigation on how often a certain pixel was identified as coal in all eight observations (scenes) has been undertaken. This supported the visualization of the process of coal storage pile growth and coal waste pile expansion over time.

The two winter scenes from December 2002 and February 2003 show an inner-annual decrease of coal coverage compared to September 2002 and May 2003. This phenomenon could be quantified and was validated through visual interpretation. While 12.4 km² were covered with coal in September 2002, only 10.34 km² were mapped in December 2002. It is assumed that coal storage pile sizes are clearly reduced in winter, since coal is heavily used for heating and electricity generation.

2. Coal fires lead to the deterioration of vegetation in the vicinity of thermally anomalous areas and cracks releasing toxic fumes. Vegetation density in the coal fire areas studied is generally low and does not exceed 50 % surface coverage. No coal fire has been showing healthy vegetation above the bedrock covering the burning seams. Above the fires vegetation density is 0 %. This was confirmed with three mapped mixture grids consisting of 349 raster cells located above fires #6, #8 and #13 in Wuda during 2002 and 2003. The phenomenon can also be observed in vegetation index data such as SAVI images. A regional increase of vegetation density with increasing distance from the subsurface fire zone could be identified. Furthermore, partial unmixing results of the vegetation fraction show values below 25% above the subsurface fires. These values above 0 % result from the overestimation of the requested spectrum in partial unmixing approaches as discussed within the thesis. However, in agricultural areas and forested regions the vegetation fraction images show values of up to 100%.

Very hot coal fires lead to the generation of pyrometamorphic rocks. These are rocks, which experience color and texture changes due to dehydration and oxidation. They occur in different colors, densities and mineral compositions depending on the parent rock and the temperature of pyrometamorphosis. Spectral differences resulting from different degrees of pyrometamorphosis and different mineral compositions were detected on surface sample spectra. Where these rocks are exposed at the surface, they can be detected in high spatial resolution satellite data. Pyrometamorphic rocks of the Ruqigou area are clearly visible in Quickbird data available for this region. Furthermore

4-5 pixels in the ETM+ data show a spectra signal dominated by such rocks. In Wuda pyrometamorphic outcrops occur only in a small area. A small region can be noted in the Quickbird data, which can only be recognized with the support of GPS data and detailed ground knowledge. In ETM+ data pyrometamorphic rock cannot be detected for Wuda.

In addition to vegetation degradation and pyrometamorphic rocks coal fires often cause numerous cracks in the overlaying bedrock. According to field mappings conducted in 2003, such cracks are 10 cm to 2 m wide, range from centimeters to 20 meters in length and strike orthogonal to the spreading direction of the subsurface coal fire. They develop due to volume loss underground. Also larger subsidence phenomena like sinkholes and collapsed mining drives exist. The cracks, sinkholes and collapsed drives can be detected clearly in high spatial resolution satellite data. In ETM+ or Aster data they cannot be seen. So far no automated extraction approach of these features has been developed. Nevertheless, manual mapping of crack fields can be done relatively quickly and indicates the underground fire situation.

Studies in the project currently investigate if released gasses and increased aerosol contents in the atmosphere above coal fires can be observed from atmospheric remote sensing data. However, in regions like Wuda, where a lot of emission results from coal industry and other anthropogenic emissions, separation from coal fire emissions will be difficult.

3. A conceptual approach for the demarcation of coal fire areas and future risk areas is presented in this thesis. Coal fire areas can be demarcated based on the automated extraction of the surface 'coal'. Coal is always present directly at or in the closer vicinity of coal fires. It can occur in outcropping coal seams, coal waste- or coal storage piles and mining entrances. Therefore, the automated extraction of this surface class is the first step for coal fire area delineation. Depending on the dip angle of the coal seam, and the assumption that coal fires only exist to ± 150 meters depth, an area can be outlined around the extracted coal surfaces. Within this demarcated area coal fires and thermal anomalies related to the fires are likely to occur.

Investigations on vegetation density and the extraction of pyrometamorphic rock within the demarcated areas can also help to specify likely or unlikely regions. However, regions of very low or zero vegetation density cannot be used directly as an indicator for coal fire occurrence. Low or zero vegetation density can also occur in settled areas, on bare rocks or on coal piles. Nevertheless, densely vegetated areas within the demarcated zone are unlikely to be coal fire areas, since healthy vegetation rarely exists above smoldering fires releasing toxic fumes. In case pyrometamorphic pixels can be identified, they can be interpreted as an indication that a hot coal fire is existing or has been burning.

All three indicators (coal, dense vegetation, pyrometamorphic rocks) can be detected in ETM+ and Aster satellite data. However, especially for the detection of pyrometamorphic surfaces data with higher spatial resolution would be more suitable. Cracks and subsidence cannot be detected in medium resolution data of ETM+ or Aster. Therefore, the automated extraction of cracks and fractures was not pursued in this thesis

Additional support for the very rough demarcation of coal fire risk areas within a country can be provided by GIS data. A vector data set on the coal bearing strata within China exists. This dataset has

a spatial scale of 1:500,000. Provided that the datasets is correct, no coal seam fire related thermal anomaly should occur outside the coal bearing area. Such data can therefore support coal fire area demarcation and detection. The polygons were used for an intersection with demarcated coal fire areas of the scene covering the main study areas. This analysis showed that none of the automatically demarcated areas was located outside the coal bearing regions.

4. Two algorithms have been implemented for coal fire area demarcation. The first is a knowledge-based spectral test sequence separated into three major parts to identify the three surfaces of interest. The test sequence can be considered as a series of spectral filters. Each image pixel of the input data set is tested in the test sequence. If a pixel passes all tests for a certain surface, it is considered to be coal, dense vegetation or pyrometamorphic rock. Confusion between the three surfaces did not occur for any pixel.

For the knowledge based extraction of coal the separation of coal and shadow, which often had identical spectral signals, could be solved employing a relative temperature threshold test. This test is based on the assumption that coal pixels will always be 'located' in the upper part (above the mean) of the thermal band histogram, while cooler shadowed areas are located in the lower part (below the mean). Coal extraction accuracies vary between 87.51 % and 95.98 % for all eleven ETM+ scenes processed and 91.32 % and 93.81 % for the two Aster scenes.

The extraction of dense vegetation based on SAVI data shows very good results. Accuracies evaluated on a limited number of ground truth ranging between one and 10 mapped polygons per scene ranged between 93.62 and 99.73 % for all scenes.

In contrast, the extraction of pyrometamorphic rock was very challenging. The algorithm is supposed to detect 4-5 pixels dominated by this surface type within 50 Mio. pixels of the whole scene. Even though the ground truth regions were extracted completely (100% producer accuracy) a relatively large number of additional pixels was extracted also. A fully automated unsupervised extraction of this surface therefore proved elusive. Nevertheless, using analyst knowledge, results can be incorporated in coal fire area maps.

The second approach developed in this work extracts the three surface types of interest on the basis of linear partial unmixing. Mixture analysis results in fraction images for each of the desired surface components. The fraction images are a quantitative measure for the spatial subpixel contribution percentage to the overall pixel reflectance. Therefore, partial unmixing enables the mapping of pixel composition on a subpixel basis. This accounts for the fact that only few pixels within image data can be considered pure.

Partial mixture analysis (PMA) was performed using self generated prototype spectra for the three surfaces of interest as a spectral reference. These spectra were designed from averaged field and laboratory measurements of numerous surface samples and were resampled to the spectral resolution of ETM+ and Aster.

The fraction images for coal have to be post-processed with a relative temperature test to differentiate shadow and coal. After this post processing classification accuracies of pixels considered as pure coal

(>85% fraction) ranged between 76.47 and 91.42 % (excluding winter scenes). Even though these results could clearly be improved when minimum noise fraction (MNF) transformed data and MNF transformed image spectra were used, this conflicted with the required automation of the algorithm. Untransformed PMA results combined with thermal post-processing were considered sufficient to extract coal automatically.

The PMA analysis for the extraction of dense vegetation shows producers accuracies between 67.33 and 91.03 % for pixels with a fraction exceeding 85 %. The exclusion of vegetation within areas delineated as coal fire risk areas is therefore feasible.

PMA analysis for the mapping of pyrometamorphic rocks encounters the same problems as analysis with the knowledge-based spectral test sequence. However, with PMA the problem is aggravated. Not only is the algorithm comparing prototype spectra to a large number of pixel spectra of which less than 0.000001 % match the prototype. The reference spectrum is furthermore not considered as spectrally extreme and is therefore a mixture itself. Hence, other pixels are mistakenly mapped as pyrometamorphic rock. Although producer's accuracies are 100%, also from PMA analysis it is concluded that the fully automated mapping of pyrometamorphic rock is not feasible at present.

Both algorithms have the advantage that no user interaction is required for the mapping of surfaces. Once a spectral test sequence has been defined, the algorithm can run on a number of scenes acquired at different times and for different regions without any analyst interaction. Also the results are reproducible in the sense that the result will be the same for identical images. The same applies for partial unmixing. Once the satellite data has been thoroughly calibrated and radiometrically preprocessed, the unmixing procedure with similar reference spectra yielded identical results. If representative prototype spectra for the surfaces of interest exist, partial unmixing can be employed for different time steps and different regions as well as for multi sensor data.

The two approaches show clear advantages over standard feature extraction and classification techniques such as maximum likelihood classification, unsupervised classification or object oriented classification. These techniques all demand extensive analyst input in the form of training areas, class definition, the definition of hierarchies or segmentation levels. Therefore they are not suited for the design of fully automated algorithms.

5. Especially the first knowledge-based test sequence approach programmed in IDL (Interactive data Language, RSI) can be combined easily with the thermal algorithm developed by ZHANG, J. (2004), which was also programmed in IDL. The fully automated implementation of the partial unmixing approach in IDL is still ongoing and more challenging. However, it is expected to be completed soon. Both algorithms for coal fire risk area demarcation can run independently from each other. They can furthermore run independently from the thermal algorithm.

To separate coal fire related thermal anomalies from false alarm thermal anomalies, the output image resulting from the thermal algorithm (0 = no thermal anomaly, 1 = thermal anomaly with > 75% probability to be coal fire related), is intersected with the result of automated coal fire risk area demarcation. Anomalies located outside the demarcated areas are assigned a low likelihood to be coal fires. Anomalies within the demarcated regions are given a higher likelihood. This is expressed in the pixel value and color coding. It is important to not delete any thermal anomaly extracted completely.

For all areas studied the demarcated risk areas and the two types of thermal anomalies are presented in 13 maps. It is more useful to leave all extracted anomalies in the final output (the map) and highlight the probable coal fire related anomalies. The accidental removal of an anomaly, which might be coal fire related or which might be of importance for the local authorities for other reasons should be avoided.

Since the algorithm of ZHANG, J. (2004) employs raw DN values and does not apply atmospheric or radiometric corrections the algorithms cannot work with the same input data sets. This however is not critical. It is very important though that both data sets have the same geometric characteristics. This means that orthorectification is required for both inputs to guarantee the spatial comparability of scenes. In addition the thermal algorithm can be modified easily to work on calibrated temperature image data also. Therefore, the algorithms can be combined to one in the future.

6. The first successful discovery of formerly unknown coal fires using remote sensing data exclusively proves that the combined approach of automated coal fire area demarcation and thermal anomaly detection is successful. This supports the creation of an operational detection and monitoring system for coal fires in large areas of northern China. It could be demonstrated that the demarcation of coal fire areas and possible coal fire risk areas can substantially reduce the spatial area in which thermal investigations are necessary. An average of only 9.8 % of the ETM+ input data set are considered relevant for the detection of thermal anomalies related to coal fires. For the full scene 129/33 (covering both study areas) only 1.5 % of the entire area is considered of relevance for coal fire investigations. For scene (128/032) of Baotou 0.59 % of the input data set area are extracted as a probable coal fire region. For scene (098/081) containing the Leigh Creek mining region 1.46 % were delineated. In India only 1.48 % of the spatial extent of the input data set 140/044) remain.

To evaluate the combination of the thermal anomaly detection algorithm developed by ZHANG, J. (2004) and the demarcation algorithm presented here, six scenes were processed. For the whole area covered by ETM+ scene nighttime scene (226/211) 451 thermal anomalies were extracted by the thermal algorithm. 243 of these (ca. 50%) are located outside the demarcated coal fire areas. These anomalies are not likely to be coal fire related. For all other daytime scenes between 1334 and 10,911 thermal anomalous clusters were extracted. This numbers could be reduced by over 80 % on average.

7. A major advantage of the multispectral algorithm for coal fire risk area demarcation is the fact that risk areas can be mapped, even if thermal anomalies have not yet developed. Maps of scale 1:100000 and 1:200,000 were generated for the study areas Wuda and Ruqigou / Gulaben, their surrounding, the broader area of Baotou as well as for transfer areas in India and Australia. These coal fire risk maps display the extracted coal surfaces, automatically generated coal fire risk areas and detected thermal anomalies. They can be extended through the intersection with additional information. Relevant parameters within the delineated zones are the coal's susceptibility to spontaneous combustion, the degree of mining activity, infrastructure density, coal seam accessibility and other parameters.

The outlined risk areas constitute locations to be closely monitored in the future. When a new thermal anomaly is detected within the delineated areas of coal fire risk a field check by local authorities is recommended.

Areas in the Wuda and Ruqigou / Gulaben surrounding, which are recommended to be kept under close observation, are:

- UL: 4398000 N, 658000 E, LR: 4390000 N, 664000 E
- UL: 4384000 N, 662000 E, LR: 4364000N, 672000 E
- UL: 4358000 N, 634000 E, LR: 4340000N, 646000 E
- UL: 4370000 N, 674000 E, LR: 4362000N, 680000 E
- UL: 4350000 N, 616000 E, LR: 4336000N, 624000 E, (all UTM, Zone 48 North, WGS 84)

Monitoring coal fire risk areas can enable a rapid response to coal fires at their initial stage. Coal fire fighting at the initial stage increases the probability to control and extinguish the fire it with low effort.

11.2 Outlook

The results presented in this thesis strongly suggest that an automated coal fire area demarcation, coal fire detection and monitoring on a large spatial scale can be achieved applying the algorithms developed.

Unfortunately, the recent failure of Landsat-7 ETM+ in May 2003 is of concern for most coal fire scientists. However, it could be demonstrated that the methods applied and the algorithms developed can work on multi sensor data and are easily transferable to different spatial and spectral resolutions. With respect to a long term monitoring concept it is important to keep automated methods as flexible as possible.

Currently, the Aster sensor is fully sufficient for coal fire analysis. Analyses of this data with the algorithms developed can be framed by other data as soon as it is available. A follow on mission of ETM+ or the thermal satellite Bird are under discussion. Furthermore, analyses can be supported by high spatial resolution data of Quickbird or Ikonos imagery. Also the MODIS sensor with a pre-dawn overpass time (5:00 am) on the platform AQUA and a daytime overpass on the platform TERRA might enable the detection of very hot fires. Obtaining several acquisitions within one day is an advantage no other sensor can offer. Furthermore, tests on thermal Envisat AATSR data are currently pursued.

Still a lot of remote sensing based coal fire research has to be undertaken on a regional and local scale. Current investigations focus on the analysis of hyperspectral Hyperion data (30m spatial resolution, >200 spectral bands). This data is of interest for the more accurate extraction of pyrometamorphic rock. Furthermore, coal types of different sulfur content might be differentiable. This would allow a remote sensing based mapping of coal types with different susceptibility for spontaneous combustion. However, hyperspectral data presently is expensive to acquire and covers only a very limited spatial area. Therefore such studies currently only serve a purely scientific interest. It is not assumed that hyperspectral data will play a key role in coal fire remote sensing for large scale approaches.

The further improvement of the coal fire area demarcation algorithm presented here may lead to results at a more detailed scale. Additional and reliable GIS data on coal bearing regions, mining operations, population density, infrastructure density, climate and many more could support the generation of a coal fire risk index map for entire China.

A long term study for a larger number of coal fire areas should be undertaken to investigate the influence of coal fires on regional atmospheric conditions. It is assumed that the rapid spatial spread of coal on the surface alone, which leads to a decrease in overall regional albedo, might influence the thermal pattern of an area.

On a China-wide and global scale, the evaluation of Kyoto relevant green-house gas emissions released by the fires is considered of high relevance concerning future coal fire research. The protocol obliges industrialized nations to cut their emissions by 5% on average below the levels of 1990 during the first commitment period between 2008 and 2012 (ROSENQVIST et al. 2003, WAGNER 2003). The magnitude of the coal fire problem in China becomes apparent keeping the first estimate of a 0.1 % - 0.2 % contribution to the annual global human induced CO₂ emissions in mind. Within the Kyoto Protocol emissions of the six greenhouse gasses (measured in terms of CO₂ equivalents) carbon dioxide (CO₂), methane (CH₄), nitrous oxides (N₂O), hydrofluorocarbons (HFCs), perfluorocarbons (PFCs) and sulphur hexafluoride (SF₆) are considered most relevant for the assessment of possibly human influenced global climate change (ROSENQVIST et al. 2003). Especially the first three gasses are emitted by coal fires.

Three steering mechanisms are introduced within the Kyoto Protocol. They all aim at the reduction of greenhouse gas emissions into the atmosphere. The Clean Development Mechanism (CDM) allows industrialized nations (Annex I nations) to earn credits for investments in developing countries. The Joint Implementation Mechanism (JI) encourages the investment of industrialized countries in other industrialized Annex I nations, to receive credits when lower emissions result. Furthermore, the general trade with greenhouse relevant emissions will increase strongly in the near future (WAGNER 2003, ROSENQVIST et al. 2003).

Even today, several European coal mining companies show interest in the coal fire problem in China. To extinguish a coal fire in China may be a cheap way of receiving credits for the reduction of CO₂ emissions. To achieve reductions in the industrialized high-wage home country equivalent to these achieved by the extinction of a few coal fires would probably be much more cost intensive. This scenario can of course be discussed intensively.

Currently, the dynamic modeling of the subsurface burning process, the estimation of the amounts of coal being burned, research on the burning efficiency as well as on the gaseous emission products are undertaken within the geoscientific Sino-German Coal Fire Research Initiative. Combining the results of the different research disciplines can lead to a quantification of coal fire induced emissions on a country wide scale. Furthermore, the estimation of resource loss and calculations on the coal fire related contribution to the annual green-house gas budget will be feasible.

The final extinction of the fires should always be considered the final goal of all coal fire research. This should not only be motivated by the monetary benefits of possible emission trades or the protection of a valuable economic resource. The extinction of the fires will clearly improve the living-, health-, and safety conditions of the local inhabitants in coal fire regions such as Wuda. To achieve this goal it is of utmost importance for scientists of different research disciplines to cross their disciplinary boundaries and face the challenges in a joint effort.

12. References

A ...

- ABRAMS, M.J. & S.J. HOOK, 1995: Simulated Aster Data for Geologic Studies. In: *IEEE Transactions on Geoscience and Remote Sensing*, Vol. 33, No. 3, pp. 692-699.
- ABRAMS, M.J., KAHLE, A.B., PALLUCONI, F.D. & J.P. SCHIELDGE, 1984: Geologic Mapping Using Thermal Images. In: *Remote Sensing of Environment*, Vol. 16, No. 1, pp. 13-33.
- ABUELGASIM, A.A., GOPAL, S., IRON, J.R. & A.H. STRAHLER, 1996: Classification of SA Multiangle and Multispectral Measurements Using Artificial Neural Networks. In: *Remote Sensing of Environment*, Vol. 57, No. 2, pp. 79-87.
- ABUELGASIM, A.A., ROSS, W.D., GOPAL, S. & C.E. WOODCOCK, 1999: Change detection using adaptive fuzzy neural networks: environmental damage assessment after the Gulf war. In: *Remote Sensing of Environment*, Vol. 70, No. 2, pp. 208-223.
- ADAMS, J.B., SABOL, D.E., KAPOS, V., ALMEIDA FILHO, R., ROBERTS, D.A., SMITH, M.O. & A.R. GILLESPIE, 1995: Classification of Multispectral Images Based on Fractions of Endmembers: Application to Land-Cover Change in the Brazilian Amazon. In: *Remote Sensing of Environment*, Vol. 52, No. 2, pp. 137-154.
- ANDRÉFOUET, S., MULLER-KARGER, F.E., HOCHBERG, E.J., HU, C. & K.L. CARDER, 2001: Change detection in shallow coral reef environment using Landsat 7 ETM+ data. In: *Remote Sensing of Environment*, Vol. 78, No. 1-2, pp. 150-162.
- ARANUVACHAPUN, S., 1983: Variation of Atmospheric Optical Depth for Remote Sensing Radiance Calculations. In: *Remote Sensing of Environment*, Vol. 13, No. 2, pp. 131-147.
- ARVIDSON, T., J. GASCH & S.N. GOWARD, 2001: Landsat 7's Long Term Acquisition Plan – an innovative approach to building a global imagery archive. *Remote Sensing of the Environment*, Vol. 78, No. 1, pp. 13-26.
- ASNER, G.P. & K.B. HEIDEBRECHT, 2003: Imaging Spectroscopy for desertification Studies: Comparing AVIRIS and EO-1 Hyperion in Argentina Drylands. In: *IEEE Transactions on Geoscience and Remote Sensing*, Vol. 41, No. 6, pp. 1283-1294.
- ATZBERGER, C., 2002: Remote sensing through the atmosphere – Physical principles and effects. unpublished manuscript, University of Trier, Germany, 7 pp.

B ...

- BACHMANN, M., 2002: Evaluation of Image Fusion Techniques for Large-Scale Mapping of Non-Green Vegetation. Example: Barrax, Spain. Master thesis at the German Remote Sensing Data Center and the Technical University of Dresden, -Dresden, Germany, 150 pp.
- BAHRENBURG, G., GIESE, E. & J. NIPPER, 1990: *Statistische Methoden in der Geographie*. Teubner. – Stuttgart, Germany, 232 pp.

- BAMLER, R., M. EINEDER, M. SCHWÄBISCH & A. ROTH 1996: SAR-Interferometrie – Sensoren, System und Produkte. In: DECH, S. & W. METT (editors): Tagungsband: 13. Nutzerseminar des DFD der DLR. –Oberpfaffenhofen, Germany, pp. 37-42.
- BANDELOW, K.-F., 2003: Personal Interview on August 5th 2003. Dr. Bandelow is head of the department of mining and geology at the German Montane Technology (DMT).
- BANERJEE S.C., 1982: A theoretical design to the determination of risk index of spontaneous fires in coal mines. In: Journal of Mines, Metals and Fuels, Vol. 30, pp. 399-406.
- BANERJEE S.C., 1985: Spontaneous Combustion of Coal and Mine Fires. –Rotterdam, Netherlands, 168 pp.
- BANERJEE S.C., NANDY D.K., BANERJEE, D.D. & R.N. CHAKRAVORTY, 1972: Classification of coal with respect to their susceptibility to spontaneous combustion. In: Transactions of the Mining and Metallurgical Institute of India, Vol. 59(2), pp. 15-31.
- BARAL, D.J. & R.P. GUPTA, 1997: Integration of satellite sensor data with DEM for the study of snow cover distribution and depletion pattern. In: International Journal of Remote Sensing, Vol. 18, No. 18, pp. 3889-3894.
- BATESON, A. & B. CURTISS, 1996: A Method for Manual Endmember Selection and Spectral Unmixing. In: Remote Sensing of Environment, Vol. 55, No. 2, pp. 229-243.
- BAUER, T. & K. STEINOCHE, 2001: Per-parcel land use classification in urban areas applying a rule based technique. In: GIS, Vol. 6, pp. 24-27.
- BAUMGARDNER, M.F., L.F. SILVA, L.F. BIEHL, L.L. STONER, 1985: Reflectance Properties of Soils. In: BRADY, N.C. (editor): Advances in Agronomy, 38, Academic Press, Orlando, FL, pp. 1-44
- BECKER, F., 1987: The impact of emissivity on the measurement of land surface temperature from a satellite. In: International Journal of Remote Sensing, Vol. 8, No. 10, pp. 1509-1522.
- BELCHANSKY, G. I. & D. C. DOUGLAS, 2000: Classification Methods for Monitoring Arctic Sea Ice Using OKEAN Passive/Active Two-Channel Microwave Data. In: Remote Sensing of Environment, Vol. 73, No. 3, pp. 307-322.
- BENEDIKTSSON, J.A. & J.R. SVEINSSON, 1997: Feature extraction for multisource data classification with artificial neural networks. In: International Journal of Remote Sensing, Vol. 18, No. 4, pp. 727-740.
- BENZ, U., HOFMANN, P., WILLHAUCK, G., LINGENFELDER, I. & M. HEYNEN, 2004: Multi-resolution object oriented fuzzy analysis of remote sensing data for GIS ready information. In: Photogrammetry and Remote Sensing, in press.
- BERK, A., BERNSTEIN, L.S. & D.C. ROBERTSON, 1989: MODTRAN: a moderate resolution model for LOWTRAN 7. GL-TR-89-0122, Massachusetts, USA
- BETHGE, P., 1999: Feuer unter China. In: Der Spiegel 44/1999, Germany, pp. 238-242
- BHATTACHARYA A. & C.S. REDDY, 1994: Underground and surface coal mine fire detection in India's Jharia coalfield using airborne thermal infra-red data. In: Asian Pacific Remote Sensing Journal. Vol. 7, pp. 59-73.

12. References

- BHATTACHARYA, A., REDDY S. & T.K. MUKHERJEE, 1991: Multi-tir remote sensing data analyses for coal fire mapping in Jharia coalfield of Bihar, India. In: Proceedings of the 12th Asian Conference on Remote Sensing. Singapore, 30 Oct. – 5 Nov. 1991, pp. 221-226.
- BLOM, R. & M. DAILY, 1982: Radar Image processing for Rock-Type Discrimination. In: IEEE Transactions on Geoscience and Remote Sensing, Vol. GE-20, No. 3, pp. 343-351.
- BOARDMAN, J.W., KRUSE, F.A. & R.O. GREEN: Mapping target signature via partial unmixing of Aviris data. Internal report at Center for the Study of the Earth from Space, University of Colorado, Boulder, USA, report CO 80309-0216, pp. 23-26.
- BOEKEMEIER R., WANG, H, ZHU, L. & S. ELLERINGMANN 2002: Hoellenfahrt durch China. In: GEO, 9, 2003. – Hamburg, Germany, pp. 21-29.
- BOREL, C.C. & S.A. GERSTL, 1994: Nonlinear Spectral Mixing Models for Vegetative and Soil Surfaces. In. Remote Sensing of Environment, Vol. 47, No. 3, pp. 403-416.
- BRADY, N.C. & R.R. WEIL 1996: The nature and properties of soils. – New Jersey, USA, 881 pp.
- BROWN DE COLSTOUN, E.C., STORY, M.H., THOMPSON, C., COMMISSO, K., SMITH, T.G. & J.R. IRONS, 2003: National Park vegetation mapping using multitemporal Landsat 7 data and a decision tree classifier. In: Remote Sensing of Environment, Vol. 85, No. 3, pp. 316-327.
- BRYANT, R., MORAN, M.S., MCELROY, S.A., HOLIFELD, C., THOME, K.J., TOMOKAI, M. & S.F. BIGGAR, 2003: Data Continuity of Earth Observing 1 (EO-1) Advanced Land Imager (ALI) and Landsat TM and ETM+. In: IEEE Transactions on Geoscience and Remote Sensing, Vol. 41, No. 6, pp. 1204-1212.
- BYLO, Z., 1960: The role of sulphonation in the sponatneous ignition of coal. In: Serie des Sciences Techniques, Vol. 8 (2), pp. 107-114.
- C ...**
- CARR, R., 1996: Spectral and textural classification of single and multiple band digital images. In: Computers and Geosciences, Vol. 22, No. 8, pp. 849-865.
- CASACCHIA, R., MAZZARINI, F., SALVATORI, R. & F. SALVINI, 1999: Rock-type discrimination by field, TM and SPOT data, Tarn Flat, Antartica. In: International Journal of Remote Sensing, Vol. 20, No. 2, pp. 403-420.
- CHAIKEN, R.F., BRENNAN, R.J., HEISEY, B.S., KIM, A.G., MALENKA, W.T. & J.T. SCHIMMEL, 1998: Problems in the Control of Anthracite Mine Fires: A Case Study of the Centralia Mine Fire. Report of Investigations 8799 of the United States Department of the Interior. –Pittsburgh, USA, 68 pp.
- CHAVEZ, P.S., 1996: Image-Based Atmospheric Corrections – Revisited and Improved. In: Photogrammetric Engineering & Remote Sensing, Vol.62, No. 9, pp. 1025-1036.
- CHEN, K.S., Y.C.TZENG, C.F. CHEN & W.L. KAO (1995): Land-Cover Classification of Multispectral Imagery Using a Dynamic Neural Network. In: Photogrammetric Engineering and Remote Sensing, Vol. 61, No.4, 1995, pp. 403-408.

- CHEN, Liding, 1997: Subsidence Assessment in the Ruqigou Coalfield, Ningxia, China, using a Geomorphological Approach. Master thesis at ITC, Enschede, Netherlands, pp. 130.
- CIHLAR, J. (2000): Land cover mapping of large areas from satellites: status and research priorities. In: *International Journal of Remote Sensing*, Vol. 21, No.6&7, pp. 1093-1114.
- CIHLAR, J., QINGHAN, X., CHEN, J., BEAUBIEN, J., FUNG, K. & R. LATIFOVIC, 1998: Classification by progressive generalization: a new automated methodology for remote sensing multichannel data. In: *International Journal of Remote Sensing*, Vol. 19, No. 14, pp. 2685-2704.
- CLARK, R.N., 1999: Spectroscopy of Rocks and Minerals and Principles of Spectroscopy. In: RENZ, A.N. (editor): *Remote Sensing for the Earth Sciences: Manual of Remote Sensing*. 3rd edition, - New York, pp. 189-248.
- CLARK, R.N. & G.A. SWAYZE, 1995: Mapping Minerals, Amorphous Materials, Environmental Materials, Vegetation, Water, Ice and Snow, and Other Materials: The USGS Tricorder Algorithm. In: *Summaries of the 5th Annual JPL Airborne Earth Science Workshop*, January 23-26, JPL publication 95-1, pp. 39-40.
- CLARK, R.N., A.J. GALLAGHER & G.A. SWAYZE, 1995: Material Absorption Band Depth Mapping of Imaging Spectrometer Data Using a Complete Band Shape Least-Squares Fit with Library Reference Spectra. In: *Proceedings of the 2nd AVIRIS Workshop*, JPL Publication 90-54, pp. 176-186.
- COCHRANE, M.A. & C.M. SOUZA, 1998 Linear mixture model classification of burned forests in the Eastern Amazon. In: *International Journal of Remote Sensing*, Vol. 19, No. 17, pp. 3433-3440.
- COLBY, G.D., 1991: Topographic Normalization in Rugged Terrain. In: *Photogrammetric Engineering & Remote Sensing*, Vol. 57, No. 5, pp. 531-537.
- COLLINS, J.B. & C.E. WOODCOCK, 1996: An assessment of several linear change detection techniques for mapping forest mortality using multitemporal Landsat TM data. In: *Remote Sensing of Environment*, Vol. 56, No. 1, pp. 66-77.
- CONGALTON, G. & K. GREEN, 1999: *Assessing the Accuracy of Remotely Sensed Data: Principles and Practices*. -Boca Raton, FL, USA, 137 pp.
- CONGHE, S., C.E. WOODCOCK, K.C. SETO, M.P. LENNEY & S.A. MACOMBER, 2001: Classification and Change Detection Using Landsat TM Date: When and How to Correct Atmospheric Effects?. In: *Remote Sensing of the Environment*, Vol. 75, No. 2, pp. 230-244.
- CORTIJO, F. & PEREZ DE LA BLANCA, N., 1997: A comparative study of some non-parametric spectral classifiers. Applications to problems with high-overlapping training sets. In: *International Journal of Remote Sensing*, Vol. 18, No. 6, pp. 1259-1275.
- COWARD, H.F., 1957: Research on spontaneous combustion of coal in mines – a review. Safety in Mines Research Establishment Research Report (SMRE), report No. 142, USA, 57 pp.
- CRACKNELL, A.P. & Y. XUE, 1996: Thermal inertia determination from space – a tutorial review. In: *International Journal of Remote Sensing*, Vol. 17, No. 3, pp. 431-461.
- CRIPPEN, R.E. (1990): Calculating the Vegetation Index Faster. In: *Remote Sensing of the Environment*, Vol. 9, No. 1, pp.71-73.

CRIST, E.P. & R.C. CICONE 1984: A physically-based transformation of Thematic mapper data – the TM Tasseled Cap. In: IEEE Transactions on Geoscience and Remote Sensing, Vol. 50, pp. 1497-1503.

D ...

DAI, S., REN, D., TANG, Y., SHAO, L. & S. LI, 2002: Distribution, isotopic variation and origin of sulfur in coals in the Wuda coalfield, Inner Mongolia, China. In: International Journal of Coal Geology, No. 57, pp. 237-250.

DANIEL, M., 1994: Chinese coal prospects to 2010. International Energy Agency, IEA on Coal Research –London, 35 pp.

DAMM, A., 1994: Anwendung spektral und geometrisch hoch auflösender Fernerkundungsdaten für stadtoökologische Fragestellungen. Master thesis at the Humboldt University Berlin, 128 pp.

DAVE, J.V., 1981: Influence on illumination and viewing geometry and atmospheric composition on the “tasseled cap” transformation of Landsat MSS data. In: Remote Sensing of Environment, Vol. 11, No. 1, pp. 37-55.

DE JONG, S., 1994: Applications of Reflective Remote Sensing for Land Degradation Studies in Mediterranean Environments. Ph.D. thesis at Utrecht University, Netherlands, 250 pp.

DEFRIES, R.S. & J.R.G. TOWNSHEND, 1994: NDVI-derived land-cover classifications at a global scale. In: International Journal of Remote Sensing, Vol. 15, No. 17, pp. 3567-3586.

DENG W., WAN Y., & R. ZHAO, 2001: Detecting coal fires with a neural network to reduce the effect of solar radiation on Landsat Thematic Mapper thermal infrared images. In: International Journal of Remote Sensing, Vol. 22, No. 6, pp. 933-944.

DEROIN, J.-P., MOTTI, E. & A. SIMONIN, 1998: A comparison of the potential for using optical and SAR data for geological mapping in an arid region: the Atar site, Western Sahara, Mauritania. In: International Journal of Remote Sensing, Vol. 19, No. 6, pp. 1115-1132.

DOUSSET, B., 1995: Synthetic aperture radar imaging of urban surfaces: a case study. In: IGARSS Proceedings, 10-14th July 1995, Firenze, pp. 2092-2096.

DRAKE, N.A., MACKIN, S. & J.J. SETTLE, 1999: Mapping Vegetation, Soils, and Geology in Semiarid Shrublands Using Spectral Matching and Mixture Modeling of SWIR AVIRIS Imagery. In: Remote Sensing of Environment, Vol. 68, No. 1, pp. 12-25.

DRIESSEN, P.M. & R. DUDAL 1991: The major soils of the world. –Leuven, Belgium, 390 pp.

E ...

EARTH REMOTE SENSING DATA ANALYSIS CENTER, 2000: DAR Guideline, Version 1.0. –Tokyo, 53 pp.

EARTH REMOTE SENSING DATA ANALYSIS CENTER, 2001: ASTER User’s Guide, Part I. Version 3.1., 42 pp.

ELLYETT C.D. & A.W. FLEMING, 1974: Thermal infrared imagery of the Burning Mountain coal fire. In: Remote Sensing of Environment, Vol. 3, No. 1, pp. 79-86.

ESCH, T., 2003: Eignung eines objektorientierten Klassifikationsverfahrens zur Gewinnung planungsrelevanter Informationen ueber urban gepraeigten Raeumen. Master thesis at the German Remote Sensing Data Center and the University of Trier, Germany, 191 pp.

F ...

FARRAND, W.H., 1997: Identification and mapping of ferric oxide and oxihydroxide minerals in imaging spectrometer data of Summitville, Colorado, U.S.A., and the surrounding San Juan Mountains. In: *International Journal of Remote Sensing*, Vol. 18, No. 7, pp. 1543-1552.

FISHER W. & W. KNUTH, 1968: Detection and delineation of subsurface coal fires by aerial infrared scanning. In: *Geological Society America*, Vol. 115, pp. 67-68.

FISHER, P., 1997: The Pixel: A Snare and a Delusion. In: *International Journal of Remote Sensing*, Vol. 18, No. 3, pp. 679-685.

FLYNN, L.P., A.J.L. HARRIS & R. WRIGHT, 2001: Improved identification of volcanic features using Landsat 7 ETM+. In: *Remote Sensing of Environment*, Vol. 78, No. 2, pp. 180-193.

FOODY, G.M. & D.P. COX, 1994: Sub-pixel land cover composition estimation using a linear mixture model and fuzzy membership functions. In: *International Journal of Remote Sensing*, Vol. 15, No. 3, pp. 619-631.

FRIEDL, M.A. & C.E. BRODLEY, 1996: Decision Tree Classification of Land Cover from Remotely Sensed Data. In: *Remote Sensing of Environment*, Vol. 61, No. 3, pp. 399-409.

FRIEDL, M.A., MCIVER, D.K., HODGES, J.C.F., ZHANG, X.Y., MUCHONEY, D., STRAHLER, A.H., WOODCOCK, C.E., GOPAL, S., SCHNEIDER, A., COOPER, A., BACCINI, A., GAO, F. & C. SCHAAF, 2002: Global land cover mapping from MODIS: algorithms and early results. In: *Remote Sensing of Environment*, No. 83, No. 2, pp. 287-302.

G ...

GAFFEY, S.J., MCFADDEN, L.A., NASH, D. & C.M. PIETERS 1: Ultraviolet, Visible, and Near Infrared Reflectance Spectroscopy: Laboratory Spectra of geologic Materials. In: Pieters, C.M. & P.A.J. Englert (editors): *Remote Geochemical Analysis: Elemental and Mineralogical Composition*. – New York, pp. 42-77.

GANGOPADHYAY, P., 2003: Coalfire Detection and Monitoring in Wuda, North China – A Multi-spectral and Multi-sensor TIR Approach. Master thesis at ITC. –Enschede, Netherlands, 72 pp.

GARCÍA-HARO, F.J., GILABERT, M.A., MELIÁ, J. & M.T. YOUNIS, 1994: Estimation of pure components spectra from spectral mixtures. In: GUYOT, G. & T. FULPIN (editors), 1994: *Physical Measurements and Signatures in Remote Sensing*. –Rotterdam, Netherlands, online version.

GARCÍA-HARO, F.J., GILABERT, M.A., & J. MELIÁ, J., 1999: Extraction of Endmembers from Spectral Mixtures. In: *Remote Sensing of Environment*, Vol. 68, No. 3, pp. 237-253.

- GAVEAU, D.L.A., BALZTER, H. & S. PLUMMER, 2003: Forest woody biomass classification with satellite based radar coherence over 90000 km² in Central Siberia. In: *Forest Ecology and Management*. Vol. 174, No. 1-3, pp. 65-75.
- GEOPHYSICAL AND ENVIRONMENT CORPORATION, 1999: GER 3700 Users Handbook (unpubl.), 112 pp.
- GIELISCH, H., 2002: Loeschung von Kohlebraenden – Statusbericht zum GTZ Projekt. Internal unpublished report of the DMT (German Montan Technology) on a project on coal fire extinction in China within the framework of a German GTZ project, 52 pp.
- GLOVER, L. 1998: Burning Beneath the Surface, In: *Tribune Review*, May 3, 1998, USA
- GOPAL, S., WOODCOCK, C.E. & A.H. STRAHLER, 1999: Fuzzy Neural Network Classification of Global Land Cover from 1° AVHRR Data Set. In: *Remote Sensing of Environment*, No. 67, No. 2, pp. 230-243.
- GOWARD, S.N., J.G. MASEK, D.L. WILLIAMS, J.R. IRONS & R.J. THOMPSON, 2001: The Landsat 7 mission. Terrestrial research and applications for the 21st century. In: *Remote Sensing of Environment*, Vol. 78, No. 1, pp. 3-12.
- GREEN, A.A., BERMAN, M., SWITZER, P., & M.D. CRAIG, 1988: A transformation for ordering multispectral data in terms of image quality with implications for noise removal. In: *IEEE Transactions on Geoscience and Remote Sensing*, Vol. 26, No. 1, pp. 65-74.
- GREENE G.W., MOXHAM R.M. & A.H. HARVEY, 1969: Aerial infrared surveys and borehole temperature measurements of coal mine fires in Pennsylvania. In: *Proceedings of the 6th Symposium on Remote Sensing of Environment*, University of Michigan, 13-16 October 1969 Institute of Science and Technology, University of Michigan, USA, pp.517-525.
- GREY, W.M., LUCKMANN, A.J. & D. HOLLAND, 2003: Mapping urban change in the UK using satellite radar interferometry. In: *Remote Sensing of Environment*, Vol. 87, No. 1, pp. 16-22.
- GUAN, H. 1989: Applications of remote sensing techniques in coal geology. In: *Acta Geologica Sinica*, Vol. 2, pp. 253-269.
- GUPTA, R.P. & A. PRAKASH, 1998: Reflectance aureoles associated with thermal anomalies due to subsurface mine fires in the Jharia coalfield, India. In: *International Journal of Remote Sensing*, Vol. 19, No. 14, pp. 2619-2622.
- GUYOT, G., 1990: Optical Properties of Vegetation Canopies. – In: STEVEN, M.D. & J.A. CLARK (editors): *Application of Remote Sensing in Agriculture*. –London, pp. 19-43.

H ...

- HALIK, U., BANDELOW, F.-K. & J. SCHLUZ, 2003: Land-use and socio-economic aspects of the Helan Shan in Ningxia and Inner Mongolia, China. Unpublished project report of the project “Innovative technologies for the exploration, extinction and monitoring of coal fires in north China”, 56 pp.
- HANSEN, M.C., DEFRIES, R.S., TOWNSHEND, J.R.G. & R. SOHLBERG, 2000: Global land cover classification at 1km spatial resolution using a classification tree approach. In: *International Journal of Remote Sensing*, Vol. 21, No. 6&7, pp. 1331-1364.

- HANSEN, M.C., DUBAYAH, R., & R.S. DEFRIES, 1996: Classification trees: an alternative to traditional land cover classifiers. In: *International Journal of Remote Sensing*, Vol. 17, No. 5, pp. 1075-1081.
- HECKER, C., 2003: Assessing the Potential of MODIS/Terra Acquired Thermal Imagery in Detecting and Monitoring Coal Fires. Internal report at ITC, Enschede, Netherlands, 26 pp.
- HILL, J. & B. STURM, 1991: Radiometric Correction of multitemporal Thematic mapper data for use in agricultural land-cover classification and vegetation monitoring. In: *International Journal of Remote Sensing*, Vol. 12, No.7, pp. 1471-1491.
- HILL, J. & D. AIFADOPOULOU, 1990: Comparative Analysis of Landsat-5 TM and SPOT HRV-1 Data for Use in Multiple Sensor Approaches. In: *Remote Sensing of the Environment*, Vol.34, No. 1, 1990, pp.55-70.
- HILL, J. & J. MÉGIER, 1988: Regional land cover and agricultural area statistics and mapping in The Département Ardèche, Franc, by use of Thematic Mapper data. In: *International Journal of Remote Sensing*, 1988 Vol. 9, No. 10 & 11, pp.1573-1595.
- HILL, J. & W. MEHL, 2003: Geo- und radiometrische Aufbereitung multi- und hyperspektraler Zeitreihen. In: *Photogrammetrie, Fernerkundung, Geoinformation*, Vol. 1, pp. 7-14.
- HILL, J., MEHL, W. & V. RADELOFF 1995: Improved forest mapping by combining corrections of atmospheric and topographic effects in Landsat TM imagery, In: ASKNE (editor) 1995: *Sensors and Environmental Applications of Remote Sensing*, Rotterdam, Netherlands, pp. 21-31.
- HILL, J., 1993a: High precision land cover mapping and inventory with multi-temporal earth observation satellite data – The Ardèche Experiment. –Luxemburg, 118 pp.
- HILL, J., 1993b: Monitoring land degradation and soil erosion in Mediterranean environments. In: *ITC Journal* No.4, Netherlands, pp. 323-331.
- HILL, J., 1998: Neue Wege zur geowissenschaftlichen Auswertung multispektraler Fernerkundungsdaten. In: *Geographische Rundschau*, Vol.50, 1998, pp.113-119.
- HILL, J., J. MÉGIER & H. KOHL, 1991: Land-use inventory and mapping in a mountainous area: the Ardèche experiment. In: *International Journal of Remote Sensing*, Vol.12, No.3, pp.445-462.
- HOFFMANN, J., ROTH, A., TETZLAFF, A. & S. VOIGT, 2003: Detecting coal fires differential interferometric synthetic aperture radar. Online proceedings of the *fringe* workshop 2003, 01.12.-05.12. 2003, Esrin, Italy.
- HOLZER-POPP, T., M. BITTNER, E. BORG, S.DECH, T. EBERTSEDER, B. FICHELTMANN & M. SCHROEDTER, 2002: Das automatische Atmosphärenkorrekturverfahren "Durchblick". In: BLASCHKE, T. (editor), 2002: *Fernerkundung und GIS. Neue Sensoren – Innovative Methoden*. Wichmann, -Karlsruhe, pp.78-87.
- HOOKE, S.J., GABELL, A.R., GREEN, A.A. & P.S. KEALY, 1992: A comparison of techniques for extracting emissivity information from thermal infrared data for geologic studies. In: *Remote Sensing of Environment*, Vol. 42, No. 2, pp. 123-135.
- HORNSTRA, T.J., MAAS, G.G. & S.M. DE JONG, 2000. Classification of Spectroscopical Imagery by Combining Spectral and Spatial Information: the SSC Method. In: proceedings of the 19th ISPRS Congress, Amsterdam, 16-23 July, pp. 550-558.

- HOSTERT, P., 2001: Monitoring von Degradationserscheinungen im europäisch-mediterranen Raum mit Methoden der Fernerkundung und GIS. Ph.D. thesis at the University of Trier, 219 pp.
- HUBER, R., 2001: Scene classification of SAR images acquired from antiparallel tracks using evidential and rule based fusion. In: *Image and Vision Computing*, Vol. 19, No. 13, pp. 1001-1010.
- HUBERT-MOY, L., COTONNEC, A., LE DU, L., CHARDIN, A. & P. PEREZ, 2001: A Comparison of Parametric Classification Procedures of Remotely Sensed Data Applied at Different Landscape Units. In: *Remote Sensing of Environment*, Vol. 75, No. 2, pp. 174-187.
- HUGHES, G.F., 1968: On the mean accuracy of statistical pattern recognizers. In: *IEEE Transactions on Information Theory*, Vol. 14, pp. 55-63.
- HUNT, G.R. & J.W. SALISBURY, 1970: Visible and near infrared spectra of minerals and rocks: I Silicate Minerals. In: *Modern Geology*, Vol. 1, pp. 283-300.
- HUNT, G.R. & J.W. SALISBURY, 1971: Visible and near infrared spectra of minerals and rocks: II Carbonates. In: *Modern Geology*, Vol. 2, pp. 23-30.
- HUNT, G.R., SALISBURY, J.W. & C.J. LENHOFF, 1971: Visible and near infrared spectra of minerals and rocks: III Oxides and Hydroxides. In: *Modern Geology*, Vol. 2, pp. 195-205.
- I ...**
- J ...**
- JAEGER, E. 2003: Personal interviews in January 2003. E. Jaeger is Professor for botany at the University of Halle, Germany. He classified the plant samples collected during the field campaign in September 2002.
- JIA, J., 2001: Rangeland degradation in Ordos Plateau, its nature and assessment. In: RALA report no. 200, Beijing, pp. 87-95.
- JIA, Y. 2002: Personal interviews during the fieldwork campaign in September 2002 (Y. Jia is the chief engineer of the coal fire fighting team Wuda).
- JIA, Y. 2003: Personal interviews during the fieldwork campaign in September 2003. (Y. Jia is the chief engineer of the coal fire fighting team Wuda).
- K ...**
- KAHLE, A.B., GILLESPIE, A.R. & A.F.H. GOETZ, 1976: Thermal Inertia Imaging: a new geological mapping tool. In: *Geophysical research Letters*, Vol. 3, No. 1, pp. 26-28.
- KARATHANASSI, V., IOSSIFIDIS, C. & D. ROKOS, 2000: A texture based method for classifying build areas according to their density. In: *International Journal of Remote Sensing*, Vol. 21, No. 9, pp. 1807-1823.
- KARTIKEYAN, B., SARKAR, A. & K.L. MAJUMDER, 1998: A segmentation approach to classification of remote sensing imagery. In: *International Journal of Remote Sensing*, Vol. 19, No. 9, pp. 1695-1709.

- KAUFMANN, Y.J. & C. SENDRA, 1988: Algorithm for automatic atmospheric corrections to visible and near-IR satellite imagery. In: *International Journal of Remote Sensing*, Vol. 9, pp. 1357-1381.
- KAUTH, R.J. & G. THOMAS, 1976: The tasseled cap – a graphic description of the spectral-temporal development of agricultural crops as seen by Landsat. In: *Proceedings of the Symposium on Machine Processing of Remotely Sensed Data 1976*, Purdue University, West Lafayette, Indiana, USA, pp. 4 B41 – 4 B51.
- KEALY, P.S. & S.J. HOOK, 1993: Separating Temperature and Emissivity in Thermal Infrared Multispectral Scanner Data: Implications for Recovering Land Surface Temperatures. In: *IEEE Transactions on Geoscience and Remote Sensing*, Vol. 31, No. 6, pp. 1155-1164.
- KEMPER, T., 2003: Reflectance Spectroscopy for Mapping and Monitoring of metal Mining related Contamination – A Case Study of the Aznalcóllar Mining Accident, Spain. Ph.D. thesis at the University of Trier and the JRC, pp. 217.
- KENEA, N.H., 1997: Improved geological mapping using Landsat TM data, Southern Red Sea Hills, Sudan: PC and HIS decorrelation stretching. In: *International Journal of Remote Sensing*, Vol. 18, No. 6, pp. 1233-1244.
- KEUCHEL, J., NAUMANN, S., HEILER, M. & A. SIEGMUND, 2003: Automatic land cover analysis for Tenerife by supervised classification using remotely sensed data. In: *Remote Sensing of Environment*, Vol. 86, No. 4, pp. 530-541.
- KIM, A.G. & R.F. CHAIKEN, 1993: Fires in Abandoned Coal Mines and Waste Banks. Bureau of Mines Information Circular 9352 of the United States Department of the Interior. –Pittsburgh, USA, 58 pp.
- KNUTH, W.M., FISHER, W.JR. & R.W. STINGELIN, 1968: Detection, delineation and monitoring of subsurface coal fires by aerial infrared scanning. In: *Geographer HRB-Singer, Inc.*, a subsidiary of the Singer Company, state College, Pennsylvania, USA, pp. 877-881.
- KOCH, M., 2000: Geological controls of land degradation as detected by remote sensing – a case study in Los Mongeros, north-east Spain. In: *International Journal of Remote Sensing*, Vol. 21, No. 3, pp. 457-473.
- KOKALY, R.F., DESPAIN, D.G., CLARK, R.N. & K.E. LIVO, 2003: Mapping vegetation in Yellowstone National Park using spectral feature analysis of AVIRIS data. In: *Remote Sensing of Environment*, Vol. 84, No. 3, pp. 437-456.
- KRAUS, K. 1988: *Fernerkundung Band 1: Physikalische Grundlagen und Aufnahmetechniken*. –Bonn, Germany, 291 pp.
- KRAUS, K. 1990: *Fernerkundung Band 2: Auswertung photographischer und digitaler Bilder*. –Bonn, Germany, 314 pp.
- KRESSLER, F., FRANZEN, M. & K. STEINOCHER, 2003: Automationsgestützte Erfassung der Landnutzung in Staedten mittels objektorientierter Auswertung von Luftbildern. In: STROBL., J., BLASCHKE, T. & G. GRIESEBNER (editors), 2003: *Angewandte Geographische Informationsverarbeitung XV*. –Salzburg, Austria, pp. 250-256.
- KRISHNAMURTHY, J., 1997: The evaluation of digitally enhanced Indian Remote Sensing Satellite (IRS) data for lithological and structural mapping. In: *International Journal of Remote Sensing*, Vol. 18, No. 16, pp. 3409-3437.

- KRUSE, F.A., BOARDMAN, J.W. & A.B. LEFKOFF, 2000: Extraction of Compositional Information for Trafficability Mapping from Hyperspectral Data. In: Proceedings of the SPIE International Symposium on Aerosense, 24-28 April 2000, Orlando, FL, pp. 262-273.
- KRUSE, F., BOARDMAN, J.W. & J.F. HUNTINGTON, 2003: Comparison of Airborne Hyperspectral Data and EO-1 Hyperion for Mineral Mapping. In: IEEE Transactions on Geoscience and Remote Sensing, Vol. 41, No. 6, pp. 1388-1400.
- KRUSE, F.A., KIERSIN-YOUNG, K.S. & J.W. BOARDMAN, 1990: Mineral Mapping at Cuprite, Nevada with a 63-Channel Imaging Spectrometer. In: Photogrammetric Engineering and Remote Sensing, Vol. 56, No.1, pp. 83-92.
- KUEMMERLE, T., 2003: Investigating the impact of livestock grazing by means of remote sensing and GIS – a case study in Northern Greece using multi-date spectral mixture analysis and cost surface modeling. Master thesis at the University of Trier, Germany, 167 pp.
- KUENZER, C., 2001: Multitemporale Untersuchung der Landnutzung des *Parc Naturel de la Haute Sûre* unter Einsatz von Fernerkundung und GIS im Hinblick auf die Wasserqualitaet des Stausees Obersauer. Master thesis at the University of Trier, Department of Remote Sensing. – Trier, 158 pp.
- KUENZER, C., NIEBERGALL, S. & S. VOIGT, 2004b: Multitemporale Untersuchungen im chinesischen Kohleabbau- und Kohlebrandgebiet Ruqigou basierend auf Landsat- und höchstauflösenden Quickbird Daten. In: STROBL, J., BLASCHKE, T. AND GRIESEBNER, G., (editors): Angewandte Geoinformatik 2004. Beitrage zum 16. AGIT-Symposium Salzburg 2004. –Heidelberg, Wichmann, pp.393-398.
- KUENZER, C., STRUNZ, G., VOIGT, S. & W. WAGNER, 2004a: Multitemporal Landcover Investigations in a Semi-arid Mining Environment: Coal Fire Areas in Northern China. In: Proceedings of the Conference of the EARSeL Special Interest Group on Land use and Land Cover, Dubrovnik, May 2004, 8 pp.
- KUENZER, C., ZHANG, J. & S. VOIGT, 2003: Set Up of a Spectral Database for Unmixing Approaches in Mining Environments in North-central China: Demarcating Coal Fire Risk Areas. In: Proceedings of the 3rd EARSeL Workshop on Imaging Spectroscopy, Herrsching, Germany, May 13-16 2003, pp. 344-348.
- KUENZER, C., ZHANG, J., TETZLAFF, A., VOIGT, S., VAN DIJK, P., WAGNER, W. & H. MEHL: Uncontrolled coal fires and their environmental impacts: Investigating two arid mining environments in north-central China. In review at: Applied Geography, 16 pp.
- L ...**
- LAPHAM, D.M., BARNES, J.H., DOWNEY, W.F. & R. FINKELMAN, 1980: Mineralogy associated with burning anthracite deposits of Eastern Pennsylvania. Mineral Resource Report 78 of the Pennsylvania Geological Survey, 82 pp.
- LAUER, W. & P. FRANKENBERG, 1986: Zur Rekonstruktion des Klimas. 2nd edition – Berlin, Germany, 54 pp.

- LE HÉGARAT-MASCALE, S., A. QUESNEY, D. VIDAL-MADJAR & O. TACONET, 2000: Land cover discrimination from multitemporal ERS images and multispectral Landsat images: a study case in an agricultural area in France. In: *International Journal of Remote Sensing*, Vol. 22, No. 3, pp. 435-456.
- LENZ, L. & B. WIEDERSICH, 1993: *Grundlagen der Geologie und Landschaftsformen*. Deutscher Verlag für Grundstoffindustrie – Stuttgart, Germany, 348 pp.
- LI, D.X., 1985: Applied study of airborne remote sensing in Taiyuan coalfield, China. Internal Report of the Remote sensing centre of the ministry of coal industry, Xian, China, pp. 3-10 (in Chinese).
- LI, X. & A.G.O. YEH, 1998: Principal component analysis of stacked multi-temporal images for the monitoring of rapid urban expansion in the Pearl River Delta. In: *International Journal of Remote Sensing*, Vol. 19, No. 8, pp. 1501-1518.
- LILLESAND, T.M. & R.W. KIEFER 1994: *Remote Sensing and Image Interpretation*. 3rd edition. –New York, USA, 748 pp.
- LIU, J.G., A. BLACK, H. LEE, H. HANIZUMI & J.M. MOORE, 2001: Land surface change detection in a desert in Algeria using multi-temporal ERS SAR coherence images. In: *International Journal of Remote Sensing*, Vol. 22, No. 13, pp. 2463-2477.
- LIVINGOOD, M., WINICATIES, J. & J. STEIN, 1999: *Centralia Mine Fire Analysis: Presence of Sulfur-bearing Mineral Deposits at Thermal Vents*. Research paper at West Chester University, Pennsylvania, USA, 9 pp.
- LOCAL FARMERS, 2002: Interviews with local farmers during field investigations in 2002. Four farmers irrigating their fields were interviewed with the help of a translator.
- LOESCHENBRAND, F., MOTT, C., ANDRESEN, T., ZIMMERMANN, S., SCHNEIDER, T. & U. KIAS, 2003: Objektorientierte Klassifikation hyperspektraler CASI-Daten zur Ableitung naturschutzfachlich relevanter Landbedeckungsparameter. In: STROBL, J., BLASCHKE, T. & G. GRIESEBNER (editors), 2003: *Angewandte Geographische Informationsverarbeitung XV*. –Salzburg, pp.268-274.
- LÖFFLER, E., 1994: *Geographie und Fernerkundung*. Teubner. –Stuttgart, Germany, 251 pp.
- LONGHI, I., SGAVETTI, M., CHIARI, R. & C. MAZZOLI, 2001: Spectral analysis and classification of metamorphic rocks from laboratory reflectance spectra in the 0.4-2.5 μm interval: a tool for hyperspectral data interpretation. In: *International Journal of Remote Sensing*, Vol. 22, No. 18, pp. 3763-3782.
- LUNETTA, R. & C.D. ELVIDGE (editors), 1999: *Remote Sensing Change Detection*. –London, Great Britain, 320 pp.
- LUNETTA, R.S. 1999: Applications, Project Formulation, and Analytical Approach. In: LUNETTA, R. & C.D. ELVIDGE (editors): *Remote Sensing Change Detection*. –London, 318 pp.

M ...

- MALYUTO, V., 2002: Simulated stellar classification combining the minimum distance method with a maximum likelihood procedure. In: *New Astronomy*, Vol. 7, No. 8, pp. 461-470.

12. References

- MANSOR S.B., CRACKNELL A.P., SHILIN B.V. & V.I. GORNYI, 1994: Monitoring of underground coal fires using thermal infrared data. In: *International Journal of Remote Sensing*, Vol. 15, No. 8, pp. 1675-1685.
- MARACCI, G, 1992: Field and laboratory narrow band spectrometers and the techniques employed. In: TOSELLI, F. & J. BODECHTEL (editors): *Imaging Spectroscopy: Fundamentals and Prospective Applications*. –Dordrecht, Netherlands, pp. 33-46.
- MARKHAM, B.L., J.L. BARKER, W.C. BONCYK, E. KAITA & D.L. HELDER, 1996: Landsat-7 Enhanced Thematic Mapper Plus – in flight radiometric calibration. In: *International Geoscience and Remote Sensing Symposium*, 2, Lincoln, Nebraska, USA, pp. 1270-1272.
- MAS, J.-F., 1999: Monitoring land-cover changes: a comparison of change detection techniques. In: *International Journal of Remote Sensing*, Vol. 20, No. 1, pp. 139-152.
- MASEK, J.G., M. HONZAK, S.N. GOWARD, P. LIU & E. PAK, 2001: Landsat7 ETM+ as an observatory for land cover. Initial radiometric and geometric comparisons with Landsat 5 Thematic Mapper. In: *Remote Sensing of the Environment*, Vol. 78, No. 1, pp.118-130.
- MATSON M. & J. DOZIER, 1981: Identification of sub-resolution high temperature sources using a thermal IR sensor. In: *Photogrammetric Engineering and Remote Sensing*, Vol. 47, No. 1, pp. 1311-1318.
- MCIVER, D.K. & M.A. FRIEDL, 2002: Using prior probabilities in decision-tree classification of remotely sensed data. In: *Remote Sensing of Environment*, Vol. 81, No. 2-3, pp. 253-261.
- MICKUS, K. & E. JOHNSON, 2001: Mapping sedimentary and volcanic units within and surrounding Petrified Forest National Park, Arizona, using Landsat-5 and SPOT panchromatic data. In: *International Journal of Remote Sensing*, Vol. 22, No. 10, pp. 1919-1935.
- MIKA, A.M., 2000: Three Decades of Landsat Instruments. In: *Photogrammetric Engineering and Remote Sensing*, Vol. 63, No. 7, pp. 839-852.
- MILTON, J. E., 1987: Principles of field spectroscopy. In: *International Journal of Remote Sensing*, Vol. 8, No. 1, pp. 1807-1827
- MOELLER-JENSEN, L., 1997: Classification of urban land cover based on expert systems, object models and texture. In: *Urban Systems*, Vol. 21, No. 3 & 4, pp. 291-302.
- MOXHAM R.M. & G.W. GREENE, 1967: Infrared surveys of coal mine fires in the anthracite and bituminous fields, Pennsylvania. USA, Geological Survey Inter-Agency Report BM-2, U.S. Bureau of Mines, 67 pp.
- MUECHER, C.A., STEINOCHEK, K.T., KRESSLER, F.P. & C. HEUNKS, 2000: Land cover characterization and change detection for environmental monitoring of pan-Europe. In: *International Journal of Remote Sensing*, Vol. 21, No. 6&7, 2000, pp. 1159-1181.
- MUENZER, H., 1972: Der Einfluss von Fremdstoffen auf das Selbstentzündungsverhalten von Steinkohle. Teil 1: Zum Einfluss des Wassers. Glückauf Forschungshefte 33, pp. 116-120. In: STACH, E., MACKOWSKY, M.-TH., TEICHMÜLLER, M., TAYLOR, G.H., CHANDRA, D & R. TEICHMÜLLER, 1975: *Stach's Text book of Coal Petrology*, 2nd edition -Berlin, Germany, 535 pp.

N ...

- NERRY, F., LABED, J. & M.P. STOLL, 1990: Spectral Properties of land Surfaces in the Thermal Infrared – Laboratory Measurements of Absolute Spectral Emissivity Signatures. In: *Journal of Geophysical Research*, Vol. 95, No. B5, pp. 7072-7044.
- NETELER, M., 1999: Spectral Mixture Analysis von Satellitendaten zur Bestimmung von Bodenbedeckungsgraden im Hinblick auf die Erosionsmodellierung. Master-thesis at the University of Hannover, Germany, 131 pp.
- NIANG, A., GROSS, L., THIRIA, S., BADRAN, F. & C. MOULIN, 2003: Automatic neural classification of ocean colour reflectance at the top of the atmosphere with introduction of expert knowledge. In: *Remote Sensing of Environment*, Vol. 86, No. 2, pp. 257-271.
- NIELSON, A.A: 1994: Analysis of regularly and irregularly sampled, spatial, multivariate, and multi-temporal data. Ph.D. thesis, Institute of Mathematical Modelling, Technical University of Denmark, Lyngsby, Denmark, 198 pp.

O ...

- OUAIDRARI, H. & E.F. VERMOTE, 1999: Operational Atmospheric Correction of Landsat TM Data. In *Remote Sensing of Environment*, Vol. 70, No. 1, pp. 4-15.

P ...

- PAGE, S.E., SIEGERT, F., RIELEY, J.O., BOEHM, H.D. & A. JAYA 1997: The amount of carbon released from peat and forest fires in Indonesia during 1997. In: *Nature*, Vol. 420, pp. 61-65.
- PAL, S.K., BANDYOPADHYAY, S. & C.A. MURTHY, 2001: Genetic classifiers for remotely sensed images: comparison with standard methods. In: *International Journal of Remote Sensing*, Vol. 22, No. 13, pp. 2545-2569.
- PALACIOS-ORUETA, A., PINZON, J., USTIN, S.L. & D.A. ROBERTS, 1999: Remote Sensing of Soils in the Santa Monica Mountains: Hierarchical Foreground and Background Analysis. In: *Remote Sensing of Environment*, Vol. 68, No. 2, pp. 138-151.
- PATRONO, A., 1996: Synergism of remotely sensed data for land cover mapping in heterogeneous alpine areas: an example combining accuracy and resolution. In: *ITC Journal*, No. 2, pp. 101-109.
- PEARLMAN, J.S., BARRY, P.S., SEGAL, C.C., SHEPANSKI, J., BEISO, D. & S.L. CARMAN, 2003: Hyperion, a Space-Based Imaging Spectrometer. In: *IEEE Transactions on Geoscience and Remote Sensing*, Vol. 41, No. 6, pp. 1160-1173.
- PENG, B., 1983: Inhibition of spontaneous combustion by controlling the water content of the coal. In: *Proceedings of the 20th International Conference of Safety in Mines.* –Sheffield, 87 pp.
- PENNIG, L., 2002: Studienprojekt: Globale Dimension der Kohlebrandproblematik. Unpublished manuscript at the University of Jena, Germany, 50 pp.
- PENNIG, L., 2003: Vergleich zweier Kohlebrandregionen in Nordchina mit Hilfe von Fernerkundungsdaten und GIS. Master Thesis at the University of Jena, 90 pp.

- PEOPLE'S REPUBLIC OF CHINA MINISTRY OF GEOLOGY AND MINERAL RESOURCES, 1990: Regional Geology of Ningxia Hui Autonomous Region. Geological Memoirs, Series 1, No. 22. Beijing, China, pp. 469-522.
- PEOPLE'S REPUBLIC OF CHINA MINISTRY OF GEOLOGY AND MINERAL RESOURCES, 1991: Regional Geology of Inner Mongolia Autonomous Region. Geological Memoirs, Series 1, No. 25. Beijing, China, pp. 667-725.
- PRAKASH, A. & R.P. GUPTA, 1998: Land-use mapping and change detection in a coal mining area – a case study in the Jharia coalfield, India. In: International Journal of Remote Sensing, Vol. 19, No. 3, pp. 391-410.
- PRAKASH, A. & R.P. GUPTA, 1999: Surface fires in Jharia Coalfield, India - their distribution and estimation of area and temperature from TM data. In: International Journal of Remote Sensing, Vol. 20, No. 10, pp. 1935-1946.
- PRAKASH, A., FIELDING, E.J., GENS, R., VAN GENDEREN, J.L. & D.L. EVANS, 2001: Data fusion for investigating land subsidence and coalfire hazards in a coal mining area. In: International Journal of Remote Sensing, Vol. 22, No. 6, pp. 921-932.
- PRAKASH, A., GENS, R. & Z. VEKERDY, 1999: Monitoring coal fires using multi-temporal night-time thermal images in a coalfield in North-west China. In: International Journal of Remote Sensing, Vol. 20, No. 14, pp. 2883-2888.
- PRAKASH, A., GUPTA, R.P. & A.K. SARAF, 1997: A Landsat TM based comparative study of surface and subsurface fires in the Jharia Coalfield, India. In: International Journal of Remote Sensing, Vol. 18, No. 14, pp. 2463-2469.
- PRAKASH, A., SARAF, A.K., GUPTA, R.P., DUTTA, M. & R.M. SUNDARAM, 1995: Surface thermal anomalies with underground fires in Jharia coal mine, India. In: International Journal of Remote Sensing, Vol. 16, No. 2, pp. 2105-2109.
- PRATT, D.A., FOSTER, S.J. & C.D. ELLYETT, 1980: A Calibration Procedure for Fourier Series Thermal Inertia Models. In: Photogrammetric Engineering & Remote Sensing, Vol. 46, No. 4, pp. 529-538.
- PROY, C., D. TANRÉ & P.Y. DESCHAMPS, 1989: Evaluation of Topographic Effects in Remotely Sensed Data. In: Remote Sensing of the Environment. Vol. 30, No 1, 1989, pp. 21-32.

Q ...

R ...

- RABCHEVSKY, G.A., 1972: Determination from available satellite and aircraft imagery of the applicability of remote sensing techniques to the detection of fires burning in abandoned coal mines and unmined coal deposits located in North Central Wyoming and Southern Montana. In: U.S. Department of Interior, Bureau of Mines, Prepared by Allied Research Associates Inc., Contract No. SO 211087, Final Report No. 8G86-F, 21 pp.
- RADELOFF, V., HILL, J. & W. MEHL (1997): Forest Mapping from Space – Enhanced satellite data processing by spectral mixture analysis and topographic corrections. –Luxemburg, 88 pp.

- RATHORE C.S. & R. WRIGHT, 1993: Monitoring environmental impacts of surface coal mining. In: *International Journal of Remote Sensing*, Vol. 14, No. 6, pp. 1021-1042.
- RAY, T.W. & B.C. MURRAY, 1996: Nonlinear Spectral Mixing in Desert Vegetation. In: *Remote Sensing of Environment*, Vol. 55, No. 1, pp. 59-64.
- REES, W.G., WILLIAMS, M. & P. VITEBSKY, 2003: Mapping land cover change in a reindeer herding area of the Russian Arctic using Landsat TM and ETM+ imagery and indigenous knowledge. In: *Remote Sensing of Environment*, Vol. 85, No. 4, pp. 441-452.
- RESMINIE, R.G., KAPPUS, M.E., ALDRICH, W.S., HARSANYI, J.C. & M. ANDERSON, 1997: Mineral mapping with Hyperspectral Digital Imagery Collection Experiment (HYDICE) sensor data at Cuprite, Nevada, U.S.A.. In: *International Journal of Remote Sensing*, Vol. 18, No. 7, pp. 1553-1570.
- RICHARDS, J.A., 1986: *Remote Sensing Digital Image Analysis – an Introduction*. –Berlin, Germany, 281 pp.
- RICHARDS, J.A., 1996: Classifier Performance and Map Accuracy. In *Remote Sensing of Environment*, Vol. 57, No. 3, pp. 161-166.
- RICHTER, G. (editor) 1996: *Handbuch ausgewählter Klimastationen der Erde*. 5th ed., -Trier, Germany, 400 pp.
- RICHTER, R., 1998: Correction of satellite imagery over mountainous terrain. *Applied Optics*, Vol. 37, No.18, pp. 4004-4015.
- RICHTER, R., 2003: *Atmospheric and Topographic Correction for Satellite Imagery*. ATCOR-2/3 User Guide, version 5.5., DLR-I3 564-02/03, Wessling, Germany, 57 pp.
- ROBERTS, D.A., GARDNER, M., CHURCH, R., USTIN, S., SCHEER, G. & R.O. GREEN, 1998: Mapping Chaparral in the Santa Monica Mountains Using Multiple Endmember Spectral Mixture Models. In: *Remote Sensing of Environment*, Vol. 65, No. 3, pp. 267-279.
- ROBERTS, D.A., SMITH, M.O. & J.B. ADAMS, 1993: Green vegetation, nonphotosynthetic vegetation, and soils in AVIRIS data. In: *Remote Sensing of Environment*, Vol. 44, No. 2-3, pp. 255-269.
- ROSEMA, A., H. GUAN, H. VELD, Z. VEKERDY, A. TEN KATEN & A. PRAKASH, 1999: *Manual of coal fire detection and monitoring*. Utrecht, Netherlands, 240 pp.
- ROSENQVIST, A., MILNE, A., LUCAS, R., IMHOFF, M. & C. DOBSON, 2003: A review of remote sensing technology in support of the Kyoto Protocol. In: *Environmental Science and Policy*, No. 6, pp. 441-455.
- ROTHERY, D.A. & P.W. FRANCIS, 1990: Short wavelength infrared images for volcano monitoring. In: *International Journal of Remote Sensing*, Vol. 11, No. 10, pp. 1665-1667.
- RSI, 2003: *Research Systems Incorporated, ENVI 3.4. online documentation*.
- RUECKER, G., 2003: Ein Satelliten- und GIS-gestuetztes Waldbrand Fruehwarnsystem fuer Tropische Regenwaelder in Ost-Kalimantan, Indonesien. In: STROBL, J., BLASCHKE, T. AND GRIESEBNER, G., (editors): *Angewandte Geographische Informationsverarbeitung XV. Beitraege zum AGIT-Symposium Salzburg 2003*. –Heidelberg, Wichmann, pp.402-410.
- RUSS, J.C., 1999: *Image Processing Handbook*. 3rd edition, -Raleigh, North Carolina, USA, 744, pp.

S ...

- SABINS, F.F., 1996: Remote Sensing. 3rd edition, - New York, USA, 450 pp.
- SAN MIGUEL-AYANZ, J. & G.S. BIGING, 1997: Comparison of Single Stage and Multi-Stage Classification Approaches for Cover Type Mapping with TM and SPOT Data. In: Remote Sensing of Environment, Vol. 59, No. 1, pp. 92-104.
- SARAF, A.K., PRAKASH, A., SENGUPTA, S., & P. GUPTA, 1995: Landsat-TM data for estimating ground temperature and depth of subsurface coal fire in the Jharia coal field, India. In: International Journal of Remote Sensing, Vol. 16, No. 12, pp. 2111-2124.
- SCHAAB, G., 2000: Modellierung und Visualisierung der räumlichen und zeitlichen Variabilität der Einstrahlungsstärke mittels eines Geo-Informationssystems. Ph.D thesis at the Technical University of Dresden., Germany, 160 pp.
- SCHARDT, M., 1990: Verwendbarkeit von Thematic Mapper-Daten zur Klassifizierung von Baumarten und natürlichen Altersklassen. Published science report, Ph.D. thesis, DLR-FB 90-44, 199 pp.
- SCHLERF, M., ATZBERGER, C., UDELHOVEN, T., JARMER, T., MADER, S., WERNER, W. & J. HILL, 2003: Spectrometric estimation of leaf pigments in Norway spruce needles using band-depth analysis, partial least-square regression and inversion of a conifer leaf model. In: Proceedings of the 3rd EARSeL Workshop on Imaging Spectroscopy, Herrsching, Germany, May 13-16 2003, pp. 559-569.
- SCHMUGGE, T.J., BECKER, F. & Z.L. LI, 1991: Spectral Emissivity Variations Observed in Airborne Surface Temperature Measurements. In: Remote Sensing of Environment, Vol. 35, No. 2, pp. 95-104.
- SCHNEIDER, W., 1996: The coal-bearing Jurassic at the southern margin of the Junggar basin, Xinjiang. In: Geowissenschaften, Vol. 14, pp. 285-287.
- SCHOTT, J.R., 1997: Remote Sensing, The Image Chain Approach. – Oxford, Great Britain, 394 pp.
- SCHOWENGERDT, R.A., 1997: Remote Sensing – Models and Methods for Image Processing. 2nd revised and expanded edition, -San Diego, 517 pp.
- SCHROEDER-BRZOSNIOWSKY, M., 2000: Stochastic Modeling of Image Content in Remote Sensing Image Archives. Ph.D. thesis at the Swiss Federal Institute of Technology, -Zurich, 177 pp.
- SCHRÖTER, W., LAUTENSCHLÄGER, K.-H. & H. BIBRACK, 1992: Chemie – Fakten und Gesetze. Buch- und Zeitverlagsgesellschaft mbH, -Cologne, Germany, 424 pp.
- SCHWARZ, J., H.-D. BETTAC & K.-D. MISSLING, 1999: Das DFD Bodensegment für Landsat 7. In: MEHL, H. & S. DECH (editors): Tagungsband: 16. Nutzerseminar des DFD der DLR, – Oberpfaffenhofen, Germany, pp. 49-57.
- SETTLE, J.J. & N.A. DRAKE, 1993: Linear mixing and the estimation of ground cover proportions. In: International Journal of Remote Sensing, Vol. 14, No. 6, pp. 1159-1177.
- SKAKUN, R.S., WULDER, M.A. & S.E. FRANKLIN, 2003: Sensitivity of the thematic mapper enhanced wetness difference index to detect mountain pine beetle red-attack damage. In: Remote Sensing of Environment, Vol. 86, No. 4, pp. 433-443.

- SLAVECKI R.J., 1964: Detection and location of subsurface coal fires. In: Proceedings of the third Symposium on Remote Sensing of Environment. 14-16 October 1964, Institute of Science and Technology, University of Michigan, USA, pp. 537-547.
- SMITH, A.C. & C.P. LAZZARA, 1987: Spontaneous combustion of US coals. Internal Report 9079 of the Department of the Interior, Bureau of Mines. –Pittsburgh, USA, 29 pp.
- SMITH, G.M. & R.M. FULLER, 2001: An integrated approach to land cover classification: an example in the Island of Jersey. In: International Journal of Remote Sensing, Vol. 22, No. 16, pp. 3123-3142.
- SMITH, M.O., J.B. ADAMS & D.E. SABOL, 1994: Spectral Mixture Analysis – New Strategies for the Analysis of Multispectral Data. In: HILL, J. & J. MÉGIER (editors): Imaging Spectrometry – a Tool for Environmental Observations. –Dordrecht, Netherlands, pp.125-145.
- SMITH, M.O., USTIN, S.L., ADAMS, J.B. & A.R. GILLESPIE, 1990: Vegetation in Deserts: I. A Regional Measure of Abundance from Multispectral Images. In: Remote Sensing of the Environment, Vol. 31, No. 1, pp. 1-26.
- SONG, C., C.E. WOODCOCK, K.C. SETO, M.P. LENNEY & S.A. MACOMBER, 2001: Classification and Change Detection using Landsat TM Data: When and How to Correct Atmospheric Effects? In: Remote Sensing of Environment, Vol. 75, No. 2, pp. 230-244.
- STAENZ, K., NADEAU, C., SECKER, J. & P. BUDKEWITSCH, 2000: Spectral Unmixing Applied to Vegetated Environments in the Canadian Arctic for Mineral Mapping. In: Proceedings of the XIX ISPRS Congress, 15.07.-23.07.2000, Amsterdam, Netherlands, 8 pp.
- STEHMAN, S.V., 1997: Selecting and Interpreting Measures of Thematic Classification Accuracy. In: Remote Sensing of Environment, Vol. 62, No. 1, pp. 77-89.
- STOLZ, R., 1998: Die Verwendung der Fuzzy Logic Theorie zur wissensbasierten Klassifikation von Fernerkundungsdaten. Ph.D. thesis at the University of Munich, Germany, 178 pp.
- SUN, Y. 2002: Personal Interviews during the fieldwork campaign in September 2002. Y. Sun is an engineer of the Wuda coal fire fighting department and leads the team on coal geology.
- SUN, Y. 2003: Personal Interviews during the fieldwork campaign in September 2003. Y. Sun is an engineer of the Wuda coal fire fighting department and leads the team on coal geology.
- SUNAR, F., 1998: An analysis of changes in a multi-date data set: a case study in the Ikitelli area, Istanbul, Turkey. In: International Journal of Remote Sensing, Vol. 19, No. 2, pp. 225-235.
- SWITZER, P. & A.A. GREEN, 1984: Min/Max Autocorrelation Factors for Multivariate Spatial Imagery. In: Tech. Report No. 6, Department of Statistics, Stanford University, Stanford, California, USA, 10 pp.

T ...

- TEILLET, P.M., BARKER, J.L., MARKHAM, B.L., IRISH, R.R., FEDOSEJEVS, G. & J.C. STOREY, 2001: Radiometric cross calibration of the Landsat-7 ETM+ and Landsat-5 TM sensors based on tandem data sets. In: Remote Sensing of Environment, Vol. 78, No. 1, pp. 39-54.

- TETZLAFF, A. 2004: Coal fire quantification using Aster, ETM and Bird satellite instrument data. Ph.D thesis at the Ludwig Maximilians University Munich, Germany, 155 pp.
- THESEIRA, M.A., THOMAS, G. & C.A.D. SANNIER, 2002: An evaluation of spectral mixture modelling applied to a semi-arid environment. In: *International Journal of Remote Sensing*, Vol. 23, No. 4, pp. 687-700.
- THOME, K.J., 2001: Absolute radiometric calibration of Landsat 7 ETM+ using the reflectance-based method. In: *Remote Sensing of Environment*, Vol. 78, No. 1, pp. 27-38.
- THOMSON, A.G., FULLER, R.M. & J.A. EASTWOOD, 1998: Supervised versus unsupervised methods for classification of coasts and river corridors from airborne remote sensing. In: *International Journal of Remote Sensing*, Vol. 19, No. 17, pp. 3423-3431.
- TIPLER, P.A., 2000: Physik. 3rd edition, Spektrum Akademischer Verlag, Heidelberg, Germany, 1520 pp.
- TODD, D. & J. FEMGJUN, 1997: Interregional coal flows in China and the problem of transport bottlenecks. In: *Applied Geography*, Vol. 17, No. 3, pp. 215-230.
- TOKOLA, T., J. SARKEALA & M. VAN DER LINDEN, 2001: Use of topographic correction in Landsat TM-based forest interpretation in Nepal. In: *International Journal of Remote Sensing*, Vol. 22, No. 4, pp. 551-563.
- TOMPKINS, S., MUSTARD, J.F., PIETERS, C.M. & D.W. FORSYTH, 1997: Optimization of Endmembers for Spectral Mixture Analysis. In: *Remote Sensing of Environment*, Vol. 59, No. 3, pp. 472-489.
- TSO, B. & MATHER, P.M., 2001: *Classification Methods for Remotely Sensed Data*. –London, Great Britain, 329 pp.

U ...

- UNDERWOOD, E., USTIN, S. & D. DIPIETRO, 2003: Mapping non-native plants using hyperspectral imagery. In: *Remote Sensing of Environment*, Vol. 86, No. 2, pp. 150-161.
- UNITED STATES GEOLOGICAL SURVEY, 1999: *Landsat 7 Data Users Handbook*. –Sioux Falls, USA

V ...

- VAN DER MEER, F.D., 1999a: Image classification through spectral unmixing. In: STEIN, A., VAN DER MEER, F.D. & B. VAN DE GORTE, (editors): *Spatial Statistics for Remote Sensing*, Kluwer Academic Publishers, Netherlands, pp. 185-193.
- VAN DER MEER, F.D. & DE JONG, S. (editors), 2001: *Imaging Spectrometry: Basic Principles and Prospective Applications*. –Dordrecht, Netherlands, 425 pp.
- VAN DER MEER, F.D., 1999b: Iterative Spectral Unmixing (ISU). In: *International Journal of Remote Sensing*, Vol. 20, No. 17, pp. 3431-3436.
- VAN DER MEER, F.D., 2000: Spectral curve shape matching with a continuum removed CCSM algorithm. In: *International Journal of Remote Sensing*, Vol. 21, No. 16, pp. 3179-3185.

- VAN DER MEER, F.D., VAZQUES-TORRES & P.M. VAN DIJK, 1997: Spectral Characterization of ophiolite lithologies in the Troodos Ophiolite complex of Cyprus and its potential in prospecting for massive sulphide deposits. In: *International Journal of Remote Sensing*, Vol. 18, No. 6, pp. 1245-1257.
- VAN GENDEREN, J.L., & H. GUAN, 1997: Environmental monitoring of spontaneous combustion in the North China coalfields. –Enschede, Netherlands, 243 pp.
- VERBURG, P.H., VELDKAMP, A. & L.O. FRESCO, 1999: Simulation of changes in the spatial pattern of land use in China. In: *Applied Geography*, Vol. 19, pp. 211-233.
- VERBYLA, D.L. & S.H. BOLES (2000): Bias in land cover change estimates due to misregistration. In: *International Journal for Remote Sensing*, Vol. 21, No.18, pp.3553-3560.
- VERMOTE, E.F., D. TANRÉ, J.L.DEUZÉ, M. HERMAN & J.-J. MORCRETTE, 1997: Second Simulation of the Satellite Signal in the Solar Spectrum, 6S: An Overview. In: *IEEE Transactions on Geosciences and Remote Sensing*, Vol. 35, No. 3, pp. 675-686.
- VIDAL, A., 1991: Atmospheric and emissivity correction of land surface temperature measured from satellite using ground measurements or satellite data. In: *International Journal of Remote Sensing*, Vol. 12, No. 12, pp. 2449-2460.
- VIOVY, N., 2000: Automatic Classification of Time Series (ACTS): a new clustering method for remote sensing time series. In: *International Journal of Remote Sensing*, Vol. 21, No. 6&7, pp. 1537-1560.
- VOGELMANN, J.E., T. SOHL & S.M. HOWARD 1998: Regional Characterization of Land Cover Using Multiple Sources of Data. In: *Photogrammetric Engineering & Remote Sensing*, Vol. 64, No.1, pp.47-57
- VOIGT, S., 2000: Advanced methods for operational mapping of Alpine snow cover using medium resolution optical satellite data. Ph.D. thesis at the University of Bern, Switzerland, 91 pp.
- VOIGT, S., TETZLAFF, A., ZHANG, J., KUENZER, C., ZHUKOV, B., STRUNZ, G., OERTEL, D., ROTH, A., VAN DIJK, P. & H. MEHL, 2004: Integrating Satellite Remote Sensing Techniques for Detection and Analysis of Uncontrolled Coal Seam Fires in North China. In: *International Journal of Coal Geology*, No. 59, pp. 121-136.

W ...

- WAGNER, W., 2003: Global Climate Change. Unpublished script for a lecture at Vienna University of Technology, 111 pp.
- WAGNER, W., LUCKMANN, A., VIETMEIER, J., TANSEY, K., BALZTER, H., SCHMULLIUS, C., DAVIDSON, M., GAVEAU, D., GLUCK, M. & T. LETOAN, 2003: Large scale mapping of boreal forest in SIBERIA using ERS tandem coherence and JERS backscatter data. In: *Remote Sensing of Environment*, Vol. 85, No. 2, pp. 125-144.
- WALKER, S., 1999: Uncontrolled fires in coal and coal wastes. International Energy Agency, IEA on Coal Research –London, Great Britain, 73 pp.
- WANG, C., 2002. Detection of coal fires in Xinjiang (China) using remote sensing techniques. Master thesis at ITC, Enschede, Netherlands, 93 pp.

- WANG, F., 1990: Fuzzy supervised classification of remote sensing images. In: *IEEE Transactions on Geoscience and Remote Sensing*, No. 28, pp. 194-201.
- WARNER, T.A. & X. CHEN, 2001: Normalization of Landsat thermal imagery for the effect of solar heating and topography. In: *International Journal of Remote Sensing*, Vol. 22, No. 5, pp. 773-788.
- WATSON, N. & D. WILCOCK, 2001: Preclassification as an Aid to the Improvement of Thematic and Spatial Accuracy in Land Cover Maps Derived from Satellite Imagery. In: *Remote Sensing of Environment*, Vol. 75, No. 2, pp. 267-278.
- WEISCHET, W. 1988: *Einführung in die Allgemeine Klimatologie. Physikalische und meteorologische Grundlagen*. 4th edition, -Stuttgart, Germany, 264 pp.
- WEN, C.G. & R. TATEISHI, 2001: 30-second degree grid land cover classification of Asia. In: *International Journal of Remote Sensing*, Vol. 22, No. 18, pp. 3845-3854.
- WRIGHT, P. & R. STOW, 1999: Detecting mining subsidence from space. In: *International Journal of Remote Sensing*, Vol. 20, No. 6, pp. 1183-1188.
- WU, W. & W. ZHANG, 2003: Present land use and cover patterns and their development potential in North Ningxia, China. In: *Journal of Geographical Sciences*, Vol. 13, No.1, pp. 54-62
- WU, W., LAMBIN, E.F. & M.-F. COUREL 2001: Land use and cover change detection and modelling for North Ningxia, China. *PRODIG-UMR8586/CNRS, Louvain, Belgium*, 37 pp.
- X ...**
- XIE, Y. 2001. Einfluss der Weidewirtschaft auf die Vegetation und die ökologischen Bedingungen der Trockensteppe in Ningxia, China. –Ph.D thesis at the University of Frankfurt, Germany, 135 pp.
- Y ...**
- YAN, G., 2003: Pixel based and object oriented image analysis for coal fire research. Master thesis at ITC, Enschede, Netherlands, 82 pp.
- YAN, H., 1995: Detection of Areas of spontaneous combustion of coal by using airborne and TM data in Xinjiang, China. Master thesis at ITC, Enschede, Netherlands, 71 pp.
- YANG, G., COLLINS, M.J. & P. GONG, 1998: Multisource data selection for lithologic classification with artificial neural networks. In: *International Journal of Remote Sensing*, Vol. 19, No. 18, pp. 3675-3680.
- YOUNG, S.S. & C.Y. WANG, 2001: Land-cover analysis of China using global-scale Pathfinder AVHRR Landcover (PAL) data, 1982-92. In: *International Journal of Remote Sensing*, Vol. 22, No. 8, pp. 1457-1477.
- YUAN, D., C.D. ELVIDGE & R.S. LUNETTA, 1999: Survey of Multispectral Methods for Land Cover Change Analysis. In: LUNETTA, R. & C.D. ELVIDGE (editors): *Remote Sensing Change Detection*. –London, pp.21-39.

Z ...

- ZHANG, J., 1996: SWIR spectra of rocks in areas affected by coal fires, Xinjiang Autonomous Region, P.R. of China. Master thesis at the ITC, Enschede, Netherlands, 74 pp.
- ZHANG, J., 2004: Spatial and Statistical Analysis of Thermal Satellite Imagery for Extraction of Coal Fire Related Anomalies. Ph.D. thesis at the Technical University Vienna, Austria, 166 pp.
- ZHANG, J., WAGNER, W., PRAKASH, A., MEHL, H., AND VOIGT, S., 2004a: Detecting Coal Fire Using Remote Sensing Techniques. In: *International Journal of Remote Sensing*, Vol. 25, No. 16, pp. 3193-3220.
- ZHANG, R. 2003: Personal interviews during the fieldwork campaign in September 2003. R. Zhang is the chief engineer of the Wuda mine.
- ZHANG, X. 1997: Regional geological mapping by using remote sensing and sedimentary characteristics of the Ruqigou basin, Ningxia, China. Master thesis at ITC, Enschede, Netherlands, 87 pp.
- ZHANG, X., 1998: Coal Fires in Northwest China – Detection, Monitoring, and Prediction Using Remote Sensing Data. PhD-thesis at ITC –Enschede, Netherlands, 235 pp.
- ZHANG, X., VAN GENDEREN, J.L. & S.B. KROONENBERG, 1997: A method to evaluate the capability of Landsat-5 TM band 6 data for sub-pixel coal fire detection. In: *International Journal of Remote Sensing*, Vol. 18, No. 15, pp. 3279-3288.
- ZHANG, X., ZHANG, J., KUENZER, C., VOIGT, S. & W. WAGNER, 2004: Capability evaluation of 3-5 μ m and 8-12,5 μ m airborne thermal data for underground coalfire detection. In: *International Journal of Remote Sensing*, Vol. 25, No. 12, pp. 2245-2258.
- ZHU, G. & D.G. BLUMBERG, 2002: Classification using ASTER data and SVM algorithms; the case study of Beer Sheva, Israel. In: *Remote Sensing of Environment*, Vol. 80, No. 2, pp. 233-240.

Internet sources:

- URL 2-1: <http://www.dwd.de/de/WundK/Klimadaten/index.html>, 16.09.2004
- URL 2-2: <http://www.cpirc.org.cn/en/eindex.htm>, 16.09.2004
- URL 3-1: http://www.hgimaging.com/PDF/Kruse_ISSSR99.pdf, 16.09.2004
- URL 4-1: http://ltpwww.gsfc.nasa.gov/IAS/handbook/handbook_htmls/chapter1/chapter1.html,
- URL 4-2: <http://landsat.gsfc.nasa.gov/>, 16.09.2004
- URL 4-3: <http://asterweb.jpl.nasa.gov/instrument/instrument.htm>, 16.09.2004
- URL 4-4: <http://asterweb.jpl.nasa.gov/>, 16.09.2004
- URL 4-5: <http://eo1.usgs.gov/>, 16.09.2004
- URL 4-6: <http://www.eurimage.com/products/quickbird.html>, 16.09.2004
- URL 4-7: http://www.esa.int/export/esaSA/GGGWBR8RVDC_earth_0.html, 16.09.2004
- URL 8-1: <http://www.pir.sa.gov.au/pages/minerals/resources/commodity/coal.htm%AsectID=245-&tempID=7>, 16.09.2004

Curriculum Vitae

Name: Claudia Künzer

Date/Place of birth: 11. May 1975, Berlin

Address: Pasinger Str. 37, 82152 Planegg, Germany

Nationality: German

- 10/02 – 03/05 **Vienna University of Technology**, Institute of Photogrammetry and Remote Sensing; enrolled as Ph.D student
- 07/01 – PRESENT **German Remote Sensing Data Center**, DLR, DFD, Project Scientist for the project „Innovative Technologies for the Exploration, Extinction and Monitoring of Coal Fires in North China“ and in the context of „Natural Hazards and Crisis Information“, analyses of multi sensor satellite data, supervision of interns, support of project management.
- 09/00 - 06/01 **Parc Naturel de la Haute Sûre**, Master thesis : „Multitemporale Untersuchung der Landnutzung des ‚Parc Naturel de la Haute Sûre‘ unter Einsatz von Fernerkundung und GIS im Hinblick auf die Wasserqualität des Stausees Obersauer“.
- 09/00 – 03/01 **Remote Sensing Department, University of Trier**, Student staff for remote sensing and GIS analyses for different projects
- 10/99 – 11/99 **United Nations Environmental Program (UNEP-GRID)**, SD, USA, Internship, analysing satellite and GIS data for transboundary protected areas in Africa and Latin America
- 7/99 – 9/99 **GAF, Gesellschaft für Angewandte Fernerkundung**, Munich, Internship, radar remote sensing analysis for flood mapping
- 6/99 – 7/99 **Regional Government Trier**, GIS-Department, freelancer Design of a Meta-database for the presentation of digital data of governmental communal and provincial GIS data in the Internet.
- 4/99 – 7/99 **Planing Community Region Trier**, Trier Internship: GIS modelling for the calculation of alternative energy (wind, solar, biomass) potential in the municipality of Trier
- 3/99 – 7/99 **Remote Sensing Department, University of Trier**, Student staff teaching introductory tutorials in remote sensing and GIS
- 12/98 – 3/99 **Remote Sensing Department, University of Trier**, freelancer Generation of digital ecotope-maps of Crete within the framework of the EU-project DEMON.
- 12/98 - 2/00 **Academic Foreign Affairs Office, University of Trier**, work contract Consultancy and supervision of students, who plan to study abroad
- 8/95 - 9/95 **Federal Ministry for Education and Science (BMBF)** Department of Environmental Systems Research, Bonn, Internship, Design of questionnaires on national and international global change research. Statistical analyses

- 1/99 – 06/01 **University of Trier, "Hauptstudium" Studies:** Applied Physical Geography. Majors: Remote Sensing, GIS, Soil Science
- 6/97 – 12/98 **Studies at Western Washington University, WWU,** at 'Huxley College of Environmental Science' Washington State, USA, Study Foci: Remote Sensing, Climate Change, Glacial Geomorphology
- 9/94 – 6/97 **University of Trier, "Grund- und Hauptstudium" Studies:** Applied Physical Geography. Majors: Remote Sensing, GIS, Soil Science
- 8/85 - 6/94 **High School,** Grade 5 to grade 13
Ernst-Kalkuhl-Gymnasium, Bonn, Abitur: June 1994
- 8/81 – 6/85 **Elementary School,** Ennertschule Bonn